FUNDAMENTALS OF TRANSPORT IN POLY(ETHYLENE TEREPHTHALATE) AND POLY(ETHYLENE FURANOATE) BARRIER MATERIALS

A Dissertation
Presented to
The Academic Faculty

By

Steven K. Burgess

In Partial Fulfillment
Of the Requirements for the Degree
Doctor of Philosophy in Chemical Engineering

Georgia Institute of Technology

May 2015

FUNDAMENTALS OF TRANSPORT IN POLY(ETHYLENE TEREPHTHALATE) AND POLY(ETHYLENE FURANOATE) BARRIER MATERIALS

Approved By:

Dr. William J. Koros
School of Chemical and Biomolecular Engineering
Georgia Institute of Technology

Dr. David S. Sholl
School of Chemical and Biomolecular Engineering
Georgia Institute of Technology

Dr. Thomas F. Fuller
School of Chemical and Biomolecular Engineering
Georgia Institute of Technology

Dr. Robert M. Kriegel
The Coca-Cola Company

Dr. Haskell W. Beckham
Exponent

Date Approved: March 30th, 2015

"'For I know the plans I have for you,' declares the Lord, 'plans to prosper you and not to harm you, plans to give you a hope and a future. Then you will call on me and come and pray to me, and I will listen to you. You will seek me and find me when you seek me with all your heart. I will be found by you,' declares the Lord"…

-Jeremiah 29:11-14

Dedicated to:

My loving wife and family

ACKNOWLEDGMENTS

Any “success” I have garnered in my life is rightfully attributed to the grace of God, and apart from God, I would be without both ability and purpose. As a graduate student in chemical engineering, I have been given the opportunity to study the wonders of this world on a microscopic level. At the completion of my PhD, I resonate most with the words of Albert Einstein, “The more I study science, the more I believe in God.”

The last five years at Georgia Tech under the guidance of Dr. William J. Koros have been absolutely incredible. I have been given a rare opportunity to learn from one of the most kind, intelligent, tactful, hard working, and enthusiastic professors I have ever met. I have learned so much about research, leadership, and life under his guidance, and I will build upon these teachings throughout the rest of my career. No question was ever inadequate in his eyes, and I cannot express how much I have truly enjoyed our collaboration throughout the past five years.

I also gladly acknowledge my thesis committee members: Dr. David Sholl, Dr. Thomas Fuller, Dr. Haskell Beckham, and Dr. Robert Kriegel, for their insightful comments and support throughout the completion of my degree. Specifically, I am grateful for our incredible collaboration with Dr. Kriegel at Coke, who provided me with a contractor badge and who acted on our behalf to help enable a large portion of the work reported in this thesis. I also gratefully acknowledge Dr. Christopher Mubarak and Dr. Ronald Moffitt at Coke, who served as extraordinary mentors and friends during these last few years. I am also sincerely grateful for the generous financial support from The Coca-Cola Company, which made this project possible in the first place.

I have had the great privilege to work with many extraordinary people throughout my time at Georgia Tech. I am grateful for the mentorship from Oğuz Karvan, J.R. Johnson, and Jong Suk Lee, and for the great friendships I have made here in the Koros research group and at Georgia Tech. I have tremendously enjoyed my friendships with Ruben Kemmerlin, Shawn Bernardy, Gaurav Agrawal, Tapesh Joshi, Nitesh Bhuwania, Justin Vaughn, Vinod Babu, Carine Achoundong, Ryan Lively, Chen Zhang, and Graham Wenz, in addition to the other past and present Koros group members. I have also been extremely privileged to share an office with Brian Kraftschik, Jong Suk Lee, Danny Kim, and Dharmik Mikkilineni during my time at Georgia Tech and will always remember the great times we had together. Last but not least, the squash, ping pong, and tennis breaks with Gaurav Agrawal, Nitesh Bhuwania, Tapesh Joshi, and Saujan Sivaram helped make my time at Georgia Tech even more memorable and will certainly be missed. In addition to everything, I am particularly grateful to Michelle Martin for keeping our group organized and for Rod Sefton, Tanya, and Rosemary for making Bunger Henry a great place to come to work every day.

Last but certainly not least, I am thankful for my best friend and love of my life, Amanda, who has unconditionally supported me over the last five years and whose companionship has made my life a joy. I am also forever grateful for my parents, Ken and Cindy, for raising me in a loving household and for instilling a desire to learn in me at a young age. I also thank my awesome sister, Ashley, for being the best sister in the world and for always wanting to spend time with me. There are undoubtedly too many additional names to mention in this acknowledgment, and to those people, thank-you for your invaluable contributions!

TABLE OF CONTENTS

LIST OF TABLES

LIST OF FIGURES

SUMMARY

Poly(ethylene terephthalate) (PET) is the dominant plastic in the beverage packaging industry; however, unacceptable barrier performance to oxygen and carbon dioxide limit advancement into more demanding markets (i.e., juice containers, alcoholic beverages, small serving packages, etc.). Due to the scale at which PET is utilized in the global market, the most cost efficient method to improve the barrier properties is to modify the existing processing platform. Such modification can be realized via the process of antiplasticization, which occurs when a low molecular weight diluent is added to the polymer and the resultant glassy mixture exhibits a reduction in penetrant transport and chain mobility vs. the neat polymer. The first portion of this thesis provides a detailed investigation regarding caffeine antiplasticization of amorphous PET by characterizing the resultant gas transport, thermal, and mechanical properties of the antiplasticized materials compared to neat PET. The goal for this work is to advance the current understanding of engineered antiplasticization as a tool for barrier property enhancement.

In addition to antiplasticization, much research has been conducted to find bio-sourced alternatives to PET to reduce petroleum dependence and carbon dioxide emissions. Particular focus has been devoted to poly(ethylene furanoate) (PEF), which is a furanic, bio-sourced alternative to PET with greatly enhanced barrier properties and attractive thermal and mechanical properties. Specifically, the transport data reported herein at 35°C illustrate that amorphous PEF exhibits significant reductions in permeability for oxygen (11X), carbon dioxide (19X), and water (2X) compared to amorphous PET. Such impressive barrier enhancements, which were experimentally

determined using complementary permeation, pressure-decay sorption, and gravimetric sorption techniques, are unexpected since PEF exhibits a higher free volume compared to PET. Further investigation into the fundamental chain motional processes which contribute to penetrant diffusion, as probed via dynamic mechanical and solid-state NMR, reveals that the polymer ring-flipping motions in PEF are largely suppressed compared to those for PET. Such behavior, while unexpected when considering the structural similarity for PET vs. PEF, allows for rationalization of the reduced transport properties for PEF compared to PET.

This work, which focuses on understanding the fundamentals of penetrant transport in antiplasticized PET and amorphous PEF, can therefore be envisioned to provide a two-pronged approach to: 1) facilitate expansion of polyester barrier materials into more demanding markets, and 2) reduce the environmental footprint of such materials.

CHAPTER 1

INTRODUCTION

1.1. Overview of Barrier Polymers and Applications

Plastic materials have achieved widespread implementation in food packaging applications due to the development of technologies to facilitate processing. The benefits of plastics versus metal or glass are founded in cost, ease of processing, durability, weight, and versatility of the final product, among others [1]. In contrast to metal and glass, which are effectively "perfect" barriers to penetrant transmission (i.e., oxygen, water, carbon dioxide, etc.), polymers are inherently permeable [2, 3]. This reality for plastics can have either positive or negative implications regarding the packaged contents. For example, it is desirable to have a "breathable" package that can accommodate respiration of live produce or living cells (e.g., blood), while a breathable package for peanut butter would be disastrous (e.g., due to hydrolytic and oxidative rancidity [4]).

Food and beverage products are often highly susceptible to the detrimental effects of oxygen. Specifically, most soups, canned vegetables, alcoholic beverages (i.e., beer), and dairy products can only tolerate an influx of 1 to 5 ppm oxygen per year at room temperature [5]. Additional packaging constraints often require barrier protection against oils or volatile organics, since the "loss" of such flavor and aroma molecules via absorption into the container walls is undesirable (i.e., "flavor scalping" [6]). These negative effects are particularly important for soft drink containers, where the beverage taste can be altered by both flavor scalping *and* oxidation of the flavor/aroma molecules

via contact with oxygen [4, 7].

In addition to barrier properties, it is also important to understand the expected shelf-life and market demands for the final packaged product. For example, while milk is highly sensitive to oxygen, the plastic container (i.e., high density polyethylene, HDPE) can exhibit high oxygen transmission rates due to the relatively short shelf life of the product [8]. HDPE is not suitable for beer bottles, however, due in part to the requirement for a longer shelf life and a smaller bottle size (i.e., increased surface area to volume ratio). This latter point is further illustrated by the carbonation requirements for soft drink containers (i.e., <15% carbon dioxide loss during the shelf life [8]), where the surface area to volume ratio for a 3L bottle is lower than in a 20 oz bottle, and consequently, the 20 oz bottle will require more stringent barrier properties vs. the 3L bottle [9].

The transport properties of a polymer are determined by a combination of factors, which include the polymer morphology (i.e., amorphous vs. semi-crystalline), temperature, affinity between penetrant and polymer, concentration, and chain orientation, among others [10-14]. The presence of crystallinity is important, since polymer crystals are impermeable to penetrant sorption and diffusion [14, 15], and thereby improve the barrier properties of the semicrystalline vs. amorphous morphology. It is also generally observed that polymers with polar moieties are typically poor barriers to water but good barriers to non-polar penetrants (i.e., hydrocarbons). Alternatively, polymers with non-polar moieties are typically poor barriers to hydrocarbons but excellent barriers to water. Illustration of this notion is provided in Table 1.1 [16], which provides a list of selected barrier polymers alongside the penetrants they hinder most effectively. Complementary oxygen and carbon dioxide barrier property data for a wide

variety of polymers is provided in Table 1.2.

Table 1.1. Selected polymers alongside the penetrants they hinder effectively (from ref. [16]).

Polymer	Effective barrier against
Poly(vinyl alcohol)	Oxygen (when dry), solvents
Poly(vinylidene chloride)	Oxygen, water vapor
Aromatic liquid crystalline polymers	Oxygen, water vapor, most solvents and vapors
Poly(ethylene-co-carbon monoxide)	Oxygen, solvents
Poly(ethylene-co-vinyl alcohol)	Oxygen
Polypropylene	Water vapor
Polyethylene	Water vapor
Semi-aromatic polyamides (6-I, MXD-6)	Oxygen
Aliphatic polyamides	Hydrocarbons

Table 1.2. Room temperature O_2 and CO_2 barrier properties for a wide variety of polymers [17].

Polymer	O_2 (Barrer[a])	CO_2 (Barrer[a])	Temp (°C)	Crystallinity class[b]
Poly(dimethyl siloxane)	440	2300	23	Amorphous
Polyethylene/vinyl acetate (85/15)	5.0	18	25	Moderately crystalline
Polystyrene (molded)	2.5	9.7	25	Amorphous
Polypropylene (molded)	1.7	7.2	25	Highly crystalline
Cellulose acetate (unplasticized)	0.68	5.0	25	Amorphous
Poly(methyl methacrylate)	0.102	—	25	Amorphous
Poly(vinyl chloride) (rigid)	0.05	0.24	30	Amorphous
Poly(vinylidene fluoride)	0.04	0.36	25	Highly crystalline
Poly(ethylene terephthalate)	0.03	0.10	25	Highly crystalline
Poly(vinylidene chloride)	0.0020	0.012	25	Highly crystalline
Poly(acrylonitrile)	0.00022	—	25	Moderately crystalline
Poly(vinyl alcohol) (bone dry)	0.000001	0.00001	25	Highly crystalline

a: 1 Barrer = $10^{-10}\,\frac{ccSTP \cdot cm}{cm^2 \cdot s \cdot cmHg}$

b: Crystallinity class is defined as follows: Amorphous (< 20% crystallinity), Moderately crystalline (< 50% crystallinity), and Highly crystalline (> 50% crystallinity), where crystallinity is measured in volume percent (data from ref. [17]).

As seen in Table 1.2, the polymers with the lowest oxygen and carbon permeabilities are semicrystalline and have at least one polar functional group. Polar moieties typically increase cohesion between neighboring chains, thereby increasing the energy needed for a penetrant molecule to separate the tightly packed chains and permeate through the matrix (i.e., compared to the energy required to separate the non-polar chains in polyethylene [18]). This notion is evident for dry poly(vinyl alcohol) as seen by the exceedingly low permeabilities in Table 1.2, which originate from the presence of hydrogen bonding between neighboring polymer chains [18]. A list of common moieties found in high barrier polymers is provided in Table 1.3 [18], where polarity is undoubtedly a unifying feature.

Table 1.3. Functional groups commonly found in high barrier polymers [18].

Moiety	Structure
Ester	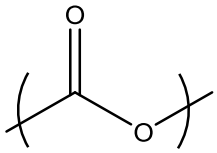
Amide	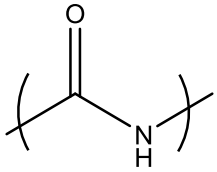
Cyano	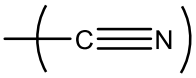
Halogen	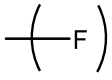
Halogen	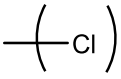
Hydroxyl	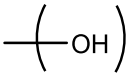

Polymers which contain one or more of the polar moieties in Table 1.3 have a natural affinity for water [18], and in some cases, the presence of water can compromise the barrier properties of the polymer. For example, poly(vinyl alcohol) exhibits a very low oxygen permeability of 0.000001 Barrer in the bone dry state, versus an increase by 5 orders of magnitude to 0.11 Barrer in the presence of 90% relative humidity [17]. This reality, coupled with the common demand for barrier protection against both water and oxygen, often necessitates packaging solutions that extend beyond pure polymers.

Barrier improvement techniques are multifaceted, and can entail polymer blending [19], multi-layered laminates [20], coatings [21], and incorporation of inorganic fillers [22] or oxygen scavengers [23], among others [24]. Incorporation of pure polymers into laminate structures is popular in the food packaging industry, where the expensive or hydrophilic oxygen barrier polymer (i.e., poly(vinyl alcohol)), can be "sandwiched" between polymer layers that are poor barriers to oxygen but good barriers to water [20]. Depositing transparent inorganic coatings on the polymer surface is also attractive [21, 25, 26]; however, the thin coating is susceptible to "cracking," which can compromise the efficacy of the entire coating. A different approach to barrier improvement involves incorporation of "scavenging" molecules inside the polymer matrix, thereby creating an "active" barrier. Oxygen scavengers, for example, reduce the oxygen influx into packages which contain highly sensitive contents (i.e., beer) by reacting with the oxygen as it permeates into the container walls [23, 27-29]. Additional barrier improvement techniques are discussed in Appendices C (graphene nanocomposites) and D (miscible and immiscible polymer blends).

The barrier improvement techniques discussed thus far, while effective, are often not

implemented due to the complexity in manufacturing (i.e., capital cost of equipment), large scale of production, and lack of recyclability regarding the finished product [24]. Such implications are the basis for the current work regarding polyester materials for beverage packaging applications, as discussed in the next section.

1.2. Motivation

Poly(ethylene terephthalate) (PET) has been the dominant polymer in the beverage packaging industry for the past four decades due to its optical clarity, barrier properties, and competitive performance-to-cost ratio [9]. While PET has met many of the current global packaging needs, high oxygen transmission rates coupled with the use of petroleum-derived terephthalic acid (TA) limit effectiveness for oxygen-sensitive beverages and environmental sustainability, respectively. Due to the scale at which PET is used in the global market, the most cost efficient method to improve the barrier properties is to modify the existing processing platform [24]. The latter technique can be accomplished via the process of antiplasticization [30-33], which occurs when a low molecular weight diluent is added to the polymer and the resultant glassy mixture exhibits a reduction in free volume and segmental chain motion. Natural consequences of antiplasticization entail a reduction in gas transport compared to the neat polymer, increased short-term mechanical modulus, and a reduction in glass transition temperature [34]. The current work investigates both the transport and thermal/mechanical property ramifications associated with antiplasticizing amorphous PET with caffeine, which has been identified by The Coca-Cola Company as a potential antiplasticizer for PET.

In addition to antiplasticization, much research has been conducted to find bio-

sourced alternatives to PET to reduce petroleum dependence and carbon dioxide emissions [7, 35-37]. Polyesters synthesized from 2,5-furandicarboxylic acid (FDCA) have received recent attention due to improved performance over PET coupled with the potential for fully renewable sourcing. Poly(ethylene furanoate) (PEF), which is the direct furan analog to PET, is particularly promising since PEF exhibits an 11X reduction in oxygen permeability [38] and 19X reduction in carbon dioxide permeability [39] vs. PET. This barrier enhancement for PEF is further accompanied by an increase in glass transition temperature, decrease in melting temperature, and increase in mechanical modulus [40]. The remainder of the work reported herein will investigate both the transport and thermal/mechanical properties of PEF, with a particular focus on relating the differences vs. PET to polymer structure and inherent chain motional processes. This fundamental information is required before PEF can be integrated into the global polyester market.

This work provides a two-pronged approach to improving the barrier properties of polyester materials to facilitate expansion into more challenging markets (i.e., beer, fruit juices, etc.). In addition to expanding the application base for polyester barrier materials, improved barrier properties will also benefit the soft drink container industry via 1) prolonged product shelf life (i.e., if the wall thickness is preserved vs. the original material), 2) reduced wall thickness to achieve the same barrier properties as the original material (i.e., reduced material costs to produce a bottle and a reduction in plastic waste), and 3) reduced environmental impact (i.e., renewable sourcing of monomers and reduction in fossil-fuel dependence).

1.3. Research Objectives

The overarching objective of this dissertation is to develop a fundamental understanding of penetrant transport in: 1) caffeine-antiplasticized PET, which will serve to advance the current understanding of engineered antiplasticization as a tool for barrier property enhancement, and 2) amorphous PEF, which is the recently introduced furanic analog to PET with greatly enhanced barrier properties and attractive thermal and mechanical properties. Specific objectives to achieve this goal are listed as follows:

1.3.1. Objective 1

Characterize the oxygen and carbon dioxide pure gas permeability at 35°C in amorphous PET antiplasticized with caffeine.

Antiplasticization occurs when a low molecular weight diluent is mixed with a polymer and the resultant glassy mixture exhibits a reduction in free volume, segmental chain mobility, and gas permeability. The extent of antiplasticization correlates directly with the amount of antiplasticizer mixed with the polymer. This objective entails characterization of the pure gas permeability of both oxygen and carbon dioxide in amorphous PET antiplasticized with varying levels of caffeine, with the goal of quantifying such barrier improvements. The reduction in penetrant permeability for all antiplasticized samples can be further separated into the specific diffusion and sorption contributions, thereby providing a more detailed understanding of the antiplasticization mechanism as it relates to PET.

1.3.2. Objective 2

Characterize the oxygen and carbon dioxide pure gas solubility at 35°C in amorphous PET antiplasticized with caffeine.

Complementary to Objective 1, which pertains to permeation testing, this objective quantifies the pure gas solubility reduction compared to neat PET for samples antiplasticized with varying levels of caffeine. Experimental measurement of the oxygen sorption properties for PET and antiplasticized PET is challenging due to low oxygen uptake resulting from minimal interaction between oxygen and the glassy matrix. Improvements to the traditional pressure-decay sorption technique, discussed later in Chapter 3, partially resolve such challenges, thereby allowing for more accurate determination of the fundamental penetrant sorption properties in glassy PET. The oxygen and carbon dioxide sorption data corresponding to this objective, in combination with the permeation data measured in Objective 1, complete the transport data set necessary for understanding the mechanism of antiplasticization in PET. Data aligned with Objectives 1 and 2 are provided in detail later in Chapter 4.

1.3.3. Objective 3

Investigate the effect of temperature on the oxygen and carbon dioxide pure gas permeability in amorphous PEF.

As mentioned previously, PEF is the recently introduced furanic analog to PET with greatly improved barrier properties. Detailed understanding of both oxygen and carbon dioxide transport in PEF is necessary to scale up industrial applications in the PET-dominated bottling industry, which is currently sized at ~15 million metric tons/year [41].

This objective quantifies the pure gas permeability of both oxygen and carbon dioxide in amorphous PEF at multiple temperatures, thereby allowing estimation of the apparent activation energies of permeation for both penetrants. Permeation data for oxygen and carbon dioxide in PEF can be separated into the diffusion and sorption contributions, which, when compared to the respective properties for amorphous PET, provides insight into the mechanism behind the greatly enhanced barrier properties for PEF vs. PET.

1.3.4. Objective 4

Investigate the effect of temperature on the pure component solubility of oxygen, carbon dioxide, and water in amorphous PEF.

Complementary to Objective 3, which discusses permeation testing in amorphous PEF, Objective 4 utilizes pressure-decay sorption to measure the solubility of oxygen and carbon dioxide in amorphous PEF at multiple temperatures. Estimates for the apparent enthalpies of sorption for both gases in PEF, when combined with the respective activation energies of diffusion, can provide estimates for the activation energies of permeation. Such estimates can be cross-verified, for internal consistency, with the values determined from permeation testing in Objective 3. The sorption data for oxygen and carbon dioxide determined in this objective, when combined with the data from Objective 3, complete the data set regarding non-condensable gas transport in amorphous PEF. Sorption measurements pertaining to water, which is significantly more soluble in PEF compared to oxygen and carbon dioxide, are determined and cross-verified using three independent gravimetric methods. Data corresponding to oxygen and carbon dioxide transport are provided later in Chapters 6 and 7, respectively, while water sorption data

are provided in Chapters 8 and 9.

1.3.5. Objective 5

Characterize the intrinsic thermal and mechanical properties of PEF compared to PET in both the dry and hydrated state.

In addition to evaluating the barrier performance of PEF compared to PET, it is also important to understand the thermal, mechanical, and chain mobility properties compared to PET. Such information has direct implications to carbonated beverage containers, which are required to maintain physical shape under pressures of ~6 atm carbon dioxide [4]. Polymer chain motions related to penetrant diffusion in PEF compared to PET are probed via dynamic mechanical and solid-state NMR methods, thereby providing insight into the underlying mechanism for the performance enhancements for PEF vs. PET. Additional insight regarding the effect of water sorption at unit activity in both polyesters is obtained via tensile testing on both wet and dry samples, and information regarding thermally-induced physical aging in PEF, measured via three independent methods, facilitates understanding of the time-dependent properties of the amorphous glass.

1.4. Thesis Organization

This dissertation comprises twelve total chapters, which includes this introduction. Chapter 2 introduces the theory governing gas and vapor transport in polymeric materials and the relevant equations used in modeling such transport processes. Chapter 3 describes the materials utilized in this work, along with descriptions for the experimental methods employed throughout the remainder of the thesis. The phenomenon of caffeine

antiplasticization in amorphous, glassy PET is discussed in Chapter 4, thereby illustrating the PET barrier improvements achievable via such approach. An introduction to PEF, including the differences compared to PET, regarding chain mobility, thermal, and mechanical properties is provided in Chapter 5, while Chapters 6 and 7 provide detailed oxygen and carbon dioxide transport studies for amorphous PEF, respectively. The latter transport data are further complemented by the investigation of water sorption and diffusion in PEF compared to PET provided in Chapters 8 and 9, respectively. Chapter 10 describes physical aging in glassy, amorphous PEF as probed via thermal, volumetric, and oxygen transport methods, and Chapter 11 outlines a MATLAB® methodology useful for fitting complex infinite series solutions directly to experimental kinetic sorption data. Chapter 12, which is the final chapter, provides a high-level overview of the major contributions realized by this work and concludes with a discussion regarding potential topics for future research. Additional selected topics, which are relevant to the overarching topic of transport in barrier materials, are provided via the Appendices at the end of this dissertation.

Much time has been devoted to organizing the many topics of this thesis into an accessible format. Chapters 4 – 11 each represent "stand-alone" studies that are relevant to the overarching goal of this thesis. This format was chosen to make the information accessible, enabling the reader to navigate directly to the topic of interest via the table of contents. Furthermore, the chapters have been organized logically to discuss PET/caffeine antiplasticization first, followed by all chapters pertaining to the fundamental properties of PEF vs. PET (i.e., chain mobility differences first, followed by non-condensable gas transport, vapor transport, and aging, in that order). Chapter 2

includes all background and theory necessary to understand the remaining thesis chapters; however, in some cases, select equations which are utilized extensively in a given chapter are reproduced for convenience to assist in readability.

1.5. References

1. Selke SEM. Understanding Plastics Packaging Technology. Cincinnati: Hanser/Gardner Publications, Inc., 1997.

2. Lee WM. Selection of barrier materials from molecular-structure. Polymer Engineering & Science 1980;20(1):65-69.

3. Comyn J. Introduction to Polymer Permeability and the Mathematics of Diffusion. In: Comyn J, editor. Polymer Permeability. New York: Elsevier Applied Science Publishers Ltd., 1985. pp. 1-10.

4. Brody AL. Food Packaging. In: Bakker M, editor. The Wiley Encyclopedia of Packaging Technology. New York: John Wiley & Sons, 1986. pp. 359-363.

5. Ryder LB. Oxygen-Barrier Containers - Their Design and Cost. Plastics Engineering 1984;40(5):41-48.

6. Sajilata MG, Savitha K, Singhal RS, and Kanetkar VR. Scalping of Flavors in Packaged Foods. Comprehensive Reviews in Food Science and Food Safety 2007;6(1):17-35.

7. Miller KS and Krochta JM. Oxygen and aroma barrier properties of edible films: A review. Trends in Food Science & Technology 1997;8(7):228-237.

8. Silvis HC. Recent advances in polymers for barrier applications. Trends in Polymer Science 1997;5(3):75-79.

9. Griff AL. Carbonated Beverage Packaging. In: Bakker M, editor. The Wiley Encyclopedia of Packaging Technology. New York: John Wiley & Sons, 1986. pp. 121-124.

10. Aitken A and Barrer RM. Transport and solubility of isomeric paraffins in rubber. Transactions of the Faraday Society 1955;51(0):116-130.

11. Barrer RM and Barrie JA. Sorption and Diffusion in Ethyl Cellulose. Part IV. Water in Ethyl Cellulose. Journal of Polymer Science 1958;XXVIII:377-386.

12. Barrer RM, Barrie JA, and Slater J. Sorption and diffusion in ethyl cellulose. Part III.

Comparison between ethyl cellulose and rubber. Journal of Polymer Science 1958;27(115):177-197.

13. Moaddeb M and Koros WJ. Effects of orientation on the transport of d-limonene in polypropylene. Journal of Applied Polymer Science 1995;57(6):687-703.

14. Michaels AS, Vieth WR, and Barrie JA. Diffusion of Gases in Polyethylene Terephthalate. Journal of Applied Physics 1963;34(1):13-20.

15. Michaels AS, Vieth WR, and Barrie JA. Solution of Gases in Polyethylene Terephthalate. Journal of Applied Physics 1963;34(1):1-12.

16. Subramanian PM and Plotzker IG. Barrier Materials by Blending. New York: John Wiley & Sons, 2000.

17. Bixler HJ and Sweeting OJ. Barrier Properties of Polymer Films: John Wiley & Sons, Inc., 1971.

18. Salame M. Barrier Polymers. In: Bakker M, editor. The Wiley Encyclopedia of Packaging Technology. New York: John Wiley & Sons, 1986. pp. 48-53.

19. Huang C-H, Wu J-S, Huang C-C, and Lin L-S. Morphological, Thermal, Barrier and Mechanical Properties of LDPE/EVOH Blends in Extruded Blown Films. Journal of Polymer Research 2004;11(1):75-83.

20. Koros WJ. Barrier Polymers and Structures: Overview. In: Koros WJ, editor. Barrier Polymers and Structures. Washington: American Chemical Society, 1990. pp. 406.

21. Erlat AG, Spontak RJ, Clarke RP, Robinson TC, Haaland PD, Tropsha Y, Harvey NG, and Vogler EA. SiOx Gas Barrier Coatings on Polymer Substrates: Morphology and Gas Transport Considerations. The Journal of Physical Chemistry B 1999;103(29):6047-6055.

22. Kim H, Miura Y, and Macosko CW. Graphene/Polyurethane Nanocomposites for Improved Gas Barrier and Electrical Conductivity. Chemistry of Materials 2010;22(11):3441-3450.

23. Di Maio L, Scarfato P, Galdi MR, and Incarnato L. Development and oxygen scavenging performance of three-layer active PET films for food packaging. Journal of Applied Polymer Science 2015;132(7).

24. Bain DR and Giles GA. Technical and commercial considerations. In: Giles GA and Bain DR, editors. Technology of Plastics Packaging for the Consumer Market. Sheffield: Sheffield Academic Press Ltd, 2001.

25. Chatham H. Oxygen diffusion barrier properties of transparent oxide coatings on polymeric substrates. Surface and Coatings Technology 1996;78(1–3):1-9.

26. Henry BM, Erlat AG, McGuigan A, Grovenor CRM, Briggs GAD, Tsukahara Y, Miyamoto T, Noguchi N, and Niijima T. Characterization of transparent aluminium oxide and indium tin oxide layers on polymer substrates. Thin Solid Films 2001;382(1–2):194-201.

27. Solis JA and Rodgers BD. Factors Affecting the Performance of New Oxygen Scavenging Polymer for Packaging Applications. Journal of Plastic Film and Sheeting 2001;17(4):339-349.

28. Solovyov SE and Goldman AY. Optimized design of multilayer barrier films incorporating a reactive layer. III. Case analysis and generalized multilayer solutions. Journal of Applied Polymer Science 2006;100(3):1966-1977.

29. Özen İ. An Investigation on Usage of Sodium Borohydride and Zinc Oxide as Oxygen Scavengers in Polyethylene Terephthalate Films. International Polymer Processing 2012;27(4):493-497.

30. Maeda Y and Paul DR. Effect of Antiplasticization on Gas Sorption and Transport. I. Polysulfone. Journal of Polymer Science: Part B: Polymer Physics 1987;25:957-980.

31. Maeda Y and Paul DR. Effect of Antiplasticization on Gas Sorption and Transport. II. Poly(phenylene Oxide). Journal of Polymer Science: Part B: Polymer Physics 1987;25:981-1003.

32. Maeda Y and Paul DR. Effect of Antiplasticization on Gas Sorption and Transport. III. Free Volume Interpretation. Journal of Polymer Science: Part B: Polymer Physics 1987;25:1005-1016.

33. Burgess SK, Lee JS, Mubarak CR, Kriegel RM, and Koros WJ. Caffeine Antiplasticization of Amorphous Poly(ethylene terephthalate): Effects on Gas Transport, Thermal, and Mechanical Properties. Polymer 2015;Submitted.

34. Lee JS, Leisen J, Choudhury RP, Kriegel RM, Beckham HW, and Koros WJ. Antiplasticization-based enhancement of poly(ethylene terephthalate) barrier properties. Polymer 2012;53:213-222.

35. Siracusa V, Rocculi P, Romani S, and Rosa MD. Biodegradable polymers for food packaging: a review. Trends in Food Science & Technology 2008;19(12):634-643.

36. Auras RA, Singh SP, and Singh JJ. Evaluation of oriented poly(lactide) polymers vs. existing PET and oriented PS for fresh food service containers. Packaging Technology and Science 2005;18(4):207-216.

37. Auras R, Harte B, and Selke S. An Overview of Polylactides as Packaging Materials. Macromolecular Bioscience 2004;4(9):835-864.

38. Burgess SK, Karvan O, Johnson JR, Kriegel RM, and Koros WJ. Oxygen Sorption and Transport in Amorphous Poly(ethylene furanoate). Polymer 2014;55(18):4748-

4756.

39. Burgess SK, Kriegel RM, and Koros WJ. Carbon Dioxide Sorption and Transport in Amorphous Poly(ethylene furanoate). Macromolecules 2015, DOI: 10.1021/acs.macromol.5b00333.

40. Burgess SK, Leisen JE, Kraftschik BE, Mubarak CR, Kriegel RM, and Koros WJ. Chain Mobility, Thermal, and Mechanical Properties of Poly(ethylene furanoate) Compared to Poly(ethylene terephthalate). Macromolecules 2014;47(4):1383-1391.

41. Eerhart AJJE, Faaij APC, and Patel MK. Replacing fossil based PET with biobased PEF; process analysis, energy and GHG balance. Energy & Environmental Science 2012;5(4):6407-6422.

CHAPTER 2

BACKGROUND AND THEORY

This chapter outlines the fundamentals of penetrant transport in polymeric materials within the framework of the sorption-diffusion model. Relatively non-condensable gases obey simple dual-mode sorption and Fickian diffusion behavior, while vapors and highly interacting penetrants often require treatment with more advanced sorption and diffusion models. This chapter provides the background and theoretical framework necessary to interpret the data presented in the remainder of the thesis.

2.1. Transport Properties

Small molecule transport across a dense polymer film occurs via the solution-diffusion model, where a penetrant molecule 1) absorbs into the polymer at the high chemical potential side of the film, 2) diffuses through the polymer down the chemical potential gradient, and 3) desorbs at the low chemical potential side of the film [1]. The flux (N_i) of penetrant "*i*" across the film is therefore described by Equation 2.1, where μ_i is the chemical potential of species *i*, *x* is the spatial dimension spanning the film thickness, and L_i is a proportionality constant [1].

$$N_i = -L_i \frac{d\mu_i}{dx} \tag{2.1}$$

The solution-diffusion model for transport in dense films assumes that the penetrant in the gaseous phase is in equilibrium with the penetrant inside the film at both film

surfaces, which allows for a continuous chemical potential gradient across the dense film [2]. The framework also assumes that the pressure throughout the film is equal to that applied on the high pressure side, thereby removing any pressure gradient across the film thickness. Such assumptions are illustrated in Figure 2.1.

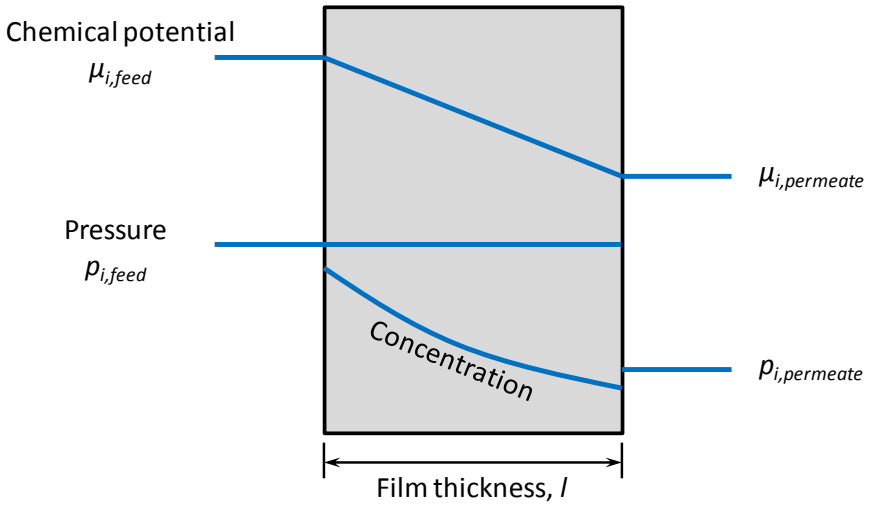

Figure 2.1. Solution-diffusion model representation for diffusion across a dense film [2].

In the absence of a pressure gradient, the chemical potential can be related to the penetrant concentration (C_i) via Equation 2.2, where R is the universal gas constant, T is the temperature in Kelvin, and γ_i is the activity coefficient [1, 2].

$$d\mu_i = RTd\ln\left(\gamma_i C_i\right) \tag{2.2}$$

Substitution of Equation 2.2 into Equation 2.1 therefore yields, after slight rearrangement, the convenient expression in Equation 2.3 for the penetrant flux in terms of concentration, which further simplifies into the known relationship for Fickian

diffusion [1-4].

$$N_i = \left(-\frac{RTL_i}{C_i}\frac{dC_i}{dx} \right) = \left(-D\frac{dC_i}{dx} \right) \tag{2.3}$$

The discussion thus far is included to illustrate the relationship between penetrant flux and chemical potential vs. concentration gradients. All discussions throughout the remainder of this work will refer to diffusion in terms of concentration, which is experimentally easier to quantify. It is now useful to examine, individually, the separate sorption and diffusion contributions to penetrant transport within the overarching context of the solution-diffusion model.

2.1.1. Solubility

Within the framework of the solution-diffusion model, a penetrant molecule must first sorb into the polymer at the high pressure side of the film before it can diffuse down the concentration gradient across the film. The concentration (C) of a pure penetrant within a polymer is related to the pressure at the polymer surface by the equilibrium sorption coefficient (S) and pressure of the penetrant (p), viz. [5]:

$$C = S(p)\,p \tag{2.4}$$

The sorption coefficient, which is typically pressure dependent for glassy polymers and ideally pressure independent for rubbery polymers in the absence of swelling [6], can

be rearranged via Equation 2.5 to yield an expression for the average sorption coefficient ($\bar{S}$) over a specified pressure interval, starting from zero pressure (i.e., both p_1 and C_1 are zero).

$$\bar{S} = \left(\frac{C_2 - C_1}{p_2 - p_1} \right) = \left(\frac{C_2}{p_2} \right) \tag{2.5}$$

The sorption of a penetrant in a polymer is determined by multiple factors, which include temperature, polymer morphology (i.e., semi-crystalline, oriented, amorphous), penetrant condensability, and the affinity between penetrant and polymer. Penetrant sorption in a polymer usually correlates with the penetrant critical temperature, in that a higher critical temperature signifies greater condensability for the penetrant [7]. A list of critical temperatures for common small-molecule penetrants is provided in Table 2.1.

Table 2.1. Critical temperatures of common small-molecule penetrants [7].

Gas	Critical Temperature (K)
H_2	33.3
N_2	126.1
O_2	154.4
CH_4	190.7
CO_2	304.2
H_2O	373.9

Equilibrium sorption coefficients, when measured at multiple temperatures, are amenable to the van't Hoff representation in Equation 2.6 [8], where S represents the sorption coefficient, S_0 is the pre-exponential factor, ΔH_S is the apparent enthalpy of sorption, R is the universal gas constant, and T is the temperature in Kelvin. Detailed

applications of Equation 2.6 to model-specific sorption coefficients are discussed later in Chapters 6 [9], 7 [10], and 8 [11].

$$S = S_0 \exp\left(-\Delta H_S \big/ RT\right) \tag{2.6}$$

Penetrant sorption in a polymer can be described thermodynamically as the penetrant sorbing into the polymer to create a "mixture." In fact, a quantifiable energy can be associated with both the penetrant "condensing" within the matrix and the actual process of mixing, such that the apparent enthalpy of sorption (ΔH_S) can be further separated into such counterparts via Equation 2.7 [5].

$$\Delta H_S = \Delta H_{cond} + \Delta \bar{H}_{mix} \tag{2.7}$$

In Equation 2.7, ΔH_{cond} is the enthalpy of penetrant condensation and $\Delta \bar{H}_{mix}$ is the partial molar enthalpy of mixing. For "permanent" gases, which have low critical temperatures (i.e., H_2, N_2, O_2 in Table 2.1), ΔH_{cond} is negative but relatively small in magnitude, while for condensable vapors (i.e., H_2O in Table 2.1), ΔH_{cond} is negative but much larger in magnitude. This notion, in combination with the reality that $\Delta \bar{H}_{mix}$ exhibits small, positive values in both cases, reveals that ΔH_S is largely dominated by the "condensability" of the penetrant. Negative values of ΔH_S, in combination with the relationship in Equation 2.6, therefore indicate that penetrant sorption will decrease with temperature in such applications.

2.1.2. Diffusivity

As mentioned previously, penetrant diffusion occurs via the Fickian relationship in Equation 2.3 within the framework of the solution-diffusion model. In a more phenomenological description, diffusion can be portrayed via Equation 2.8 from random walk theory [12, 13], where λ is the path length of a molecular jump, f is the frequency of jumps, and the factor 1/6 relates to a random walk in an isotropic medium. The jump frequency is a measure of how often molecular-sized holes form in the medium, and for polymers, is fundamentally related to the segmental chain mobility. A more detailed discussion regarding Equation 2.8 is provided later in Chapter 6 [9].

$$D = \frac{1}{6} f \lambda^2 \tag{2.8}$$

Similar to the sorption coefficient in Equation 2.5, which reflects the average value over a specified pressure or concentration interval, an average diffusion coefficient can be estimated via Equation 2.9, which originates from the mean value theorem for definite integrals [14].

$$\bar{D} = \frac{1}{C_2 - C_1} \int_{C_1}^{C_2} D(C)\, dC \tag{2.9}$$

It naturally follows from Equation 2.9 that $\bar{D} = D$ for the case of a constant diffusion coefficient (i.e., ideal diffusion at a fixed temperature in a rubbery material [6]). Concentration dependent diffusion coefficients are commonly observed in many diffusion

cases involving polymers. For example, ideal diffusion in glassy polymers, as described by the partial immobilization model (discussed later in Section 2.3.3), naturally invokes a variable average or local diffusion coefficient. Such variability can be even more pronounced in complicated diffusion cases involving plasticization or clustering [15, 16], as will be discussed later in Chapter 9 [17].

In practice, it is common to experimentally measure the effective diffusion coefficient (i.e., $\bar{D}$ from Equation 2.9) over a discrete pressure or concentration interval. Such measurement, which yields an estimate for the average diffusion coefficient, gives little information regarding the functional dependence of D on concentration (i.e., $D(C)$ from Equation 2.9). If multiple concentration intervals are measured in series, however, the functional form of D can be inferred by plotting $\bar{D}$ versus the average concentration employed in the discrete interval [3]. A commonly observed functional form for $D(C)$ is provided via the exponential relationship in Equation 2.10 [18-21], where D_∞ is the infinite dilution diffusion coefficient (i.e., $D(C=0)$) and β is a constant. Application of Equation 2.10 for water diffusion in PET and PEF is provided in Chapter 9 [17], and a comprehensive list of potential functional dependencies for $D(C)$ can be found elsewhere [3].

$$D(C) = D_\infty \exp(\beta C) \tag{2.10}$$

As will be discussed in Section 2.4, $\bar{D}$ can be estimated via kinetic sorption experiments during either penetrant sorption *into* the polymer or penetrant desorption *out of* the polymer. Such detailed estimates are useful, however, a more accurate

approximation for $\bar{D}$ can be obtained by averaging the estimate determined from sorption (i.e., $\bar{D}_{sorption}$) and desorption (i.e., $\bar{D}_{desorption}$) via Equation 2.11 [3]. Direct application of Equation 2.11 is discussed later in Chapter 9 [17].

$$\bar{D} = \left(\frac{\bar{D}_{sorption} + \bar{D}_{desorption}}{2} \right) \tag{2.11}$$

Similar to penetrant sorption in polymers, diffusion is also governed by a variety of factors, which include temperature, kinetic diameter of the penetrant, free volume of the polymer, and polymer morphology (i.e., semi-crystalline, oriented, amorphous), among others [6]. As mentioned previously, a molecular sized hole must form in the polymer and remain open long enough for the penetrant to "jump" into the hole for diffusion to occur. It is therefore logical to imagine that a relatively large penetrant molecule (i.e., methane) will diffuse more slowly through a polymer compared to helium, which is smaller, due to the larger penetrant size and reduced frequency of formation for "holes" large enough to accommodate the larger penetrant. Such behavior results in the commonly observed negative correlation between kinetic diameter and diffusivity, where a list of kinetic diameters for a variety of common penetrants is provided in Table 2.2.

Table 2.2. Kinetic diameters for various common penetrants [7, 22].

Gas	Critical Temperature (K)
H_2	33.3
N_2	126.1
O_2	154.4
CH_4	190.7
CO_2	304.2
H_2O	373.9

The penetrant diffusivity, when measured as a function of temperature, is amenable to the Arrhenius analysis provided in Equation 2.12 [23], where D_0 is the pre-exponential factor, E_D is the apparent activation energy of diffusion, R is the universal gas constant, and T is the temperature in Kelvin. The pre-exponential factor for diffusion can be further described using transition state theory via Equation 2.13 [6, 24-26], where λ is the diffusion path length during a diffusive "jump," k is Boltzmann's constant, h is Planck's constant, R is the universal gas constant, and S_D is the apparent activation entropy of diffusion.

$$D = D_0 \exp\left(-E_D \big/ RT\right) \tag{2.12}$$

$$D_0 = e\lambda^2 \frac{kT}{h} \exp\left(\frac{S_D}{R}\right) \tag{2.13}$$

Since diffusion in polymers is known to be an "activated" process [27], estimates for E_D are typically positive, and consequently, the diffusion coefficient often exhibits a positive correlation with increasing temperature. Estimates for the activation entropy of

diffusion from Equation 2.13 are useful in assessing the entropic contributions to "size selective" diffusion in materials with well defined pore structures [26]; however, such applications are rather limited for polymers due to the lack of permanent pores within the amorphous morphology of barrier materials [25].

2.1.3. Permeability

The permeability coefficient of a pure penetrant in a polymer (P) characterizes the steady-state flux (N) of the penetrant across a film of thickness l under a given partial pressure driving force (Δp) as shown in Equation 2.14.

$$P = \frac{N}{\left(\Delta p / l\right)} \tag{2.14}$$

Although useful for engineering calculations, for fundamental understanding factorization of the constituent sorption (S) and diffusion (D) coefficients is necessary, viz.,

$$\bar{P} = \bar{D}\bar{S} \tag{2.15}$$

In Equation 2.15, $\bar{P}$ represents the average permeability between upstream and downstream conditions at the film surface, and similarly, the diffusivity and sorption parameters represent the average values discussed previously in Equations 2.9 and 2.5, respectively. Derivation of Equation 2.15 can be achieved via substitution of Equation 2.3, which is the Fickian expression for the flux (N), into the general expression for the

permeability in Equation 2.14, viz.,

$$\bar{P} = \frac{\left(-\bar{D}\frac{dC}{dx}\right)}{\left(\Delta p/l\right)} \tag{2.16}$$

Equation 2.16 can be rearranged and integrated over both concentration and spatial variables to yield the expression provided in Equation 2.17, which is further simplified in Equation 2.18 and shown to be equivalent to the expression provided previously in Equation 2.15.

$$\frac{P}{l}\int_0^l dx = \frac{\left(D\int_{C_1}^{C_2} dC\right)}{-\Delta p} \tag{2.17}$$

$$\bar{P} = \bar{D}\left(\frac{C_2 - C_1}{p_2 - p_1}\right) = \bar{D}\bar{S} \tag{2.18}$$

The transport parameters discussed thus far (i.e., permeability, diffusivity, and solubility) represent “pressure-averaged” constant values; however, it is common for all three parameters to vary with feed pressure [28, 29]. Such dependencies vs. pressure are provided and discussed later in Section 2.3.

Similar to diffusivity, permeability data measured at multiple temperatures can be analyzed using the Arrhenius representation in Equation 2.19, where P_0 is the pre-exponential factor, E_P is the apparent activation energy of permeation, and R and T are

defined previously. Substitution of Equations 2.19, 2.12, and 2.6 into Equation 2.15 yields, after minor simplification, the expression provided in Equation 2.20.

$$P = P_0 \exp\left(-E_P \big/ RT\right) \tag{2.19}$$

$$E_P = E_D + \Delta H_S \tag{2.20}$$

Values of the activation energy of permeation (E_P) are typically positive for most penetrants; however, a large negative value for ΔH_S (which can originate from a high critical temperature for the penetrant) can sometimes offset the positive value of E_D, rendering a negative value for E_P, and consequently, a permeability that decreases with increasing temperature [30].

2.2. Effect of Crystallinity

All transport data reported in this thesis correlate with the amorphous morphology; however, transport estimates for the semicrystalline morphology can be obtained if the amorphous volume fraction (ϕ_a) of the sample is known. Expressions for the solubility (S), diffusivity (D), and permeability (P) for semicrystalline samples are provided in Equations 2.21, 2.22, and 2.23, respectively, where the subscript "a" refers to the amorphous morphology and "sc" refers to the semicrystalline morphology [8, 23].

$$S_{SC} = S_a \phi_a \tag{2.21}$$

$$D_{SC} = D_a \phi_a \tag{2.22}$$

$$P_{SC} = P_a \left(\phi_a\right)^2 \tag{2.23}$$

Such expressions can provide a first approximation for the transport properties in semicrystalline samples; however, deviations from the idealized behavior represented by the two-phase model are known to exist for PET [31]. Moreover, transport studies involving the semicrystalline morphology are needed to validate the applicability of Equations 2.21 – 2.23 for PEF.

2.3. Transport Modeling

As mentioned previously, transport in polymeric materials is defined by the product of sorption and diffusion factors. The transport parameters discussed thus far have referred to "pressure-averaged" values; however, large pressure (or concentration) dependencies can exist depending on the specific transport application. This section provides an overview of the relevant transport models useful for describing such dependencies, and consequently, provides the majority of information necessary for interpreting the data in the remainder of the thesis.

2.3.1. Dual-Mode Model Framework

Description of penetrant transport in rubbery polymers (i.e., above the glass transition temperature) is simple, in that all transport parameters are pressure independent in the absence of swelling or plasticization [6]. Since both diffusivity and permeability are

constant at a fixed temperature in such materials, Equation 2.24 applies, where k_D represents the Henry's law sorption parameter which characterizes the penetrant uptake.

$$P = k_D D \tag{2.24}$$

In glassy polymers, however, the total sorbed penetrant concentration equals the sum of two populations that exist at local equilibrium with each other, as determined by the chemical potential that can be written in terms of the penetrant partial pressure. This local effective partial pressure, of course, varies from the upstream to the downstream face of the film. The dual-mode model accommodates the non-equilibrium nature of glassy polymers by visualizing a simple "dissolved" population (i.e., C_D), and a more complex sorbed population reflecting the non-equilibrium nature of the glass (i.e., C_H) [8, 32, 33]. Sorption in this latter mode is visualized as occurring in packing defects represented by a Langmuir isotherm with characteristic Langmuir capacity constant (C_H') and affinity parameter (b). On the other hand, sorption in the simple dissolved mode (i.e., Henry's environment) is characterized by a Henry's law parameter (k_D) like that in a simple rubber with similar nature, but without non-equilibrium microvoids. The dual-mode model is therefore conveniently written in Equations 2.25 and 2.26:

$$C = C_D + C_H \tag{2.25}$$

$$C = \left(k_D p + \frac{C_H' bp}{1 + bp} \right) \tag{2.26}$$

Graphical representation of the dual-mode model is provided in Figure 2.2, which illustrates the shape of the dual-mode isotherm as a summation of Henry's law and Langmuir isotherms.

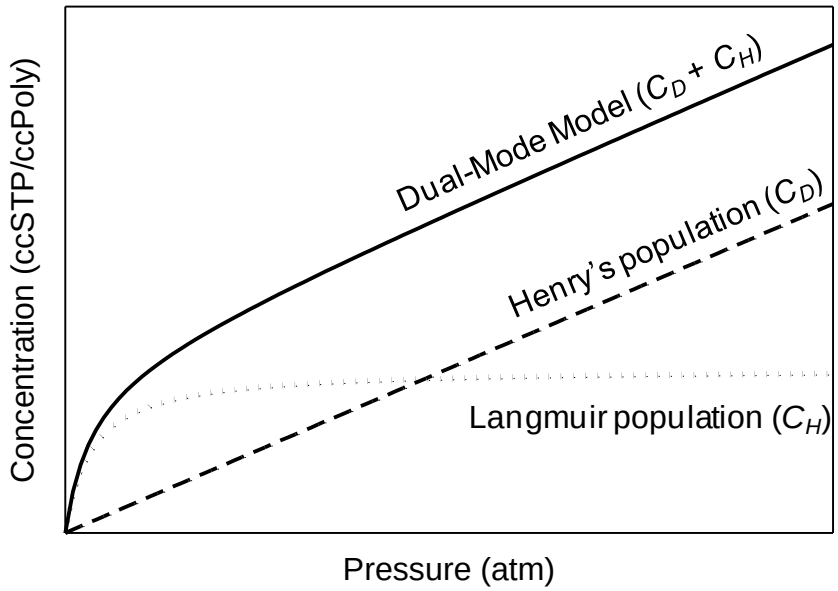

Figure 2.2. Graphical representation of the dual-mode model from Equation 2.26.

The low pressure limit of Equation 2.26, given by Equation 2.27, provides an effective infinite dilution sorption coefficient, where $\lim_{p\to 0} S = k*$. This coefficient reflects the low pressure contributions from both sorbed populations in the glass, and will be referenced often throughout the remainder of this thesis.

$$k^* = \left(k_D + C_H' b\right) \tag{2.27}$$

The sorption parameters defined in Equations 2.26 and 2.27 are typically determined via pressure-decay sorption testing (discussed later in Section 3.3). Complementary estimates of the effective solubility parameter (k^*) can be determined from transient permeation data (discussed later in Section 3.2.3) via Equation 2.28 [29], provided that the upstream driving pressure is sufficiently low. In Equation 2.28, P represents the steady-state penetrant permeability, θ represents the time-lag (discussed later in Section 3.2.3), and l is the film thickness. Ideally, k^* estimated from independent equilibrium sorption and combined transient and low pressure steady-state permeation should be identical.

$$k^* = 6\theta P / l^2 \tag{2.28}$$

The dual-mode framework described thus far focuses solely on pure penetrant sorption. While not required in this work, extensions exist, which allow dual-mode analysis of sorption cases involving multiple components [34].

2.3.2. Diffusion Estimates from Permeation

Similar to Equation 2.28, which utilizes transient permeation data to estimate the effective solubility coefficient, an estimate for the diffusion coefficient can also be obtained from the time-lag (θ) via Equation 2.29 [23], where l is the film thickness.

$$D = l^2 / 6\theta \tag{2.29}$$

Graphical representation and determination of the permeation time-lag is described in detail later in Section 3.2.3. For internal consistency, another estimate of the infinite dilution diffusion coefficient can also be obtained via Equation 2.30, which combines transport measurements from both low pressure steady-state permeation and pressure-decay sorption testing [6], viz.,

$$D = \left(\frac{P}{k^*_{sorption}} \right) = \left(\frac{P}{k_D + C_H' b} \right) \tag{2.30}$$

As with the k^* estimates from Equations 2.27 and 2.28, the independently estimated values of the infinite dilution diffusion coefficient from Equations 2.29 and 2.30 should be the same at low feed pressures.

2.3.3. Partial Immobilization Model Framework

As mentioned previously, the non-equilibrium nature of glassy polymers can give rise to pressure-dependent transport parameters. Such dependencies are common, and can be explained within the framework of the partial immobilization model introduced by Petropoulos [33] and also discussed by Paul and Koros [35]. The basis of the partial immobilization model is that the gas population sorbed into the Langmuir mode is 'partially immobilized' as opposed to the earlier assumption of total immobilization. As a result, the penetrant mobility in each sorption mode is assigned a diffusion coefficient *D*. The partial immobilization analog to Fick's first law, using the model of Paul and Koros [35], is provided in Equation 2.31, with the expression for the effective diffusion

coefficient provided in Equation 2.32. The subscripts "*D*" and "*H*" refer to the dissolved (C_D) and Langmuir populations (C_H), respectively.

$$N = -D_D \frac{\partial C_D}{\partial x} - D_H \frac{\partial C_H}{\partial x} \tag{2.31}$$

$$N = \left(-D \frac{\partial C}{\partial x} \right) = -D_D \left(\frac{1 + \dfrac{FK}{\left(1 + \alpha C_D\right)^2}}{1 + \dfrac{K}{\left(1 + \alpha C_D\right)^2}} \right) \frac{\partial C}{\partial x} \tag{2.32}$$

In Equations 2.31 and 2.32, $K = C_H'b/k_D$, $F = D_H/D_D$, $\alpha = b/k_D$. Further manipulation of the effective diffusivity and sorption parameters yields the permeability expression in Equation 2.33, assuming that the downstream pressure is effectively zero. Inspection of Equation 2.33 reveals that the permeability will be approximately independent of pressure if $F \approx 0$ (i.e., $D_H \approx 0$) or if the values of K and b are small. The former case corresponds to the limit of "total immobilization," where the penetrant is effectively "immobilized" in the Langmuir microvoids and only the dissolved mode contributes to transport. However, due to the assumption that equilibrium exists between the dissolved and Langmuir populations, F cannot truly equal zero [35].

$$P = k_D D_D \left(1 + \frac{FK}{1 + bp} \right) \tag{2.33}$$

In addition to permeability, the partial immobilization model also allows for

concentration dependence regarding the diffusion coefficient. Combination of the partial immobilization model representation of the diffusion coefficient from Equation 2.32 with the expression in Equation 2.9 for the average diffusion coefficient yields Equation 2.34 [36-38].

$$\bar{D} = D_D \left(\frac{1 + \frac{FK}{(1+bp_1)(1+bp_2)}}{1 + \frac{K}{(1+bp_1)(1+bp_2)}} \right) \tag{2.34}$$

The dependence of $\bar{D}$ from Equation 2.34 on F, which is a measure of penetrant mobility within the microvoids, is illustrated in Figure 2.3 using hypothetical, typical values for the dual-mode model parameters for CO_2 in amorphous PEF at 35°C.

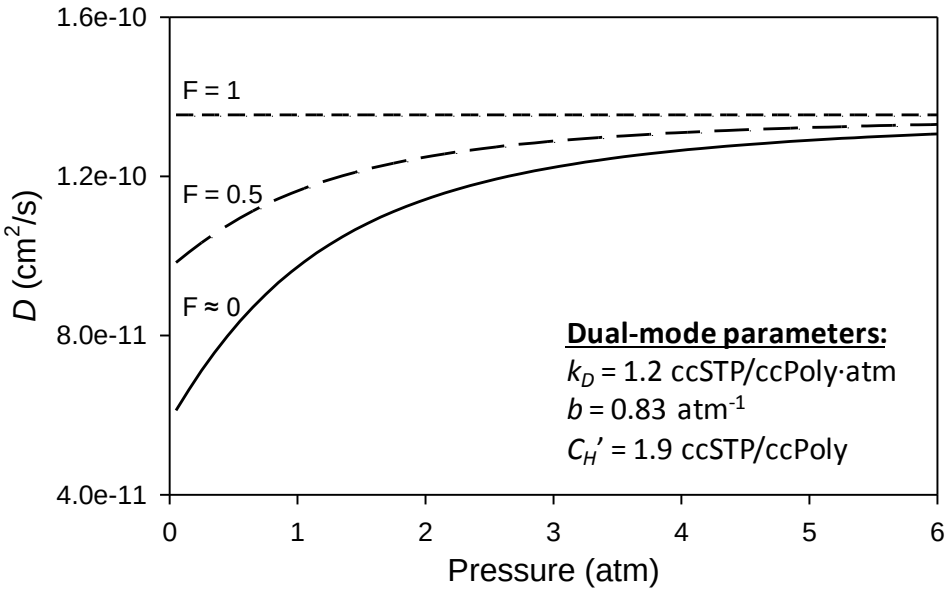

Figure 2.3. Example dependence of $\bar{D}$ calculated from Equation 2.31 on F, using hypothetical values for the dual-mode model parameters.

As seen in Figure 2.3, pressure independent behavior for the diffusion coefficient is observed when $F = 1$, thereby indicating equivalent mobility for a penetrant sorbed in a microvoid vs. the dissolved mode, while a strong pressure dependence is observed when $F \approx 0$, which indicates the limit of "total immobilization" within the microvoids.

The partial immobilization framework described thus far focuses solely on pure penetrant transport. Similar to the equations for dual-mode sorption, extensions exist which allow partial immobilization analysis of transport cases involving multiple components [39].

2.3.4. Flory Huggins Framework

In contrast to the typical dual-mode sorption isotherm shown in Figure 2.2 for ideal penetrant sorption in glassy polymers, high activity vapor sorption is often characterized by an upturn in sorption with respect to activity [16, 21, 40-42]. Such isotherms have been described using the modified dual-mode model proposed by Mauze and Stern [43] or more recently by the unified dual-mode model proposed by Guo and Barbari [44]. Satisfactory description of such data can also be provided by the Flory-Huggins representation developed for sorption in rubbery materials via Equation 2.35 [45]. In Equation 2.35, p is the penetrant pressure, p_0 is the saturation vapor pressure, ϕ_1 is the volume fraction of the penetrant, and χ is the "effective" Flory-Huggins interaction parameter. Calculation of ϕ_1 can be achieved through Equation 2.36 [41], where V_1 is the sorbed molar volume of the penetrant at the test temperature and C is the penetrant concentration. The molar volume denoted by V_1 is generally similar to the van der Waal volume of the specific penetrant [46].

$$\ln\left(\frac{p}{p_0}\right) = \ln\phi_1 + \left(1-\phi_1\right) + \chi\left(1-\phi_1\right)^2 \tag{2.35}$$

$$\phi_1 = \frac{V_1\left(C/22400\right)}{1+V_1\left(C/22400\right)} \tag{2.36}$$

Use of Equation 2.35 in combination with a constant interaction parameter signifies the ideal case of random mixing between penetrant and polymer [15, 47, 48]. Sorption data for iso-propanol, ethanol, and methanol in PET are well described via this simplified methodology [21, 40]. More complicated sorption cases, however, require a concentration dependant expression for χ and can suggest deviations from random mixing. Equation 2.37 represents a simple, empirical model for capturing the concentration dependence of χ, where χ_0, χ_1, and χ_2 are constants associated with the model fit [49, 50].

$$\chi = \chi_0 + \chi_1\left(1-\phi_1\right) + \chi_2\left(1-\phi_1\right)^2 \tag{2.37}$$

Applications of Equations 2.35 – 2.37 to water sorption isotherms at 35°C for amorphous PET and PEF are discussed later in Chapter 8 [11].

2.3.5. Zimm-Lundberg Clustering Analysis

The onset of clustering can be qualitatively determined using the analysis proposed

by Zimm and Lundberg [51], which interprets the shape of the equilibrium sorption isotherm in terms of a so-called cluster integral (G_{11}). Equation 2.38 reflects their methodology, where a_1 is the activity of the penetrant (i.e. p/p_0), ϕ_1 is the volume fraction of the penetrant, and $\bar{V}_1$ represents the penetrant partial molar volume.

$$\frac{G_{11}}{\bar{V}_1} = -\left(1-\phi_1\right)\left[\frac{\partial\left(a_1/\phi_1\right)}{\partial a_1}\right]_{p,T} - 1 \tag{2.38}$$

The quantity $\phi_1 G_{11}/\bar{V}_1$ represents the number of penetrant molecules in a cluster in excess of single, isolated penetrant molecules. Consequently, this parameter can be non-zero at high activity and approximately zero at low activities, where clustering is less common. Both clustering and uniform swelling phenomena exhibit an upturn in solubility at high activities. Equation 2.38 can be used to detect a departure from ideality and the onset of plasticization or clustering as indicated by values of $\phi_1 G_{11}/\bar{V}_1$ greater than zero. To detect whether simple swelling or more complex clustering is occurring, one must determine the concentration (or activity) dependence of the diffusion coefficient. If plasticization occurs, an increase in diffusion coefficient accompanies the upturn in sorption. If clustering occurs, the diffusion coefficient decreases, despite such an upturn in sorption. Application of Equation 2.38 to water sorption data for PET and PEF is provided later in Chapter 8 [11].

2.3.6. Free Volume and Antiplasticization vs. Plasticization

The notion of "free volume" is often used to rationalize penetrant transport behavior in polymeric materials. The specific free volume ($\hat{V}_F$) of a glassy polymer can be defined as the difference between specific volume (i.e., $\hat{V}_g$, which is the inverse of density) and the specific occupied volume ($\hat{V}_0$) via Equation 2.39, while a definition for the fractional free volume (*FFV*), which is a simple extension of the specific free volume, is provided in Equation 2.40.

$$\hat{V}_F = \hat{V}_g - \hat{V}_0 \tag{2.39}$$

$$FFV = \frac{\hat{V}_g - \hat{V}_0}{\hat{V}_g} \tag{2.40}$$

The occupied volume represents the specific volume of the polymer at 0 Kelvin, and can be estimated using the group contribution methods of Sugden [52], Bondi [53], van Krevelen [54], or Park and Paul [55]. Occupied volume calculations for PET, PEF, and caffeine using the method of Sugden are provided later in Chapters 4 [56] and 5 [57]. A graphical representation of the free volume is provided in Figure 2.4, where the "excess free volume" is defined as the "extra" volume that exists in the form of non-equilibrium "microvoids" in the glassy state compared to the equilibrium rubbery state. The excess free volume correlates directly with penetrant sorption in the Langmuir mode of the dual-mode model, which was discussed previously.

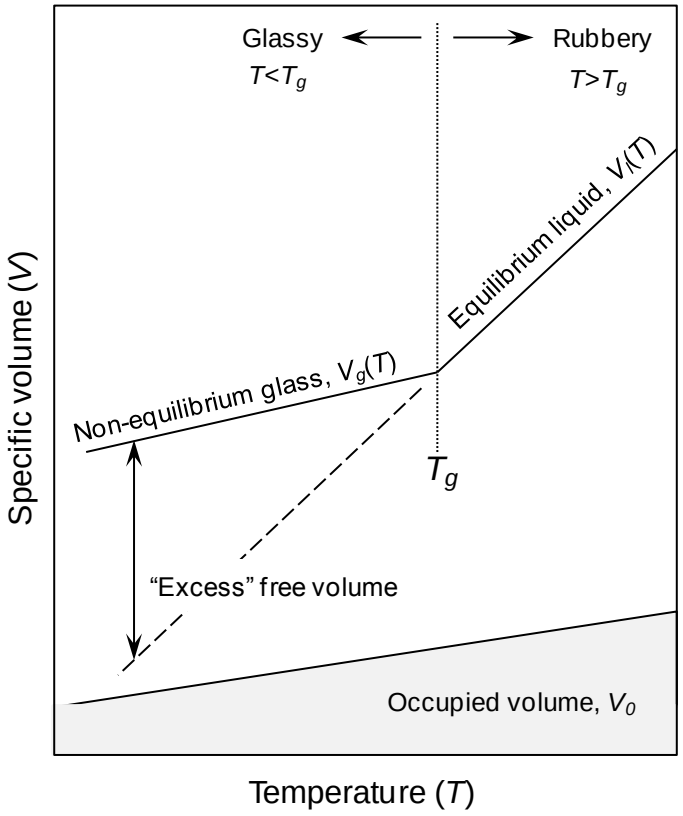

Figure 2.4. Graphical representation of free volume (V_F) and the general specific volume versus temperature behavior for a typical polymer.

Multiple authors have related various macroscopic properties of a polymer to free volume [58-60]; however, the free volume framework proposed by Fujita [60] in Equation 2.41 is perhaps the most straightforward for penetrant diffusivity, where B_D and A_D are penetrant-specific empirical parameters and FFV is defined previously in Equation 2.40.

$$D = A_D \exp\left(\frac{-B_D}{FFV}\right) \tag{2.41}$$

The concept of using free volume to describe penetrant diffusion is logical, since in

theory, diffusive “jumps” within a polymer are thought to occur via a continual redistribution of free volume due to random thermal/density fluctuations [61]. Since the free volume of a polymer can depend on temperature, penetrant size and shape, and penetrant concentration, it is therefore convenient to express diffusion in terms of free volume, since undoubtedly the diffusivity of a penetrant depends on the same underlying factors.

The relationship between diffusivity and free volume in Equation 2.41 can be substituted into the previous expression for permeability in Equation 2.15 (i.e., $P = D \cdot S$), and along with the assumption that penetrant solubility exhibits a weak dependence on free volume, produces the correlation in Equation 2.42 between permeability and free volume [62]. In Equation 2.42, B_P and A_P are penetrant-specific empirical parameters and FFV is defined previously in Equation 2.40.

$$P = A_P \exp\left(\frac{-B_P}{FFV}\right) \tag{2.42}$$

It is now convenient to introduce the topic of plasticization and antiplasticization in polymer/diluent mixtures, which both involve changes in free volume. In the most simplistic description, plasticization results when a polymer/diluent mixture exhibits an *increase* in free volume for the mixture compared to the neat polymer, while antiplasticization results when a polymer/diluent exhibits a *decrease* in free volume for the mixture compared to the neat polymer. Reductions in free volume vs. the neat polymer, as seen for antiplasticization, have been linked to reductions in chain mobility, penetrant transport, and elongation at break [63-68], while the opposite behavior has been

observed for plasticization [69-71]. It is also believed that the phenomenon of antiplasticization is concentration dependent, meaning that a polymer/diluent mixture can exhibit both antiplasticization and plasticization type behavior depending on the diluent concentration. Such a notion is depicted graphically in Figure 2.5 via the hypothetical plot of permeability and diffusivity vs. diluent content, where a working definition for antiplasticization useful in the current work entails *any* diluent content that produces a reduced permeability or diffusivity compared to the neat polymer.

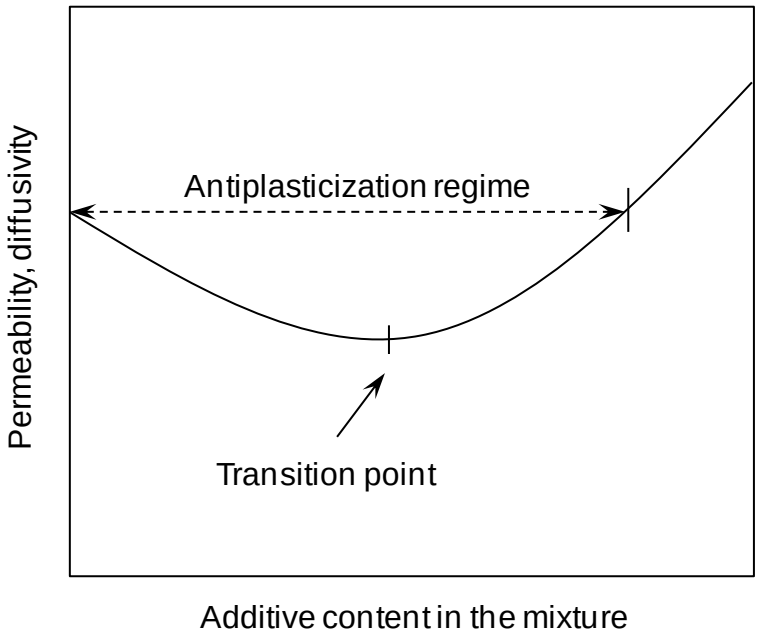

Figure 2.5. Graphical representation of antiplasticization in a hypothetical polymer/diluent mixture.

The reduction in free volume for an antiplasticized polymer/diluent mixture can be described using modified versions of Equations 2.39 and 2.40, which are defined for pure polymers. Corresponding relationships for a polymer/diluent mixture are provided in Equations 2.43 and 2.44 [68], where w is the weight fraction of the diluent and the

subscripts *m*, *d*, and *p* stand for *mixture*, *diluent*, and *polymer*, respectively.

$$\hat{V}_{F,m} = \hat{V}_{g,m} - \hat{V}_{0,m} \tag{2.43}$$

$$\hat{V}_{0,m} = w\hat{V}_{0,d} + (1-w)\hat{V}_{0,p} \tag{2.44}$$

Equation 2.44 represents ideal additivity of the occupied volume of the diluent and polymer, where the values of $\hat{V}_0$ for the pure components can be calculated using Sugden's method [52], as described previously. The fractional free volume of the polymer-diluent mixture (FFV_m) is obtained by dividing Equation 2.43 by the specific volume of the glassy mixture. Application of Equations 2.43 and 2.44 for caffeine antiplasticized PET is provided later in Chapter 4 [56].

Aside from plasticization of a polymer/diluent mixture, plasticization can also occur due to "swelling" of the polymer chains resulting from penetrant sorption at high concentration [72-77]. Detailed discussion regarding plasticization-type phenomena is provided later in Chapter 8 [11].

2.4. Diffusion Coefficient Modeling—Kinetic Sorption

Penetrant uptake data, when measured via pressure-decay sorption or gravimetric sorption methods (discussed later in Section 3.3 and 3.4, respectively), can be normalized such that the non-dimensional mass gained by the polymer during diffusion varies from zero to one. Such data, which is represented via M_t/M_∞ (i.e., mass of penetrant uptake at time *t* divided by the equilibrium mass uptake after equilibrium), can be modeled using an infinite series solution to the time-dependent diffusion equation in Equation 2.45,

provided that the sample geometry is known.

$$\frac{\partial C}{\partial t} = \bar{D}\frac{\partial^2 C}{\partial x^2} \tag{2.45}$$

Equation 2.45 represents the partial differential equation for time-dependent, uniaxial diffusion in an infinite sheet, where $\bar{D}$ is the average diffusion coefficient over the uptake interval, as discussed previously. This section will discuss various solutions of Equation 2.45 corresponding to the multiple diffusion cases encountered in this work, while a MATLAB® methodology useful for applying such solutions to experimental kinetic sorption data is provided in Chapter 11 [78].

2.4.1. Fickian Kinetics—Constant Initial and Boundary Conditions

The most straightforward solution to Equation 2.45 involves implementation of the constant initial and boundary conditions (i.e., IC and BC, respectively) provided in Equation 2.46, where l is the film thickness. The infinite series solution obtained under such conditions is represented via Equation 2.47 [3] in terms of the non-dimensional quantity M_t/M_∞, discussed previously.

$$\begin{aligned} &\text{IC: } \left(C = C_0, \quad -l/2 < x < l/2, \quad t = 0\right) \\ &\text{BC: } \left(C = C_1, \qquad x = \pm l/2, \qquad t \geq 0\right) \end{aligned} \tag{2.46}$$

$$\frac{M_t}{M_\infty}(t) = 1 - \sum_{n=0}^{\infty} \frac{8}{(2n+1)^2 \pi^2} \exp\left(\frac{-\bar{D}(2n+1)^2 \pi^2 t}{l^2}\right) \tag{2.47}$$

Equation 2.47 is valid for ideal penetrant diffusion cases which do not involve the superposition of non-Fickian relaxations (discussed later in Section 2.4.4). Application of Equation 2.47 is demonstrated for the case of oxygen diffusion in amorphous PEF in Chapter 6 [9].

2.4.2. Fickian Kinetics—Flux Boundary Condition

Implementation of a constant boundary condition at the film surface is not strictly valid for penetrant uptake data measured via pressure-decay techniques (discussed later in Section 3.3), due to the necessary decay in pressure at the film surface during sorption. As will be discussed in Chapter 6 [9], this effect is negligible for oxygen uptake in PEF due to the small decay in pressure (i.e., ~2%) observed during sorption, therefore rendering the assumption of a constant boundary condition valid in that application. Carbon dioxide, however, is notably more sorptive in PEF compared to oxygen, and thereby results in a much larger change in pressure at the film boundary compared to oxygen and renders the aforementioned constant boundary condition assumption less valid. Accommodation of this reality can be obtained through implementation of the flux boundary condition in Equation 2.48, which specifies that the rate of carbon dioxide "loss" in the cell headspace outside the film ($\partial C/\partial t$) is proportional to the rate of carbon dioxide flux into the film at the film surface ($-\bar{D}\partial C/\partial x$) [3], where l is the film half-thickness, V_R is the volume of the sample cell reservoir in the pressure-decay apparatus (discussed later in Section 3.3), and V_S is the volume of the polymer sample in the pressure-decay apparatus.

$$\text{IC: } \left(C = C_0, \quad -l < x < l, \quad t = 0\right)$$
$$\text{BC: } \left(\left(l\frac{V_R}{V_S}\right)\frac{\partial C}{\partial t} = \mp\bar{D}\frac{\partial C}{\partial x}, \ \ x = \pm l, \ \ t > 0\right) \tag{2.48}$$

Solutions of the transient diffusion equation (i.e., Equation 2.45) with respect to the conditions specified in Equation 2.48 are provided via the infinite series solution in Equation 2.49 [3], where l is the film half-thickness, q_n is defined via the non-zero positive roots of Equation 2.50, and α is related to the final fractional uptake of the film in Equation 2.51 (i.e., the number of moles of carbon dioxide *in the film* at the end of diffusion divided by the total number of moles *in the sample cell* at the start of the sorption run).

$$\frac{M_t}{M_\infty}(t) = 1 - \sum_{n=1}^{\infty}\frac{2\alpha(1+\alpha)}{1+\alpha+\alpha^2 q_n{}^2}\exp\left(\frac{-Dq_n{}^2 t}{l^2}\right) \tag{2.49}$$

$$\tan(q_n) = -\alpha q_n \tag{2.50}$$

$$\frac{n_{film,\,final}}{n_{total,initial}} = \left(\frac{1}{1+\alpha}\right) \tag{2.51}$$

The solution specified in Equation 2.49 reduces to the simple Fickian solution (i.e., Equation 2.47) in the limit of $\alpha \to \infty$. Such conditions are realized in the case of oxygen sorption in PEF [9], where the fractional uptake of oxygen is small compared to the total

amount of oxygen in the cell headspace. Application of Equation 2.49 is demonstrated for the case of carbon dioxide diffusion in amorphous PEF in Chapter 7 [10].

2.4.3. Fickian Kinetics—Time-Dependent Boundary Condition

In contrast to oxygen and carbon dioxide uptake in polymers, which can be studied using pressure-decay sorption, water is more condensable and the resultant uptake can be studied using gravimetric techniques (cf. Section 3.4). In regards to water uptake measured using a vapor laden carrier gas and an automated instrument control scheme, anomalous diffusion behavior can occur due to the presence of a time dependent boundary condition due to relaxations or other complex phenomena at the film surface. Such boundary and initial conditions can be described by Equation 2.52 [3, 79, 80], where l is the film thickness and τ_S is the time constant which characterizes the time required to reach equilibrium saturation at the film surface. In the current work, this time dependence represents an instrumental parameter related to how fast the automated control scheme of the vapor analyzer can implement a step-change in concentration (discussed further in Section 3.4.2).

$$\begin{aligned} &\text{IC: } \left(C = C_0, \quad -l/2 < x < l/2, \quad t = 0\right) \\ &\text{BC: } \left(C = C_1\left(1 - \exp\left(-\frac{t}{\tau_S}\right)\right), \quad x = \pm l/2, \quad t > 0\right) \end{aligned} \tag{2.52}$$

Solution of the transient diffusion equation (i.e., Equation 2.45) with respect to the conditions specified in Equation 2.52 is provided via the infinite series solution in

Equation 2.53 [79, 80]. Detailed explanation regarding the experimental conditions which justify the usage of Equation 2.53 in the current work is discussed later in Section 3.4.2 and Chapter 9 [17].

$$\frac{M_t}{M_\infty}(t) = \left[1 - \exp\left(-\frac{t}{\tau_S}\right)\left(\frac{4\tau_S D_{Avg}}{l^2}\right)^{1/2} \tan\left(\frac{l^2}{4\tau_S D_{Avg}}\right)^{1/2} - \frac{8}{\pi^2}\sum_{n=0}^{\infty}\frac{\exp\left(-D_{Avg}(2n+1)^2\pi^2\frac{t}{l^2}\right)}{(2n+1)^2\left(1-(2n+1)^2\left(\frac{\tau_S D_{Avg}\pi^2}{l^2}\right)\right)}\right] \tag{2.53}$$

A useful feature regarding Equation 2.53 is that the original Fickian solution (Equation 2.47) is recovered when $\tau_S = 0$, thereby signifying an "instantaneous approach" in surface concentration to the final equilibrium value (i.e., the instrumental control scheme "guesses" the correct wet/dry flow rates on the first guess during the step-change in concentration, discussed further in Section 3.4.2). To reiterate, the parameter τ_S in the current work represents an instrumental time constant *and does not represent a fundamental property of the polymer*. Additional applications of Equation 2.53 and variations thereof can be found in multiple articles in the literature [80-83].

2.4.4. Non-Fickian Kinetics—Berens-Hopfenberg Framework

The discussion thus far has focused on simple penetrant diffusion in the absence of long-term non-Fickian relaxations. Such relaxations are known to occur in a wide variety of penetrant and polymer systems [84-86], and can indicate the occurrence of

morphological changes in the polymer. Informative discussions regarding the physical origins of non-Fickian relaxations can be found in the works by Sanopoulou et al. [87, 88] and Crank [3]. Non-Fickian relaxations can be modeled using the formalism proposed by Berens and Hopfenberg [42], shown in Equations 2.54 and 2.55, which states that both Fickian diffusion and first-order relaxation processes can be idealized as occurring independently and can be combined using simple linear superposition. In Equation 2.54, M_t represents the total mass uptake from both mechanisms at time t, $M_{t,F}$ is the mass uptake from the Fickian mode, and $M_{t,R}$ is the mass uptake from the first-order relaxation mode.

$$M_t = M_{t,F} + M_{t,R} \tag{2.54}$$

$$\left.\frac{M_t}{M_\infty}\right|_{BH} = \left[\phi_F \left(\left.\frac{M_t}{M_\infty}\right|_F\right) + \left(1-\phi_F\right)\left(1-\exp\left(-\frac{t}{\tau_R}\right)\right)\right] \tag{2.55}$$

In Equation 2.55, ϕ_F represents the weighting factor which specifies the relative contribution of each uptake mode, τ_R is the time constant for the non-Fickian relaxations, and the subscripts "*BH*" and "*F*" represent the infinite series solutions obtained using the Berens-Hopfenberg (BH) and Fickian (Equation 2.47) formalisms, respectively. Additional models exist in the literature for describing diffusion/relaxation phenomenon [89-91], but none are as simple and straightforward to implement as the BH model. Moreover, the BH framework specified in Equation 2.55 is versatile in that the infinite series solution from the simple Fickian case (Equation 2.47) can be replaced with the

more complex solutions provided previously in Equations 2.49 and 2.53, which result from the implementation of non-constant boundary conditions. The final representation is therefore capable of modeling diffusion cases involving the superposition of non-Fickian relaxations *and* non-constant boundary conditions, depending on the specific application. Implementation of the Berens-Hopfenberg framework in combination with Equation 2.53 is discussed later in Chapter 9 [17], and implementation of the Berens-Hopfenberg framework in combination with Equation 2.49 is discussed later in Chapter 11 [78].

2.5. References

1. Wijmans JG and Baker RW. The solution-diffusion model: a review. Journal of Membrane Science 1995;107(1–2):1-21.
2. Baker RW. Membrane Technology and Applications, Third ed. West Sussex: John Wiley and Sons Ltd, 2012.
3. Crank J. The Mathematics of Diffusion, 2nd ed.: Oxford Science Publications, 1975.
4. Comyn J. Introduction to Polymer Permeability and the Mathematics of Diffusion. In: Comyn J, editor. Polymer Permeability. New York: Elsevier Applied Science Publishers Ltd., 1985. pp. 1-10.
5. Rogers CE. Permeation of Gases and Vapours in Polymers. In: Comyn J, editor. Polymer Permeability. New York: Elsevier Applied Science Publishers Ltd., 1985. pp. 11-73.
6. Crank J and Park GS. Diffusion in Polymers. London: Academic Press, 1968.
7. Mulder M. Basic Principles of Membrane Technology, 2nd ed. Boston: Kluwer Academic Publishers, 1996.
8. Michaels AS, Vieth WR, and Barrie JA. Solution of Gases in Polyethylene Terephthalate. Journal of Applied Physics 1963;34(1):1-12.
9. Burgess SK, Karvan O, Johnson JR, Kriegel RM, and Koros WJ. Oxygen Sorption and Transport in Amorphous Poly(ethylene furanoate). Polymer 2014;55(18):4748-4756.
10. Burgess SK, Kriegel RM, and Koros WJ. Carbon Dioxide Sorption and Transport in

Amorphous Poly(ethylene furanoate). Macromolecules 2015, DOI: 10.1021/acs.macromol.5b00333.

11. Burgess SK, Mikkilineni DS, Yu DB, Kim DJ, Mubarak CR, Kriegel RM, and Koros WJ. Water Sorption in Poly(ethylene furanoate) Compared to Poly(ethylene terephthalate). Part 1: Equilibrium Sorption. Polymer 2014;55(26):6861-6869.

12. Chandrasekhar S. Stochastic problems in physics and astronomy. Reviews of Modern Physics 1943;15(1):1-89.

13. Petropoulos JH. Some fundamental approaches to membrane gas permeability and permselectivity. Journal of Membrane Science 1990;53(3):229-258.

14. Spiegel MR and Liu J. Mathematical Handbook of Formulas and Tables, 2nd ed. New York: McGraw-Hill, 1999.

15. Williams JL, Hopfenberg HB, and Stannett V. Water transport and clustering in poly[vinyl cloride], poly[oxymethylene], and other polymers. Journal of Macromolecular Science, Part B 1969;3(4):711-725.

16. Wellons JD and Stannett V. Permeation, sorption, and diffusion of water in ethyl cellulose. Journal of Polymer Science Part A-1: Polymer Chemistry 1966;4(3):593-602.

17. Burgess SK, Mikkilineni DS, Yu DB, Kim DJ, Mubarak CR, Kriegel RM, and Koros WJ. Water Sorption in Poly(ethylene furanoate) Compared to Poly(ethylene terephthalate). Part 2: Kinetic Sorption. Polymer 2014;55(26):6870-6882.

18. Serad GE, Freeman BD, Stewart ME, and Hill AJ. Gas and vapor sorption and diffusion in poly(ethylene terephthalate). Polymer 2001;42:6929-6943.

19. Dhoot SN, Freeman BD, Stewart ME, and Hill AJ. Sorption and transport of linear alkane hydrocarbons in biaxially oriented polyethylene terephthalate. Journal of Polymer Science Part B: Polymer Physics 2001;39(11):1160-1172.

20. Dhoot SN, Freeman BD, and Stewart ME. Sorption and Transport of Linear Esters and Branched Alkanes in Biaxially Oriented Poly(ethylene terephthalate). Industrial & Engineering Chemistry Research 2004;43(12):2966-2976.

21. Chandra P and Koros WJ. Sorption of lower alcohols in poly(ethylene terephthalate). Polymer 2009;50:4241-4249.

22. Yampolskii Y, Pinnau I, and Freeman BD. Materials Science of Membranes for Gas and Vapor Separation. John Wiley & Sons Ltd., 2006. pp. 466.

23. Michaels AS, Vieth WR, and Barrie JA. Diffusion of Gases in Polyethylene Terephthalate. Journal of Applied Physics 1963;34(1):13-20.

24. Koros WJ. Barrier Polymers and Structures: Overview. In: Koros WJ, editor. Barrier

Polymers and Structures. Washington: American Chemical Society, 1990. pp. 406.

25. Singh-Ghosal A and Koros WJ. Energetic and Entropic Contributions to Mobility Selectivity in Glassy Polymers for Gas Separation Membranes. Industrial & Engineering Chemistry Research 1999;38(10):3647-3654.

26. Singh A and Koros WJ. Significance of Entropic Selectivity for Advanced Gas Separation Membranes. Industrial & Engineering Chemistry Research 1996;35(4):1231-1234.

27. Freeman BD. Basis of Permeability/Selectivity Tradeoff Relations in Polymeric Gas Separation Membranes. Macromolecules 1999;32(2):375-380.

28. Koros WJ and Paul DR. CO2 Sorption in Poly(ethylene Terephthalate) above and below the Glass Transition. Journal of Polymer Science: Polymer Physics Edition 1978;16:1947-1963.

29. Koros WJ and Paul DR. Transient and Steady-State Permeation in Poly(ethylene Terephthalate) Above and Below the Glass Transition. Journal of Polymer Science: Polymer Physics Edition 1978;16:2171-2187.

30. Merkel TC, Gupta RP, Turk BS, and Freeman BD. Mixed-gas permeation of syngas components in poly(dimethylsiloxane) and poly(1-trimethylsilyl-1-propyne) at elevated temperatures. Journal of Membrane Science 2001;191(1–2):85-94.

31. Lin J, Shenogin S, and Nazarenko S. Oxygen solubility and specific volume of rigid amorphous fraction in semicrystalline poly(ethylene terephthalate). Polymer 2002;43(17):4733-4743.

32. Barrer RM, Barrie JA, and Slater J. Sorption and diffusion in ethyl cellulose. Part III. Comparison between ethyl cellulose and rubber. Journal of Polymer Science 1958;27(115):177-197.

33. Petropoulos JH. Quantitative analysis of gaseous diffusion in glassy polymers. Journal of Polymer Science Part A-2: Polymer Physics 1970;8(10):1797-1801.

34. Koros WJ. Model for Sorption of Mixed Gases in Glassy Polymers. Journal of Polymer Science: Polymer Physics Edition 1980;18:981-992.

35. Paul DR and Koros WJ. Effect of Partially Immobilizing Sorption on Permeability and the Diffusion Time Lag. Journal of Polymer Science: Polymer Physics Edition 1976;14:675-685.

36. Koros WJ and Hopfenberg HB. Small Molecule Migration in Products Derived from Glassy Polymers. Industrial & Engineering Chemistry Product Research and Development 1979;18(4):353-358.

37. Koros WJ, Patton CJ, Felder RM, and Fincher SJ. Kinetics and equilibria of sulfur

dioxide sorption in kapton polyimide. Journal of Polymer Science: Polymer Physics Edition 1980;18(7):1485-1495.

38. Patton CJ, Felder RM, and Koros WJ. Sorption and transport of benzene in poly(ethylene terephthalate). Journal of Applied Polymer Science 1984;29(4):1095-1110.

39. Koros WJ, Chern RT, Stannett V, and Hopfenberg HB. A Model for Permeation of Mixed Gases and Vapors in Glassy Polymers. Journal of Polymer Science: Polymer Physics Edition 1981;19:1513-1530.

40. Chandra P and Koros WJ. Sorption and transport of methanol in poly(ethylene terephthalate). Polymer 2009;50:236-244.

41. Singh A, Freeman BD, and Pinnau I. Pure and mixed gas acetone/nitrogen permeation properties of polydimethylsiloxane [PDMS]. Journal of Polymer Science Part B: Polymer Physics 1998;36(2):289-301.

42. Berens AR and Hopfenberg HB. Diffusion and relaxation in glassy polymer powders: 2. Separation of diffusion and relaxation parameters. Polymer 1978;19(5):489-496.

43. Mauze GR and Stern SA. The solution and transport of water vapor in poly(acrylonitrile): a re-examination. Journal of Membrane Science 1982;12(1):51-64.

44. Guo J and Barbari TA. Unified Dual Mode Description of Small Molecule Sorption and Desorption Kinetics in a Glassy Polymer. Macromolecules 2009;42(15):5700-5708.

45. Flory PJ. Stastical Mechanics of Swelling of Network Structures. The Journal of Chemical Physics 1950;18(1):108-111.

46. Edward JT and Farrell PG. Relation between van der Waals and Partial Molal Volumes of Organic Molecules in Water. Canadian Journal of Chemistry 1975;53(19):2965-2970.

47. Orofino TA, Hopfenberg HB, and Stannett V. Characterization of penetrant clustering in polymers. Journal of Macromolecular Science, Part B 1969;3(4):777-788.

48. Stannett V, Haider M, Koros WJ, and Hopfenberg HB. Sorption and Transport of Water Vapor in Glassy Poly(Acrylonitrile). Polymer Engineering and Science, Mid-March 1980;20(4):300-304.

49. Schuld N and Wolf BA. Solvent quality as reflected in concentration- and temperature-dependent Flory–Huggins interaction parameters. Journal of Polymer Science Part B: Polymer Physics 2001;39(6):651-662.

50. Kamide K, Sugamiya K, Kawai T, and Miyazaki Y. The Concentration Dependence

of the Polymer-Solvent Interaction Parameter for Polystyrene-Methylcyclohexane System. Polym J 1980;12(1):67-69.

51. Zimm BH and Lundberg JL. Sorption of Vapors by High Polymers. Journal of Physical Chemistry 1956;60(4):425-428.

52. Sugden S. Molecular Volumes at Absolute Zero. Part II. Zero Volumes and Chemical Composition. Journal of the Chemical Society 1927:1786-1798.

53. Bondi A. Physical Properties of Molecular Crystals, Liquids, and Glasses. New York: John Wiley & Sons, 1968.

54. van Krevelen DW and te Nijenhuis K. Properties of Polymers: Their Correlation with Chemical Structure, Their Numerical Estimation and Prediction from Additive Group Contributions, 4th ed. Amsterdam: Elsevier Science & Technology, 2009.

55. Park JY and Paul DR. Correlation and prediction of gas permeability in glassy polymer membrane materials via a modified free volume based group contribution method. Journal of Membrane Science 1997;125(1):23-39.

56. Burgess SK, Lee JS, Mubarak CR, Kriegel RM, and Koros WJ. Caffeine Antiplasticization of Amorphous Poly(ethylene terephthalate): Effects on Gas Transport, Thermal, and Mechanical Properties. Polymer 2015, DOI: 10.1016/j.polymer.2015.03.051.

57. Burgess SK, Leisen JE, Kraftschik BE, Mubarak CR, Kriegel RM, and Koros WJ. Chain Mobility, Thermal, and Mechanical Properties of Poly(ethylene furanoate) Compared to Poly(ethylene terephthalate). Macromolecules 2014;47(4):1383-1391.

58. Cohen MH and Turnbull D. Molecular Transport in Liquids and Glasses. The Journal of Chemical Physics 1959;31(5):1164-1169.

59. Doolittle AK. Studies in Newtonian Flow. II. The Dependence of the Viscosity of Liquids on Free-Space. Journal of Applied Physics 1951;22(12):1471-1475.

60. Fujita H, Kishimoto A, and Matsumoto K. Concentration and temperature dependence of diffusion coefficients for systems polymethyl acrylate and n-alkyl acetates. Transactions of the Faraday Society 1960;56(0):424-437.

61. Duda JL, Romdhane IH, and Danner RP. Diffusion in glassy polymers - relaxation and antiplasticization. Journal of Non-Crystalline Solids 1994;172-174:715-720.

62. Lee WM. Selection of barrier materials from molecular-structure. Polymer Engineering & Science 1980;20(1):65-69.

63. Jackson WJ and Caldwell JR. Antiplasticization. II. Characteristics of antiplasticizers. Journal of Applied Polymer Science 1967;11(2):211-226.

64. Jackson WJ and Caldwell JR. Antiplasticization. III. Characteristics and properties of antiplasticizable polymers. Journal of Applied Polymer Science 1967;11(2):227-244.

65. Robeson LM and Faucher JA. Secondary Loss Transitions in Antiplasticized Polymers. Journal of Polymer Science Part B: Polymer Letters 1969;7:35-40.

66. Maeda Y and Paul DR. Effect of Antiplasticization on Gas Sorption and Transport. I. Polysulfone. Journal of Polymer Science: Part B: Polymer Physics 1987;25:957-980.

67. Maeda Y and Paul DR. Effect of Antiplasticization on Gas Sorption and Transport. II. Poly(phenylene Oxide). Journal of Polymer Science: Part B: Polymer Physics 1987;25:981-1003.

68. Maeda Y and Paul DR. Effect of Antiplasticization on Gas Sorption and Transport. III. Free Volume Interpretation. Journal of Polymer Science: Part B: Polymer Physics 1987;25:1005-1016.

69. Bos A, Pünt IGM, Wessling M, and Strathmann H. CO2-induced plasticization phenomena in glassy polymers. Journal of Membrane Science 1999;155(1):67-78.

70. Ismail AF and Lorna W. Penetrant-induced plasticization phenomenon in glassy polymers for gas separation membrane. Separation and Purification Technology 2002;27(3):173-194.

71. Martin O and Avérous L. Poly(lactic acid): plasticization and properties of biodegradable multiphase systems. Polymer 2001;42(14):6209-6219.

72. Achoundong CSK, Bhuwania N, Burgess SK, Karvan O, Johnson JR, and Koros WJ. Silane Modification of Cellulose Acetate Dense Films as Materials for Acid Gas Removal. Macromolecules 2013;46(14):5584-5594.

73. Wind JD, Sirard SM, Paul DR, Green PF, Johnston KP, and Koros WJ. Relaxation Dynamics of CO2 Diffusion, Sorption, and Polymer Swelling for Plasticized Polyimide Membranes. Macromolecules 2003;36(17):6442-6448.

74. Wind JD, Sirard SM, Paul DR, Green PF, Johnston KP, and Koros WJ. Carbon Dioxide-Induced Plasticization of Polyimide Membranes: Pseudo-Equilibrium Relationships of Diffusion, Sorption, and Swelling. Macromolecules 2003;36(17):6433-6441.

75. Schult KA and Paul DR. Water sorption and transport in blends of poly(vinyl pyrrolidone) and polysulfone. Journal of Polymer Science Part B: Polymer Physics 1997;35(4):655-674.

76. Schult KA and Paul DR. Water sorption and transport in blends of polyethyloxazoline and polyethersulfone. Journal of Polymer Science Part B: Polymer Physics 1997;35(6):993-1007.

77. Schult KA and Paul DR. Water sorption and transport in a series of polysulfones. Journal of Polymer Science Part B: Polymer Physics 1996;34(16):2805-2817.

78. Burgess SK, Kriegel RM, and Koros WJ. Diffusion Coefficient Modeling in Polyester Barrier Materials: Applications of Infinite Series Solutions. Society of Plastics Engineers - ANTEC Las Vegas, Nevada, 2014. pp. 830 - 835.

79. Long FA and Richman D. Concentration Gradients for Diffusion of Vapors in Glassy Polymers and their Relation to Time Dependent Diffusion Phenomena1,2. Journal of the American Chemical Society 1960;82(3):513-519.

80. Rodríguez O, Fornasiero F, Arce A, Radke CJ, and Prausnitz JM. Solubilities and diffusivities of water vapor in poly(methylmethacrylate), poly(2-hydroxyethylmethacrylate), poly(N-vinyl-2-pyrrolidone) and poly(acrylonitrile). Polymer 2003;44(20):6323-6333.

81. Arce A, Fornasiero F, Rodriguez O, Radke CJ, and Prausnitz JM. Sorption and transport of water vapor in thin polymer films at 35 [degree]C. Physical Chemistry Chemical Physics 2004;6(1):103-108.

82. Weinmüller C, Langel C, Fornasiero F, Radke CJ, and Prausnitz JM. Sorption kinetics and equilibrium uptake for water vapor in soft-contact-lens hydrogels. Journal of Biomedical Materials Research Part A 2006;77A(2):230-241.

83. Mamaliga I and Negoescu C. Some aspects of two stage diffusion in polymer films and membranes. Environmental Engineering & Management Journal (EEMJ) 2012;11(11):2091-2099.

84. Detallante V, Langevin D, Chappey C, Métayer M, Mercier R, and Pinéri M. Kinetics of water vapor sorption in sulfonated polyimide membranes. Desalination 2002;148(1–3):333-339.

85. Berens AR. The solubility of vinyl chloride in poly(vinyl chloride). Die Angewandte Makromolekulare Chemie 1975;47(1):97-110.

86. Potreck J, Uyar F, Sijbesma H, Nijmeijer K, Stamatialis D, and Wessling M. Sorption induced relaxations during water diffusion in S-PEEK. Physical Chemistry Chemical Physics 2009;11(2):298-308.

87. Sanopoulou M, Roussis PP, and Petropoulos JH. A detailed study of the viscoelastic nature of vapor sorption and transport in a cellulosic polymer. I. Origin and physical implications of deviations from Fickian sorption kinetics. Journal of Polymer Science Part B: Polymer Physics 1995;33(7):993-1005.

88. Sanopoulou M and Petropoulos JH. Systematic Analysis and Model Interpretation of Micromolecular Non-Fickian Sorption Kinetics in Polymer Films. Macromolecules 2001;34(5):1400-1410.

89. Sun Y-M. Sorption/desorption properties of water vapour in poly(2-hydroxyethyl methacrylate): 2. Two-stage sorption models. Polymer 1996;37(17):3921-3928.

90. Joshi S and Astarita G. Diffusion-relaxation coupling in polymers which show two-stage sorption phenomena. Polymer 1979;20(4):455-458.

91. Pomerantsev AL. Phenomenological modeling of anomalous diffusion in polymers. Journal of Applied Polymer Science 2005;96(4):1102-1114.

CHAPTER 3

MATERIALS AND EXPERIMENTAL METHODS

Two industrially important polyesters, poly(ethylene terephthalate) (PET) and poly(ethylene furanoate) (PEF), are studied in the current work. This chapter provides specific details regarding polymer processing (i.e., PET/caffeine compounding, amorphous film preparation, etc.), transport characterization (i.e., permeation, pressure-decay sorption, and gravimetric vapor sorption testing), and material property characterization (i.e., thermal, mechanical, and supplemental characterization techniques).

3.1. Materials

3.1.1. PET, PEF, and Caffeine

Caffeine, poly(ethylene terephthalate) (PET), and poly(ethylene furanoate) (PEF) materials were all provided by the Coca-Cola Company. The PET exhibits an intrinsic viscosity of 0.84 dL/g measured at 30°C using 60/40 phenol/1,1,2,2-tetrachloroethane, which correlates with a M_w of approximately 61,000 g/mol and a M_n of approximately 39,000 g/mol as estimated via the Mark-Houwink relationship [1]. Regarding PEF, both M_w and M_n values were measured by Polymer Standards Service (Germany) using multi-angle laser light scattering (MALLS) and refractive index (RI) methods calibrated with known poly(methyl methacrylate) (PMMA) standards. A combined eluent of hexafluoroisopropanol and 0.05 M potassium trifluoroacetate and a polymer concentration of ~2.5 mg/mL was used for all injections. Since the change in refractive

index versus concentration (d*n*/d*c*) is unknown for PEF, an RI-factor calculated from a PMMA standard was obtained and used to calculate d*n*/d*c* values for PEF. Furthermore, the M_w and M_n values measured by these methodologies are PMMA equivalent molecular weights and are not absolute. Table 3.1 lists relevant structural information for caffeine and both polyesters, while Table 3.2 lists molecular weight information for PEF. An uncertainty of ~5% is estimated for M_w values calculated via both methods, while ~5% and ~15% uncertainties are estimated for M_n values calculated via RI and MALLS methods, respectively.

Table 3.1. Structural information for PET, PEF, and caffeine.

Material	Structure
Poly(ethylene terephthalate)	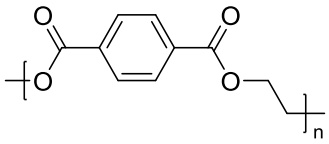
Poly(ethylene furanoate)	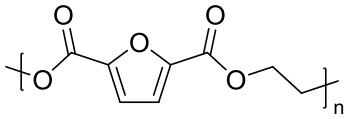
Caffeine	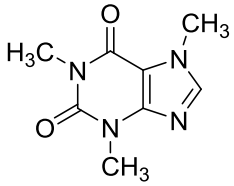

Table 3.2. PMMA equivalent molecular weight values for PEF measured by Polymer Standards Service using multi-angle laser light scattering (MALLS) and refractive index (RI) methods.

Method	M_w (g/mol)	M_n (g/mol)
MALLS	87,000	66,000
RI	110,000	47,000

As a note, all PET and PEF samples characterized throughout the remainder of the thesis were taken from the same respective "master" batch of polymer, thereby allowing for consistent and meaningful comparisons to be made regarding the data reported herein.

3.1.2. PET/Caffeine Melt-Mixing

As mentioned previously, a main goal of this work is to investigate the effect of antiplasticization as it relates to the PET/caffeine system. A Brabender batch mixer (Intelli-Torque Plasti-Corder®, 3 piece mixer) was used to mix PET batches with variable caffeine loading. Roller-type blades were used to provide homogeneous mixing in the melt via high shear, and the final recovered PET/caffeine batches weighed ~35 g each. All batches were prepared at 265°C with a head speed of 60 rpm with the following nominal caffeine loadings: 0, 3, 5, 10, 15, and 20 wt%. Prior to melt-compounding, the polymer was dried at 120ºC under vacuum for at least 12 hours, and the caffeine was dried at 95ºC and 0% RH (via dry nitrogen purge) for 110 minutes to minimize polyester degradation due to hydrolysis. Once dried, the PET was introduced into the preheated, rotating mixing head over a period of ~1.5 minutes, followed by the addition of caffeine over the next thirty seconds. After all materials had been added to the mixing head, the batch was allowed to mix with the head closed for a total time of 11 minutes before

opening the head and allowing the sample to collect on aluminum foil and air cool. The mixing period of 11 minutes was found to give uniform differential scanning calorimetry thermograms for multiple samples from the same batch. Great care was taken to ensure that the mixing head was clean before processing the next PET/caffeine batch. The cleaning procedure began by mixing a batch of glass-filled styrenic resin (NewEX Asaclean) in the PET-contaminated mixing head for 10 minutes at 265ºC, followed by cooling the mixing head to 170ºC before mixing a batch of 20 wt% $CaCO_3$—80 wt% polyethylene/polypropylene (PE/PP) copolymer for 20 minutes. After processing the first polyolefin batch at 170ºC, three subsequent batches of 100% PE/PP were each mixed for 20 min at 170ºC before finally re-heating the head to 265ºC and proceeding with the next PET/caffeine batch.

3.1.3. Film Preparation

Amorphous polyester films were prepared via a melt press procedure similar to that developed by Lee et al. [2]. When preparing pure polymer films, the as-received polymers were cryogenically ground into powder and dried at 120°C under vacuum for 24 hours prior to melt pressing to remove residual water. A similar drying step was followed for all PET/caffeine samples; however, an additional cryogenic grinding step was needed prior to drying to reduce the size of the batch taken from the Brabender into smaller pieces to facilitate further processing. Films were pressed under vacuum between two non-stick metal sheets (Faberware®) in a Wabash press at 30 tons and 270°C for 30 seconds before immediately quenching in a bath of room temperature water. Special care was taken to evenly spread the polymer powder over the entire pressing surface prior to

pressing to minimize possible melt-orientation effects. The film thickness was controlled by the thickness of stacked aluminum shim layers (hard-temper aluminum foil, McMaster Carr, three mils thick), which had two 9 cm circles cut out for where the dried polymer was placed before pressing. The quenched films were dried at 35°C under vacuum overnight before storing in plastic sample bags at room temperature. All films were amorphous as determined by differential scanning calorimetry and x-ray diffraction (discussed later in Sections 3.5.1 and 3.7.3, respectively). Additional description of the melt-press process, including a schematic representation, is provided in the work of Lee [3].

3.1.4. Gases and Vapors

Research grade oxygen and carbon dioxide (>99.999%) were provided by Airgas (Radnor, PA), and were used as-received. De-ionized water, which was obtained "in-house," was used for all water sorption testing experiments. As discussed previously, the aforementioned species represent the most important penetrants for barrier property testing in beverage packaging applications.

3.2. Gas Permeation Testing

3.2.1. Isochoric Permeation Apparatus

All permeation data reported herein were measured using a similar constant-volume variable-pressure system utilized in prior work [2, 4]. A schematic representation of a typical *pure gas* permeation system is provided in Figure 3.1, where the upstream and downstream sections (with respect to the permeation sample cell) are represented by the

red and blue lines, respectively. Permeation systems which allow for multicomponent feeds are slightly more complex, and descriptions of such systems can be found in prior work [3, 5].

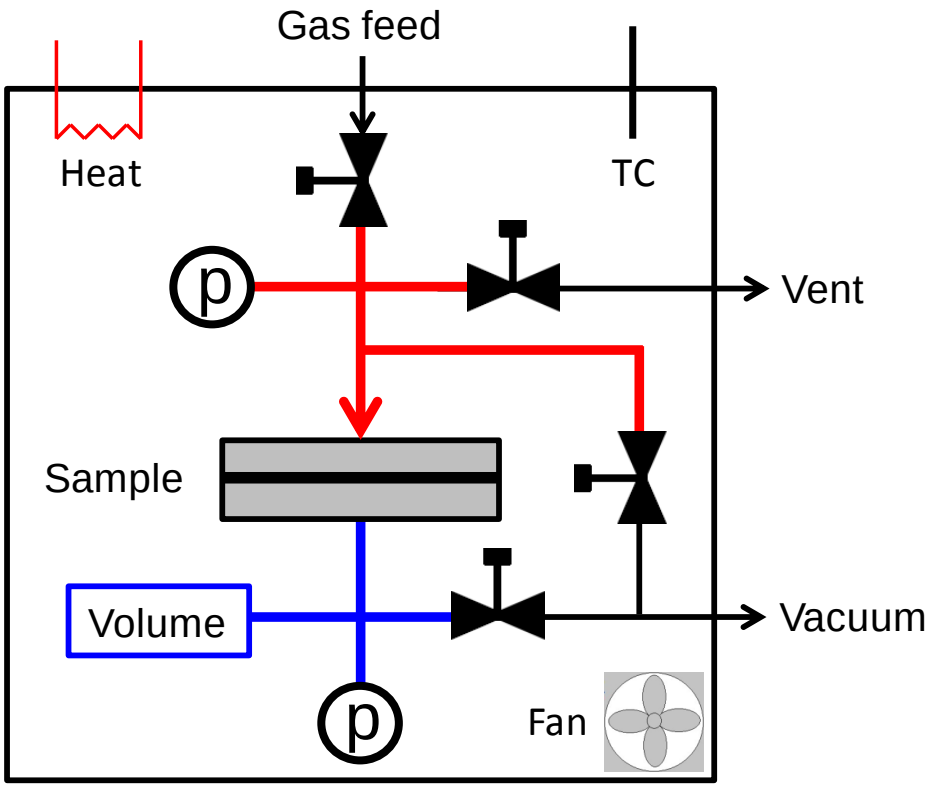

Figure 3.1. Representation of the constant-volume, variable-pressure pure-gas permeation system used in the current work. The red and blue lines represent the upstream and downstream, respectively, and pressure transducers are represented by a lowercase p. "TC" stands for thermocouple.

All permeation measurements reported herein were measured at constant temperature, which was maintained inside the insulated permeation box by a temperature controller (Thermoworks, Alpine, UT) attached to a thermocouple and heat tape. Temperature uniformity throughout the box was achieved via incorporation of a fan, and the box was kept closed during testing. Swagelok® fittings and valves made of 316 SS were used to

construct the system, and VCR fittings, which utilized nickel or stainless steel gaskets, were used to construct the downstream portion of the system to minimize the leakage of atmospheric gas into the downstream. The upstream pressure transducer, which is a Model Z transducer with a 1000 psia maximum pressure rating (Sensotec, Columbus, OH), was shunt-calibrated at each temperature to ensure accuracy of the pressure reading prior to testing. The downstream pressure transducer, which is a Baratron® 121AA capacitance manometer, had a much lower pressure rating of 10 torr in order to detect the small change in downstream pressure resulting from the permeating gas. Vacuum conditions were maintained on the downstream, prior to testing, using a rotary vacuum pump (RV3, Edwards, Wilmington, MA). Permeability calculations were performed using the method discussed later in Section 3.2.3, which employs characteristic properties of the system illustrated in Figure 3.1 (i.e., temperature, upstream pressure, etc.).

3.2.2. Permeation Cell Design and Film Masking

A schematic representation of the permeation cell, which was designed specifically herein for barrier testing, is provided in Figure 3.2 (top view) and Figure 3.3 (side view). The design illustrated in Figures 3.2 and 3.3 provides multiple improvements to that reported previously for barrier material testing [4]. Specifically, clamping the finished cell into a vice is facilitated by the two flat faces cut into the cell as shown by the top view in Figure 3.2. Furthermore, the cell was machined from a sheet of highly polished stainless steel, which improves adhesion between the surface and aluminum tape and reduces the leak of atmospheric gases into the downstream.

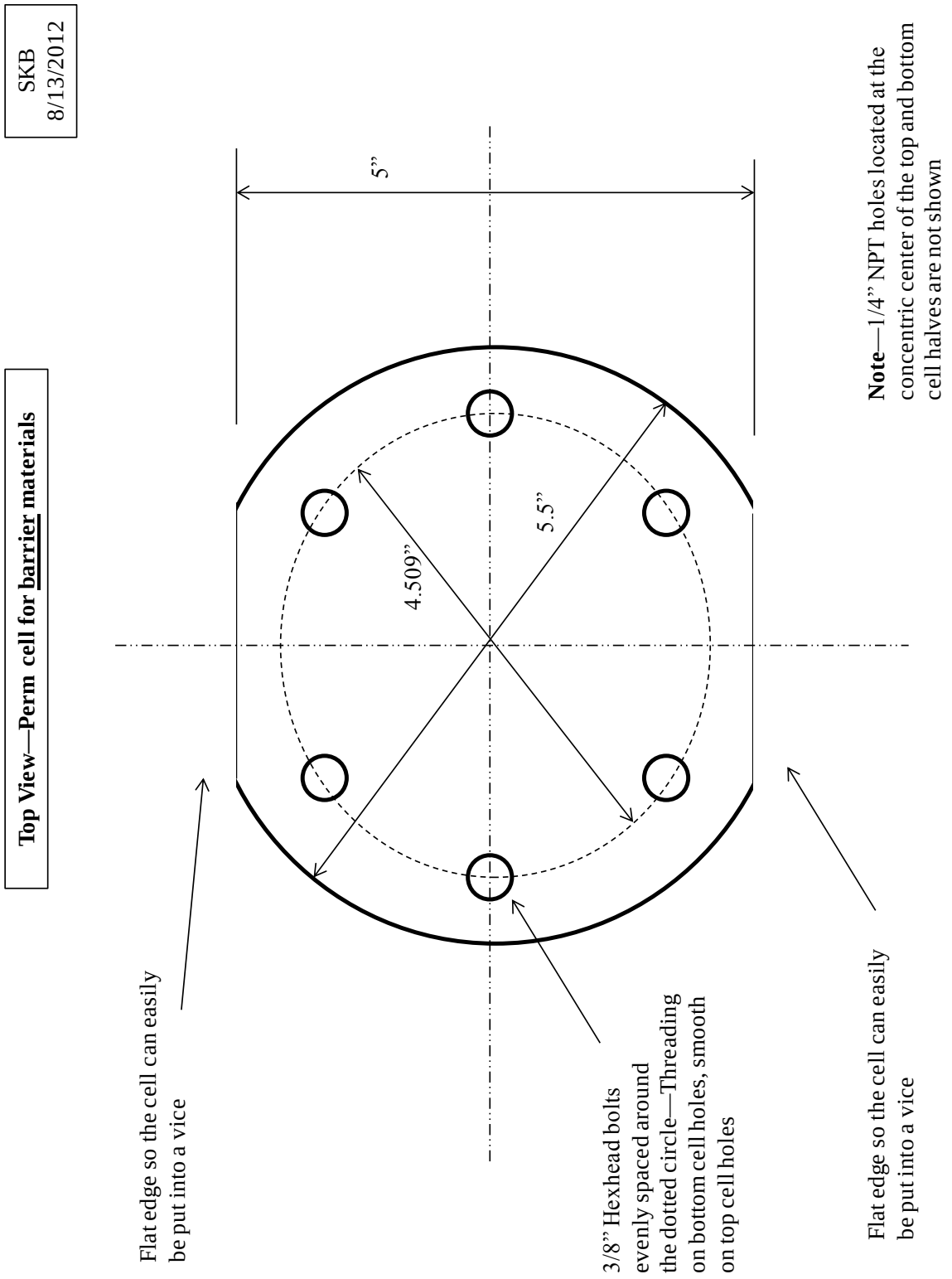

Figure 3.2. Top-view of the permeation cell designed for barrier material testing.

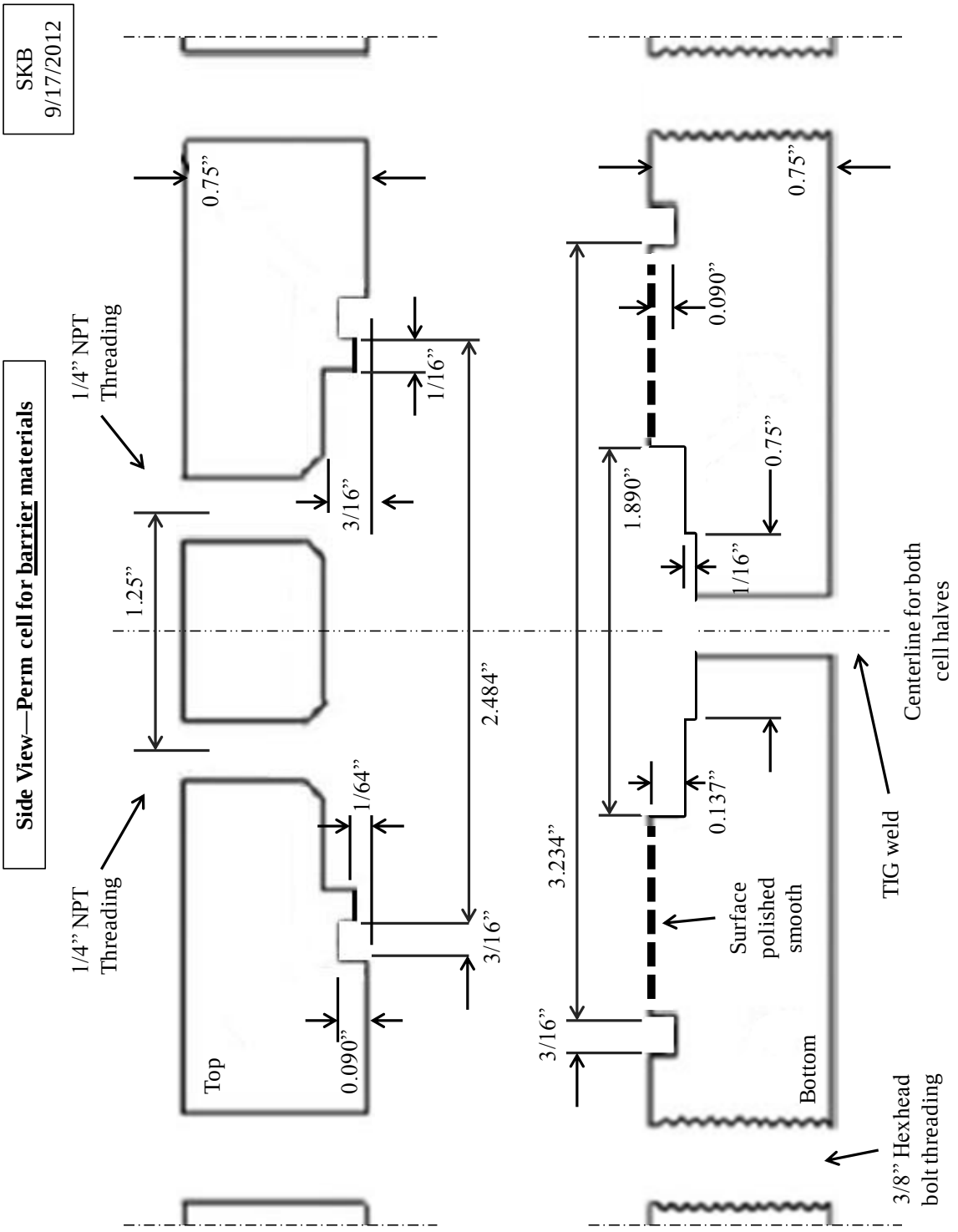

Figure 3.3. Side-view of the permeation cell designed for barrier material testing.

A schematic of the polymer film masking technique is provided in Figure 3.4. The polyester films ("d" in Figure 3.4) were masked onto the permeation cell using aluminum tape (Intertape ALF200L, "e" in Figure 3.4) and the polymer/tape interface sealed using Duralco 4525 epoxy (Cotronics, "f" in Figure 3.4) via a similar procedure reported by Moore et al. [6]. The letter "a" in Figure 3.4 represents a porous, sintered stainless steel disc, while "b" is perforated metal frit and "c" represents at least two pieces of Whatman™ filter paper. The O-rings which make the seal between the top and bottom cell halves are indicated by letter "g" in Figure 3.4. Thickness values for the polymer films were measured using a digital micrometer (Mitutoyo Series 293), and the permeation area of each film was determined via computer imaging software analysis (ImageJ) of the scanned films. Additional details regarding the experimental permeation apparatus are also available in prior work [3, 5].

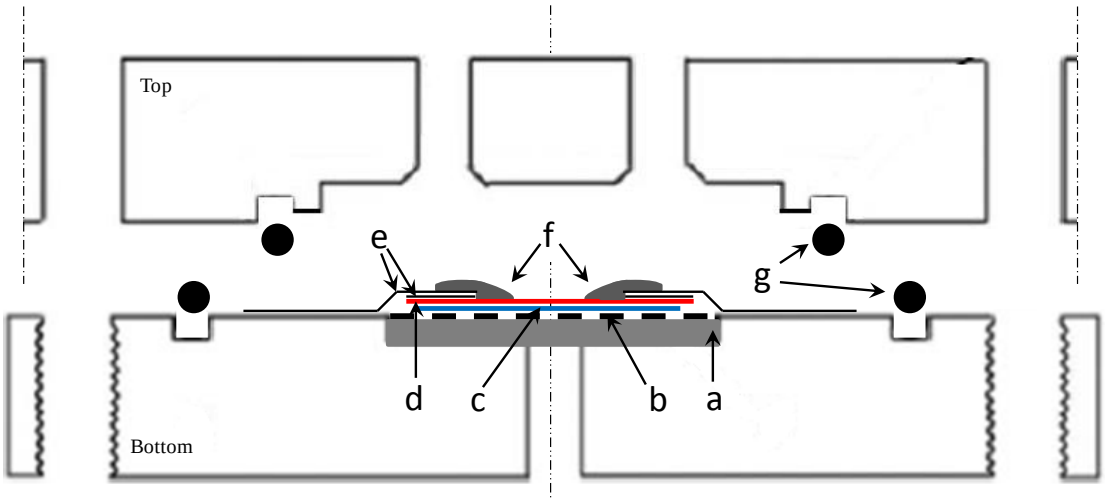

Figure 3.4. Film masking technique used for permeation testing of barrier materials.

3.2.3. Permeation-Specific Calculations

All permeability data in the current work are reported in units of Barrer, via Equation 3.1.

$$1\ \text{Barrer} = 10^{-10}\ \frac{ccSTP \cdot cm}{cm^2 \cdot s \cdot cmHg} \tag{3.1}$$

A typical isochoric permeation test first requires degassing the polymer film for a set amount of time (i.e., greater than 10 time-lags), before applying a non-zero pressure on the upstream face of the film and tracking the downstream pressure as a function of time. The downstream pressure will remain constant until the penetrant diffuses through the entire film and "breaks through" the downstream face, after which the downstream pressure will begin to increase versus time. Such transient behavior in downstream pressure is characterized by the time-lag, θ, which was discussed previously in Chapter 2. Graphical representation of the time-lag is illustrated in Figure 3.5, along with the corresponding relationship between θ and diffusivity (cf. Equation 2.29, discussed previously), and a graphical representation of the steady-state penetrant flux (N). Recall that the time-lag can also be used to estimate the penetrant solubility in the polymer via Equation 2.28, as discussed previously.

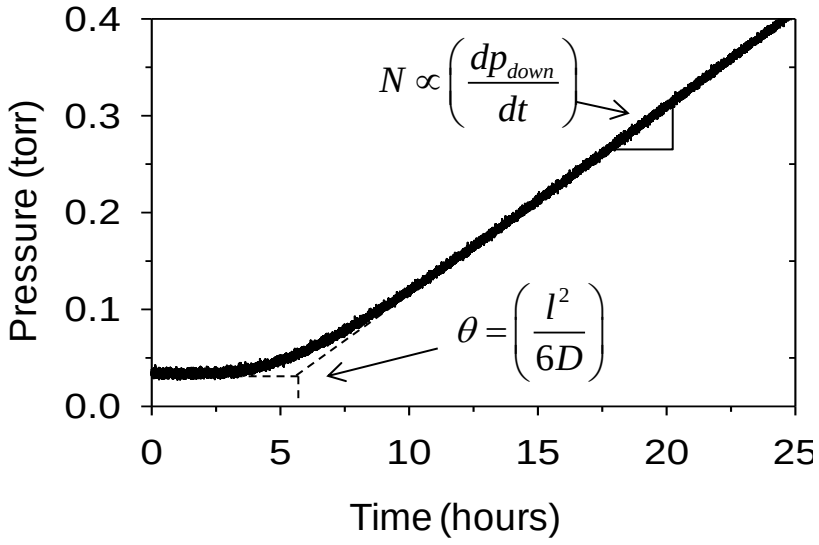

Figure 3.5. Graphical representation of the time-lag (θ) from a transient permeation test.

As discussed in Chapter 2, the permeability is related to the steady-state flux across the film via Equation 2.14. A more detailed expression for the permeability, as it pertains to determination via the isochoric methodology described previously, is provided in Equation 3.2.

$$P = \left(\frac{dp_{down}}{dt} \right) \left(\frac{V_{down}}{RT} \right) \left(\frac{l}{Ap_{up}} \right) \tag{3.2}$$

In Equation 3.2, P is the penetrant permeability, dp_{down}/dt is the steady-state change in downstream pressure versus time, V_{down} is the downstream volume of the permeation apparatus, R is the universal gas constant, T is the temperature of the polymer film in Kelvin, l is the polymer film thickness, A is the film area, and p_{up} is the upstream pressure.

For cases involving permeation testing at multiple temperatures, permeation measurements were recorded starting at the lowest temperature using fully degassed films after thorough degassing for >24 hours (which was >10 time-lags for all cases). After final exposure to the highest pressure at a given temperature, the samples were again thoroughly degassed before proceeding to the next temperature. Time-lags were recorded at 1 atm pressure for each temperature, and steady-state permeation values were calculated using the slope of pressure vs. time data (dp/dt) between approximately 5 – 10 time-lags for each permeation run [7]. The time-lags recorded at 1 atm were used in further transport analysis and parameter cross-verification. In all cases, replicate measurements were recorded for both time-lag and steady-state permeation values, and uncertainty limits estimated from the standard error.

Special care was taken to measure the downstream leak rate prior to recording permeation data due to the high barrier nature of both PET and PEF materials, and leak corrections were applied to all respective measurements. Any isochoric permeation system which utilizes a downstream vacuum is subject to a non-zero leak of atmospheric gases into the system. This leak rate, while negligible when compared to the permeation rate for non-barrier polymers, must be considered when testing barrier polymers such as PET and PEF. The atmospheric leak rate was measured on each fully degassed film prior to permeation testing by isolating the downstream from vacuum and recording the pressure vs. time response over a duration of ~1 hr. The leak rate was then determined from the slope in data as shown in Figure 3.6. After leak testing, the downstream was degassed once more prior to commencing the actual permeation test.

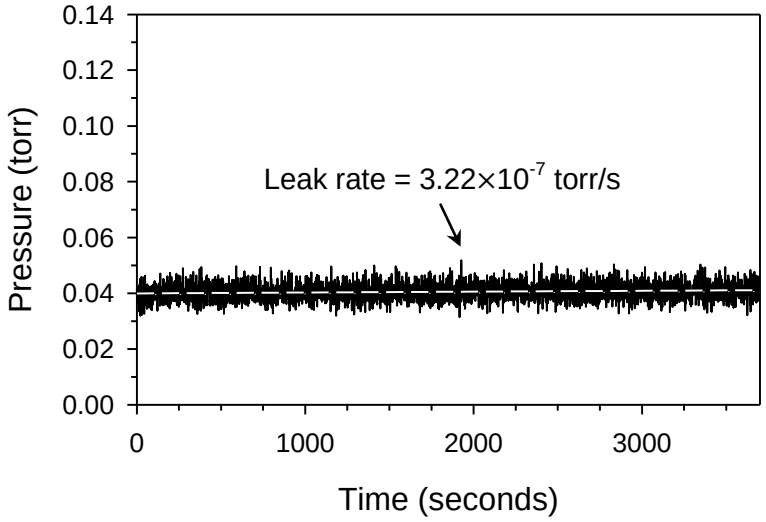

Figure 3.6. Example downstream leak rate data at 30°C for oxygen in PEF.

Application of the measured leak rate correction to actual permeation data was straightforward. The atmospheric leak contribution to the downstream pressure during each permeation test was calculated by multiplying the predetermined leak rate with the elapsed measurement time. Simple subtraction of the small leaked pressure contribution from the total downstream pressure for each measurement thereby allowed determination of the downstream pressure response resulting solely from permeation. These corrections were largest for oxygen at 1 atm, and became subsequently smaller with increasing feed pressure. Figure 3.7 shows example permeation data at 30°C and 1 atm oxygen for PEF, both before (black data) and after (blue data) application of the leak rate correction illustrated in Figure 3.6. Permeation time-lags were also slightly affected as a result of the leak rate correction. The permeation results reported herein for both PET and PEF were found to exhibit excellent reproducibility *only* after application of the leak correction methodology outlined in this section. Furthermore, the difference between corrected and un-corrected data illustrated in Figure 3.7 will become increasingly smaller as the

upstream pressure is increased beyond 1 atm oxygen (i.e., the permeation rate will increase while the leak rate will remain unchanged).

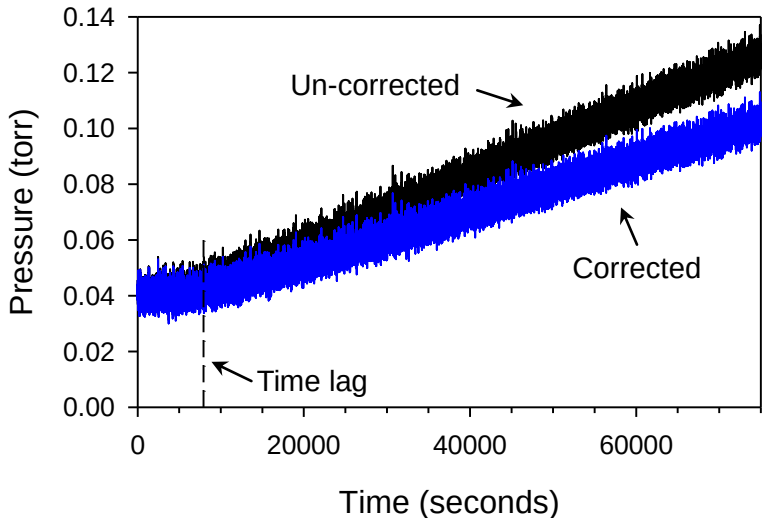

Figure 3.7. Example permeation data for oxygen at 1 atm in PEF at 30°C. The black data represents permeation data without the leak correction, while the blue data represents permeation data with the leak correction [8]. The magnitude of the leak correction decreases as the feed pressure increases.

3.3. Pressure-Decay Sorption

3.3.1. Isochoric Sorption Apparatus

As mentioned previously in Chapter 2, both equilibrium and kinetic sorption isotherms for oxygen and carbon dioxide uptake in polyester barrier materials can be measured using a constant-volume, pressure-decay technique. A graphical representation of the system used herein, which resembles that described elsewhere [9, 10], is provided in Figure 3.8.

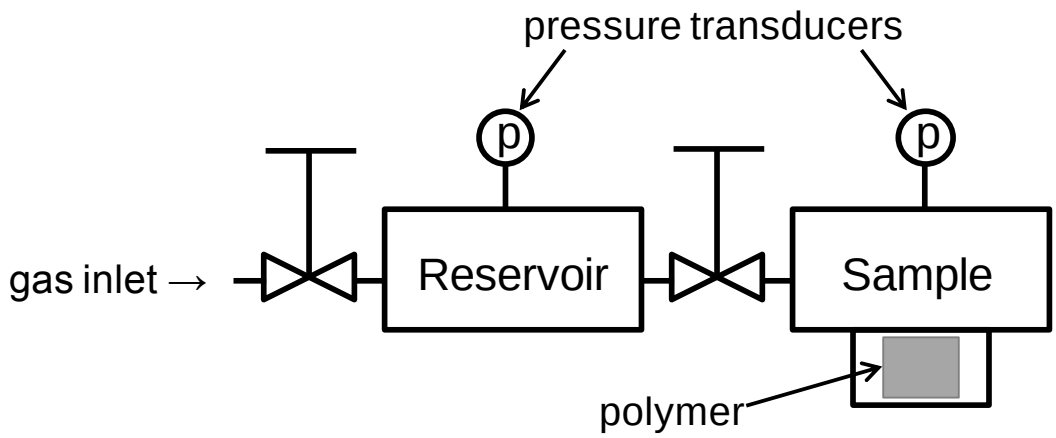

Figure 3.8. Representation of the constant-volume, pressure-decay apparatus used in the current work.

Due to the low solubility of oxygen in both PET and PEF, special precautions were needed to obtain accurate sorption measurements. High accuracy 500 psia transducers (Honeywell STJE) were used in conjunction with a custom-built high capacity sample cell designed to decrease the void volume to sample volume ratio. A constant testing temperature was obtained by immersing the sorption apparatus in an oil bath (Duratherm S) controlled using a bath heater/circulator (PolyScience). Temperature and pressure dependent compressibility factors (z) were used to correct for the relatively small gas phase non-ideality of oxygen and carbon dioxide at the testing conditions, and were calculated using the NIST extended corresponding states equation via the NIST SUPERTRAPP program (cf. Appendix K). Pressure-decay sorption measurements were typically recorded in 1 atm intervals from 0 – 10 atm for oxygen and 0 – 6 atm for carbon dioxide at 35°C first, followed by degassing the sample and repeating the measurements at the next higher temperature. Use of accurate density values for both polyesters is important for accurate sorption measurements due to the exceedingly low solubility of

oxygen.

Calibration of the reservoir and sample volumes was performed using a series of mole balances (i.e., pressure expansions), which were performed using both an empty sample volume and a sample volume filled with precision ball bearings of known dimension. Once calibrated, the sorption uptake of carbon dioxide in polydimethylsiloxane (PDMS), which is well characterized in the literature, was measured and compared against literature values to verify the accuracy of the sorption apparatus.

3.3.2. Pressure-Decay Sorption Data Transform

As briefly mentioned in Section 2.4, the raw pressure-decay data can be transformed to represent a non-dimensional mass uptake which varies from zero to one (i.e., M_t/M_∞, which represents the mass of penetrant uptake at time t divided by the equilibrium mass uptake after equilibrium). Such a transform, as it relates to pressure-decay data, is provided in Equation 3.3, where p represents the pressure in the sample cell, and *final* and *initial* represent the pressure at the end and beginning of the diffusion process, respectively.

$$\frac{M_t}{M_\infty}(t) = \left(\frac{p_{initial} - p(t)}{p_{initial} - p_{final}} \right) \tag{3.3}$$

Example raw pressure-decay data for oxygen in amorphous PEF at 35°C during sorption between the pressure interval 0 to 1.1 atm oxygen is provided in Figure 3.9, while the corresponding data, after transformation via Equation 3.3, is provided in Figure

3.10. A model fit of the Fickian diffusion model (cf. Equation 2.47) to the transformed data in Figure 3.10 is illustrated later in Chapter 6 [8].

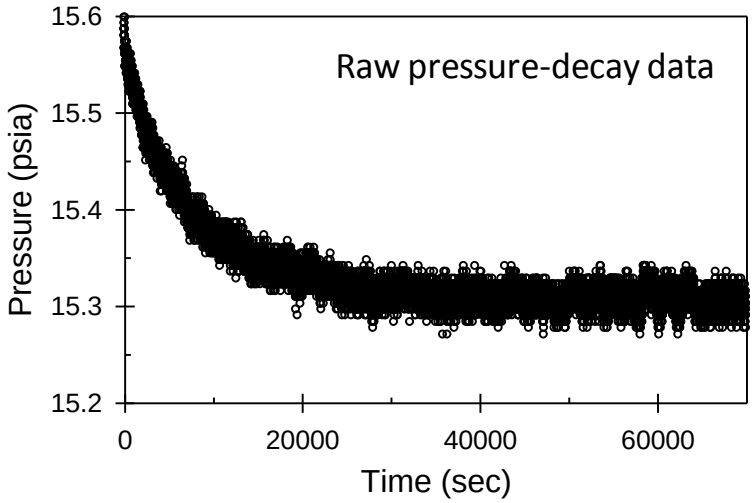

Figure 3.9. Example pressure-decay data for oxygen in amorphous PEF at 35°C from the pressure interval 0 to 1.1 atm oxygen [8].

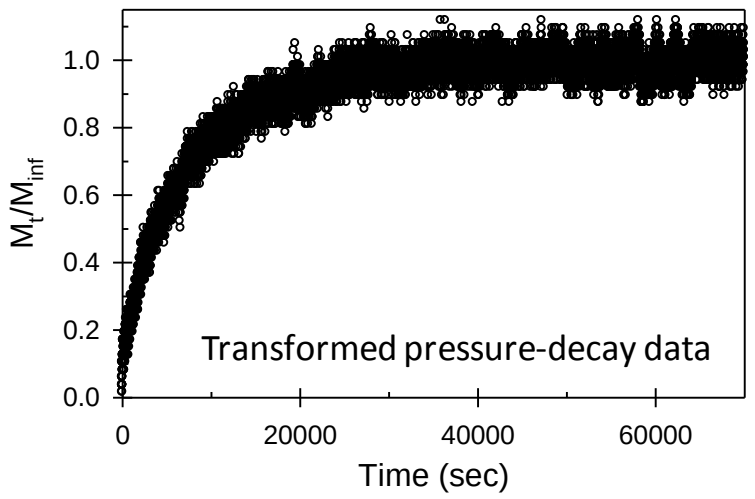

Figure 3.10. Transformed pressure-decay data, which varies from zero to one, from Figure 3.9 after application of Equation 3.3.

Estimation of the penetrant solubility from pressure-decay sorption involves a simple penetrant mole balance. Example sorption calculations are not provided in this chapter;

however, such information can be found in the work of Koros and Paul [9].

3.4. Gravimetric Vapor Sorption

Water is more condensable than oxygen and carbon dioxide, and consequently, exhibits a much larger uptake in both polyesters that can be studied via gravimetric methods. This section outlines the three independent water sorption techniques that are employed in the current work, and concludes with a description of the data transform required to normalize the water uptake data prior to diffusion coefficient modeling.

3.4.1. Quartz Spring Sorption

Water vapor uptake at relatively low activities (i.e., <0.7) can be measured accurately with the manual McBain quartz spring technique [11], which is described in detail in prior work [5, 12-14]. The quartz spring technique functions by hanging a polymer film on a sensitive spring made of quartz glass, and the vertical position of the polymer is monitored by a cathetometer during the process of penetrant sorption. Since the spring constant is known via prior calibration, any vertical change in position of the film can be converted directly, via Hooke's law, to the corresponding mass of water uptake by the polymer. The quartz spring apparatus operates at a fixed temperature under vacuum conditions, where the temperature of the chamber is controlled by a water jacket. Vapor condensation on the inner apparatus walls can be problematic at high penetrant activity, and as a result, the quartz spring system is best suited to testing at low and intermediate activities. A schematic of the quartz spring technique utilized in the current work is provided in Figure 3.11 (taken from ref. [5]), and data corresponding to water uptake in

amorphous PET and PEF are provided in Chapters 8 and 9 [15, 16].

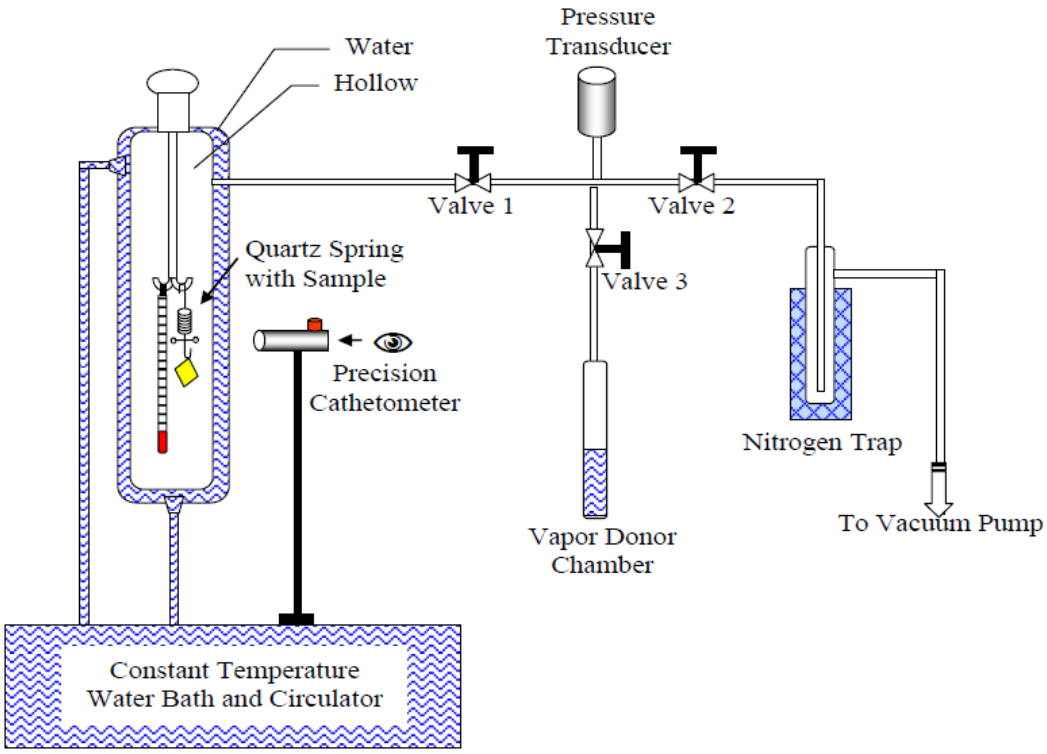

Figure 3.11. Schematic of the McBain quartz spring apparatus used in the current work, from ref. [5].

3.4.2. Automated Vapor Sorption

In contrast to the quartz spring technique, which is manually operated, the TA VTI-SA+ vapor sorption analyzer (TA Instruments, New Castle, DE) provides an additional gravimetric sorption technique that allows for fully automated control between 0 – 0.95 activity. The accuracy and calibration of the instrument was verified by performing routine water vapor sorption experiments on sodium chloride and polyvinylpyrrolidone according to the methodology established by the instrument vendor. This system provides a humidified nitrogen stream by mixing a separate wet and dry stream, which are

controlled by two individual mass flow controllers. The resulting humidified stream flows through a dew point analyzer, which continuously measures the water content in the stream and provides feedback to the instrument to allow for automated control. After exiting the dew point analyzer, the humid stream passes over a quartz basket containing the polymer sample, which is attached to a sensitive microgram balance (accuracy ± 0.1%). Once the mass uptake for a given activity has reached equilibrium, the system automatically proceeds to the next programmed activity step. Equilibrium is realized when the mass uptake over a specified time interval falls below a threshold limit, e.g. 0.0015% mass change in 99 minutes. Multiple equilibration intervals were needed at high activity for sorption testing involving both PET and PEF due to the protracted gradual increase in water uptake resulting from non-Fickian relaxations. Film samples with an approximate thickness of ~160 microns were initially dried in the instrument at 45°C until constant mass was achieved, prior to commencing sorption. Interval sorption measurements were recorded using water activities ranging from 0 – 0.9 in increments of 0.1, along with a final value of 0.95. Both sorption and desorption interval measurements were recorded over the entire activity range, followed by a second set of interval sorption and desorption measurements recorded at 0.3, 0.6, and 0.95 activity. The presence of long-term non-Fickian relaxations prevented attainment of true equilibrium mass uptake between the sorption values of 0.7 – 0.95. However, as will be shown and discussed later in Chapters 8 and 9 [15, 16], the overall implications of this reality appear to be negligible.

As previously discussed in Section 2.4.3, the automated system produces anomalous sorption behavior that, for modeling purposes, can be accommodated by implementation

of a time-dependent boundary condition. The anomalous kinetics result primarily from a lag introduced by the process control scheme employed by the instrument. Recall that the VTI instrument produces a desired water concentration by mixing a dry nitrogen stream with a completely humidified stream and selectively controlling the respective flow rates using two separate mass flow controllers. After uptake equilibrium is achieved at the current water activity, the instrument automatically adjusts the flow rates of the wet and dry streams to produce the next desired activity. The automated control scheme obtains feedback from the measured water content determined by a dew point analyzer. Upon any activity change (sorption or desorption), the instrument will initially adjust the wet/dry flow rates to obtain a first guess for obtaining the new set-point activity. With the new flow rates held constant, the instrument then averages multiple activity readings over a discrete period of time (~1 min). If the averaged activity is different from the set-point after this period, the instrument implements a small change to the wet/dry flow rates, and the process is repeated until the perfect set-point activity is achieved. While the system typically achieves the desired set-point after only a few minutes, this variability is enough to produce anomalous sorption kinetics. Further description and justification for the usage of the time-dependent boundary condition implemented in Section 2.4.3 is provided later in Chapter 9 [16].

Water sorption data measured by the automated VTI instrument for amorphous PET and PEF are provided in Chapters 8 and 9 [15, 16], and are shown to be consistent with the uptake data measured by the quartz spring apparatus, which was described previously.

3.4.3. Liquid Water Sorption

Both the automated VTI sorption system and the manual quartz spring system are unable to measure water sorption data at complete saturation (i.e., unit activity) due to water condensation. To circumvent this problem, measurements at unit activity were made by submerging thick, amorphous PET and PEF samples in de-ionized liquid water at 35°C and periodically removing the samples and recording their masses on a sensitive microgram balance (Mettler Toledo XP6). The samples were sufficiently thick (i.e., ~500 microns for PEF, ~890 microns for PET) so that desorption during the weighing step was negligible. Mass measurements were recorded until constant uptake was achieved, and the corresponding values represent the integral sorption step between zero and unit activity. Four replicate samples were tested for both polyesters to allow calculation of uncertainty limits via the standard error. Thickness values for the polymer films were measured on the initially dry samples and again after exposure to liquid water at 35°C for approximately four months to quantify the effect of swelling. This gravimetric sorption technique allows for completion of the sorption data set by covering the entire activity range from zero to unit activity. The water uptake measured via this technique allowed determination of the true equilibrium uptake at unit activity, and provides a consistency check for data obtained using the other two sorption techniques.

3.4.4. Gravimetric Vapor Sorption Data Transform

Gravimetric water sorption data are typically reported in units of weight percent water (wt%, g H_2O/g dry polymer) and, similar to the pressure–decay data transform in Equation 3.3, can be converted via Equation 3.4 to a non-dimensional form useful for

extracting kinetic information.

$$\frac{M_t}{M_\infty}(t) = \left(\frac{m(t) - m_{initial}}{m_{final} - m_{initial}} \right) \tag{3.4}$$

In Equation 3.4, M_t represents the water uptake at time t, M_∞ is the water uptake at equilibrium (i.e., infinite time), m is the sample mass measured by the balance, *initial* represents the beginning of the sorption interval, and *final* represents the end of the sorption interval. Similar to the transformed pressure-decay data, the M_t/M_∞ parameter in Equation 3.4 therefore represents a normalized, non-dimensional quantity that varies from zero to unity. Equation 3.4 is valid for all three independent gravimetric sorption techniques discussed previously.

3.5. Thermal Characterization

3.5.1. Differential Scanning Calorimetry

Differential scanning calorimetry (DSC) is a useful characterization technique that is used to investigate the relevant thermal properties of the melt-pressed PET and PEF films described throughout the remainder of this work. A typical heat-flux DSC operates by comparing the heat flow in a sample pan (i.e., crimped aluminum pan which contains the polymer sample) to the corresponding heat flow in an empty aluminum reference pan while both are subjected to the same defined temperature ramp. Various descriptions of polymer thermal analysis as it relates to DSC testing can be found in multiple works in the literature [17-20].

A TA Q1000 DSC (TA Instruments, New Castle, DE) was used to measure all DSC data reported in the current work. Temperature ramps of either 10 or 20°C/min were used when heating and cooling between 0 and approximately 300°C, and a dry nitrogen purge in the sample cell was used in all tests. Instrument calibrations were performed using indium and sapphire standards, as per the methodology described by the instrument vendor. Application-specific DSC test methods for general thermal analysis are provided later in each corresponding chapter, along with a description for the method used to determine the glass transition temperature (T_g). The general thermal properties of a polymer which can be measured by DSC are illustrated in Figure 3.12 for PET.

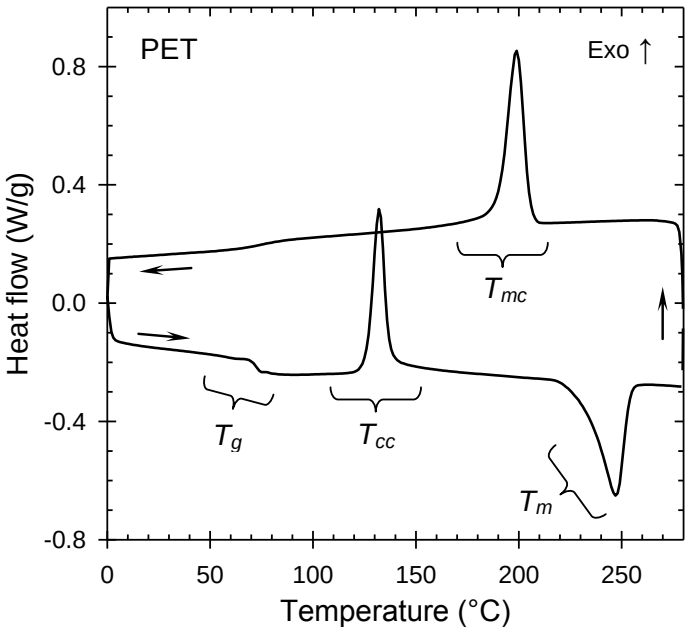

Figure 3.12. Example DSC trace for PET during heating and subsequent cooling at 10°C/min. The heat-cool cycle illustrates the four major thermal events as indicated by the following subscripts: *g* = glass transition, *cc* = cold crystallization, *m* = melting, and *mc* = melt crystallization [21].

As mentioned previously, DSC can also be used to verify the amorphous morphology of all PET, PEF, and PET/caffeine films obtained using the melt-press procedure

described in Section 3.1.3. A representation of the crystalline weight fraction (X_c) of a polymer is provided in Equation 3.5 [18], where ΔH_f is the enthalpy of fusion, ΔH_c is the enthalpy of cold crystallization, and ΔH_f^0 is an estimate for the enthalpy of fusion for the material at 100% crystallinity. Values of $X_c \approx 0$ were determined experimentally for all samples obtained using the melt-press procedure described previously, thereby confirming the amorphous morphology of the samples.

$$X_c = \left(\frac{\Delta H_f - \Delta H_c}{\Delta H_f^0} \right) \tag{3.5}$$

In addition to verifying the amorphous morphology and characterizing the thermal features illustrated in Figure 3.12, DSC can also be used to investigate the physical aging properties of glassy polymers. Enthalpic recovery measurements via DSC are convenient to perform, since aging and thermal cycling of the sample can be conducted accurately *in situ* within the DSC instrument. Detailed information regarding the DSC method used to characterize the aging properties of amorphous PEF is provided later in Chapter 10 [22].

3.5.2. Thermogravimetric Analysis

Thermogravimetric analysis (TGA) provides information regarding the weight loss of a polymer sample as a function of both time and temperature, and is useful for characterizing the melt-pressed PET/caffeine films discussed previously. Caffeine can show sublimation/vaporization at the melt processing temperature of PET [23], and as a result, the final caffeine content of the PET mixtures after processing can be reduced

slightly compared to the nominal content that was initially loaded into the mixing head. Furthermore, any subsequent drying or melting step (i.e., melt pressing) could result in small caffeine losses. Lee et al. [2] used thermogravimetric analysis to determine the final weight fraction of volatile additives (i.e., phenacetin and acetanilide) in their PET film samples, and a modified method was adopted for this work, where the primary difference concerns the assignment of water content in the samples. In the current method, a film sample was heated from room temperature to 110°C at a rate of 20°C/min, held isothermally at 110°C for 30 min, and subsequently heated to 270°C at a rate of 20°C/min before a final isothermal step lasting one hour. The weight percent water for a given sample is assigned to the weight loss during the initial holding time of 30 minutes at 110°C, and the weight percent caffeine is assigned to the weight loss during a final isothermal step of one hour at 270°C. Interestingly, the 0 wt% caffeine films (i.e., pure PET) experienced ~0.28 ± 0.02 wt% loss during the isothermal step at 270°C. This weight loss is attributed to the evolution of acetaldehyde and cyclic oligomers formed during melt-mixing [24], and was subtracted from all subsequent PET/caffeine film samples. A weight loss versus time and temperature profile for an example PET/caffeine film is provided in Figure 3.13, which is similar to that observed for PET/phenacetin and PET/acetanilide reported elsewhere (cf. Figure 1 in ref. [2]). All caffeine composition data were measured on a TA Q5000 TGA instrument operated with a dry nitrogen purge, and the composition values reported throughout the remainder of this work represent the final actual caffeine content in the compounded polymer films. Data corresponding to PET/caffeine films are provided later in Chapter 4 [21].

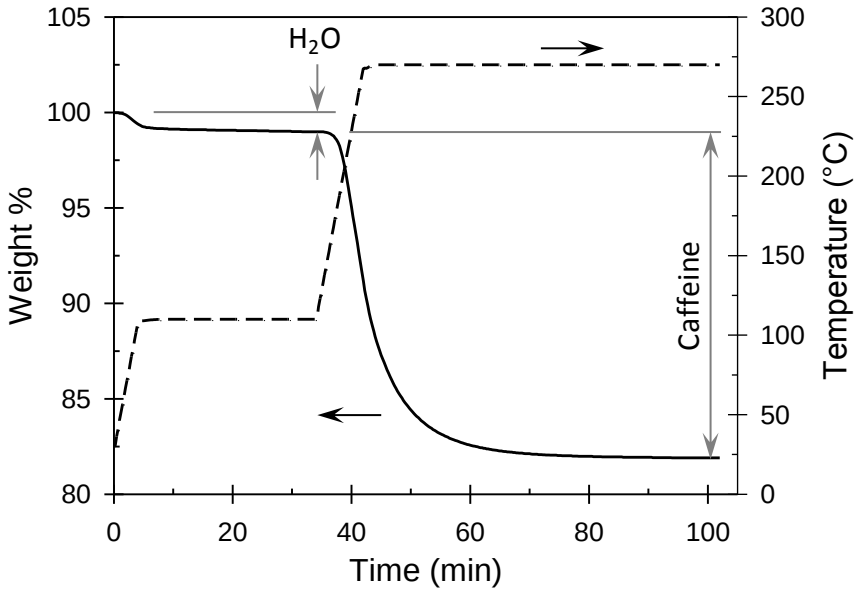

Figure 3.13. Example TGA trace for a PET/caffeine film, illustrating the method for determining the actual caffeine content.

In addition to caffeine content determination, thermogravimetric analysis can also provide information regarding the decomposition temperature of a polymer. For the case of PEF compared to PET, amorphous films were heated at 10°C/min from room temperature to 800°C under 20 mL/min nitrogen purge using a Perkin Elmer Pyris 1 TGA. Decomposition temperatures (T_d) were recorded at the temperature corresponding to 10% weight loss on the decomposition curves for pure PET and PEF, which are illustrated later in Chapter 5 [25].

3.6. Mechanical Characterization

3.6.1. Dynamic Mechanical Analysis

Dynamic mechanical analysis (DMA), as employed in the current work, involves characterization of the polymeric storage modulus (*E'*), loss modulus (*E''*), and tan δ (i.e., *E''*/*E'*) as a function of temperature and frequency via application of an oscillatory strain

on a rectangular strip in tensile geometry mode. DMA is useful for gaining a more molecular level understanding of the fundamental chain motional processes which contribute to penetrant diffusion in both PET and PEF, as will be discussed in further detail in Chapters 4 [21] and 5 [25]. More information regarding mechanical characterization of polymers via DMA can be found in multiple works in the literature [26-30]. A typical plot of storage and loss modulus at 1 Hz as a function of temperature for amorphous PET is provided in Figure 3.14, thereby illustrating the relative location of the alpha and beta relaxations.

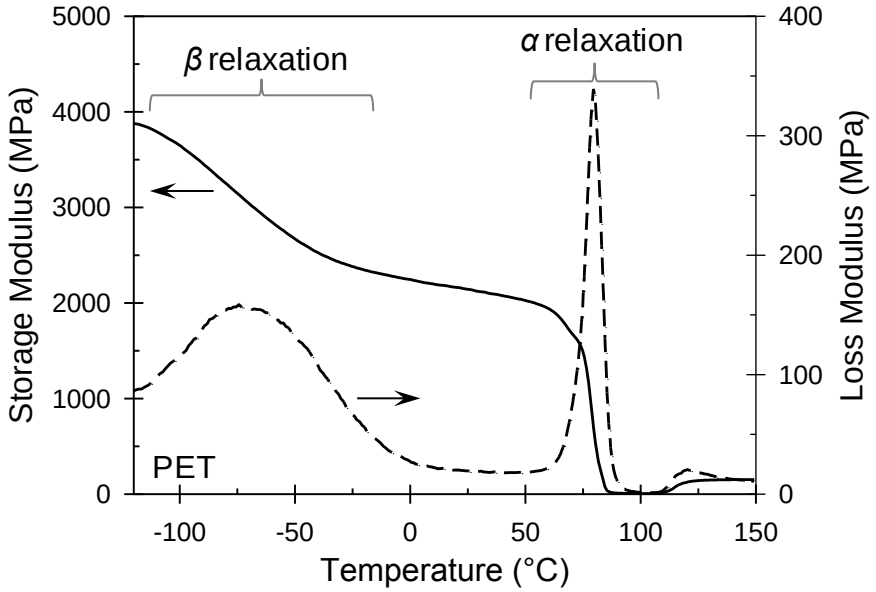

Figure 3.14. Example DMA trace for amorphous PET at 1 Hz.

All dynamic mechanical data reported herein were recorded on a TA Q800 DMA in tensile geometry mode using a simultaneous frequency sweep and temperature ramp. The discrete frequencies ranged from 1, 2, 5, 10, and 20 Hz, while the furnace heated at

1.5°C/min from –120°C to 0°C and 0.5°C/min from 0°C to 150°C. Glass transition temperature (T_g) measurements were recorded using the maximum in tan δ peak. All DMA test strips were dried overnight at 35°C under vacuum to remove residual water, as water can decrease the activation energy of the low-temperature beta relaxation in PET [28]. Furthermore, essentially non-oriented films were used for DMA measurements, as orientation can affect the characteristics of the beta relaxation for both polyesters.

The activation energy (E_A, kJ/mol) of the both the alpha and beta relaxation can be calculated by applying the Arrhenius relationship in Equation 3.6 to data corresponding to the shift in β peak temperature (T, Kelvin) as a function of the dynamic test frequency (f, Hz), where A is a constant and R (8.314 J/mol·K) is the gas constant.

$$f = A\exp\left(-E_A \big/ RT\right) \tag{3.6}$$

Further information regarding the energetics of the β relaxation can be obtained via the activation entropy (ΔS), which is provided from Starkweather [31] in Equation 3.7.

$$E_A = RT\left[1+\ln\left(\frac{k}{2\pi h}\right)+\ln\left(\frac{T}{f}\right)\right]+T\Delta S \tag{3.7}$$

In Equation 3.7, ΔS is the activation entropy of the β relaxation, k and h represent Boltzmann's and Planck's constants, respectively, and T, f, R, and E_A are the same respective parameters employed in Equation 3.6. The activation entropy, in the context of Starkweather, provides an estimate of the cooperativity between moieties and

neighboring polymer chains involved in the respective relaxation [31-33]. Detailed characterization of PET/caffeine and PEF within such framework is provided later in Chapters 4 [21] and 5 [25], respectively.

3.6.2. Tensile Testing

DMA testing, while useful, is not designed to measure the Young's modulus of a glassy polymer due to the relatively low maximum tensile force that the instrument can exert (i.e., approximately 18 N for the TA Q800). Calculation of the Young's modulus from tensile testing involves the initial slope of the stress vs. strain curve (cf. ASTM D638); however, such data are difficult to measure using the Q800 DMA due to the limited force range. Such data are better measured using a dedicated tensile testing instrument, such as the Instron 5566, which was utilized with a 10,000 N load cell in the current wok. Young's modulus data, which were measured using a crosshead speed of 10 mm/min, for both wet and dry PET and PEF are provided and discussed later in Appendix G.

3.7. Supplementary Characterization Techniques

3.7.1. Density Measurement

The densities of all film samples (i.e., PET, PET/caffeine, and PEF) were measured at 23°C using a density gradient column (Techne^{TM}, NJ) containing water and calcium nitrate. The density values were recorded after twenty minutes from introduction of the samples into the column to limit the effect of water uptake on sample density. Such methodology was valid, since multiple films with significantly different thickness values

tested for PEF produced the same density measurement, thereby confirming the negligible effect of water uptake. Density estimates for amorphous PET and all PET/caffeine samples are provided later in Chapter 4 [21], while the density for amorphous PEF compared to PET is provided in Chapter 5 [25].

Although not utilized in this work, the density of a semicrystalline sample can be used to estimate the corresponding crystalline weight fraction (X_c), provided that the density of the completely amorphous (ρ_a) and crystalline (ρ_c) materials are known. Such methodology is provided in Equation 3.8 [5], where ρ is the experimentally measured density of the sample with unknown crystallinity, and ρ_a and ρ_c are tabulated in the literature.

$$X_c = \left(\frac{\rho - \rho_a}{\rho_c - \rho_a} \right) \frac{\rho_c}{\rho} \tag{3.8}$$

3.7.2. Infrared Spectroscopy

Fourier transform infrared (FTIR) spectroscopy operated in attenuated total reflectance (ATR) mode was used to characterize the functional groups in both amorphous PET and PEF. Amorphous polyester films were tested on a Bruker Hyperion 1000 microscope between 4000 – 600 cm^{-1} at 1 cm^{-1} intervals using an average of 128 scans. A blank scan was used to correct for atmospheric noise and all measured values were converted into absorbance units. Functional group motions are assigned and compared to other literature reports. Example FTIR scans for PET compared to PET/caffeine are provided in Chapter 4 [21], while scans for PET compared to PEF are

provided in Chapter 5 [25].

3.7.3. X-Ray Diffraction

The amorphous morphology of both PET and PEF films prepared using the melt-press procedure described previously was verified using X-ray diffraction (XRD). Scans were recorded on a PANalytical XRD instrument between 5 to 55° using a Cu Kα source. Such technique also allowed characterization of semicrystalline PEF, and revealed that the crystal peaks reported herein exhibit agreement with those found in literature. XRD scans for both PET and PEF are provided in Chapter 4 [25].

3.7.4. ^{13}C Solid-State NMR

Two separate solid-state NMR techniques were used to investigate the fundamental chain mobility differences between amorphous PET and PEF. A Bruker AV3-400 spectrometer was used in conjunction with magic-angle spinning (MAS) and proton decoupling to measure variable contact-time solid state NMR data. Rf-frequencies of 100 MHz and 400 MHz were used for ^{13}C and ^{1}H, respectively. All cross-polarization (CP) variable contact-time measurements were performed at 35°C using a radio frequency field of 50 kHz and contact-times varying from 0.01 – 10 ms using a total of 512 scans for each data point. A recycle delay of 4 s was used. These experiments worked best under conditions of slow MAS spinning speeds. A spinning speed of 4.5 kHz was chosen, where no overlap between spinning-sidebands and peaks corresponding to isotropic chemical shifts were observed. Amorphous, non-oriented polymer films were cryogenically ground prior to loading into the ZrO_2 Bruker 4 mm MAS rotor, which were

then sealed using Kel-F caps.

Centerband-Only Detection of Exchange (CODEX) measurements were performed at room temperature using a small z-filter time (t_z) of 100 μs to improve the signal-to-noise ratio. Spectra were measured using a spinning speed of 10 kHz and recycle delay of 4 s at a mixing time (t_m) of 1 s. The CODEX experiment requires a reference spectrum, which was measured using identical conditions as for the CODEX experiment, however the time delays t_m and t_z were switched. A total of more than 20,000 scans was used for both the CODEX and the reference experiment to obtain data with a sufficient signal-to-noise ratio. The functioning of the experiment was verified by conducting the identical experiment on dimethyl sulfone (DMS), where large angle jump-type motions could be readily detected using only a few scans. Solid-state NMR data pertaining to both amorphous PET and PEF are provided in Chapter 5 [25].

3.8. References

1. Sanches NB, Dias ML, and Pacheco EBAV. Comparative techniques for molecular weight evaluation of poly (ethylene terephthalate) (PET). Polymer Testing 2005;24(6):688-693.

2. Lee JS, Leisen J, Choudhury RP, Kriegel RM, Beckham HW, and Koros WJ. Antiplasticization-based enhancement of poly(ethylene terephthalate) barrier properties. Polymer 2012;53:213-222.

3. Lee JS. Fundamentals of Transport in Advanced Barrier Materials Based on Engineered Antiplasticization. Chemical and Biomolecular Engineering. Atlanta: Georgia Institute of Technology, 2011.

4. Lee JS, Chandra P, Burgess SK, Kriegel R, and Koros WJ. An advanced gas/vapor permeation system for barrier materials: Design and applications to poly(ethylene terephthalate). Journal of Polymer Science Part B: Polymer Physics 2012;50(17):1262-1270.

5. Chandra P. Chemical and Biomolecular Engineering, vol. PhD. Atlanta: Georgia

Institute of Technology, 2006.

6. Moore TT, Damle S, Williams PJ, and Koros WJ. Characterization of low permeability gas separation membranes and barrier materials; design and operation considerations. Journal of Membrane Science 2004;245(1–2):227-231.

7. Rogers CE. Permeation of Gases and Vapours in Polymers. In: Comyn J, editor. Polymer Permeability. New York: Elsevier Applied Science Publishers Ltd., 1985. pp. 11-73.

8. Burgess SK, Karvan O, Johnson JR, Kriegel RM, and Koros WJ. Oxygen Sorption and Transport in Amorphous Poly(ethylene furanoate). Polymer 2014;55(18):4748-4756.

9. Koros WJ and Paul DR. Design considerations for measurement of gas sorption in polymers by pressure decay. Journal of Polymer Science: Polymer Physics Edition 1976;14(10):1903-1907.

10. Koros WJ, Paul DR, and Rocha AA. Carbon dioxide sorption and transport in polycarbonate. Journal of Polymer Science: Polymer Physics Edition 1976;14(4):687-702.

11. McBain JW and Bakr AM. A new sorption balance. Journal of the American Chemical Society 1926;48(3):690-695.

12. Chandra P and Koros WJ. Sorption and transport of methanol in poly(ethylene terephthalate). Polymer 2009;50:236-244.

13. Chandra P and Koros WJ. Sorption of lower alcohols in poly(ethylene terephthalate). Polymer 2009;50:4241-4249.

14. Lee JS, Adams RT, Madden W, and Koros WJ. Toluene and n-heptane sorption in Matrimid® asymmetric hollow fiber membranes. Polymer 2009;50(25):6049-6056.

15. Burgess SK, Mikkilineni DS, Yu DB, Kim DJ, Mubarak CR, Kriegel RM, and Koros WJ. Water Sorption in Poly(ethylene furanoate) Compared to Poly(ethylene terephthalate). Part 1: Equilibrium Sorption. Polymer 2014;55(26):6861-6869.

16. Burgess SK, Mikkilineni DS, Yu DB, Kim DJ, Mubarak CR, Kriegel RM, and Koros WJ. Water Sorption in Poly(ethylene furanoate) Compared to Poly(ethylene terephthalate). Part 2: Kinetic Sorption. Polymer 2014;55(26):6870-6882.

17. Schick C. Differential scanning calorimetry (DSC) of semicrystalline polymers. Analytical and Bioanalytical Chemistry 2009;395(6):1589-1611.

18. Khanna YP and Kuhn WP. Measurement of crystalline index in nylons by DSC: Complexities and recommendations. Journal of Polymer Science Part B: Polymer Physics 1997;35(14):2219-2231.

19. Hourston DJ, Song M, Hammiche A, Pollock HM, and Reading M. Modulated differential scanning calorimetry: 6. Thermal characterization of multicomponent polymers and interfaces. Polymer 1997;38(1):1-7.

20. Cañadas JC, Diego JA, Sellarès J, Mudarra M, Belana J, Díaz-Calleja R, and Sanchis MJ. Comparative study of amorphous and partially crystalline poly(ethylene-2,6-naphthalene dicarboxylate) by TSDC, DEA, DMA and DSC. Polymer 2000;41(8):2899-2905.

21. Burgess SK, Lee JS, Mubarak CR, Kriegel RM, and Koros WJ. Caffeine Antiplasticization of Amorphous Poly(ethylene terephthalate): Effects on Gas Transport, Thermal, and Mechanical Properties. Polymer 2015, DOI: 10.1016/j.polymer.2015.03.051.

22. Burgess SK, Mubarak CR, Kriegel RM, and Koros WJ. Physical Aging in Amorphous Poly(ethylene furanoate): Enthalpic Recovery, Density, and Oxygen Transport Considerations. Journal of Polymer Science Part B: Polymer Physics 2015;53(6):389-399.

23. Emel'yanenko VN and Verevkin SP. Thermodynamic properties of caffeine: Reconciliation of available experimental data. The Journal of Chemical Thermodynamics 2008;40(12):1661-1665.

24. Rossbach V. Analysis of Low Molecular Weight Homologues of Fiber-Forming Polycondensates. Angewandte Chemie International Edition in English 1981;20(10):831-840.

25. Burgess SK, Leisen JE, Kraftschik BE, Mubarak CR, Kriegel RM, and Koros WJ. Chain Mobility, Thermal, and Mechanical Properties of Poly(ethylene furanoate) Compared to Poly(ethylene terephthalate). Macromolecules 2014;47(4):1383-1391.

26. Maxwell AS, Monnerie L, and Ward IM. Secondary relaxation processes in polyethylene terephthalate-additve blends: 2. Dynamic mechanical and dielectric investigations. Polymer 1998;39(26):6851-6859.

27. Hardy L, Stevenson I, Boiteux G, Seytre G, and Schönhals A. Dielectric and dynamic mechanical relaxation behaviour of poly(ethylene 2,6 naphthalene dicarboxylate). I. Amorphous films. Polymer 2001;42(13):5679-5687.

28. Illers KH and Breuer H. Molecular Motions in Polyethylene Terephthalate. Journal of Colloid Science 1963;18:1-31.

29. Comer AC, Kalika DS, Rowe BW, Freeman BD, and Paul DR. Dynamic relaxation characteristics of Matrimid® polyimide. Polymer 2009;50(3):891-897.

30. Light RR and Seymour RW. Effect of sub-Tg relaxations on the gas transport properties of polyesters. Polymer Engineering & Science 1982;22(14):857-864.

31. Starkweather HW. Simple and Complex Relaxations. Macromolecules 1981;14(5):1277-1281.

32. Starkweather HW. Noncooperative Relaxations. Macromolecules 1988;21:1798-1802.

33. Starkweather HW. Aspects of simple, non-cooperative relaxations. Polymer 1991;32(13):2443-2448.

CHAPTER 4

CAFFEINE ANTIPLASTICIZATION OF AMORPHOUS PET[1]

This chapter investigates the phenomenon of caffeine antiplasticization of amorphous poly(ethylene terephthalate) (PET). Oxygen and carbon dioxide permeation measurements at 35°C reveal significant barrier improvement for all PET/caffeine samples studied, and penetrant solubility and diffusivity estimates are used to deconvolute the relative transport contributions to the overall barrier reduction determined via permeation testing. The data reported herein suggest that antiplasticization of PET occurs via a combination of both "hole filling" and chain mobility restriction mechanisms, and that the relative mechanistic contributions to transport reduction depend largely on the penetrant solubility and diffusivity within the polymer matrix.

4.1. Introduction

Poly(ethylene terephthalate) (PET), despite being the most widely used polymer in the beverage packaging industry, exhibits inadequate barrier performance for challenging oxygen and carbon dioxide applications [1]. While various complicated methods of PET barrier improvement exist (i.e., multi-layered polymers, polymer blends, coatings, etc.), the most economical method would involve minimal modifications to the current processing platform [2]. As will be demonstrated, the incorporation of low molecular weight diluents into the PET matrix via antiplasticization can provide such barrier

[1]Reprinted in part from *Polymer*, Burgess, S.K.; Lee, J.S.; Mubarak, C.R.; Kriegel, R.M.; Koros, W.J., *Caffeine Antiplasticization of Amorphous Poly(ethylene terephthalate): Effects on Gas Transport, Thermal, and Mechanical Properties*, DOI: 10.1016/j.polymer.2015.03.051, Copyright 2015, with permission from Elsevier.

enhancements while requiring minimal processing equipment modification.

Antiplasticization occurs when a polymer/diluent mixture exhibits an overall reduction in chain mobility, penetrant transport, and free volume compared to the respective pure glassy polymer [3-5]. Multiple authors in the literature support the notion that antiplasticization occurs primarily via a simple "hole filling" mechanism, where the additive reduces the free volume of the mixture by filling a portion of the excess free volume inherent to the non-equilibrium glass [6-11]. Evidence from the PET/caffeine system reported herein supports this hypothesis; however, additional interrelated factors such as chain mobility are also shown to contribute to the antiplasticization phenomena.

Caffeine, which is the chosen antiplasticizer for this study, is generally regarded as "safe" for human consumption, and consequently, avoids toxicity issues associated with previously considered antiplasticizers for both PET [11-13] and other polymers [9, 10, 14]. This factor is particularly important for applications involving direct food/beverage contact, to address concerns regarding additive migration into the container contents. Besides safety advantages, caffeine is highly soluble in the PET matrix, and as will be shown, produces significant barrier improvements for oxygen and carbon dioxide when mixed with PET.

This chapter investigates caffeine antiplasticization of amorphous PET using detailed oxygen and carbon dioxide transport studies (i.e., permeation, sorption, and diffusion), density and free volume characterization, and thermal/mechanical techniques. PET/caffeine samples are studied with caffeine concentrations ranging from 0 to ~15 wt%. In support of prior work, the results reported herein provide evidence that antiplasticization occurs, in part, via the overall reduction in free volume (i.e., "hole

filling") for the PET/caffeine samples compared to neat PET. Further evidence correlates the diffusion reductions for the antiplasticized samples to chain mobility as probed by dynamic mechanical investigation of the sub-ambient beta relaxation, where caffeine is observed to hinder polymer phenyl ring-flipping motions in glassy PET. This chapter provides a "base case" investigation regarding caffeine antiplasticization of the amorphous morphology for PET as a starting point for future studies involving both crystallinity and orientation.

4.2. Experimental Methods

4.2.1. Materials, PET/Caffeine Mixing, and Film Preparation

The caffeine and poly(ethylene terephthalate) (PET) used herein are the same materials described previously in Section 3.1.1. All PET/caffeine batches were mixed according to the procedure outlined in Section 3.1.2, and amorphous films were pressed via the method in Section 3.1.3. Due to the volatile nature of caffeine at the melt processing temperature of PET [15], the final caffeine content of each PET/caffeine film differed from the nominal loading. Such behavior required determination of the actual, final caffeine content in the films via the TGA procedure described in Section 3.5.2. The final caffeine content in the films was also affected by the film thickness. For example, permeation films pressed from the PET/caffeine batch with 20 wt% nominal caffeine content had a final caffeine content of ~10.7 wt% as measured via TGA, while DMA films, which were approximately 3X thicker than the permeation films (i.e., 150 μm vs. 50 μm), exhibited a final caffeine content of ~15.0 wt%. All composition values reported throughout the remainder of this chapter represent the final *actual* caffeine content in the

compounded polymer films. The FTIR spectra for films of virgin PET and PET mixed with ~15 wt% caffeine are provided in Appendix A.

4.2.2. Transport Characterization

Pure gas permeation data for oxygen and carbon dioxide were measured at 35°C using the variable-pressure, constant-volume permeation method described in Section 3.2. Similarly, all pure gas solubility data were measured at 35°C using the standard pressure-decay method described in Section 3.3. The permeation and sorption data reported herein for all PET/caffeine samples reflect characterization of the amorphous morphology. The absence of crystallinity was verified, as stated in Chapter 3, by X-Ray and differential scanning analysis of the melt-pressed samples.

4.2.3. Thermal, Mechanical, and Density Characterization

Differential scanning calorimetry (DSC) was used to investigate relevant thermal properties of the melt-pressed PET/caffeine films. Heat-cool-heat scans were recorded at a rate of 10°C/min between 0 and 280°C on a TA Q1000 DSC, and glass transition (T_g) temperatures were estimated on the first heat via the onset in heat flow versus temperature. The T_g values reported in this chapter correlate with the amorphous morphology.

Dynamic mechanical analysis (DMA) was used to investigate the effect of caffeine on the T_g and sub-ambient beta (β) relaxation of PET. Polymer strips were tested in tensile geometry mode on a TA Q800 DMA using a concurrent temperature ramp (1.5°C/min) and frequency sweep (1, 2, 5, 10, and 20 Hz). As described in Chapter 3, all test strips

were dried at 35°C for at least 12 hours under vacuum prior to testing to remove excess sorbed water. Glass transition temperature (T_g) measurements were recorded for the amorphous films at 1 Hz via the onset in storage modulus (E').

Density values were measured for all PET/caffeine samples at 23C using the density gradient methodology described previously in Section 3.7.1.

4.3. Results and Discussion

4.3.1. Permeation

Permeation data measured at 35°C for oxygen and carbon dioxide in various PET/caffeine samples are reported in Figures 4.1 and 4.2, respectively. The reported data represent the average of multiple tests (2 to 3 samples, at least), with uncertainty limits originating from the standard error. Complementary data are plotted later in Appendix A as penetrant permeability at 1 atm vs. caffeine content. As expected, Figures 4.1 and 4.2 show that all caffeine-containing samples exhibit a reduced permeability compared to the respective permeability for neat PET. Such barrier improvement can be quantified by the so-called Barrier Improvement Factor (BIF_P) [11], which is defined as the pure gas permeability in pure, amorphous PET divided by the respective permeability in the caffeine containing samples. Table 4.1 lists values for the average BIF_P (averaged over all pressures tested) for each respective PET/caffeine sample and test gas.

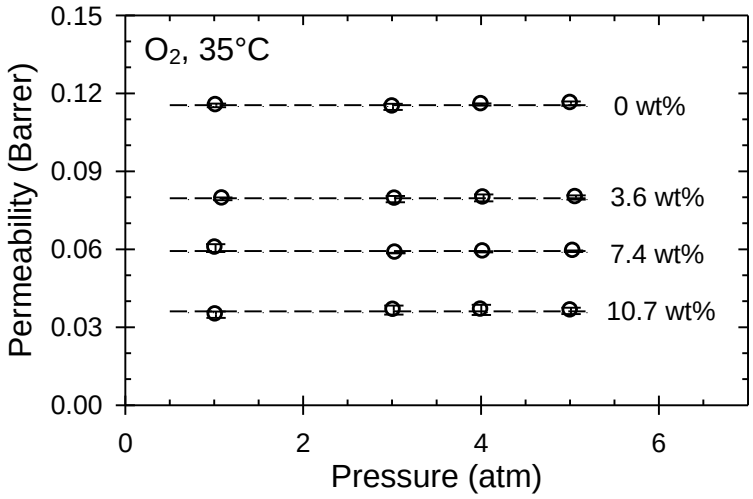

Figure 4.1. Oxygen permeability at 35°C for various PET/caffeine samples. Dashed lines are drawn to aid the eye. Uncertainty bounds are smaller than the size of the specific data points in all cases. Each weight percent indicates the actual concentration of caffeine for each PET/caffeine sample.

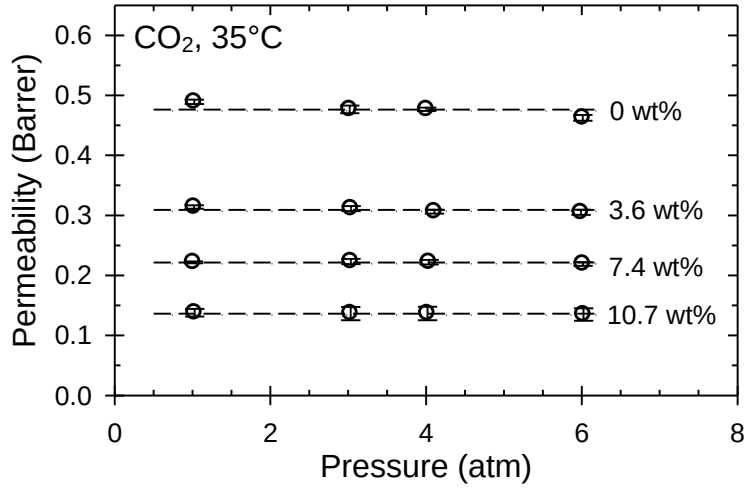

Figure 4.2. Carbon dioxide permeability at 35°C for various PET/caffeine samples. Dashed lines are drawn to aid the eye.

Table 4.1. Oxygen and carbon dioxide Barrier Improvement Factors (BIF_P) estimated from permeation at 35°C averaged over all pressures for various PET/caffeine samples. Uncertainty limits for all BIF_P values are $\leq \pm 0.04$.

wt% Caffeine	O_2 BIF_P	CO_2 BIF_P
0	1	1
3.6 ± 0.2	1.5	1.5
7.4 ± 0.2	1.9	2.1
10.7 ± 0.1	3.2	3.5

BIF_P values greater than unity in Table 4.1 indicate that barrier improvement (i.e., antiplasticization) is achieved for all caffeine-containing samples, with improvements >3X observed for both gases in PET blended with ~10.7 wt% caffeine. The BIF_P values in Table 4.1 can be further separated into respective Barrier Improvement Factors specific to the penetrant solubility and diffusivity, and will be discussed in more detail in Section 4.3.3 (cf. Table 4.4). It is also noted that the BIF_P values for carbon dioxide are slightly larger than the respective values for oxygen in all caffeine concentrations tested. As will be shown, such differences exist due to the differences in relative contributions of solubility and diffusivity for each penetrant in the antiplasticized samples.

The oxygen permeability data in Figure 4.1 exhibit very little, if any, pressure dependence for all caffeine compositions, while the respective data for carbon dioxide in Figure 4.2 exhibit a slightly decreasing permeability trend with increasing pressure for all caffeine compositions. Such pressure dependencies can be examined within the context of the so-called partial immobilization model [16, 17], which considers the solubility of the penetrant in the polymer when modeling permeability data. Since oxygen exhibits a significantly reduced solubility in PET compared to carbon dioxide (discussed further in

Section 4.3.2), it is not surprising to observe pressure independence over the small pressure range illustrated in Figure 4.1. Similar pressure independent behavior for oxygen has been observed for permeation in glassy poly(ethylene furanoate) (PEF) [18].

Aside from the steady-state permeation data reported in Figures 4.1 and 4.2, analysis of the initial transient data prior to steady-state can provide an estimate of both the penetrant solubility and diffusivity. This procedure, while already described in Chapter 2, is provided again for convenience via Equations 4.1 and 4.2 [19, 20], where k^* (ccSTP/ccPoly·atm) is an "effective" solubility coefficient, θ (s) is the time-lag, P is the low pressure penetrant permeability, l (cm) is the film thickness, and D (cm^2/s) is the diffusion coefficient. Recall that graphical determination of the time-lag (θ) has been illustrated previously in Section 3.2.3.

$$k^* = \frac{6\theta P}{l^2} \tag{4.1}$$

$$D = \frac{l^2}{6\theta} \tag{4.2}$$

Carbon dioxide k^* data for various PET/caffeine samples measured via permeation testing are provided in Appendix A, and diffusion coefficient data are provided in Section 4.3.3 (cf. Table 4.3).

4.3.2. Equilibrium Sorption

Recall from Chapter 2 that the so-called dual-mode model, reproduced in Equation

4.3, is often used to describe the equilibrium sorption of gases in glassy polymers.

$$C = \left(k_D p + \frac{C_H^{'} bp}{1 + bp} \right) \tag{4.3}$$

While sorption in glassy polymers involves two idealized modes, relatively non-condensable gases, which exhibit low solubility and minimal interaction with the polymer matrix, approach simple Henry's law type sorption in the glassy state. This notion is described via Equation 4.4, where k^* represents an *effective* Henry's law solubility coefficient. Equation 4.4 also describes the low-pressure limit behavior of the dual-mode model in Equation 4.3, via $k^* = (k_D + C_H'b)$. The parameter k^* measured via sorption testing from Equation 4.4 should be equivalent to k^* measured via permeation testing from Equation 4.1, since both k^* estimates effectively combine the sorption contributions from both the Henry's law and Langmuir environments. Consequently, both k^* estimates are typically larger in magnitude than the true Henry's law coefficient (k_D), which ideally probes only the dissolved mode [18, 21, 22].

$$C = \left(k^* \right) p = \left(k_D + C_H^{'} b \right) p \tag{4.4}$$

Equilibrium sorption data measured at 35°C for oxygen in various PET/caffeine samples are reported in Figure 4.3, with analogous sorption data for carbon dioxide reported in Figure 4.4. The solid lines drawn through the data in Figure 4.3 (oxygen) represent linear model fits from Equation 4.4, while the lines drawn in Figure 4.4 (carbon

dioxide) represent fits from the dual-mode model in Equation 4.3. Corresponding model parameters for the fits in Figures 4.3 and 4.4 are provided in Table 4.2.

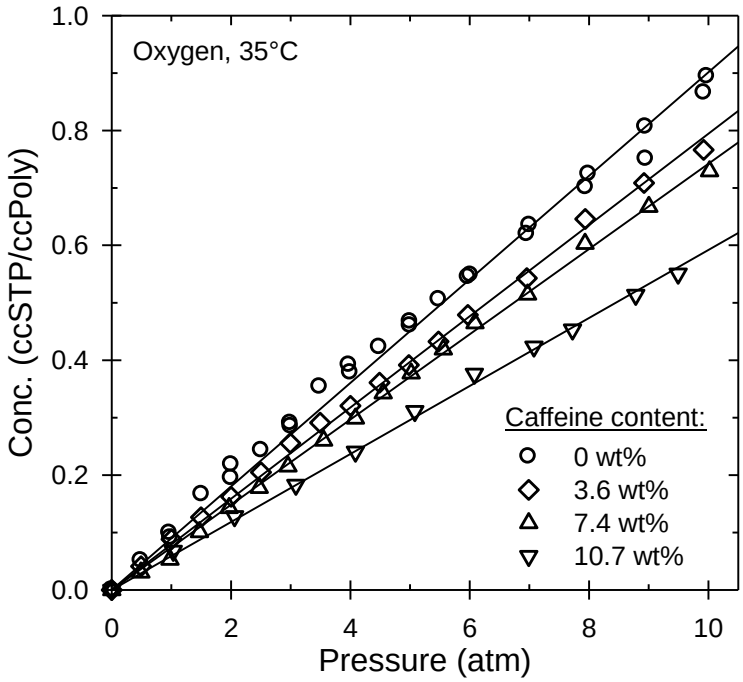

Figure 4.3. Oxygen sorption data at 35°C for various PET/caffeine samples. Lines represent the respective linear fits from Equation 4.4.

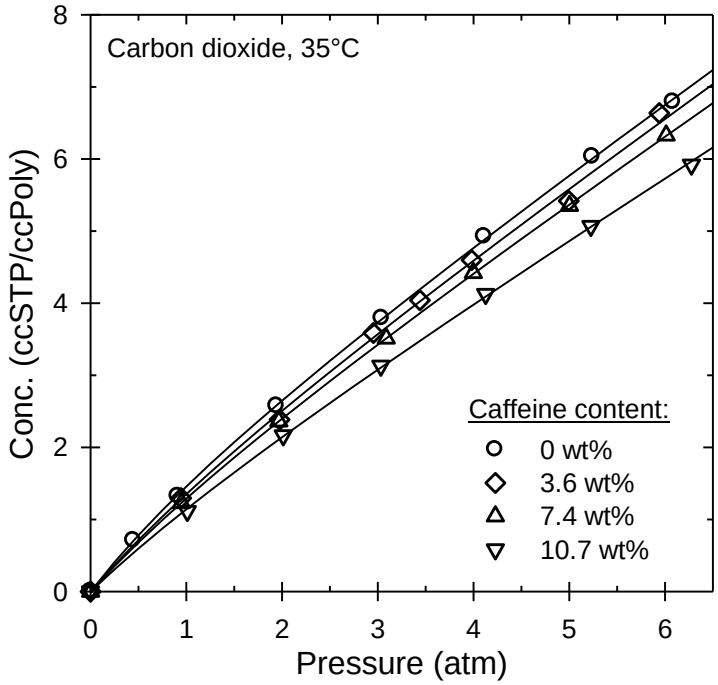

Figure 4.4. Carbon dioxide sorption data at 35°C for various PET/caffeine samples. Lines represent the respective dual-mode model fits from Equation 4.3.

Table 4.2. Sorption parameters at 35°C for oxygen and carbon dioxide uptake in various PET/caffeine samples. Standard errors were determined via the fitting program.

	Oxygen	**Carbon dioxide**			
wt% Caffeine	***k**** **(ccSTP/ccPoly·atm)**	k_D **(ccSTP/ccPoly·atm)**	b **(atm^{-1})**	C_H' **(ccSTP/ccPoly)**	$k^* = (k_D + C_H'b)$ **(ccSTP/ccPoly·atm)**
0	0.090 ± 0.0007	0.93 ± 0.04	0.50 ± 0.2	1.6 ± 0.4	1.7 ± 0.3
3.6 ± 0.2	0.079 ± 0.0005	0.92 ± 0.1	0.42 ± 0.5	1.5 ± 1	1.5 ± 0.9
7.4 ± 0.2	0.074 ± 0.0004	0.89 ± 0.02	0.42 ± 0.1	1.4 ± 0.2	1.5 ± 0.2
10.7 ± 0.1	0.059 ± 0.0004	0.82 ± 0.07	0.40 ± 0.3	1.1 ± 0.9	1.3 ± 0.5

As seen in Figure 4.3, all caffeine-containing samples exhibit reduced oxygen solubility compared to neat PET, and the oxygen sorption data for neat PET agree well with prior literature reports [18, 19, 23]. The linear sorption isotherms (i.e., Equation 4.4) in Figure 4.3 describe the oxygen sorption data well, despite the presence of the

Langmuir sorption mode in the glassy samples. In fact, the slight curvature in the sorption isotherm for neat PET, which originates from sorption in the Langmuir mode, is observed to decrease in prominence as caffeine is introduced into the matrix. This behavior is consistent with the notion that caffeine is filling a portion of the Langmuir environment (i.e., excess free volume), thereby reducing the contribution of oxygen sorption in the Langmuir environment and serving to "linearize" the isotherms.

Similar to oxygen, all caffeine-containing samples exhibit reduced carbon dioxide solubility compared to neat PET (cf. Figure 4.4), and the sorption data for neat PET agree well with prior literature reports [11, 23]. While oxygen exhibits low solubility and minimal interaction with the PET matrix, carbon dioxide is more condensable and exhibits higher solubility compared to oxygen. The dual-mode model parameters in Table 4.2 indicate that k_D, which correlates with sorption in the dissolved mode, is effectively unchanged by the addition of caffeine into the polymer matrix. On the other hand, the Langmuir parameters reflect a slight decrease in b and apparent decrease in C_H' for all caffeine containing samples compared to neat PET. The latter behavior is consistent with the notion that caffeine acts primarily to fill a portion of the excess free volume corresponding to the Langmuir environment. Complementary sorption data for carbon dioxide estimated via permeation testing (i.e., Equation 4.1) are provided in Appendix A, and a more complete discussion regarding the free volume reductions observed in the current work for all caffeine-containing samples is provided in Section 4.3.4.

As a final note, all PET/caffeine compositions investigated in this chapter reflect characteristics of antiplasticization. It is expected that the PET/caffeine system will transition to a plasticization-type behavior at a sufficiently high caffeine loading. This

transition point is postulated to occur after the excess free volume of the glassy material is ideally "filled," thereby indicating that any additional caffeine added to the system must enrich the dissolved environment and serve to increase the inter-chain spacing between polymer chains (i.e., plasticization). While the transition point was not directly observed in the current study, it is expected to occur at a concentration slightly above the practical maximum concentration studied herein based on trends in the sorption data and mechanical data (cf. Section 4.3.6).

4.3.3. Diffusion

As mentioned previously, diffusion coefficients can be determined from the time-lag approach via transient permeation (i.e., Equation 4.2), or through the relationship $D = P/k^*$ (i.e., diffusivity = permeability / solubility). Diffusion coefficients can also be obtained from pressure-decay data when the sample geometry is known [18, 24]; however, this approach was not pursued in the current work due to some variability in the sample film thickness values and the need for a large sorption sample size. It should be noted, however, that long-term non-Fickian relaxations were observed in all carbon dioxide pressure-decay sorption isotherms for all PET samples studied herein. Such plasticization/conditioning behavior is known to occur with carbon dioxide at high pressure [25-27]; however, detailed characterization of the non-Fickian diffusion behavior is outside the scope of the current work.

Low concentration diffusion coefficient data measured via the relationship $D = P/k^*$ for oxygen and carbon dioxide are plotted in Figure 4.5 (circles) and listed in Table 4.3, where P represents the steady-state permeability at 1 atm and k^* is the effective solubility

coefficient taken from Table 4.2. Diffusivity estimates from the time-lag approach for carbon dioxide (i.e., Equation 4.2) are also plotted in Figure 4.5 (triangles) for comparison; however, corresponding diffusivity estimates for oxygen using this approach were impractical, due in part to uncertainties associated with the relatively small time-lags. As a point of comparison, the oxygen and carbon dioxide diffusivities at 35°C for neat PET exhibit satisfactory agreement with prior literature reports [20, 23]. Estimates for the activation entropies of oxygen and carbon dioxide diffusion in PET are provided later in Appendix F.

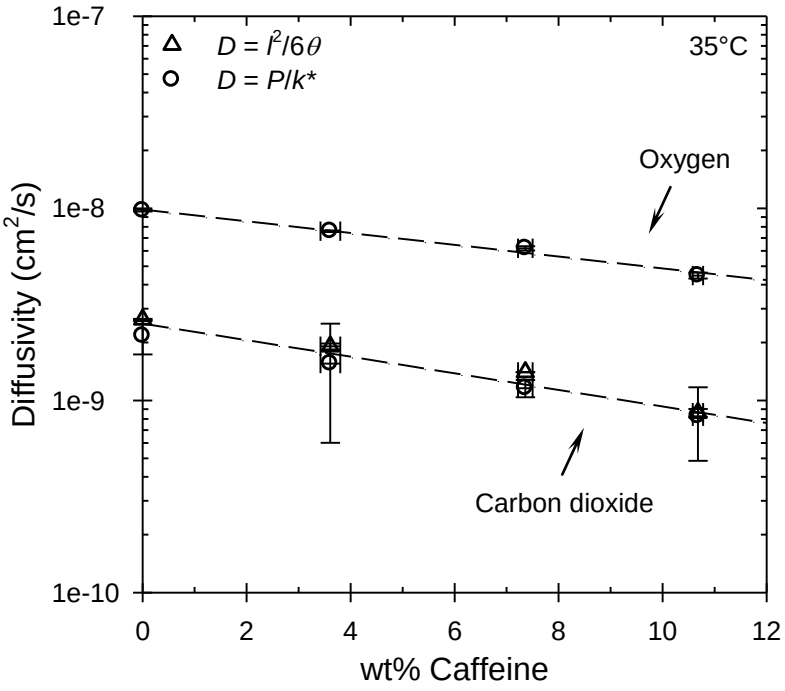

Figure 4.5. Diffusivity data at 35°C for oxygen and carbon dioxide in various PET/caffeine samples measured via the relationship $D = P/k^*$ (circles) for both gases and the time-lag approach ($D = l^2/6\theta$) for carbon dioxide (triangles). Lines are drawn to aid the eye.

Table 4.3. Diffusion coefficient data at 35°C for oxygen and carbon dioxide in various PET/caffeine samples measured via the relationship $D = P/k^*$ for both gases and the time-lag approach ($D = l^2/6\theta$) for carbon dioxide, with an upstream permeation pressure of 1 atm.

	$D\times10^9$ (cm^2/s) (P/k^*)		$D\times10^9$ (cm^2/s) ($l^2/6\theta$)
wt% Caffeine	**Oxygen**	**Carbon dioxide**	**Carbon dioxide**
0	9.7 ± 0.1	2.2 ± 0.4	2.6 ± 0.02
3.6 ± 0.2	7.6 ± 0.1	1.6 ± 1	1.9 ± 0.07
7.4 ± 0.2	6.2 ± 0.2	1.2 ± 0.1	1.4 ± 0.001
10.7 ± 0.1	4.5 ± 0.2	0.83 ± 0.3	0.86 ± 0.04

From Figure 4.5, it is evident that the diffusivities of both oxygen and carbon dioxide decrease with increasing caffeine content. Such diffusivity reduction primarily implies a reduction in segmental chain mobility for the antiplasticized samples compared to neat PET, and this notion will be discussed in relation to free volume (Section 4.3.4) and fundamental chain motional processes (i.e., polymer phenyl ring-flipping) later in the document (Section 4.3.6).

As mentioned previously, the Barrier Improvement Factors (BIF_P) for the antiplasticized samples measured via permeation testing can be separated into contributions from the diffusivity and solubility via the relationship $P = Dk^*$ (i.e., permeability = diffusivity × solubility). A separate Barrier Improvement Factor can be defined for each of the equation components such that $BIF_P = BIF_D \times BIF_{k^*}$, where the BIF is again defined as the ratio of the property for pure PET divided by the same respective property for the antiplasticized sample [11]. Component Barrier Improvement Factors are provided for both oxygen and carbon dioxide transport in the various PET/caffeine samples in Table 4.5, where the BIF_D values originate from the diffusion

coefficients measured via $D = P/k^*$ in Table 4.3 and the BIF_{k^*} values originate from the solubility coefficients (i.e., k^* from Equation 4.4) in Table 4.2. As seen in Table 4.4, the BIF_P estimates (i.e., $BIF_P = BIF_D \times BIF_{k^*}$) obtained from multiplying the independent diffusion and sorption contributions are within 10% error of the actual BIF_P values determined from experimental permeation testing (Table 4.1).

Table 4.4. Oxygen and carbon dioxide Barrier Improvement Factors (BIFs) at 35°C for various PET/caffeine samples. BIF_D values are calculated from $D = P/k^*$ in Table 4.3, BIF_{k^*} values are calculated from the k^* sorption values from Table 4.2 (i.e., Equation 4.4), and the experimental BIF_P values originate from Table 4.1.

	wt% Caffeine	**BIF_D**	**BIF_{k^*}**	**BIF_P (calculated) ($BIF_D \cdot BIF_{k^*}$)**	**BIF_P (experimental) (Table 4.1)**	**% Error**
O_2	3.6 ± 0.2	1.3	1.1	1.4	1.5	-7
	7.4 ± 0.2	1.6	1.2	1.9	1.9	0
	10.7 ± 0.1	2.2	1.5	3.3	3.2	3
CO_2	3.6 ± 0.2	1.4	1.1	1.5	1.5	0
	7.4 ± 0.2	1.9	1.2	2.3	2.1	10
	10.7 ± 0.1	2.6	1.4	3.6	3.5	3

Inspection of Table 4.4 reveals that the values of BIF_D for both gases are larger than the respective values of BIF_{k^*}, implying that caffeine antiplasticization has a greater impact on reducing diffusion versus sorption. A more detailed discussion regarding sorption is provided in Section 4.3.2, while a discussion regarding diffusion is provided in Section 4.3.4 (i.e., free volume) and Section 4.3.6 (i.e., phenyl ring-flipping and chain mobility).

4.3.4. Antiplasticization and Free Volume

The permeability and diffusivity reductions observed in the PET/caffeine system can be examined in the context of free volume theory. Antiplasticized polymer-diluent systems often exhibit a negative deviation from pure component volume additivity via the diluent acting to partially fill the free volume between polymer chains [5, 9, 10]. Such negative departures are enhanced when a strong interaction exists between polymer and diluent [14], and quantitative models have been developed to predict the volumetric behavior of polymer-diluent mixtures based on pure component property data [7, 28]. Lee [29] empirically correlated permeability to free volume across a wide variety of polymers by assuming similar sorption contributions to the permeability (i.e., $P = Dk^*$). This approximation is more accurate for carbon dioxide in the PET/caffeine samples as evidenced by the relative magnitudes of BIF_D compared to BIF_{k^*} found in Table 4.4. Definitions of specific free volume ($\hat{V}_F$), fractional free volume (*FFV*), and Lee's permeability-free volume correlation [29], are provided in Chapter 2 for pure polymers and polymer/diluent mixtures.

Density data measured at 23°C for all PET/caffeine samples are plotted vs. caffeine content in Figure 4.6 and listed in Table 4.5 along with values of the specific volume, occupied volume, free volume, and fractional free volume. The dashed curve in Figure 4.6 represents a quadratic regression to the density data, which allows interpolation of density values between the plotted data. The regression was particularly useful in estimating the density of the ~10.7 wt% caffeine films used in sorption testing, since pressure-decay sorption requires accurate sample density *and* thin films (e.g., ~50 μm) to achieve experimentally accessible sorption time-scales.

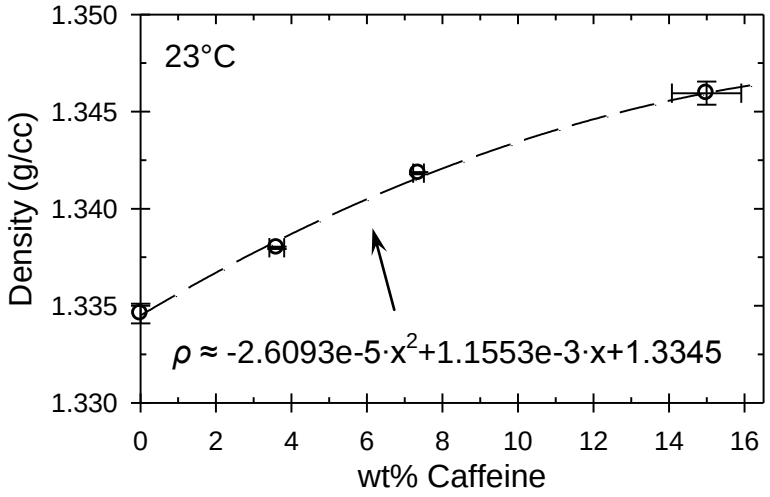

Figure 4.6. Density data measured at 23°C for various *amorphous* PET/caffeine samples. The dashed line represents a simple quadratic regression of the plotted data.

Table 4.5. Density and free volume calculations using Sugden's method [30] for various PET/caffeine samples at 23°C. All quantities, with the exception of 0 wt% caffeine, represent values pertaining to the respective PET/caffeine mixture.

wt% Caffeine	**ρ (g/cc)[a]**	**$\hat{V}_g$ (cc/g)[b]**	**$\hat{V}_0$ (cc/g)**	**$\hat{V}_F$ (cc/g)**	***FFV* (–)**
0	1.3346	0.749	0.652	0.098	0.130
3.6 ± 0.2	1.3380	0.747	0.653	0.094	0.126
7.4 ± 0.2	1.3418	0.745	0.655	0.091	0.122
15.0 ± 0.9	1.3459	0.743	0.658	0.085	0.115

[a] Uncertainty limits for ρ are $\leq \pm$ 6e-4 g/cc for all samples.

[b] Uncertainty limits for $\hat{V}_g$ are $\leq \pm$ 4e-4 cc/g for all samples.

Consistent with the notion of antiplasticization, the free volume and fractional free volume values in Table 4.5 decrease noticeably with increasing caffeine content. Such data are consistent with the transport results for both oxygen and carbon dioxide observed in Sections 4.3.1, 4.3.2, and 4.3.3, and provide a basis for understanding the observed barrier improvement. In fact, the permeability reductions observed in Figures 4.1 and 4.2 can be rationalized in part by the permeability/free volume correlation proposed by Lee

[29] in Equation 4.7. Additional details regarding the application of such correlations can be found in various literature reports [6, 9, 10, 29, 31].

As a final note, the concept of solubility parameters has been used by several researchers to correlate and predict antiplasticizer/polymer compatibility [11, 14, 32, 33]. This concept was not employed in this work, as the structural complexity of caffeine precluded accurate assignment of the group contributions required by the method of Hoy, Hoftyzer, and van Krevelen [34].

4.3.5. Differential Scanning Calorimetry

Differential scanning calorimetry (DSC) was used to investigate the effect of caffeine on the relevant thermal properties of the PET/caffeine samples. For illustration purposes, the DSC thermograms corresponding to pure PET and PET mixed with ~15.0 wt% caffeine are shown in Figure 4.7 as the solid and dashed lines, respectively, during the first complete heat/cool cycle. Recall that both samples are initially amorphous prior to the first heat, and therefore exhibit large cold crystallization peaks (T_{cc}) while heating followed by subsequent melting peaks (T_m) at higher temperatures.

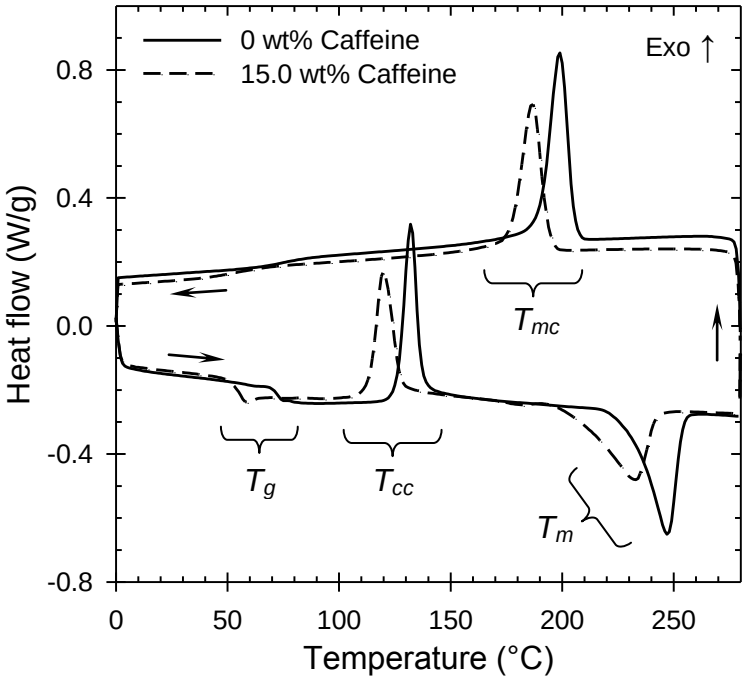

Figure 4.7. DSC thermogram for PET (solid line) and PET mixed with 15.0 ± 0.9 wt% caffeine (dashed line) during heating and subsequent cooling. The heat-cool cycles illustrate the four major thermal events as indicated by the following subscripts: *g* = glass transition, *cc* = cold crystallization, *m* = melting, and *mc* = melt crystallization.

As observed in Figure 4.7, all major thermal transitions for the caffeine containing sample are shifted to lower temperatures compared to the respective transitions for neat PET. Reduction of the glass transition temperature for the antiplasticized polymer is counterintuitive to the notion of increased chain rigidity at room temperature; however, this behavior can be physically rationalized. As mentioned previously in Sections 4.3.2 and 4.3.4, caffeine reduces the free volume of the glassy mixture by filling a portion of the idealized Langmuir "microvoids." It is known that the excess free volume of a glassy polymer decreases as temperature is increased to the glass transition temperature, with the excess free volume (Langmuir environment) disappearing completely at the glass transition temperature [21, 27]. Any caffeine which exists in the Langmuir environment will be liberated to enrich (or "plasticize") the dissolved mode as the temperature is

increased towards the T_g [11]. The latter effect produces the reduction in T_g for the mixture compared to the neat polymer.

In addition to the ~15.0 wt% caffeine sample illustrated in Figure 4.7, all caffeine containing samples studied herein exhibited reduced T_g's compared to neat PET. The T_g of a polymer/diluent mixture often exists at some temperature between the T_g's of both respective pure components. For the PET/caffeine system in the current work, the T_g of neat PET was measured to be ~69°C, while the T_g of caffeine has been reported at –17°C [35]. Polymer/diluent mixture T_g dependencies vs. diluent weight fraction can be described using various methods in the literature, where the empirical model of Fox [36] in Equation 4.5 has been useful to describe T_g effects in the presence of diluents:

$$\frac{1}{T_{g,m}} = \frac{w_1}{T_{g,1}} + \frac{w_2}{T_{g,2}} \tag{4.5}$$

In Equation 4.5, components w_1 and w_2 represent the weight fractions of the diluent and polymer, and *m* stands for *mixture*. Experimental T_g data vs. caffeine content measured via DSC and DMA (i.e., from the onset in *E*') in the current work are plotted in Figure 4.8, with the solid line in Figure 4.8 representing Equation 4.5. Inspection of Figure 4.8 reveals that Equation 4.5 provides a satisfactory description of the T_g data reported in this work pertaining to the relatively small range of 0 – 15 wt% caffeine studied.

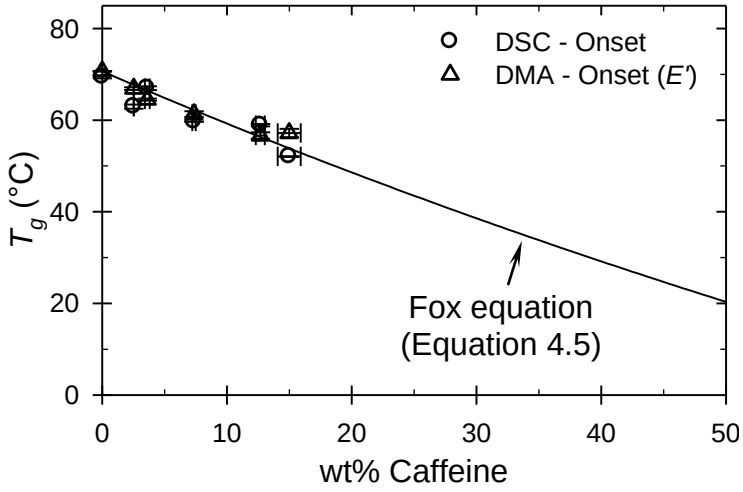

Figure 4.8. Glass transition temperature (T_g) data for amorphous PET/caffeine mixtures measured by DSC on the first heat (circles) and by DMA testing at 1 Hz (triangles). The solid line represents the Fox equation from Equation 4.5.

4.3.6. Dynamic Mechanical Analysis

Dynamic mechanical data recorded via tan δ (i.e., *E''/E'*, or the ratio of loss modulus to storage modulus) as a function of temperature and frequency can provide useful information regarding the viscoelastic relaxations in PET. Specifically, characteristics of the sub-ambient beta (β) relaxation are of interest in the current work, as such properties have been previously correlated with a wide variety of macroscopic properties for PET [12, 13, 37, 38] and other polymers [5, 39]. The β peak for PET, which occurs at approximately –60°C, differs from the alpha relaxation (α, or T_g) in that only localized chain motions can exist at temperatures so far below T_g in the glassy state [5, 40, 41]. As discussed in Chapter 3, the activation energy (E_A, kJ/mol) of the β relaxation can be calculated by applying the Arrhenius relationship in Equation 4.6 to data corresponding to the shift in β peak temperature (T, Kelvin) as a function of the dynamic test frequency (f, Hz), where A is a constant and R (8.314 J/mol·K) is the gas constant.

$$f = A\exp\left(-E_A \big/ RT\right) \tag{4.6}$$

Further information regarding the energetics of the β relaxation can be obtained via the activation entropy (ΔS), which is provided from Starkweather [42] in Equation 4.7.

$$E_A = RT\left[1+\ln\left(\frac{k}{2\pi h}\right)+\ln\left(\frac{T}{f}\right)\right]+T\Delta S \tag{4.7}$$

In Equation 4.7, ΔS is the activation entropy of the β relaxation, k and h represent Boltzmann's and Planck's constants, respectively, and T, f, R, and E_A are the same respective parameters employed in Equation 4.6. The activation entropy, in the context of Starkweather, provides an estimate of the cooperativity between moieties and neighboring polymer chains involved in the respective relaxation [42-44]. Viscoelastic relaxations which involve significant long-range motion, such as the glass transition, incur large values of ΔS, while values pertaining to the β relaxation are significantly smaller in magnitude [41, 42]. As will be shown, the beta peak energetic parameters pertaining to the various PET/caffeine samples in the current work are useful in assessing the impact of caffeine antiplasticization on the motional processes pertaining to penetrant diffusion.

Example tan δ data at 1 Hz over the temperature range of the β relaxation are plotted in Figure 4.9 for various PET/caffeine samples, where the data were smoothed over an interval of 10°C prior to plotting.

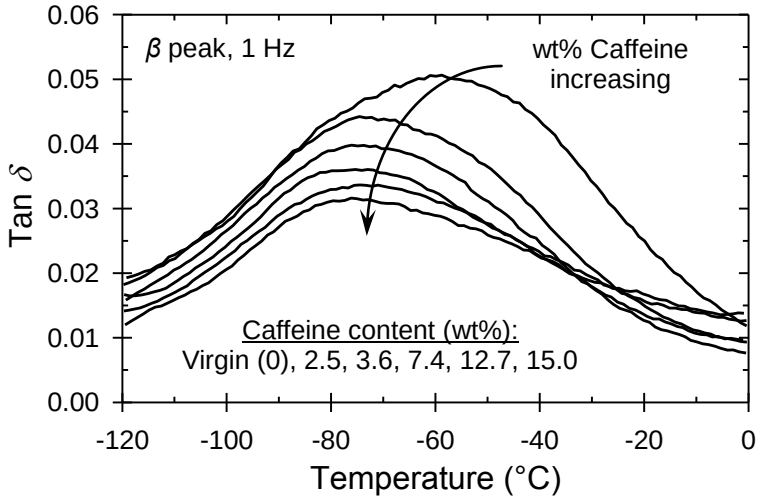

Figure 4.9. Example tan δ data at 1 Hz plotted over the temperature range of the β relaxation for various PET/caffeine samples. Data were smoothed over an interval of 10°C prior to plotting.

From Figure 4.9, it is apparent that the overall magnitude of the β peak is continually suppressed with increasing caffeine content. Such peak suppression has been observed in other PET antiplasticization reports in the literature [11-13, 37], and also in cases involving copolymerizing PET with increasing quantities of mobility-restricting co-monomers [12, 38, 45, 46]. Additional work has correlated a reduction in β peak intensity or area under the β peak curve to reduction in penetrant diffusivity [38, 47], and as seen in Figure 4.9 and Table 4.3, such correlation clearly exists in the current work.

The curves in Figure 4.9 also reveal that peak suppression occurs more significantly on the high temperature side of the curve, while the low temperature side is less suppressed with increasing caffeine content. Maxwell and coworkers [13, 37] observed similar trends in their work regarding PET antiplasticization, and used a combination of NMR, mechanical (DMA), and dielectric methods to correlate an ideal flipping motion of the phenyl rings to the high temperature side of the peak and motions of the carbonyl groups to the low temperature side of the peak. The results in Figure 4.9, when examined

within this context, suggest that caffeine antiplasticization suppresses the phenyl ring-flipping motion more significantly than the motions of the carbonyl groups. As will be shown, this notion is consistent with the implications from the energetic parameters measured for the various PET/caffeine mixtures.

A plot of the β peak E_A values for the various PET/caffeine mixtures vs. caffeine content is provided in Figure 4.10, with the corresponding values also listed in Table 4.6 along with the β peak max temperatures, ΔS values, and T_g values measured via DSC (cf. Section 4.3.5). The activation energy of ~72 kJ/mol for virgin PET listed in Table 4.6 exhibits excellent agreement with multiple literature reports [11, 37, 41, 48], and as a control, is very similar to the value for pure PET which was melt-processed without caffeine in the Brabender (i.e., ~68 kJ/mol). The latter depression may be a small antiplasticization effect resulting from the presence of minor thermo-oxidative degradation byproducts inevitably formed during processing in the melt. However, as will be shown, this small effect on the resultant E_A values for the PET/caffeine mixtures is secondary to the much larger effect of caffeine.

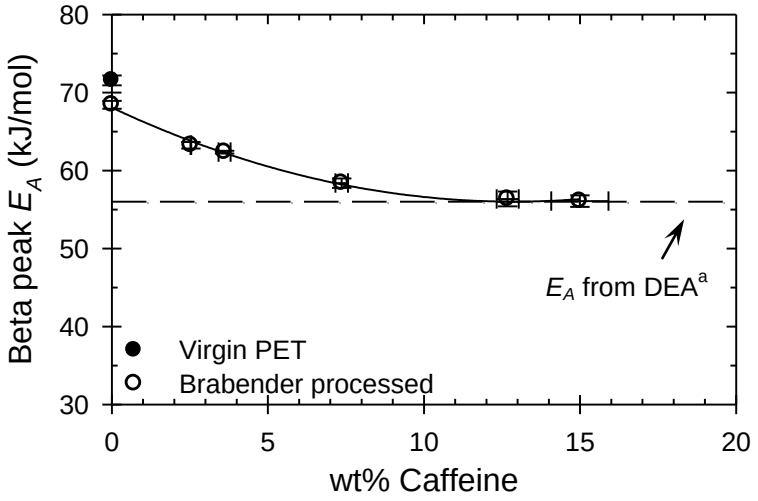

Figure 4.10. Beta peak E_A values for various PET/caffeine samples vs. caffeine content. The solid line is drawn to aid the eye, and the dashed line represents the beta peak E_A measured for pure PET via dielectric analysis ([a]DEA) (i.e., 56 ± 10 kJ/mol from [37]).

Table 4.6. Thermal and mechanical data for various amorphous PET/caffeine samples.

wt% Caffeine	DSC	DMA			
	T_g[a] (°C)	T_g[b] (°C)	β peak temp at 1 Hz (°C)	$E_A(\beta)$ (kJ/mol)	$\Delta S(\beta)$ (J/mol·K)
0 (Virgin[c])	–	–	-61 ± 1	72 ± 1	102 ± 3
0 (Brabender[d])	69 ± 0.3	71 ± 0.1	-66 ± 0.8	68 ± 0.5	94 ± 1
2.5 ± 0.01	63 ± 0.5	67 ± 0.3	-70 ± 0.4	63 ± 0.4	77 ± 1
3.6 ± 0.2	67 ± 0.4	64 ± 0.2	-73 ± 0.1	62 ± 0.2	77 ± 1
7.4 ± 0.2	60 ± 0.1	61 ± 0.6	-73 ± 0.9	58 ± 0.6	58 ± 2
12.7 ± 0.4	59 ± 0.3	57 ± 0.7	-72 ± 1	56 ± 1	45 ± 4
15.0 ± 0.9	52 ± 0.1	57 ± 0.9	-74 ± 2	56 ± 0.7	47 ± 4

a: T_g data measured via the onset on the first heat.
b: T_g data measured at 1 Hz via the onset in storage modulus (E').
c: Virgin PET *not* brabender-processed.
d: Pure PET processed in the brabender.

As seen in Figure 4.10, the β peak E_A values decrease with increasing caffeine content. Such behavior can be rationalized using the notion of reduced free volume and

increased chain packing. For example, since the antiplasticized samples exhibit reduced free volume compared to neat PET (cf. Section 4.3.4), the antiplasticized chains experience less motional freedom in the glassy state and therefore require less energy to activate the small-scale localized motions associated with the β relaxation. Interestingly, the beta peak E_A values in Figure 4.10 appear to plateau at a minimum value of ~56 kJ/mol at a caffeine loading of ~15.0 wt%. The dashed line in Figure 4.10 corresponding to this minimum represents data measured by Maxwell et al. [37] using dielectric analysis (DEA), which probes the polar contributions (i.e., carbonyl motions) to the activation energy. The E_A approach in Figure 4.10 to the minimum E_A measured by DEA signifies that the motions of the phenyl rings are being continually suppressed by caffeine addition, and that the motions of the carbonyl moieties are ideally unaffected. Evidence to support this notion is provided by Choudhury et al. [49], who used solid-state NMR measurements to verify that phenyl ring-flipping motions in antiplasticized PET were suppressed compared to neat PET.

Similar to the β peak activation energies, the corresponding activation entropies in Table 4.6 also continually decrease with increasing caffeine content. This behavior, in the context of Starkweather [42-44], indicates that the localized pendant motions are becoming more "simple" and less cooperative in nature. The latter notion is consistent with the overall reduction in free volume for the caffeine antiplasticized samples compared to neat PET (cf. Sections 4.3.2 and 4.3.4), and is related to the suppression of the phenyl ring-flipping motions in the glassy state.

The mechanical measurements reported thus far provide a framework for unifying the entire discussion regarding caffeine antiplasticization of PET. For example, while

antiplasticization occurs in part via the overall reduction in free volume for the mixture compared to neat PET (cf. Section 4.3.4), the mechanical measurements indicate that the primary mechanism for improvement originates from suppression of the phenyl ring-flipping motion. This concept is consistent with both the equilibrium sorption and diffusion results discussed in Sections 4.3.2 and 4.3.3, respectively, which indicate that the transport reductions measured via diffusion (and by default, chain mobility) are more dominant than the transport reductions measured via sorption (cf. Table 4.4). The conclusion that barrier improvement from caffeine antiplasticization of PET is related to the hindrance of the phenyl ring-flipping is therefore logical, and provides additional evidence to that already found in the literature [12, 13, 37, 49].

One final note should be mentioned regarding the ring-flipping motions in PET. Similar to the terephthalate group in PET, caffeine assumes a planar three-dimensional structure. It is perhaps logical to hypothesize that a synergistic attraction exists between caffeine and the terephthalate group, such that a caffeine molecule may in fact interact with the terephthalate group in a way that hinders ring-flipping. This notion warrants additional investigation, and could serve as a platform for guiding design of next-generation antiplasticizer molecules.

4.4. Summary and Conclusions

Caffeine antiplasticization of amorphous poly(ethylene terephthalate) (PET) was investigated using complementary transport (i.e., O_2 and CO_2), density, thermal, and mechanical methods. While previous work has investigated the performance of other antiplasticizers for PET (i.e., phenacetin and acetanilide [11]), caffeine is attractive due to

its food-grade compatibility.

Oxygen and carbon dioxide permeation measurements at 35°C demonstrate that significant reductions in transport are possible for caffeine antiplasticized samples compared to neat PET. Specifically, PET mixed with ~10.7 wt% caffeine exhibits >3X barrier improvements for both penetrants. Equilibrium sorption measurements from pressure-decay sorption allow quantification of the reductions in penetrant solubility for all PET/caffeine mixtures vs. neat PET. These solubility reductions, when combined with the diffusivity reductions measured via transient permeation, provide a means to understand the fundamental sorption vs. diffusion contributions to the overall permeability reduction in caffeine antiplasticized PET. Such investigation revealed that diffusion is significantly more important than sorption in determining carbon dioxide transport in antiplasticized PET, and revealed a similar, although less pronounced, trend for oxygen transport.

Density measurements for all PET/caffeine samples exhibit densification and reduction in free volume for the mixtures compared to neat PET. This behavior is consistent with the improved transport properties for the antiplasticized samples, where known correlations exist which relate permeability to an exponential dependence on free volume [29, 31]. Furthermore, solubility coefficients measured via both permeation and equilibrium sorption methods corroborate the notion that caffeine fills a portion of the excess free volume (i.e., Langmuir “microvoids”) in the glassy matrix.

Reduction in the glass transition temperature (T_g) measured via differential scanning calorimetry was observed for all PET/caffeine mixtures compared to neat PET, despite antiplasticization behavior occurring in the glassy state at 35°C. The T_g dependence was

effectively described over the concentration range using the Fox equation, which utilized values of the pure component T_g's. Not surprisingly, significant T_g reductions were observed for the PET/caffeine mixtures with high caffeine content due to the low T_g of pure caffeine (i.e., –17°C [35]).

Dynamic mechanical investigation of the sub-ambient beta (β) relaxation for the PET/caffeine mixtures provided insight into the effect of caffeine on the fundamental motional processes accessible in the glassy state. Testing at multiple frequencies allowed determination of both the activation energies and entropies associated with the β relaxation, and revealed that both parameters decrease with increasing caffeine content. The latter notion occurs via caffeine suppressing the phenyl ring-flipping motion in the PET/caffeine samples, and serves to explain the diffusion reductions compared to neat PET. The conclusion that the permeability reductions resulting from antiplasticization of PET originate from reductions in both solubility (i.e, "hole filling") and diffusivity (i.e., hindered phenyl ring-flipping) is logical, since undoubtedly, the two mechanisms are interrelated.

While caffeine antiplasticization serves as a promising technique to improve the barrier properties of PET, both improvements and drawbacks inevitably exist. The volatility of caffeine during melt-processing is a factor that must be addressed, since antiplasticization is only ideally possible when the diluent exhibits homogeneous mixing with the polymer. Despite the attraction of the improved barrier properties, the T_g reduction for the PET/caffeine samples is a drawback due to the already low T_g for pure PET. The latter T_g reduction in the caffeine containing samples is further amplified when humidity is introduced, since water induces plasticization in PET [50, 51] and since water

exists in the end-use applications regarding beverage containers. It should be reiterated, however, that the current study only investigates the effect of caffeine antiplasticization regarding *amorphous* PET, and that the presence of both crystallinity and orientation will help mitigate the T_g reductions observed in the current work pertaining to the amorphous state.

The logical next step will be to investigate the effect of caffeine antiplasticization on both semicrystalline and biaxially oriented PET samples, since blow-molding introduces such features. Specifically, it will be of interest to understand the effect of caffeine on the three phase model of crystallinity in PET [52], and to investigate the synergy in transport reduction that can be realized via combination of both antiplasticization and crystallization phenomena. While it is necessary to study such complicated cases, the current work provides an important "base-case" investigation that undoubtedly must begin with the simplified amorphous morphology.

4.5. References

1. Lange J and Wyser Y. Recent Innovations in Barrier Technologies for Plastic Packaging - a Review. Packaging Technology and Science 2003;16:149-158.
2. Bain DR and Giles GA. Technical and commercial considerations. In: Giles GA and Bain DR, editors. Technology of Plastics Packaging for the Consumer Market. Sheffield: Sheffield Academic Press Ltd, 2001.
3. Jackson WJ and Caldwell JR. Antiplasticization. II. Characteristics of antiplasticizers. Journal of Applied Polymer Science 1967;11(2):211-226.
4. Jackson WJ and Caldwell JR. Antiplasticization. III. Characteristics and properties of antiplasticizable polymers. Journal of Applied Polymer Science 1967;11(2):227-244.
5. Robeson LM and Faucher JA. Secondary Loss Transitions in Antiplasticized Polymers. Journal of Polymer Science Part B: Polymer Letters 1969;7:35-40.

6. Maeda Y and Paul DR. Effect of Antiplasticization on Gas Sorption and Transport. III. Free Volume Interpretation. Journal of Polymer Science: Part B: Polymer Physics 1987;25:1005-1016.

7. Vrentas JS, Duda JL, and Ling H-C. Antiplasticization and Volumetric Behaviour in Glassy Polymers. Macromolecules 1988;21:1470-1475.

8. Anderson SL, Grulke EA, DeLassus PT, Smith PB, Kocher CW, and Landes BG. A Model for Antiplasticization in Polystyrene. Macromolecules 1995;28(8):2944-2954.

9. Maeda Y and Paul DR. Effect of Antiplasticization on Gas Sorption and Transport. I. Polysulfone. Journal of Polymer Science: Part B: Polymer Physics 1987;25:957-980.

10. Maeda Y and Paul DR. Effect of Antiplasticization on Gas Sorption and Transport. II. Poly(phenylene Oxide). Journal of Polymer Science: Part B: Polymer Physics 1987;25:981-1003.

11. Lee JS, Leisen J, Choudhury RP, Kriegel RM, Beckham HW, and Koros WJ. Antiplasticization-based enhancement of poly(ethylene terephthalate) barrier properties. Polymer 2012;53:213-222.

12. Gohil RM. Designing polyethylene terephthalate-based barrier resins. Journal of Applied Polymer Science 2012;126(1):260-272.

13. Maxwell AS, Ward IM, Lauprêtre F, and Monnerie L. Secondary relaxation processes in polyethylene terephthalate-additive blends: 1. N.m.r. investigation. Polymer 1998;39(26):6835-6849.

14. Larocca NM and Pessan LA. Effect of antiplasticisation on the volumetric, gas sorption and transport properties of polyetherimide. Journal of Membrane Science 2003;218(1–2):69-92.

15. Emel'yanenko VN and Verevkin SP. Thermodynamic properties of caffeine: Reconciliation of available experimental data. The Journal of Chemical Thermodynamics 2008;40(12):1661-1665.

16. Paul DR and Koros WJ. Effect of Partially Immobilizing Sorption on Permeability and the Diffusion Time Lag. Journal of Polymer Science: Polymer Physics Edition 1976;14:675-685.

17. Petropoulos JH. Quantitative analysis of gaseous diffusion in glassy polymers. Journal of Polymer Science Part A-2: Polymer Physics 1970;8(10):1797-1801.

18. Burgess SK, Karvan O, Johnson JR, Kriegel RM, and Koros WJ. Oxygen Sorption and Transport in Amorphous Poly(ethylene furanoate). Polymer 2014;55(18):4748-4756.

19. Michaels AS, Vieth WR, and Barrie JA. Solution of Gases in Polyethylene

Terephthalate. Journal of Applied Physics 1963;34(1):1-12.

20. Michaels AS, Vieth WR, and Barrie JA. Diffusion of Gases in Polyethylene Terephthalate. Journal of Applied Physics 1963;34(1):13-20.

21. Koros WJ and Paul DR. Transient and Steady-State Permeation in Poly(ethylene Terephthalate) Above and Below the Glass Transition. Journal of Polymer Science: Polymer Physics Edition 1978;16:2171-2187.

22. Burgess SK, Mubarak CR, Kriegel RM, and Koros WJ. Physical Aging in Amorphous Poly(ethylene furanoate): Enthalpic Recovery, Density, and Oxygen Transport Considerations. Journal of Polymer Science Part B: Polymer Physics 2015;53(6):389-399.

23. Lee JS, Chandra P, Burgess SK, Kriegel R, and Koros WJ. An advanced gas/vapor permeation system for barrier materials: Design and applications to poly(ethylene terephthalate). Journal of Polymer Science Part B: Polymer Physics 2012;50(17):1262-1270.

24. Burgess SK, Kriegel RM, and Koros WJ. Diffusion Coefficient Modeling in Polyester Barrier Materials: Applications of Infinite Series Solutions. Society of Plastics Engineers - ANTEC Las Vegas, Nevada, 2014. pp. 830 - 835.

25. Kamiya Y, Hirose T, Mizoguchi K, and Naito Y. Gravimetric study of high-pressure sorption of gases in polymers. Journal of Polymer Science Part B: Polymer Physics 1986;24(7):1525-1539.

26. Wonders AG and Paul DR. Effect of CO2 exposure history on sorption and transport in polycarbonate. Journal of Membrane Science 1979;5(0):63-75.

27. Koros WJ and Paul DR. CO2 Sorption in Poly(ethylene Terephthalate) above and below the Glass Transition. Journal of Polymer Science: Polymer Physics Edition 1978;16:1947-1963.

28. Ruiz-Trevino FA and Paul DR. A Quantitative Model for the Specific Volume of Polymer-Diluent Mixtures in the Glassy State. Journal of Polymer Science: Part B: Polymer Physics 1997;36:1037-1050.

29. Lee WM. Selection of barrier materials from molecular-structure. Polymer Engineering & Science 1980;20(1):65-69.

30. Sugden S. Molecular Volumes at Absolute Zero. Part II. Zero Volumes and Chemical Composition. Journal of the Chemical Society 1927:1786-1798.

31. Park JY and Paul DR. Correlation and prediction of gas permeability in glassy polymer membrane materials via a modified free volume based group contribution method. Journal of Membrane Science 1997;125(1):23-39.

32. Slark AT. The effect of intermolecular forces on the glass transition of solute-polymer blends. Polymer 1997;38(10):2407-2414.

33. Vidotti SE, Chinellato AC, Hu GH, and Pessan LA. Effects of low molar mass additives on the molecular mobility and transport properties of polysulfone. Journal of Applied Polymer Science 2006;101(2):825-832.

34. van Krevelen DW and te Nijenhuis K. Properties of Polymers: Their Correlation with Chemical Structure, Their Numerical Estimation and Prediction from Additive Group Contributions, 4th ed. Amsterdam: Elsevier Science & Technology, 2009.

35. Descamps M, Correia NT, Derollez P, Danede F, and Capet F. Plastic and Glassy Crystal States of Caffeine. Journal of Physical Chemistry B 2005;109:16092-16098.

36. Fox TG. The Bulletin of the American Physical Society 1952;1:123.

37. Maxwell AS, Monnerie L, and Ward IM. Secondary relaxation processes in polyethylene terephthalate-additve blends: 2. Dynamic mechanical and dielectric investigations. Polymer 1998;39(26):6851-6859.

38. Light RR and Seymour RW. Effect of sub-Tg relaxations on the gas transport properties of polyesters. Polymer Engineering & Science 1982;22(14):857-864.

39. Ngai KL, Rendell RW, Yee AF, and Plazek DJ. Antiplasticization effects on a secondary relaxation in plasticized glassy polycarbonates. Macromolecules 1991;24(1):61-67.

40. English AD. Macromolecular dynamics in solid poly(ethylene terephthalate): proton and carbon-13 solid-state NMR. Macromolecules 1984;17(10):2182-2192.

41. Burgess SK, Leisen JE, Kraftschik BE, Mubarak CR, Kriegel RM, and Koros WJ. Chain Mobility, Thermal, and Mechanical Properties of Poly(ethylene furanoate) Compared to Poly(ethylene terephthalate). Macromolecules 2014;47(4):1383-1391.

42. Starkweather HW. Simple and Complex Relaxations. Macromolecules 1981;14(5):1277-1281.

43. Starkweather HW. Noncooperative Relaxations. Macromolecules 1988;21:1798-1802.

44. Starkweather HW. Aspects of simple, non-cooperative relaxations. Polymer 1991;32(13):2443-2448.

45. Polyakova A, Liu RYF, Schiraldi DA, Hiltner A, and Baer E. Oxygen-barrier properties of copolymers based on ethylene terephthalate. Journal of Polymer Science Part B: Polymer Physics 2001;39(16):1889-1899.

46. Polyakova A, Connor DM, Collard DM, Schiraldi DA, Hiltner A, and Baer E.

Oxygen-barrier properties of polyethylene terephthalate modified with a small amount of aromatic comonomer. Journal of Polymer Science Part B: Polymer Physics 2001;39(16):1900-1910.

47. Hiltner A, Liu RYF, Hu YS, and Baer E. Oxygen transport as a solid-state structure probe for polymeric materials: A review. Journal of Polymer Science Part B: Polymer Physics 2005;43(9):1047-1063.

48. Cristea M, Ionita D, and Simionescu BC. A new insight in the dynamo-mechanical behavior of poly(ethylene terephthalate). European Polymer Journal 2010;46:2005-2012.

49. Choudhury RP, Lee JS, Kriegel RM, Koros WJ, and Beckham HW. Chain Dynamics in Antiplasticized and Annealed Poly(ethylene terephthalate) Determined by Solid-State NMR and Correlated with Enhanced Barrier Properties. Macromolecules 2012;45(2):879-887.

50. Burgess SK, Mikkilineni DS, Yu DB, Kim DJ, Mubarak CR, Kriegel RM, and Koros WJ. Water Sorption in Poly(ethylene furanoate) Compared to Poly(ethylene terephthalate). Part 1: Equilibrium Sorption. Polymer 2014;55(26):6861-6869.

51. Burgess SK, Mikkilineni DS, Yu DB, Kim DJ, Mubarak CR, Kriegel RM, and Koros WJ. Water Sorption in Poly(ethylene furanoate) Compared to Poly(ethylene terephthalate). Part 2: Kinetic Sorption. Polymer 2014;55(26):6870-6882.

52. Lin J, Shenogin S, and Nazarenko S. Oxygen solubility and specific volume of rigid amorphous fraction in semicrystalline poly(ethylene terephthalate). Polymer 2002;43(17):4733-4743.

CHAPTER 5

CHAIN MOBILITY, THERMAL, AND MECHANICAL PROPERTIES OF PEF COMPARED TO PET[1]

This chapter investigates the fundamental chain mobility, thermal, and mechanical properties of poly(ethylene furanoate) (PEF), which is the furan-derived analog to poly(ethylene terephthalate) (PET), and relates performance enhancements vs. PET to underlying chain motional mechanisms. The improved barrier for PEF compared to PET is unexpected due to the higher free volume of PEF vs. PET. Segmental motions related to penetrant diffusion in both polyesters are studied using dynamic mechanical analysis, ^{13}C-CP/MAS solid-state NMR variable contact-time experiments, and Centerband-Only Detection of Exchange (CODEX) measurements. Unlike the active phenyl ring-flipping mechanism in PET, furan ring-flipping is greatly suppressed, thereby reducing beta relaxation motions and diffusion in PEF due to the energy penalty associated with the non-linear axis of ring rotation and ring polarity.

5.1. Introduction

Poly(ethylene terephthalate) (PET) has been the dominant polymer for beverage packaging for the past four decades due to its optical clarity, barrier properties, and competitive performance-to-cost ratio. While PET has met many of the current global packaging needs, high oxygen transmission rates coupled with the use of petroleum-

[1]Reproduced in part with permission from Burgess, S.K; Leisen, J.E.; Kraftschik, B.E.; Mubarak, C.R.; Kriegel, R.M.; Koros, W.J., *Chain Mobility, Thermal, and Mechanical Properties of Poly(ethylene furanoate) Compared to Poly(ethylene terephthalate)*, *Macromolecules*, 47, 1383-1391, Copyright 2014 American Chemical Society.

derived terephthalic acid (TA) limit effectiveness for oxygen-sensitive beverages [1] and environmental sustainability [2], respectively. Moreover, much research has been conducted to find bio-sourced alternatives to PET to reduce petroleum dependence and carbon dioxide emissions. Polyesters synthesized from 2,5-furandicarboxylic acid (FDCA) have received recent attention due to improved performance over PET coupled with the potential for fully renewable sourcing [2-7]. Poly(ethylene furanoate) (PEF), which is the direct furan analog to PET, is the primary focus of this chapter.

While FDCA is strikingly similar to TA, differences in ring size, polarity, and linearity result in significantly different performance metrics. TA exhibits an inter-atomic distance of 5.731 Å between carboxylic acid groups, while FDCA is notably shorter at 4.830 Å [4]. Moreover, the linear *para*- phenyl connection in TA results in an angle of 180° between carboxylic acid carbons while the non-linear structure of FDCA yields an angle of 129.4° [4]. Additionally, the non-linear character in FDCA combined with the permanent dipole frustrates the crystallization process, resulting in the slow isothermal crystallization rates observed by Knoop et al. [5].

Synthesis of PEF and fundamental property characterizations have been performed on a lab-scale by various researchers. Gandini et al. [3] synthesized PEF using an antimony catalyst in the transesterification step and subsequently characterized the results using differential scanning calorimetry (DSC), infrared spectroscopy (IR), and NMR methods. Gomes et al. [8] synthesized PEF and poly(3-propylene 2,5-furandicarboxylate) among others and characterized the products via IR and NMR methods. PEF analogs containing successively longer aliphatic segments were synthesized and characterized by Jiang et al. [9], while Gruter et al. [10] screened dozens of catalysts using small scale reactors.

Ambient-to-high temperature mechanical property characterization has been performed by Knoop et al. [5], in addition to preliminary crystallization studies. While the previous studies synthesized PEF on the lab-scale, recent advancement in catalyst technology by Avantium in the Netherlands has now enabled prospects for large-scale production.

Although much work has focused on synthesis and preliminary characterization of PEF, little has been reported on characterization of the barrier properties and its relationship to fundamental chain motion. Of particular importance is the significant reduction in reported oxygen permeability by a factor of ~10X for PEF compared to PET [11], despite PEF exhibiting a *higher* free volume. Preliminary work in our lab, discussed later, also shows similar permeability reductions for PEF compared to PET, along with similar oxygen solubilities for both polyesters. These factors, coupled with diffusion coefficient estimates from transient permeation measurements, prove that the large reduction in oxygen permeability for PEF is due primarily to a reduction in diffusion coefficient. This result is unexpected when considering the free volume framework of Cohen and Turnbull [12], and is the primary motivation for examining the chain mobility of PEF compared to PET.

The current chapter examines motional processes in high molecular weight PEF as revealed by thermal, mechanical, and solid-state NMR methods. Moreover, the observed performance differences between PET and PEF are inherently related to molecular structure and respective chain motional processes. We hypothesize that the asymmetric axis of ring rotation coupled with the dipolar furan moiety in PEF significantly hinders the furan ring-flipping mechanism from contributing to penetrant diffusion as observed via preliminary transport testing and the sub-ambient relaxation process as observed via

mechanical methods. ^{13}C cross-polarization magic-angle spinning (CP/MAS) solid-state NMR measurements corresponding to Centerband-Only Detection of Exchange (CODEX) and variable contact-time measurements will be shown to support this conclusion.

5.2. Experimental Methods

5.2.1. Materials and Film Preparation

The poly(ethylene furanoate) (PEF) and poly(ethylene terephthalate) (PET) used herein are the same materials described previously in Section 3.1.1, and all amorphous films were melt-pressed using the method in Section 3.1.3. Table 5.1 lists relevant structural and physical property information for both polyesters, while molecular weight information is available in Section 3.1.1.

Table 5.1: Structural and physical property information for amorphous PEF and PET.

Polymer	**Structure**	**ρ (g/cc)**	**T_g (°C)**	**T_m (°C)**	**T_d (°C)**
PEF	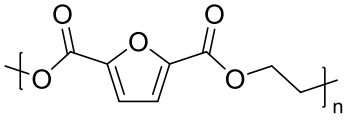	1.4299[a]	85[b]	211[b]	389[c]
PET	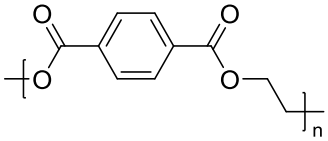	1.3346[a]	76[b]	247[b]	413[c]

a: Density, from density gradient column at 23°C.
b: Glass transition temperature, T_g, of amorphous sample and melting temperature, T_m, from differential scanning calorimetry.
c: Thermal degradation onset, T_d, from thermogravimetric analysis at 10°C/min under nitrogen.

5.2.2. Thermal, Mechanical, and ^{13}C Solid-State NMR Characterization

Differential scanning calorimetry (DSC) allowed measurement of relevant polymeric thermal properties. Heat-cool scans were recorded between 0°C and 280°C on a TA Q1000 DSC. Glass transition (T_g) temperatures were measured on the melt pressed samples using the half-C_p extrapolated tangent method on the second heat, which was measured using a heating rate of 20°C/min. The second heat was chosen for T_g determination because the first heat scan exhibited some noise due to the relaxation of residual stresses introduced from melt pressing. The film samples were dried overnight at 35°C prior to loading into aluminum pans for testing, as water is known to induce plasticization [13].

Similar to Chapter 4, dynamic mechanical data were recorded on a TA Q800 DMA in tensile geometry mode using a simultaneous frequency sweep and temperature ramp. The discrete frequencies ranged from 1, 2, 5, 10, and 20 Hz, while the furnace heated at 1.5°C/min from –120°C to 0°C and 0.5°C/min from 0°C to 150°C. T_g measurements were recorded using the maximum in tan δ peak.

Information regarding the experimental conditions for the solid-state NMR characterization data reported in this chapter is available in Section 3.7.4.

5.2.3. Supplemental Characterization

Density estimates for the sample films were measured at 23°C using a density gradient column (Techne™, NJ) containing water and calcium nitrate, as discussed previously in Section 3.7.1. All transport data reported herein were measured using the permeation and pressure-decay sorption methodologies provided in Chapter 3, which also

contains information regarding the methods employed for XRD, FTIR, and TGA characterization.

5.3. Results and Discussion

5.3.1. Preliminary Characterization

Density data for amorphous PEF and PET measured using a density gradient column at 23°C are reported in Table 5.1. Measurements were recorded after twenty minutes from introduction of the sample into the column to allow minimal time for water uptake to occur. The amorphous morphology for PET is further verified through excellent amorphous density agreement with other literature reports [14-16]. From Table 5.1, it is evident that PEF exhibits a considerably higher amorphous density than PET. So-called specific free volume ($\hat{V}_F$) and fractional free volume (*FFV*) are defined previously in Chapter 2 via Equations 2.39 and 2.40, respectively.

The occupied volume of the polymer, as utilized in Equation 2.39, can be estimated through group contribution techniques proposed by Sugden [17] and van Krevelen [18], among others. The method of van Krevelen utilizes the van der Waals specific volume ($\hat{V}_w$) and partitions the molecule into separate functional groups, while Sugden's method provides a direct estimation of $\hat{V}_0$ by summing contributions of individual atoms and structural features such as the presence of multiple bonds or rings. Although van Krevelen's method is slightly more accurate because it accounts for minor differences in atomic molecular volumes due to the presence of neighboring atoms, one difficulty is that successful parameter estimation requires accurate accounting of all functional groups in

the repeat structure. Since the furan moiety is absent in the functional groups tabulated by van Krevelen, Sugden's method was chosen despite having slightly reduced accuracy. Furthermore, meaningful comparison is possible since the same method is used for both polymers. Free volume calculations for both polyesters are provided in Table 5.2. Interestingly, PEF exhibits a higher fractional free volume than PET despite possessing a higher density.

Table 5.2: Fractional free volume (*FFV*) calculations for PEF and PET based on density measurements at 23°C and Sugden's method [17], and preliminary oxygen transport measurements at 35°C.

	MW[a] (g/mol)	$\hat{V}_g$ **(cc/g)**	$\hat{V}_0$ **(cc/g)**	***FFV*** **(–)**	**Permeability (Barrer)**	***k**** **(ccSTP/ccPoly·atm)**	$D_{eff}\cdot 10^9$ **(cm^2/s)**
PEF	182.1	0.699	0.592	0.153	0.0107	0.094	1.04 ± 0.06
PET	192.2	0.749	0.652	0.130	0.114	0.102	11.6 ± 0.44

a: Molecular weight of the repeat unit.

Preliminary oxygen transport data in both polyesters are provided in Table 5.2. Equilibrium oxygen sorption data measured at 35°C for both polyesters are given in the form of a single effective low-pressure solubility coefficient (k^*) [19], where $k^* = (k_D + C'_H b)$ and k_D, C'_H, and b are the parameters of the dual-mode model discussed previously in Chapter 2 [20]. A more detailed description of oxygen sorption and transport in PEF is outside the scope of this chapter, and is provided later in Chapter 6. From Table 5.2, it is evident that PEF and PET exhibit strikingly similar oxygen solubilities at 35°C. Consequently, the large reduction in oxygen permeability by ~11X for PEF vs. PET results from a reduction in diffusion coefficient as evidenced by the D_{eff} values in Table 5.2.

FTIR scans between 4000 – 600 cm^{-1} for both polyesters are provided in Figure 5.1. Corresponding peak assignments are listed in Table 5.3, and exhibit excellent agreement with prior reports for both PET [21] and PEF [8, 9].

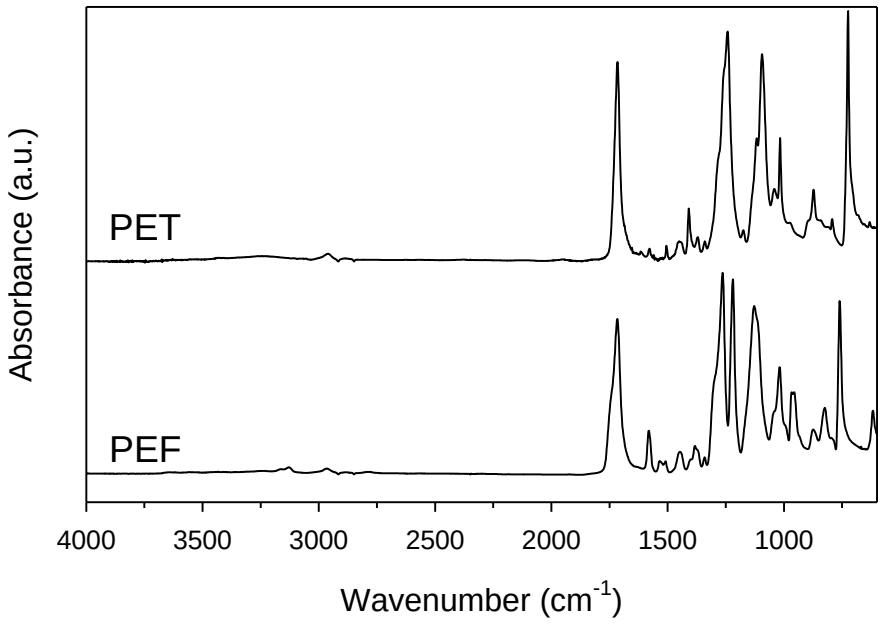

Figure 5.1: FTIR spectra for amorphous PEF and PET films.

Table 5.3: FTIR peak assignments for amorphous PEF and PET.

Functional Group	Wavenumbers (cm^{-1})	
	PEF	**PET**
=CH (furan ring)	3129	—
C-H (CH_2)	2965	2960
C=O stretch (ester)	1716	1716
C-C stretch (ring)	1581	1578
C-O stretch (ester)	1264	1258
C-C-C bend (ring) C-C stretch (ring)	1018	1017
Ring torsion C=O out-of-plane bend (ester) C-H out-of-plane bend (ring)	760	725

X-ray diffraction (XRD) was used to verify the amorphous morphology of both polyesters after the quench step in the melt press procedure. XRD measurements were also performed on a PEF film crystallized for 6 hours at 160°C under vacuum for comparative purposes. Figure 5.2 shows XRD spectra for both amorphous and semicrystalline PEF films, and the primary peak locations for semicrystalline PEF agree with other reports [9].

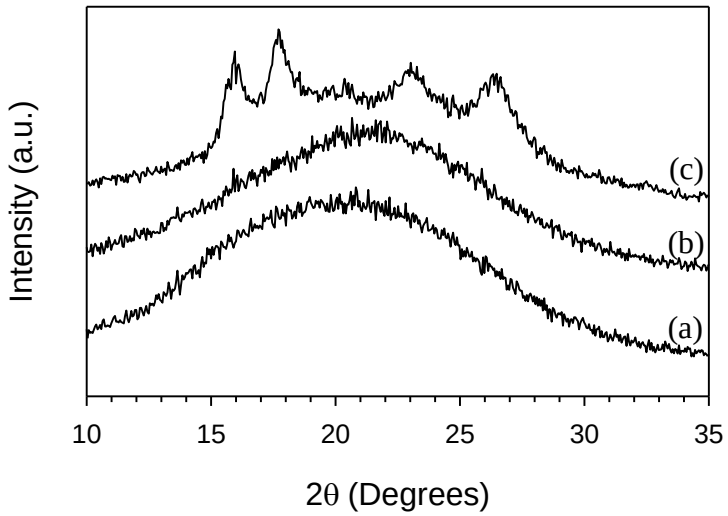

Figure 5.2: X-ray diffraction patterns of amorphous PET (a), amorphous PEF (b), and semicrystalline PEF (c).

Decomposition temperatures were recorded via thermogravimetric analysis (TGA) for PEF and PET under nitrogen atmosphere. Example TGA traces for both polyesters are provided in Figure 5.3, with decomposition data listed in Table 5.1. A 24°C reduction in decomposition temperature for PEF is notable considering that PEF exhibits a higher degree of chain rigidity than PET.

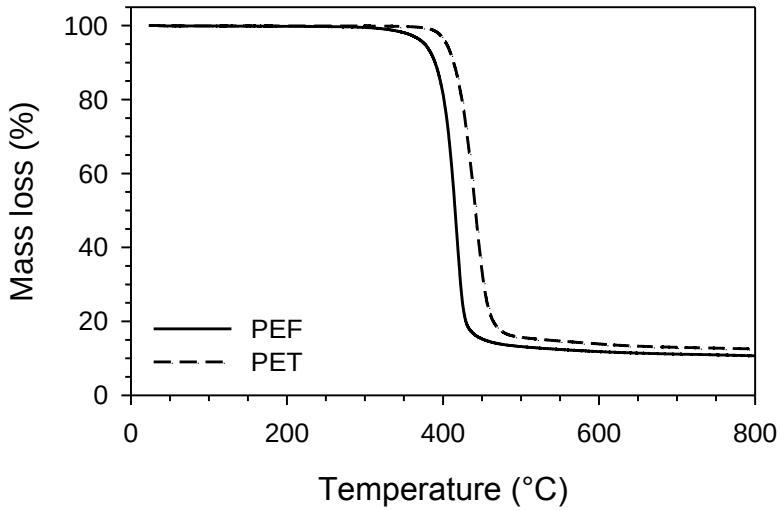

Figure 5.3: TGA decomposition curves for amorphous PEF and PET under N_2 atmosphere, 10°C/min.

5.3.2. Differential Scanning Calorimetry

Thermal transitions for both polyesters recorded during the first heat cycle are shown in Figure 5.4. The pronounced glass transition signatures are consistent with the amorphous morphology. The anomalous shape of the curves near the T_g for both polyesters is due to relaxation of minor residual stresses imparted during the melt press procedure. Furthermore, the small endothermic peak near the high temperature side of the T_g corresponds to enthalpic relaxation from aging and has been observed in other studies [14, 15]. Glass transition measurements were recorded using the half-C_p extrapolated tangent method on the heat capacity data, and are listed in Table 5.1 for both polyesters. The T_g increase of 9°C for PEF compared to PET is consistent with a higher degree of chain rigidity for PEF. In comparison, a significantly reduced T_g of 59°C has been reported for poly(ethylene isophthalate) (PEI) [22], which exhibits a similar non-linear structure to PEF due to the *meta*- phenyl ring conformation. Due to the reduced T_g, PEI is regarded as a non-viable replacement for PET. A simple comparison of the T_g values from PEF and PEI to PET can help distinguish between property enhancements resulting from solely the non-linearity in PEI or the non-linear furanic moiety in PEF.

From Figure 5.4, it is apparent that PET exhibits a large cold-crystallization and melting peak, whereas the heat flow curve for PEF above T_g is flat. The absence of cold-crystallization and subsequent melting peaks for PEF indicates the long time-scale of the crystallization process. Crystallization in PEF is presumably hindered by increased structural rigidity and the asymmetric axis of rotation around the furan ring. Small melting endotherms for PEF appeared on the second heat, and apparent melting points measured by heating at 10°C/min for both polyesters are reported in Table 5.1.

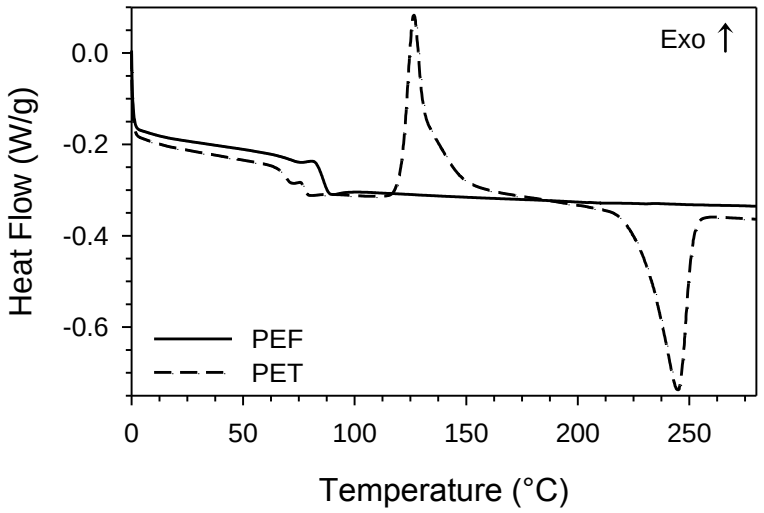

Figure 5.4: DSC curves for amorphous PEF (solid line) and PET (dashed line) on first heat, 10°C/min.

5.3.3. Dynamic Mechanical Analysis

Temperature and frequency dependent mechanical relaxation data for PEF and PET were recorded via storage modulus (*E'*), loss modulus (*E"*), and tan δ, which is the ratio of the loss modulus to storage modulus. Figures 5.5 and 5.6 show representative *E'* and *E"* traces for both polyesters, respectively. *E'* values of 3285 ± 47 MPa and 2120 ± 38 MPa are reported at 35°C for PEF and PET, respectively. The larger storage modulus for PEF is attributed to increased chain rigidity, and similar observations have been made for modulus increases [23] and decreases [24] based on respective changes in chain rigidity. The glass transition temperature is recognized in Figure 5.5 by the large drop in storage modulus and in Figure 5.6 by the corresponding peak maximum in loss modulus. Crystallization is observed by the increase in storage modulus after 100°C for both polymers, but is much less pronounced for PEF due to the considerably slower crystallization rate.

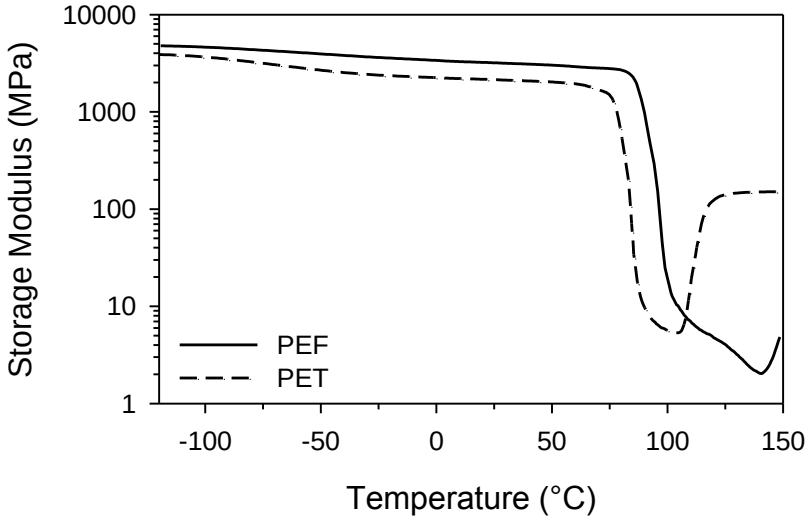

Figure 5.5: Storage modulus (*E'*) curves for PEF and PET. Recorded at 1 Hz, 1.5°C/min between –120°C to 0°C, 0.5°C/min between 0°C and 150°C.

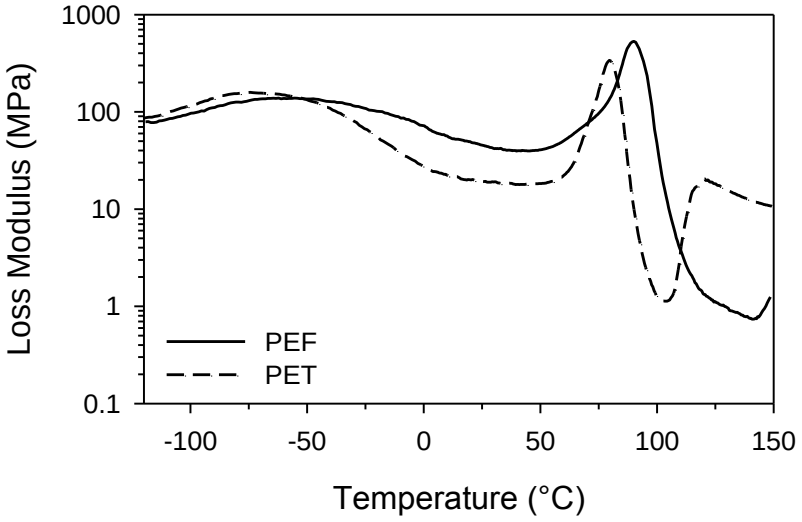

Figure 5.6: Loss modulus (*E"*) curves for PEF and PET. Recorded at 1 Hz, 1.5°C/min between 120°C to 0°C, 0.5°C/min between 0°C and 150°C.

A frequency dependent Arrhenius relationship can be used to calculate the activation energy (E_A) of both the T_g relaxation (alpha) and the sub-T_g relaxation (beta) specific to both polyesters.

$$f = A\exp\left(-E_A \diagup RT\right) \tag{5.1}$$

In Equation 5.1, f is the frequency of the dynamic oscillations (Hz), A is the pre-exponential factor, E_A is the activation energy (kJ/mol), R is the universal gas constant (8.314 J/mol·K), and T is the temperature in Kelvin of the maximum in the tan δ peak. A linearized form of Equation 5.1 can be used with experimental data to determine the activation energy for both alpha and beta relaxations. The activation energy of a viscoelastic process can be further related to the activation entropy (ΔS) through the relationship derived by Starkweather [25].

$$E_A = RT\left[1+\ln\left(\frac{k}{2\pi h}\right)+\ln\left(\frac{T}{f}\right)\right]+T\Delta S \tag{5.2}$$

In Equation 5.2, h is Planck's constant, k is Boltzmann's constant, T is the peak temperature (Kelvin) of tan δ for the viscoelastic relaxation, f is the frequency (Hz) of the experiment, and ΔS is the activation entropy (kJ/mol·K) of the transition. Relaxation processes involving large-scale cooperative chain motion have large activation entropies, while relaxations pertaining to localized and non-cooperative motions have increasingly reduced, and in some cases, essentially zero activation entropies [26, 27]. The former is typical of the glass transition, which signifies the beginning of micro-Brownian chain motion. The latter, however, is more common to all sub-T_g relaxations, as sub-T_g relaxations primarily involve only localized chain motion [28-31]. Quantitative values of the activation entropy are useful in assessing the degree of cooperativity associated with

the relaxation process, and give information regarding the underlying motional processes occurring at the molecular level.

A linearized Arrhenius relationship is generally not applicable to the alpha relaxation, as curvature induced by the spectrum of relaxation times precludes accurate calculation of the E_A. For such cases, the Williams-Landel-Ferry (WLF) equation [32] or the Vogel-Fulcher-Tamman (VFT) equation [33] can be used to account for curvature. As commonly observed with mechanical testing [34, 35], the limited scale of frequencies accessible via DMA prevented accurate parameter estimation for the WLF or VFT equations in the current work. Nevertheless, observed linearity as described by the Arrhenius relationship yields a first estimate of the alpha peak E_A and provides a basis for comparison between the two polyesters. The alpha peak E_A approximations for PEF and PET are given in Table 5.4, with uncertainty limits derived from the standard error. The E_A value of 550 ± 6 kJ/mol for PET is similar to the value of 432 kJ/mol reported by Cristea et al. [36] and significantly lower than the value of 775 kJ/mol reported by Mackintosh and Liggat [35]. A higher activation energy for PET compared to PEF is consistent with other reports showing a higher value for PET when compared to analogously more rigid polymers, such as poly(ethylene naphthalate) (PEN) [35]. The large activation entropies observed at the T_g for both polyesters are consistent with the onset of long-range, highly cooperative segmental chain motion.

Table 5.4: Arrhenius approximation for the activation energy (E_A) and entropy (ΔS at 1 Hz) of the alpha relaxation for PEF and PET.

	Peak temperature at 1 Hz (T_g) (°C)	**E_A (alpha) (kJ/mol)**	**ΔS (alpha) (J/mol·K)**
PEF	98 ± 0.1	475 ± 5	1040 ± 14
PET	86 ± 0.3	550 ± 6	1290 ± 18

Analysis of the beta relaxation for PEF and PET using the Arrhenius relationship is considerably more accurate than for the alpha relaxation due to the expected linear relationship between ln(f) and 1/T. Moreover, the beta relaxation is of primary interest in this work, as researchers have linked characteristics of the beta peak to numerous macroscopic polymer properties [28, 30, 31, 37, 38]. Light and Seymour [37] observed that the area under the tan δ curve and tan δ peak maximum for the beta relaxation increased or decreased when PET was copolymerized with mobility-enhancing and mobility-restricting monomers, respectively. They further illustrated a direct correlation between beta peak area and oxygen diffusivity, demonstrating that the molecular motions associated with the beta peak were directly related to gas diffusivity. Their claims were further justified through direct permeability measurements at temperatures below and above the beta peak temperature for PET. A more detailed analysis of the beta transition was conducted by Maxwell et al. [30, 31], who used a combination of mechanical (DMA), dielectric, and NMR techniques to probe the specific molecular contributions to the beta peak. They give evidence that the beta peak E_A for PET consists of two primary contributions—one from phenyl ring-flipping and the other from carbonyl motions. Further testing by Maxwell and coworkers [30, 31] on PET samples mixed with mobility-restricting low-molecular weight diluents (i.e. antiplasticizers) showed that increased

antiplasticizer loadings resulted in further reduced beta peak E_A values. An accompanying suppression of the high temperature side of the beta peak was also observed, which the authors attributed primarily to suppression of the phenyl ring-flipping mechanism. Their final conclusion argues that the mechanism for beta peak E_A reduction during antiplasticization consists solely of phenyl ring motion suppression, and that the antiplasticizer loading is not effective at suppressing the carbonyl contribution to the beta peak E_A.

Figure 5.7 shows the tan δ curves at 1 Hz for PEF and PET over the temperature range of the beta relaxation. First inspection of Figure 5.7 reveals that the beta peak for PEF is shifted to a higher temperature and the magnitude is considerably suppressed compared to PET. Activation energies and entropies calculated from Equations 5.1 and 5.2 are given in Table 5.5. The beta peak activation energy of 72 kJ/mol for PET is consistent with various literature reports [14, 30, 36]. Clearly, differences in peak shape and activation energy/entropy between polyesters must be related to polymer structure and inherent molecular motions. Interpretation of the experimentally observed differences can be elucidated through comparison with data from structurally similar polymers.

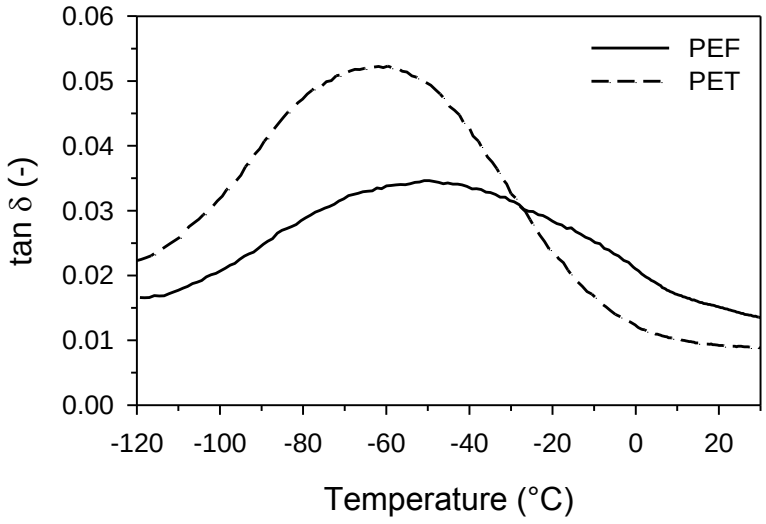

Figure 5.7: Tan δ curves at 1 Hz for PEF and PET over the temperature range of the beta relaxation.

Table 5.5: Activation energies (E_A) and entropies (ΔS at 1 Hz) of the beta relaxation for PEF and PET.

	Sample	**Peak Temperature at 1 Hz (°C)**	**E_A (beta) (kJ/mol)**	**ΔS (beta) (J/mol·K)**
DMA	PEF	–50 ± 1	68 ± 2	68 ± 9
	PET	–61 ± 1	72 ± 1	102 ± 3
DEA[a]	PET	–70	56 ± 10	53 ± 10

a: Dielectric measurements (DEA) [30].

Poly(ethylene isophthalate) (PEI) is a structural isomer of PET, with the sole difference being the *meta*- and *para*- phenyl ring connections, respectively. The *meta*-connection gives PEI a bent structure that resembles the non-linear structure of PEF, and similar to PET and PEF, PEI exhibits a comparable beta relaxation. Light and Seymour [37] note in studying copolyesters of PET and PEI that introduction of the isophthalate group restricts sub-T_g motion as evidenced by a suppression in magnitude of the tan δ

corresponding to the beta relaxation. This trend was also observed by the results of Polyakova et al. [16], which showed a notable reduction in peak intensity of the beta relaxation for PEI when compared to PET. The difference in beta peak magnitude between polyesters can be examined in the context set forth by Maxwell et al. [30], who separated the tan δ peak for PET into separate contributions from the carbonyl motions and phenyl ring-flipping. Since PEI does not possess a symmetric axis of rotation around the phenyl ring, a phenyl ring flip in PEI will require a semi-cooperative motion of the neighboring carbonyl and ethylene units [39]. Moreover, the energy penalty for phenyl ring-flipping in PEI precludes this flipping mechanism from contributing to the magnitude of the beta peak. Abis et al. [39] provide NMR confirmation of this notion, where a significant difference in mobility between PET and PEI has been attributed to the respective *para*- and *meta*- phenyl ring connections. Similar results regarding mobility have also been observed with poly(ethylene naphthalate) (PEN), which has a bulky naphthalate group in place of the mobile phenyl group found in PET.

The relaxation data for PEF can be examined using the comparison between PET, PEI, and PEN. Similar to PEI and PEN, the asymmetric axis of furan ring rotation and ring polarity for PEF is thought to hinder this mechanism from contributing to the beta peak magnitude and activation energy. Figure 5.7 corroborates this claim through suppression in magnitude of the PEF beta peak when compared to PET. Additionally, the beta peak temperature for PEF is shifted ~11°C higher than for PET. This shift is attributed to increased chain rigidity for PEF, as shifts to both higher temperatures [16, 37, 40] and lower temperatures [24, 41] have been reported for mobility restricting and mobility enhancing co-monomers in PET copolymers, respectively. If the furan ring-

flipping mechanism in PEF does not significantly contribute to the beta peak activation energy, the resultant activation energy should represent the carbonyl motions alone, based on the work of Maxwell et al. [30, 31] for PET and the NMR results discussed below. If this is the case, then the beta peak activation energy for PEF might be expected to compare well with the activation energy contribution from solely the carbonyl motions in PET. Such selective characterization in PET is possible with dielectric analysis (DEA), which measures the relaxations induced by permanent dipoles such as the carbonyl moiety and neglects the contributions from non-polar moieties such as the phenyl ring. As a result, beta peak characteristics measured by DEA for PET therefore represent only the carbonyl contributions and can be used to compare directly with mechanical data for PEF.

Since carbonyl motions provide the dominant contribution to the beta peak activation energy in PEF, the activation energy and entropy measured from mechanical methods for PEF simplistically might be expected to have similar values to those measured by dielectric methods for PET. In fact, the beta activation energy of 68 kJ/mol for PEF measured by DMA is much higher than the 56 kJ/mol for PET measured by DEA [30] (Table 5.5), and almost equals the 72 kJ/mol for PET measured by DMA. Additionally, the activation entropy of 68 J/mol·K for PEF is considerably higher than the activation entropy of 53 J/mol·K resulting from the carbonyl motions alone for PET (Table 5.5).

While the furan rings are not thought to significantly contribute to the beta relaxation in PEF, the surprisingly high activation energy and entropy for the carbonyl motions warrant additional explanation. In the context of Starkweather [25-27], a large activation entropy signifies the presence of complex interactions involving either multiple functional groups or interaction between neighboring chains. A larger beta activation

energy and entropy for PEF when compared to PET therefore implies that the carbonyl motions in PEF are more complex and interactive than the respective motions in PET. This conclusion is logical, as the furan rings in PEF are highly polar when compared to the non-polar phenyl rings in PET. Moreover, a smaller distance between carbonyls is observed in PEF due to the smaller size of the furan ring versus the larger phenyl ring in PET. The previous reasoning suggests that the carbonyl groups in PEF must undergo some type of concerted motion that is possibly coupled with small scale furan ring oscillations, a coupling that is apparently dampened by the non-polar phenyl ring spacers present in PET. To illustrate, a useful comparison can be made between the beta peak characteristics of PET and PEN. The bulky napthalate group in PEN isolates the carbonyl motions more so than the single phenyl ring in PET. A report [34] that the activation energy and entropy of the carbonyl motions in PEN is slightly lower than that for PET is therefore not surprising, as isolation of the carbonyl groups causes a reduction in cooperative motion. The increased activation entropy and energy for the carbonyl motions in PEF therefore reflect a *higher degree* of cooperativity than the motions in PET.

Preliminary oxygen transport measurements for PEF and PET show the large significance of the suppression of ring flips in PEF, despite PEF exhibiting a larger free volume than PET. The similarity of oxygen sorption, coupled with the large reduction in diffusion coefficient for PEF compared to PET, proves that the significantly reduced permeability is a result of the reduced diffusion and, consequently, the chain motion. Similar permeability reductions are also observed when comparing permeability in PEI and PEN to PET [16, 37, 39], where drastic transport differences are attributed to reduced

motion resulting from the rigid isophthalate and naphthalate groups, respectively.

A final note should be mentioned regarding the sensitivity of both polyesters to orientation effects. As mentioned previously, only non-oriented polyester films were tested and reported in this work. In the case of PEF, the large as-received pellets were cryogenically ground into powder and evenly spread across the pressing plate to allow for sufficient heat transfer and melting prior to pressing. If cryogenic grinding was not performed, the large pellets would not completely melt prior to pressing and a slightly oriented film could potentially result. DMA testing of such oriented films show reduced beta peak E_A's for both PEF and PET, and is likely due to increased chain packing from melt orientation.

5.3.4. NMR Spectroscopy and Chain Mobility

Detailed ^{13}C solid state NMR measurements have been used to corroborate the mechanical relaxation data by verifying the hindrance of furan ring-flipping in PEF. Figure 5.8 shows the CP/MAS spectra recorded at 35°C for both polyesters, and Table 5.6 lists the primary isotropic peak resonances.

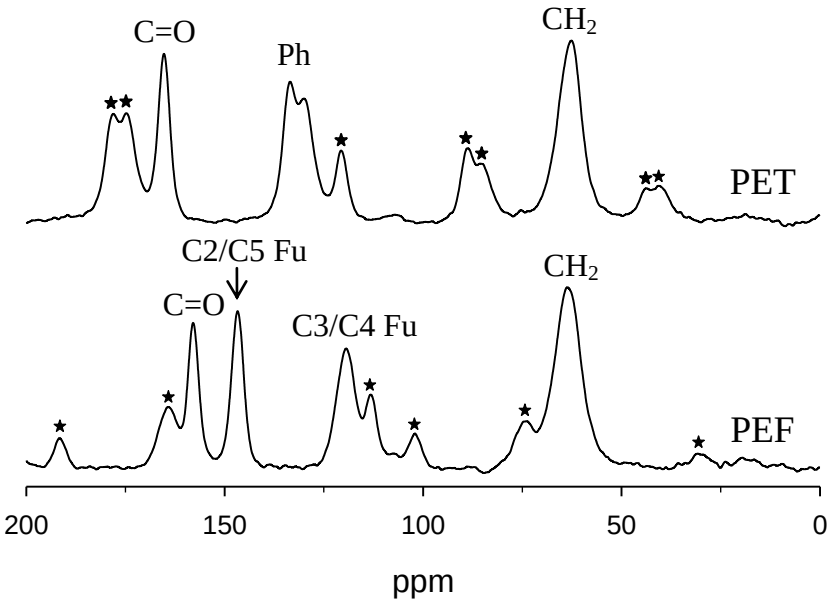

Figure 5.8: ^{13}C-CP/MAS solid-state NMR spectra for amorphous PEF and PET at 35°C. Asterisks indicate spinning sidebands. Ph = phenyl, Fu = furan.

Table 5.6: Isotropic peak resonance locations for PEF and PET at 35°C.

Sample	Carbon type	Resonance (ppm)
PEF	Carbonyl	158
	Non-protonated aromatic	147
	Protonated aromatic	119
	Aliphatic	64
PET	Carbonyl	165
	Non-protonated aromatic	134
	Protonated aromatic	130
	Aliphatic	63

Variable contact-time experiments were used to study the dipolar coupling between ^{1}H and ^{13}C species for all carbon types in both polyesters. This technique provides the time constants for magnetization buildup (T_{CH}) and subsequent decay ($T_{1\rho}(^{1}H)$) for each

carbon type. T_{CH} describes the magnetization buildup and depends on mobility and the internuclear distance between ^{1}H and ^{13}C species. Since T_{CH} depends on the neighboring proton environment and since PEF contains two fewer protons in the repeat structure than PET, this parameter cannot be used for a meaningful comparison between PET and PEF. Alternatively, $T_{1\rho}(^{1}\mathrm{H})$ *is* useful for comparison because it reflects molecular mobility on a more general scale. A simplified analytical description of the signal intensities M measured for each peak as a function of contact time τ can be achieved using the following equation [42-44]:

$$M(\tau) = \sum_i M_{0i} \left[\frac{e^{-\tau/T_{1\rho i}(^{1}\mathrm{H})} - e^{-\tau/T_{\mathrm{CH}i}}}{1 - T_{\mathrm{CH}i}/T_{1\rho i}(^{1}\mathrm{H})} \right] \tag{5.3}$$

The multiple terms in the summation of Equation 5.3 are due to buildup/decay processes corresponding to multiple correlation times or variable distances between ^{1}H and ^{13}C atoms. If multiple terms in Equation 5.3 are required, independent measurement of the $T_{1\rho i}(^{1}\mathrm{H})$ parameters should be performed to provide a rigorous model fit to the data [42]. The current study avoids independent $T_{1\rho i}(^{1}\mathrm{H})$ measurement by considering only the data measured from the carbonyl carbons, which can be fitted well by Equation 5.3 using a single component for $T_{1\rho}(^{1}\mathrm{H})$ and T_{CH}. This is likely due to the presence of spin-diffusion (see below) leading to a single effective value for $T_{1\rho}(^{1}\mathrm{H})$ together with the low density of protons at the site of the carbonyl group. This sparsity of protons leads to long values for T_{CH}, which also lends itself to spin-diffusion averaging. Figure 5.9 illustrates intensities as measured for the carbonyl carbon peak as a function of the contact time τ.

A good fit is achieved for both PET and PEF using Equation 5.3, while Table 5.7 lists the relevant model fit parameters.

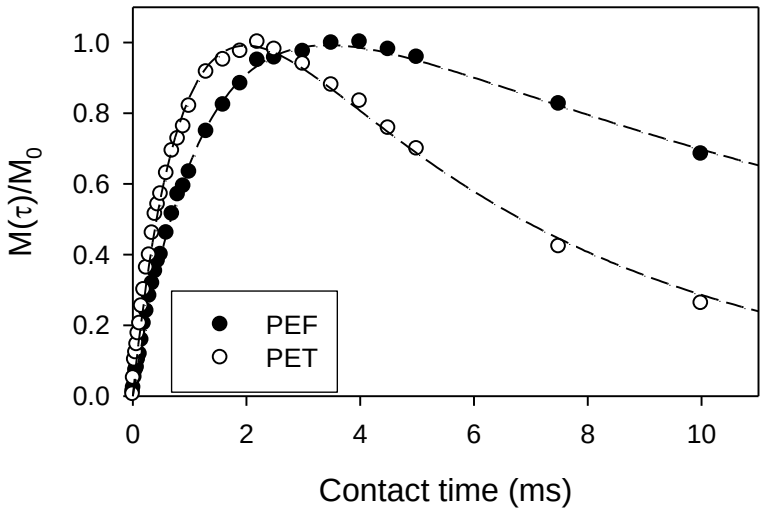

Figure 5.9: Variable contact-time curves for the carbonyl carbons in PEF and PET, measured at 50 kHz and 35°C. Dashed lines represent model fits from Equation 5.3 (i = 1) to the experimental data.

Table 5.7: Comparison between $T_{1\rho}(^1H)$ values for PEF and related amorphous polyesters. All $T_{1\rho}(^1H)$ values measured in the current work reflect motions detected through the carbonyl carbons.

	Reference	**Temperature (°C)**	**Frequency (kHz)**	$T_{1\rho}(^1H)$ **(ms)**	T_{CH} **(ms)**
PET	This work	35	50	5.6	0.91
PEF	This work	35	50	14.9	1.27
PET	[42]	25	50	4.7	—
PET-phenacetin	[42]	25	50	5.6	—
PET-semicrystalline	[42]	25	50	11.5	—
PET	[39]	24	38	5.1	—
PEI	[39]	24	38	10.6	—
PEN	[39]	24	38	10.0	—

Due to spin-diffusion the $T_{1\rho}(^1H)$ parameter reflects a general measure of chain rigidity. Spin-diffusion averaging is realized due to the "diffusion like" propagation of magnetization caused by dipolar coupling between individual ^1H sites, which results in the measurement of a single "averaged" $T_{1\rho}(^1H)$ at all sites despite each site having potentially different mobilities [45]. $T_{1\rho}(^1H)$ is therefore suitable for the comparison of mobility in various polyesters. While independent site-specific $T_{1\rho}(^1H)$ measurements are needed to verify the occurrence of spin diffusion, comparison of our experimental conditions to that in other works and the findings described therein suggest that it is observed in our measurements. Furthermore, the $T_{1\rho}(^1H)$ parameters listed in Table 5.7 from other works represent spin-diffusion averaged values, so a semi-quantitative comparison with the values from the current work is valid.

Choudhury et al. [42] report that $T_{1\rho}(^1H)$ sequentially increased for amorphous PET, amorphous PET mixed with 2.32 wt% phenacetin (acting as an antiplasticizer), and semicrystalline PET, thus showing a positive $T_{1\rho}(^1H)$ correlation with increasing chain rigidity. Abis et al. [39] measured $T_{1\rho}(^1H)$ and $T_{1\rho}(^{13}C)$ values for all carbon types in PET, PEI, and PEN and correlated the results to chain mobility. Interestingly, the authors found that PEI and PEN exhibited similar largely increased $T_{1\rho}(^1H)$ values when compared to PET, and used the $T_{1\rho}(^{13}C)$ values measured at two separate field strengths to assign mobile and rigid regions. The explanation for the lower $T_{1\rho}(^1H)$ value and increased mobility for PET as compared to PEI and PEN was based on the presence of ring-flipping. The *para*- phenyl connection in PET provides a lower energy barrier to ring-flipping when compared to the asymmetric *meta*- phenyl connection and bulky naphthalene rings in PEI and PEN, respectively. The current $T_{1\rho}(^1H)$ value for PET agrees

well with other literature reports (Table 5.7), while the $T_{1\rho}(^1H)$ value for PEF is comparable in magnitude to the values for PEI and PEN. The similarity in $T_{1\rho}(^1H)$ values of PEF, PEI, and PEN suggests that all three polymers exhibit a similar increased rigidity when compared to PET. Furthermore, the proclivity or hindrance of ring-flipping appears to correlate with our results.

Quantitative information regarding the ring-flipping mechanisms in PEF and PET can be obtained through Centerband-Only Detection of Exchange (CODEX) measurements. This technique is able to probe dynamics in the range of kHz – Hz by comparing the intensities measured for individual peaks in a ^{13}C NMR spectrum with the respective intensities of a corresponding reference spectrum. The CODEX experiment therefore requires subtraction of two similar spectra, and as such, the scale of noise in the CODEX spectrum will be larger than in the reference spectrum. Two-fold jump-type motions lead to a reduced intensity of the CODEX spectrum I_{CODEX} with respect to the reference spectrum I_{ref} by a factor ~0.5. The observable $S(t_m) = (I_{ref} - I_{CODEX})/I_{ref}$ measured as a function of the mixing time provides a correlation function, which allows the extraction of information regarding the time scale and mechanism of molecular motions.

We found the recording of CODEX experiments for our specific samples experimentally challenging. This is due to the fact that phenyl flips in polymers are often associated with a broad distribution of correlation times spanning over several decades. A distribution of correlation times ranging over 6 decades has been observed for PET using ^2H NMR [46]. Consequently, peaks in the ^{13}C-CP/MAS spectrum corresponding to the aromatic moieties will be associated with flips occurring on this broadly distributed time scale. Phenyl ring flips occur at any temperature between –30°C and the melting

temperature of PET; a significant fraction of these components is either too slow or too fast for detection by the CODEX experiment. These slow and fast fractions contribute to I_{ref} and I_{CODEX} such that $S(t_m)$, which only detects motions between ~ 10^{-3} – 10^{0} Hz, becomes quite small. Using long measuring times it was possible to reliably detect a signal $S(t_m$=1s) for the aromatic moieties in PET at room temperature, while for PEF it was not possible to conclusively detect any signal using the same experimental conditions (cf. Figure 5.10). This provides evidence that the ring-flip in PEF is strongly hindered in comparison to PET.

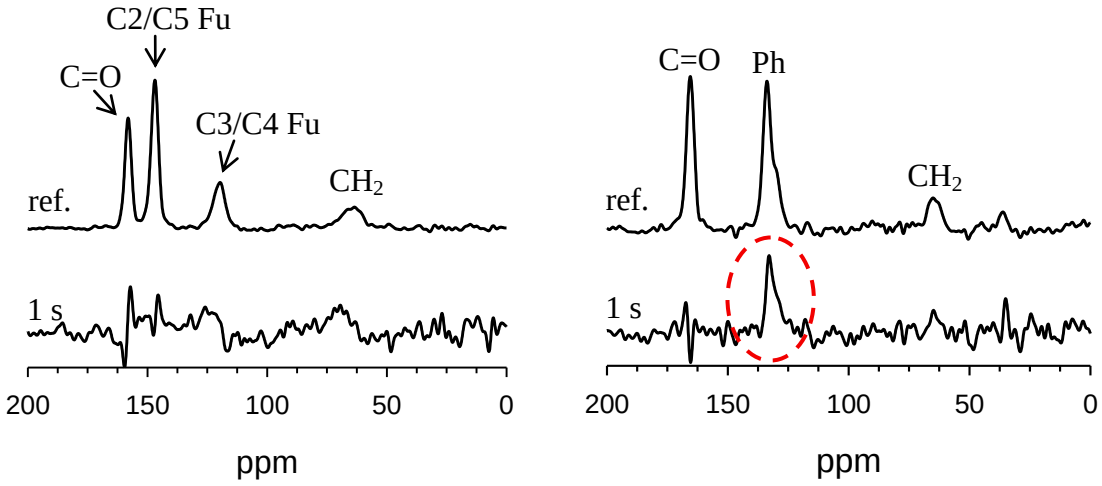

Figure 5.10: CODEX spectra (bottom) for amorphous PEF (left) and PET (right) measured at room temperature for t_m=1s. The top curve represents the corresponding reference spectra. Conclusive evidence for an aromatic peak in the CODEX spectrum is found only for PET (encircled), while the absence in the PEF spectra provides evidence for the hindrance of furan ring flips.

5.4. Summary and Conclusions

Poly(ethylene furanoate) (PEF), a bio-sourced polyester derived from 2,5-furandicarboxylic acid, exhibits improved mechanical properties, reduced oxygen permeability, a higher glass transition temperature, and slower chain mobility than its

terephthalic acid counterpart. A detailed comparison of the sub-ambient mechanical relaxation behavior of PEF and PET reveals contributions from different respective motional processes. While both phenyl ring-flipping and carbonyl motions contribute to the relaxation behavior of PET, the ring-flipping motion in PEF is strongly hindered such that only the carbonyl motions and small scale cooperative furan ring motions are believed to contribute to the relaxation behavior of PEF. Moreover, actual furan ring-flipping in PEF is frustrated by the asymmetric axis of furan ring rotation coupled with the ring polarity. Corroborating proof is found through a significantly increased $T_{1\rho}(^1H)$ value for PEF compared to PET, along with the absence of the furan peak for PEF as observed by CODEX measurements. The hindrance of furan ring-flipping explains the significant reduction in oxygen diffusion coefficient and permeability measured for PEF compared to PET, and provides a fundamental framework for future work.

5.5. References

1. Bain DR and Giles GA. Technical and commercial considerations. In: Giles GA and Bain DR, editors. Technology of Plastics Packaging for the Consumer Market. Sheffield: Sheffield Academic Press Ltd, 2001.

2. Bozell JJ and Petersen GR. Technology development for the production of biobased products from biorefinery carbohydrates-the US Department of Energy's "Top 10" revisited. Green Chemistry 2010;12(4):539-554.

3. Gandini A, Silvestre AJD, Neto CP, Sousa AF, and Gomes M. The furan counterpart of poly(ethylene terephthalate): An alternative material based on renewable resources. Journal of Polymer Science Part A: Polymer Chemistry 2009;47(1):295-298.

4. Wu J, Eduard P, Thiyagarajan S, van Haveren J, van Es DS, Koning CE, Lutz M, and Fonseca Guerra C. Isohexide Derivatives from Renewable Resources as Chiral Building Blocks. ChemSusChem 2011;4(5):599-603.

5. Knoop RJI, Vogelzang W, van Haveren J, and van Es DS. High molecular weight poly(ethylene-2,5-furanoate); critical aspects in synthesis and mechanical property

determination. Journal of Polymer Science Part A: Polymer Chemistry 2013;51(19):4191-4199.

6. Jong Ed, Dam MA, Sipos L, and Gruter GJM. Furandicarboxylic Acid (FDCA), A Versatile Building Block for a Very Interesting Class of Polyesters. Biobased Monomers, Polymers, and Materials, vol. 1105: American Chemical Society, 2012. pp. 1-13.

7. Eerhart AJJE, Faaij APC, and Patel MK. Replacing fossil based PET with biobased PEF; process analysis, energy and GHG balance. Energy & Environmental Science 2012;5(4):6407-6422.

8. Gomes M, Gandini A, Silvestre AJD, and Reis B. Synthesis and characterization of poly(2,5-furan dicarboxylate)s based on a variety of diols. Journal of Polymer Science Part A: Polymer Chemistry 2011;49(17):3759-3768.

9. Jiang M, Liu Q, Zhang Q, Ye C, and Zhou G. A series of furan-aromatic polyesters synthesized via direct esterification method based on renewable resources. Journal of Polymer Science Part A: Polymer Chemistry 2012;50(5):1026-1036.

10. Gruter G-JM, Sipos L, and Adrianus Dam M. Accelerating research into bio-based FDCA-polyesters by using small scale parallel film reactors. Combinatorial Chemistry & High Throughput Screening 2012;15(2):180-188.

11. Avantium - PEF bottles. http://avantium.com/yxy/products-applications/fdca/PEF-bottles.html.

12. Cohen MH and Turnbull D. Molecular Transport in Liquids and Glasses. The Journal of Chemical Physics 1959;31(5):1164-1169.

13. Langevin D, Grenet J, and Saiter JM. Moisture Sorption in PET: Influence on the Thermokinetic Parameters. European Polymer Journal 1994;30(3):339-345.

14. Lee JS, Leisen J, Choudhury RP, Kriegel RM, Beckham HW, and Koros WJ. Antiplasticization-based enhancement of poly(ethylene terephthalate) barrier properties. Polymer 2012;53:213-222.

15. McGonigle E-A, Daly JH, Jenkins SD, Liggat JJ, and Pethrick RA. Influence of Physical Aging on the Molecular Motion and Structural Relaxation in Poly(ethylene terephthalate) and Related Polyesters. Macromolecules 2000;33(2):480-489.

16. Polyakova A, Liu RYF, Schiraldi DA, Hiltner A, and Baer E. Oxygen-barrier properties of copolymers based on ethylene terephthalate. Journal of Polymer Science Part B: Polymer Physics 2001;39(16):1889-1899.

17. Sugden S. Molecular Volumes at Absolute Zero. Part II. Zero Volumes and Chemical Composition. Journal of the Chemical Society 1927:1786-1798.

18. van Krevelen DW and te Nijenhuis K. Properties of Polymers: Their Correlation with Chemical Structure, Their Numerical Estimation and Prediction from Additive Group Contributions, 4th ed. Amsterdam: Elsevier Science & Technology, 2009.

19. Michaels AS, Vieth WR, and Barrie JA. Solution of Gases in Polyethylene Terephthalate. Journal of Applied Physics 1963;34(1):1-12.

20. Petropoulos JH. Quantitative analysis of gaseous diffusion in glassy polymers. Journal of Polymer Science Part A-2: Polymer Physics 1970;8(10):1797-1801.

21. Donelli I, Freddi G, Nierstrasz VA, and Taddei P. Surface structure and properties of poly-(ethylene terephthalate) hydrolyzed by alkali and cutinase. Polymer Degradation and Stability 2010;95(9):1542-1550.

22. Hsiue G-H, Yeh T-S, and Chang S. The thermal shrinkage of the drawing poly(ethylene isophthalate terephthalate) copolyester films. Journal of Applied Polymer Science 1989;37(10):2803-2816.

23. Seo YW, Pang K, and Kim YH. Property Modulation of Poly(trimethylene terephthalate) by Incorporation of Nonlinear Isophthalate Units. Macromolecular Materials and Engineering 2006;291(11):1327-1337.

24. Yip HK and Williams HL. Transitions and Relaxations of Linear Polyesters Related to Poly(ethylene Terephthalate). II. Glassy and Gamma. Journal of Applied Polymer Science 1976;20:1217-1230.

25. Starkweather HW. Simple and Complex Relaxations. Macromolecules 1981;14(5):1277-1281.

26. Starkweather HW. Noncooperative Relaxations. Macromolecules 1988;21:1798-1802.

27. Starkweather HW. Aspects of simple, non-cooperative relaxations. Polymer 1991;32(13):2443-2448.

28. Robeson LM and Faucher JA. Secondary Loss Transitions in Antiplasticized Polymers. Journal of Polymer Science Part B: Polymer Letters 1969;7:35-40.

29. English AD. Macromolecular dynamics in solid poly(ethylene terephthalate): proton and carbon-13 solid-state NMR. Macromolecules 1984;17(10):2182-2192.

30. Maxwell AS, Monnerie L, and Ward IM. Secondary relaxation processes in polyethylene terephthalate-additve blends: 2. Dynamic mechanical and dielectric investigations. Polymer 1998;39(26):6851-6859.

31. Maxwell AS, Ward IM, Lauprêtre F, and Monnerie L. Secondary relaxation processes in polyethylene terephthalate-additive blends: 1. N.m.r. investigation. Polymer 1998;39(26):6835-6849.

32. Williams ML, Landel RF, and Ferry JD. The Temperature Dependence of Relaxation Mechanisms in Amorphous Polymers and Other Glass-forming Liquids. Journal of the American Chemical Society 1955;77(14):3701-3707.

33. Fulcher GS. ANALYSIS OF RECENT MEASUREMENTS OF THE VISCOSITY OF GLASSES. Journal of the American Ceramic Society 1925;8(6):339-355.

34. Hardy L, Stevenson I, Boiteux G, Seytre G, and Schönhals A. Dielectric and dynamic mechanical relaxation behaviour of poly(ethylene 2,6 naphthalene dicarboxylate). I. Amorphous films. Polymer 2001;42(13):5679-5687.

35. Mackintosh AR and Liggat JJ. Dynamic mechanical analysis of poly(trimethylene terephthalate)—A comparison with poly(ethylene terephthalate) and poly(ethylene naphthalate). Journal of Applied Polymer Science 2004;92(5):2791-2796.

36. Cristea M, Ionita D, and Simionescu BC. A new insight in the dynamo-mechanical behavior of poly(ethylene terephthalate). European Polymer Journal 2010;46:2005-2012.

37. Light RR and Seymour RW. Effect of sub-Tg relaxations on the gas transport properties of polyesters. Polymer Engineering & Science 1982;22(14):857-864.

38. Ngai KL, Rendell RW, Yee AF, and Plazek DJ. Antiplasticization effects on a secondary relaxation in plasticized glassy polycarbonates. Macromolecules 1991;24(1):61-67.

39. Abis L, Floridi G, Merlo E, Pò R, and Zannoni C. Investigation on the dynamics of aromatic polyesters by means of high resolution solid state CPMAS 13C NMR. Journal of Polymer Science Part B: Polymer Physics 1998;36(9):1557-1566.

40. Chen D and Zachmann HG. Glass transition temperature of copolyesters of PET, PEN and PHB as determined by dynamic mechanical analysis. Polymer 1991;32(9):1612-1621.

41. Roupakias CP, Bikiaris DN, and Karayannidis GP. Synthesis, thermal characterization, and tensile properties of alipharomatic polyesters derived from 1,3-propanediol and terephthalic, isophthalic, and 2,6-naphthalenedicarboxylic acid. Journal of Polymer Science Part A: Polymer Chemistry 2005;43(17):3998-4011.

42. Choudhury RP, Lee JS, Kriegel RM, Koros WJ, and Beckham HW. Chain Dynamics in Antiplasticized and Annealed Poly(ethylene terephthalate) Determined by Solid-State NMR and Correlated with Enhanced Barrier Properties. Macromolecules 2012;45(2):879-887.

43. Stejskal EO, Schaefer J, Sefcik MD, and McKay RA. Magic-angle carbon-13 nuclear magnetic resonance study of the compatibility of solid polymeric blends. Macromolecules 1981;14(2):275-279.

44. Gabrielse W, Angad Gaur H, Feyen FC, and Veeman WS. 13C Solid-State NMR Study of Differently Processed Poly(ethylene terephthalate) Yarns. Macromolecules 1994;27(20):5811-5820.

45. Packer KJ, Pope JM, Yeung RR, and Cudby MEA. The effects of morphology on 1H NMR spectra and relaxation in semicrystalline polyolefins. Journal of Polymer Science: Polymer Physics Edition 1984;22(4):589-616.

46. Kawaguchi T, Mamada A, Hosokawa Y, and Horii F. 2H n.m.r. analysis of the phenylene motion in different poly(ethylene terephthalate) samples. Polymer 1998;39(13):2725-2732.

CHAPTER 6

OXYGEN SORPTION AND TRANSPORT IN AMORPHOUS PEF[1]

This chapter expands on the limited oxygen transport data for amorphous PEF described in the previous chapter by providing a more complete oxygen transport study at various temperatures using complementary permeation and pressure-decay sorption techniques. In Chapter 5, the limited oxygen data were only shown to complement the traditional polymer characterization, while this chapter focuses detailed attention on the PEF oxygen sorption and transport properties. A significant reduction in oxygen permeability of 11X was observed at 35°C for PEF compared to PET, and is attributed primarily to reduction in chain segment mobility for PEF resulting from a hindrance of furan ring-flipping. A custom-built high accuracy sorption system allowed determination of temperature-dependent so-called dual-mode parameters that have not been reported as a function of temperature for oxygen in any polyester. Energetic parameters, i.e., the apparent enthalpy of sorption and apparent activation energies of diffusion and permeation, were measured for oxygen in PEF and discussed in the context of PET and related polyesters.

6.1. Introduction

Many attempts have been made to improve the barrier properties of poly(ethylene terephthalate) (PET), which has an undesirably high oxygen permeability that hinders

[1]Reprinted in part from *Polymer*, 55/18, Burgess, S.K.; Karvan, O.; Johnson, J.R.; Kriegel, R.M.; Koros, W.J., *Oxygen Sorption and Transport in Amorphous Poly(ethylene furanoate)*, 4748-4756, Copyright 2014, with permission from Elsevier.

juice and vitamin water packaging [1]. Barrier-improvement techniques are diverse and include organic barrier coatings, multi-layered barrier polymers, nanocomposite materials, polymer blends, and vacuum deposited coatings [2]. While the barrier properties of PET can be improved by such techniques, complex processing steps coupled with high capital investment can hinder production on a large scale [1]. As a result, much work has also focused on the development of novel pure-polymer replacements for PET with the goal of providing enhanced performance.

Poly(ethylene furanoate) (PEF) is the recently developed high-barrier polyester synthesized from ethylene glycol and 2,5-furandicarboxylic acid (FDCA). Due to the production of FDCA from renewable sugars [3], PEF also offers a bio-sourced replacement to poly(ethylene terephthalate) (PET) in addition to offering improved mechanical, thermal, and barrier properties [4]. Large-scale production of bio-sourced PEF can significantly reduce greenhouse gas emissions and non-renewable energy usage compared to petroleum-sourced PET [5]. Multiple studies have focused on small-scale synthesis and subsequent property characterization of PEF and related furan-derived polyesters [6-13]; however, only one brief report exists regarding the barrier efficacy to oxygen [14].

This chapter can be motivated by an abbreviated table which compares the oxygen permeability properties in amorphous PET, which is the base case for comparison, to PEF and other analogously rigid polymers to PEF such as poly(ethylene naphthalate) (PEN) and poly(ethylene isophthalate) (PEI). A useful metric to normalize and compare permeability results from different studies is the so-called Barrier Improvement Factor (BIF_P), which can be defined as the permeability of oxygen in PET divided by the

permeability of oxygen in either PEF, PEI, or PEN ($BIF_P = P_{PET}/P_{PEF,PEN,PEI}$) [15]. Consequently, BIF_P's greater than unity illustrate barrier improvement compared to amorphous PET. Table 6.1 provides such permeability data and BIF comparisons between PET and related polyesters.

Table 6.1. Permeability and Barrier Improvement Factor (BIF_P) comparison between amorphous PET and amorphous PEF, PEI, and PEN.

Polyester	**Temp (°C)**	**Permeability (Barrer)**	**BIF_P (-)**	**Reference**
PET	35	0.114	1	Ch 5, this work
PEF	35	0.0107	11	Ch 5, this work
PET	35	0.103	1	[16]
PEN	36	0.037	2.8	[16]
PET	30	0.054	1	[17]
PEN	30	0.019	2.9	[17]
PEI	30	0.015	3.6	[17]

From Table 6.1, it is apparent that PEF exhibits largely improved oxygen barrier properties compared to PET as evidenced by the large BIF_P of 11, while PEN exhibits a smaller BIF_P of 2.9 and PEI a BIF_P of 3.6. Although significantly lower than PET, the oxygen permeability for amorphous PEF is still higher than for semicrystalline barrier polymers such as dry Nylon-MXD6 (0.002 Barrer at 35°C [18]) and dry ethylene vinyl alcohol (EVOH, 0.0003 Barrer at 35°C [18]), however the latter polymers, especially EVOH, typically exhibit poor oxygen permeability performance in humid environments. Nevertheless, the significant oxygen barrier improvements for PEF compared to PET

greatly expand the opportunities for introduction of PEF into markets beyond that of beverage packaging applications. This notion is complemented by PEF exhibiting improved mechanical and thermal properties compared to PET [4], which enhancements can be further improved via transitioning into the semicrystalline domain.

The large BIF_P for PEF vs. PET listed in Table 6.1 and discussed in Chapter 5 motivated the current study, which provides a more detailed investigation regarding the oxygen transport characteristics of PEF. Fundamental understanding of the solubility and diffusivity contributions to oxygen transport in PEF will help elucidate the dominant mechanism of barrier enhancement compared to PET and can guide development of increasingly advanced barrier resins. Previous research, described in Chapter 5, using NMR methods and dynamic mechanical analysis has revealed that penetrant diffusion in PEF and PET is strongly affected by chain mobility originating from the ring-flipping mechanism. The symmetry about the ring-flipping axis and lack of phenyl ring polarity promotes ring-flipping in PET. On the other hand, the nonsymmetrical axis of ring rotation and polarity in the furan ring hinders ring-flipping in PEF [4] and thus suggested a basis for understanding our limited preliminary oxygen transport data.

The current chapter utilizes complementary permeation and pressure-decay sorption methods to probe the dissolved and Langmuir sorbed populations in amorphous PEF, thus providing a detailed understanding of the complex transport environment in the glassy polymer. The significant permeability reduction of 11X for oxygen in PEF compared to PET is explained primarily by a difference in chain mobility [4], since both polyesters exhibit similar oxygen solubilities at 35°C. Furthermore, energetic transport parameters derived from permeation and pressure-decay sorption techniques will be shown to have

excellent internal consistency between the independently measured parameters.

6.2. Transport Background and Theory

A detailed discussion regarding the transport background and theory utilized in this chapter is available in Chapter 2 (cf. Section 2.3), where Equations 6.1 – 6.4 are reproduced below for convenience.

$$D = {l^2}/{6\theta} \tag{6.1}$$

$$k* = {6\theta P}/{l^2} \tag{6.2}$$

$$C = \left(k_D p + \frac{C_H' bp}{1+bp} \right) \tag{6.3}$$

$$k^* = \left(k_D + C_H' b \right) \tag{6.4}$$

6.3. Experimental Methods

6.3.1. Materials and Film Preparation

The poly(ethylene furanoate) (PEF) and poly(ethylene terephthalate) (PET) polymers used in this chapter are the same materials described previously in Section 3.1.1, and all

amorphous films were melt-pressed using the method in Section 3.1.3. All transport measurements reported herein for PEF and PET reflect data corresponding to the amorphous morphology.

6.3.2. Transport Characterization

Permeation data at 1, 2.5, 4, 6, and 8 atm were measured for O_2 in amorphous PEF at 30, 35, 45, and 55°C using the constant-volume, variable-pressure system described previously in Chapter 3.

Equilibrium and kinetic sorption isotherms were measured between 0 – 10 atm for O_2 in amorphous PEF at 35, 45, 55, and 65°C using the constant-volume, pressure-decay technique described previously in Chapter 3. Sorption measurements were recorded using ~6 g PEF per sample cell, which amplified the transducer response due to a minimized void volume to sample volume ratio of ~4. Pressure-decay sorption measurements were recorded in 1 atm O_2 intervals from 0 – 10 atm O_2 at 35°C first, followed by degassing the sample and repeating the measurements at the next higher temperature. Use of an accurate density value for amorphous PEF, which was measured to be 1.4299 g/cc at 23°C in the previous chapter, was important for accurate sorption measurements due to the exceedingly low solubility of O_2 in PEF.

6.4. Results and Discussion

6.4.1. Permeation

Oxygen permeation data in amorphous PEF at 30, 35, 45, and 55°C are shown in Figure 6.1, along with dashed lines drawn to aid the eye. The observed constant

permeability vs. pressure behavior in Figure 6.1 for all temperatures might suggest applying the limit of total penetrant immobilization within the framework of the well known partial immobilization model [19]. However, total immobilization in the Langmuir environment is physically unlikely, due to the small penetrant size and exceedingly low O_2 solubility. A more likely explanation for the apparent pressure-independent permeability behavior in Figure 6.1 is low sorption uptake of O_2 in PEF and the low degree of Langmuir site saturation at the relatively low pressures considered. A more complete discussion of the permeability data within the context of the partial immobilization model is provided in Appendix B.

Oxygen permeation data in amorphous PET at 35°C also exhibited approximate pressure independence (not shown) over the pressure range tested, and consequently, can be represented by an average permeability value of ~0.11 Barrer. The ratio between average O_2 permeabilities at 35°C for PET to PEF therefore reveals a significant permeability reduction of ~11X (0.11/0.01=11) for PEF compared to PET [4]. The O_2 permeability value for PET at 35°C exhibit excellent agreement with prior literature reports [15, 16, 20], and the permeability reduction of ~11X for PEF compared to PET agrees with the ~10X reduction reported by Avantium [14]. The apparent activation energy of permeation (E_P) for O_2 in amorphous PEF can be obtained via the Arrhenius relationship in Equation 2.19 (discussed previously) and the semi-logarithmic plot in Figure 6.2, resulting in a value of 24.6 ± 2.4 kJ/mol for O_2 in amorphous PEF. The uncertainty limit for E_P was calculated using the standard error of the slope in Figure 6.2 via regression analysis. Furthermore, the uncertainty limits for the data points in Figure 6.2 are smaller than the size of the data points, and are approximately $\pm 1 \times 10^{-4}$ Barrer in

magnitude.

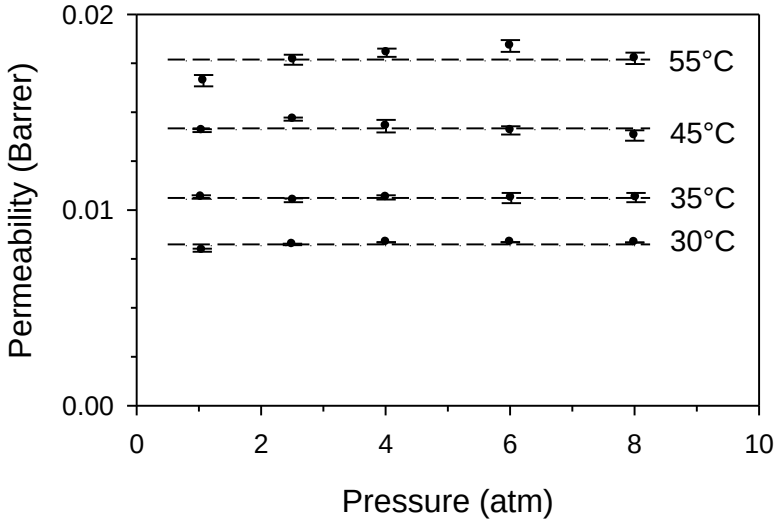

Figure 6.1. Oxygen permeability in amorphous PEF. Dashed lines represent the average permeability at each respective temperature.

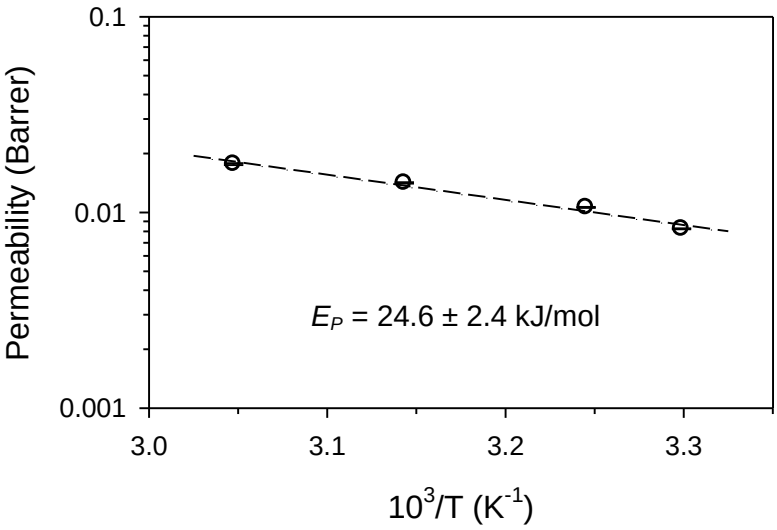

Figure 6.2. Arrhenius plot of average oxygen permeability data in amorphous PEF.

6.4.2. Equilibrium Sorption

Oxygen sorption testing was performed on amorphous PEF films at 35, 45, 55, and 65°C. Duplicate measurements were made at all temperatures and exhibited good reproducibility. Equilibrium sorption isotherms and corresponding dual-mode model fits for O_2 in amorphous PEF are illustrated in Figure 6.3, with the model parameters listed in Table 6.2. Equilibrium O_2 sorption in amorphous PET at 35°C is shown in Figure 6.3 via the dashed line for comparison, and the low-pressure solubility constant (k*) value of 0.102 ccSTP/ccPoly·atm for PET agrees well with other literature reports [21, 22]. A detailed discussion regarding the temperature dependence of the dual-mode model parameters is provided in Appendix B.

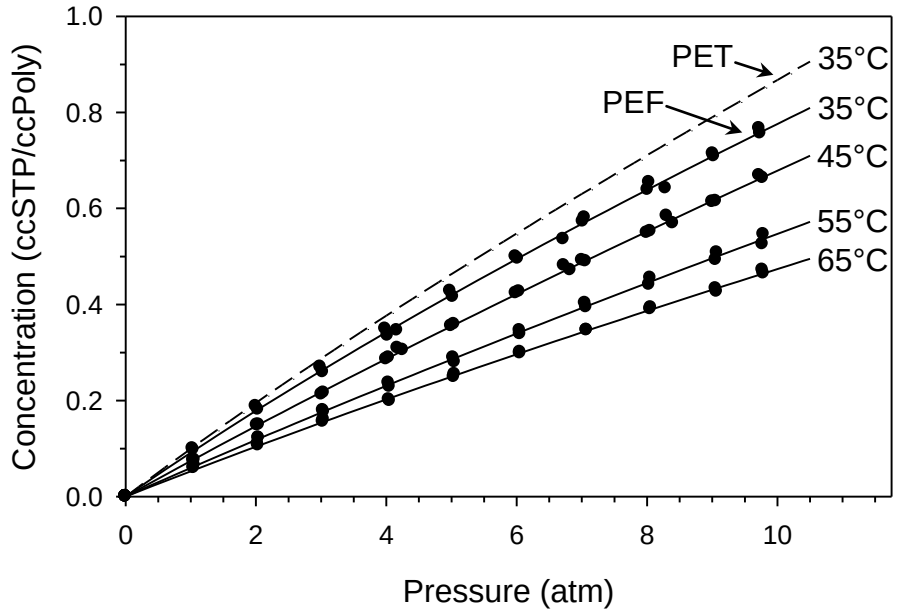

Figure 6.3. Equilibrium oxygen sorption in amorphous PEF. Solid lines represent the respective dual-mode model fits from Equation 6.3. The dashed line represents the dual-mode model fit for oxygen in amorphous PET at 35°C.

Table 6.2. Dual-mode model parameters for oxygen sorption in amorphous PEF. Model parameters are included for oxygen in amorphous PET at 35°C for comparison. $K = C_H'b/k_D$.

Sample	Temp (°C)	k_D (ccSTP/ccPoly·atm)	b (atm^{-1})	C_H' (ccSTP/ccPoly)	k^* (ccSTP/ccPoly·atm)	K (—)
PET	35	0.059	0.055	0.78	0.102	0.73
PEF	35	0.048	0.054	0.85	0.094	0.96
PEF	45	0.047	0.035	0.81	0.075	0.60
PEF	55	0.038	0.033	0.69	0.060	0.60
PEF	65	0.031	0.038	0.58	0.054	0.71

From Figure 6.3, it is apparent that PEF exhibits a very similar O_2 sorption to PET at 35°C, despite the significant (11X) O_2 permeability reduction for PEF. The similar O_2 solubility for PET and PEF at 35°C, in combination with the relationship $P=DS$, therefore demonstrates that the large permeability reduction for PEF is primarily due to a reduction in chain mobility and diffusion coefficient [4]. A detailed discussion regarding chain mobility and its fundamental relationship to diffusion and permeation is provided later in Section 6.4.4.

While many studies in the literature have examined the temperature-dependent dual-mode characteristics of condensable gases [23, 24] and vapors [25] in polymers, this study is the first to report such temperature-dependent parameters for a non-condensable gas as a function of temperature in a polyester. In fact, only one report was found to provide the dual-mode model parameters for O_2 sorption in PET [22], which is surprising since PET has dominated the beverage packaging industry for the last forty years. The lack of data in the literature presumably results from difficulty in achieving the high level of accuracy needed for pressure-decay measurements using insoluble gases. Furthermore, extracting accurate dual-mode model parameters for O_2 in PEF is difficult due to the lack

of curvature in the isotherms (cf. Figure 6.3) resulting from low O_2 solubility. This process is complicated by the 'initial guess' parameters used by the non-linear curve fitting program, which can influence the final model parameters due to the inherent coupling of b and C_H' in Equation 6.3. While care has been taken to select dual-mode model parameters that appear physically significant, alternative parameter sets can also represent the data. Fortunately, as will be shown, the accuracy of the dual-mode model parameters listed in Table 6.2 can be verified and corroborated through independent permeation measurements.

As noted earlier, in the absence of isotherm curvature [26], Equations 6.1 and 6.2 can be used in conjunction with a single permeation experiment to accurately specify both the penetrant sorption and diffusion coefficients. The solubility coefficient calculated from permeation for a glassy polymer represents an effective solubility coefficient (k^*), where k^* will be larger than the true solubility coefficient (k_D) due to the presence of the Langmuir environment [21]. As expected, k^* calculated from permeation will approach the true k_D calculated from sorption as the temperature approaches T_g and the polymer transitions from the glassy to the rubbery state. Permeation experiments can therefore be used to validate the accuracy of the transport parameters obtained via pressure-decay sorption. Values of k^* (from permeation) and k_D (from sorption) are plotted in Figure 6.4 in van't Hoff form, thus illustrating the convergence of k^* to k_D at elevated temperatures approaching T_g and demonstrating the internal consistency between permeation and sorption measurements. The small difference between k^* and k_D at 35°C originates from the low critical temperature and low affinity constant for O_2. Michaels et al. [21] also demonstrated close agreement between pressure-decay and permeation-based solubility

measurements for non-condensable gases such as O_2 in PET. Larger deviations between k^* and k_D are observed for gases exhibiting higher critical temperatures (i.e., CO_2 in PET [21, 27]); however, these differences also disappear near T_g [21, 27].

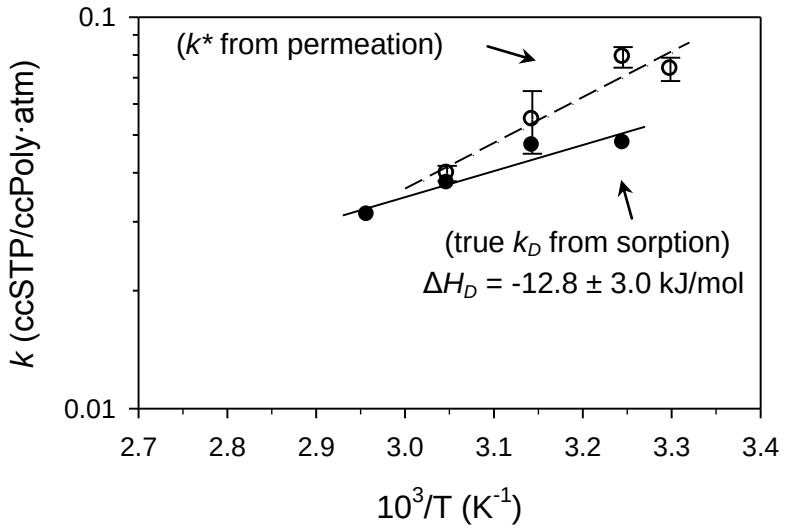

Figure 6.4. Semi-logarithmic van't Hoff plot of the true sorption coefficient (k_D) from equilibrium sorption (solid circles) and the effective sorption coefficient (k^*) from permeation testing (hollow circles) for oxygen in PEF.

Thermodynamic van't Hoff analysis of the true k_D data from the semi-logarithmic plot in Figure 6.4 reveals a value of -12.8 ± 3.0 kJ/mol for the apparent enthalpy of sorption in the dissolved mode (ΔH_D), where the uncertainty was calculated in a manner similar to E_P. Similar analysis of the Langmuir affinity parameter b is provided in Appendix B. The sorption coefficient obtained in the limit of zero pressure (k^*, Equation 6.4) measured by pressure-decay sorption is also subject to a van't Hoff interpretation. The apparent enthalpy of sorption value derived via this method is an effective parameter and physical interpretation is complex due to inclusion of the Langmuir capacity constant (C_H') [25]. Michaels et al. [21] report an effective enthalpy of sorption ($\Delta H_{S,eff}$) value of -14.6

kJ/mol for O_2 in amorphous PET, which is similar in magnitude to the $\Delta H_{S,eff}$ value of -16.5 ± 1.2 kJ/mol for O_2 in amorphous PEF from the current work. A theoretical discussion regarding the enthalpy of sorption derived from the various dual-mode model parameters is provided by Koros et al. [28].

6.4.3. Kinetic Sorption

Aside from equilibrium sorption data, pressure-decay sorption experiments also allow measurement of temperature-dependent diffusion coefficient data as indicated previously in Section 2.4 and Section 3.3.2. As described previously, the raw pressure-decay data vs. time can be transformed via Equation 6.5 into a non-dimensional form that can be modeled using the solution of the time-dependent diffusion equation in Equation 6.6.

$$\frac{M_t}{M_\infty}(t) = \left(\frac{p_{initial} - p(t)}{p_{initial} - p_{final}} \right) \tag{6.5}$$

$$\frac{M_t}{M_\infty}(t) = 1 - \sum_{n=0}^{\infty} \frac{8}{(2n+1)^2 \pi^2} \exp\left(\frac{-D_{Avg}(2n+1)^2 \pi^2 t}{l^2} \right) \tag{6.6}$$

Oxygen diffusion in PEF is accurately described by simple Fickian kinetics due to low penetrant solubility and lack of strong interaction with the polymer matrix. Highly sorbing penetrants, which can induce long-term non-Fickian relaxations (e.g., lower alcohols in PET [29]), require more sophisticated models to accurately describe the diffusion process.

One hundred terms in the summation were used to accurately approximate the infinite series solution in Equation 6.6, and the resulting function was modeled to experimental data using the MATLAB®-based non-linear least squares fitting routine described later in Chapter 11 [30]. Care was taken to accurately measure the average thickness values of the PEF films, as the value of D_{Avg} from Equation 6.6 is highly sensitive to l [20, 31]. Since the experiments were conducted using discrete sorption intervals, D_{Avg} calculated from Equation 6.6 represents an average diffusion coefficient over the concentration interval via Equation 6.7 [32]. Average diffusion coefficients were measured from 0 to 10 atm O_2 over 1 atm intervals, and a plot of D_{Avg} vs. pressure will reveal any dependence of the diffusion coefficient on concentration. A detailed discussion of such data in the context of the partial immobilization model is presented in Appendix B.

$$D_{Avg} = \frac{\int_{C_1}^{C_2} D_{eff}\, dC}{C_2 - C_1} \tag{6.7}$$

Figure 6.5 shows example M_t/M_∞ data and the corresponding model fit from Equation 6.6 (dashed white line) for a kinetic sorption interval from 0 to 1.1 atm O_2 in amorphous PEF at 35°C. From Figure 6.5, it is apparent that the simple Fickian model defined by Equation 6.6 accurately describes the O_2 kinetic uptake data. Values for D_{Avg} averaged over all pressure intervals, indicated as $\overline{D_{Avg}}$, are listed in Table 6.3 at each temperature along with diffusion coefficients derived from transient permeation for comparison. The permeation-based diffusion coefficients were calculated using the time-lag measured at 1 atm O_2 and Equation 6.1. A D_{eff} value of 11.6×10^{-9} cm^2/s has been previously reported in

Chapter 5 for amorphous PET at 35°C using the time-lag method at 1 atm O_2 [4], thereby confirming the reduction in chain mobility for PEF vs. PET. Figure 6.6 illustrates the Arrhenius dependence of the diffusion coefficients listed in Table 6.3 from both permeation and sorption measurements. The excellent agreement in diffusion coefficients from Figure 6.6 between sorption and permeation-based values demonstrates the internal consistency in the reported measurements. Values of the activation energy of diffusion (E_D) from Figure 6.6 are similar at 43.1 ± 4.7 kJ/mol for sorption-derived values and 46.0 ± 2.4 kJ/mol for permeation-derived values, where the uncertainty is calculated as noted earlier.

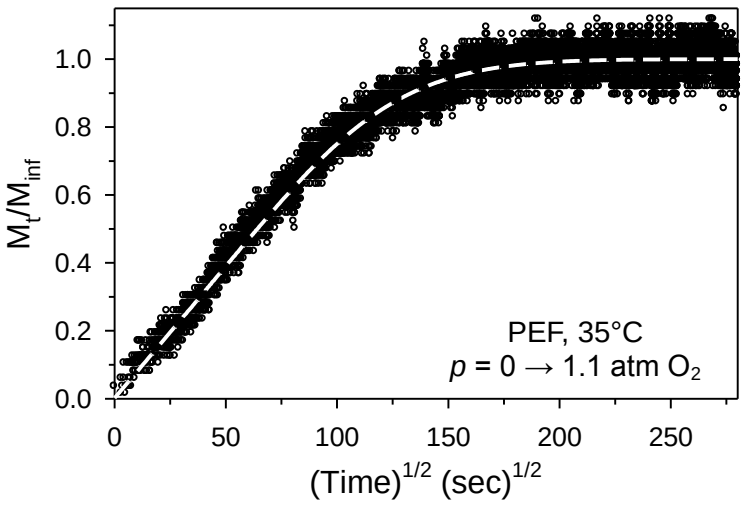

Figure 6.5. Kinetic sorption isotherm for oxygen in amorphous PEF at 35°C from the pressure interval 0 to 1.1 atm O_2. The white dashed line represents the Fickian model fit from Equation 6.6 with $D_{Avg} = 8\times10^{-10}$ cm^2/s.

Table 6.3. Diffusion coefficients (D) for oxygen in amorphous PEF. Values from sorption represent the average value over all pressure intervals, while values from permeation originate from the time-lag at 1 atm O_2.

	$D\times10^9$ (cm^2/s)	
Temp (°C)	**Permeation (D_{eff})**	**Sorption ($\overline{D_{Avg}}$)**
30	0.82 ± 0.06	—
35	1.04 ± 0.06	1.03 ± 0.04
45	2.02 ± 0.36	1.40 ± 0.05
55	3.18 ± 0.15	2.79 ± 0.12
65	—	4.31 ± 0.27

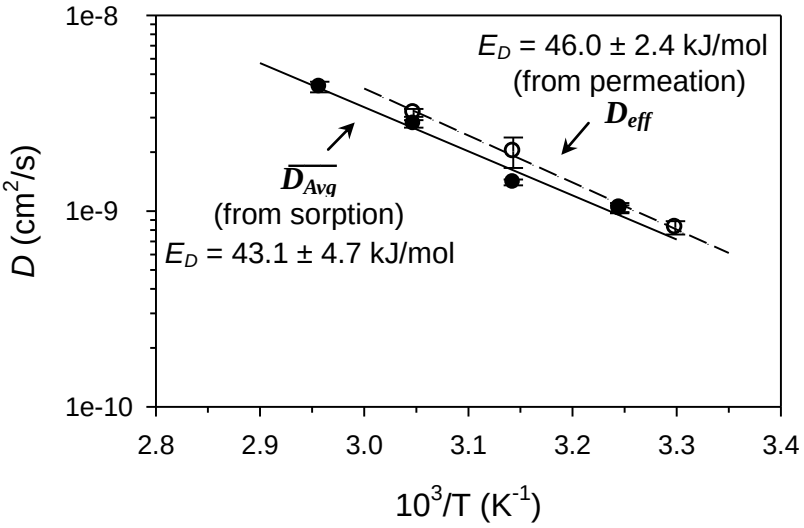

Figure 6.6. Arrhenius plot of the diffusion coefficients estimated from permeation (D_{eff}, hollow circles) and sorption ($\overline{D_{Avg}}$, solid circles) for oxygen in amorphous PEF.

6.4.4. Chain Mobility and Transport Energetics

As mentioned previously, the sorption of O_2 in amorphous PEF and PET is surprisingly similar at 35°C (cf. Figure 6.3), despite a reduction in O_2 permeability of 11X for PEF compared to PET. This result indicates that the permeability difference is

primarily due to a reduction in chain mobility for PEF compared to PET. Corroborating evidence for the importance of chain mobility is the similarity in static fractional free volume (*FFV*) measurements for both polyesters measured by density and group contribution methods (i.e., 0.153 for PEF and 0.130 for PET, from Chapter 5). The Sugden method for *FFV* estimation was used in this calculation since a value for the van der Waals volume of the furan ring is not available using the van Krevelen method. A more complete discussion regarding the choice of Sugden's method as opposed to van Krevelen's method is provided in Chapter 5. Furthermore, transport predictions based solely on *FFV* measurements [33] suggest *incorrectly* that PEF will exhibit a higher permeability than PET.

Previous work, described in Chapter 5, examined the mobility of the sub-T_g localized segments that contribute to the diffusion process in amorphous PEF and PET. Complementary results from mechanical and NMR methods demonstrate that the reduction in chain mobility for PEF compared to PET results from the hindrance of furan-ring-flipping in PEF due to ring polarity and structural non-linearity [4]. The phenyl ring in PET, however, is non-polar and exhibits a higher degree of mobility due to the symmetrical axis of ring rotation [34]. A ring flip in either PEF or PET can be envisioned to include or induce small-scale semi-cooperative motions of the carbonyl and ethylene linkages [35] which also contribute to the diffusion process. The presence of cooperativity between the furan ring and adjoining glycol linkages in PEF is greater due to the conformational strain associated with a complete flip. Atomistic simulations of the chain dynamics of poly(ethylene isophthalate) (PEI) and PET verify this behavior [36], where PEI and PEF exhibit similar nonsymmetrical axes of ring rotation when compared

to PET. Further evidence for the importance of the ring-flipping mechanism to diffusion has been provided by Tonelli [37], who studied the conformational characteristics of PET, PEI, and poly(ethylene phthalate) (PEP, the *ortho*-substituted isomer of PET) [38], and also poly(butylene terephthalate) and poly(ethylene naphthalate) [39, 40].

Various researchers have also linked characteristics of the sub-T_g beta relaxation to transport properties in PET and related polyesters [17, 20, 41, 42]. In particular, a decrease in beta relaxation intensity for the loss modulus or tan δ compared to PET correlates well with reduced oxygen diffusivity. Similar intensity reductions in tan δ have been observed for PEF compared to PET [4], however, PEF exhibits a larger than expected activation energy and entropy for the beta relaxation due to enhanced cooperativity originating from the smaller ring size, asymmetric axis of rotation, and ring polarity. Consequently, the general correlation between the activation energy of the beta peak and the activation energy of oxygen diffusion in structurally similar polyesters suggested by Hiltner et al. [31] may be questionable for PEF.

A summary of the energetic transport parameters measured for PEF is provided in Table 6.4, along with a comparison of similar values for PET obtained from the literature. Corresponding values for PEI and PEN, which have a similar rigidity to PEF, will be referenced in the text as needed. From Table 6.4, the apparent activation energy of O_2 diffusion (E_D) in PEF is slightly larger than the value for PET. As a note, the E_D value of 48.5 kJ/mol reported by Michaels et al. [43] is much larger than other reports, but is included in Table 6.4 for completeness. Values of E_D for O_2 in PEI and PEN are reported at 43 kJ/mol and 44 kJ/mol [16], respectively, and are both slightly larger than the value of 39.7 kJ/mol for PET from the same study. The results therefore indicate that the E_D

value for PEF, PEI, and PEN, which are more rigid than PET, are all slightly larger than the E_D for PET. Such correlation with chain rigidity is partially expected, and will be explained shortly. As a side note, it should also be mentioned that the energetic values for O_2 diffusion in glassy PEF agree well with the known correlation of $\log(D_0)$ with E_D/T for glassy polymers as illustrated by Koros [44].

The effective enthalpy of sorption ($\Delta H_{S,eff}$) values in Table 6.4 reveal a more negative value of -21.4 ± 3.4 kJ/mol for PEF compared to -10.8 kJ/mol for PET. Furthermore, PEN exhibits an intermediate value of -14.2 kJ/mol, while PEI exhibits a value of -19.8 kJ/mol [45], which is more similar to PEF. These results indicate that the $\Delta H_{S,eff}$ for O_2 in PEF and PEI are quite similar to each other and lower than the value for PET, while the value for PEN is intermediate between the two limiting values. These results are interesting and perhaps originate from the similarity in non-symmetrical bonding and small ring structures for PEF and PEI, whereas PEN contains a more bulky naphthalene ring than the smaller furan and phenyl rings in PEF and PEI, respectively. The apparent enthalpy of O_2 sorption in the dissolved mode (ΔH_D) of PEF cannot be compared to that for PET due to lack of data in the literature for PET.

Simple addition of the E_D and $\Delta H_{S,eff}$ values in Table 6.4 measured from sorption yield an estimate of the apparent activation energy of permeation E_P, which can be compared directly to the E_P value estimated from permeation measurements. As seen in Table 6.4, close agreement between the E_P values calculated via the two independent methods for O_2 in PEF demonstrates the internal consistency of the measurements. The E_P value of 24.6 ± 2.4 kJ/mol for PEF is slightly lower than the average value of 29.3 kJ/mol for PET. Based on the previous similarity between PEF and PEI, it is not

surprising that the E_P for PEF compares well with the value of 23.2 kJ/mol reported for PEI [45]. Furthermore, an E_P for PEN reported at 29.8 kJ/mol [16] agrees well with the value of PET.

Table 6.4. Apparent energetic parameters for O_2 transport in amorphous PEF and PET.

	Method	E_P **(kJ/mol)**	E_D **(kJ/mol)**	$\Delta H_{S,eff}$ **(kJ/mol)**	ΔH_D **(kJ/mol)**	**Reference**
PEF	Permeation	24.6 ± 2.4	46.0 ± 2.4	-21.4[a] ± 3.4	—	This work
	Sorption	26.6[b] ± 4.9	43.1 ± 4.7	-16.5[f] ± 1.2	-12.8 ± 3.0	This work
PET	Permeation	30.5	—	—	—	[17]
	Permeation	37.7[c]	48.5[c]	-10.8[a]	—	[43]
	Permeation	29.0	39.7	-10.7[a]	—	[16]
	Permeation	30.3[d]	—	—	—	[46]
	Permeation	27.3[e]	—	—	—	[47]
	Permeation	—	42.3[d]	—	—	[48]
	Sorption	—	—	-14.6	—	[21]

a: Estimated from $\Delta H_{S,eff} = E_P - E_D$
b: Estimated from $E_P = E_D + \Delta H_{S,eff}$
c: Values are larger than other reported values but are reported for completeness.
d: For semi-crystalline PET.
e: For biaxially oriented PET.
f: This estimate was obtained from the temperature dependence of k^* derived from the low pressure limit of the dual-mode model (i.e., $k^* = k_D + C_H'b$). The temperature dependence of a model-independent k^* obtained from fitting a general cubic polynomial expression to the sorption data provided a statistically equivalent estimate for $\Delta H_{S,eff}$.

As discussed previously in Chapter 2, penetrant diffusion is often portrayed via Equation 6.8 from random walk theory [49, 50], where λ is the path length of a molecular jump, f is the frequency of jumps, and the factor 1/6 represents a random walk in an isotropic medium. The jump frequency is a measure of how often molecular-sized gaps

form in the medium, and for polymers, is fundamentally related to the segmental chain mobility. From Equation 6.8, if the diffusion path lengths are similar between PEF and PET, then the drastic reduction in diffusion coefficient for PEF correlates directly to a significant reduction in the frequency of hole formation and diffusive jumps compared to PET. This result can be explained by the reduction in chain mobility for PEF due to the hindrance of ring-flipping when compared to PET [4]. Furthermore, f can be interpreted using an activation energy or free volume approach, which are inherently different methods for describing the same diffusion process. The activation energy interpretation has been chosen for the current discussion, however both methodologies are extensively reviewed in previous works [51, 52].

$$D = \frac{1}{6} f \lambda^2 \tag{6.8}$$

A simplistic, yet useful activation energy model was first proposed by Meares [53], who expressed the apparent activation energy of diffusion as the energy needed to open a penetrant-sized cylindrical cavity within the polymer. The dimensions of the cylindrical cavity are defined by the diameter of the penetrant molecule (d_A) and the length of a diffusive jump (λ), while the energy required to open the cavity is proportional to the cohesive energy density of the polymer (E_{CD}). Meares' interpretation is provided in Equation 6.9, where N_0 is Avogadro's constant.

$$E_D \approx \frac{1}{4} N_0 \pi d_A{}^2 \lambda E_{CD} \tag{6.9}$$

Equation 6.9 has realized some success [54], however the model is generally viewed as being too simplistic for describing the complex diffusion process within a polymer [51, 52]. Nevertheless, the model can still provide a first-approximation to understanding the diffusive process in related polymers. The cohesive energy density (E_{CD}) from Equation 6.9 can be estimated by the highly approximated group contribution method of Fedors as reported by van Krevelen [55], thus yielding values of 560 J/cc for PEF and 540 J/cc for PET. Similar values of 550 J/cc and 530 J/cc have been reported for PEI and PEN, respectively [45]. If the diffusive path length is assumed to be similar for PET, PEF, PEI, and PEN, then the larger E_{CD} values for PEF and PEI compared to PET successfully predict via Equation 6.9 the slight increase in E_D for PEF and PEI compared to PET. Alternatively, a lower E_{CD} for PEN compared to PET would suggest a lower E_D for PEN, but this is not experimentally observed by measurements in the literature [16]. This inaccurately low prediction is either from an inadequacy in the model (most likely) or perhaps from the assumption of similar jump lengths for PEN and PET, however the latter assumption may still be reasonably valid in a tightly packed glassy matrix.

A more instructive molecular model, although still idealized, is provided by Brandt [52, 56] in Equation 6.10, where p_I is related to E_{CD}, d_p is the approximate diameter of a polymer chain, a_d is the length of the polymer segment involved in a diffusive jump, d_A is the diameter of the penetrant molecule, d_s is the inter-chain spacing of the polymer segments prior to chain separation, ψ_0 is the energy barrier associated with internal rotation around a chain bond, and b_d is the projected length on the chain axis of a

backbone chain bond [52].

$$E_D \approx \left(\frac{N_0 p_I d_p a_d \left(d_A - d_s \right)}{2} \right) + \left(\frac{18 \psi_0 b_d \left(d_A - d_s \right)^2}{a_d{}^3} \right) \tag{6.10}$$

While quantitative evaluation of Equation 6.10 is difficult for PEF and PET, a qualitative comparison between the two polyesters can help explain the slightly increased E_D for PEF. X-ray diffraction measurements reported in Chapter 5 reveal that the peak maximum of the amorphous halo for PEF is shifted to a higher 2θ value than for PET, thus indicating a slightly smaller average inter-chain spacing (d_s) for PEF. Since the diameter of the penetrant (d_A) is the same for PEF and PET, the term (d_A – d_s) will therefore be larger for PEF. Additionally, since PEF is more rigid than PET, the barrier to internal rotation (ψ_0) will be increased for PEF compared to PET. Increased rigidity for PEF might also indicate a reduced length for the projection of the backbone bond onto the chain axis (b_d), in addition to a possible increase in length of the polymer segment involved during the chain separation step (a_d). Since O_2 in PEF exhibits a slightly larger E_D than for PET, the results can be rationalized using Equation 6.10.

As seen in Equation 6.10, accurately modeling the energetics of the diffusion process is challenging. Additional activation energy and free volume-based models not discussed here, but deserve mention, are Barrer's activated zone theory [57], the free volume theory of Cohen and Turnbull [58], and the volume fluctuation theory proposed by Dibenedetto and Paul [59-62].

6.5. Summary and Conclusions

Poly(ethylene furanoate) (PEF), when manufactured using bio-sourced ethylene glycol, provides a 100% renewable alternative to petroleum-sourced poly(ethylene terephthalate) (PET) with significantly enhanced barrier properties. Oxygen transport in amorphous PEF was studied at temperatures between 30°C to 65°C using permeation and pressure-decay sorption techniques. Internal consistency in the values from both methods was demonstrated through detailed analysis and comparison of the temperature-dependent transport parameters. Significant differences in chain mobility between PEF and PET explain the large reduction in O_2 permeability of 11X for PEF [4]. Moreover, hindrance in complete ring-flipping for PEF arises from the large energy barrier associated with the ring polarity and nonsymmetrical axis of ring rotation. Further analysis reveals that the common permeability vs. free volume correlation established by Lee [33] cannot accurately predict the permeability reduction of PEF compared to PET, since both polyesters share similar static free volumes. Application of the partial immobilization model to pressure dependent permeation and diffusion was demonstrated in Appendix B, thus highlighting the significance of the Henry's law sorption mode in PEF due to low O_2 solubility. Energetic transport parameters were successfully measured for O_2 in PEF and discussed in the context of PET and related polyesters.

The current chapter provides a "base case" investigation of oxygen transport in amorphous PEF at multiple temperatures. The idealized two-phase model [21, 43] can be used to provide an estimate of the transport properties in semicrystalline PEF samples based on the amorphous volume fraction; however, it has already been shown that deviations from such ideal behavior exist for PET [63], which is structurally similar to

PEF. Consequently, detailed transport studies are needed in semicrystalline PEF to further examine the effect of crystallinity and the corresponding applicability of the idealized two-phase model.

PEF, due to the possibility of complete bio-renewable sourcing and improved barrier, thermal, and mechanical properties, serves as an excellent replacement for the currently dominant petroleum-based PET. This chapter presents the first detailed study of penetrant transport in PEF, thereby proving the high barrier efficacy to oxygen and highlighting the underlying, fundamental connection to chain mobility.

6.6. References

1. Bain DR and Giles GA. Technical and commercial considerations. In: Giles GA and Bain DR, editors. Technology of Plastics Packaging for the Consumer Market. Sheffield: Sheffield Academic Press Ltd, 2001.

2. Lange J and Wyser Y. Recent Innovations in Barrier Technologies for Plastic Packaging - a Review. Packaging Technology and Science 2003;16:149-158.

3. Bozell JJ and Petersen GR. Technology development for the production of biobased products from biorefinery carbohydrates-the US Department of Energy's "Top 10" revisited. Green Chemistry 2010;12(4):539-554.

4. Burgess SK, Leisen JE, Kraftschik BE, Mubarak CR, Kriegel RM, and Koros WJ. Chain Mobility, Thermal, and Mechanical Properties of Poly(ethylene furanoate) Compared to Poly(ethylene terephthalate). Macromolecules 2014;47(4):1383-1391.

5. Eerhart AJJE, Faaij APC, and Patel MK. Replacing fossil based PET with biobased PEF; process analysis, energy and GHG balance. Energy & Environmental Science 2012;5(4):6407-6422.

6. Jong Ed, Dam MA, Sipos L, and Gruter GJM. Furandicarboxylic Acid (FDCA), A Versatile Building Block for a Very Interesting Class of Polyesters. Biobased Monomers, Polymers, and Materials, vol. 1105: American Chemical Society, 2012. pp. 1-13.

7. Knoop RJI, Vogelzang W, van Haveren J, and van Es DS. High molecular weight poly(ethylene-2,5-furanoate); critical aspects in synthesis and mechanical property

determination. Journal of Polymer Science Part A: Polymer Chemistry 2013;51(19):4191-4199.

8. Gandini A, Silvestre AJD, Neto CP, Sousa AF, and Gomes M. The furan counterpart of poly(ethylene terephthalate): An alternative material based on renewable resources. Journal of Polymer Science Part A: Polymer Chemistry 2009;47(1):295-298.

9. Ma J, Pang Y, Wang M, Xu J, Ma H, and Nie X. The copolymerization reactivity of diols with 2,5-furandicarboxylic acid for furan-based copolyester materials. Journal of Materials Chemistry 2012;22(8):3457-3461.

10. Ma J, Yu X, Xu J, and Pang Y. Synthesis and crystallinity of poly(butylene 2,5-furandicarboxylate). Polymer 2012;53(19):4145-4151.

11. Gruter G-JM, Sipos L, and Adrianus Dam M. Accelerating research into bio-based FDCA-polyesters by using small scale parallel film reactors. Combinatorial Chemistry & High Throughput Screening 2012;15(2):180-188.

12. Gomes M, Gandini A, Silvestre AJD, and Reis B. Synthesis and characterization of poly(2,5-furan dicarboxylate)s based on a variety of diols. Journal of Polymer Science Part A: Polymer Chemistry 2011;49(17):3759-3768.

13. Jiang M, Liu Q, Zhang Q, Ye C, and Zhou G. A series of furan-aromatic polyesters synthesized via direct esterification method based on renewable resources. Journal of Polymer Science Part A: Polymer Chemistry 2012;50(5):1026-1036.

14. Avantium - PEF bottles. http://avantium.com/yxy/products-applications/fdca/PEF-bottles.html.

15. Lee JS, Leisen J, Choudhury RP, Kriegel RM, Beckham HW, and Koros WJ. Antiplasticization-based enhancement of poly(ethylene terephthalate) barrier properties. Polymer 2012;53:213-222.

16. Liu RYF, Hiltner A, and Baer E. Free volume and oxygen transport in cold-drawn polyesters. Journal of Polymer Science Part B: Polymer Physics 2004;42(3):493-504.

17. Light RR and Seymour RW. Effect of sub-Tg relaxations on the gas transport properties of polyesters. Polymer Engineering & Science 1982;22(14):857-864.

18. Permeability and other film properties of plastics and elastomers. Norwich, NY: Plastics Design Library, 1995.

19. Paul DR and Koros WJ. Effect of Partially Immobilizing Sorption on Permeability and the Diffusion Time Lag. Journal of Polymer Science: Polymer Physics Edition 1976;14:675-685.

20. Polyakova A, Liu RYF, Schiraldi DA, Hiltner A, and Baer E. Oxygen-barrier properties of copolymers based on ethylene terephthalate. Journal of Polymer Science

Part B: Polymer Physics 2001;39(16):1889-1899.

21. Michaels AS, Vieth WR, and Barrie JA. Solution of Gases in Polyethylene Terephthalate. Journal of Applied Physics 1963;34(1):1-12.

22. Lee JS, Chandra P, Burgess SK, Kriegel R, and Koros WJ. An advanced gas/vapor permeation system for barrier materials: Design and applications to poly(ethylene terephthalate). Journal of Polymer Science Part B: Polymer Physics 2012;50(17):1262-1270.

23. Koros WJ and Paul DR. CO2 Sorption in Poly(ethylene Terephthalate) above and below the Glass Transition. Journal of Polymer Science: Polymer Physics Edition 1978;16:1947-1963.

24. Felder RM, Patton CJ, and Koros WJ. Dual-mode sorption and transport of sulfur dioxide in kapton polyimide. Journal of Polymer Science: Polymer Physics Edition 1981;19(12):1895-1909.

25. Patton CJ, Felder RM, and Koros WJ. Sorption and transport of benzene in poly(ethylene terephthalate). Journal of Applied Polymer Science 1984;29(4):1095-1110.

26. Aitken A and Barrer RM. Transport and solubility of isomeric paraffins in rubber. Transactions of the Faraday Society 1955;51(0):116-130.

27. Koros WJ and Paul DR. Transient and Steady-State Permeation in Poly(ethylene Terephthalate) Above and Below the Glass Transition. Journal of Polymer Science: Polymer Physics Edition 1978;16:2171-2187.

28. Koros WJ, Paul DR, and Huvard GS. Energetics of gas sorption in glassy polymers. Polymer 1979;20(8):956-960.

29. Chandra P and Koros WJ. Sorption of lower alcohols in poly(ethylene terephthalate). Polymer 2009;50:4241-4249.

30. Burgess SK, Kriegel RM, and Koros WJ. Diffusion Coefficient Modeling in Polyester Barrier Materials: Applications of Infinite Series Solutions. Society of Plastics Engineers - ANTEC Las Vegas, Nevada, 2014. pp. 830 - 835.

31. Hiltner A, Liu RYF, Hu YS, and Baer E. Oxygen transport as a solid-state structure probe for polymeric materials: A review. Journal of Polymer Science Part B: Polymer Physics 2005;43(9):1047-1063.

32. Crank J and Park GS. Diffusion in Polymers. London: Academic Press, 1968.

33. Lee WM. Selection of barrier materials from molecular-structure. Polymer Engineering & Science 1980;20(1):65-69.

34. Tonelli AE. Effect of the terephthaloyl residue on chain flexibility of poly(ethylene terephthalate). Journal of Polymer Science: Polymer Letters Edition 1973;11(7):441-447.

35. Abis L, Floridi G, Merlo E, Pò R, and Zannoni C. Investigation on the dynamics of aromatic polyesters by means of high resolution solid state CPMAS 13C NMR. Journal of Polymer Science Part B: Polymer Physics 1998;36(9):1557-1566.

36. Karayiannis NC, Mavrantzas VG, and Theodorou DN. Detailed Atomistic Simulation of the Segmental Dynamics and Barrier Properties of Amorphous Poly(ethylene terephthalate) and Poly(ethylene isophthalate). Macromolecules 2004;37(8):2978-2995.

37. Kotek R, Pang K, Schmidt B, and Tonelli A. Synthesis and gas barrier characterization of poly(ethylene isophthalate). Journal of Polymer Science Part B: Polymer Physics 2004;42(23):4247-4254.

38. Tonelli AE. Conformational characteristics of poly(ethylene phthalate)s. Journal of Polymer Science Part B: Polymer Physics 2002;40(12):1254-1260.

39. Tonelli AE. The conformations of poly(butylene-terephthalate) and poly(butylene-2,6-naphthalate) chains in their α and β crystalline polymorphs. Polymer 2002;43(22):6069-6072.

40. Tonelli AE. PET versus PEN: what difference can a ring make? Polymer 2002;43(2):637-642.

41. Maxwell AS, Ward IM, Lauprêtre F, and Monnerie L. Secondary relaxation processes in polyethylene terephthalate-additive blends: 1. N.m.r. investigation. Polymer 1998;39(26):6835-6849.

42. Maxwell AS, Monnerie L, and Ward IM. Secondary relaxation processes in polyethylene terephthalate-additve blends: 2. Dynamic mechanical and dielectric investigations. Polymer 1998;39(26):6851-6859.

43. Michaels AS, Vieth WR, and Barrie JA. Diffusion of Gases in Polyethylene Terephthalate. Journal of Applied Physics 1963;34(1):13-20.

44. Koros WJ. Barrier Polymers and Structures: Overview. In: Koros WJ, editor. Barrier Polymers and Structures. Washington: American Chemical Society, 1990. pp. 406.

45. Hu YS, Liu RYF, Schiraldi DA, Hiltner A, and Baer E. Oxygen Barrier Properties of Copolyesters Containing a Mesogenic Monomer. Macromolecules 2004;37(6):2136-2143.

46. Auras R, Harte B, and Selke S. Effect of Water on the Oxygen Barrier Properties of Poly(ethylene terephthalate) and Polylactide Films. Journal of Applied Polymer Science 2004;92:1790-1803.

47. Deng CS, Assender HE, Dinelli F, Kolosov OV, Briggs GAD, Miyamoto T, and Tsukahara Y. Nucleation and growth of gas barrier aluminium oxide on surfaces of poly(ethylene terephthalate) and polypropylene: effects of the polymer surface properties. Journal of Polymer Science Part B: Polymer Physics 2000;38(23):3151-3162.

48. Yasuda H and Stannett V. Permeation, Solution, and Diffusion of Water in Some High Polymers. Journal of Polymer Science 1962;57:907-923.

49. Chandrasekhar S. Stochastic problems in physics and astronomy. Reviews of Modern Physics 1943;15(1):1-89.

50. Petropoulos JH. Some fundamental approaches to membrane gas permeability and permselectivity. Journal of Membrane Science 1990;53(3):229-258.

51. Kumins CA and Kwei TK. Free Volume and Other Theories. In: Crank J and Park GS, editors. Diffusion in Polymers. London: Academic Press Inc. Ltd., 1968. pp. 107-139.

52. Petropoulos JH. Mechanisms and Theories for Sorption and Diffusion of Gases in Polymers. In: Paul DR and Yampol'skii YP, editors. Polymeric Gas Separation Membranes. Boca Raton: CRC Press, Inc., 1994. pp. 17-83.

53. Meares P. The Diffusion of Gases Through Polyvinyl Acetate1. Journal of the American Chemical Society 1954;76(13):3415-3422.

54. Alentiev AY and Yampolskii YP. Meares equation and the role of cohesion energy density in diffusion in polymers. Journal of Membrane Science 2002;206(1–2):291-306.

55. van Krevelen DW and te Nijenhuis K. Properties of Polymers: Their Correlation with Chemical Structure, Their Numerical Estimation and Prediction from Additive Group Contributions, 4th ed. Amsterdam: Elsevier Science & Technology, 2009.

56. Brandt WW. Model Calculation of the Temperature Dependence of Small Molecule Diffusion in High Polymers. The Journal of Physical Chemistry 1959;63(7):1080-1085.

57. Barrer RM. Some Properties of Diffusion Coefficients in Polymers. The Journal of Physical Chemistry 1957;61(2):178-189.

58. Cohen MH and Turnbull D. Molecular Transport in Liquids and Glasses. The Journal of Chemical Physics 1959;31(5):1164-1169.

59. DiBenedetto AT. Molecular properties of amorphous high polymers. I. A cell theory for amorphous high polymers. Journal of Polymer Science Part A: General Papers 1963;1(11):3459-3476.

60. DiBenedetto AT. Molecular properties of amorphous high polymers. II. An

interpretation of gaseous diffusion through polymers. Journal of Polymer Science Part A: General Papers 1963;1(11):3477-3487.

61. DiBenedetto AT and Paul DR. An interpretation of gaseous diffusion through polymers using fluctuation theory. Journal of Polymer Science Part A: General Papers 1964;2(2):1001-1015.

62. Paul DR and DiBenedetto AT. Diffusion in amorphous polymers. Journal of Polymer Science Part C: Polymer Symposia 1965;10(1):17-44.

63. Lin J, Shenogin S, and Nazarenko S. Oxygen solubility and specific volume of rigid amorphous fraction in semicrystalline poly(ethylene terephthalate). Polymer 2002;43(17):4733-4743.

CHAPTER 7

CARBON DIOXIDE SORPTION AND TRANSPORT IN AMORPHOUS PEF[1]

Complementary to Chapter 6, which examined oxygen transport in PEF, this chapter investigates carbon dioxide transport in amorphous PEF at various temperatures using permeation and pressure-decay sorption techniques. Detailed measurements for PEF at 35°C indicate a significant, surprisingly large reduction in carbon dioxide permeability of 19X at 1 atm compared PET, despite both an increase in free volume and carbon dioxide solubility of 1.6X for PEF vs. PET. The solubility increase for PEF, which originates from greater interaction between carbon dioxide and the polar furan moiety, is offset by a substantial reduction in diffusivity of 31X compared to PET. Such diffusion reduction for PEF, which is 3X greater than the 9.7X reduction in oxygen diffusivity compared to PET, is thought to originate from a hindrance of polymer ring-flipping motions compared to PET. A possible mechanism for the surprising barrier improvement for carbon dioxide in PEF vs. PET is provided in this chapter, along with a detailed comparison to oxygen and preliminary water transport data. Additional discussion is provided regarding the larger barrier improvement seen for carbon dioxide vs. oxygen in PEF vs. PET.

7.1. Introduction

Poly(ethylene furanoate) (PEF) is the furan-based analog to poly(ethylene terephthalate) (PET), which is the dominant polymer used in the beverage packaging

[1]Reproduced in part with permission from Burgess, S.K; Kriegel, R.M.; Koros, W.J., *Carbon Dioxide Sorption and Transport in Amorphous Poly(ethylene furanoate)*, *Macromolecules*, DOI: 10.1021/acs.macromol.5b00333, Copyright 2015 American Chemical Society.

industry. PEF and other related furanic polymers have been the subject of much recent research [1-20], due in part to the increased rigidity resulting from the furan moiety and attractive bio-renewable sourcing [21]. Currently, no published data exist regarding the sorption and transport of carbon dioxide in PEF; however, such data are necessary to enable large-scale industrial applications in the PET-dominant beverage packaging market, which currently comprises approximately 15 million metric tons/year [5].

A careful, fundamental study is required to understand the surprising carbon dioxide barrier advantages for PEF compared to PET and related polyesters such as poly(ethylene isophthalate) (PEI) and poly(ethylene naphthalate) (PEN). In fact, PET exhibits the highest carbon dioxide permeability of the aforementioned four polyesters, and consequently, provides a useful base case for comparison. Such comparisons can be quantified in terms of the Barrier Improvement Factor (BIF_P) [22], which represents the permeability of carbon dioxide in PET divided by the respective carbon dioxide permeability in PEF, PEN, or PEI. Permeability data and related BIF_P values provided in Table 7.1 emphasize the surprisingly large 19-fold permeability reduction for PEF compared to PET versus the smaller reductions compared to PET for PEI (ranging from 8 to 13) and for PEN of only 3-fold. Moreover, the carbon dioxide BIF_P of 19 for PEF vs. PET reported herein is significantly greater than the PEF BIF_P value of 4 reported in a prior study [23]. Such large differences in BIF_P values potentially originate from differences in polymer morphology and the chosen permeation test method. Specifically, the permeation values reported in this study were measured using amorphous, un-oriented PEF films, while most industry methods for carbon dioxide permeation testing typically utilize the entire finished package, which may include package “creep” during testing. If

creep happens, however, it could potentially make PEF less attractive, even if it is a better intrinsic barrier.

Table 7.1. Carbon dioxide permeability comparison (i.e., Barrier Improvement Factor, BIF_P) between transport in PET and related polyesters (i.e., PEF, PEI, and PEN). All values reflect data for essentially amorphous and un-oriented samples, with test conditions performed at low pressure (i.e., ≤1 atm).

Polyester	**Temp (°C)**	**Permeability (Barrer)**	**BIF_P**	**Reference**
PET	35	0.49	1	This work
PEF	35	0.026	19	This work
PET	30	0.57	1	[24]
PEI	30	0.045	13	[24]
PET	25	0.53	1	[25]
PEN	25	0.17	3.1	[25]
PET	30	0.32	1	[26]
PEN	30	0.11	2.9	[26]
PEI	30	0.038	8.4	[26]

The current study extends our prior work regarding PEF fundamental chain mobility (Chapter 5) and oxygen sorption and transport (Chapter 6). It is important to note that the independent carbon dioxide transport data for PEF recorded at multiple temperatures via complementary pressure-decay sorption and permeation methods presented in this chapter will be shown to be internally consistent. Since permeability is equal to a product of sorption and diffusion contributions (cf. Chapter 2), the carbon dioxide permeability reduction of 19X for PEF compared to PET at 1 atm can be factored further into

respective sorption and diffusion contributions. This factorization gives valuable insight into the fundamental basis for the difference in PEF vs. PET barrier performance.

In addition to providing the first transport study for carbon dioxide in amorphous PEF, the current chapter concludes with a detailed side-by-side comparison of the sorption and diffusion contributions to penetrant permeability in amorphous PEF vs. PET for carbon dioxide, oxygen, and water at 35°C (cf. Tables 7.6 and 7.7). This comparison clearly shows the detailed basis for the attractive barrier properties of PEF vs. PET, which combined with fully renewable PEF sourcing and improved thermal and mechanical properties, make it an attractive substitute for PET. The preliminary water transport data included herein (for comparison purposes) are taken from Chapters 8 and 9, which provide much a much more detailed investigation regarding equilibrium and kinetic water sorption, respectively, in both polyesters over the entire water activity range.

7.2. Transport Background and Theory

A detailed discussion regarding the transport background and theory utilized in this chapter is available in Chapter 2 (cf. Section 2.3), and select equations which will be referenced often in this chapter are reproduced below for convenience.

$$C = \left(k_D p + \frac{C_H' bp}{1 + bp} \right) \tag{7.1}$$

$$k^* = \left(k_D + C_H' b \right) \tag{7.2}$$

$$D = l^2 / 6\theta \tag{7.3}$$

$$k^* = 6\theta P / l^2 \tag{7.4}$$

$$D = \left(\frac{P}{k^*_{sorption}} \right) = \left(\frac{P}{k_D + C_H' b} \right) \tag{7.5}$$

7.3. Experimental Methods

7.3.1. Materials and Film Preparation

The poly(ethylene furanoate) (PEF) and poly(ethylene terephthalate) (PET) used in this chapter are the same materials described previously in Section 3.1.1, and all amorphous films were melt-pressed using the method in Section 3.1.3. All transport measurements reported in this study for PEF and PET reflect data corresponding to the amorphous morphology.

7.3.2. Transport Characterization

Carbon dioxide permeation data (i.e., 1, 2.5, 4, and 6 atm carbon dioxide at 30, 35, 45, and 55°C) were measured for amorphous PEF via the same constant-volume, variable-pressure apparatus and procedure described previously in Chapter 3. Permeation isotherms were measured in steps of increasing pressure at the lowest temperature first, followed by similar testing at the next highest temperature. Since carbon dioxide can induce plasticization/conditioning in polyester films [27], the permeability at 1 atm was

re-checked after testing at 6 atm at each temperature to verify that the values were reproducible and that the amorphous morphology was not detectably altered via testing at the highest pressure. Previous researchers have employed a "pre-conditioning" step at the highest carbon dioxide test pressure for PET to avoid plasticization during the course of testing (i.e., max pressure 20 atm carbon dioxide [27, 28]); however, this practice was not employed in the current work due to the relatively low pressures investigated. Transport testing at elevated temperatures near the glass transition temperature of the polymer can induce physical aging; however, our investigation regarding the effect of aging on transport in PEF reveals that this effect is minor (cf. Chapter 10 [19]). Permeation time-lags were measured at 1 atm and used in combination with $D = l^2/6\theta$ and Equation 7.4 for additional transport analysis. All permeation-related data reported in this study reflect the average of at least three measurements, with uncertainty limits derived from the standard error.

Carbon dioxide sorption data (i.e., 1 to 6 atm in steps of 1 atm at 35, 45, 55, and 65°C) were measured in amorphous PEF using the same constant-volume pressure-decay apparatus and procedure described in Chapter 3. Unlike the oxygen study discussed in Chapter 6, which utilized the same PEF sample for oxygen sorption testing at all temperatures, fresh films were used at each temperature for carbon dioxide testing in the current chapter. Such precautions were used, since carbon dioxide sorption at high pressure might induce sorption hysteresis, thereby possibly altering the morphology of PET [27-30] and other glassy polymers [31-33]. In fact, in this work, non-Fickian relaxations were observed at almost all carbon dioxide sorption pressures tested for PEF, despite the relatively low maximum pressure of 6 atm tested. This "conditioning"

behavior was not observed in the permeation measurements, resulting likely from the vacuum conditions on the downstream side of the permeation film at all times (i.e., there is a partial pressure differential across the permeation film, while a uniform partial pressure exists throughout the sorption films). Similar non-Fickian uptake behavior, as measured via pressure-decay methods, was also observed in our prior work regarding carbon dioxide sorption in amorphous PET, discussed previously in Chapter 4. Each complete sorption isotherm at 35, 45, 55, and 65°C in the current chapter (cf. Figure 7.4) was measured using at least two different samples to verify the reproducibility of the reported data.

7.4. Results and Discussion

7.4.1. Permeation

Carbon dioxide permeation data are provided for amorphous PEF as a function of pressure and temperature in Figure 7.1, with dashed lines drawn to aid the eye. The pressure dependencies reported in Figure 7.1 are significantly more pronounced than the corresponding pressure independence for oxygen in PEF reported in Chapter 6. This behavior is expected, due to the higher condensability and solubility of carbon dioxide in PEF compared to oxygen. Such pressure dependent permeability data are amenable to analysis via the partial immobilization model [34], provided that the dual-mode model parameters from Equation 7.1 are known. A detailed discussion regarding the partial immobilization model as it pertains to carbon dioxide transport in amorphous PEF is provided later in Appendix C, but is not the main focus of this chapter.

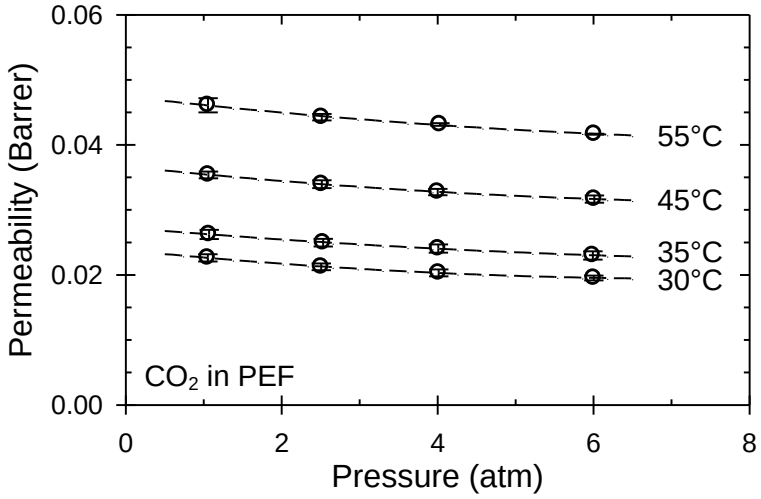

Figure 7.1. Carbon dioxide permeability in amorphous PEF. Dashed lines are drawn to aid the eye.

Permeability data for carbon dioxide in amorphous PET at 35°C are reported in Chapter 4 and plotted in Figure 7.2 alongside the respective permeability data at 35°C for PEF. Inspection of Figure 7.2 reveals a significant permeability reduction of 19X at 1 atm for carbon dioxide in PEF compared to PET (i.e., 0.49/0.026 = 19). It is interesting to note that the permeability reduction for carbon dioxide is larger than the 11X reduction in oxygen permeability observed for PEF compared to PET in Chapter 6. A detailed discussion regarding the respective sorption and diffusion contributions to the reduction in carbon dioxide permeability for PEF compared to PET is provided later in the document (cf. Tables 7.6 and 7.7).

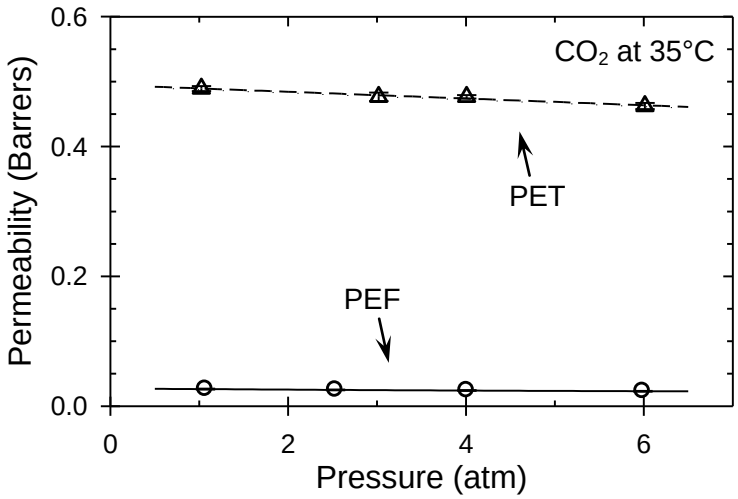

Figure 7.2. Carbon dioxide permeability in amorphous PEF and PET at 35°C. Data corresponding to PET (triangles) are from Chapter 4 and are included herein for comparison purposes.

The permeability data for PEF in Figure 7.1 were re-plotted in semi-logarithmic form to perform an Arrhenius analysis. Temperature-dependent permeability data at 1 atm (circles) and 6 atm (triangles) are plotted versus the inverse of temperature in Figure 7.3 in such fashion, thereby yielding values of 23.7 ± 0.2 kJ/mol at 1 atm and 25.2 ± 0.4 kJ/mol at 6 atm for the apparent activation energies of permeation (E_P). A slightly larger E_P value corresponding to the highest pressure is not surprising, and originates in part from a difference in degree of Langmuir site saturation at the two pressures [28]. The E_P estimate at 6 atm is included for illustration purposes, and all additional apparent energetic parameters discussed throughout the remainder of the work reflect values corresponding to the low pressure limit (i.e., ≤1 atm carbon dioxide). The 1 atm values can be considered an effective infinite dilution limit, consistent with the previous discussion of these parameters in Equations 7.2 – 7.5.

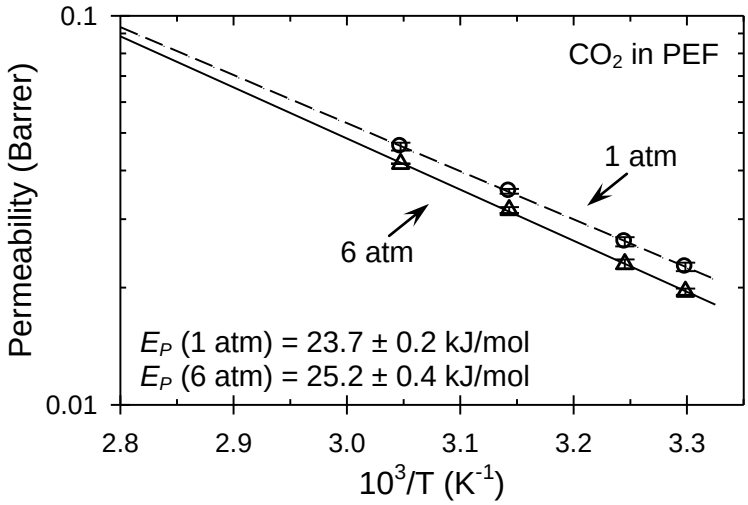

Figure 7.3. Arrhenius plot of carbon dioxide permeability at 1 atm (circles) and 6 atm (triangles) data in amorphous PEF. Lines represent the respective model fits from Equation 2.19 (discussed previously).

7.4.2. Equilibrium Sorption

Equilibrium sorption data for carbon dioxide in amorphous PEF at multiple temperatures are plotted in Figure 7.4 along with the corresponding dual-mode fits from Equation 7.1. The carbon dioxide sorption isotherm at 35°C for amorphous PET is reported in Chapter 4 and plotted for comparison in Figure 7.5 alongside the respective sorption data at 35°C for amorphous PEF. The dual-mode parameters corresponding to the data in Figures 7.4 and 7.5 are provided in Table 7.2, and a discussion regarding the temperature dependence of the parameters from Table 7.2 is available in Appendix C. The uncertainty limits for k_D, b, and C_H' in Table 7.2 represent the standard error of the model fit parameters from Equation 7.1 determined via the fitting program (SigmaPlot 8.0). Furthermore, the relative lack of isotherm curvature (cf. Figure 7.4) and the inherent coupling of C_H' and b in Equation 7.1 produce large uncertainty estimates for C_H' and b. The uncertainty limits for k* were determined via a standard propagation of uncertainty

analysis [35] applied to the definition of k^* (i.e., $k^* = k_D + C_H'b$).

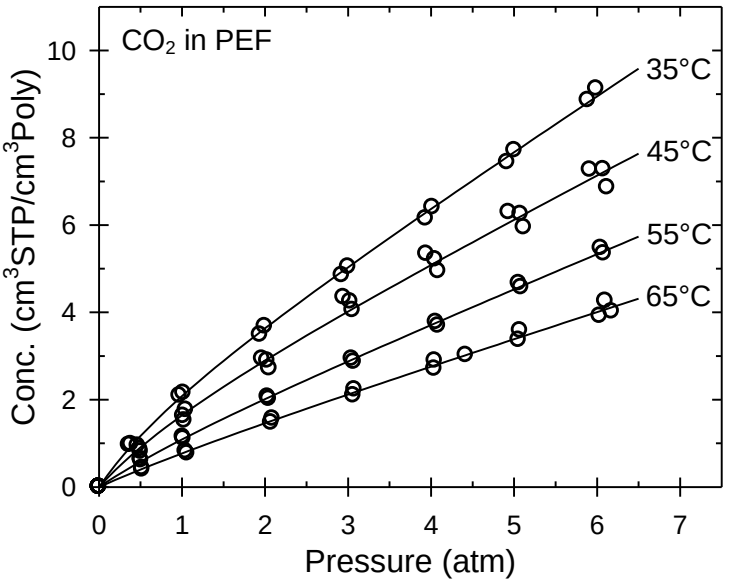

Figure 7.4. Equilibrium carbon dioxide sorption data for amorphous PEF. Solid lines represent the respective dual-mode model fits from Equation 7.1.

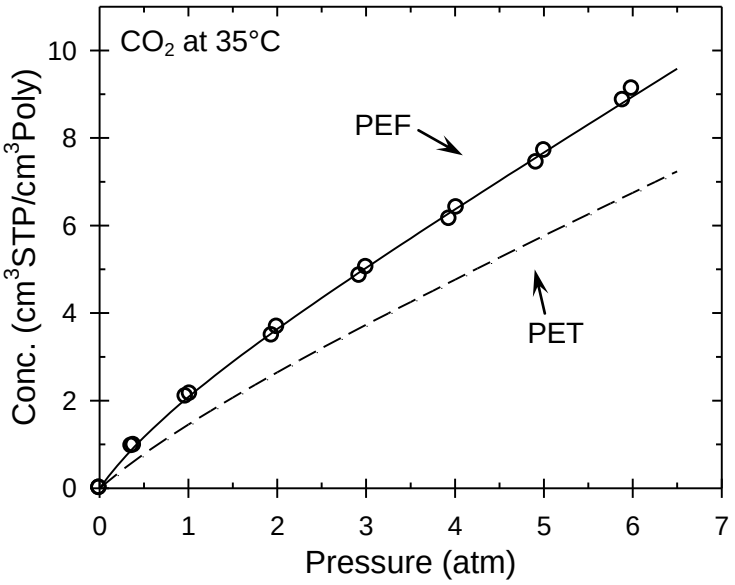

Figure 7.5. Equilibrium carbon dioxide sorption data for amorphous PEF and PET. Data corresponding to PET (dashed line) are from Chapter 4 and are included in this figure for comparison purposes.

Table 7.2. Dual-mode model (Equation 7.1) parameters for carbon dioxide sorption in amorphous PEF.

Sample	Temp (°C)	k_D (ccSTP/ccPoly·atm)	b (atm^{-1})	C_H' (ccSTP/ccPoly)	k^*, ($k_D + C_H'b$) (ccSTP/ccPoly·atm)	K,($C_H'b/k_D$) (—)
PET[a]	35	0.93 ± 0.04	0.50 ± 0.2	1.6 ± 0.4	1.7 ± 0.3	0.86 ± 0.4
PEF	35	1.2 ± 0.06	0.83 ± 0.3	1.9 ± 0.5	2.8 ± 0.7	1.3 ± 0.5
PEF	45	0.96 ± 0.1	0.68 ± 0.6	1.7 ± 0.9	2.1 ± 1	1.2 ± 1
PEF	55	0.78 ± 0.05	0.58 ± 0.4	0.85 ± 0.5	1.3 ± 0.4	0.63 ± 0.5
PEF	65	0.60 ± 0.07	0.42 ± 0.9	0.58 ± 0.8	0.84 ± 0.6	0.41 ± 1

a: Data corresponding to PET are from Chapter 4 and are included in this table for comparison purposes.

First inspection of Figure 7.5 reveals that carbon dioxide is noticeably more soluble in PEF compared to PET, which is the opposite behavior observed for oxygen sorption in PEF vs. PET from Chapter 6. Examination of the dual-mode model parameters for carbon dioxide at 35°C in Table 7.2 reveals both a larger carbon dioxide k_D and b for PEF compared to PET, probably reflecting a greater interaction between carbon dioxide and the PEF matrix compared to PET. Such behavior can be rationalized by carbon dioxide exhibiting a greater affinity for the polar furan ring in PEF compared to the non-polar phenyl ring in PET. The Langmuir capacity constant (C_H') for carbon dioxide is also apparently larger for PEF compared to PET, which agrees with the trend in C_H' observed for oxygen (cf. Chapter 6). Despite the overall increase in carbon dioxide solubility for PEF compared to PET, a significant reduction in overall permeability of 19X at 1 atm for PEF vs. PET is still observed. A more detailed discussion regarding this interesting effect and how it pertains to the overall transport comparison between PEF and PET is provided later in Section 7.4.4.

As mentioned previously, the effective solubility coefficient (k^*) reflects sorption

contributions from both the Langmuir and Henry's populations, and by nature, is larger than the respective sorption coefficient for the Henry's population (k_D) [16, 27, 28]. A list of relevant sorption parameters measured via pressure-decay sorption (i.e., k_D and $k^* = k_D+C_H'b$) and permeation (i.e., $k^* = 6\theta P/l^2$) is provided in Table 7.3, where satisfactory agreement is observed between k^* values measured via the independent permeation and sorption methodologies noted earlier.

Table 7.3. Sorption parameters for carbon dioxide in amorphous PEF measured via pressure-decay sorption and permeation techniques. The sorption estimates from permeation were measured with an upstream pressure of 1 atm.

	Sorption		**Permeation**
Temp (°C)	**k_D (Eq. 7.1) ($cm^3STP/cm^3Poly \cdot atm$)**	**k^*, ($k_D+C_H'b$) ($cm^3STP/cm^3Poly \cdot atm$)**	**k^*, ($6\theta P/l^2$) ($cm^3STP/cm^3Poly \cdot atm$)**
30	–	–	2.5 ± 0.1
35	1.2 ± 0.06	2.8 ± 0.7	2.2 ± 0.07
45	0.96 ± 0.1	2.1 ± 1	1.7 ± 0.04
55	0.78 ± 0.05	1.3 ± 0.4	1.1 ± 0.02
65	0.60 ± 0.07	0.84 ± 0.6	–

The sorption parameters from Table 7.3 can be re-plotted in semi-logarithmic form as a function of inverse temperature to perform a van't Hoff analysis based on Equation 2.6. Sorption parameters determined from permeation testing (i.e., $k^* = 6\theta P/l^2$) are plotted in Figure 7.6 (hollow circles) along with values of k_D measured from sorption (solid circles), while data corresponding to k^* determined from sorption (i.e., $k^* = k_D+C_H'b$) are plotted in Appendix C. Inspection of Figure 7.6 reveals that k^* approaches k_D as the temperature increases towards the glass transition temperature (i.e., $T_g \approx 85$°C [15]). Such behavior is expected, since the Langmuir contribution to k^* will decrease and effectively disappear at

T_g, leaving $k^* = k_D$ at and above T_g [27, 28]. The van't Hoff analysis illustrated in Figure 7.6 yields estimates for the apparent enthalpies of carbon dioxide sorption in PEF from the two independent methods. Specifically, analysis of k_D yields the apparent enthalpy of sorption in the dissolved Henry's mode (ΔH_D = -20.5 ± 0.8 kJ/mol), while analysis of k^* determined from permeation yields the apparent enthalpy of sorption in both the dissolved and microvoid populations ($\Delta H_{S,eff}$ = -26.5 ± 3 kJ/mol). A more exothermic value of $\Delta H_{S,eff}$ compared to ΔH_D is consistent with the notion that sorption via molecular dissolution includes the endothermic step of penetrant-sized "hole formation" between the polymer chains [36], while a molecular scale "hole" ideally already exists for sorption in the Langmuir population [27, 37, 38]. Additional information pertaining to the van't Hoff analysis of sorption parameters is provided in Appendix C.

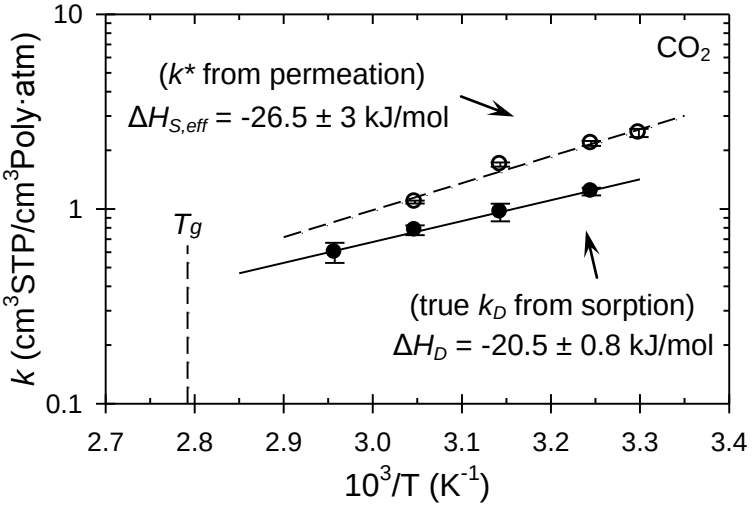

Figure 7.6. Van't Hoff analysis of the sorption parameters for carbon dioxide in amorphous PEF. The vertical dashed line represents the T_g of 85°C reported in Chapter 5.

7.4.3. Kinetic Sorption and Diffusion

Aside from equilibrium sorption data, pressure-decay sorption experiments also allow measurement of temperature-dependent diffusion coefficient data as indicated previously in Section 2.4 and Section 3.3.2. As described previously, the raw pressure-decay data vs. time can be transformed via Equation 7.6 into a non-dimensional form that can be modeled using the solution of the time-dependent diffusion equation in Equations 7.7 – 7.9, which specifically applies to carbon dioxide sorption in PEF (cf. Section 2.4.2). As a note, Equation 7.7 will be called the "Fick-LV" model throughout the remainder of this chapter.

$$\frac{M_t}{M_\infty}(t) = \left(\frac{p_{initial} - p(t)}{p_{initial} - p_{final}} \right) \tag{7.6}$$

$$\frac{M_t}{M_\infty}(t) = 1 - \sum_{n=1}^{\infty} \frac{2\alpha(1+\alpha)}{1+\alpha+\alpha^2 q_n^{\,2}} \exp\left(\frac{-Dq_n^{\,2}t}{L^2} \right) \tag{7.7}$$

$$\tan(q_n) = -\alpha q_n \tag{7.8}$$

$$\frac{n_{film,\,final}}{n_{total,initial}} = \left(\frac{1}{1+\alpha} \right) \tag{7.9}$$

While Equation 7.7 can successfully account for the variable pressure at the film surface during diffusion, more complex models are needed for diffusion cases involving

the superposition of true non-Fickian relaxations with the polymer [39-41]. Such uptake-induced relaxations and/or conditioning-type behavior have been observed for carbon dioxide uptake in PET at both relatively low [42] and high [27, 28, 43] pressures, and similarly, are also observed in the current work to some degree regarding PEF at all carbon dioxide uptake pressures >0.5 atm. Detailed investigation of such non-Fickian behavior is beyond the scope of the current chapter, and consequently, only kinetic sorption isotherms corresponding to the lowest pressure step (i.e., 0 to ~0.5 atm carbon dioxide) are investigated and reported herein. Example kinetic data for carbon dioxide uptake in PEF at 35°C are reported in Figure 7.7 along with the model fit from Equation 7.7 (dashed white line). Optimization of the diffusion coefficient from Equation 7.7 was performed using the MATLAB® procedure described later in Chapter 11 [44].

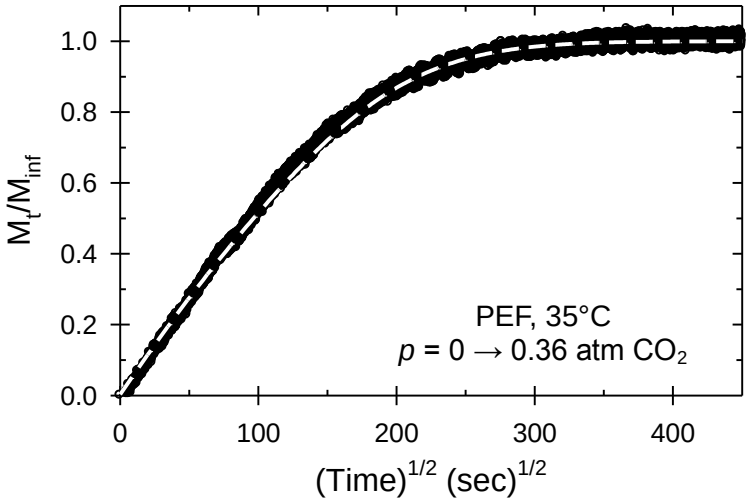

Figure 7.7. Kinetic sorption isotherm between 0 to 0.36 atm for carbon dioxide uptake in amorphous PEF at 35°C. The Fick-LV model fit from Equation 7.7 is depicted via the white dashed line, with $D = 7 \times 10^{-11}$ cm^2/s and $\alpha = 2.3$.

Diffusivity estimates via Equation 7.7 represent the average value over the discrete pressure uptake interval (i.e., approximately 0 to ~0.5 atm carbon dioxide). Due to the relatively low maximum pressures tested, the diffusivities determined from sorption should ideally agree with the diffusivities determined via permeation testing at 1 atm (i.e., $D = l^2/6\theta$). The diffusivities determined from sorption and permeation discussed thus far are independent of the actual solubility and permeability, respectively (i.e., M_t/M_∞ is dimensionless, and the estimates from permeation originate from the time-lag). A third diffusivity estimate, which can be used to further cross-verify the internal consistency of the measurements, can be provided via $D = P/k^*$, where P is the steady-state permeability at 1 atm from permeation testing, and k^* is the effective solubility coefficient from sorption testing (i.e., $k^* = k_D + C_H'b$). Carbon dioxide diffusivities in amorphous PEF from all three methods (i.e., sorption, permeation, and permeation/sorption) are provided in Table 7.4, where excellent agreement is observed among the reported parameters. Any small impact of non-Fickian relaxations, even for feed pressures of 1 atm appear to be less than the experimental uncertainty in general; however, at higher pressures, e.g., both of these effects would need to be considered.

Table 7.4. Effective diffusion coefficients at low pressure for carbon dioxide in amorphous PEF.

	$D\times10^{10}$ (cm^2/s)			$\left(\frac{1}{1+\alpha}\right)$
Temp (°C)	**Transient Permeation[a] ($l^2/6\theta$)**	**Steady-state Permeation/Sorption[b] (P/k^*)**	**Kinetic Sorption[c] (Fick-LV, Eq. 7.7)**	**for Sorption (Eq. 7.9)**
30	0.70 ± 0.05	–	–	–
35	0.92 ± 0.05	0.72 ± 0.2	0.76 ± 0.07	0.28 ± 0.02
45	1.6 ± 0.03	1.3 ± 0.8	1.6 ± 0.1	0.13 ± 0.02
55	3.2 ± 0.1	2.8 ± 0.9	2.8 ± 0.2	0.11 ± 0.002
65	–	–	5.1 ± 1	0.067 ± 0.009

a: Measured via the time-lag method with an upstream pressure equal to 1 atm.
b: P represents the steady-state carbon dioxide permeability at 1 atm, and k^* represents the sorption derived effective solubility parameter from Table 7.2 (i.e., $k^* = k_D + C_H'b$).
c: Measured via the model fit of Equation 7.7 to kinetic sorption data over the pressure interval 0 to ~0.5 atm carbon dioxide.

Inspection of Table 7.4 reveals that $1/(1+\alpha)$ (i.e., Equation 7.9) exhibits a negative correlation with temperature, which represents an expected decreasing fractional uptake with increasing temperature due to the reduced carbon dioxide solubility in PEF at higher temperatures (cf. Figure 7.4). Diffusivities determined via the permeation and sorption methods are plotted in Arrhenius form in Figure 7.8, while the respective values from P/k^* are not shown to avoid cluttering the figure. As seen in Figure 7.8, the apparent activation energy of diffusion (E_D) from sorption (53.9 ± 4 kJ/mol) is consistent with the respective value determined from permeation (50.0 ± 3 kJ/mol).

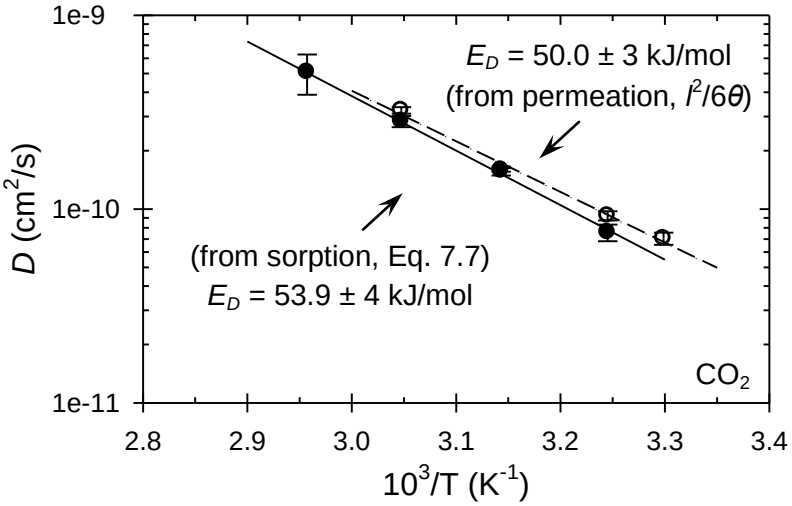

Figure 7.8. Effective diffusion coefficients determined via kinetic sorption (solid circles) and permeation (hollow circles) for carbon dioxide in amorphous PEF.

7.4.4. Transport Energetics and Comparison to O_2 and H_2O Transport

It is useful to compare the energetic parameters for carbon dioxide in PEF reported in this chapter to analogous data in the literature for carbon dioxide in PET. Such data are provided in Table 7.5, where satisfactory agreement is observed between the energetic parameters from the independent pressure-decay sorption and permeation methods reported herein. Estimates for the activation entropies of carbon dioxide diffusion in PET and PEF are provided later in Appendix F.

Table 7.5. Apparent energetic parameters corresponding to carbon dioxide transport at low pressure (i.e., ≤1 atm) in amorphous, un-oriented PEF and PET, unless otherwise noted.

	Method	E_P (kJ/mol)	E_D (kJ/mol)	$\Delta H_{S,eff}$[a] (kJ/mol)	ΔH_D (kJ/mol)	Reference
PEF	Permeation	23.7 ± 0.2	50.0 ± 3	-26.5 ± 3	–	This work
	Sorption	20.5[b] ± 10	53.9 ± 4	-33.4 ± 10	-20.5 ± 0.8	This work
PET	Permeation	24.9[c]	51.3[d]	-26.4[e]	–	[28]
	Permeation	27.6	52.3	-24.7[e]	–	[45]
	Sorption	–	40 ± 7[f]	–	–	[43]
	Sorption	–	–	-24.0[g,h]	-7.1[h]	[27]
	Sorption	18.7[b]	41.2	-22.5	–	[46]

a: Estimated from van't Hoff analysis of k^* as determined via permeation or sorption measurements, unless otherwise noted.
b: Estimated from $E_P = E_D + \Delta H_{S,eff}$
c: Estimated from permeability data at 1 atm from Figure 1 in ref. [28] for semicrystalline PET.
d: Estimated from D_{eff} data at 1 atm from Figure 5 in ref. [28] for semicrystalline PET.
e: Estimated from $\Delta H_{S,eff} = E_P - E_D$.
f: Measured via carbon dioxide sorption in amorphous PET at high pressure.
g: Estimated from van't Hoff analysis of k^* determined from Table 1 in ref. [27] for semicrystalline PET.
h: For semicrystalline PET.

From Table 7.5, the activation energy of diffusion (E_D) for carbon dioxide in PEF is slightly larger than the average value reported for PET (i.e., 46.2 kJ/mol). A similar trend was also observed for the activation energy of oxygen diffusion in PEF compared to PET in Chapter 6. The variability in the E_D estimates for CO_2 diffusion in PET reported in Table 7.5 likely originates from either differences in sample morphology or test method, since such data were not measured for PET in the current work. The notion that PEF exhibits larger E_D's for both penetrants compared to PET can be examined in the context of fundamental polymer properties based on the framework of Meares [47] and Brandt [48, 49], which is discussed previously in Chapter 6. The transport data for carbon

dioxide provided in this chapter complement prior work pertaining to oxygen (Chapter 6) and work pertaining to water sorption and diffusion in amorphous PEF compared to PET (Chapters 8 and 9, respectively). It is useful to provide an abbreviated side-by-side comparison of the transport parameters (i.e., permeability, diffusivity, and solubility) at 35°C for the three relevant penetrants in PEF vs. PET, and to examine the relative sorption and diffusion contributions to the permeability reductions for PEF compared to PET. Such transport data at 35°C for carbon dioxide, oxygen, and water in amorphous PEF and PET are provided in Table 7.6. Recall that the water transport data reported in Figure 7.6 represent a small subset of the measured data, which are available over the entire concentration range in Chapters 8 and 9. Estimates for the activation entropies of oxygen, carbon dioxide, and water diffusion in PET and PEF are provided later in Appendix F.

Table 7.6. Sorption and transport parameters at low pressure and 35°C for carbon dioxide, oxygen, and water in amorphous PEF and PET. All k^* values reflect estimates from sorption ($k^* = k_D + C_H'b$), and the permeability values for carbon dioxide and oxygen represent experimental values at 1 atm.

	Value at 35°C	**Carbon dioxide[a]**	**Oxygen[b]**	**Water[c]**
PEF	$D \times 10^{10}$ (cm^2/s)	0.72 ± 0.2	10 ± 0.6	17
	k^* ($cm^3STP/cm^3Poly \cdot atm$)	2.8 ± 0.7	0.094	787 ± 110
	P (Barrer)	0.026	0.0107	180[d]
PET	$D \times 10^{10}$ (cm^2/s)	22 ± 4	97 ± 1	96
	k^* ($cm^3STP/cm^3Poly \cdot atm$)	1.7 ± 0.3	0.102	290 ± 140
	P (Barrer)	0.49	0.114	370[d]

a: Data for PET from Chapter 4.
b: Data from Chapters 4 and 6.
c: Data from Chapters 8 and 9. Diffusivity values are taken from Figure 9.8 in Chapter 9 between the activity interval 0.1 – 0.2.
d: Estimated from $P = Dk^*$, and not explicitly measured.

Additional analysis of the data reported in Table 7.6 is possible through a modified form of the Barrier Improvement Factor (BIF) [22], which was introduced previously. The original definition of the BIF pertains to the permeability ratio between the base case material (i.e., PET) and the new material with reduced permeability (i.e., PEF). Sorption and diffusion-specific Barrier Improvement Factors can be defined in a similar manner to further illustrate the respective sorption and diffusion reductions for PEF compared to PET. Such factors are defined as BIF_{k^*}, equal to the ratio of k^* parameters in Table 7.6 for PET divided by PEF, and BIF_D, equal to the ratio of D values from Table 7.6 for PET divided by PEF. Clearly, since $P = Dk^*$ (i.e., permeability = diffusivity × solubility), the infinite dilution BIF based on permeability (i.e., BIF_P) must equal the product of BIF_{k^*} and BIF_D. Barrier Improvement Factors derived from the data in Table 7.6 are provided in Table 7.7.

Table 7.7. Carbon dioxide, oxygen, and water Barrier Improvement Factors at 35°C (i.e., property from Table 7.6 corresponding to amorphous PET divided by the respective property from Table 7.6 for amorphous PEF). Data for oxygen are from Chapters 4 and 6. Data for water are from Chapters 8 and 9, while data for carbon dioxide in PET are from Chapter 4.

BIF (PET/PEF)	Carbon dioxide	Oxygen	Water[a]
BIF_D	31	9.7	5.6
BIF_{k^*}	0.61	1.1	0.37
BIF_P	19	11	2.1[b]

a: All BIF values for water reported herein were estimated over the activity interval of 0.1 – 0.2 to represent water transport at low concentration, while the BIF values reported in Chapters 8 and 9, which are similar in magnitude, are averaged over the entire activity range 0 – 1.
b: Calculated from $BIF_P = BIF_D \cdot BIF_{k^*}$.

Inspection of Table 7.7 reveals BIF_D values greater than unity for all three penetrants, thereby indicating reductions in penetrant diffusivity for PEF compared to PET. Such

behavior is believed to be related to the hindrance of furan ring-flipping motions in PEF compared to the respective phenyl ring-flipping motions in PET, as determined in our prior work described in Chapter 5 via solid-state NMR and dynamic mechanical methods. Corresponding values of BIF_{k^*} less than unity for carbon dioxide and water indicate increased penetrant sorption in PEF compared to PET, originating from greater interaction between the penetrant and the polar furan moiety in the PEF matrix compared to the non-polar phenyl moiety in PET. The trend in BIF_{k^*} values for the various penetrants (i.e., $BIF_{k^*,O2} > BIF_{k^*,CO2} > BIF_{k^*,H2O}$) correlates with the trend of increasing penetrant condensability as determined via the critical temperature (i.e., $T_{c,O2} < T_{c,CO2} < T_{c,H2O}$). Such a correlation of BIF_{k^*} with critical temperature is interesting, and may be related somehow to the more polar nature of PEF vs. PET; however, the complex nature of k^* makes the source of such correlation unclear at this time.

It should also be noted that the BIF_D for carbon dioxide (i.e., 31) is significantly larger than the respective value for oxygen (i.e., 9.7), despite both penetrants exhibiting similar kinetic diameters (i.e., 3.3 Å for carbon dioxide and 3.46 Å for oxygen [50]). Such behavior indicates that the mobility of carbon dioxide in PEF is reduced more significantly by the chain mobility differences and ring polarity compared to PET than oxygen. One possible explanation for this notion might entail a combination of interrelated factors. For example, it is possible that a synergistic relationship exists between the increase in carbon dioxide affinity for PEF and the hindered flipping motion of the polar furan moiety. The reduced frequency of ring-flipping in PEF undoubtedly reduces the frequency of free volume "reorganization" within the matrix (and hence, the frequency of successful diffusive jumps). The notion of a more rigid matrix for PEF vs.

PET can be coupled with the hypothesis that a diffusive jump in PEF likely occurs via some type of motion involving the polar carbonyl moieties, which are effectively "unhindered" in motion compared to PET, as described in Chapter 5. Diffusion of a carbon dioxide molecule, which can have an induced dipole, will therefore experience greater interaction with the polar carbonyl moieties in PEF compared to PET due to the hindered ring-flipping motions and increased chain rigidity. Similar to carbon dioxide, diffusion of the non-polar oxygen molecule in PEF will still be hindered compared to PET due to the hindered ring-flipping motions (hence, $BIF_D = 9.7$). Despite this fact, the non-polar nature of oxygen compared to carbon dioxide results in less affinity for the polar carbonyl moieties, which consequently, may produce a higher diffusion coefficient compared to carbon dioxide. Corroboration of this notion is provided by examination of the BIF_P values for oxygen and carbon dioxide transport in poly(ethylene isophthalate) (PEI) compared to PET as shown in Table 7.8. The non-symmetrical axis of ring rotation in PEI results in hindered ring-flipping events compared to PET [51], which is similar in behavior to PEF; however, the phenyl ring in PEI is non-polar compared to the furan ring in PEF. As seen in Table 7.8, the $BIF_P(CO_2)$ for PEI is larger than the respective $BIF_P(O_2)$ for PEI, which is the same behavior observed for CO_2 and O_2 in PEF. Such a large reduction in CO_2 permeation compared to O_2 for both rigid polyesters compared to PET can be explained using the prior reasoning that penetrant diffusion in analogously rigid polyesters with hindered ring-flipping motions, such as PEF and PEI, may occur via some type of motions involving the polar carbonyl moieties. This notion is also supported via CO_2 exhibiting a larger apparent activation energy of diffusion in PEF compared to O_2 (i.e., ~52.0 kJ/mol for CO_2 vs. ~44.6 kJ/mol for O_2), despite CO_2 exhibiting a smaller

kinetic diameter than O_2.

Table 7.8. Comparison between PET, PEF, and poly(ethylene isophthalate) (PEI).

	PET 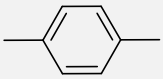	**PEI** 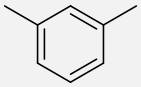	**PEF** 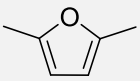
"Polar" ring?	No	No	Yes
Hindered ring-flipping?	No	Yes	Yes
$BIF_P(O_2)$ vs. PET	1	3.6[a]	11[a]
$BIF_P(CO_2)$ vs. PET	1	11[b]	19

a: From Table 6.1 in Chapter 6.
b: From Table 7.1.

The aforementioned synergy between carbon dioxide affinity and matrix rigidity for PEF is partially lost for water diffusion in PEF vs. PET (i.e., BIF_D = 5.6); however, a much smaller kinetic diameter for water (2.65 Å [50]) compared to carbon dioxide (3.3 Å [50]) likely explains the less "selective" nature of water vs. carbon dioxide diffusion in PEF compared to PET. The relatively small value of BIF_D for water (i.e., 5.6), in combination with the BIF_{k^*} lower than unity (i.e., 0.37), results in a projected permeability reduction of only ~2X at low activity for PEF compared to PET. While the BIF_P for water is lower than for carbon dioxide and oxygen, the observed reduction in penetrant permeability for all three penetrants still demonstrates the viability of PEF as an attractive replacement for PET.

7.5. Summary and Conclusions

Independent permeation and pressure-decay sorption data corresponding to carbon dioxide transport in amorphous poly(ethylene furanoate) (PEF) were measured at

multiple temperatures and shown to be internally consistent. Surprisingly large reductions in both carbon dioxide permeability (19X) and diffusivity (31X) were observed at 1 atm when compared to the respective properties for carbon dioxide in amorphous PET, despite both an increase in free volume and carbon dioxide solubility of 1.6X for PEF vs. PET. It appears that this effect may reflect greater carbon dioxide interaction with the PEF matrix as compared to the case for oxygen. Such behavior indicates the importance of reduced chain mobility for PEF vs. PET in determining the overall carbon dioxide transport properties. Transport energetic parameters (i.e., apparent enthalpy of sorption, apparent activation energies of permeation and diffusion) were determined for carbon dioxide in amorphous PEF, thereby allowing parameter estimation for a wide range of temperatures in the glassy state.

In combination with penetrant transport data from Chapters 4, 6, 8, and 9, a side-by-side comparison was made between the relative sorption and diffusion contributions to the reduction in permeability for carbon dioxide, oxygen, and water in amorphous PEF compared to PET. The reductions for carbon dioxide diffusion (31X) in PEF compared to PET were significantly larger than the respective diffusion reductions for oxygen (9.7X) and water (5.6X), while both carbon dioxide and water were found to exhibit increased solubility in PEF, possibly due in part to greater affinity for the polar furan moiety. The surprisingly large magnitude of BIF_D for carbon dioxide (31X) is believed to occur through a synergistic relationship between the carbon dioxide affinity for the polar moieties in PEF and the relative hindrance of ring-flipping motions compared to the respective properties for PET. Such synergy is partially lost for water diffusion in PEF compared to PET, since a much smaller kinetic diameter compared to carbon dioxide

renders PEF less “selective.”

The current chapter investigates carbon dioxide transport in only the amorphous morphology for PEF; however, estimates for transport in semicrystalline PEF (i.e., permeability, solubility, and diffusivity) can be determined from the idealized two-phase model of crystallinity [38, 45]. Additional studies involving transport in semicrystalline PEF are needed to verify the applicability of the two-phase model for PEF, since transport estimates for semicrystalline PET are known to deviate slightly from such ideal behavior [52]. Furthermore, the current work can serve as a starting point for future transport studies involving orientation and crystallinity, since comparisons to the amorphous morphology are undoubtedly required. As mentioned previously, this chapter provides the first transport data for carbon dioxide in PEF, and in combination with Chapters 6, 8, and 9, illustrates the impressive barrier performance of PEF and viability as a potential replacement for PET.

7.6. References

1. Gandini A, Silvestre AJD, Neto CP, Sousa AF, and Gomes M. The furan counterpart of poly(ethylene terephthalate): An alternative material based on renewable resources. Journal of Polymer Science Part A: Polymer Chemistry 2009;47(1):295-298.

2. Gomes M, Gandini A, Silvestre AJD, and Reis B. Synthesis and characterization of poly(2,5-furan dicarboxylate)s based on a variety of diols. Journal of Polymer Science Part A: Polymer Chemistry 2011;49(17):3759-3768.

3. Knoop RJI, Vogelzang W, van Haveren J, and van Es DS. High molecular weight poly(ethylene-2,5-furanoate); critical aspects in synthesis and mechanical property determination. Journal of Polymer Science Part A: Polymer Chemistry 2013;51(19):4191-4199.

4. Jong Ed, Dam MA, Sipos L, and Gruter GJM. Furandicarboxylic Acid (FDCA), A Versatile Building Block for a Very Interesting Class of Polyesters. Biobased Monomers, Polymers, and Materials, vol. 1105: American Chemical Society, 2012.

pp. 1-13.

5. Eerhart AJJE, Faaij APC, and Patel MK. Replacing fossil based PET with biobased PEF; process analysis, energy and GHG balance. Energy & Environmental Science 2012;5(4):6407-6422.

6. Jiang M, Liu Q, Zhang Q, Ye C, and Zhou G. A series of furan-aromatic polyesters synthesized via direct esterification method based on renewable resources. Journal of Polymer Science Part A: Polymer Chemistry 2012;50(5):1026-1036.

7. Gruter G-JM, Sipos L, and Adrianus Dam M. Accelerating research into bio-based FDCA-polyesters by using small scale parallel film reactors. Combinatorial Chemistry & High Throughput Screening 2012;15(2):180-188.

8. Papageorgiou GZ, Tsanaktsis V, and Bikiaris DN. Synthesis of poly(ethylene furandicarboxylate) polyester using monomers derived from renewable resources: thermal behavior comparison with PET and PEN. Physical Chemistry Chemical Physics 2014;16:7946-7958.

9. Codou A, Guigo N, van Berkel J, de Jong E, and Sbirrazzuoli N. Non-isothermal Crystallization Kinetics of Biobased Poly(ethylene 2,5-furandicarboxylate) Synthesized via the Direct Esterification Process. Macromolecular Chemistry and Physics 2014;215(21):2065-2074.

10. Wilsens CHRM, Verhoeven JMGA, Noordover BAJ, Hansen MR, Auhl D, and Rastogi S. Thermotropic Polyesters from 2,5-Furandicarboxylic Acid and Vanillic Acid: Synthesis, Thermal Properties, Melt Behavior, and Mechanical Performance. Macromolecules 2014;47(10):3306-3316.

11. Wilsens CHRM, Deshmukh YS, Noordover BAJ, and Rastogi S. Influence of the 2,5-Furandicarboxamide Moiety on Hydrogen Bonding in Aliphatic–Aromatic Poly(ester amide)s. Macromolecules 2014;47(18):6196-6206.

12. Matos M, Sousa AF, Fonseca AC, Freire CSR, Coelho JFJ, and Silvestre AJD. A New Generation of Furanic Copolyesters with Enhanced Degradability: Poly(ethylene 2,5-furandicarboxylate)-co-poly(lactic acid) Copolyesters. Macromolecular Chemistry and Physics 2014;215(22):2175-2184.

13. Wu J, Eduard P, Thiyagarajan S, Noordover BAJ, van Es DS, and Koning CE. Semi-Aromatic Polyesters Based on a Carbohydrate-Derived Rigid Diol for Engineering Plastics. ChemSusChem 2015;8(1):67-72.

14. Papageorgiou GZ, Tsanaktsis V, Papageorgiou DG, Exarhopoulos S, Papageorgiou M, and Bikiaris DN. Evaluation of polyesters from renewable resources as alternatives to the current fossil-based polymers. Phase transitions of poly(butylene 2,5-furan-dicarboxylate). Polymer 2014;55(16):3846-3858.

15. Burgess SK, Leisen JE, Kraftschik BE, Mubarak CR, Kriegel RM, and Koros WJ.

Chain Mobility, Thermal, and Mechanical Properties of Poly(ethylene furanoate) Compared to Poly(ethylene terephthalate). Macromolecules 2014;47(4):1383-1391.

16. Burgess SK, Karvan O, Johnson JR, Kriegel RM, and Koros WJ. Oxygen Sorption and Transport in Amorphous Poly(ethylene furanoate). Polymer 2014;55(18):4748-4756.

17. Burgess SK, Mikkilineni DS, Yu DB, Kim DJ, Mubarak CR, Kriegel RM, and Koros WJ. Water Sorption in Poly(ethylene furanoate) Compared to Poly(ethylene terephthalate). Part 1: Equilibrium Sorption. Polymer 2014;55(26):6861-6869.

18. Burgess SK, Mikkilineni DS, Yu DB, Kim DJ, Mubarak CR, Kriegel RM, and Koros WJ. Water Sorption in Poly(ethylene furanoate) Compared to Poly(ethylene terephthalate). Part 2: Kinetic Sorption. Polymer 2014;55(26):6870-6882.

19. Burgess SK, Mubarak CR, Kriegel RM, and Koros WJ. Physical Aging in Amorphous Poly(ethylene furanoate): Enthalpic Recovery, Density, and Oxygen Transport Considerations. Journal of Polymer Science Part B: Polymer Physics 2015;53(6):389-399.

20. van Berkel JG, Guigo N, Kolstad JJ, Sipos L, Wang B, Dam MA, and Sbirrazzuoli N. Isothermal Crystallization Kinetics of Poly (Ethylene 2,5-Furandicarboxylate). Macromolecular Materials and Engineering 2015, DOI: 10.1002/mame.201400376.

21. Bozell JJ and Petersen GR. Technology development for the production of biobased products from biorefinery carbohydrates-the US Department of Energy's "Top 10" revisited. Green Chemistry 2010;12(4):539-554.

22. Lee JS, Leisen J, Choudhury RP, Kriegel RM, Beckham HW, and Koros WJ. Antiplasticization-based enhancement of poly(ethylene terephthalate) barrier properties. Polymer 2012;53:213-222.

23. Avantium - PEF bottles. http://avantium.com/yxy/products-applications/fdca/PEF-bottles.html.

24. Kotek R, Pang K, Schmidt B, and Tonelli A. Synthesis and gas barrier characterization of poly(ethylene isophthalate). Journal of Polymer Science Part B: Polymer Physics 2004;42(23):4247-4254.

25. Brolly JB, Bower DI, and Ward IM. Diffusion and sorption of CO2 in poly(ethylene terephthalate) and poly(ethylene naphthalate). Journal of Polymer Science Part B: Polymer Physics 1996;34(4):769-780.

26. Light RR and Seymour RW. Effect of sub-Tg relaxations on the gas transport properties of polyesters. Polymer Engineering & Science 1982;22(14):857-864.

27. Koros WJ and Paul DR. CO2 Sorption in Poly(ethylene Terephthalate) above and below the Glass Transition. Journal of Polymer Science: Polymer Physics Edition

1978;16:1947-1963.

28. Koros WJ and Paul DR. Transient and Steady-State Permeation in Poly(ethylene Terephthalate) Above and Below the Glass Transition. Journal of Polymer Science: Polymer Physics Edition 1978;16:2171-2187.

29. Vieth WR, Dao LH, and Pedersen H. Non-equilibrium microstructural and transport characteristics of glassy poly (ethylene terephthalate). Journal of Membrane Science 1991;60(1):41-62.

30. Hirose T, Mizoguchi K, Kamiya Y, and Terada K. Sorption and transport of CO2 in poly(ethylene terephthalate) crystallized by sorption of high-pressure CO2. Journal of Applied Polymer Science 1989;37(6):1513-1525.

31. Wonders AG and Paul DR. Effect of CO2 exposure history on sorption and transport in polycarbonate. Journal of Membrane Science 1979;5(0):63-75.

32. Kamiya Y, Hirose T, Mizoguchi K, and Naito Y. Gravimetric study of high-pressure sorption of gases in polymers. Journal of Polymer Science Part B: Polymer Physics 1986;24(7):1525-1539.

33. Wang J-S, Kamiya Y, and Naito Y. Effects of CO2 conditioning on sorption, dilation, and transport properties of polysulfone. Journal of Polymer Science Part B: Polymer Physics 1998;36(10):1695-1702.

34. Paul DR and Koros WJ. Effect of Partially Immobilizing Sorption on Permeability and the Diffusion Time Lag. Journal of Polymer Science: Polymer Physics Edition 1976;14:675-685.

35. Harris DC. Quantitative Chemical Analysis, 6th ed. New York: W.H. Freeman and Company, 2003.

36. Barrer RM and Rees LVC. Henry's law adsorption constants. Transactions of the Faraday Society 1961;57(0):999-1007.

37. Felder RM, Patton CJ, and Koros WJ. Dual-mode sorption and transport of sulfur dioxide in kapton polyimide. Journal of Polymer Science: Polymer Physics Edition 1981;19(12):1895-1909.

38. Michaels AS, Vieth WR, and Barrie JA. Solution of Gases in Polyethylene Terephthalate. Journal of Applied Physics 1963;34(1):1-12.

39. Berens AR and Hopfenberg HB. Diffusion and relaxation in glassy polymer powders: 2. Separation of diffusion and relaxation parameters. Polymer 1978;19(5):489-496.

40. Chandra P and Koros WJ. Sorption and transport of methanol in poly(ethylene terephthalate). Polymer 2009;50:236-244.

41. Chandra P and Koros WJ. Sorption of lower alcohols in poly(ethylene terephthalate). Polymer 2009;50:4241-4249.

42. Burgess SK, Lee JS, Mubarak CR, Kriegel RM, and Koros WJ. Caffeine Antiplasticization of Amorphous Poly(ethylene terephthalate): Effects on Gas Transport, Thermal, and Mechanical Properties. Polymer 2015, DOI: 10.1016/j.polymer.2015.03.051.

43. Brantley NH, Kazarian SG, and Eckert CA. In situ FTIR measurement of carbon dioxide sorption into poly(ethylene terephthalate) at elevated pressures. Journal of Applied Polymer Science 2000;77(4):764-775.

44. Burgess SK, Kriegel RM, and Koros WJ. Diffusion Coefficient Modeling in Polyester Barrier Materials: Applications of Infinite Series Solutions. Society of Plastics Engineers - ANTEC Las Vegas, Nevada, 2014. pp. 830 - 835.

45. Michaels AS, Vieth WR, and Barrie JA. Diffusion of Gases in Polyethylene Terephthalate. Journal of Applied Physics 1963;34(1):13-20.

46. Toi K. Diffusion and sorption of gases in poly(ethylene terephthalate). Journal of Polymer Science: Polymer Physics Edition 1973;11(9):1829-1839.

47. Meares P. The Diffusion of Gases Through Polyvinyl Acetate1. Journal of the American Chemical Society 1954;76(13):3415-3422.

48. Petropoulos JH. Mechanisms and Theories for Sorption and Diffusion of Gases in Polymers. In: Paul DR and Yampol'skii YP, editors. Polymeric Gas Separation Membranes. Boca Raton: CRC Press, Inc., 1994. pp. 17-83.

49. Brandt WW. Model Calculation of the Temperature Dependence of Small Molecule Diffusion in High Polymers. The Journal of Physical Chemistry 1959;63(7):1080-1085.

50. Yampolskii Y, Pinnau I, and Freeman BD. Materials Science of Membranes for Gas and Vapor Separation. John Wiley & Sons Ltd., 2006. pp. 466.

51. Tonelli AE. Conformational characteristics of poly(ethylene phthalate)s. Journal of Polymer Science Part B: Polymer Physics 2002;40(12):1254-1260.

52. Lin J, Shenogin S, and Nazarenko S. Oxygen solubility and specific volume of rigid amorphous fraction in semicrystalline poly(ethylene terephthalate). Polymer 2002;43(17):4733-4743.

CHAPTER 8

EQUILIBRIUM WATER SORPTION IN PEF COMPARED TO PET[1]

In Chapter 7, limited water sorption data at low concentrations for both PET and PEF were discussed in comparison to oxygen and carbon dioxide sorption. This chapter focuses *solely on the equilibrium water uptake properties* in both polyesters at 35°C over the entire water activity range. PEF exhibits a largely increased equilibrium water sorption capacity of ~1.8X averaged over the entire concentration range compared to PET, resulting from substitution of the non-polar phenyl ring in PET with the polar furan ring in PEF. Both polyesters exhibit dual-mode sorption up to ~0.6 activity, after which the onset of plasticization produces a noticeable upturn in concentration vs. activity for both polyesters. Excellent agreement was observed between three independent sorption measurement techniques, thereby providing a consistency check for the reported data. Sorption measurements performed at 15, 25, 35, and 45°C also allowed estimation of the effective enthalpy of water sorption for both polyesters, which were similar to the enthalpy of condensation for pure water. Diffusion coefficient data complementary to the data reported in this chapter are provided in Chapter 9.

8.1. Introduction

Understanding the sorption and transport behavior of water in polymeric materials is important for barrier applications involving contact with liquid water and high activity

[1]Reprinted in part from *Polymer*, 55/26, Burgess, S.K.; Mikkilineni, D.S.; Yu, D.B.; Kim, D.J.; Mubarak, C.R.; Kriegel, R.M.; Koros, W.J., *Water Sorption in Poly(ethylene furanoate) Compared to Poly(ethylene Terephthalate). Part 1: Equilibrium Sorption*, 6861-6869, Copyright 2014, with permission from Elsevier.

water vapor. Moisture can have significant detrimental effects on mechanical, thermal, and barrier properties of such polymers [1-4], due primarily to swelling and plasticization of the matrix. Recent advancements have enabled cost-effective production of poly(ethylene furanoate) (PEF), a new biologically sourced polyester showing enhanced performance compared to petroleum-based PET [5]. Currently, very limited data exist in the literature regarding the water sorption properties of PEF compared to PET; however, detailed understanding of these properties is needed before PEF can be integrated into the global polyester market.

The current chapter provides a detailed investigation of the equilibrium water sorption properties in amorphous PEF and PET at 35°C via three different gravimetric techniques, while complementary kinetic sorption data are provided in Chapter 9. Compared to PET, PEF exhibits a 1.8X higher water sorption capacity averaged over the entire water activity range. Increased water uptake for PEF reflects the substitution of the non-polar phenyl ring in PET with the polar furan ring in PEF, and also occurs in part from the higher free volume in PEF compared to PET discussed in Chapter 5 [6]. Related observations were made by Rueda et al. [7, 8] for water solubility in poly(ethylene naphthalate) (PEN), where the authors explained increased water uptake for PEN compared to PET based on respective differences in free volume.

Both polyesters in the current chapter exhibit so-called “dual-mode sorption” reflected by concavity in the isotherms up to ~0.6 activity, after which distinct upturns occurred at high water activity. Morphological changes induced at high activity are indicated for both polyesters via distinct sorption hysteresis during desorption. These hysteretic responses correlate with the presence of non-Fickian relaxations during

sorption at high activity described in Chapter 9. Excellent agreement is observed in sorption values over the entire water activity range for all three independent methods, thereby providing internal consistency for the reported data. Additional measurements performed at different temperatures allowed calculation of the enthalpy of water sorption for both polyesters, which can be combined with the diffusion activation energy presented in Chapter 9 to estimate values for the activation energy of water permeation for both polyesters. The current chapter, in combination with the kinetic sorption counterpart, presents the first in-depth study of water transport in PEF.

8.2. Experimental Methods

8.2.1. Materials and Film Preparation

The poly(ethylene furanoate) (PEF) and poly(ethylene terephthalate) (PET) polymers used in this chapter are the same materials described previously in Section 3.1.1, and all amorphous films were melt-pressed using the method in Section 3.1.3. All transport measurements reported herein for PEF and PET reflect data corresponding to the amorphous morphology.

8.2.2. Sorption Measurements

Gravimetric water sorption uptake measurements were recorded for amorphous PEF and PET at 35°C using three independent and complementary techniques, which are described in detail in Chapter 3 (cf. Section 3.4).

8.3. Results and Discussion

8.3.1. Initial Sorption at 35°C

Vapor sorption in glassy polymers is often characterized by dual-mode sorption at low activities, and can be described by the dual-mode model [9] in Equation 8.1, which is discussed in-depth in Chapter 2. Such data exhibit concavity in concentration with respect to penetrant pressure, and resemble the dual-mode sorption behavior for non-condensable gases (i.e., oxygen [10] and nitrogen [11]) in glassy polymers.

$$C = k_D p + \frac{C_H' b p}{1 + b p} \tag{8.1}$$

Water sorption data at 35°C are plotted in Figure 8.1 up to 0.6 activity for PEF (diamonds) and PET (circles), and reflect data measured from both the VTI system (solid points) and the quartz spring system (hollow points). Dual-mode model fits from Equation 8.1 are plotted via the solid lines in Figure 8.1, and the corresponding model parameters are listed in Table 8.1. Excellent agreement between data measured from the two independent sorption methodologies provides a consistency check for the reported data. Noticeable deviation from dual-mode behavior was observed after 0.6 activity, and will be discussed later in the chapter.

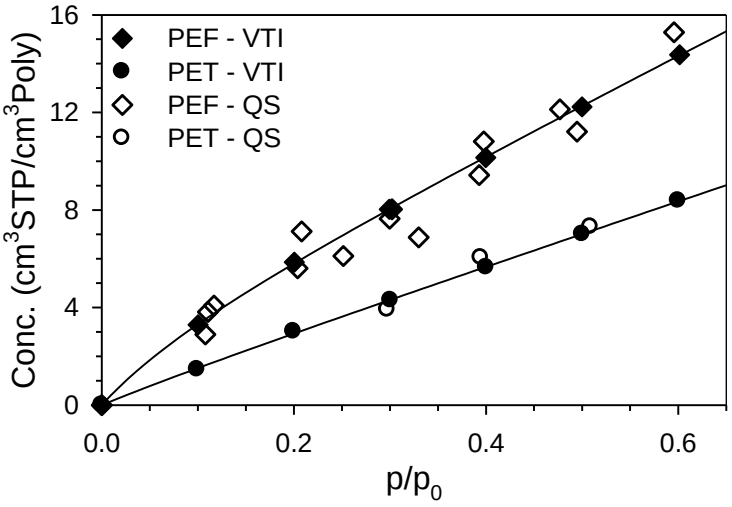

Figure 8.1. Initial equilibrium water sorption values for water at 35°C in PEF (diamonds) and PET (circles). Solid data points represent measurements from the automated VTI system, while hollow points represent measurements from the quartz spring (QS) apparatus.

Table 8.1. Dual-mode parameters from Equation 8.1 for water sorption and subsequent desorption in PEF and PET at 35°C. The uncertainty limits represent the standard error as determined from the curve fitting program. Parameters for desorption are described in Section 8.3.3, and $k^* = (k_D + C_H'b)$.

Activity Range	**Sample**	k_D **(ccSTP/ccPoly·atm)**	b **(atm^{-1})**	C_H' **(ccSTP/ccPoly)**	k^* **(ccSTP/ccPoly·atm)**
Sorption (0 – 0.6)	PEF	354 ± 7	141 ± 30	3.07 ± 0.4	787 ± 110
	PET	237 ± 16	88.7 ± 180	0.599 ± 0.9	290 ± 140
Desorption (0.95 – 0)	PEF	421 ± 25	141[a]	5.82 ± 1.7	1240 ± 297
	PET	274 ± 7	88.7[a]	1.62 ± 0.6	418 ± 297

a: The value of b from sorption was fixed in the determination of desorption parameters.

The sorption values reported in Figure 8.1 for water in amorphous PET exhibit excellent agreement with the results from various studies in the literature on amorphous PET [1, 7, 12]. Water sorption results from semicrystalline PET can be compared to the current amorphous data via the relationship $S = S_a X_a$ validated by Lasoski and Cobbs

[13], where S represents the sorption coefficient for the penetrant in the semicrystalline material (analogous to k_D from Equation 8.1), S_a represents the sorption coefficient for the penetrant in the completely amorphous material, and X_a represents the amorphous fraction of the polymer (i.e., subscript "*a*" denotes "amorphous"). Comparisons performed in this manner reveal that the data for amorphous PET in Figure 8.1 are slightly lower than the normalized semicrystalline data from various studies [14, 15]. This behavior can be rationalized by the likelihood of increased sorption in the less densified rigid amorphous fraction surrounding the immediate vicinity of the crystallites in the semicrystalline samples [16]. However, the current study only investigates water sorption in completely amorphous PEF and PET, and as a result, future studies on sorption in semicrystalline materials are needed to verify this notion.

The Langmuir affinity parameter (b) value of 88.7 atm^{-1} for water in amorphous PET reported in Table 8.1 agrees well with the value of 94.6 atm^{-1} reported by Shigetomi et al. [15] for water in semicrystalline PET. This result is expected, since the impermeable crystallites should ideally not affect the thermodynamic interaction between the penetrant and polymer sites within the amorphous domain [9]. The k_D and C_H' parameters for the semicrystalline sample, however, will be affected by the presence of crystallinity [9]. A value of 237 ccSTP/ccPoly·atm for k_D in the present study (Table 8.1) is similar in magnitude to the amorphous value of 285 ccSTP/ccPoly·atm by Fukuda et al. [12] and the normalized semicrystalline value of 284 ccSTP/ccPoly·atm from Shigetomi et al. [15]. In contrast to b and k_D, the value of C_H' in the current study differs significantly from the value of 2.58 ccSTP/ccPoly reported by Shigetomi et al. [15]. This difference can be explained by potential variations in either sample processing [17], prior thermal

history, or from differences in crystallinity [9].

Figure 8.1 reveals that water is noticeably more sorptive in PEF compared to PET. This result can be interpreted via the dual-mode parameters listed in Table 8.1, which show a larger k_D for PEF compared to PET. The interaction parameter (b) for PEF is also significantly larger than the value for PET, thus indicating a stronger interaction between water and the polymer matrix. This behavior is expected, especially when considering the polar nature of the furan ring in PEF compared to the non-polar phenyl ring in PET. Values of b for water in both polyesters are also significantly larger than the respective values for oxygen and carbon dioxide reported in Chapters 6 and 7, respectively, which is attributable to large differences in critical temperature and the Lennard-Jones force constant for the three penetrants [18]. Aside from k_D and b, a larger C_H' is observed for PEF compared to PET and likely originates from the larger fractional free volume (*FFV*) for PEF, which was reported previously in Chapter 5.

High activity vapor sorption in glassy polymers is often characterized by an upturn in solubility with respect to activity [17-21], which can be described using the Flory-Huggins representation in Equations 8.2 – 8.4 (cf. Chapter 2, Section 2.3.4 for more details).

$$\ln\left(\frac{p}{p_0}\right) = \ln\phi_1 + \left(1-\phi_1\right) + \chi\left(1-\phi_1\right)^2 \tag{8.2}$$

$$\phi_1 = \frac{V_1\left(C/22400\right)}{1+V_1\left(C/22400\right)} \tag{8.3}$$

$$\chi = \chi_0 + \chi_1\left(1-\phi_1\right) + \chi_2\left(1-\phi_1\right)^2 \tag{8.4}$$

Water sorption data for both polyesters are provided over the entire activity range in Figure 8.2 via units of concentration (cm^3STP/cm^3Poly) and in Figure 8.3 via units of wt% (g H_2O/g Poly), along with the Flory-Huggins fit from Equation 8.2 coupled with a concentration-dependent interaction parameter. A graph of the Flory-Huggins interaction parameter vs. volume fraction water is provided in Figure 8.4, with model parameters from Equation 8.4 for PEF as follows: χ_0 = -2273 ± 157, χ_1 = 4623 ± 318, and χ_2 = -2347 ± 161. Corresponding model parameters for PET are: χ_0 = -3373 ± 277, χ_1 = 6800 ± 558, and χ_2 = -3424 ± 281. The solid points in Figures 8.2 and 8.3 represent data measured via the automated VTI sorption system, while the hollow points represent data measured in liquid water. The data point for equilibrium sorption at unit activity for PEF in Figure 8.3 is in agreement with the value reported by Matos et al. [22].

As mentioned previously in Chapter 3 (cf. Section 3.4.2), the solid data points in Figures 8.2 and 8.3 measured between 0.7 – 0.95 activity from the automated VTI system are slightly lower than the true equilibrium values due to the presence of long-term non-Fickian relaxations at high activity [23]. Similar termination of sorption before achieving true equilibrium was also done by Berens, who noted that determination of the true equilibrium sorption isotherm at high activity "would be excessively time-consuming" [24]. The differences between the equilibrium values reported in Figures 8.2 and 8.3 between 0.7 – 0.95 activity and the true equilibrium values are minor (estimated to be <10%), due to small "extra" relaxation-induced uptake associated with the non-Fickian relaxations [23]. Further verification of this notion is provided by excellent agreement of

the data in Figures 8.2 and 8.3 (solid points) with the data recorded at unit activity and true equilibrium (hollow points) measured via the independent and complementary liquid water method.

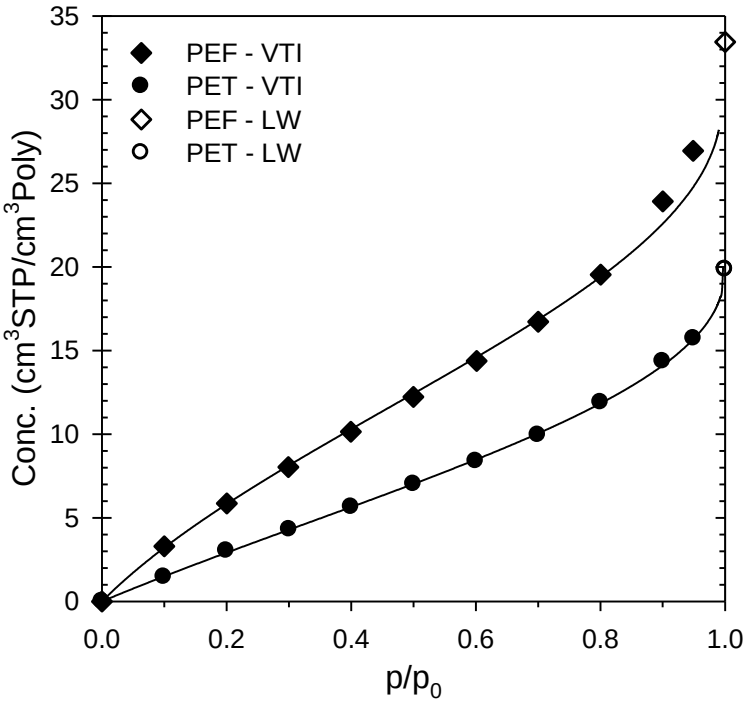

Figure 8.2. Equilibrium sorption values for water at 35°C in PEF (diamonds) and PET (circles) at 35°C during the first sorption cycle. Solid data points represent measurements from the automated VTI system, while hollow points at unit activity represent gravimetric sorption data measured in liquid water (LW).

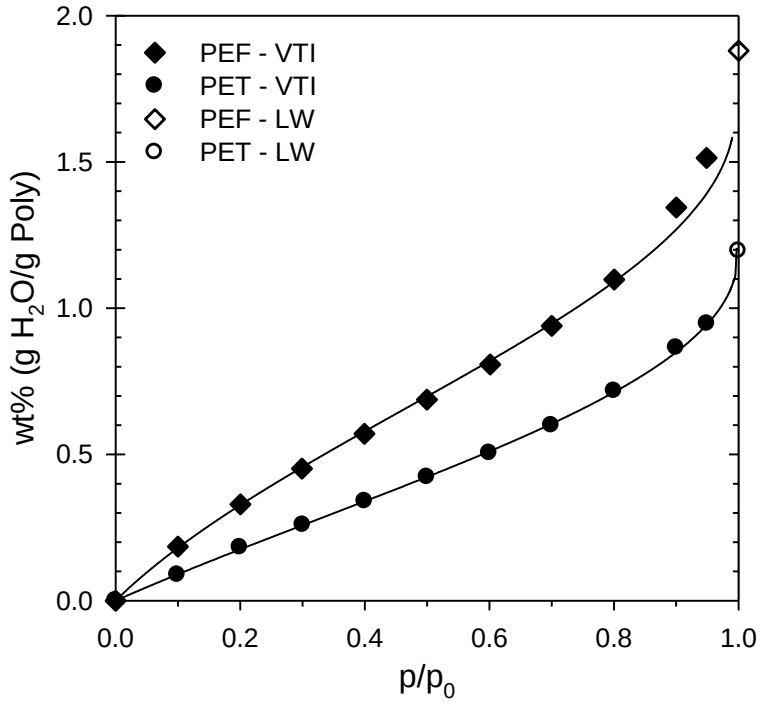

Figure 8.3. Equilibrium sorption values for water at 35°C in PEF (diamonds) and PET (circles) at 35°C during the first sorption cycle. Solid data points represent measurements from the automated VTI system, while hollow points at unit activity represent gravimetric sorption data measured in liquid water (LW).

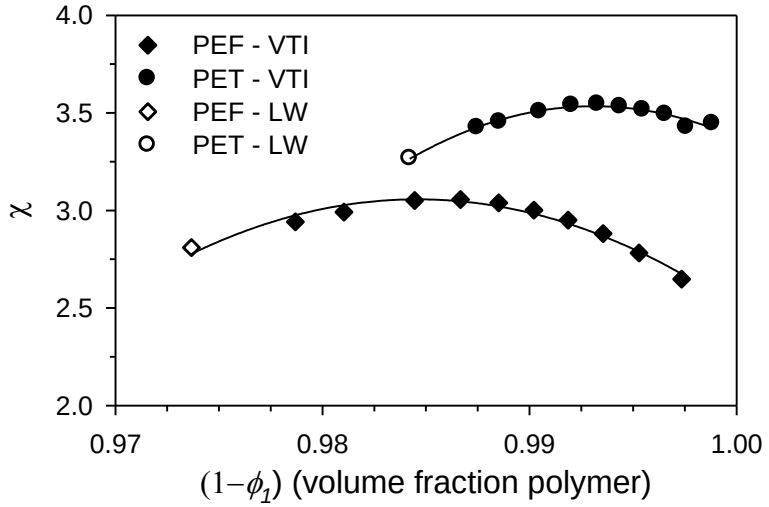

Figure 8.4. Interaction parameters for water at 35°C in PEF (diamonds) and PET (circles) at 35°C. Solid data points represent measurements from the automated VTI system, while hollow points represent gravimetric sorption data measured in liquid water (LW). Lines represent model fits from Equation 8.4.

From Figure 8.2, it is apparent that the water uptake data in both PEF and PET exhibit an upturn in concentration at high activity and that the Flory-Huggins model coupled with a concentration-dependent χ interaction parameter accurately describes the data. A distinct sorption upturn at high activity for PET has also been reported for both amorphous [12] and semicrystalline PET samples [14, 25], however, the degree of upturn in the semicrystalline samples is less significant than in the current work due to the presence of impermeable crystallites acting to stabilize the matrix against swelling. Additional studies have reported linear sorption isotherms for both amorphous [1, 26] and semicrystalline PET [27], which contrasts to the trend observed in the current work. The water sorption value for PET measured in liquid water (hollow circle in Figure 8.3) agrees well with the normalized semicrystalline value reported by Park [28] using a similar measurement methodology. Deviations from dual-mode equilibrium behavior above 0.6 activity correlate with the onset of non-Fickian kinetic relaxations observed in Figures 9.4 and 9.5 of Chapter 9 for both polyesters [23].

Similar to PET, PEF also exhibits a distinct upturn in concentration at high activities as seen in Figures 8.2 and 8.3. As mentioned previously, higher water sorption in PEF compared to PET is expected to be due to the increased polarity of the furan ring compared to the non-polar phenyl ring in PET. The upturn for both polyesters signifies the presence of either water clustering, plasticization, or both, and will be discussed in the next section.

8.3.2. Clustering vs. plasticization

A positive deviation from dual-mode or Henry's law sorption at high vapor activities

can indicate simple swelling or clustering, where the latter case reflects the nonrandom distribution of a penetrant within the polymer matrix [29, 30]. Plasticization is indicated when the upturn in solubility accompanies a simultaneous increase in diffusion coefficient, thus giving evidence for increased segmental mobility. Alternatively, clustering is indicated when the upturn in solubility accompanies a decrease in diffusion coefficient, which results from an increase in the effective diameter of the diffusing water (i.e., water molecules cluster together) [31]. Permeation experiments can also be used to differentiate between the two phenomena, as plasticization yields an increase in permeability at high activity while clustering exhibits a more or less constant permeability with increasing activity. Both plasticization [30, 32-34] and clustering [19, 29, 31, 35-39] phenomena have been reported for a wide range of penetrants and polymers.

Besides clustering, penetrant plasticization in glassy polymers is quite common. Numerous studies have focused on carbon dioxide-induced dilation and plasticization in polymer membranes [40-48], since such behavior can compromise the separation efficiency of the membrane. Several recent studies have examined related plasticizing effects via various computer modeling techniques [49-52]. Using molecular dynamics simulations, Neyertz and Brown determined that the free volume within a polyimide increased with carbon dioxide–induced swelling [52]. A further study by the same authors examined both *para*- and *meta*-substituted polyimide isomers, and concluded that the swelling behavior upon carbon dioxide sorption resulted from localized relaxations in the respective matrices rather than larger structural changes [53]. Aside from carbon dioxide, which typically plasticizes glassy polymers at relatively high pressures [54], water and

organic vapors are also prone to induce plasticization effects in various polymers as evidenced by sorption hysteresis due to increased condensability and interactions with the matrix [17, 30, 32, 33, 39, 55].

The onset of clustering or plasticization can be qualitatively assessed using the analysis proposed by Zimm and Lundberg [56] in Equation 8.5, which is discussed further in Chapter 2 (cf. Section 2.3.5). Application of Equation 8.5 to the sorption data from Figure 8.2 for both polyesters is provided in Figure 8.5.

$$\frac{G_{11}}{\bar{V}_1} = -\left(1-\phi_1\right)\left[\frac{\partial\left(a_1/\phi_1\right)}{\partial a_1}\right]_{p,T} - 1 \tag{8.5}$$

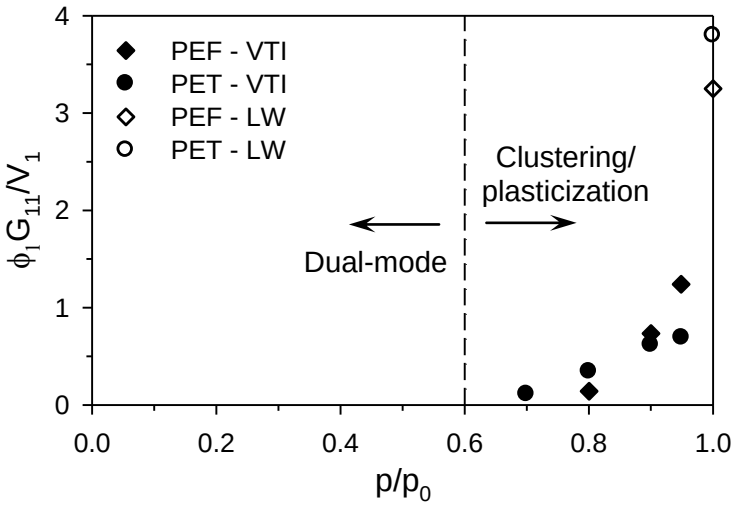

Figure 8.5. The onset of clustering/plasticization is realized when the quantity $\phi_1 G_{11}/\bar{V}_1$ is greater than zero.

From Figure 8.5, it is evident that the onset of either clustering or plasticization occurs at an activity of ~0.6 for both polyesters. Caution should be emphasized regarding the physical interpretation of Figure 8.5 as definite proof for the presence of clustering, as

some authors have found notable differences between the results from this methodology and other techniques, such as FTIR spectroscopy [38]. Analysis of the diffusion coefficient behavior vs. activity for both PEF and PET can help distinguish between clustering and plasticization. Detailed kinetic data reported in Chapter 9 reveal that both PEF and PET exhibit increasing diffusion coefficients with increasing concentration over the entire activity interval, which is consistent with the notion of plasticization [23]. However, as noted above, it is still a possibility that *both* clustering and plasticization could be occurring simultaneously.

Additional differentiation between the clustering and plasticization phenomena can be obtained by examining the permeability vs. activity dependence for both polyesters [35]. While not measured in this work, various researchers have reported both an activity independent permeability [27] and a slight increase in permeability at high activity for semicrystalline PET [25, 57]. The latter behavior is consistent with increased chain mobility resulting from the onset of plasticization in the amorphous environment at high activity; however, the presence of impermeable crystallites may dampen the magnitude of the permeability increase due to reduction of the amorphous fraction which is available for plasticization. Regardless, the permeability increase resulting from plasticization in amorphous PET is not expected to be large due to the minor positive correlation between diffusion coefficient and activity reported in Chapter 9. Currently, to our knowledge, there exists no literature report on the water permeability in PEF vs. activity. The diffusion coefficient for water in PEF slightly increases with increasing activity, thereby suggesting the possibility of plasticization. However, independent permeability measurements are needed to verify the presence or absence of either clustering or

plasticization.

Agreement between solubility coefficients obtained from both permeation time-lags and independent sorption measurements can also indicate the absence of clustering [29], since the entirety of the sorbed penetrant population contributes to the permeation process. Such agreement has been observed for semicrystalline PET by multiple researchers [25, 27], and thus corroborates the evidence that plasticization occurs in PET at high activity.

8.3.3. Hysteresis

Sorption hysteresis occurs when the penetrant sorption and subsequent desorption cycles do not superimpose, and can occur in a wide variety of penetrant-material combinations [58-60]. Various authors have linked hysteretic behavior to swelling of the polymer matrix, where the chains relax to incorporate the extra penetrant at high concentrations [17, 24, 61-63]. Time-dependent non-Fickian relaxations induced by this swelling have been directly observed in Chapter 9 at high water vapor activities (cf. Figures 9.4 and 9.5).

Water uptake in both PEF and PET in the current study exhibited distinct hysteresis between sorption and subsequent desorption cycles. This behavior correlates with the upturn in concentration vs. activity for both polyesters in Figure 8.2 and the presence of non-Fickian relaxations at high activities in Chapter 9. Initial sorption/desorption data measured using the automated VTI instrument up to 0.95 activity for PEF and PET at 35°C are provided in Figures 8.6 and 8.7, respectively, where the solid circles represent sorption and the hollow circles represent subsequent desorption. The samples were dried

at 45°C after completion of the first cycle, and followed by a second sorption/desorption cycle, which consisted of fewer data points (filled and hollow triangles for the second sorption and desorption cycle, respectively).

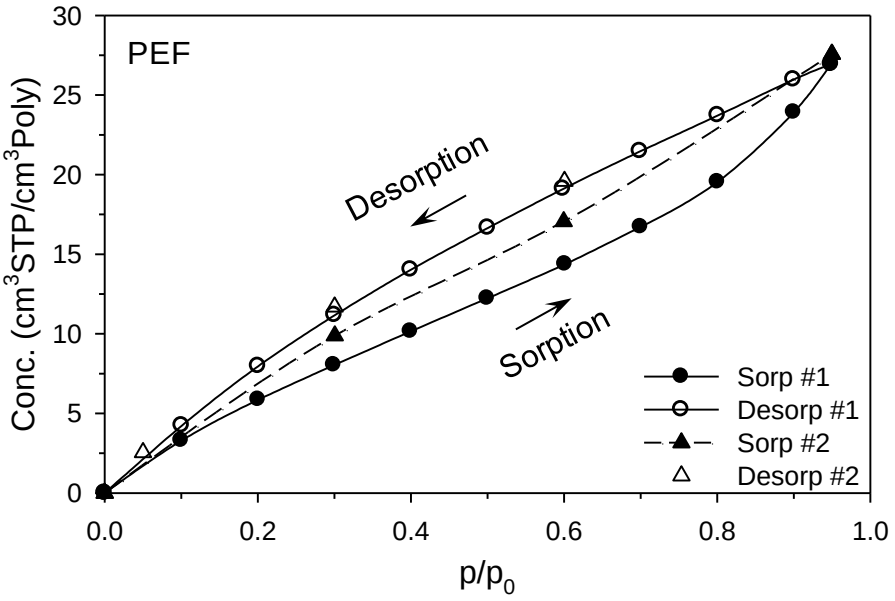

Figure 8.6. Sorption hysteresis at 35°C for PEF recorded using the automated VTI sorption system. Filled and hollow circles represent the initial sorption and desorption cycle, respectively, while filled and hollow triangles represent the second sorption and desorption cycle, respectively. Lines are drawn to aid the eye and do not represent model fits.

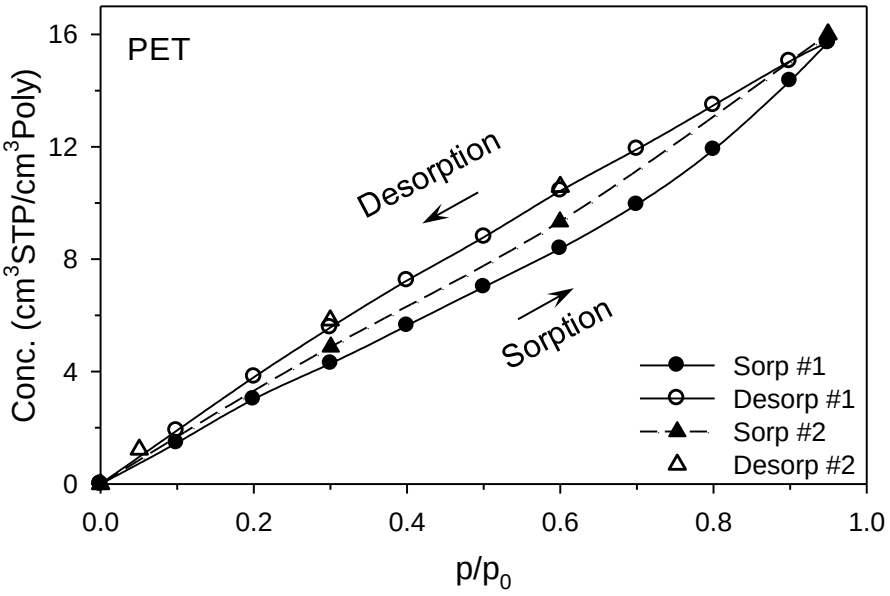

Figure 8.7. Sorption hysteresis at 35°C for PET recorded using the automated VTI sorption system. Filled and hollow circles represent the initial sorption and desorption cycle, respectively, while filled and hollow triangles represent the second sorption and desorption cycle, respectively. Lines are drawn to aid the eye and do not represent model fits.

Dual-mode model parameters for both sorption (from 0 – 0.6 activity) and desorption data (from 0.95 – 0 activity) are provided in Table 8.1 for both polyesters. The Langmuir affinity parameter (*b*) is associated with the thermodynamic polymer/penetrant interactions, and is not ideally expected to change during the sorption process. Consequently, values of *b* obtained from the initial sorption isotherms were fixed when calculating the model parameters for desorption. Inspection of the parameters in Table 8.1 reveals that both k_D and C_H' for desorption are larger when compared to the respective sorption values for both polyesters. Such behavior can be understood as reflecting morphological changes in the glassy matrix resulting from swelling. Larger values of C_H' are consistent with an increase in either number and/or approximate size of the Langmuir microvoids, and as a result, represent an increase in free volume in the swollen samples. The increased water sorption capacity is readily observed by the upturn in concentration

vs. activity in Figure 8.2. Quantitative interpretation of the classic dual-mode parameters for sorption and subsequent hysteretic desorption suggest that the glass has been conditioned to a different non-equilibrium state before and after exposure to the maximum conditioning activity. As a result, the dual-mode parameters for desorption should be considered approximate, and are included in Table 8.1 for completeness.

The desorption trajectory and degree of hysteresis for both polyesters is directly related to the maximum value obtained during initial sorption, as observed in the acetonitrile/cellulose acetate system in other works [61, 62]. Hysteresis is not expected to occur appreciably in the water/polyester systems for initial sorption values up to ~0.6 activity, which marks the transition between dual-mode and plasticization behavior (cf. Figure 8.5). The presence of simple Fickian diffusion up to ~0.6 activity corroborates this notion, as observed in Figures 9.4 and 9.5 from Chapter 9.

A second sorption/desorption cycle using larger sorption intervals was performed after drying both polyesters at 45°C to investigate the permanence of the morphological changes. Resorption values in both polyesters at 0.3 and 0.6 activity (solid triangles in Figures 8.6 and 8.7) exhibit an increase in sorption capacity when compared to the initial sorption isotherm (solid circles), which is consistent with sorption in the increased free volume in the conditioned samples compared to the virgin samples. These results also suggest that the timescale of free volume collapse is slower than the experimental sorption experiments, thereby corroborating the observation of predominantly Fickian kinetics over the entire activity range during desorption (cf. Figures 9.4 and 9.5 in Chapter 9). The resorption data points are slightly reduced when compared to the initial desorption isotherms (hollow circles). Such behavior suggests that the morphological

changes induced during swelling of the glassy matrix at high activity are only semi-permanent and that deswelling is indeed occurring. Resorption values at 0.95 activity for both polyesters (solid triangles) are approximately equal to the initial sorption values at 0.95 activity (solid circles), and the subsequent desorption values for both cycles (hollow circles, hollow triangles) are satisfyingly similar. These results corroborate the notion that the desorption trajectory is dependent on the maximum sorption level achieved. Similar hysteretic behavior to that observed in the current work (Figures 8.6 and 8.7) has been reported for multiple polymer/penetrant systems [24, 30, 32, 33, 55].

A recent study by Visser and Wessling [64] illustrates the importance of volume dilation in determining the onset of sorption-induced relaxations in Matrimid polyimide. The authors show how any gas, even relatively inert gases such as Krypton, can cause non-Fickian sorption relaxations above a threshold volume dilation. Equation 8.6 can be used to estimate the swelling (volume change, ΔV) of a polymer sample based on the change in sample thickness (l) [62, 65], with the assumption that the sample is an isotropic medium. In Equation 8.6, V_0 and l_0 represent the volume and thickness of the pure, dry polymer, respectively.

$$\frac{\Delta V}{V_0} = \left[\left(\frac{l}{l_0} \right)^3 - 1 \right] = \left[\left(1 + \frac{\Delta l}{l_0} \right)^3 - 1 \right] \tag{8.6}$$

Calculation of swelling data via Equation 8.6 was only possible using the thick samples from sorption testing in liquid water. Thickness values were measured on both dry samples prior to sorption testing, and again after sorption equilibrium was achieved.

Values for the percent change in thickness and volume change are provided in Table 8.2 for both PEF and PET, along with the final concentration of water at unit activity. At least four different samples were measured for both PEF and PET, and the uncertainty limits originate from the standard error. In the context of Visser and Wessling [64], a threshold dilation of ~1.2% was found for the onset of non-Fickian relaxations for various gases in Matrimid. This threshold value will vary for different polymers; however, the swelling values for PEF and PET at unit activity in Table 8.2 are undoubtedly above the respective unknown threshold limits. The swelling data reported in Table 8.2 also allows calculation of the partial molar volume for water in both polyesters, denoted by $\bar{V}$, via Equation 8.7 [44].

Table 8.2. Swelling values for amorphous PEF and PET at 35°C in liquid water calculated from Equation 8.6.

	Conc. at a = 1 (cm^3STP/cm^3Poly)	**$\Delta l/l_0$ (%)**	**$\Delta V/V_0$ (%)**
PEF	33.4 ± 0.1	1.3 ± 0.3	4.1 ± 0.8
PET	19.8 ± 0.1	0.8 ± 0.2	2.4 ± 0.6

$$\bar{V} = \left(\frac{\partial V}{\partial n}\right) \approx \left(\frac{\Delta V}{\Delta n}\right) \tag{8.7}$$

Values of $\bar{V}$ obtained for PEF and PET are 27.5 ± 5.6 cm^3/mol and 26.9 ± 6.3 cm^3/mol, respectively, which are both larger than the molar volume of pure, liquid water

(~18 cm^3/mol). Such seemingly anomalous behavior can be explained by three possibilities: 1) that plasticization at high activity in the polymer matrix is creating extra free volume which, in fact, is unoccupied by water molecules, thus resulting in a disproportionate volume change for the polymer/water "mixture" compared to the true amount of water added in the system, 2) the thickness measurements are not accurate enough to estimate the true values of $\bar{V}$, or 3) the assumption of an isotropic medium for both polyesters is inaccurate. Due to the large uncertainty limits reported in the values of $\bar{V}$ for both polyesters, it is believed that option 2 likely reflects reality. Consequently, ellipsometry or other techniques more suited to performing dilation measurements should be used to verify the data reported in Table 8.2 for both polyesters.

8.3.4. Apparent Enthalpy of Sorption

In addition to the equilibrium sorption measurements at 35°C, uptake values were also measured at 0.2 activity and 15, 25, and 45°C for water in both polyesters. Kinetic uptake data between 0.1 – 0.2 activity are discussed in Chapter 9, which also reports estimates for the apparent activation energy of diffusion and apparent activation energy of permeation for water at low activity in PEF and PET. Measurements were recorded at 0.2 activity on virgin films to ensure dual-mode behavior applied and to avoid the upturn in concentration observed in Figure 8.2 at high activity. The van't Hoff relationship in Equation 2.6 (discussed previously) can describe the temperature dependence of the equilibrium uptake data. Uptake data at 0.2 activity and 15, 25, 35, and 45°C are plotted in Figure 8.8 for PEF (diamonds) and PET (circles), where the lines represent the respective model fit from Equation 2.6. The uncertainty limits for the ΔH_S values

depicted in Figure 8.8 originate from the standard error of the model fit.

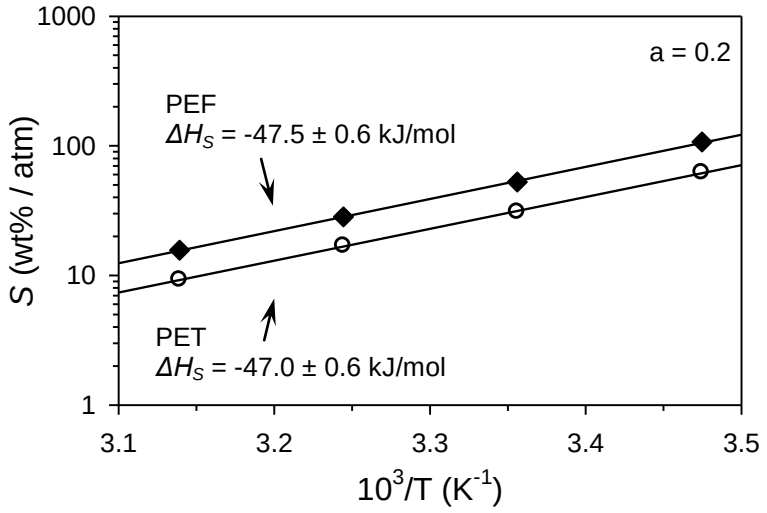

Figure 8.8. Semi-logarithmic van't Hoff plot of water sorption at 0.2 activity in amorphous PEF (filled diamonds) and amorphous PET (hollow circles). Lines represent the van't Hoff representation from Equation 2.6.

The data in Figure 8.8 exhibit excellent linearity for both polyesters, and produce estimates of ΔH_S which are quite similar in magnitude to the enthalpy of condensation for pure water [66]. Such behavior is expected, and indicates that the overall enthalpy of sorption is dominated by the exothermic contribution from the enthalpy of condensation [37]. The remaining contribution from the enthalpy of mixing is therefore rationalized to be small. Values of ΔH_S for water in PET from the literature are sparse and variable [15, 28, 67], while no additional data exist in the literature for PEF. Values of ΔH_S can be estimated from the Hildebrand equation [68]; however, predictions which utilize the solubility parameter for water are not recommended due to the likelihood of non-ideal behavior [69]. The value of ΔH_S for water sorption in PEF is apparently slightly more negative than the respective value for PET. Such result can be rationalized by the

additional interaction between water and the polar furan ring in PEF vs. the non-polar phenyl ring in PET; however, the uncertainty limits in ΔH_S render the estimates statistically identical and additional measurements need to be performed to verify this notion.

8.4. Summary and Conclusions

The current chapter examines the equilibrium water uptake properties of amorphous PEF and PET at 35°C over the entire water activity range, with the corresponding kinetic uptake data discussed in Chapter 9. Water sorption values were measured using the following activity ranges and techniques: 1) 0 – 0.6 activity with the McBain quartz spring technique, 2) 0 – 0.95 activity with the automated TA VTI-SA+ sorption apparatus, and 3) at unit activity using samples immersed in liquid water, with the water uptake determined using a microgram balance. A consistency check was provided through excellent agreement in the uptake data measured from all three independent methods.

PEF exhibits higher equilibrium water uptake compared to PET over the entire activity range. This behavior is attributed to the higher affinity between water and the polar furan ring vs. the non-polar phenyl ring in PET. A lower average value of the Flory-Huggins interaction parameter (χ) for PEF compared to PET also indicates a higher degree of compatibility between water and PEF. Dual-mode sorption behavior was observed at low water activity, and an upturn in the water sorption isotherm was analyzed and not found to be primarily due to clustering above 0.6 activity for either of the polyesters. Verification of penetrant plasticization at high activity is provided in Chapter 9, and is evidenced by the positive correlation between diffusion coefficients and

increasing activity for both polymers. Further verification between either plasticization or clustering behavior will require permeation experiments at high activity, which were not conducted in these studies. Additional complementary data and related discussions regarding the kinetic uptake analogy of the current work are provided in Chapter 9.

The current chapter, in combination with Chapter 9, presents the first detailed report of water sorption in PEF compared to PET. Such information can assist in advancing the large-scale commercialization of PEF for a variety of markets. Information regarding the effect of water at unit activity on the resultant thermal and mechanical properties of both polyesters is discussed later in Appendix G.

8.5. References

1. Langevin D, Grenet J, and Saiter JM. Moisture Sorption in PET: Influence on the Thermokinetic Parameters. European Polymer Journal 1994;30(3):339-345.

2. Lahokallio S, Saarinen K, and Frisk L. Changes in water absorption and modulus of elasticity of flexible printed circuit board materials in high humidity testing. Microelectronics and Packaging Conference (EMPC), 2011 18th European, 2011. pp. 1-6.

3. Mali S, Sakanaka LS, Yamashita F, and Grossmann MVE. Water sorption and mechanical properties of cassava starch films and their relation to plasticizing effect. Carbohydrate Polymers 2005;60(3):283-289.

4. Auras R, Harte B, and Selke S. Effect of Water on the Oxygen Barrier Properties of Poly(ethylene terephthalate) and Polylactide Films. Journal of Applied Polymer Science 2004;92:1790-1803.

5. Avantium - PEF bottles. http://avantium.com/yxy/products-applications/fdca/PEF-bottles.html.

6. Burgess SK, Leisen JE, Kraftschik BE, Mubarak CR, Kriegel RM, and Koros WJ. Chain Mobility, Thermal, and Mechanical Properties of Poly(ethylene furanoate) Compared to Poly(ethylene terephthalate). Macromolecules 2014;47(4):1383-1391.

7. Rueda DR and Varkalis A. Water Sorption/Desorption Kinetics in Poly(Ethylene

Naphthalene-2,6-Dicarboxylate) and Poly(Ethylene Terephthalate). Journal of Polymer Science Part B: Polymer Physics 1995;33:2263-2268.

8. Rueda DR, Viksne A, Kajaks J, Balta-Calleja FJ, and Zachmann HG. Properties of arylpolyesters with reference to water content. Macromolecular Symposia 1995;94(1):259-268.

9. Michaels AS, Vieth WR, and Barrie JA. Solution of Gases in Polyethylene Terephthalate. Journal of Applied Physics 1963;34(1):1-12.

10. Burgess SK, Karvan O, Johnson JR, Kriegel RM, and Koros WJ. Oxygen Sorption and Transport in Amorphous Poly(ethylene furanoate). Polymer 2014;55(18):4748-4756.

11. Koros WJ, Chan AH, and Paul DR. Sorption and transport of various gases in polycarbonate. Journal of Membrane Science 1977;2(0):165-190.

12. Fukuda M, Kawai H, Yagi N, Kimura O, and Ohta T. FTi.r. study on the nature of water sorbed in poly(ethylene terephthalate) film. Polymer 1990;31(2):295-302.

13. Lasoski SW and Cobbs WH. Moisture permeability of polymers. I. Role of crystallinity and orientation. Journal of Polymer Science 1959;36(130):21-33.

14. Myers AW, Meyer JA, Rogers CE, Stannett V, and Szwarc M. Studies in the Gas and Vapor Permeability of Plastic Films and Coated Papers. Part VI. The Permeation of Water Vapor. Tappi 1961;44(1):58-64.

15. Shigetomi T, Tsuzumi H, Toi K, and Ito T. Sorption and diffusion of water vapor in poly(ethylene terephthalate) film. Journal of Applied Polymer Science 2000;76(1):67-74.

16. Lin J, Shenogin S, and Nazarenko S. Oxygen solubility and specific volume of rigid amorphous fraction in semicrystalline poly(ethylene terephthalate). Polymer 2002;43(17):4733-4743.

17. Chandra P and Koros WJ. Sorption and transport of methanol in poly(ethylene terephthalate). Polymer 2009;50:236-244.

18. Chandra P and Koros WJ. Sorption of lower alcohols in poly(ethylene terephthalate). Polymer 2009;50:4241-4249.

19. Singh A, Freeman BD, and Pinnau I. Pure and mixed gas acetone/nitrogen permeation properties of polydimethylsiloxane [PDMS]. Journal of Polymer Science Part B: Polymer Physics 1998;36(2):289-301.

20. Berens AR and Hopfenberg HB. Diffusion and relaxation in glassy polymer powders: 2. Separation of diffusion and relaxation parameters. Polymer 1978;19(5):489-496.

21. Wellons JD and Stannett V. Permeation, sorption, and diffusion of water in ethyl cellulose. Journal of Polymer Science Part A-1: Polymer Chemistry 1966;4(3):593-602.

22. Matos M, Sousa AF, Fonseca AC, Freire CSR, Coelho JFJ, and Silvestre AJD. A New Generation of Furanic Copolyesters with Enhanced Degradability: Poly(ethylene 2,5-furandicarboxylate)-co-poly(lactic acid) Copolyesters. Macromolecular Chemistry and Physics 2014;215(22):2175-2184.

23. Burgess SK, Mikkilineni DS, Yu DB, Kim DJ, Mubarak CR, Kriegel RM, and Koros WJ. Water Sorption in Poly(ethylene furanoate) Compared to Poly(ethylene terephthalate). Part 2: Kinetic Sorption. Polymer 2014;55(26):6870-6882.

24. Berens AR. Effects of sample history, time, and temperature on the sorption of monomer vapor by PVC. Journal of Macromolecular Science, Part B 1977;14(4):483-498.

25. Hubbell WH, Brandt H, and Munir ZA. Transient and steady-state water vapor permeation through polymer films. Journal of Polymer Science: Polymer Physics Edition 1975;13(3):493-507.

26. Jabarin SA and Lofgren EA. Effects of water absorption on physical properties and degree of molecular orientation of poly (ethylene terephthalate). Polymer Engineering & Science 1986;26(9):620-625.

27. Yasuda H and Stannett V. Permeation, Solution, and Diffusion of Water in Some High Polymers. Journal of Polymer Science 1962;57:907-923.

28. Park H. Characterization of Moisture Diffusion into Polymeric Thin Film. Experimental Mechanics 2013;53(9):1693-1703.

29. Orofino TA, Hopfenberg HB, and Stannett V. Characterization of penetrant clustering in polymers. Journal of Macromolecular Science, Part B 1969;3(4):777-788.

30. Schult KA and Paul DR. Water sorption and transport in a series of polysulfones. Journal of Polymer Science Part B: Polymer Physics 1996;34(16):2805-2817.

31. Williams JL, Hopfenberg HB, and Stannett V. Water transport and clustering in poly[vinyl cloride], poly[oxymethylene], and other polymers. Journal of Macromolecular Science, Part B 1969;3(4):711-725.

32. Schult KA and Paul DR. Water sorption and transport in blends of poly(vinyl pyrrolidone) and polysulfone. Journal of Polymer Science Part B: Polymer Physics 1997;35(4):655-674.

33. Schult KA and Paul DR. Water sorption and transport in blends of polyethyloxazoline and polyethersulfone. Journal of Polymer Science Part B: Polymer Physics 1997;35(6):993-1007.

34. Wellons JD, Williams JL, and Stannett V. Preparation and characterization of some cellulose graft copolymers. Part IV. Some properties of isolated cellulose acetate–styrene graft copolymers. Journal of Polymer Science Part A-1: Polymer Chemistry 1967;5(6):1341-1357.

35. Barrer RM and Barrie JA. Sorption and Diffusion in Ethyl Cellulose. Part IV. Water in Ethyl Cellulose. Journal of Polymer Science 1958;XXVIII:377-386.

36. Zhang Z, Britt IJ, and Tung MA. Water absorption in EVOH films and its influence on glass transition temperature. Journal of Polymer Science Part B: Polymer Physics 1999;37(7):691-699.

37. Stannett V, Haider M, Koros WJ, and Hopfenberg HB. Sorption and Transport of Water Vapor in Glassy Poly(Acrylonitrile). Polymer Engineering and Science, Mid-March 1980;20(4):300-304.

38. Davis EM and Elabd YA. Water Clustering in Glassy Polymers. The Journal of Physical Chemistry B 2013;117(36):10629-10640.

39. Barrie JA and Platt B. The diffusion and clustering of water vapour in polymers. Polymer 1963;4(0):303-313.

40. Achoundong CSK, Bhuwania N, Burgess SK, Karvan O, Johnson JR, and Koros WJ. Silane Modification of Cellulose Acetate Dense Films as Materials for Acid Gas Removal. Macromolecules 2013;46(14):5584-5594.

41. Horn NR and Paul DR. Carbon dioxide plasticization and conditioning effects in thick vs. thin glassy polymer films. Polymer 2011;52(7):1619-1627.

42. Horn NR and Paul DR. Carbon dioxide plasticization of thin glassy polymer films. Polymer 2011;52(24):5587-5594.

43. Pantoula M and Panayiotou C. Sorption and swelling in glassy polymer/carbon dioxide systems: Part I. Sorption. The Journal of Supercritical Fluids 2006;37(2):254-262.

44. Kamiya Y, Hirose T, Naito Y, and Mizoguchi K. Sorptive dilation of polysulfone and poly(ethylene terephthalate) films by high-pressure carbon dioxide. Journal of Polymer Science Part B: Polymer Physics 1988;26(1):159-177.

45. Wonders AG and Paul DR. Effect of CO2 exposure history on sorption and transport in polycarbonate. Journal of Membrane Science 1979;5(0):63-75.

46. Kamiya Y, Hirose T, Mizoguchi K, and Naito Y. Gravimetric study of high-pressure sorption of gases in polymers. Journal of Polymer Science Part B: Polymer Physics 1986;24(7):1525-1539.

47. Wind JD, Sirard SM, Paul DR, Green PF, Johnston KP, and Koros WJ. Relaxation

Dynamics of CO2 Diffusion, Sorption, and Polymer Swelling for Plasticized Polyimide Membranes. Macromolecules 2003;36(17):6442-6448.

48. Wind JD, Sirard SM, Paul DR, Green PF, Johnston KP, and Koros WJ. Carbon Dioxide-Induced Plasticization of Polyimide Membranes: Pseudo-Equilibrium Relationships of Diffusion, Sorption, and Swelling. Macromolecules 2003;36(17):6433-6441.

49. Hölck O, Heuchel M, Böhning M, and Hofmann D. Simulation of experimentally observed dilation phenomena during integral gas sorption in glassy polymers. Journal of Polymer Science Part B: Polymer Physics 2008;46(1):59-71.

50. Neyertz S, Brown D, Pandiyan S, and van der Vegt NFA. Carbon Dioxide Diffusion and Plasticization in Fluorinated Polyimides. Macromolecules 2010;43(18):7813-7827.

51. Hölck O, Böhning M, Heuchel M, Siegert MR, and Hofmann D. Gas sorption isotherms in swelling glassy polymers—Detailed atomistic simulations. Journal of Membrane Science 2013;428(0):523-532.

52. Neyertz S and Brown D. Molecular Dynamics Study of Carbon Dioxide Sorption and Plasticization at the Interface of a Glassy Polymer Membrane. Macromolecules 2013;46(6):2433-2449.

53. Neyertz S and Brown D. The effect of structural isomerism on carbon dioxide sorption and plasticization at the interface of a glassy polymer membrane. Journal of Membrane Science 2014;460(0):213-228.

54. Koros WJ and Paul DR. CO2 Sorption in Poly(ethylene Terephthalate) above and below the Glass Transition. Journal of Polymer Science: Polymer Physics Edition 1978;16:1947-1963.

55. Potreck J, Uyar F, Sijbesma H, Nijmeijer K, Stamatialis D, and Wessling M. Sorption induced relaxations during water diffusion in S-PEEK. Physical Chemistry Chemical Physics 2009;11(2):298-308.

56. Zimm BH and Lundberg JL. Sorption of Vapors by High Polymers. Journal of Physical Chemistry 1956;60(4):425-428.

57. Thornton ER, Stannett V, and Szwarc M. The permeation of vapors and liquids through polymer films. Journal of Polymer Science 1958;28(117):465-468.

58. Martin RT. Water-vapor sorption on kaolinite: hysteresis. Clays and Clay Minerals. Berkeley, CA: Pergamon Press, 1959. pp. 259-278.

59. Okubayashi S, Griesser UJ, and Bechtold T. Moisture sorption/desorption behavior of various manmade cellulosic fibers. Journal of Applied Polymer Science 2005;97(4):1621-1625.

60. Champion D, Loupiac C, Simatos D, Lillford P, and Cayot P. Structural Relaxation During Drying and Rehydration of Food Materials—the Water Effect and the Origin of Hysteresis. Food Biophysics 2011;6(1):160-169.

61. Guo J and Barbari TA. Unified Dual Mode Description of Small Molecule Sorption and Desorption Kinetics in a Glassy Polymer. Macromolecules 2009;42(15):5700-5708.

62. Guo J and Barbari TA. A dual mode interpretation of the kinetics of penetrant-induced swelling and deswelling in a glassy polymer. Polymer 2010;51(22):5145-5150.

63. Berens AR. The solubility of vinyl chloride in poly(vinyl chloride). Die Angewandte Makromolekulare Chemie 1975;47(1):97-110.

64. Visser T and Wessling M. When Do Sorption-Induced Relaxations in Glassy Polymers Set In? Macromolecules 2007;40(14):4992-5000.

65. Böhning M and Springer J. Sorptive dilation and relaxational processes in glassy polymer/gas systems—I. Poly(sulfone) and poly(ether sulfone). Polymer 1998;39(21):5183-5195.

66. Felder RM and Rousseau RW. Elementary Principles of Chemical Processes, 3rd ed.: John Wiley & Sons, Inc., 2005.

67. Launay A, Thominette F, and Verdu J. Water sorption in amorphous poly(ethylene terephthalate). Journal of Applied Polymer Science 1999;73(7):1131-1137.

68. Comyn J. Introduction to Polymer Permeability and the Mathematics of Diffusion. In: Comyn J, editor. Polymer Permeability. New York: Elsevier Applied Science Publishers Ltd., 1985. pp. 1-10.

69. Hansen CM. Hansen Solubility Parameters: A User's Handbook, 2 ed. Boca Raton: CRC Press, Taylor & Francis Group, 2007.

CHAPTER 9

KINETIC WATER SORPTION IN PEF COMPARED TO PET[1]

Complementary to Chapter 8, which examined the equilibrium water sorption properties for PEF and PET at 35°C, this chapter investigates the corresponding diffusion coefficient behavior over the entire water activity range. PEF was found to exhibit a ~5X reduction in diffusion coefficient averaged over the entire concentration interval compared to PET. Fickian diffusion was observed for water in both polyesters up to ~0.6 activity, after which the presence of non-Fickian relaxations required treatment using the Berens-Hopfenberg modeling framework. Penetrant plasticization at high activity was found for both PEF and PET, as evidenced by a positive correlation between diffusion coefficient and increasing water concentration. Arrhenius interpretation of diffusion coefficients measured at 15, 25, 35, and 45°C allowed calculation of the activation energies of diffusion for PEF and PET, which were similar at 47.1 ± 2.8 kJ/mol and 46.4 ± 3.0 kJ/mol, respectively.

9.1. Introduction

Studies involving water transport in polymeric materials are important, since most polymers will realistically encounter humid environments at some point during their usable lifetime. Such transport data are particularly important for materials which will be in direct contact with liquid water, since water at unit activity can cause undesirable plasticization and swelling effects in a wide variety of polymers [1-4].

[1]Reprinted in part from *Polymer*, 55/26, Burgess, S.K.; Mikkilineni, D.S.; Yu, D.B.; Kim, D.J.; Mubarak, C.R.; Kriegel, R.M.; Koros, W.J., *Water Sorption in Poly(ethylene furanoate) Compared to Poly(ethylene Terephthalate). Part 2: Kinetic Sorption*, 6870-6882, Copyright 2014, with permission from Elsevier.

Recent innovation by Avantium (The Netherlands) has enabled economical, large-scale production of 2,5-furandicarboxylic acid (FDCA), which is one of two monomers needed to manufacture poly(ethylene furanoate) (PEF). Integration of PEF into the global polyester market is desirable, due to renewable sourcing of the monomers and the largely improved barrier, mechanical, and thermal properties compared to PET [5]. Multiple studies have focused on various aspects of PEF synthesis and/or material property characterization [6-11], however, no data exist in the literature regarding the fundamental water transport properties. Applications of PEF in the beverage and food packaging industry involve high humidity environments, and knowledge of the water transport properties at ambient temperature is therefore required for accurate shelf-life predictions.

In comparison to PET, the current study indicates that PEF exhibits ~5X reduced water diffusion coefficients averaged over the entire concentration interval. This reduction is attributed to fundamental differences in segmental mobility, which originate from the rigid furan moiety in PEF compared to the mobile phenyl moiety in PET (cf. Chapter 5). The results from the current chapter can be compared to the diffusion of water in poly(ethylene naphthalate) (PEN), which exhibits somewhat analogous rigidity to PEF due to hindered flipping of the bulky naphthalene moiety [12]. Rueda and Varkalis report a ~3.2X reduction in diffusion coefficient for PEN compared to PET, where both polymers are amorphous and in the hydrated state [13]. Interestingly, the authors also report a higher equilibrium sorption in PEN compared to PET due to differences in free volume [13, 14], although the disparity in equilibrium uptake is not as significant as the difference between equilibrium uptake in PEF and PET as discussed in Chapter 8.

This chapter presents a detailed kinetic investigation of water diffusion in amorphous PEF and PET, and complements prior work regarding equilibrium sorption properties for water (Chapter 8), carbon dioxide transport (Chapter 7), oxygen transport (Chapter 6), and fundamental segmental chain mobility (Chapter 5). Similar to Chapter 8, gravimetric sorption experiments were performed using three independent techniques, thereby allowing verification of the reported diffusion coefficients. Concentration dependent diffusion coefficients are presented for amorphous PEF and PET at 35°C over the entire water activity range, and exhibit plasticization type behavior as evidenced by the positive correlation with increasing activity. The presence of non-Fickian relaxations at high activity is consistent with this notion, as is the sorption/desorption hysteresis observed for both polyesters reported in Chapter 8. Additional measurements of the activation energy of diffusion can be combined with the enthalpy of sorption measurements provided in Chapter 8, thereby allowing a means to estimate the apparent activation energy of water permeation in both polyesters. Similar calculations involving the diffusivity and solubility reveal a reduction in permeability of ~2.8X averaged across the entire concentration interval for PEF compared to PET, which is consistent with the reduction of ~2X for PEF vs. PET reported by Avantium [15].

9.2. Experimental Methods

9.2.1. Materials and Film Preparation

The poly(ethylene furanoate) (PEF) and poly(ethylene terephthalate) (PET) polymers used in this chapter are the same materials described previously in Section 3.1.1, and all amorphous films were melt-pressed using the method in Section 3.1.3. All transport

measurements reported herein for PEF and PET reflect data corresponding to the amorphous morphology.

9.2.2. Sorption Measurements

Gravimetric water sorption uptake measurements were recorded for amorphous PEF and PET at 35°C using three independent and complementary techniques, which are described in detail in Chapter 3 (cf. Section 3.4).

9.3. Results and discussion

9.3.1. Diffusion Model Development

As described in Chapter 3 (cf. Section 3.4.4), the raw gravimetric water uptake data vs. time can be transformed via Equation 9.1 into a non-dimensional form that can be modeled using a solution of the time-dependent diffusion equation.

$$\frac{M_t}{M_\infty}(t) = \left(\frac{m(t) - m_{initial}}{m_{final} - m_{initial}} \right) \tag{9.1}$$

The Fickian solution discussed previously in Equation 2.47 accurately describes the kinetic sorption behavior of relatively non-condensable gases in polymer materials (i.e., O_2 in PEF [16]) and some vapors at low activity [17, 18], consistent with the validity of the boundary and initial conditions in these applications. Equation 2.47 can also describe the water sorption data measured by the quartz spring system in the current work (cf. Figure 9.1, discussed later in the document). Since $\bar{D}$ from Equation 2.47 naturally

represents the average "effective" diffusion coefficient over the specified concentration interval (cf. Equation 2.9), diffusion coefficients reported in this chapter are plotted at the midpoint of the respective sorption intervals.

Uptake data measured from the automated VTI instrument at low activities could not be accurately described by the Fickian model from Equation 2.47. All data recorded from this instrument exhibited a slight but distinct curvature convex to the time axis at short times, before approaching Fickian-like behavior at longer times (cf. Figure 9.3, discussed later in the document). A discussion regarding the cause of the anomalous sorption kinetics is available in Chapter 3 (cf. Section 3.4.2).

The sigmoidal sorption data from Figure 9.3 (discussed later in the chapter) can be modeled formally using the Long and Richman formulation of the time-dependent boundary condition from Equation 2.52 (discussed previously), which states that the equilibrium concentration at the film surface is described by an exponential approach to equilibrium [19]. Solution of the time-dependent diffusion equation with the boundary conditions in Equation 2.52 is reproduced in Equation 9.2 [19, 20], where the subscript "*F-Exp*" denotes the Fickian solution obtained after application of the exponential-type boundary condition.

$$\left.\frac{M_t}{M_\infty}\right|_{F-Exp} = \left[1-\exp\left(-\frac{t}{\tau_S}\right)\left(\frac{4\tau_S D_{Avg}}{l^2}\right)^{1/2}\tan\left(\frac{l^2}{4\tau_S D_{Avg}}\right)^{1/2} - \frac{8}{\pi^2}\sum_{n=0}^{\infty}\frac{\exp\left(-D_{Avg}\left(2n+1\right)^2\pi^2\frac{t}{l^2}\right)}{(2n+1)^2\left(1-\left(2n+1\right)^2\left(\frac{\tau_S D_{Avg}\pi^2}{l^2}\right)\right)}\right] \tag{9.2}$$

Additional experimental verification of the validity of Equation 9.2 in the current application is provided in Appendix D, which provides values of D_{Avg} and τ_S measured using nitrogen, argon, and helium as carrier gases along with variable flow rates. Equation 9.2 can be combined with the Berens-Hopfenberg representation discussed previously (cf. Section 2.4.4) to produce Equation 9.3, which describes kinetic sorption measured via the VTI instrument in the presence of non-Fickian relaxations.

$$\left.\frac{M_t}{M_\infty}\right|_{BH-Exp} = \left[\phi_F\left(\left.\frac{M_t}{M_\infty}\right|_{F-Exp}\right) + \left(1-\phi_F\right)\left(1-\exp\left(-\frac{t}{\tau_R}\right)\right)\right] \tag{9.3}$$

In the following discussions throughout the chapter, Equation 9.3 will be referenced as the "BH-Exp" model. It is important to recognize that Equations 2.55, 2.53, and 2.47 (provided in Chapter 2) can all be recovered from Equation 9.3 depending on the shape of the kinetic curve. For example, use of Equation 9.3 to model a strictly Fickian uptake curve (cf. Figure 9.1, discussed later in the chapter) will return values of $\phi_F \approx 1$ and $\tau_S \approx 0$. Similarly, use of Equation 9.3 to model the kinetic data from the VTI system at low water concentrations (cf. Figure 9.3, i.e., absence of non-Fickian relaxations) will return values of $\phi_F \approx 1$ and $\tau_S \neq 0$. The model in Equation 9.3 therefore represents a robust representation which is capable of describing a wide variety of kinetic phenomena.

Application of Equation 9.3 to experimental kinetic sorption data was achieved using a similar MATLAB® non-linear least squares fitting routine as described later in Chapter 11. Due to the presence of four unknown parameters in Equation 9.3, caution should be exercised regarding the selection of "initial guess" parameters required by the non-linear

least squares fitting routine and how these parameters affect the final optimized model parameters. For example, the functional form of Equation 9.2 (cf. Figure 9.3), especially for large values of τ_S, can resemble the sigmoidal shape of the exponential relaxation term in Equation 9.3. Selecting a purely non-physical initial guess of 3000 s for τ_S when modeling the data in Figure 9.3b (which clearly has a τ_S on the order of 200 s), could result in the MATLAB® routine "optimizing" the solution by selecting a local minima in the solution-optimization space which exhibits no physical significance. Consequently, care must be taken to ensure that the final optimized parameters truly reflect the physical phenomena occurring during diffusion. An additional discussion regarding the selection of initial guess parameters in the MATLAB® fitting routine is provided in Chapter 11.

A final note should be mentioned regarding the relative time-scales of both Fickian diffusion and first-order relaxations. Direct comparison of these parameters can be obtained via the Deborah number (*De*) for diffusion given in Equation 9.4 [21], where τ_R is the time constant for the first-order relaxations obtained from Equations 9.3, and τ_D is the time constant for Fickian diffusion.

$$De = \frac{\tau_R}{\tau_D} = \frac{\tau_R}{\left(l^2 \diagup D\right)} \tag{9.4}$$

Simple Fickian behavior will be observed in the kinetic uptake data for both limiting cases where $De \gg 1$ and $De \ll 1$, while diffusion cases which involve comparable diffusion and relaxation time scales ($De \approx 1$) require treatment with a relaxation-based model (i.e., Berens-Hopfenberg model). Further discussions on the Deborah diffusion

number can be found in the literature [21-23].

9.3.2. Sorption/Desorption at 35°C (First Cycle)

Water uptake data for both polyesters measured by the manual quartz spring apparatus at low activities can be accurately described by the simple Fickian model from Equation 2.47. Example quartz spring data are provided in Figure 9.1 for water vapor at 35°C in PEF (diamonds) and PET (circles), and are plotted on the same graph via normalization using a non-dimensional time $(D_{Avg}t/l^2)^{1/2}$. The solid line in Figure 9.1 represents the model fit from Equation 2.47. Similar agreement between Equation 2.47 and uptake data was also observed for measurements conducted in liquid water at 35°C, and will be discussed later in Section 9.3.3. Diffusion coefficients obtained via the quartz spring method for both polyesters are provided in Appendix D, and exhibit excellent agreement with the values obtained from automated VTI system.

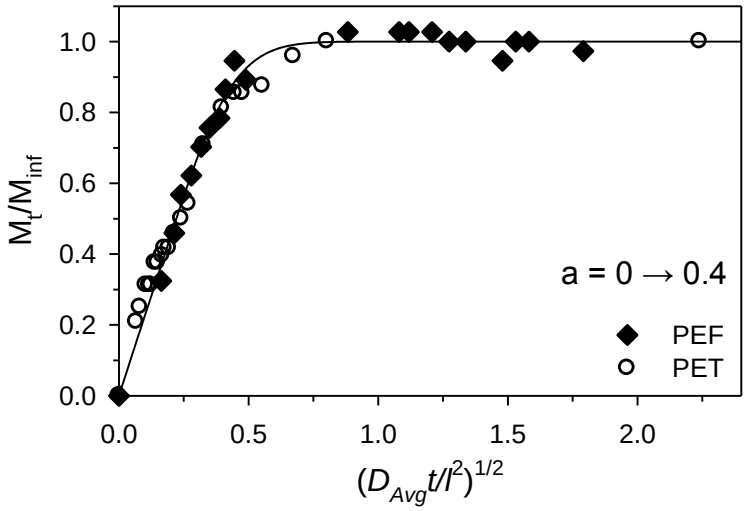

Figure 9.1. Water uptake data at 35°C for PEF (diamonds) and PET (circles) measured during sorption between 0 – 0.4 activity using the quartz spring system. Data are plotted versus a non-dimensional time, with the corresponding Fickian fit from Equation 2.47. Respective D_{Avg} values are provided in Appendix D.

The raw kinetic sorption data measured at 35°C from the automated VTI system are shown in Figure 9.2a for PEF and Figure 9.2b for PET between the activity range of 0 – 0.95 for sorption and subsequent desorption. First examination of Figure 9.2 for both polyesters reveals a Fickian-type uptake behavior during sorption up to ~0.6 activity, as evidenced by a functional approach to equilibrium similar to that illustrated in Figure 9.1 (i.e., negligible long-term relaxations). After ~0.6 activity, however, long-term non-Fickian relaxations are observed via a protracted incremental increase in sorption capacity. In fact, examination of Figure 9.2 for both polyesters reveals that true sorption equilibrium was not reached for uptake curves between 0.6 – 0.95 activity during initial sorption. Implications of this reality on the final kinetic model parameters, although minor, will be discussed later in the chapter. The non-Fickian relaxation behavior observed at high activity is consistent with the onset of sorption-induced morphological changes associated with plasticization and swelling and an overall increase in free volume in the conditioned samples. This behavior coincides with the positive deviation from dual-mode sorption observed in Chapter 8 above ~0.6 activity. Data similar to that in Figure 9.2 have also been observed for kinetic water sorption in sulfonated polyimide membranes [24].

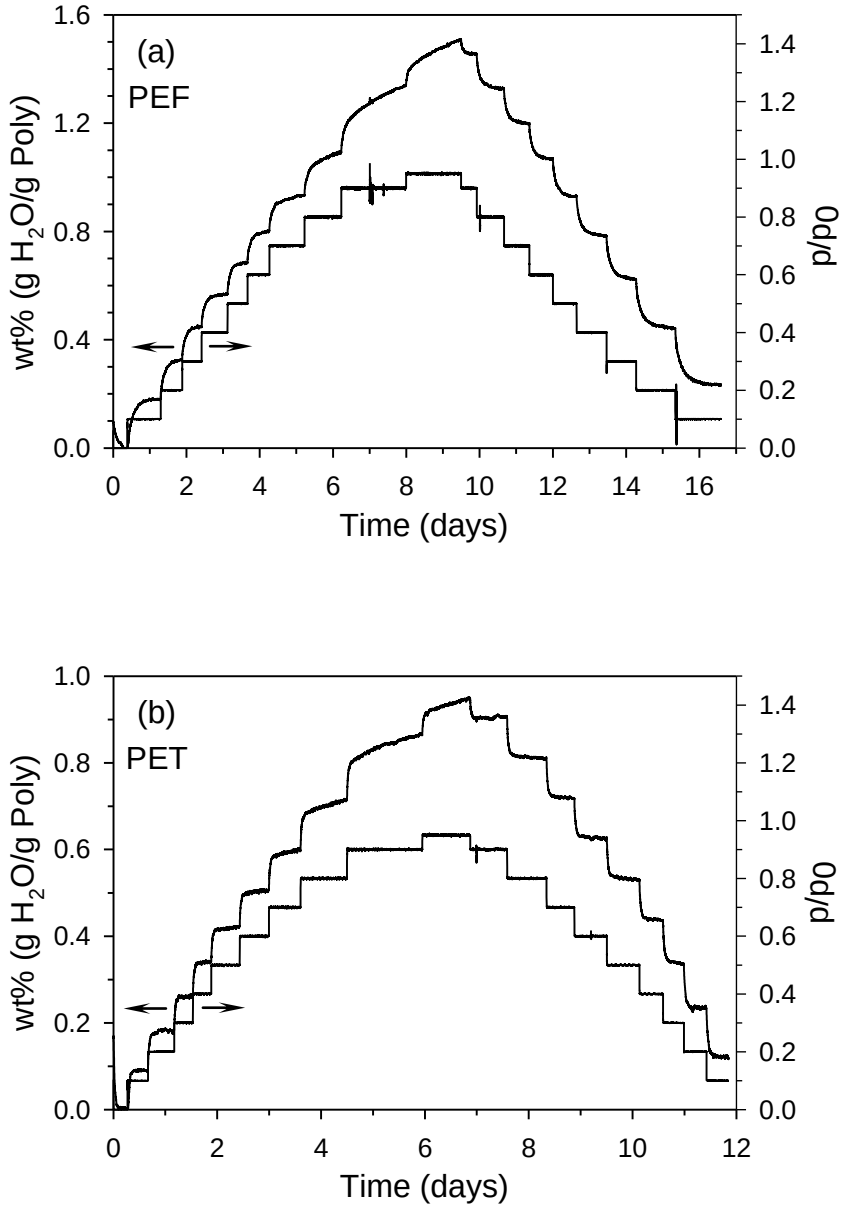

Figure 9.2. Sorption/desorption data for water in PEF (a) and PET (b) at 35°C measured by the automated VTI instrument. Both (a) and (b) contain complementary kinetic and equilibrium sorption data, where the equilibrium sorption data are summarized in Figures 8.6 and 8.7 of Chapter 8.

The data in Figure 9.2 can be partitioned into individual sorption/desorption curves via Equation 9.1, thereby facilitating application of Equation 9.3 and extraction of model parameters. The anomalous kinetics introduced by the process control lag are not

apparent in Figure 9.2 due to the small magnitude of τ_S (minutes) compared to the time-scale of the overall experiment (days). Closer examination of the kinetic uptake data for PEF from Figure 9.2a is provided in Figure 9.3a for the sorption interval 0 – 0.1 activity and in Figure 9.3b for the sorption interval 0.1 – 0.2 activity. The uptake data in Figure 9.3 are plotted versus $(\text{time})^{1/2}$ to better illustrate the anomalous kinetics introduced by the control scheme lag, and both the Fickian model from Equation 2.47 (dashed line) and the BH-Exp model from Equation 9.3 (solid line) are shown in the figure for comparison. It was consistently observed during VTI operation that any concentration step starting from zero activity exhibited a much larger value of τ_S than if the instrument initiated a step change starting from a nonzero activity. This notion is demonstrated in Figure 9.3a and 9.3b, where τ_S = 1820 s in Figure 9.3a (activity step 0 – 0.1) and τ_S = 214 s in Figure 9.3b (activity step 0.1 – 0.2). Anomalous kinetic uptake curves similar to Figure 9.3b have also been observed by Detallante et al. [24], who used a different automated vapor sorption system than in the current work and attributed the anomalous behavior to similar variability in the water vapor concentration at the film surface.

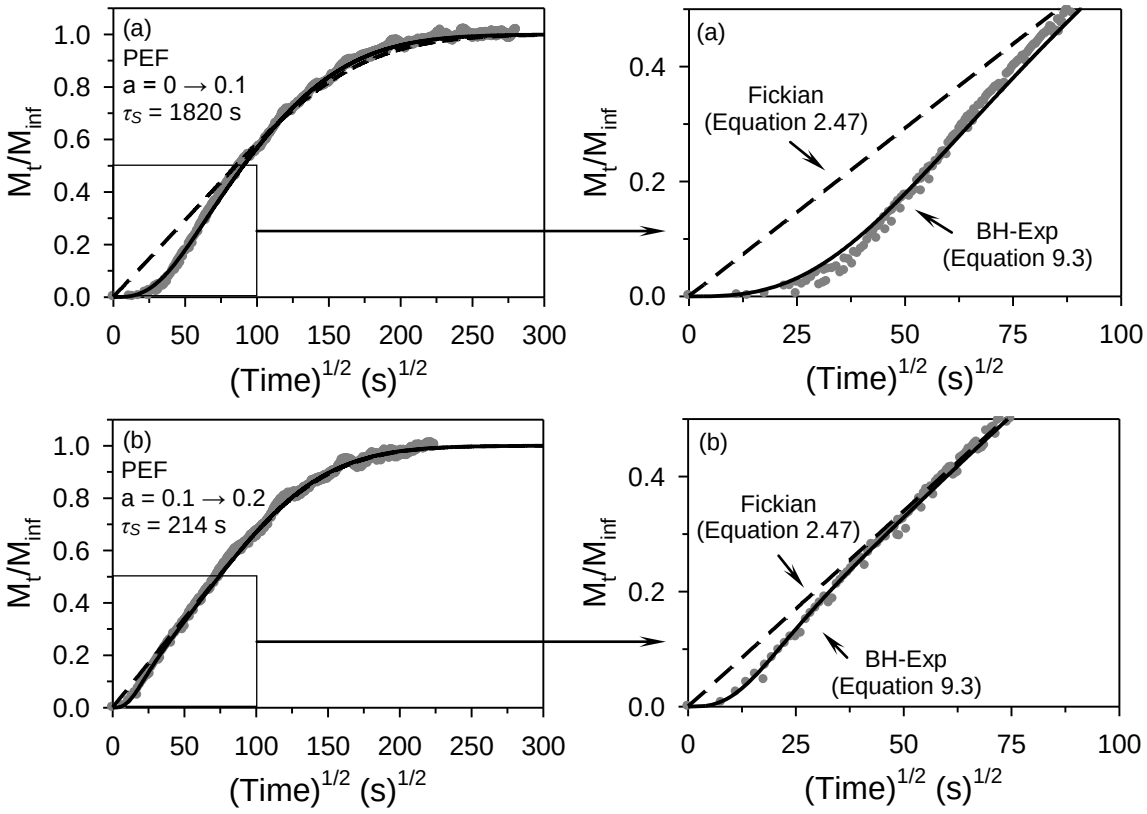

Figure 9.3. Water uptake data at 35°C measured by the automated VTI system during sorption between 0 – 0.1 activity (a) and 0.1 – 0.2 activity (b). Dashed lines represent the Fickian fit from Equation 2.47, while solid lines represent the BH-Exp fit from Equation 9.3. Model parameters are as follows: (a) Fickian (D_{Avg} = 1.55×10^{-9} cm^2/s), BH-Exp (D_{Avg} = 1.83×10^{-9} cm^2/s, ϕ_F = 1, τ_R = not used, τ_s = 1820 s), and for (b) Fickian (D_{Avg} = 2.09×10^{-9} cm^2/s), BH-Exp (D_{Avg} = 2.14×10^{-9} cm^2/s, ϕ_F = 1, τ_R = not used, τ_s = 214 s).

In Figure 9.3, it is apparent that the BH-Exp model from Equation 9.3 more accurately describes the experimental data than the ideal Fickian model from Equation 2.47. The model parameters for all four best fit lines in Figure 9.3 are provided in the figure caption. Not surprisingly, differences between diffusion coefficients calculated from the two models are accentuated in Figure 9.3a due to the larger value of τ_S compared to that illustrated in Figure 9.3b. Furthermore, a value of τ_S = 214 s in Figure 9.3b results in only a minor correction to D_{Avg} calculated from the simple Fickian model. Values of ϕ_F = 1 were obtained from modeling Equation 9.3 to the data shown in Figure 9.3, thereby

indicating the absence of non-Fickian relaxations over the time-scale of these experiments. Significantly larger deviations between D_{Avg} values calculated from the two models are realized when ϕ_F <<1, as observed in the current work during sorption at high activity for both polyesters.

Individual partitioning of the sorption/desorption uptake curves depicted in Figure 9.2a for PEF is provided in Figure 9.4, while the corresponding curves in Figure 9.2b for PET are provided in Figure 9.5. Sorption/desorption curves measured over the same activity interval (i.e., 0.1 – 0.2 for sorption, and 0.2 – 0.1 for desorption) are plotted on the same respective graphs to allow for simple comparison. The solid lines in Figures 9.4 and 9.5 represent the BH-Exp model fit from Equation 9.3 to the experimental sorption data, while the dashed lines represent corresponding fits to the desorption data. Desorption data were not measured for the interval 0.1 – 0, and consequently, only the sorption curves between 0 – 0.1 activity are represented in Figures 9.4a and 9.5a.

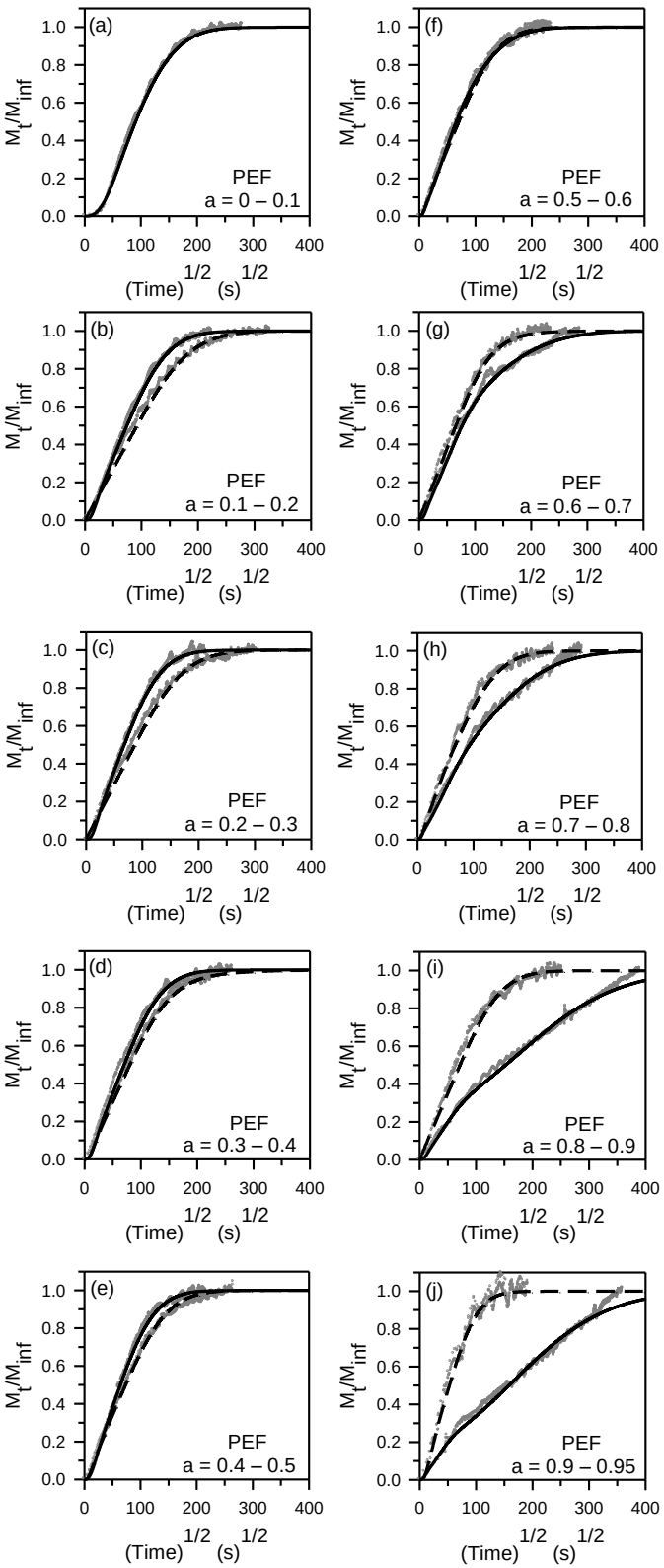

Figure 9.4. Kinetic sorption data from Figure 9.2a for water in PEF at 35°C measured by the VTI system. Lines represent model fits from Equation 9.3 corresponding to sorption (solid) and subsequent desorption (dashed), while experimental data are represented in grey. The sorption intervals are labeled in each respective graph.

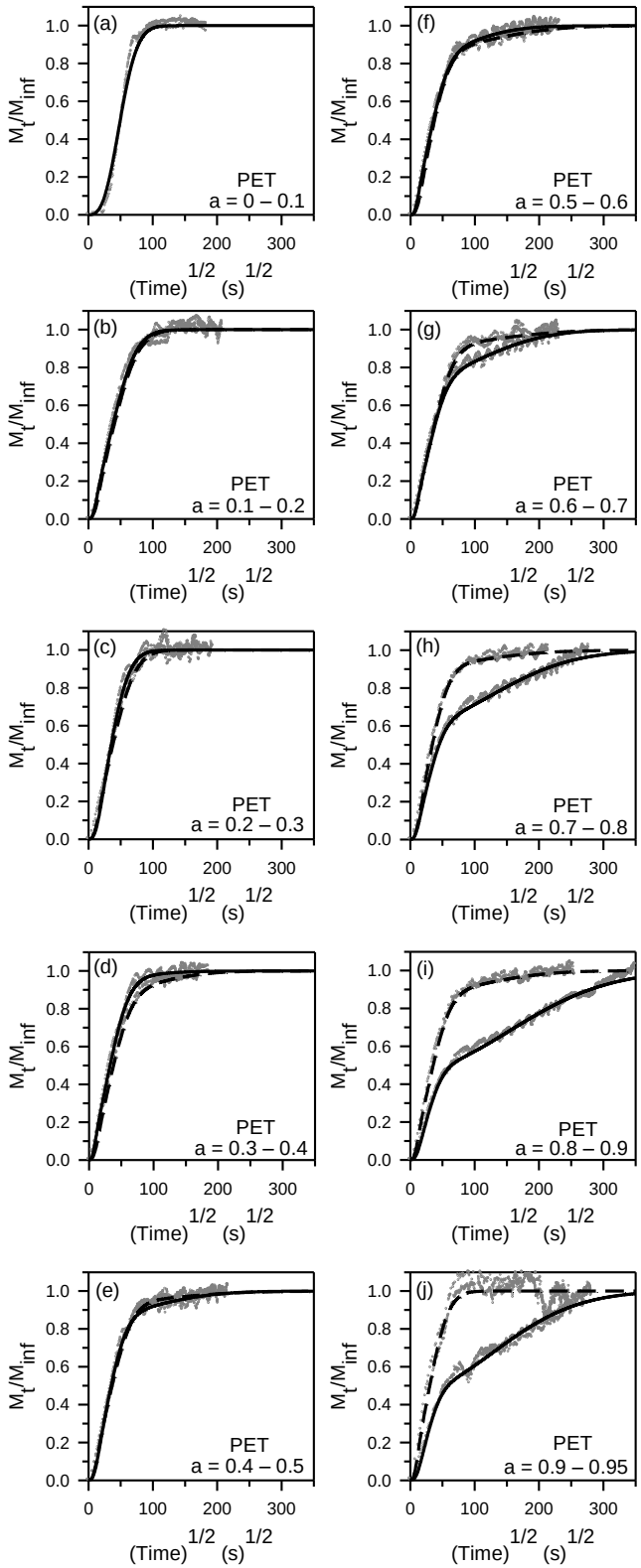

Figure 9.5. Kinetic sorption data from Figure 9.2b for water in PET at 35°C measured by the VTI system. Lines represent model fits from Equation 9.3 corresponding to sorption (solid) and subsequent desorption (dashed), while experimental data are represented in grey. The sorption intervals are labeled in each respective graph.

Effective diffusion coefficients (D_{Avg}) obtained from the BH-Exp model fit to the sorption/desorption data for PEF in Figure 9.4 are provided in Figure 9.6, with corresponding values for PET from Figure 9.5 provided in Figure 9.7. From these figures, it is apparent that D_{Avg} exhibits a positive correlation with increasing concentration during sorption for both polyesters, with the same behavior observed during subsequent desorption. The initial increase in D_{Avg} values up to 0.6 activity can be described by typical dual-mode behavior, and is discussed in Appendix D. Above 0.6 activity, however, positive deviations from ideal dual-mode behavior correlate with increased segmental mobility resulting from penetrant-induced plasticization. *This behavior is opposite to that expected for penetrant clustering*, which exhibits a decrease in diffusion coefficient with increasing concentration due to the larger kinetic diameter of the diffusing species [25, 26].

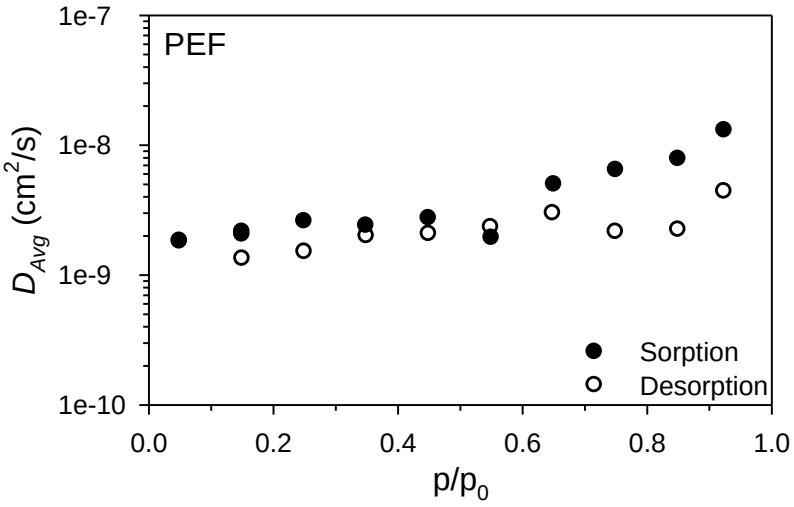

Figure 9.6. D_{Avg} values from Equation 9.3 for water in PEF at 35°C measured from the VTI system. Sorption (solid circles) and subsequent desorption values (hollow circles) are plotted at the midpoint activity of the respective sorption interval, and correlate with model fits to the data in plots (a) – (j) from Figure 9.4.

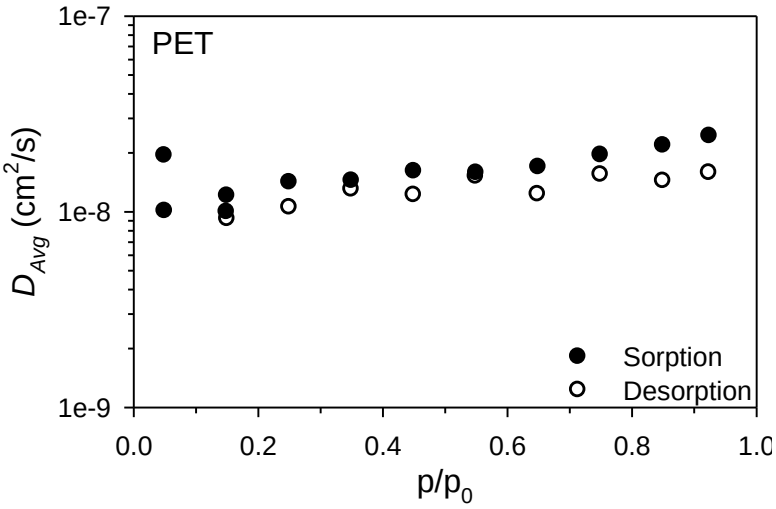

Figure 9.7. D_{Avg} values from Equation 9.3 for water in PET at 35°C measured from the VTI system. Sorption (solid circles) and subsequent desorption (hollow circles) values are plotted at the midpoint activity of the respective sorption interval, and correlate with model fits to the data in plots (a) – (j) from Figure 9.5.

Data in Figures 9.6 and 9.7 also reveal slightly larger D_{Avg} values for sorption compared to respective desorption values for both polyesters. This behavior is consistent when considering the positive correlation between D_{Avg} and concentration. Crank notes that sorption is typically faster than desorption when the diffusion coefficient increases with concentration [20]. Regardless, the D_{Avg} values for sorption and desorption are similar in magnitude over the entire concentration range, which is similar to the behavior observed for water diffusion in polysulfone (PSF) [27]. The trends in Figures 9.6 and 9.7 for PEF and PET, respectively, contrast those observed for water in polyethersulfone [28], 20% poly(vinyl pyrrolidone)/PSF [27], and water in some polyimides [29], where the latter polymers exhibit a decreasing D_{Avg} with increasing concentration for sorption at high activity due to the presence of clustering.

A more accurate estimate of the true diffusion coefficient dependence vs. activity can be obtained by averaging the diffusion coefficients obtained during sorption and

subsequent desorption over the same respective interval (cf. Equation 2.11, discussed previously) [20, 30]. Average diffusion coefficients obtained via this method are represented by $D_{(s+d)/2}$, where *s* and *d* represent *sorption* and *desorption*, respectively. $D_{(s+d)/2}$ values corresponding to both PEF and PET are plotted together in Figure 9.8 to allow for simple comparison. A note regarding this average is that the morphology of the polyester material is slightly altered after initial sorption at high activity. Recall that the sorption steps were performed in series between 0 – 0.95 activity, followed by the desorption steps in series between 0.95 – 0 activity. Morphological changes in the polymer are observed via the non-Fickian relaxations in the current work and by the distinct sorption hysteresis observed in Figures 8.6 and 8.7 presented in Chapter 8. Values of $D_{(s+d)/2}$ for PET divided by respective values for PEF between 0 – 0.95 activity vary from ~6.2 to ~2.3 at the low and high activity limits, respectively, with an average value of 5.0 across the entire concentration range. Reduced diffusion coefficients for PEF compared to PET originate from inherent differences in segmental mobility, as discussed in Chapter 5. Similar diffusion coefficient behavior to that observed in Figure 9.8 has been observed for both semicrystalline PET and amorphous poly(ethylene naphthalate) (PEN) [13], which exhibits similar rigidity to PEF.

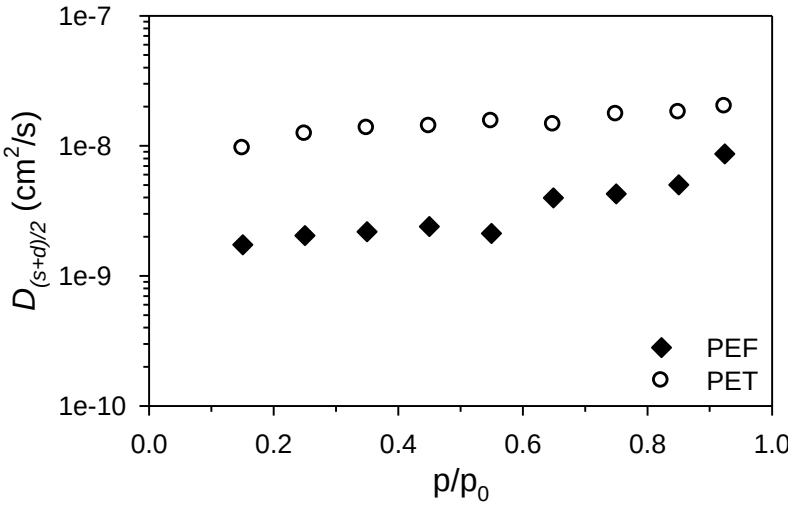

Figure 9.8. Sorption and desorption averaged diffusion coefficients ($D_{(s+d)/2}$) measured from the VTI system for water in PEF (diamonds) and PET (circles) at 35°C.

The average diffusion coefficient data presented in Figure 9.8 for both polyesters can also be plotted as a function of equilibrium water concentration (cm^{3}STP/cm^{3}Poly), which can be obtained from Figures 8.6 and 8.7 in Chapter 8 for PEF and PET, respectively. Values of $D_{(s+d)/2}$ from Figure 9.8 are plotted in Figure 9.9 versus the average equilibrium concentration, which reflects the average concentration from beginning to end of the interval and averaged again between sorption and desorption concentrations to account for sorption hysteresis. The lines in Figure 9.9 represent model fits from Equation 9.5, which assumes an exponential dependence for the diffusion coefficient on concentration.

$$D = D_{\infty} \exp\left(\beta C_{Avg}\right) \tag{9.5}$$

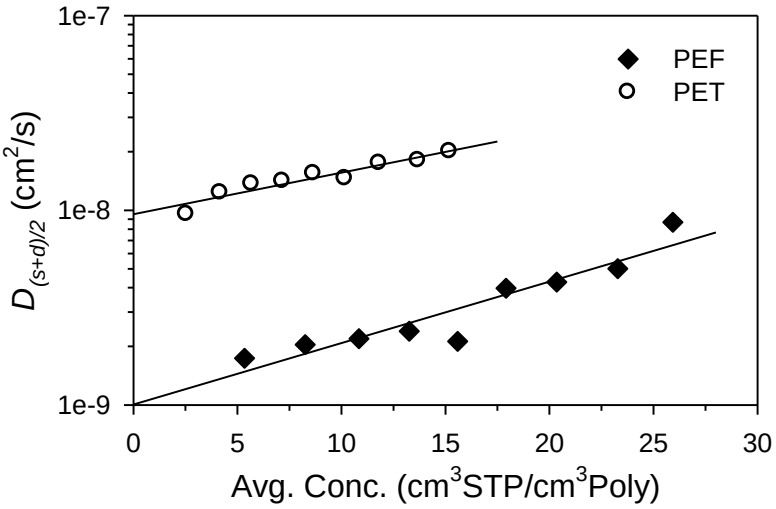

Figure 9.9. Diffusion coefficients from Figure 9.8 versus equilibrium water concentration at 35°C for PEF (diamonds) and PET (circles). Lines reflect model fits from Equation 9.5, and respective model parameters are included in the text.

In Equation 9.5, C_{Avg} represents the aforementioned average concentration, β is a constant, and D_∞ is the infinite dilution diffusion coefficient. Model parameters from Equation 9.5 for PEF are $D_\infty = 1.0\times10^{-9}$ cm^2/s and $\beta = 0.073$ (cm^{3}STP/cm^{3}Poly)$^{-1}$, while corresponding model parameters for PET are $D_\infty = 9.6\times10^{-9}$ cm^2/s and $\beta = 0.049$ (cm^{3}STP/cm^{3}Poly)$^{-1}$. Reports in the literature suggest that values for β increase with increasing penetrant size for diffusion in PET, and the value of 0.049 for PET from the current work is significantly lower than values reported for ethanol, n-propanol, i-propanol, i-butane, and ethyl acetate [18, 31, 32]. Additionally, PEF exhibits a larger concentration dependence than PET as evidenced by the slightly larger value for β. Such results are consistent with the observation of Chandra and Koros [18], who suggested a positive correlation between concentration dependence and interaction between penetrant and polymer matrix. The latter notion is discussed in Chapter 8, where water is shown to exhibit higher compatible with PEF vs. PET due to the polar furan ring.

The presence of non-Fickian relaxations during sorption at high activity (>0.6) for both polyesters is apparent via the long, protracted approach to equilibrium observed in Figures 9.2, 9.4, and 9.5. Similar non-Fickian behavior to that reported in the current work has been reported by Schult and Paul [33] in their work regarding water sorption in polyethyloxazoline and polyethersulfone, and in additional studies regarding water sorption in PET [2, 34]. The onset of non-Fickian behavior in the current work is best visualized by a plot of the respective ϕ_F values from Equation 9.3 for the best-fit models illustrated in Figure 9.4 for PEF and Figure 9.5 for PET. A plot of ϕ_F vs. activity during initial sorption is provided in Figure 9.10a for both PEF (diamonds) and PET (circles), with the corresponding graph for desorption provided in Figure 9.10b. Simple Fickian diffusion is dominant during sorption up to 0.6 activity, as evidenced by ϕ_F values near unity for both polyesters in Figure 9.10a. Alternatively, a large systematic decrease in ϕ_F is observed above 0.6 activity during sorption, thereby indicating a transition to relaxation-dominated mass uptake. Fickian kinetics dominate the desorption process, as observed by ϕ_F values near unity for both polyesters in Figure 9.10b over the entire concentration range. It is also known that a slightly retarded approach to equilibrium during the final stages of desorption can accompany the specific type of concentration dependence observed in the current work [20]. This protracted approach to equilibrium during desorption can also potentially result from deswelling of the previously swollen matrix, as observed by Berens [35] in the case of vinyl chloride sorption in poly(vinyl chloride) or by Bagley and Long [36] in the case of acetone sorption in cellulose acetate. Consequently, the values of ϕ_F not equal to unity in Figure 9.10b are potentially a result of the relaxation-based model attempting to describe this deswelling process or the

protracted approach resulting from the concentration dependence of the diffusion coefficient. Nevertheless, the observation of predominantly Fickian kinetics upon desorption is consistent with the notion that the collapse of extra free-volume which was introduced during sorption occurs significantly slower than the Fickian desorption process, thereby resulting in the appearance of Fickian kinetics [27, 35]. A brief discussion regarding the persistence of the morphological changes is provided in Chapter 8, which illustrates sorption hysteresis in both polyesters [37]. The remaining BH-Exp model parameters from Equation 9.3 for the best-fit curves in Figures 9.4 and 9.5 are provided in Figure 9.11 for τ_R and in Figure 9.12 for τ_S.

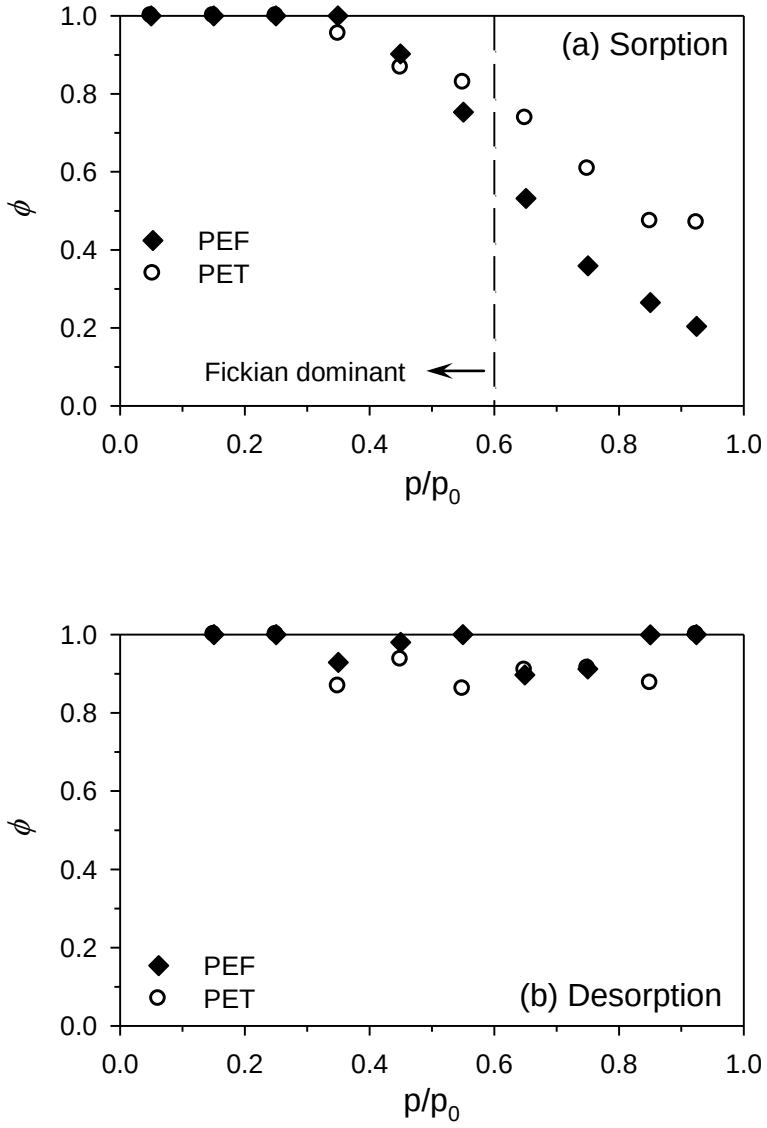

Figure 9.10. Plot of ϕ_F from Equation 9.3 for water at 35°C in PEF (solid diamonds) and PET (hollow circles) measured by the VTI system for sorption (a) and desorption (b).

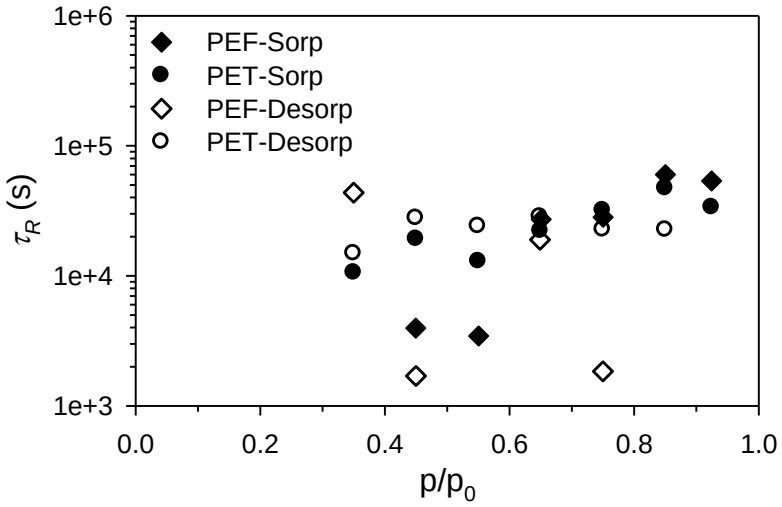

Figure 9.11. Plot of τ_R from Equation 9.3 for water at 35°C in PEF (diamonds) and PET (circles) measured by the VTI system for sorption (filled) and desorption (hollow). Values of τ_R are only provided for values of ϕ_F <1 from Figure 9.10.

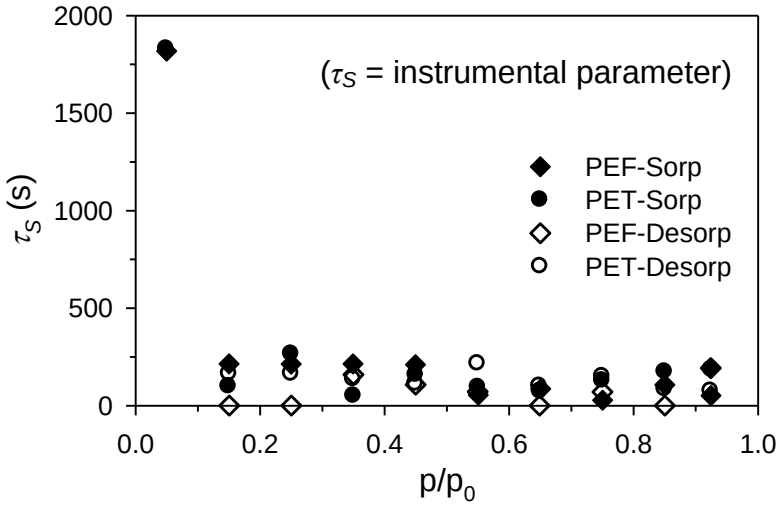

Figure 9.12. Plot of τ_S from Equation 9.3 for water at 35°C in PEF (diamonds) and PET (circles) measured by the VTI system for sorption (filled) and desorption (hollow). *Recall that τ_S is an instrumental parameter, and does not reflect intrinsic properties of the polymer.*

Values of τ_R from Equation 9.3 can only be evaluated accurately via the MATLAB® modeling technique when ϕ_F < 1. Consequently, Figure 9.11 only reports τ_R values in conjunction with the respective ϕ_F parameters depicted in Figures 9.10a during sorption, which are less than unity above ~0.5 activity. Corresponding τ_R values for desorption are

also only provided for values of $\phi_F < 1$ as reported in Figure 9.10b. It is interesting to observe that both PEF and PET exhibit similar relaxation rates during sorption at high activity despite seemingly large differences in segmental mobility [5]. It should be reiterated, however, that only one relaxation term in the Berens-Hopfenberg expression (cf. Equation 9.3) was used in this study, and as a result, τ_R represents an empirical parameter.

Values of the instrumental time constant associated with the process control lag (τ_S) are plotted in Figure 9.12 for PEF (diamonds) and PET (circles) during both sorption (solid) and desorption (hollow). To reiterate, τ_S is not a fundamental polymer parameter and is employed solely to remove the anomalous behavior introduced by the instrument control lag. Consequently, τ_S is approximately constant during the activity range between 0.1 – 0.95 for both polyesters. The exception is the interval starting from zero, which consistently produced larger values of τ_S. As a consistency check, all values of τ_S reported in Figure 9.12 were significantly smaller than (l^2/D_{Avg}), which is the respective time scale for diffusion. Automated VTI measurements using argon and helium in addition to nitrogen are provided in Appendix D between the interval 0.1 – 0.2 activity to further explain the choice of Equation 9.3 and role of τ_S in the current work.

As mentioned previously, extra time was allotted to allow for completion of sorption at activities greater than 0.6 (cf. Figures 9.2, 9.4, and 9.5); however, the uptake curves did not reach complete equilibrium and were still increasing when the system proceeded to the next activity step. This effect is accentuated at the highest sorption interval between 0.9 – 0.95 activity, which corresponds with the upswing in equilibrium vs. concentration reported in Chapter 8 [37]. Berens [35], who studied vinyl chloride sorption in poly(vinyl

chloride), also terminated his runs before true equilibrium was reached due to excessively lengthened experiment times.

Recall that the diffusion model provided in Equation 9.3 represents a linear superposition of both Fickian and relaxation terms, where both are assumed to occur independently of the other [38]. Since enough time was allowed in Figures 9.4 and 9.5 to fully span the timescale needed for Fickian diffusion, it is possible, in theory, to ideally obtain physically meaningful values of the diffusion coefficient without reaching true uptake equilibrium [36]. Furthermore, not achieving true equilibrium due to the presence of relaxations should ideally only affect the model parameters associated with the relaxation process, which are ϕ_F and τ_R in Equation 9.3. The end-result for the relaxation-based model parameters will be: 1) a further decrease in ϕ_F than illustrated in Figure 9.10a due to the larger contribution from the relaxation mode, and 2) an increase in τ_R for the values illustrated in Figure 9.11 due to longer time needed for completion of the relaxation process. Only one relaxation term in the Berens-Hopfenberg framework was considered in Equation 9.3 for simplicity and to achieve "uniqueness" in the final model parameters. It is possible, however, that additional relaxation terms in the BH framework might be needed to model the complete uptake curve in the case of achieving true equilibrium. Consequently, the relaxation parameters provided in Figures 9.10 and 9.11 serve the purpose of providing a workable, phenomenological description of the relaxation process in both polyesters. Continuing with the aforementioned discussion, the diffusion coefficients calculated in the absence of long-term relaxations (i.e., $p/p_0 < 0.6$ during sorption, and all activities during desorption) reflect a higher degree of confidence in the optimized values, while more uncertainty exists in the optimized values for D_{Avg}

during sorption at high activity due to the large relaxation contribution from Equation 9.3.

9.3.3. Sorption/Desorption at 35°C (Second Cycle) and Sorption at Unit Activity

The values for D_{Avg} reported in Figures 9.6 (PEF) and 9.7 (PET) are for initial sorption (solid circles) and subsequent desorption (hollow circles). Recall that equilibrium uptake hysteresis was reported in Chapter 8, which included data for a second sorption cycle to examine the persistence of the sorption-induced morphological changes (cf. Figures 8.6 and 8.7 in Chapter 8). The kinetic counterpart to the equilibrium data during the second sorption cycle at 35°C will now be presented.

Sorption during the second cycle consisted of larger concentration intervals than used initially (i.e., 0 – 0.3, 0.3 – 0.6, and 0.6 – 0.95 for sorption, and 0.95 – 0.6, 0.6 – 0.3, 0.3 – 0.05 for desorption). Values of the average diffusion coefficient from sorption and desorption (i.e., $D_{(s+d)/2}$, discussed previously) during the second cycle at 35°C are plotted via the hollow circles at the midpoint of the concentration interval in Figure 9.13 for PEF and Figure 9.14 for PET. Corresponding $D_{(s+d)/2}$ values obtained during the first cycle are plotted in Figures 9.13 and 9.14 (hollow diamonds) for comparison. Parameter values for the additional model parameters from the BH-Exp model (Equation 9.3) are similar to those reported for initial sorption (cf. Figures 9.10 – 9.12), and are not included.

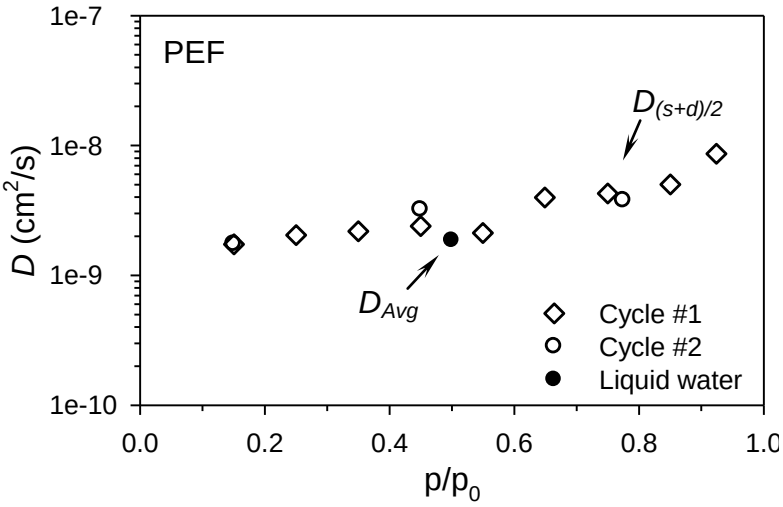

Figure 9.13. Diffusion coefficients for water in PEF at 35°C. Data for the first sorption cycle (hollow diamonds) and second sorption cycle (hollow circles) represent values of $D_{(s+d)/2}$, while the solid circle represents D_{Avg} measured during sorption from 0 – 1 activity. Values are plotted at the midpoint of their respective activity intervals.

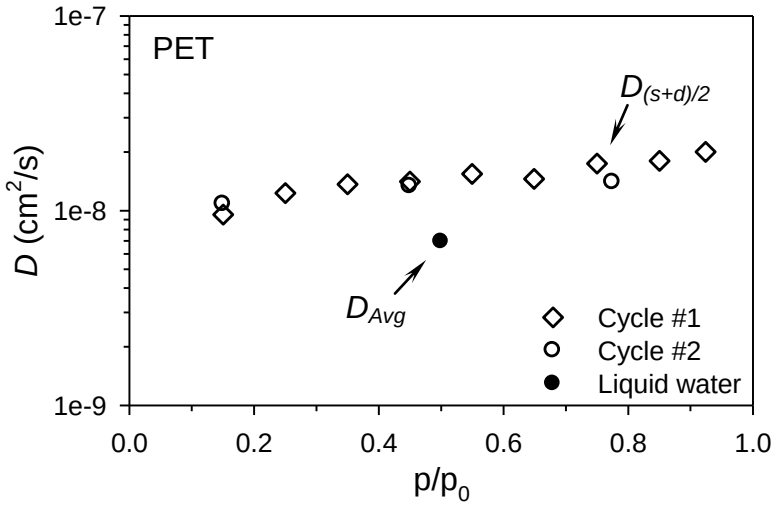

Figure 9.14. Diffusion coefficients for water in PET at 35°C. Data for the first sorption cycle (hollow diamonds) and second sorption cycle (hollow circles) represent values of $D_{(s+d)/2}$, while the solid circle represents D_{Avg} measured during sorption from 0 – 1 activity. Values are plotted at the midpoint of their respective activity intervals.

Inspection of the diffusion coefficients in Figures 9.13 and 9.14 reveals excellent reproducibility between the average values during sorption/desorption for both the initial and subsequent sorption cycles. Not shown in Figures 9.13 and 9.14 are the separate

diffusion coefficients obtained during sorption and subsequent desorption during the second sorption cycle. In fact, these respective values for both polyesters exhibited much closer agreement than the sorption/desorption values during the initial sorption cycle reported in Figures 9.6 and 9.7. This notion is consistent with the work of Berens [35], who hypothesized that the diffusion coefficients obtained during sorption and desorption would eventually converge if enough sorption cycles were performed.

As mentioned previously, uptake experiments at unit activity were performed using a gravimetric liquid water method. Kinetic uptake curves resulting from this method were predominantly Fickian despite the high activity of water, due to the thickness of the films needed to ensure long, experimentally accessible timescales for diffusion. Correspondingly, Deborah numbers (*De*) for both polyesters were significantly less than unity (i.e., $De \approx 0.04$ for PEF, $De \approx 0.03$ for PET), so the appearance of Fickian kinetics is not surprising. Kinetic uptake curves representing data from four separate sorption experiments are provided in Figure 9.15 (a) for PEF and (b) for PET, and are plotted versus a non-dimensional time $(D_{Avg}t/l^2)^{1/2}$ to normalize differences in film thickness. Values for the diffusion coefficient measured during sorption (D_{Avg}) are provided for both polyesters in Figures 9.13 and 9.14 via the filled circles, and are plotted at the midpoint of the sorption interval (0.5 activity).

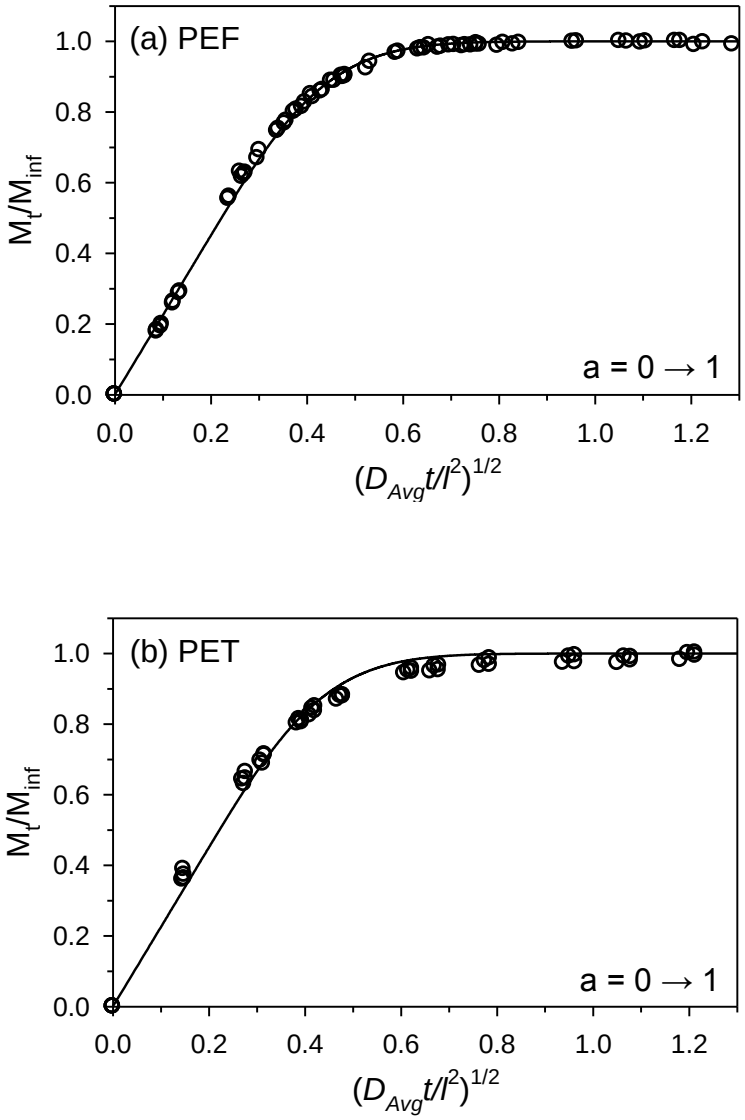

Figure 9.15. Kinetic sorption data during sorption between 0 – 1 activity for water at 35°C in PEF (a) and PET (b). Lines represent the Fickian model fit from Equation 2.47, and corresponding D_{Avg} values for PEF and PET plotted in Figures 9.13 and 9.14, respectively. Both (a) and (b) reflect normalized data from four separate sorption experiments.

The value of D_{Avg} plotted in Figure 9.13 (filled circle) for PEF exhibits excellent agreement with the corresponding diffusion coefficients measured from the automated VTI instrument. However, the respective value for PET plotted in Figure 9.14 (filled circle) is slightly lower than the values measured from the VTI instrument. Diffusion coefficients measured at unit activity in the literature for amorphous PET are somewhat

varied [34, 39, 40], but are similar in magnitude to the value reported in the current study.

9.3.4. Transport Energetics

In addition to the above measurements at 35°C, kinetic uptake curves were also measured at 15, 25, and 45°C between the activity interval 0.1 – 0.2 for both polyesters. Equilibrium uptake data at 0.2 activity for all four temperatures are presented in Chapter 8, which also reports estimates for the apparent enthalpy of sorption for water in both polyesters. Measurements were performed between 0.1 – 0.2 activity to ensure simple Fickian diffusion (ϕ_F = 1) and to avoid large values of τ_S (discussed previously) associated with the sorption interval starting from zero. The resulting kinetic uptake curves were predominantly Fickian, with correspondingly small values of τ_S consistent with those reported in Figure 9.12. The temperature dependence of the diffusion coefficients can be described via the Arrhenius representation in Equation 2.12 (discussed previously). Values of D_{Avg} measured at 15, 25, 35, and 45°C are plotted in semi-logarithmic form in Figure 9.16 for both PEF (diamonds) and PET (circles). The lines represent the corresponding fits from Equation 2.12, and the uncertainty limits for E_D are taken from the standard error of the model fits.

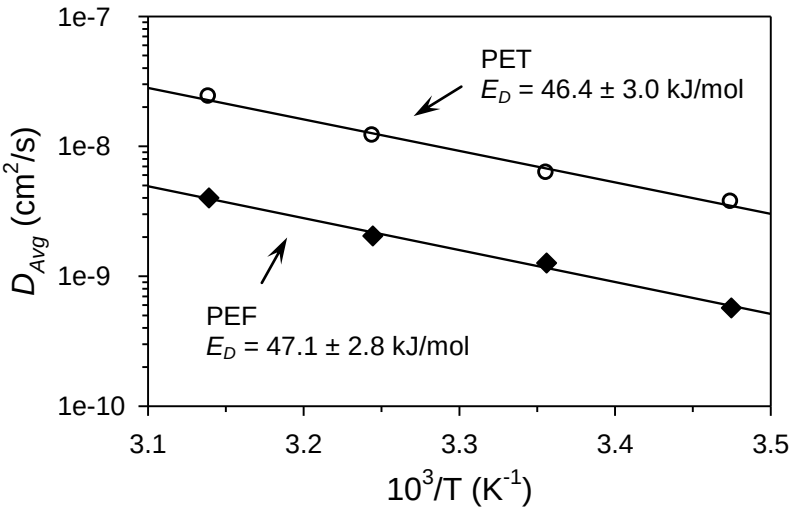

Figure 9.16. Temperature-dependent diffusion coefficients for PEF (diamonds) and PET (circles) measured during sorption between 0.1 – 0.2 activity. Lines reflect model fits from Equation 2.12.

Excellent linearity is observed in the Arrhenius model fits in Figure 9.16, thereby giving confidence to the E_D values of 47.1 ± 2.8 kJ/mol for PEF and 46.4 ± 3.0 kJ/mol for PET. Values of E_D reported in the literature for water diffusion in both semicrystalline and amorphous PET are similar to those reported in the current work for amorphous PET [34, 40-42], while no additional data exists in the literature for PEF. Quick inspection of the E_D values for PEF and PET in Figure 9.16 reveals a slightly higher value for PEF; however, the uncertainty limits result in statistically indistinguishable values for both polyesters. The E_D values shown in Figure 9.16 for water diffusion reveal distinct similarity to the respective E_D values for oxygen diffusion in both polyesters from Chapter 6. Such behavior is consistent with the work of Yasuda and Stannett, who reported similar E_D values for water and oxygen in the same polymer for rubber hydrochloride, PET, ethyl cellulose, and polypropylene [41]. Estimates for the activation entropies of water diffusion in PET and PEF are provided later in Appendix F.

Values of the effective enthalpy of water sorption (ΔH_S) for both polyesters are

estimated in Chapter 8, and reflect values of -47.5 ± 0.6 kJ/mol for PEF and -47.0 ± 0.6 kJ/mol for PET. Combination of the enthalpy of sorption with the activation energy of diffusion for both polyesters yields an estimate for the effective activation energy of permeation (E_P), which can be calculated via Equation 2.19 (discussed previously). Estimates of E_P for water in PEF and PET are provided in Table 9.1, where the uncertainty limits originate from the standard error of the fit.

Table 9.1. Transport energetics for water in PEF and PET. Values of ΔH_S are reproduced from Chapter 8.

	E_D (kJ/mol)	ΔH_S (kJ/mol)	E_P (kJ/mol)
PEF	47.1 ± 2.8	-47.5 ± 0.6	-0.4 ± 2.8
PET	46.4 ± 3.0	-47.0 ± 0.6	-0.6 ± 3.1

Values of E_P reported in Table 9.1 exhibit small values close to zero, thereby reflecting a weak temperature dependence for water permeability in both polyesters over the measured activity range (0.1 – 0.2). Similar E_P values for semicrystalline PET are reported in the literature [43, 44]. As a reminder, the E_P values for both polyesters reported in Table 9.1 are first estimates, and will ideally be validated in the future by independent permeation tests.

9.4. Summary and Conclusions

The current chapter investigates the kinetic uptake properties of water in amorphous PEF and PET across the entire water activity interval at 35°C, and complements the work in Chapter 8 which investigates the corresponding equilibrium uptake properties at the

same conditions. Similar to Chapter 8, uptake data were measured using three independent methodologies. Excellent agreement was observed between all three methodologies, thereby providing a consistency check for the reported data.

Simple Fickian behavior was observed for water diffusion in both polyesters up to ~0.6 activity, after which the presence of non-Fickian relaxations required treatment with the Berens-Hopfenberg model. Anomalous curvature was introduced in all uptake data measured by the automated VTI instrument due to lag introduced by the control scheme. Such anomalous behavior was successfully accounted for via implementation of the formal diffusion model proposed by Long and Richman [19]; however, the physical significance of the parameters are totally different in the two cases. In fact, the use of the Long and Richman model in the present case is simply for the sake of convenience, while the coefficients in the original Long and Richman work related to actual molecular relaxation times.

Both polyesters exhibited a positive correlation between diffusion coefficient and increasing concentration over the entire concentration range. Diffusion coefficient data between 0 – 0.6 activity can be described using the partial immobilization model (cf. Appendix D), after which positive deviations from dual mode behavior indicate the likely presence of plasticization. Permeation experiments, which were not conducted in this study, are ultimately needed to further verify the presence of either plasticization or clustering at high activity in both polyesters.

PEF exhibits a significantly reduced water diffusion coefficient of ~5X averaged over the entire concentration range compared to PET at 35°C. The reduction in diffusion coefficient for PEF vs. PET originates from the reduction in segmental mobility due to

the non-symmetrical furan ring in PEF compared to the symmetrical phenyl ring in PET [5]. Additionally, the added polarity of the furan ring in PEF imparts the increased equilibrium water solubility of ~1.8X averaged over the entire concentration range compared to PET. The respective increase in solubility and decrease in diffusivity for water in PEF vs. PET can be combined using the common relationship $P = DS$ to provide a permeability comparison for both polyesters. Multiplication of the aforementioned parameters yields an average permeability reduction of ~2.8X for water in PEF compared to PET at 35°C over the entire concentration interval. This value is similar to the ~2X permeability reduction for PEF vs. PET reported by Avantium [15]. The permeability reduction for water reported in the current chapter complements the significant permeability reductions for oxygen and carbon dioxide discussed in Chapters 6 and 7, respectively, and further confirms the notion that PEF can potentially serve as a viable alternative to PET in the beverage container market. This chapter, in combination with Chapter 8, provides the first detailed investigation of water transport in PEF.

9.5. References

1. Hodge RM, Bastow TJ, Edward GH, Simon GP, and Hill AJ. Free Volume and the Mechanism of Plasticization in Water-Swollen Poly(vinyl alcohol). Macromolecules 1996;29(25):8137-8143.

2. Bastioli C, Guanella I, and Romano G. Effects of water sorption on the physical properties of PET, PBT, and their long fibers composites. Polymer Composites 1990;11(1):1-9.

3. Mali S, Sakanaka LS, Yamashita F, and Grossmann MVE. Water sorption and mechanical properties of cassava starch films and their relation to plasticizing effect. Carbohydrate Polymers 2005;60(3):283-289.

4. Lahokallio S, Saarinen K, and Frisk L. Changes in water absorption and modulus of elasticity of flexible printed circuit board materials in high humidity testing.

Microelectronics and Packaging Conference (EMPC), 2011 18th European, 2011. pp. 1-6.

5. Burgess SK, Leisen JE, Kraftschik BE, Mubarak CR, Kriegel RM, and Koros WJ. Chain Mobility, Thermal, and Mechanical Properties of Poly(ethylene furanoate) Compared to Poly(ethylene terephthalate). Macromolecules 2014;47(4):1383-1391.

6. Gruter G-JM, Sipos L, and Adrianus Dam M. Accelerating research into bio-based FDCA-polyesters by using small scale parallel film reactors. Combinatorial Chemistry & High Throughput Screening 2012;15(2):180-188.

7. Gandini A, Silvestre AJD, Neto CP, Sousa AF, and Gomes M. The furan counterpart of poly(ethylene terephthalate): An alternative material based on renewable resources. Journal of Polymer Science Part A: Polymer Chemistry 2009;47(1):295-298.

8. Gomes M, Gandini A, Silvestre AJD, and Reis B. Synthesis and characterization of poly(2,5-furan dicarboxylate)s based on a variety of diols. Journal of Polymer Science Part A: Polymer Chemistry 2011;49(17):3759-3768.

9. Papageorgiou GZ, Tsanaktsis V, and Bikiaris DN. Synthesis of poly(ethylene furandicarboxylate) polyester using monomers derived from renewable resources: thermal behavior comparison with PET and PEN. Physical Chemistry Chemical Physics 2014;16:7946-7958.

10. Knoop RJI, Vogelzang W, van Haveren J, and van Es DS. High molecular weight poly(ethylene-2,5-furanoate); critical aspects in synthesis and mechanical property determination. Journal of Polymer Science Part A: Polymer Chemistry 2013;51(19):4191-4199.

11. Gopalakrishnan P, Narayan-Sarathy S, Ghosh T, Mahajan K, and Belgacem M. Synthesis and characterization of bio-based furanic polyesters. Journal of Polymer Research 2013;21(1):1-9.

12. Tonelli AE. PET versus PEN: what difference can a ring make? Polymer 2002;43(2):637-642.

13. Rueda DR and Varkalis A. Water Sorption/Desorption Kinetics in Poly(Ethylene Naphthalene-2,6-Dicarboxylate) and Poly(Ethylene Terephthalate). Journal of Polymer Science Part B: Polymer Physics 1995;33:2263-2268.

14. Rueda DR, Viksne A, Kajaks J, Balta-Calleja FJ, and Zachmann HG. Properties of arylpolyesters with reference to water content. Macromolecular Symposia 1995;94(1):259-268.

15. Avantium - PEF bottles. http://avantium.com/yxy/products-applications/fdca/PEF-bottles.html.

16. Burgess SK, Karvan O, Johnson JR, Kriegel RM, and Koros WJ. Oxygen Sorption

and Transport in Amorphous Poly(ethylene furanoate). Polymer 2014;55(18):4748-4756.

17. Chandra P and Koros WJ. Sorption and transport of methanol in poly(ethylene terephthalate). Polymer 2009;50:236-244.

18. Chandra P and Koros WJ. Sorption of lower alcohols in poly(ethylene terephthalate). Polymer 2009;50:4241-4249.

19. Long FA and Richman D. Concentration Gradients for Diffusion of Vapors in Glassy Polymers and their Relation to Time Dependent Diffusion Phenomena1,2. Journal of the American Chemical Society 1960;82(3):513-519.

20. Crank J. The Mathematics of Diffusion, 2nd ed.: Oxford Science Publications, 1975.

21. Vrentas JS, Jarzebski CM, and Duda JL. A Deborah number for diffusion in polymer-solvent systems. AIChE Journal 1975;21(5):894-901.

22. Potreck J, Uyar F, Sijbesma H, Nijmeijer K, Stamatialis D, and Wessling M. Sorption induced relaxations during water diffusion in S-PEEK. Physical Chemistry Chemical Physics 2009;11(2):298-308.

23. Sun Y-M. Sorption/desorption properties of water vapour in poly(2-hydroxyethyl methacrylate): 2. Two-stage sorption models. Polymer 1996;37(17):3921-3928.

24. Detallante V, Langevin D, Chappey C, Métayer M, Mercier R, and Pinéri M. Kinetics of water vapor sorption in sulfonated polyimide membranes. Desalination 2002;148(1–3):333-339.

25. Williams JL, Hopfenberg HB, and Stannett V. Water transport and clustering in poly[vinyl cloride], poly[oxymethylene], and other polymers. Journal of Macromolecular Science, Part B 1969;3(4):711-725.

26. Wellons JD and Stannett V. Permeation, sorption, and diffusion of water in ethyl cellulose. Journal of Polymer Science Part A-1: Polymer Chemistry 1966;4(3):593-602.

27. Schult KA and Paul DR. Water sorption and transport in blends of poly(vinyl pyrrolidone) and polysulfone. Journal of Polymer Science Part B: Polymer Physics 1997;35(4):655-674.

28. Schult KA and Paul DR. Water sorption and transport in a series of polysulfones. Journal of Polymer Science Part B: Polymer Physics 1996;34(16):2805-2817.

29. Okamoto K-I, Tanihara N, Watanabe H, Tanaka K, Kita H, Nakamura A, Kusuki Y, and Nakagawa K. Sorption and diffusion of water vapor in polyimide films. Journal of Polymer Science Part B: Polymer Physics 1992;30(11):1223-1231.

30. Petropoulos JH, Sanopoulou M, and Papadokostaki KG. Beyond Fick: How Best to Deal with non-Fickian Behavior in a Fickian Spirit. Diffusion Fundamentals 2009;11:1-21.

31. Dhoot SN, Freeman BD, Stewart ME, and Hill AJ. Sorption and transport of linear alkane hydrocarbons in biaxially oriented polyethylene terephthalate. Journal of Polymer Science Part B: Polymer Physics 2001;39(11):1160-1172.

32. Dhoot SN, Freeman BD, and Stewart ME. Sorption and Transport of Linear Esters and Branched Alkanes in Biaxially Oriented Poly(ethylene terephthalate). Industrial & Engineering Chemistry Research 2004;43(12):2966-2976.

33. Schult KA and Paul DR. Water sorption and transport in blends of polyethyloxazoline and polyethersulfone. Journal of Polymer Science Part B: Polymer Physics 1997;35(6):993-1007.

34. Park H. Characterization of Moisture Diffusion into Polymeric Thin Film. Experimental Mechanics 2013;53(9):1693-1703.

35. Berens AR. Effects of sample history, time, and temperature on the sorption of monomer vapor by PVC. Journal of Macromolecular Science, Part B 1977;14(4):483-498.

36. Bagley E and Long FA. Two-stage Sorption and Desorption of Organic Vapors in Cellulose Acetate1,2. Journal of the American Chemical Society 1955;77(8):2172-2178.

37. Burgess SK, Mikkilineni DS, Yu DB, Kim DJ, Mubarak CR, Kriegel RM, and Koros WJ. Water Sorption in Poly(ethylene furanoate) Compared to Poly(ethylene terephthalate). Part 1: Equilibrium Sorption. Polymer 2014;55(26):6861-6869.

38. Berens AR and Hopfenberg HB. Diffusion and relaxation in glassy polymer powders: 2. Separation of diffusion and relaxation parameters. Polymer 1978;19(5):489-496.

39. Langevin D, Grenet J, and Saiter JM. Moisture Sorption in PET: Influence on the Thermokinetic Parameters. European Polymer Journal 1994;30(3):339-345.

40. Launay A, Thominette F, and Verdu J. Water sorption in amorphous poly(ethylene terephthalate). Journal of Applied Polymer Science 1999;73(7):1131-1137.

41. Yasuda H and Stannett V. Permeation, Solution, and Diffusion of Water in Some High Polymers. Journal of Polymer Science 1962;57:907-923.

42. Henry BM, Erlat AG, McGuigan A, Grovenor CRM, Briggs GAD, Tsukahara Y, Miyamoto T, Noguchi N, and Niijima T. Characterization of transparent aluminium oxide and indium tin oxide layers on polymer substrates. Thin Solid Films 2001;382(1–2):194-201.

43. Thornton ER, Stannett V, and Szwarc M. The permeation of vapors and liquids through polymer films. Journal of Polymer Science 1958;28(117):465-468.

44. Hubbell WH, Brandt H, and Munir ZA. Transient and steady-state water vapor permeation through polymer films. Journal of Polymer Science: Polymer Physics Edition 1975;13(3):493-507.

CHAPTER 10

PHYSICAL AGING IN PEF: DSC, DENSITY, AND OXYGEN TRANSPORT[1]

This chapter continues the investigation of poly(ethylene furanoate) (PEF) by utilizing three separate techniques to study the physical aging process of the amorphous glass. Differential scanning calorimetry (DSC) aging experiments were conducted at multiple aging temperatures and times, and the resultant enthalpic recovery values compared to the theoretical maximum enthalpy loss evaluated from calculations involving extrapolation of the equilibrium liquid line. Density measurements reveal densification of the matrix for the aged vs. unaged samples, and provide an estimate for the reduction in free volume for the aged samples. Furthermore, complementary oxygen permeation and pressure-decay sorption experiments provide independent verification of the free volume reduction mechanism for physical aging in glassy polymers.

10.1. Introduction

Physical aging in glassy polymers is defined as the temperature and time-dependent approach of the material properties (enthalpy, specific volume, dielectric, and mechanical properties) from a non-equilibrium excess state towards a stabilized equilibrium state [1]. Such property changes, altered via physical aging, can be reversed by heating through the glass transition temperature (T_g), and thereby differ from the permanent changes induced by chemical aging. Understanding the physical aging process is an important topic of

[1]Reprinted in part from *Journal of Polymer Science Part B: Polymer Physics*, 53/6, Burgess, S.K.; Mubarak, C.R..; Kriegel, R.M.; Koros, W.J., *Physical Aging in Amorphous Poly(ethylene furanoate): Enthalpic Recovery, Density, and Oxygen Transport Considerations*, 389–399, Copyright 2014, with permission from John Wiley & Sons.

research, since numerous industrially relevant polymers have end-use applications below T_g. One example of a recently introduced engineering thermoplastic is poly(ethylene furanoate) (PEF), which is a bio-sourced polyester with improved barrier, mechanical, and thermal properties compared to poly(ethylene terephthalate) (PET) [2, 3]. Despite the importance and promise of PEF, there exist no physical aging data yet in the literature. Such information is needed, and will help facilitate integration of PEF into the polyester market.

Aging properties of glassy polymers can be studied using multiple techniques, including enthalpic recovery via differential scanning calorimetry (DSC) [4-7], dielectric spectroscopy [8, 9], transport testing [10-13], and mechanical methods [14, 15], among others. Enthalpic recovery measurements via DSC are perhaps the most convenient to perform, since aging and thermal cycling of the sample can be conducted accurately *in situ* within the DSC. Moreover, the enthalpic recovery induced by aging at some sub-T_g temperature is only an indirect measurement of the physical aging process [16]. Direct measurement is possible using volumetric measurements (e.g., density and specific volume), which can detect the densification of the glassy matrix resulting from the aging process. Furthermore, the reduction in specific volume and free volume associated with aging have direct and well correlated implications regarding penetrant transport [17].

The data reported in this chapter complement our prior work regarding various aspects of PEF compared to PET, such as fundamental chain mobility (Chapter 5), oxygen sorption and transport (Chapter 6), carbon dioxide sorption and transport (Chapter 7), and equilibrium and kinetic water sorption (Chapters 8 and 9, respectively). The current work utilizes a three pronged approach to study the physical aging process in

amorphous PEF. DSC aging experiments are performed at a number of different aging temperatures and aging times, and the corresponding enthalpic recovery values are evaluated and compared to the theoretical maximum enthalpy loss estimated from calculations involving extrapolation of the equilibrium liquid line. Direct verification of matrix densification resulting from aging is evident from specific volume measurements, thereby demonstrating a concurrent reduction in free volume for the aged sample. Furthermore, oxygen was chosen to "probe" the accessible free volume in aged and unaged PEF via complementary permeation and pressure-decay sorption experiments due to oxygen exhibiting minimal interaction with the glassy matrix, as discussed previously in Chapter 6. The independent transport results corroborate the specific volume measurements and provide additional confirmation regarding the free volume reduction mechanism of physical aging in glassy polymers.

The different testing methodologies (i.e., DSC, density, and transport) and the corresponding aging conditions associated with each method are summarized for convenience in Table 10.1, where specific details associated with each methodology are provided in the experimental section. As will be shown, enthalpic aging occurs in parallel with free volume aging, which in turn is reflected in the transport measurements for the aged vs. unaged samples.

Table 10.1. Summary of testing methods and aging conditions for the data reported in this chapter. Additional details are provided in Section 10.2.

Differential scanning calorimetry (DSC)	
Unaged	Measured by the DSC instrument concurrently with data for the aged samples
Aged	Samples aged *in situ* at 65, 70, 75, 78, and 81°C for time periods ranging from 0 ~ 1 day
Density	
Unaged	Measured in a density gradient column concurrently with the aged samples
Aged	Measured after aging in an oven at 65°C for greater than the max DSC aging time
Oxygen permeation	
Unaged	Measured at 35°C
Aged	Re-measured at 35°C after aging for ~4.5 days at 45°C and ~3.5 days at 55°C
Oxygen sorption	
Unaged	Measured at 35°C
Aged	Re-measured at 35°C after aging for ~17 days at 45°C, ~24 days at 55°C, and 12 days at 65°C

10.2. Experimental Methods

10.2.1. Materials and Film Preparation

The poly(ethylene furanoate) (PEF) and poly(ethylene terephthalate) (PET) polymers used in this chapter are the same materials described previously in Section 3.1.1, and all amorphous films were melt-pressed using the method in Section 3.1.3. All transport and aging measurements reported herein for PEF and PET reflect data corresponding to the amorphous morphology.

10.2.2. Differential Scanning Calorimetry

Heat capacity curves were measured via differential scanning calorimetry (DSC) using a TA Q1000 DSC, which was previously calibrated using indium and sapphire

standards according to the method provided by TA Instruments. Each heat capacity measurement was recorded using ~10 mg of amorphous PEF film crimped into an aluminum sample pan (Perkin Elmer part # 02190041). The common convention of heating a glassy polymer to T_g + 50°C in order to erase the prior thermal history [18] could not be applied in the current work due to the semicrystalline nature of PEF. Fortunately, PEF crystallizes slowly when cooled from the melt [19] and can be quenched in the amorphous, glassy state using the cooling rates accessible to the Q1000 DSC. Fresh sample pans were prepared and utilized for measurement at each respective aging temperature (T_a) and aging time (t_a) to avoid excessive degradation at high temperature due to repeated thermal cycling. The amorphous PEF films were dried overnight at 35°C under vacuum prior to loading into the sample pans, and all DSC measurements were conducted in the presence of a dry nitrogen purge.

All samples were aged within the DSC instrument and tested according to the method provided in Table 10.2. The first temperature ramp step in Table 10.2 involves heating the sample to 300°C to erase the prior thermal history of the sample, followed by cooling at 30°C/min to 0°C. Due to the slow crystallization kinetics of PEF, the latter step quenches the material into an amorphous glass. Evidence for the amorphous nature of the quenched material is observed directly in the thermogram by the absence of a crystallization peak upon cooling from the melt, and a lack of melting peak upon subsequent re-heating to the melt. After cooling to 0°C, the sample is then re-heated to 300°C to provide the heat capacity baseline corresponding to zero aging during the previous cooling step (i.e., t_a = 0). This baseline provides a direct comparison to the heat capacity curve for the aged sample, which is measured in subsequent steps. After heating to 300°C (step 10, Table

10.2), the sample is then cooled to the aging temperature (T_a) and held isothermally at T_a for a discrete aging time (t_a) before cooling to 0°C. The final subsequent heating step to 300°C then measures the heat capacity curve corresponding to the previous aging conditions. The method outlined in Table 10.2 was chosen to enhance reproducibility in the measured data and to enable meaningful comparisons between data measured at different aging times and temperatures. Data collection was turned off during the isothermal aging period to avoid creation of unmanageably large file sizes, especially for experiments involving extended aging times.

Table 10.2. DSC method used to study the enthalpic recovery process in amorphous PEF.

Objective	Step #	Step description
Erase prior thermal history in the film sample	1	Equilibrate at 40°C
	2	Data storage: On
	3	Ramp 20°C/min to 300°C
	4	Data storage: Off
	5	Isothermal for 1 min
	6	Data storage: On
	7	Ramp 30°C/min to 0°C
	8	Isothermal for 1 min
	9	Mark end of cycle
Measure ***unaged*** heat capacity	10	Ramp 20°C/min to 300°C
Age at T_a°C for t_a minutes	11	Data storage: Off
	12	Isothermal for 1 min
	13	Ramp 30°C/min to T_a (aging temp)
	14	Isothermal for t_a (aging time)
	15	Ramp 30°C/min to 0°C
	16	Isothermal for 1 min
Measure ***aged*** heat capacity	17	Data storage: On
	18	Ramp 20°C/min to 300°C
	19	End of method

A cooling rate of 30°C/min was chosen to provide a compromise between instrument capability and sample history reproducibility. The maximum cooling rate for this instrument between 300 – 0°C was experimentally observed to be on the order of 40°C/min. Higher cooling rates resulted in loss of temperature control at the low end of the specified range. Alternatively, very low cooling rates (i.e., <10°C/min) could allow PEF crystallization during cooling from the melt. The chosen value of 30°C/min allowed accurate, reproducible temperature control between different samples, while cooling at a

fast enough rate to avoid crystallization.

Aging temperatures (T_a) of 65, 70, 75, 78, and 81°C were chosen below the T_g of amorphous PEF (85°C, measured in Chapter 5 via the midpoint in C_p between the extrapolated liquid and glassy tangents); however, lower temperatures were not tested due to experimentally inaccessible time-scales of aging. Corresponding aging times (t_a) of 1.5, 3, 5.5, 10, 17, 30, 60, 125, 240, 475, 950, and 1500 min were studied at each of the aforementioned aging temperatures to study the evolution of the enthalpic relaxation peak as a function of aging time. Aging measurements for each time/temperature combination were duplicated using fresh samples to verify reproducibility of the reported data. Consequently, each aging data point in the current work reflects an independent measurement performed on a separate sample.

10.2.3. Density Measurement

Density values were measured after 20 minutes from introduction into the column, as described previously in Chapter 3. Accurate density measurement of the amorphous PEF films aged during permeation (~50 μm thick) and sorption testing (~80 μm thick) was not possible after 20 minutes, due to viscous drag or interfacial tension effects in the column resulting from the reduced film thickness required for transport testing. Consequently, a separate amorphous PEF film of ~200 μm thickness was utilized for all density measurements. Aging was induced on the latter sample by placement in an oven at 65°C for 12 days to simulate the thermal treatment experienced by sorption testing, which is discussed in the next section. As a side note, all films used in the current study are well above the ~1 μm "thin film" threshold value, where previous work has shown that glassy

films with thickness values below this limit can age at faster rates than the bulk material [13].

10.2.4. Transport Characterization

Oxygen permeation measurements were recorded at 35°C for unaged, amorphous PEF using a constant-volume, variable pressure system at selected pressures ranging from 1 – 8 atm, where the system details are described in Chapter 3. Permeation data for the *unaged* samples at 35°C (cf. Figure 10.7, discussed later) are reported in Chapter 6, and are reproduced in the current chapter as a direct comparison to data for the *aged* samples. Film samples are identical to those used in Chapter 6, and the data reported in this chapter were measured in conjunction with that from Chapter 6 to ensure a consistent comparison between aged and unaged samples. Film samples were tested sequentially at 35, 45, and 55°C in order of increasing temperature while loaded into the permeation cell during the course of measurement. The exposure time of each film at 45°C was approximately 4.5 days, followed by exposure to 55°C for approximately 3.5 days. After the oxygen permeation data were measured at 55°C, the films were re-tested at 35°C to investigate the cumulative effect of exposure to elevated temperature on the resultant permeation properties. Consequently, the comparison illustrated in the current work is for oxygen permeation at 35°C for the unaged (*before* exposure to 45 and 55°C) and aged (*after* exposure to 45 and 55°C) samples. Replicate measurements were made for the data reported in this chapter.

Oxygen sorption data were measured for amorphous PEF using a constant-volume, pressure-decay apparatus identical to that used in Chapter 6. Data were measured in 1

atm intervals between 0 – 10 atm at 35, 45, 55, and 65°C in order of increasing temperature. Equilibrium sorption values for the unaged samples at 35, 45, 55, and 65°C are reported in Chapter 6, and only the values measured at 35°C are included in the current chapter as a direct comparison to the aged sample data. Similar to the permeation methodology, the films used for sorption testing were aged within the apparatus during sequential testing at elevated temperatures. The exposure time at 45°C was approximately 17 days, followed by exposure at 55°C for ~24 days and exposure at 65°C for ~12 days. After testing oxygen sorption at 65°C, sorption was retested at 35°C to investigate the cumulative effect of high temperature exposure on the subsequent sorption properties. The comparison provided in the current chapter reflects oxygen sorption at 35°C for the unaged (*before* exposure to 45, 55, and 65°C) and aged (*after* exposure to 45, 55, and 65°C) samples. Recall that a summary of all testing methodologies and aging conditions utilized in this work is provided in Table 10.1.

10.3. Results and Discussion

10.3.1. Differential Scanning Calorimetry

The enthalpy vs. temperature behavior for glassy polymers is often described by the qualitative diagram in Figure 10.1. The glass transition temperature (T_g) is noted by point *B* in Figure 10.1, and exists at the intersection of the equilibrium liquid line and the glassy line. A typical aging experiment occurs via pathway *ABCD* in Figure 10.1, which depicts the process of cooling a rubbery polymer from above T_g to a defined aging temperature (T_a, point *C*), and subsequently isothermally aging the polymer at T_a for a specified aging time (t_a). The instantaneous structure of the glass during the aging process

can be described by the so-called fictive temperature (T_f) [20], which is observed in Figure 10.1 by the intersection of the extrapolated liquid equilibrium line and the dashed line parallel to the non-equilibrium glassy line originating from point *D*. Given enough time during isothermal aging at T_a, the prior pathway depicted by *ABCD* will proceed to point *E*, which corresponds to the sample achieving the maximum possible enthalpy loss as dictated by the extrapolation of the equilibrium liquid line. As a natural consequence, the value of T_f equals T_a at point *E*.

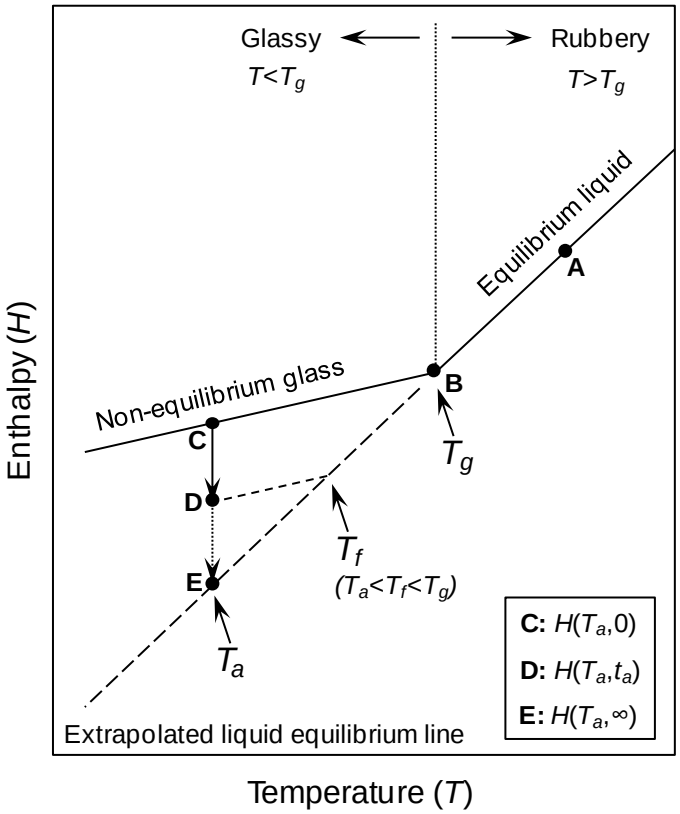

Figure 10.1. Qualitative diagram of enthalpy vs. temperature for a typical glassy polymer.

The modeling framework of Tool-Narayanaswamy-Moynihan (TNM) [20-22] is often used to provide a phenomenological description of the enthalpic aging process. Equations

10.1 and 10.2 illustrate the mechanics of this framework, where ϕ is the non-dimensional enthalpic relaxation function, τ is the characteristic relaxation time, T_f is the fictive temperature (illustrated in Figure 10.1), β is the stretching parameter (or non-exponentiality parameter) in the Kohlrausch-William-Watts (KWW) function [23], A is the pre-exponential factor, x is the non-linearity parameter, R is the universal gas constant, and Δh^* is the apparent activation energy of the glass transition.

$$\phi(t) = \exp\left[-\left(\int_0^t \frac{\mathrm{d}t}{\tau}\right)^{\beta}\right] \tag{10.1}$$

$$\tau = A\exp\left(\frac{x\Delta h^*}{RT} + \frac{(1-x)\Delta h^*}{RT_f}\right) \tag{10.2}$$

Equations 10.1 and 10.2 take into account both the non-exponentiality and non-linearity of the structural recovery process. While multiple authors have noted shortcomings of the TNM representation [5, 7, 24, 25], it remains probably the most widely adopted model in the literature to date.

Equation 10.3, shown below, can be used to calculate enthalpic recovery values via application to experimental heat capacity data measured using the DSC method in Table 10.2. In Equation 10.3, $\Delta H(T_a, t_a)$ is the enthalpic recovery associated with aging for t_a minutes at temperature T_a, C_p^{aged} is the curve measured upon heating after aging for t_a minutes at temperature T_a, C_p^{unaged} is the reference curve measured upon heating after zero aging, and T_1 and T_2 are temperatures well below and above T_g, respectively. The

value of T_1 was chosen to be 60°C in this context, while T_2 was selected to be approximately 110°C. The method outlined in Table 10.2 was chosen to enhance reproducibility of the C_p baseline between unaged and aged samples; however, a very small baseline offset (on the order of ±0.01 J/g°C) was sometimes observed between the unaged and aged C_p data. For such cases, a correction was employed by vertically shifting the C_p data corresponding to the aged run until the baseline matched that for the unaged data. C_p curves for the respective unaged and aged runs were integrated numerically using the *trapz* function in MATLAB®, and the resultant areas subtracted according to Equation 10.3. Graphical interpretation of Equation 10.3 is provided in Figure 10.2, where the enthalpic recovery resulting from aging is visualized by the difference in areas below the unaged and aged C_p curves (dark gray regions in Figure 10.2).

$$\Delta H\left(T_a, t_a\right) = \int_{T_1}^{T_2} \left(C_p{}^{aged}\left(T_a, t_a\right) - C_p{}^{unaged} \right) \mathrm{d}T \tag{10.3}$$

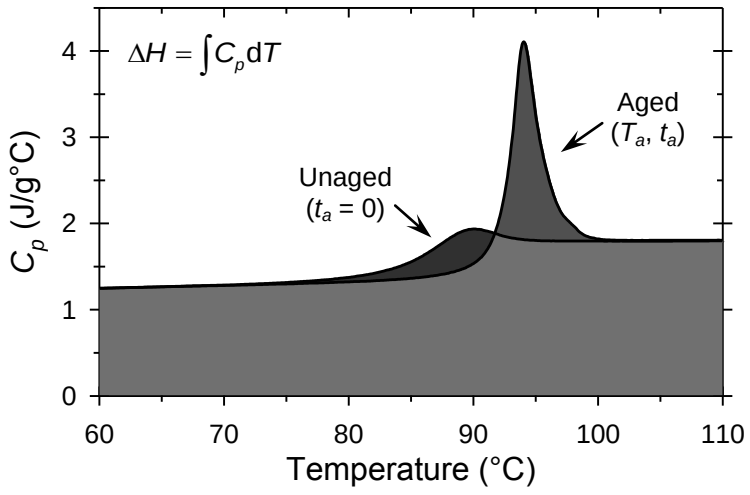

Figure 10.2. Graphical representation of ΔH from Equation 10.3. $\Delta H(T_a,t_a)$ is calculated numerically by the difference in areas corresponding to the two dark gray regions.

Since different PEF samples were used for each respective aging temperature and aging time combination, some minor variability in the C_p baseline is expected across separate runs. As mentioned previously, such variability was removed from the calculation of the enthalpic recovery via measurement of the unaged C_p curve alongside each aged C_p curve. DSC data for various aged samples measured at the same aging temperature can be meaningfully compared after normalization of the data via application of Equation 10.4. Graphing the normalized C_p simply allows for easier comparison between the different sample pans tested at each of the different aging times. Without this small normalization, even small baseline scatter from the different samples would obscure the comparison.

$$C_p{}^N(T) = \frac{C_p(T) - C_{pg}(T_2)}{C_{pl}(T_1) - C_{pg}(T_2)} \tag{10.4}$$

In Equation 10.4, $C_p(T)$ is the experimental heat capacity at temperature T, $C_{pg}(T_1)$ is the glassy heat capacity at T_1 (i.e., 60°C), $C_{pl}(T_2)$ is the liquid heat capacity at T_2 (i.e., ~110°C), and $C_p{}^N(T)$ is the normalized experimental heat capacity which varies from zero to one. Normalized heat capacity data measured at all aging times and temperatures are provided in Figure 10.3, and all ΔH values corresponding to each aging time and temperature are provided in Figure 10.4.

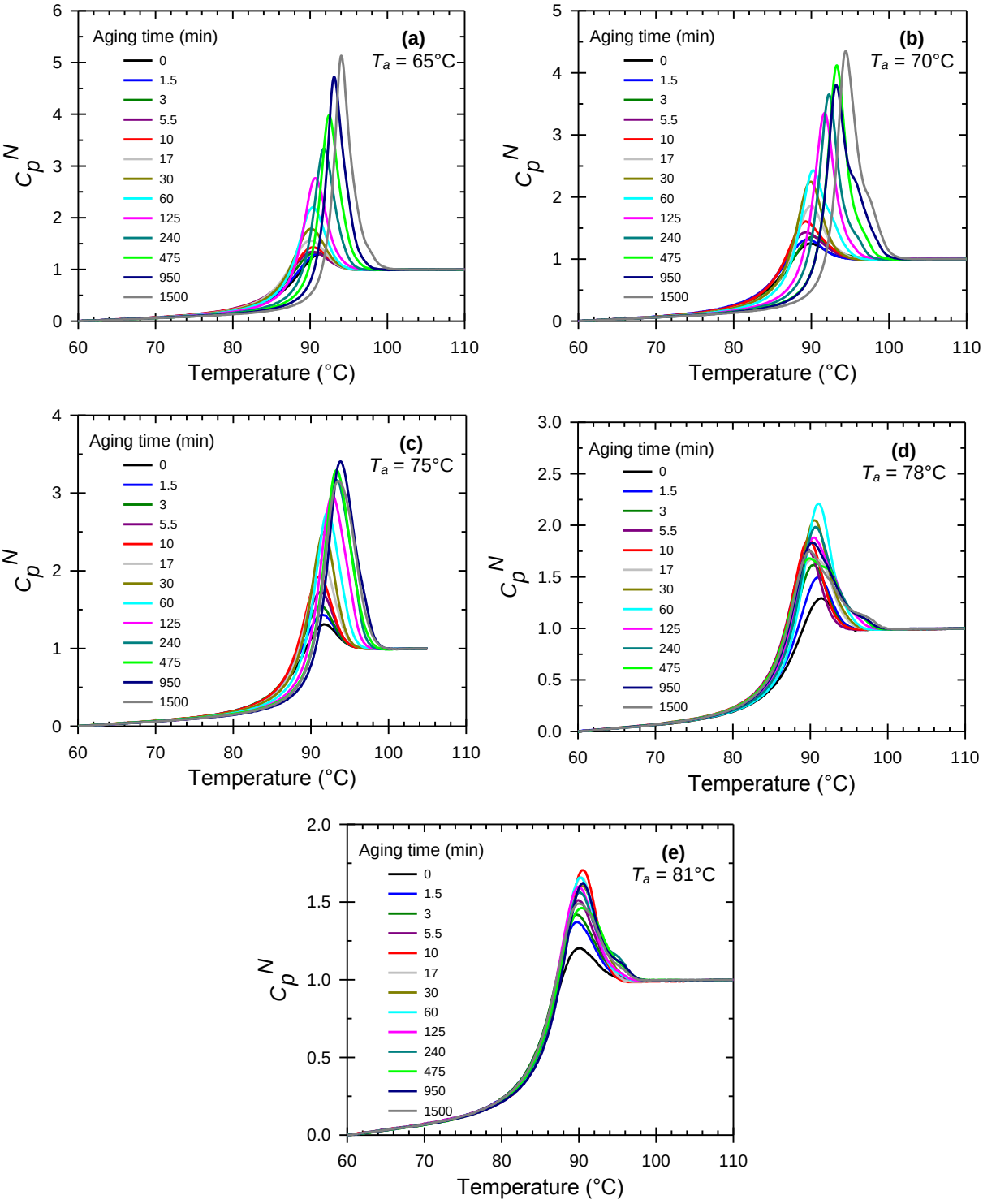

Figure 10.3. Normalized heat capacity (C_p^N) data for amorphous PEF at each respective aging temperature. Each curve in (a) through (e) represents an independent DSC measurement using a fresh sample. View in color for best results.

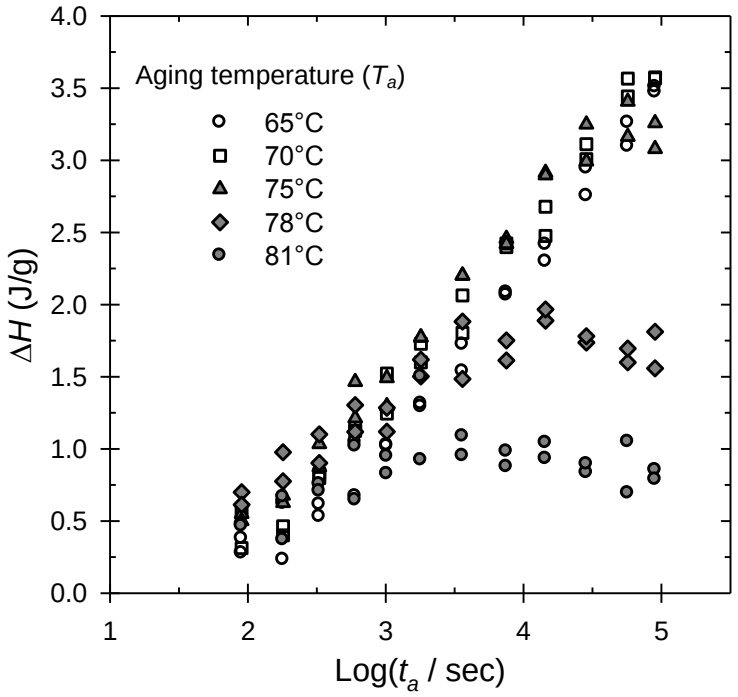

Figure 10.4. Enthalpic recovery data (ΔH) for amorphous PEF measured at various aging temperatures and aging times. Each data point represents an independent DSC test performed using a fresh sample.

In Figure 10.3, the typical behavior signified by an increasing peak height and peak temperature with increasing aging time is observed for plots *a*, *b*, and *c*. Similar behavior has been observed for analogous DSC studies on a wide variety of glassy polymers [1]. Alternatively, plots *d* and *e*, which represent data recorded after aging at the two highest temperatures, exhibit a single main peak at low aging times and a developing shoulder on the high temperature side at long aging times. Some scatter also exists in the peak heights for plots *d* and *e*, resulting in part from the experimental requirement to use separate samples for each respective aging time. The latter notion is also observed in Figure 10.4, which illustrates the application of Equation 10.3 to the curves in Figure 10.3. Multiple peaks and shoulders in the enthalpic recovery landscape have been observed elsewhere in the literature [24, 26-29], and have been attributed to relaxation effects associated with

the breadth of retardation times. Other authors have attributed multiple peaks to the presence of crystallinity [15, 30-32]; however, this explanation is unlikely for the data reported herein due to the verified amorphous morphology.

Examination of Figure 10.4 reveals that the enthalpic recovery values at 75, 78, and 81°C reach a plateau after a certain threshold aging time at the respective temperatures. These enthalpic recovery values can be compared to the theoretical maximum enthalpy loss estimated by the extrapolation of the equilibrium liquid and glass heat capacity lines through the T_g. Equation 10.5 provides an estimate of the theoretical equilibrium enthalpy loss after infinite time ($\Delta H(T_a,\infty)$) [33], where T_a is the aging temperature, T_{fo} is the fictive temperature measured on the unaged sample upon heating through the T_g after previously cooling from the rubbery state at 30°C/min, and ΔC_p provided in Equation 10.6 is the difference in heat capacity between the extrapolated liquid (C_{pl}) and glass (C_{pg}) lines with T in units of °C. A discussion regarding the different methodologies for estimating $\Delta H(T_a,\infty)$ is provided by Koh and Simon [33], and the approximation provided by Equation 10.5 will be proven valid later in the chapter.

$$\Delta H\left(T_a,\infty\right) \approx -\int_{T_{fo}}^{T_a} \Delta C_p \mathrm{d}T \tag{10.5}$$

$$\Delta C_p = \left(C_{pl} - C_{pg}\right) = \left(0.599 - 0.00217T\right) \tag{10.6}$$

The equation for the liquid heat capacity line was estimated to be C_{pl} = (1.617 + 0.00125T), with T in units of °C, via averaging the slope and y-intercepts of at least ten

separate DSC samples during heating from the glass at 20°C/min. The equation for the glassy heat capacity was estimated to be C_{pg} = (1.018 + 0.00342T), with T in units of °C, thereby producing ΔC_p in Equation 10.6 after subtraction from C_{pl}. A temperature range of 30 to 55°C was used for calculating the parameters of the glassy regression, while a range of 120 to 145°C was used for calculating the parameters of the liquid regression. Standard errors on the order of 4×10^{-5} and 0.01 were observed for the slope and y-intercept values, respectively, corresponding to both glassy and liquid regressions. Caveats regarding the measurement of absolute ΔC_p values via DSC are discussed by Badrinarayanan et al. [34]. A value for the fictive temperature during heating can be estimated by the equal areas method proposed by Moynihan [35] in Equation 10.7, where T_1 and T_2 are temperatures well below (55°C) and above (120°C) the T_g, respectively.

$$\int_{T_1}^{T_2}\left(C_p - C_{pg}\right)\mathrm{d}T = \int_{T_{fo}}^{T_2}\left(C_{pl} - C_{pg}\right)\mathrm{d}T \tag{10.7}$$

Estimation of T_{fo} via Equation 10.7 was performed automatically via the Universal Analysis software provided by TA Instruments. A value of 82.2 ± 0.2°C for T_{fo} was estimated by averaging the results from multiple samples. Note that the value of T_{fo}, which was measured during heating, is lower than the estimate for the T_g (i.e., 85°C), which was also measured during heating. This result is not surprising, since the T_g should actually be measured during cooling from the liquid as opposed to the accepted convention of measurement during heating [34, 36]. Glass transition temperatures measured during cooling typically produce values slightly lower than those measured

during subsequent heating [36]. Consequently, usage of the T_g measured during heating in place of T_{fo} in Equation 10.5 can result in slight overestimation of $\Delta H(T_a,\infty)$. A graph of $\Delta H(T_a,\infty)$ from Equation 10.5 vs. aging temperature is provided in Figure 10.5 by the dashed line, where experimental values of $\Delta H(T_a, t_a = 1500$ min) from Figure 10.4 are plotted as hollow circles.

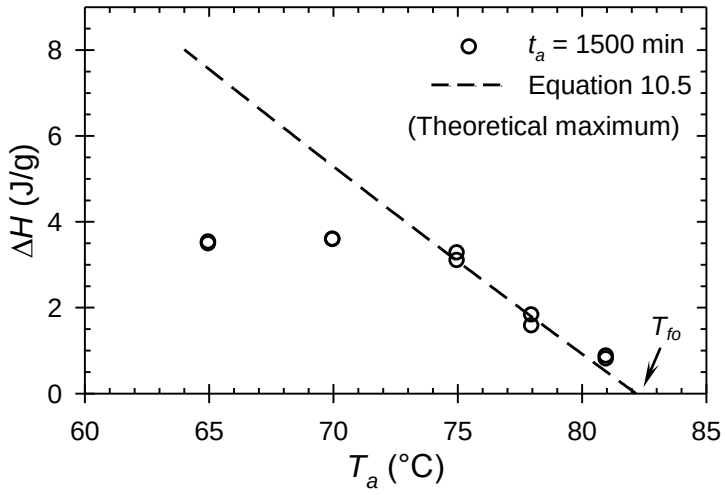

Figure 10.5. Plot of experimental $\Delta H(T_a, t_a = 1500$ min) values from Figure 10.4 at each aging temperature for amorphous PEF. The dashed line represents the equilibrium value of $\Delta H(T_a,\infty)$ estimated from Equation 10.5.

In Figure 10.5, agreement between the dashed line (Equation 10.5) and the experimental enthalpic recovery data at temperatures near T_{fo} suggest that the approximation provided in Equation 10.5 is valid for the current application. It is also not surprising that the equilibrium liquid line was not reached in the short 1500 min time period at 65 or 70°C, which exist approximately 20 and 15°C below the T_g of amorphous PEF. This notion is further observed at 65 and 70°C in Figure 10.4 by the absence of a plateau in ΔH after 1500 min. Koh and Simon [33] report in their study using polystyrene

that time-scales on the order of one year were needed to approach the equilibrium liquid line at 15°C below T_g.

10.3.2. Density and Free Volume

The specific volume vs. temperature behavior for a glassy polymer is commonly depicted by the qualitative diagram in Figure 10.6, and is similar to the enthalpy vs. temperature behavior described previously in Figure 10.1. Recall that the maximum temperature used for oxygen transport testing was 55°C for permeation and 65°C for permeation (cf. Table 10.1). As mentioned previously, the unaged, amorphous PEF samples were initially tested at 35°C, before incrementally increasing the testing temperature up to the aforementioned maximum values. The enthalpic recovery measurements from DSC at 65°C reported in Figure 10.5 reveal that approximately half of the equilibrium recovery is reached after aging for 1500 minutes (~1 day). It is therefore logical that sorption testing at 65°C for 12 days will produce a sample that is closer to the theoretical maximum enthalpy and maximum specific volume loss than the halfway point reported after ~1 day in Figure 10.5. A similar conclusion is reached for the permeation sample which was aged at 55°C during testing for ~3.5 days; however, the extent of aging for this sample is less due to the lower temperature and shorter exposure time at the elevated temperature.

A graphical, idealized specific volume vs. temperature representation of the aging process during transport testing is provided in Figure 10.6. For example, sorption testing was initially performed on unaged PEF at 35°C (i.e., point *A* in Figure 10.6), followed by incrementally increasing the testing temperature to 45°C, 55°C, and finally 65°C before

reducing the temperature back to 35°C (i.e., point *D* in Figure 10.6). Sorption testing at 35°C followed by aging during testing at 65°C can therefore be visualized by pathway *ABC* in Figure 10.6, which neglects any reduction in specific volume at 45 and 55°C for simplicity. It can be assumed, for illustration purposes, that aging at 65°C (pathway *BC*) reaches the extrapolation of the equilibrium liquid line. Cooling to 35°C after sorption testing at 65°C follows pathway *CD*, and final sorption testing at 35°C (point *D*) results in the measurement of transport properties corresponding to the aged sample.

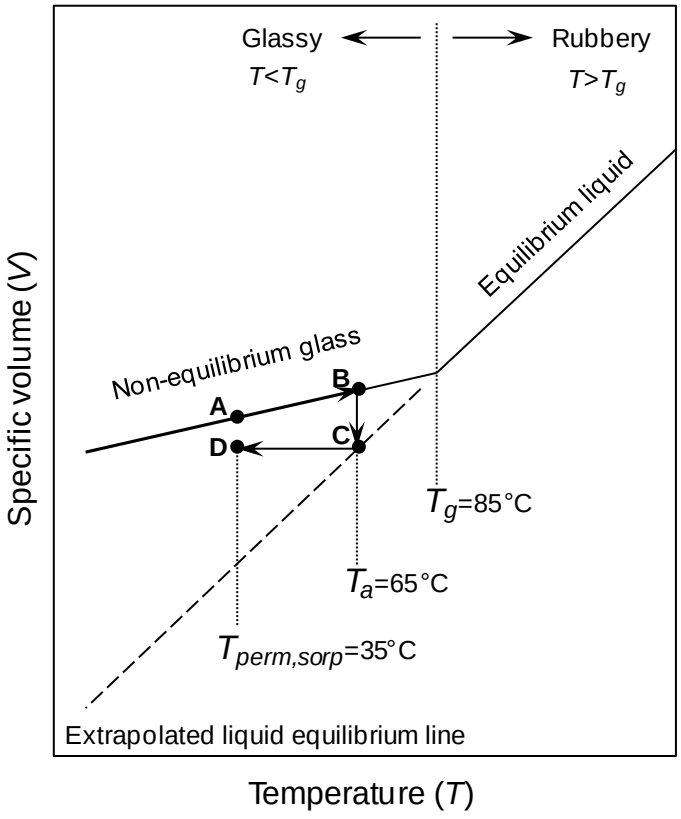

Figure 10.6. Qualitative specific volume vs. temperature behavior for a glassy polymer. Explanation of the figure is provided in the text.

Direct measurement of the specific volume corresponding to points *A* and *D* in Figure 10.6 can be approximated through density measurement at 23°C via density gradient

column. An estimate of the fractional free volume (*FFV*) is provided by Equation 2.40 (discussed previously). As discussed previously, both the permeation and sorption films were too thin to allow accurate density characterization during the 20 minute equilibrium interval in the column. Consequently, density measurements were recorded using a separate amorphous PEF film of ~200 μm thickness. Aging was induced on the latter sample by placement in an oven at 65°C for 12 days to simulate the thermal treatment experienced by sorption testing. Density measurements and *FFV* calculations for the unaged and aged PEF samples are provided in Table 10.3, where the density of the unaged, amorphous PEF exhibits good reproducibility compared to the value reported in Chapter 5.

Table 10.3. Density values at 23°C and free volume calculations for unaged and aged amorphous PEF.

PEF sample	Density (g/cc)	$\hat{V}_g$ (cc/g)	$\hat{V}_0$ (cc/g)	*FFV* (–)
Unaged	1.4308	0.699	0.592[b]	0.153
Aged[a]	1.4338	0.697	0.592[b]	0.151

a: Aged at 65°C in an oven for 12 days.
b: Calculated using Sugden's method [37].

In corroboration of the enthalpic recovery results measured by DSC at 65°C, the reduction in *FFV* reported in Table 10.3 for the aged PEF sample compared to the unaged sample provides evidence that physical aging is indeed occurring during extended thermal treatment at 65°C. Such changes in free volume have direct implications regarding penetrant transport, and a complete discussion regarding this notion is provided in the next section.

10.3.3. Oxygen Transport

A discussion regarding the theory of penetrant transport in glassy polymers is provided in Chapter 2, where Equations 2.26 and 2.28 will be utilized in this chapter. As discussed previously, the time-scale of physical aging increases dramatically as the temperature is reduced further below T_g. While the aging temperatures used in this study (i.e., 55°C for permeation and 65°C for sorption) were low compared to the T_g of 85°C for amorphous PEF [2], densification of the matrix can still occur during the time-scale of transport testing as evidenced by the *FFV* measurements in the prior section. Oxygen permeability data at 35°C for unaged and aged PEF (aged at 55°C) are provided in Figure 10.7, illustrating a ~16% reduction in permeability for the aged sample compared to the unaged sample. Equilibrium O_2 sorption data at 35°C for unaged and aged PEF (aged at 65°C) are provided in Figure 10.8, with the respective dual-mode model parameters listed in Table 10.4. The data corresponding to the unaged PEF samples in Figures 10.7 and 10.8 have been reproduced from Chapter 6, and are included in this chapter to provide a direct comparison to the aged sample data.

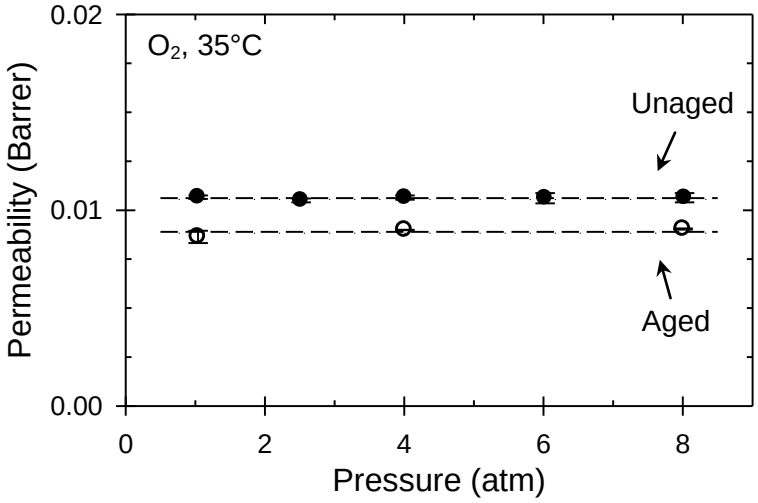

Figure 10.7. Oxygen permeability data for unaged PEF (solid circles) and PEF aged at 55°C (hollow circles). Data corresponding to the filled circles are reproduced from Chapter 6. The dashed horizontal lines represent the average of each respective data set.

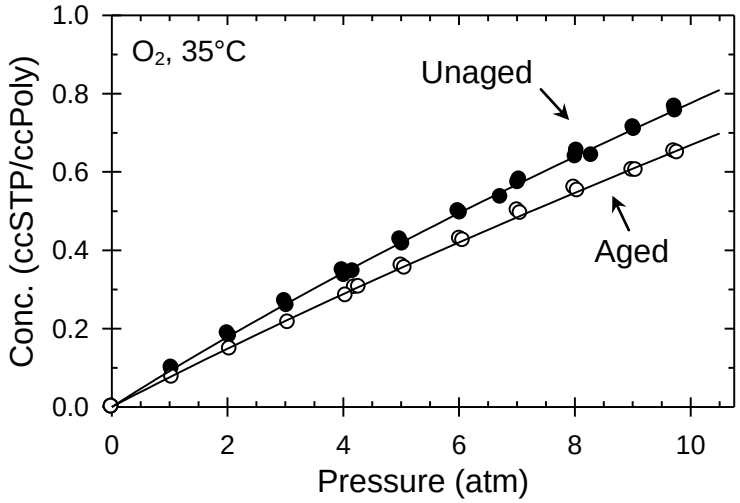

Figure 10.8. Equilibrium O_2 sorption at 35°C for unaged PEF (solid circles) and PEF aged according to the method in Table 10.1 (hollow circles). Lines represent the respective dual-mode model fits. Data corresponding to the filled circles are reproduced from Chapter 6.

Table 10.4. Dual-mode model parameters for oxygen sorption at 35°C in unaged and aged PEF. $k^* = (k_D + C_H'b)$.

PEF	Temp (°C)	k_D (ccSTP/ccPoly·atm)	b (atm^{-1})	C_H' (ccSTP/ccPoly)	k^* (ccSTP/ccPoly·atm)
Unaged[a]	35	0.048	0.054	0.85	0.094
Aged[b]	35	0.047	0.051	0.59	0.077

a: Reproduced from Chapter 6.
b: Aged during sequential sorption testing at 45, 55, and 65°C.

The reduction in permeability and solubility for the aged samples observed in Figures 10.7 and 10.8, respectively, are consistent with the *FFV* result that indicates physical aging is indeed occurring at the elevated temperatures used in this study. In fact, the permeability reduction illustrated in Figure 10.7 can be rationalized when examined within the context of the permeability–FFV correlation proposed by Lee [17] and discussed further by Park and Paul [38]. The transport results in Figures 10.7 and 10.8 also confirm the notion that some degree of aging is inevitable when performing permeation and sorption measurements at elevated temperatures due to the lengthy experiment time required by such techniques.

The mechanism for how aging affects transport in glassy PEF is enlightened through inspection of the dual-mode parameters listed in Table 10.4. From Table 10.4, it is evident that the Langmuir capacity constant C_H' is reduced from 0.85 to 0.59 for the unaged and aged samples, respectively, while the Henry's constant k_D and Langmuir affinity parameter b remain unchanged. In fact, C_H' is a measure of the excess free volume in a glassy polymer [39, 40], and the reduction observed for the aged sample is consistent with the notion that physical aging involves the relaxation of the non-equilibrium *excess* free volume towards an equilibrium state. A reduction in the size or number of Langmuir

microvoids should therefore ideally not affect the Henry's parameter for the dissolved mode or the affinity parameter, since the interactions between oxygen and PEF remain ideally unchanged for both aged and unaged samples [39]. Similar C_H' and b behavior to that in the current work for aged vs. unaged samples has also been observed for oxygen and nitrogen transport in glassy poly(methyl methacrylate) by Hu et al. [41].

Further investigation of the aging mechanism is observed via estimation of k^* from Equation 2.28 by transient permeation measurements on the aged samples. True k_D values from sorption testing on the aged and unaged PEF samples are listed in Table 10.5 along with k^* values for the aged and unaged samples obtained from transient permeation measurements. From Table 10.5, it is evident that the k^* for the aged sample has decreased in magnitude from the value for the unaged sample and is approaching the true k_D value measured from independent sorption measurements. As a reminder, the true k_D values from sorption testing for both the aged and unaged samples are approximately equal due to the negligible effect of aging on the dissolved environment. Oxygen diffusivity estimates from the raw pressure-decay sorption data further reveal that the average diffusion coefficient (averaged over all pressure intervals) is reduced by ~15% for the aged samples when compared to the corresponding value for the unaged samples. The permeability reduction observed in Figure 10.7 for the aged samples therefore results from a concurrent reduction in both oxygen solubility and diffusivity. These results can be ideally rationalized within the framework of the partial immobilization model [42], where specific applications to oxygen transport are described in Chapter 6.

Table 10.5. Sorption coefficients for oxygen at 35°C in amorphous PEF from pressure-decay sorption (k_D) and permeation (k^*).

PEF	k_D (sorption) (ccSTP/ccPoly·atm)	k^* (permeation) (ccSTP/ccPoly·atm)
Unaged[a]	0.048	0.079 ± 0.005
Aged	0.047[b]	0.063 ± 0.004[c]

a: Reproduced from Chapter 6.
b: Aged during sequential sorption testing at 45, 55, and 65°C (cf. Table 10.1).
c: Aged during sequential permeation testing at 45 and 55°C (cf. Table 10.1).

Inspection of Table 10.5 also reveals that the k^* for the aged sample has decreased in magnitude but has not yet reached the true k_D value measured from sorption testing. This observation indicates that while the glass has indeed aged via relaxation of a portion of the non-equilibrium excess free volume, some excess free volume still remains in the glass. A graphical representation of this notion is provided in the idealized specific volume vs. temperature diagram discussed previously in Figure 10.6. Further evidence for the presence of residual excess free volume in the aged sample is observed from sorption measurements by the reduced *but still non-zero* C_H' for the aged sample as noted in Table 10.4. The fact that some excess free volume remains at 35°C is not surprising, especially when considering the extraordinary time-scales needed for aging to occur at temperatures significantly below T_g.

A final note should be mentioned regarding the difference in aging temperatures used for permeation testing (55°C) and sorption testing (65°C). While the aging temperatures were not the same for both methods, the final transport results are indeed complementary. For example, aging at the maximum temperature of 55°C for the permeation-tested samples reduces the oxygen permeability at 35°C when compared to the original permeability at 35°C for the unaged sample. Transient permeation measurements on the

aged samples further reveal a reduction in k^* when compared to the respective value for the unaged samples, and the oxygen diffusion coefficients estimated via pressure-decay sorption reflect a drop in diffusivity for the aged vs. the unaged samples. These observations are consistent with a reduction in free volume for the aged vs. the unaged sample, which was proven to occur in the previous section via experimental density measurements. Alternatively, aging at the maximum temperature of 65°C for the sorption-tested samples produces a reduction in overall oxygen solubility at 35°C for the aged sample compared to the corresponding transport data at 35°C for the unaged sample. This reduction can be further analyzed within the context of the idealized dual-mode model, where reduction in C_H' for the aged sample suggests a decrease in excess free volume when compared to the unaged sample. In conclusion, the oxygen permeation and sorption results reported in the current work provide independent and complementary confirmation regarding the free volume reduction mechanism of physical aging in glassy PEF.

10.4. Summary and Conclusions

Physical aging in amorphous poly(ethylene furanoate) (PEF) was studied using three complementary techniques. Enthalpic recovery experiments were recorded after aging at various temperatures and times using differential scanning calorimetry (DSC). Separate samples were used for each aging temperature/time combination to avoid excessive degradation associated with repeated thermal cycling at elevated temperatures. The resultant heat capacity curves measured during heating through the glass transition temperature after aging were numerically integrated and benchmarked against the

integrated area for the unaged heat capacity curve to provide an estimate for the enthalpic recovery. The latter values corresponding to aging at the maximum time (i.e., 1500 min) were compared to the theoretical maximum enthalpy loss, thereby illustrating that only the three highest aging temperatures (75, 78, and 81°C) reached the theoretical maximum value within the timescale of the measurements.

Density measurements performed on unaged PEF and PEF aged for 12 days at 65°C provide an estimate for the specific volume, which can be used in conjunction with the occupied volume obtained via group contribution methods to estimate the free volume within the glassy matrix. Not surprisingly, specific volume measurements on the aged sample reveal a reduction in free volume when compared to the unaged sample.

Oxygen permeation measurements on aged and unaged PEF reveal a reduction in permeability of ~16% at 35°C for PEF samples sequentially aged at 45 and 55°C. This permeability reduction can be rationalized when examined within the context of the free volume-permeability correlation set forth by Lee [17] and discussed further by Park and Paul [38]. Complementary pressure-decay sorption experiments reveal a reduction in C_H' for the aged vs. the unaged sample, while the additional k_D and b dual mode model parameters remain effectively unchanged. The latter results are fully consistent with the aged sample exhibiting reduced free volume when compared to the unaged sample. The data reported in this chapter provide a first examination of the physical aging properties of amorphous PEF, and further corroborate the notion that physical aging in glassy polymers occurs via the temperature and time dependent reduction in free volume.

10.5. References

1. Hutchinson JM. Physical aging of polymers. Progress in Polymer Science 1995;20(4):703-760.

2. Burgess SK, Leisen JE, Kraftschik BE, Mubarak CR, Kriegel RM, and Koros WJ. Chain Mobility, Thermal, and Mechanical Properties of Poly(ethylene furanoate) Compared to Poly(ethylene terephthalate). Macromolecules 2014;47(4):1383-1391.

3. Burgess SK, Karvan O, Johnson JR, Kriegel RM, and Koros WJ. Oxygen Sorption and Transport in Amorphous Poly(ethylene furanoate). Polymer 2014;55(18):4748-4756.

4. Flory AL, Ramanathan T, and Brinson LC. Physical Aging of Single Wall Carbon Nanotube Polymer Nanocomposites: Effect of Functionalization of the Nanotube on the Enthalpy Relaxation. Macromolecules 2010;43(9):4247-4252.

5. Li Q and Simon SL. Enthalpy recovery of polymeric glasses: Is the theoretical limiting liquid line reached? Polymer 2006;47(13):4781-4788.

6. Murphy TM, Langhe DS, Ponting M, Baer E, Freeman BD, and Paul DR. Enthalpy recovery and structural relaxation in layered glassy polymer films. Polymer 2012;53(18):4002-4009.

7. Boucher VM, Cangialosi D, Alegría A, and Colmenero J. Enthalpy Recovery of Glassy Polymers: Dramatic Deviations from the Extrapolated Liquidlike Behavior. Macromolecules 2011;44(20):8333-8342.

8. McGonigle E-A, Daly JH, Jenkins SD, Liggat JJ, and Pethrick RA. Influence of Physical Aging on the Molecular Motion and Structural Relaxation in Poly(ethylene terephthalate) and Related Polyesters. Macromolecules 2000;33(2):480-489.

9. Boucher VM, Cangialosi D, Alegrìa A, Colmenero J, González-Irun J, and Liz-Marzan LM. Physical aging in PMMA/silica nanocomposites: Enthalpy and dielectric relaxation. Journal of Non-Crystalline Solids 2011;357(2):605-609.

10. Horn NR and Paul DR. Carbon dioxide plasticization and conditioning effects in thick vs. thin glassy polymer films. Polymer 2011;52(7):1619-1627.

11. Cui L, Qiu W, Paul DR, and Koros WJ. Responses of 6FDA-based polyimide thin membranes to CO2 exposure and physical aging as monitored by gas permeability. Polymer 2011;52(24):5528-5537.

12. Huang Y, Wang X, and Paul DR. Physical aging of thin glassy polymer films: Free volume interpretation. Journal of Membrane Science 2006;277(1–2):219-229.

13. Huang Y and Paul DR. Physical aging of thin glassy polymer films monitored by gas

permeability. Polymer 2004;45(25):8377-8393.

14. Odegard GM and Bandyopadhyay A. Physical aging of epoxy polymers and their composites. Journal of Polymer Science Part B: Polymer Physics 2011;49(24):1695-1716.

15. Pan P, Zhu B, and Inoue Y. Enthalpy Relaxation and Embrittlement of Poly(l-lactide) during Physical Aging. Macromolecules 2007;40(26):9664-9671.

16. Hutchinson JM and Kumar P. Enthalpy relaxation in polyvinyl acetate. Thermochimica Acta 2002;391(1–2):197-217.

17. Lee WM. Selection of barrier materials from molecular-structure. Polymer Engineering & Science 1980;20(1):65-69.

18. Cowie JMG and Arrighi V. Miscibility and Relaxation Processes in Blends. In: Shonaike GO and Simon GP, editors. Polymer Blends and Alloys. New York: Marcel Dekker, Inc., 1999. pp. 81-124.

19. Codou A, Guigo N, van Berkel J, de Jong E, and Sbirrazzuoli N. Non-isothermal Crystallization Kinetics of Biobased Poly(ethylene 2,5-furandicarboxylate) Synthesized via the Direct Esterification Process. Macromolecular Chemistry and Physics 2014;215(21):2065-2074.

20. Tool AQ. RELATION BETWEEN INELASTIC DEFORMABILITY AND THERMAL EXPANSION OF GLASS IN ITS ANNEALING RANGE*. Journal of the American Ceramic Society 1946;29(9):240-253.

21. Narayanaswamy OS. A Model of Structural Relaxation in Glass. Journal of the American Ceramic Society 1971;54(10):491-498.

22. Moynihan CT, Macedo PB, Montrose CJ, Gupta PK, DeBolt MA, Dill JF, Dom BE, Drake PW, Easteal AJ, Elterman PB, Moeller RP, Sasabe H, and Wilder JA. STRUCTURAL RELAXATION IN VITREOUS MATERIALS*. Annals of the New York Academy of Sciences 1976;279(1):15-35.

23. Williams G and Watts DC. Non-symmetrical dielectric relaxation behaviour arising from a simple empirical decay function. Transactions of the Faraday Society 1970;66(0):80-85.

24. Hodge IM. Effects of annealing and prior history on enthalpy relaxation in glassy polymers. 6. Adam-Gibbs formulation of nonlinearity. Macromolecules 1987;20(11):2897-2908.

25. Mauro JC, Allan DC, and Potuzak M. Nonequilibrium viscosity of glass. Physical Review B: Condensed Matter and Materials Physics 2009;80(9):094204.

26. Hutchinson JM and Ruddy M. Thermal cycling of glasses. III. Upper peaks. Journal

of Polymer Science Part B: Polymer Physics 1990;28(11):2127-2163.

27. Hodge IM and Berens AR. Effects of annealing and prior history on enthalpy relaxation in glassy polymers. 2. Mathematical modeling. Macromolecules 1982;15(3):762-770.

28. Hodge IM. Enthalpy relaxation and recovery in amorphous materials. Journal of Non-Crystalline Solids 1994;169(3):211-266.

29. Ribelles JLG, Greus AR, and Calleja RD. A phenomenological study of the structural relaxation of poly(methyl methacrylate). Polymer 1990;31(2):223-230.

30. Wang Y, Gómez Ribelles JL, Salmerón Sánchez M, and Mano JF. Morphological Contributions to Glass Transition in Poly(l-lactic acid). Macromolecules 2005;38(11):4712-4718.

31. Alves NM, Mano JF, Balaguer E, Meseguer Dueñas JM, and Gómez Ribelles JL. Glass transition and structural relaxation in semi-crystalline poly(ethylene terephthalate): a DSC study. Polymer 2002;43(15):4111-4122.

32. Ruddy M and Hutchinson JM. Multiple peaks in differential scanning calorimetry of polymer glasses. Polymer Communications 1988;29(5):132-134.

33. Koh YP and Simon SL. Enthalpy Recovery of Polystyrene: Does a Long-Term Aging Plateau Exist? Macromolecules 2013;46(14):5815-5821.

34. Badrinarayanan P, Zheng W, Li Q, and Simon SL. The glass transition temperature versus the fictive temperature. Journal of Non-Crystalline Solids 2007;353(26):2603-2612.

35. Moynihan CT, Easteal AJ, De Bolt MA, and Tucker J. Dependence of the Fictive Temperature of Glass on Cooling Rate. Journal of the American Ceramic Society 1976;59(1-2):12-16.

36. Plazek DJ and Frund ZN. Epoxy resins (DGEBA): The curing and physical aging process. Journal of Polymer Science Part B: Polymer Physics 1990;28(4):431-448.

37. Sugden S. Molecular Volumes at Absolute Zero. Part II. Zero Volumes and Chemical Composition. Journal of the Chemical Society 1927:1786-1798.

38. Park JY and Paul DR. Correlation and prediction of gas permeability in glassy polymer membrane materials via a modified free volume based group contribution method. Journal of Membrane Science 1997;125(1):23-39.

39. Michaels AS, Vieth WR, and Barrie JA. Solution of Gases in Polyethylene Terephthalate. Journal of Applied Physics 1963;34(1):1-12.

40. Koros WJ and Paul DR. CO2 Sorption in Poly(ethylene Terephthalate) above and

below the Glass Transition. Journal of Polymer Science: Polymer Physics Edition 1978;16:1947-1963.

41. Hu C-C, Fu Y-J, Hsiao S-W, Lee K-R, and Lai J-Y. Effect of physical aging on the gas transport properties of poly(methyl methacrylate) membranes. Journal of Membrane Science 2007;303(1–2):29-36.

42. Paul DR and Koros WJ. Effect of Partially Immobilizing Sorption on Permeability and the Diffusion Time Lag. Journal of Polymer Science: Polymer Physics Edition 1976;14:675-685.

CHAPTER 11

DIFFUSION COEFFICIENT MODELING: APPLICATIONS OF INFINITE SERIES SOLUTIONS[1]

The transport performance of new polyester resins can be evaluated through gravimetric or pressure-decay kinetic sorption experiments, as described in previous chapters; however, estimation of model parameters can be challenging. Accurate diffusion coefficient determination is particularly difficult, as applications of the time-dependent diffusion equation yield non-intuitive infinite series solutions. Furthermore, complex diffusion processes often produce intractable models which require either short- or long-time approximations for parameter estimation. This chapter circumvents such approximations by describing a modeling methodology useful for fitting complex infinite series solutions directly to experimental kinetic sorption data. Two specific modeling cases pertaining to polyester films are used to validate the methodology. Furthermore, the diffusion coefficients estimated from kinetic sorption in Chapters 6, 7, and 9 were all determined using the MATLAB® procedure described in this chapter.

11.1. Introduction

Poly(ethylene terephthalate) (PET) has long been the industry standard for water and carbonated beverage containers [1]. Although PET has many desirable properties, an insufficient barrier to oxygen limits applications to more demanding markets such as fruit juice, beer, and vitamin water containers [2]. Evaluating the performance of more

[1]Reprinted in part from Burgess, S.K.; Kriegel, R.M.; Koros, W.J., *Diffusion Coefficient Modeling in Polyester Barrier Materials: Applications of Infinite Series Solutions*, Society of Plastics Engineers ANTEC Proceedings, Las Vegas, Nevada, 2014, pgs. 830 – 835.

advanced resins to replace PET can be accomplished by estimating the permeability (P) through combination of the sorption (S) and diffusion (D) coefficients, as discussed previously in Chapter 2 (cf. Section 2.1). Kinetic sorption experiments are particularly useful for transport evaluation, as both D and S parameters can be determined through time-dependent penetrant uptake and equilibrium uptake, respectively. While accurate solubility coefficients are easily measured from the equilibrium penetrant uptake, modeling of the time-dependent approach to equilibrium can introduce large errors in the diffusion coefficient. Furthermore, significant errors in D can result when applying a simple Fickian model to diffusion cases where non-Fickian relaxations, non-constant boundary conditions, or combinations of the two factors are present.

The current chapter describes a MATLAB® based modeling technique for determining accurate diffusion coefficient information from complicated experimental kinetic sorption data, thus improving the accuracy of permeability predictions derived from this method. Kinetic sorption data have been collected via a pressure-decay method for oxygen and carbon dioxide, and as discussed previously, a simple normalization procedure allows a common framework for analysis by converting the raw data into the form of mass uptake at time t (M_t) divided by the mass uptake at infinite time (M_∞). Once normalized, the kinetic sorption curves can be modeled using known infinite series solutions of the time-dependent diffusion equation and relevant model parameters determined through using a widely available non-linear least squares fitting routine. Since the infinite series solutions are discretized in MATLAB®, hundreds of terms in the infinite summation can be easily used to accurately approximate the model. Fickian models for non-constant and constant boundary conditions in films, cylinders, and

spheres can also be incorporated into more complicated diffusion models which take into account non-Fickian relaxations, such as the Berens-Hopfenberg model discussed in Chapter 9.

The proposed method evaluates relevant model parameters after application of the discretized analytical model to the entire data set, and does not rely on short- or long-time analytical approximations as typically used in past methods [3]. The method described in this chapter therefore provides a more accurate estimation of the effective diffusion coefficient which is uncomplicated by confounding long-term relaxations or sample geometry considerations. The end result is a more realistic prediction of barrier properties through the relationship $P = DS$, which was introduced in Chapter 2. The methodology is demonstrated and validated for two specific modeling cases involving diffusion in an infinite sheet: simple Fickian diffusion with constant boundary conditions (O_2 in PET), and non-Fickian diffusion coupled with a variable boundary condition (CO_2 in PEF).

11.2. Materials and Experimental Methods

The poly(ethylene furanoate) (PEF) and poly(ethylene terephthalate) (PET) polymers used in this chapter are the same materials described previously in Section 3.1.1, and all amorphous films were melt-pressed using the method in Section 3.1.3. All transport measurements reported herein for PEF and PET reflect data corresponding to the amorphous morphology.

Kinetic sorption data for O_2 and CO_2 were measured by the standard pressure-decay method at 35°C, which is described in Chapter 3. Since the pressure-decay method records pressure in the sample cell versus time, it is possible for highly sorbing penetrants

to cause a significant drop in pressure from the start to end of the experiment. For such cases, the concentration of gas at the polymer surface will not be constant throughout the diffusion process and the variable pressure must be taken into consideration during diffusion modeling, as discussed for the case of CO_2 sorption in PEF in Chapter 7. Alternatively, oxygen exhibits low solubility in PET, and consequently, a constant boundary condition during the diffusion process is valid as discussed in Chapter 6.

11.3. Diffusion Equations

The differential equation used to describe diffusive transport of a penetrant in a polymer is shown in Equation 11.1, which represents diffusion in an isotropic material and neglects convective transport and chemical reaction terms [4].

$$\frac{\partial C_i}{\partial t} = div\left(D\nabla C_i\right) \tag{11.1}$$

Where D is the diffusion coefficient (cm^2/s), C_i is the mass or molar concentration of species i, and div represents the divergence. Equation 11.1 simplifies to Equation 2.45 (discussed previously) for diffusion in an infinite sheet and where D is constant. The three infinite series solutions utilized in this chapter are discussed in detail in Chapter 2 (cf. Section 2.4), but are reproduced in this chapter for convenience. From Section 2.4.1, the simple Fickian solution of the time-dependent diffusion equation is provided in Equation 11.2, where the subscript F represents "Fickian."

$$\left.\frac{M_t}{M_\infty}\right|_F = 1 - \sum_{n=0}^{\infty} \frac{8}{(2n+1)^2 \pi^2} \exp\left(\frac{-D(2n+1)^2 \pi^2 t}{l^2}\right) \tag{11.2}$$

From Section 2.4.2, the Fickian solution of the time-dependent diffusion equation with a flux boundary condition is provided in Equations 11.3 – 11.5, where the subscript *LV* represents "limited volume."

$$\left.\frac{M_t}{M_\infty}\right|_{LV} = 1 - \sum_{n=1}^{\infty} \frac{2\alpha(1+\alpha)}{1+\alpha+\alpha^2 q_n^{\,2}} \exp\left(\frac{-D q_n^{\,2} t}{l^2}\right) \tag{11.3}$$

$$\tan(q_n) = -\alpha q_n \tag{11.4}$$

$$\frac{n_{film,\,final}}{n_{total,\,initial}} = \left(\frac{1}{1+\alpha}\right) \tag{11.5}$$

From Section 2.4.4, the Berens-Hopfenberg (*BH*) representation can be described via Equation 11.6, where $k = 1/\tau_R$ and the subscripts *F* and *BH* represent the Fickian and Berens-Hopfenberg formalisms, respectively.

$$\left.\frac{M_t}{M_\infty}\right|_{BH} = \left[\phi_F \left(\left.\frac{M_t}{M_\infty}\right|_F\right) + (1-\phi_F)(1-\exp(-kt))\right] \tag{11.6}$$

The *LV* model in Equation 11.3 can be substituted into the *BH* representation from Equation 11.6 to produce Equation 11.7, which can describe complex diffusion cases that

require accommodation of both the flux boundary conditions and superposition of non-Fickian relaxations. As a note, the infinite series solution in Equation 11.7 still requires Equations 11.4 and 11.5 to completely specify the general solution.

$$\left.\frac{M_t}{M_\infty}\right|_{BH,LV} = \left[\phi_F\left(\left.\frac{M_t}{M_\infty}\right|_{LV}\right) + \left(1-\phi_F\right)\left(1-\exp\left(-kt\right)\right)\right] \tag{11.7}$$

Although seemingly complex, all diffusion models presented thus far in Equations 11.2 – 11.7 can be easily implemented using the proposed MATLAB® modeling methodology.

11.4. Modeling Methodology

The raw pressure-decay data vs. time can be transformed via Equation 3.3 (discussed previously) into a non-dimensional form that can be modeled using the solution of the time-dependent diffusion equation in Equations 11.2 – 11.7. In addition to transforming the pressure data, the time data (in seconds) must exist such that $t = 0$ represents the beginning of the diffusion process. Once transformed, the data can be saved into an empty excel file (*currentData.xlsx*) such that the time data resides in the "A" column and the M_t/M_∞ data in the "B" column. Upon initializing MATLAB®, the "*xlsread*" command is used to import the normalized kinetic sorption data. This command imports the data into MATLAB® such that the "*x*" matrix contains the time data and the "*y*" matrix contains the M_t/M_∞ data, viz.,

```
A = xlsread('currentData.xlsx');
x = A(:,1);
y = A(:,2);
```

The proposed modeling technique uses a widely available non-linear least squares fitting routine available on the MathWorks website [5]. This routine, entitled "*easyfit*," is useful because it applies any user-defined function to the entirety of the experimental dataset and returns the relevant model parameters based on the optimized fit. The command shown below is a simplified syntax for the *easyfit* routine, where *pbest* is the matrix containing the output model parameters (i.e., *D* for the Fickian model), *x* and *y* represent the experimental kinetic sorption data (which have already been imported into MATLAB® using the *xlsread* command), [*IG*] represents the matrix containing the initial guess of the model parameters, and *@function* represents the function name for the user-defined function.

```
[pbest]=easyfit(x,y,[IG],@function)
```

The remaining step is to define the function file that the routine will use to fit the desired model to the experimental data. Shown below is the function to implement the simple Fickian model with constant boundary conditions from Equation 11.2. The *U* matrix in the function syntax represents the matrix containing the adjustable model parameters (i.e., *D* is the only adjustable parameter for the simple Fickian case). In the function code, *U(1)* represents the first adjustable model parameter, or the diffusion coefficient. The dimension of the [*IG*] matrix and *U* matrix must be the same. For example, since there are three adjustable parameters in the *BH* model from Equation 11.6,

the [*IG*] matrix will take the form of [*value, value, value*] and the adjustable parameters will take the form of *U(1), U(2),* and *U(3)* in the respective code. The benefit of using a function file to represent the model rests in the ability to discretize the infinite summation by using a "*for*" loop, where the number of terms in the infinite series can be changed by altering the number of iterations in the loop.

```
function y=Fick(U,x)
L = 0.00226;            %Half-film thickness in cm
Sum = 0;
for i = 0:1:100;        %Number of terms in the infinite series
        m = 8/(pi^2*(2*i+1)^2)*exp(-U(1)*(2*i+1)^2*pi^2*…
        x./(4*L^2));
        Sum = m + Sum;
end
y = 1 - Sum;
end
```

Once the function file has been defined, the following syntax can be used to apply the Fickian model directly to the experimental data:

```
[pbest]=easyfit(x,y,[1e-9],@Fick)
```

After executing the fitting routine, the MATLAB® output will be the [*pbest*] matrix and a graph of the optimized model plotted along with the experimental data. The [*pbest*] matrix contains the optimized values of the adjustable parameters from the selected model, i.e., [*pbest*] will contain one value for the simple Fickian fit and three values for the *BH* fit.

Extension of the function file to represent solutions of more complex diffusion problems is straightforward. For CO_2 diffusion in PEF, the application of either Equation 11.3 or 11.7 requires solution of the transcendental equation in Equation 11.4. The non-repeating, positive solutions of Equation 11.4 can be computed using MATLAB®'s *fzero* command, where the following code stores the first "*n*" positive solutions of Equation 11.4 into the vector q_n.

```
n = 100;
ep = 1e-4;
qn = zeros(1,n);
for i = 1:n
        qn(i) = fzero(@(q) tan(q)+alpha*(q),[pi/2+(i-1)*pi+ep
        pi/2+i*pi-ep]);
end
```

Calculation of q_n can be included in the larger function file specific to Equation 11.7. Accordingly, the function file for modeling CO_2 diffusion in PEF in the presence of non-Fickian relaxations is provided on the next page, where the adjustable parameters for the *BH-LV* model from Equation 11.7 are assigned as follows: *U(1)* = D (cm^2/s), *U(2)* = φ_F, and *U(3)* = k (1/s).

```
function y = BH_LV(U,x)
L = 0.0107;                %Half-film thickness in cm
alpha = 2.0329;            %Obtained experimentally from Equation 11.5
n = 100;                   %Number of terms in the infinite series

ep = 1e-4;
qn = zeros(1,n)
for i = 1:n                %Calculating solutions of Equation 11.4
        qn(i) = fzero(@(q) tan(q)+alpha*(q),[pi/2+(i-1)*pi+ep
        pi/2+i*pi-ep]);
end

Sum = 0;
for i = 0:1:n-1;
        m = 2*alpha*(1+alpha)/(1+alpha+alpha^2*qn(i+1)^2)*
        exp(-U(1)*(qn(i+1))^2*x./L^2);
        Sum = m + Sum;
end
w = 1 - Sum;
y = U(2)*w + (1 - U(2))*(1 - exp(-U(3)*x./1));  %BH model
end
```

Computational execution of the *BH-LV* model from Equation 11.7 is performed by the following command:

```
[pbest]=easyfit(x,y,[5e-10,1,5e-7],@BH_LV)
```

The output from executing this command is a graph of the model along with the experimental data and the [*pbest*] matrix, which now contains three optimized values. Care should be taken when selecting the initial values for the [*IG*] matrix. Since this procedure utilizes a non-linear least squares fitting routine, poorly selected initial guesses

can yield non-physical model results. Minor trial and error is recommended to verify the accuracy of the modeling results. As an example, a good initial value for the diffusion coefficient in the *BH* or *BH-LV* model is the optimized value obtained after modeling the simple Fickian fit to the model data. A good initial value for φ_F is usually 1 or 0.5, based on the nature and magnitude of deviations from the Fickian fit in Equation 11.2 [6], and a good initial value for k is ~1×10^{-5} 1/s for relaxation in glassy polymers. Clearly, optimized model outputs of φ_F which are negative or greater than one are non-physical and the initial guess parameters should be adjusted. In some cases, initial guesses of φ_F and k in the *BH* model can be obtained independently by the long-time approximation procedure outlined by Patton et al. [7].

11.5. Results and Discussion

11.5.1. Fickian Diffusion: O_2 in PET

As discussed in Chapter 6, the Fickian model from Equation 11.2 is valid for modeling O_2 diffusion in both PEF and PET. Example O_2 sorption data for PET from 0 to 3.6 atm is provided in Figure 11.1 (recall that a similar plot is provided for O_2 sorption in PEF from 0 to 1.1 atm in Figure 6.5). As mentioned in Chapter 6, the pressure-decay data are slightly noisy due to the low solubility of O_2 in polyester barrier materials (i.e., the pressure drop from beginning to end of sorption is only ~0.6 psia in this example). The diffusion coefficient for O_2 in PET at 35°C determined via this methodology is represented in Figure 11.1, and agrees with other literature reports [8, 9].

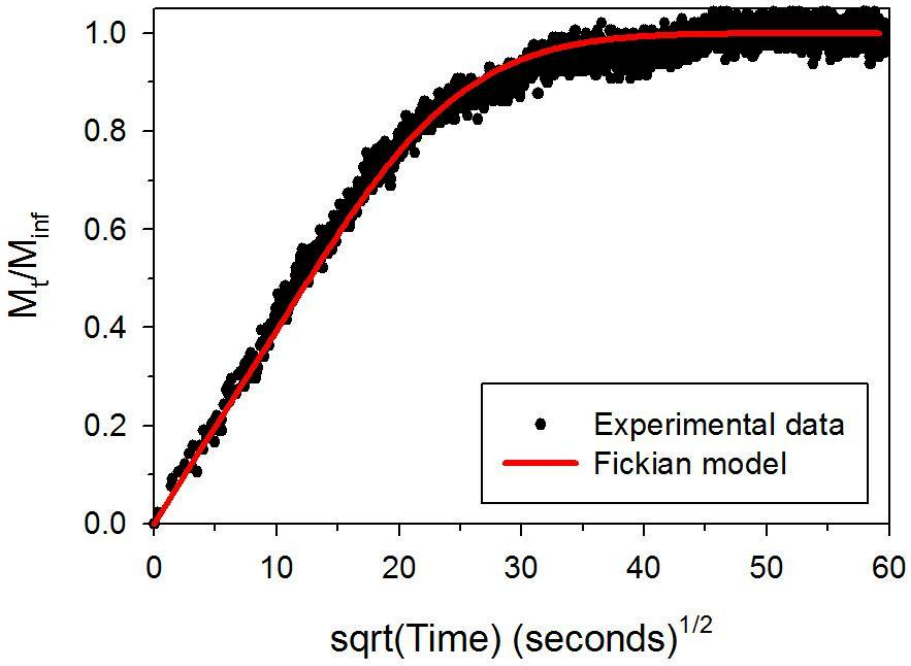

Figure 11.1. O_2 sorption in amorphous PET at 35°C. Equation 11.2 is represented by the red curve. 100 terms were used in the infinite series, $D = 6.3\times10^{-9}$ cm^2/s, and the film thickness is 45.2 ± 0.8 μm.

11.5.2. Non-Fickian Diffusion: CO_2 in PEF

As described in Chapter 7, the Fickian solution combined with the flux boundary conditions (i.e., Equations 11.3 – 11.5) is adequate for modeling CO_2 diffusion in PEF at *low pressure* (i.e., <0.5 atm), *in the absence of non-Fickian relaxations*. Pressure-decay data recorded at higher CO_2 pressures, however, reflected the presence of non-Fickian relaxations. Modeling such complex behavior can be accomplished via Equation 11.7, which can effectively describe diffusion cases that require accommodation of both the flux boundary conditions and superposition of non-Fickian relaxations.

To illustrate the utility of the proposed MATLAB® technique, it is useful to compare the CO_2 diffusion coefficients obtained from all three modeling equations described thus far against the same dataset. Figure 11.2 shows the simple Fickian model fit from

Equation 11.2 plotted against experimental CO_2 sorption data for PEF measured between 0 to 0.82 atm CO_2 (which is >0.5 atm, and therefore induces non-Fickian relaxations in the uptake curve). Figure 11.3 shows the same experimental CO_2 uptake data along with the *BH* model fit from Equation 11.6, and Figure 11.4 illustrates the *BH-LV* model fit from Equation 11.7. The film thickness corresponding to the data in Figures 11.2 – 11.4 is 215 ± 1 μm, α is 2.03 (determined experimentally from Equation 11.5), and the higher sorption of CO_2 in PEF vs. O_2 in PET yields an improved signal-to-noise ratio for the CO_2 pressure-decay data in Figures 11.2 – 11.4 compared to the O_2 data in Figure 11.1. Relevant model parameters for all three diffusion models are provided in Table 11.1, along with a comparison between the calculated CO_2 permeability from $P=DS$ (i.e., both D and S are estimated from the same pressure-decay sorption dataset) and the actual experimental permeability (P_{exp}) at 35°C.

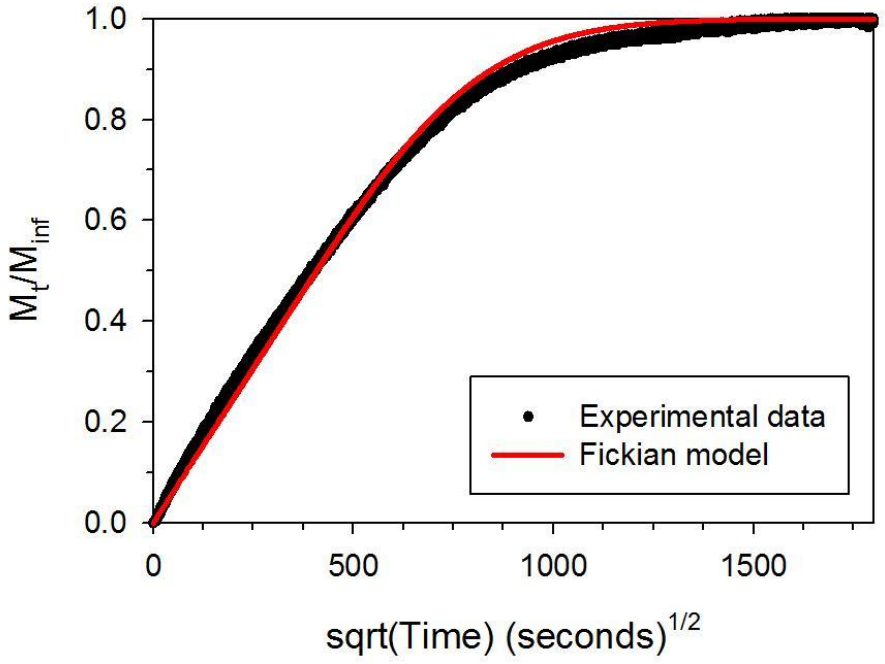

Figure 11.2. CO_2 sorption in amorphous PEF at 35°C between 0 to 0.82 atm. The Fickian model from Equation 11.2 is represented by the red curve, and 100 terms were used to approximate the infinite series.

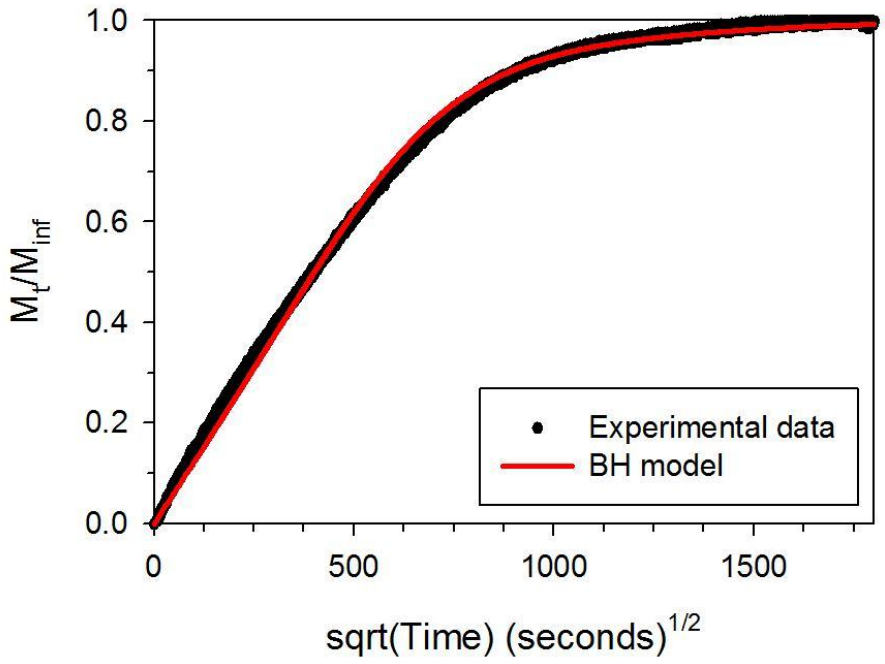

Figure 11.3. CO_2 sorption in amorphous PEF at 35°C between 0 to 0.82 atm. The Berens-Hopfenberg (*BH*) model from Equation 11.6 is represented by the red curve, and 100 terms were used to approximate the infinite series.

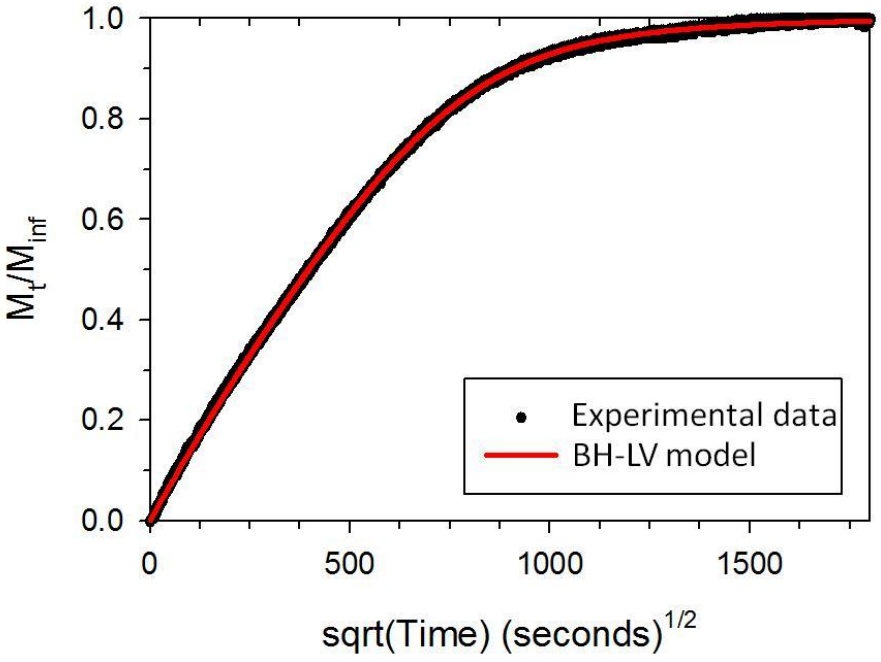

Figure 11.4. CO_2 sorption in amorphous PEF at 35°C between 0 to 0.82 atm. The *BH-LV* model from Equation 11.7 is represented by the red curve, and 100 terms were used to approximate the infinite series.

Table 11.1. Relevant model parameters for CO_2 diffusion in amorphous PEF at 35°C.

	Fickian **Eq. 11.2**	***BH*** **Eq. 11.6**	***BH-LV*** **Eq. 11.7**
D (cm^2/s)	1.4e-10	1.7e-10	1.0e-10
φ_F (-)	—	0.87	0.91
k (1/s)	—	8.8e-7	8.9e-7
$\left(\frac{P_{P=DS}-P_{exp}}{P_{exp}}\right)100\%$	42	81	4.2

A visual comparison of Figures 11.2 – 11.4 reveals that the *BH-LV* model provides the best fit to the experimental CO_2 sorption data. The applicability of the *BH-LV* model is also demonstrated in Table 11.1, where the permeability calculation (i.e., *P=DS*) resulting from using the *D* from the *BH-LV* model exhibits only 4.2% error for the calculated

permeability compared to the experimental permeability, while the Fickian and *BH* models exhibit 42% and 81% errors for the calculated permeability compared to the experimental permeability, respectively. The errors in the permeability calculation resulting from using the incorrect diffusion model are therefore significant, and can be avoided by application of the correct diffusion model via the method described in this chapter. As a side note, the experimental permeability utilized in Table 11.1 (i.e., P_{exp} = 0.027 Barrer) was measured at 1 atm CO_2, and provides a meaningful comparison to the permeability calculated from the kinetic sorption data measured at ~0.82 atm CO_2.

11.6. Summary and Conclusions

Accurate determination of transport parameters, including the sorption and diffusion coefficients, is important for estimating penetrant permeability from kinetic sorption data. The methodology described in this chapter provides a framework for applying complex infinite series diffusion models to experimental kinetic sorption data, with special applicability to complex diffusion models.

The proposed MATLAB® modeling technique has only been illustrated for two diffusion cases corresponding to the infinite sheet sample geometry; however, the methods described in this chapter are applicable to more complex geometries and to analogous heat conduction problems. The only requirement is that the analytical solution of the partial differential equation be known, and that all experimental parameters required by the model are accurately characterized (accurate sample dimensions, α from Equation 11.5, etc.). Tabulated solutions of the diffusion equation are provided by Crank [3], while tabulated solutions of the analogous heat conduction equation are provided by

Carslaw and Jaeger [10]. Additional discussion regarding the MATLAB modeling technique is provided in Appendix E, along with MATLAB® code useful for describing diffusion in bounded and infinite cylinders.

11.7. References

1. Bain DR and Giles GA. Technical and commercial considerations. In: Giles GA and Bain DR, editors. Technology of Plastics Packaging for the Consumer Market. Sheffield: Sheffield Academic Press Ltd, 2001.

2. Hotchkiss JH. Overview on Chemical Interactions between Food and Packaging Materials. In: P. Ackermann MJ, T. Ohlsson, editor. Foods and Packaging Materials - Chemical Interactions. Cambridge: The Royal Society of Chemistry, 1995. pp. 231.

3. Crank J. The Mathematics of Diffusion, 2nd ed.: Oxford Science Publications, 1975.

4. Deen WM. Analysis of Transport Phenomena. New York: Oxford University Press, 1998.

5. Fit experimental data is easy. http://www.mathworks.com/matlabcentral/fileexchange/10625-fit-experimental-data-is-easy/content/easyfit.m.

6. Berens AR and Hopfenberg HB. Diffusion and relaxation in glassy polymer powders: 2. Separation of diffusion and relaxation parameters. Polymer 1978;19(5):489-496.

7. Patton CJ, Felder RM, and Koros WJ. Sorption and transport of benzene in poly(ethylene terephthalate). Journal of Applied Polymer Science 1984;29(4):1095-1110.

8. Lewis ELV, Duckett RA, Ward IM, Fairclough JPA, and Ryan AJ. The barrier properties of polyethylene terephthalate to mixtures of oxygen, carbon dioxide and nitrogen. Polymer 2003;44:1631-1640.

9. Polyakova A, Stepanov EV, Sekelik D, Schiraldi DA, Hiltner A, and Baer E. Effect of Crystallization on Oxygen-Barrier Properties of Copolyesters Based on Ethylene Terephthalate. Journal of Polymer Science: Part B: Polymer Physics 2001;39:1911-1919.

10. Carslaw HS and Jaeger JC. Conduction of Heat in Solids, 2nd ed.: Oxford Science Publications, 1986.

CHAPTER 12

CONCLUSIONS AND RECOMMENDATIONS

As noted in Chapter 1, the overarching goal of this dissertation was to develop a fundamental understanding of penetrant transport in: 1) caffeine antiplasticized, amorphous poly(ethylene terephthalate) (PET), and 2) amorphous poly(ethylene furanoate) (PEF), which are industrially relevant polyester barrier materials. This chapter will discuss the most important contributions of this thesis, and will conclude with recommendations for future research.

12.1. Summary of Contributions

12.1.1. PET/Caffeine Antiplasticization (Chapter 4)

The first portion of this thesis focused on investigating the effect of caffeine antiplasticization of amorphous PET on the resultant barrier, thermal, and mechanical properties vs. neat PET. Much time was initially spent developing a method to homogeneously mix PET with caffeine via melt-processing at high temperature, with the additional goal of preventing measurable thermo-oxidative polymer degradation. As described in Chapter 3, an extensive procedure for cleaning the batch mixer was also developed to prevent contamination between batches. Once mixed, all PET/caffeine batches were processed into amorphous films by methods described in the literature [1, 2].

Multiple characterization techniques were used to investigate the effect of caffeine antiplasticization of amorphous PET. The study presented in Chapter 4 is unique for PET,

since it provides relevant transport, mechanical, density, and thermal property data for the mixed PET/caffeine samples as a function of caffeine content. Such data provide insight into the evolution and interrelated nature of the aforementioned properties as a function of caffeine content, and provide a more detailed understanding of antiplasticization as a tool for PET barrier property enhancement. Specifically, the permeability reductions for antiplasticized PET vs. neat PET were observed to originate from reductions in both solubility (i.e., via "hole-filling") and diffusivity (i.e., via hindered phenyl ring-flipping), since logically, the two mechanisms are interrelated.

12.1.2. Characterization of PEF Compared to PET (Chapters 5 – 10)

The bulk of this thesis has been devoted to understanding the fundamentals of transport in PEF, which is the recently introduced furanic, bio-sourced alternative to PET with greatly enhanced barrier properties and attractive thermal and mechanical properties. The significant property enhancements for PEF compared to PET are surprising, especially when considering the structural similarity between the two polyesters. In fact, it was this structural similarity, combined with the large reduction in oxygen permeability of 10X for PEF vs. PET [3], that provided the initial motivation for examining PEF in this thesis.

The fundamental chain mobility study for PEF compared to PET in Chapter 5 revealed, via dynamic mechanical and solid-state NMR methods, that the polymer furan ring-flipping motions in PEF are hindered compared to the "mobile" phenyl ring-flipping motions in PET. Such reductions in chain mobility for PEF are closely related to the 10X reduction in oxygen permeability for PEF vs. PET, and explain the large differences in

oxygen transport between the two polyesters, despite the similarity in structure.

The comprehensive transport studies for oxygen and carbon dioxide in Chapters 6 and 7, respectively, provide both temperature and pressure dependent permeation and sorption data for amorphous PEF. These studies are unique, due to the extensive cross-verification of the reported transport parameters as performed via complementary permeation and pressure-decay sorption techniques. Moreover, a custom-built, high accuracy pressure-decay sorption system was developed to enable accurate uptake measurements for gases with low solubility in PET and PEF (i.e., oxygen). The data presented in Chapters 6 and 7 provide the first detailed reports of non-condensable penetrant transport in PEF.

Aside from "non-condensable" gas transport (i.e., oxygen and carbon dioxide), it is also important to understand the transport behavior of water in both PEF and PET. Such data are provided via the equilibrium and kinetic investigations in Chapters 8 and 9, respectively, which utilized three independent gravimetric water sorption techniques to cross-verify the accuracy of the reported data. Furthermore, sorption measurements at multiple temperatures allowed determination of the relevant transport energetic parameters (i.e., apparent enthalpy of sorption and apparent activation energies of diffusion and permeation) for water in both polyesters. Similar to the oxygen and carbon dioxide data in Chapters 6 and 7, the data for water in Chapters 8 and 9 provide the first detailed reports of water transport in PEF compared to PET.

In addition to studying the three most relevant penetrants for beverage containers (i.e., oxygen, carbon dioxide, and water), it is also important to understand the physical aging properties of the amorphous glass. Preparation of an amorphous glass was simple for PEF, since the reduced chain mobility for PEF vs. PET discussed in Chapter 5

correlates with a reduction in crystallization rate compared to PET. Such reality allowed for the study in Chapter 10, which provided a detailed investigation of the physical aging properties of amorphous, glassy PEF via complementary thermal, volumetric, and oxygen transport characterization techniques. The data in Chapter 10 provide the first aging study for PEF, and illustrate, using complementary techniques, that physical aging in PEF occurs via the time-dependent reduction in excess free volume.

12.1.3. Diffusion Coefficient Modeling (Chapter 11)

As discussed in Chapters 2 and 3, kinetic sorption data measured via pressure-decay sorption and gravimetric sorption techniques can be modeled using solutions of the time-dependent diffusion equation. Estimation of model parameters can be challenging, however, since complex diffusion processes often require complicated models with multiple fitting parameters. Chapter 11 addressed this challenge by describing a modeling methodology useful for fitting complex infinite series solutions directly to experimental kinetic sorption data. The utility of the modeling methodology was further illustrated via direct application to the kinetic sorption data provided in Chapters 6, 7, and 9.

12.2. Recommendations for Future Work

12.2.1. Antiplasticization of Semicrystalline/Oriented PET

The antiplasticization data in Chapter 4 were measured using amorphous samples to eliminate the complicating effects of crystallinity and orientation; however, such effects are present in typical beverage containers. It will be of great interest to understand the effect of antiplasticization on the three phase model of crystallinity in PET [4], and to

investigate the synergy in transport reduction that can be realized via combination of both antiplasticization and crystallization phenomena [5].

While not investigated in the current work, it is hypothesized that glassy mixtures of PEF and caffeine will *not* exhibit the same antiplasticization properties as observed for the PET/caffeine samples. Such hypothesis is logical for PEF, since the furan ring-flipping motions are already hindered in PEF vs. PET (cf. Chapter 5), and since the transport reductions in antiplasticized PET result primarily from caffeine hindering the phenyl ring-flipping motions compared to neat PET. It would be useful, however, to experimentally verify this notion.

12.2.2. Penetrant Transport in Semicrystalline/Oriented PEF

The transport data from Chapters 6 – 9 for amorphous PEF provide a first look into the interesting transport properties for PEF compared to PET in the absence of crystallinity and orientation; however, transport data corresponding to semicrystalline and oriented PEF are undoubtedly necessary, since blow-molding introduces such complicating features. It will be of further interest to investigate the applicability of the idealistic two-phase model of crystallinity [6, 7] to PEF, since it has already been shown that deviations from such ideal behavior exist for PET [4].

Additional investigation into the two-phase model of crystallinity for PEF can also be accomplished via complementary volumetric (i.e., density), X-Ray diffraction, and thermal (i.e., modulated DSC) investigation of semicrystalline vs. amorphous PEF as described by Lee for PET [1]. Data from the aforementioned techniques can be further evaluated in light of transport data measured for semicrystalline samples to help

determine the applicability of the idealized two-phase model for PEF.

12.2.3. Multicomponent Penetrant Transport

All penetrant transport data for PET and PEF reported in the current work represent pure component measurements; however, conditions involving multicomponent transport are ubiquitous in real-world beverage container applications. Specifically, it is of interest to investigate the transport properties of combined O_2/CO_2 feeds in both PET/caffeine and PEF materials in the amorphous and semicrystalline/oriented morphologies, with the subsequent introduction of additional feed components (i.e., H_2O, and potentially methanol to simulate flavor molecules [8-10]). Such evaluation would provide a better understanding of transport in PET/caffeine and PEF materials as it relates to real-world beverage container applications.

12.2.4. PET/PEF Blends and Copolymers

The data reported in this thesis, up to this point, have focused on either PET/caffeine blends or PEF samples, with no mention regarding PET/PEF blends or copolymers; however, data pertaining to such mixtures are important since PEF will eventually enter the PET recycle stream. Preliminary data regarding PET/PEF blends and copolymers are provided in Appendix H, and illustrate that blends of PET and PEF are surprisingly compatible after mixing in the melt state using the same mixing procedure described in Chapter 3. The thermal data reported in Appendix H further illustrate that blends of PET and PEF can be "compatibilized" via transesterification of the polymer chains resulting from extended exposure to high temperature [11, 12]. In addition to pure component

transport data, measurements involving multicomponent feeds (as described in the previous section) will also be useful for evaluating the transport performance of such blends and copolymers in real-world applications.

12.2.5. Barrier Susceptibility to Flavor Scalping

"Flavor scalping" is the terminology used to describe the unwanted removal of flavor compounds from a packaged food/beverage by means of absorption into the plastic container [13]. While secondary in importance compared to the overall transport performance of O_2, CO_2, and H_2O, it is still necessary to understand the resistance to flavor scalping of the PET/caffeine and PEF barrier materials studied in this work. Such investigation can be performed via transport studies involving small, low molecular weight "flavor simulants", such as limonene, methanol, or other lower alcohols [1, 8, 9, 14, 15].

12.3. References

1. Lee JS. Fundamentals of Transport in Advanced Barrier Materials Based on Engineered Antiplasticization. Chemical and Biomolecular Engineering. Atlanta: Georgia Institute of Technology, 2011.
2. Lee JS, Leisen J, Choudhury RP, Kriegel RM, Beckham HW, and Koros WJ. Antiplasticization-based enhancement of poly(ethylene terephthalate) barrier properties. Polymer 2012;53:213-222.
3. Avantium - PEF bottles. http://avantium.com/yxy/products-applications/fdca/PEF-bottles.html.
4. Lin J, Shenogin S, and Nazarenko S. Oxygen solubility and specific volume of rigid amorphous fraction in semicrystalline poly(ethylene terephthalate). Polymer 2002;43(17):4733-4743.

5. Burgess SK, Lee JS, Mubarak CR, Kriegel RM, and Koros WJ. Caffeine Antiplasticization of Amorphous Poly(ethylene terephthalate): Effects on Gas Transport, Thermal, and Mechanical Properties. Polymer 2015, DOI: 10.1016/j.polymer.2015.03.051.

6. Michaels AS, Vieth WR, and Barrie JA. Solution of Gases in Polyethylene Terephthalate. Journal of Applied Physics 1963;34(1):1-12.

7. Michaels AS, Vieth WR, and Barrie JA. Diffusion of Gases in Polyethylene Terephthalate. Journal of Applied Physics 1963;34(1):13-20.

8. Chandra P. Chemical and Biomolecular Engineering, vol. PhD. Atlanta: Georgia Institute of Technology, 2006.

9. Chandra P and Koros WJ. Sorption and transport of methanol in poly(ethylene terephthalate). Polymer 2009;50:236-244.

10. Lee JS, Chandra P, Burgess SK, Kriegel R, and Koros WJ. An advanced gas/vapor permeation system for barrier materials: Design and applications to poly(ethylene terephthalate). Journal of Polymer Science Part B: Polymer Physics 2012;50(17):1262-1270.

11. Kimura M, Porter RS, and Salee G. Blends of poly(butylene terephthalate) and a polyarylate before and after transesterification. Journal of Polymer Science: Polymer Physics Edition 1983;21(3):367-378.

12. Huang ZH and Wang LH. Infrared studies of transesterification in poly(ethylene terephthalate)/polycarbonate blends. Die Makromolekulare Chemie, Rapid Communications 1986;7(5):255-259.

13. Sajilata MG, Savitha K, Singhal RS, and Kanetkar VR. Scalping of Flavors in Packaged Foods. Comprehensive Reviews in Food Science and Food Safety 2007;6(1):17-35.

14. Moaddeb M and Koros WJ. Effects of orientation on the transport of d-limonene in polypropylene. Journal of Applied Polymer Science 1995;57(6):687-703.

15. Chandra P and Koros WJ. Sorption of lower alcohols in poly(ethylene terephthalate). Polymer 2009;50:4241-4249.

APPENDIX A

SUPPORTING INFORMATION FOR CHAPTER 4

(CAFFEINE ANTIPLASTICIZATION OF PET)[1]

A.1. FTIR of PET and PET/Caffeine Films

The FTIR spectra for films of virgin PET and PET mixed with ~15 wt% caffeine are provided in Figure A.1, where the characteristic double carbonyl peak for caffeine at ~1700 cm^{-1} is observed in the PET/caffeine spectra.

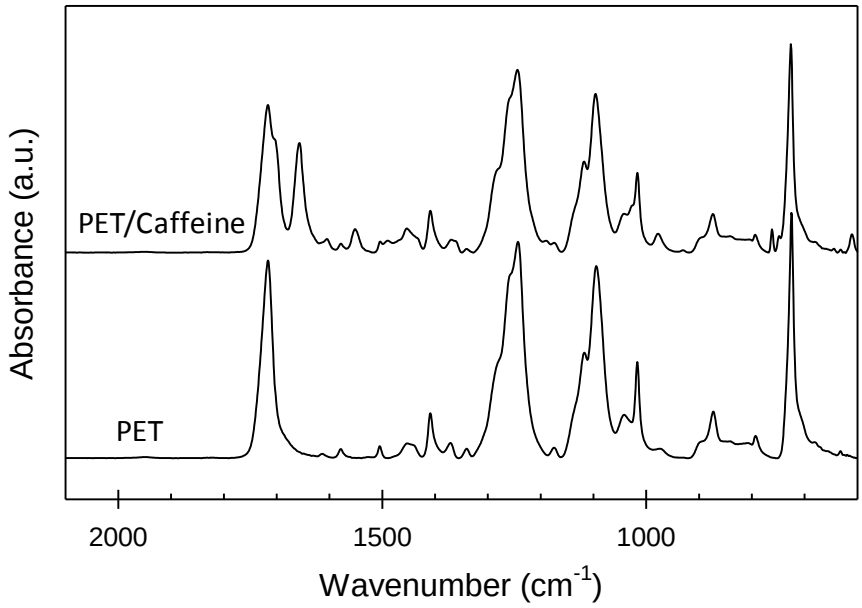

Figure A.1. FTIR spectra for virgin PET and PET/caffeine (i.e., caffeine content ~15 wt%).

[1]Reprinted in part from *Polymer*, Burgess, S.K.; Lee, J.S.; Mubarak, C.R.; Kriegel, R.M.; Koros, W.J., *Caffeine Antiplasticization of Amorphous Poly(ethylene terephthalate): Effects on Gas Transport, Thermal, and Mechanical Properties*, DOI: 10.1016/j.polymer.2015.03.051, Copyright 2015, with permission from Elsevier.

A.2. Permeation Data vs. Caffeine Concentration

The permeability data for oxygen and carbon dioxide plotted in Figures 4.1 and 4.2 can be re-plotted to more clearly demonstrate the permeability reductions vs. caffeine concentration. Accordingly, the oxygen permeability data at 1 atm are plotted in Figure A.2 vs. caffeine concentration along with additional data measured by Lee [1], with the corresponding data for carbon dioxide plotted in Figure A.3. The solid lines in Figures A.2 and A.3 represent quadratic regressions to the data, and appear to indicate that the permeability data are approaching a minimum that exists at a higher caffeine concentration than ~10.7 wt% caffeine. This behavior is consistent with the trend in DMA results reported in Figure 4.10, which appears to indicate that a minimum value for the activation energy of the beta relaxation occurs at a concentration near ~15 wt%. It is hypothesized that a transition to plasticization behavior will occur at some caffeine concentration slightly greater than 15 wt%; however, caffeine concentrations greater than 15 wt% were not tested in the current work and this notion has not been explicitly verified.

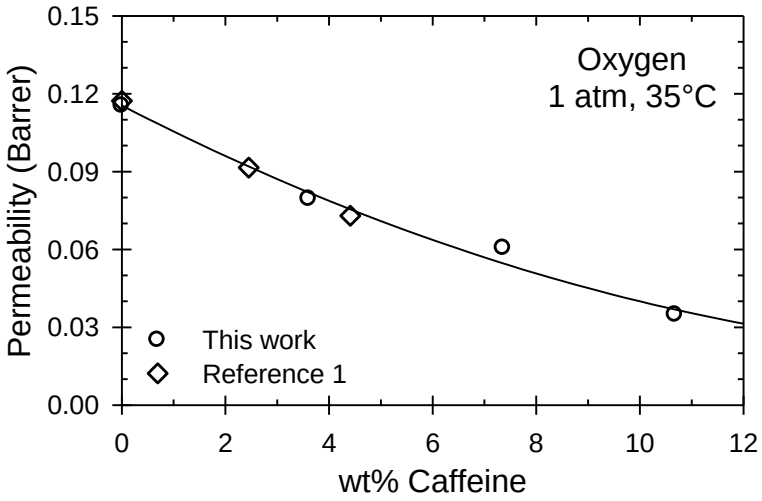

Figure A.2. Oxygen permeability at 1 atm and 35°C for various PET/caffeine samples. The solid line represents a quadratic regression to the data.

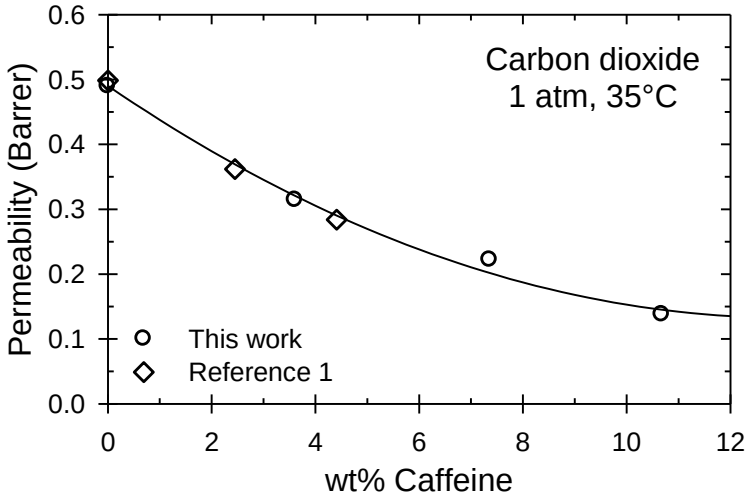

Figure A.3. Carbon dioxide permeability at 1 atm and 35°C for various PET/caffeine samples. The solid line represents a quadratic regression to the data.

A.3. Effect of Antiplasticization on the Effective Solubility Coefficient for CO_2

Additional insight regarding the effect of caffeine antiplasticization on gas solubility can be obtained by complementary permeation testing. The effective solubility parameters measured via transient permeation (i.e., $k^* = 6\theta P/l^2$) and pressure-decay sorption (i.e., $k^* = k_D + C_H'b$) reflect solubility contributions from both the Henry's law and Langmuir environments, and consequently, typically exhibit positive deviations from the true Henry's law parameter (k_D) measured via pressure-decay sorption [2-4]. Solubility coefficients for carbon dioxide measured in the current work via sorption (k_D and $k^* = k_D + C_H'b$) and permeation ($k^* = 6\theta P/l^2$) are provided in Table A.1. As seen in Table A.1, the effective solubility coefficients (k^*) measured via permeation and sorption decrease with increasing caffeine content, while the true k_D values measured via sorption remain essentially unchanged. The former notion is consistent with reduced sorption in the Langmuir mode for the caffeine-containing samples, and corroborates the "hole-filling" notion of caffeine antiplasticization discussed in the main paper. Furthermore,

satisfactory agreement is observed between the k^* values measured from the independent permeation and pressure-decay sorption methodologies.

Table A.1. Carbon dioxide solubility coefficients measured at 35°C via pressure-decay sorption (i.e., k_D and $k^* = k_D + C_H'b$) and transient permeation ($k^* = 6\theta P/l^2$) for various PET/caffeine samples.

	Carbon dioxide		
wt% Caffeine	**k_D (sorp) (ccSTP/ccPoly·atm)**	**k^* (sorp, $k^* = k_D + C_H'b$) (ccSTP/ccPoly·atm)**	**k^* (perm, $k^* = 6\theta P/l^2$) (ccSTP/ccPoly·atm)**
0	0.93 ± 0.04	1.7 ± 0.3	1.4 ± 0.01
3.6 ± 0.2	0.92 ± 0.1	1.5 ± 0.9	1.3 ± 0.03
7.4 ± 0.2	0.89 ± 0.02	1.5 ± 0.2	1.2 ± 0.02
10.7 ± 0.10	0.82 ± 0.07	1.3 ± 0.5	1.2 ± 0.04

A.4. References

1. Lee JS. Fundamentals of Transport in Advanced Barrier Materials Based on Engineered Antiplasticization. Chemical and Biomolecular Engineering. Atlanta: Georgia Institute of Technology, 2011.

2. Koros WJ and Paul DR. Transient and Steady-State Permeation in Poly(ethylene Terephthalate) Above and Below the Glass Transition. Journal of Polymer Science: Polymer Physics Edition 1978;16:2171-2187.

3. Burgess SK, Karvan O, Johnson JR, Kriegel RM, and Koros WJ. Oxygen Sorption and Transport in Amorphous Poly(ethylene furanoate). Polymer 2014;55(18):4748-4756.

4. Burgess SK, Mubarak CR, Kriegel RM, and Koros WJ. Physical Aging in Amorphous Poly(ethylene furanoate): Enthalpic Recovery, Density, and Oxygen Transport Considerations. Journal of Polymer Science Part B: Polymer Physics 2015;53(6):389-399.

APPENDIX B

SUPPORTING INFORMATION FOR CHAPTER 6 (O_2 TRANSPORT IN PEF)[1]

B.1. Temperature Dependence of Dual-Mode Model Parameters

The dual-mode model parameters listed in Table 6.2 are plotted in Figures B.1 and B.2 vs. temperature, and exhibit the expected negative correlation with increasing temperature. The Langmuir capacity constant (C_H'), which is associated with the excess free volume of the polymer, is expected to approach a value of zero near the glass transition temperature (T_g). From Figure B.1, it is apparent that the linear extrapolation of C_H' will intersect the temperature axis at a value somewhat higher than the reported T_g of 85°C for PEF measured via DSC [1]. This "overshoot" in C_H' past the polymeric T_g has also been observed for CO_2 in semicrystalline PET [2], although the overshoot for CO_2 in PET is less pronounced than in the current study. Consequently, it is not understood why C_H' does not intersect the temperature axis closer to T_g for the case of O_2 in PEF.

Aside from C_H', the low pressure effective solubility coefficient (k*) should approach the true solubility coefficient for the dissolved mode (k_D) near T_g, and the two parameters will be equal above T_g due to the absence of the Langmuir sorption environment. This trend is represented in Figure B.3 by the semi-logarithmic van't Hoff plots of k* and k_D.

[1]Reprinted in part from *Polymer*, 55/18, Burgess, S.K.; Karvan, O.; Johnson, J.R.; Kriegel, R.M.; Koros, W.J., *Oxygen Sorption and Transport in Amorphous Poly(ethylene furanoate)*, 4748-4756, Copyright 2014, with permission from Elsevier.

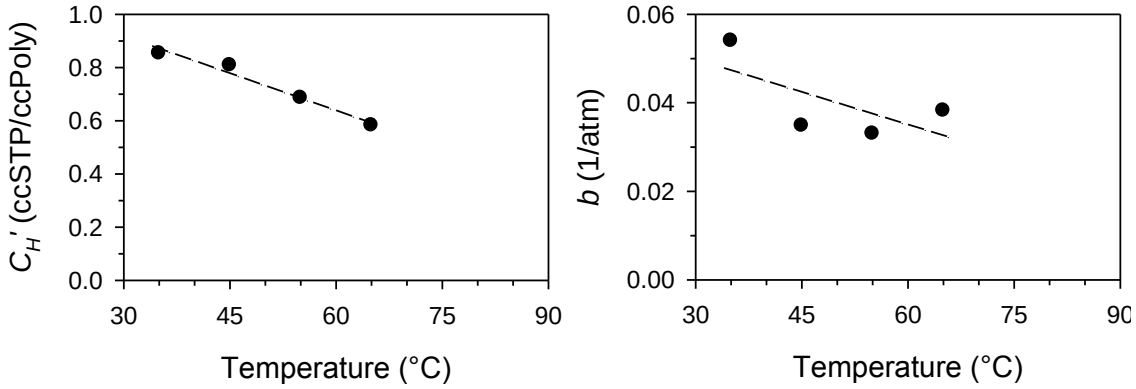

Figure B.1. Temperature dependence of C_H' and b dual-mode model parameters from Table 6.2.

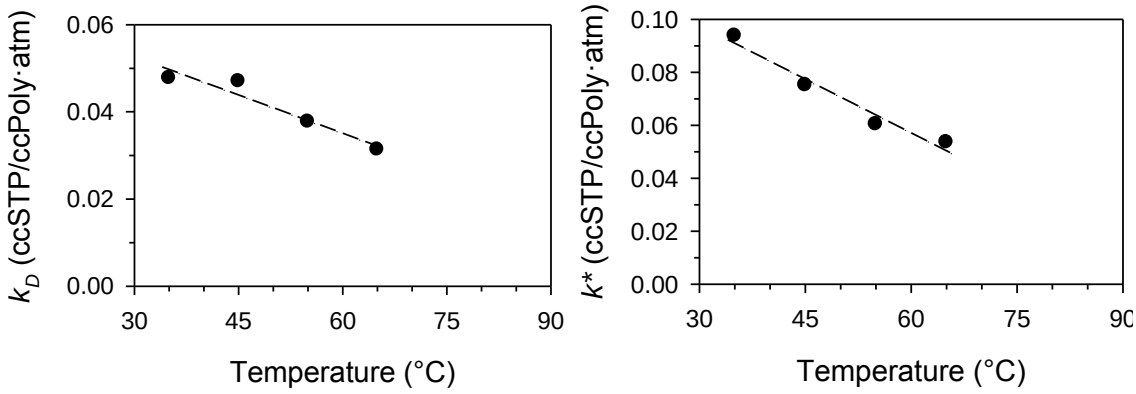

Figure B.2. Temperature dependence of k_D and k^* dual-mode model parameters from Table 6.2.

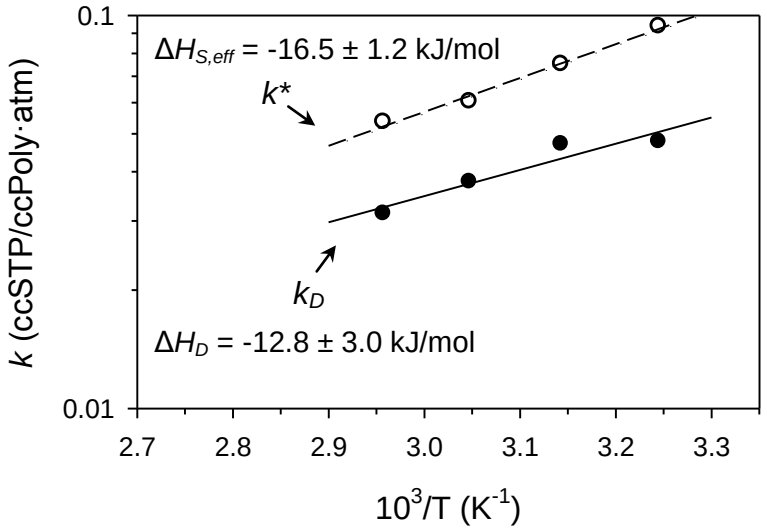

Figure B.3. Van't Hoff plot of the true k_D and k^* approximation from sorption testing.

Similar to k_D, the Langmuir hole affinity parameter b also represents an equilibrium constant and is subject to the same van't Hoff interpretation as described previously in Equation 2.6. Respective apparent enthalpy of sorption values, which represent the enthalpy difference between the sorbed and gaseous state, can therefore be obtained for the dissolved species (ΔH_D) and the Langmuir species (ΔH_b). Figures B.3 and B.4 illustrate the van't Hoff representations for k_D and b, respectively, yielding values of -12.8 ± 3.0 kJ/mol for ΔH_D and -9.8 ± 7.9 kJ/mol for ΔH_b. In contrast to CO_2 in PET [2], the enthalpy of O_2 sorption in the dissolved mode of PEF is actually *lower* than the Langmuir mode by ~3 kJ/mol. This behavior is interesting, since sorption via dissolution is postulated to include the endothermic process of chain separation to form the penetrant-sized holes [3], while this endothermic step is not needed during exothermic sorption in the preexisting microvoids of the Langmuir environment [2, 4, 5]. A lower value of ΔH_D than ΔH_b has also been observed for the case of a polyimide containing residual solvent [4], and this trend is predicted in certain mixed gas systems containing highly sorbing penetrants [6]. Further examination of Figure B.4 reveals significant scatter, and as a result, additional data points are needed to verify the accuracy of ΔH_b.

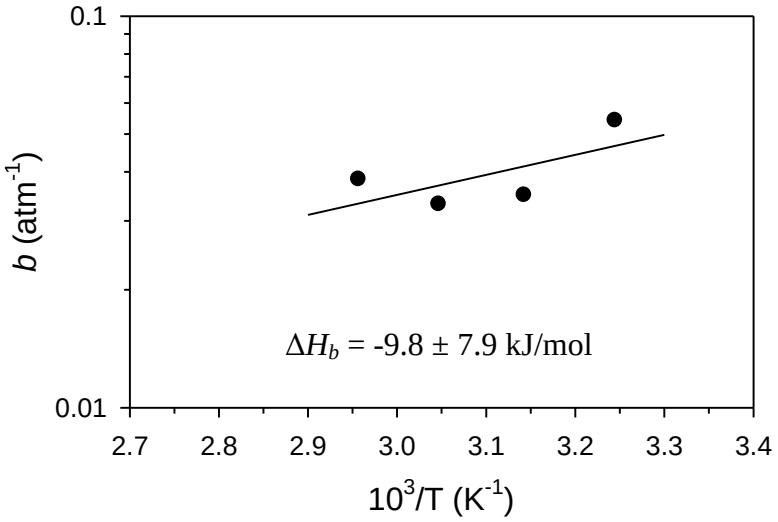

Figure B.4. Thermodynamic van't Hoff plot of the Langmuir affinity parameter *b* for O_2 in amorphous PEF.

B.2. Partial Immobilization Model Interpretation

The partial immobilization model representations of the permeability and diffusivity are provided in Equations 2.33 and 2.34, respectively, with addition details provided in Chapter 2. As mentioned in Section 6.4.1, the pressure independence of the O_2 permeability in Figure 6.1 does not necessarily reflect total immobilization (i.e., $F \approx 0$); rather, a weak pressure dependence is expected for even large values of *F* due to the low solubility of O_2 in PEF. The critical temperature and penetrant size can act as qualitative indicators for the likelihood of penetrant immobilization in the Langmuir environment, where large penetrants with high critical temperatures are prone to apparent immobilization. The limit of total immobilization has been approached for methanol in PET at 35°C [7], benzene in PET at 40°C [8], and SO_2 in Kapton polyimide at 25°C [4], which is not surprising when considering the large penetrant sizes and higher critical temperatures than O_2. For CO_2, which has a critical temperature above O_2 and below that

for benzene and methanol, partial immobilization is observed at 35°C via *F* values of 0.093 and 0.071 for amorphous [7] and semicrystalline [9] PET, respectively. Following this trend, O_2 should have a higher mobility than methanol, benzene, and CO_2 in the Langmuir environment of PET due to the smaller diameter and significantly lower critical temperature.

Very little reported data exists on the dual-mode characteristics of O_2 transport in PET. Only one measurement of *F* has been reported in the literature [7], and as expected, a value of 0.213 for O_2 in amorphous PET at 35°C is significantly higher than reported values for CO_2 in PET [7, 9]. A value of *F* similar to that for O_2 in PET might also be expected to represent O_2 transport in amorphous PEF.

The pressure dependence of O_2 permeability in PEF at 35°C will now be illustrated. The assumption is made that *F* arbitrarily equals a value of 0.20, which is similar to the *F* for O_2 in amorphous PET. The partial immobilization model expression for permeability (Equation 2.33) can then be applied to the experimental permeability data at 35°C from Figure 6.1 in the paper, and simple optimization reveals that $D_D = 1.46\times10^{-9}$ cm^2/s best represents the data. The experimental permeability data for O_2 in PEF at 35°C is re-plotted in Figure B.5, along with the model fit from Equation 2.33 *assuming arbitrary values* of $F = 0.20$ and $D_D = 1.46\times10^{-9}$ cm^2/s. Alternate values could be used; however, in any case, using these or any other reasonable combination in Figure B.5 illustrates that very little pressure dependence exists when using the partial immobilization model at the low site saturation conditions considered here. The large value of *F* is offset by the low values of *K* and *b* from Equation 2.33, thereby reiterating the impact of reduced gas/polymer interactions for the case of O_2 in PEF. While no pressure dependence in

permeability was observed in the current study for O_2 in PEF over the pressure range tested, it is expected that higher pressures would reveal the underlying trend of decreasing permeability. This was not pursued due to safety issues associated with long permeation times with unattended operation.

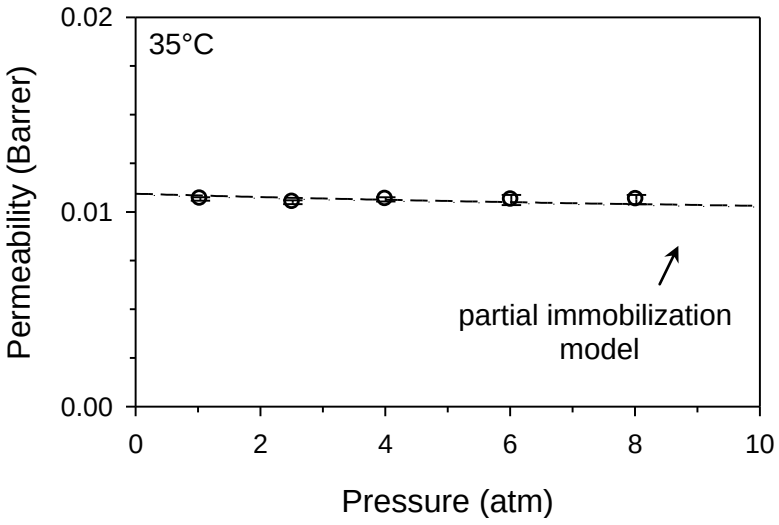

Figure B.5. O_2 permeability in PEF at 35°C, re-plotted from Figure 6.1. The dashed line represents Equation 2.33 with the assumed parameters $F = 0.20$ and $D_D = 1.46\times10^{-9}$ cm^2/s.

In addition to permeability, the partial immobilization model can also explain the concentration dependence of the diffusion coefficients (D_{Avg}) obtained from the kinetic sorption measurements in Section 6.4.3, as indicated via Equation 2.34 [8, 10, 11]. Figure B.6 shows the experimental O_2 sorption data at 35°C vs. pressure, along with the partial immobilization model fit from Equation 2.34 and the *arbitrarily assumed* parameters $F = 0.20$ and $D_D = 1.46\times10^{-9}$ cm^2/s discussed earlier for illustration purposes.

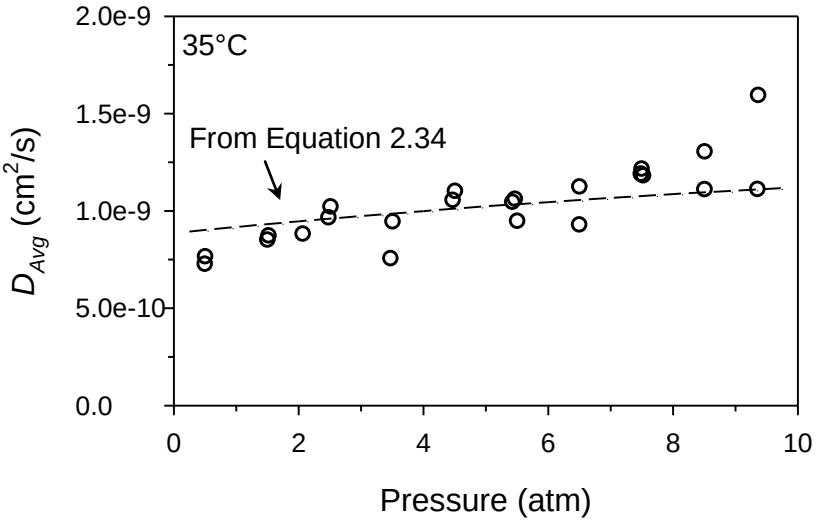

Figure B.6. Average diffusion coefficients (D_{Avg}) from kinetic oxygen sorption in PEF plotted at the midpoint of each respective sorption interval. The dashed line represents the partial immobilization model fit from Equation 2.34 with the arbitrarily assumed parameters F = 0.20 and $D_D = 1.46\times10^{-9}$ cm^2/s.

From Figure B.6, it is apparent that the partial immobilization model captures the general trend of increasing diffusion coefficient with pressure. Recall that the D_{Avg} values in Figure B.6 were extracted from the application of Equation 6.6 to experimental pressure-decay data (cf. Figure 6.5). The low solubility of O_2 in PEF causes an exceedingly low pressure differential from start to end of sorption after each successive interval of 1 atm O_2, thus contributing to the error and scatter in D_{Avg} values in Figure B.6.

As noted above, the partial immobilization model parameters of F = 0.20 and $D_D = 1.46\times10^{-9}$ cm^2/s were *chosen arbitrarily* to illustrate the almost negligible pressure dependence of both permeability and diffusivity resulting from the low critical temperature and low solubility of O_2 in PEF. Although other combinations could fit the data, accurate determination of actual F and D_D parameters for O_2 in PEF was not allowed in the current study due to the small range of pressures tested. However, the

partial immobilization model is still a useful framework for understanding the transport behavior of O_2 when considered in the broader context of transport in an important glassy polymer like PEF.

B.3. References

1. Burgess SK, Leisen JE, Kraftschik BE, Mubarak CR, Kriegel RM, and Koros WJ. Chain Mobility, Thermal, and Mechanical Properties of Poly(ethylene furanoate) Compared to Poly(ethylene terephthalate). Macromolecules 2014;47(4):1383-1391.

2. Koros WJ and Paul DR. CO2 Sorption in Poly(ethylene Terephthalate) above and below the Glass Transition. Journal of Polymer Science: Polymer Physics Edition 1978;16:1947-1963.

3. Barrer RM and Rees LVC. Henry's law adsorption constants. Transactions of the Faraday Society 1961;57(0):999-1007.

4. Felder RM, Patton CJ, and Koros WJ. Dual-mode sorption and transport of sulfur dioxide in kapton polyimide. Journal of Polymer Science: Polymer Physics Edition 1981;19(12):1895-1909.

5. Michaels AS, Vieth WR, and Barrie JA. Solution of Gases in Polyethylene Terephthalate. Journal of Applied Physics 1963;34(1):1-12.

6. Koros WJ. Model for Sorption of Mixed Gases in Glassy Polymers. Journal of Polymer Science: Polymer Physics Edition 1980;18:981-992.

7. Lee JS, Chandra P, Burgess SK, Kriegel R, and Koros WJ. An advanced gas/vapor permeation system for barrier materials: Design and applications to poly(ethylene terephthalate). Journal of Polymer Science Part B: Polymer Physics 2012;50(17):1262-1270.

8. Patton CJ, Felder RM, and Koros WJ. Sorption and transport of benzene in poly(ethylene terephthalate). Journal of Applied Polymer Science 1984;29(4):1095-1110.

9. Koros WJ and Paul DR. Transient and Steady-State Permeation in Poly(ethylene Terephthalate) Above and Below the Glass Transition. Journal of Polymer Science: Polymer Physics Edition 1978;16:2171-2187.

10. Koros WJ and Hopfenberg HB. Small Molecule Migration in Products Derived from Glassy Polymers. Industrial & Engineering Chemistry Product Research and

Development 1979;18(4):353-358.

11. Koros WJ, Patton CJ, Felder RM, and Fincher SJ. Kinetics and equilibria of sulfur dioxide sorption in kapton polyimide. Journal of Polymer Science: Polymer Physics Edition 1980;18(7):1485-1495.

APPENDIX C

SUPPORTING INFORMATION FOR CHAPTER 7 (CO_2 TRANSPORT IN PEF)[1]

C.1. Temperature Dependence of the Dual-Mode Model Parameters

As mentioned previously, the dual-mode model parameters from Table 7.2 are illustrated in Figures C.1 and C.2 as a function of temperature, thereby demonstrating a reduction in magnitude as a function of increasing temperature for all parameters. Linear extrapolation of the Langmuir capacity constant (i.e., C_H') to the temperature axis indicates that C_H' will approximately equal zero at a temperature near the reported glass transition temperature (T_g) of 85°C for amorphous PEF from Chapter 5. Such behavior is consistent with the relationship between C_H' and the excess free volume accessible to penetrant sorption in the glassy state, which effectively disappears at T_g during the transition to the rubbery morphology. Similar behavior has also been observed for carbon dioxide sorption in semicrystalline poly(ethylene terephthalate) (PET) [1].

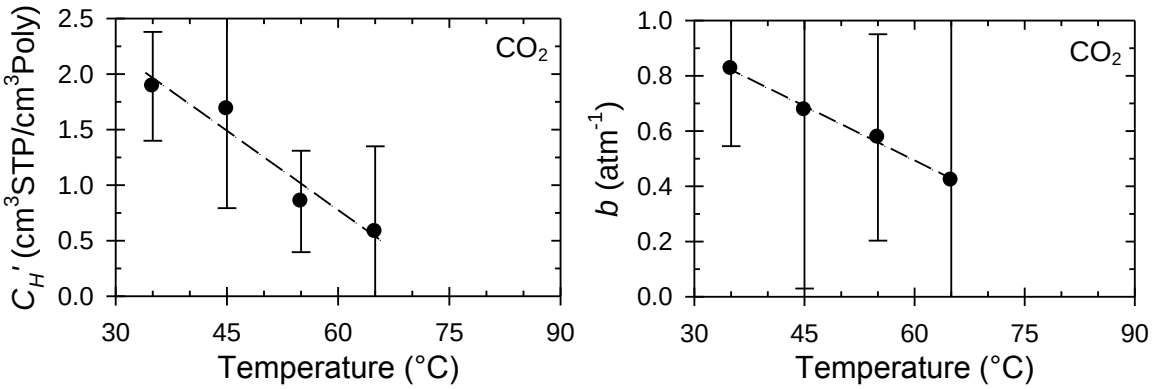

Figure C.1. Dependence of C_H' and b (from sorption) on temp for PEF (values from Table 7.2).

[1]Reproduced in part with permission from Burgess, S.K; Kriegel, R.M.; Koros, W.J., *Carbon Dioxide Sorption and Transport in Amorphous Poly(ethylene furanoate)*, *Macromolecules*, DOI: 10.1021/acs.macromol.5b00333, Copyright 2015 American Chemical Society.

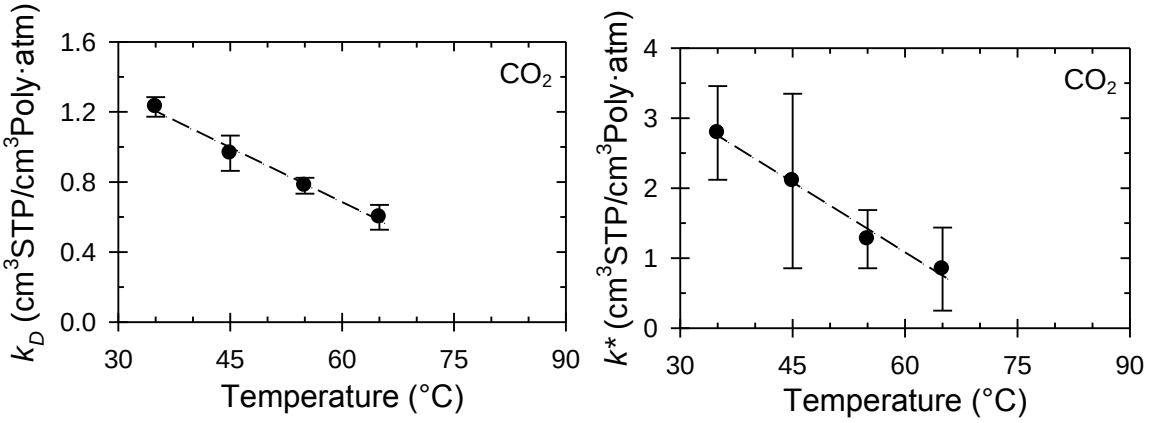

Figure C.2. Dependence of k_D and k^* (from sorption) on temp for PEF (values from Table 7.2).

Similar to the temperature-dependent behavior of k^* determined via permeation (i.e., $k^* = 6\theta P/l^2$) reported in Figure 7.6, k^* determined from sorption (i.e., $k^* = k_D + C_H'b$) should also approach the limiting value of k_D as temperature increases towards the T_g. Such behavior is illustrated in the van't Hoff plot in Figure C.3, which includes estimates for the apparent enthalpy of sorption in the dissolved mode (i.e., ΔH_D) and the apparent enthalpy of sorption in the combined Langmuir and dissolved environments (i.e., $\Delta H_{S,eff}$).

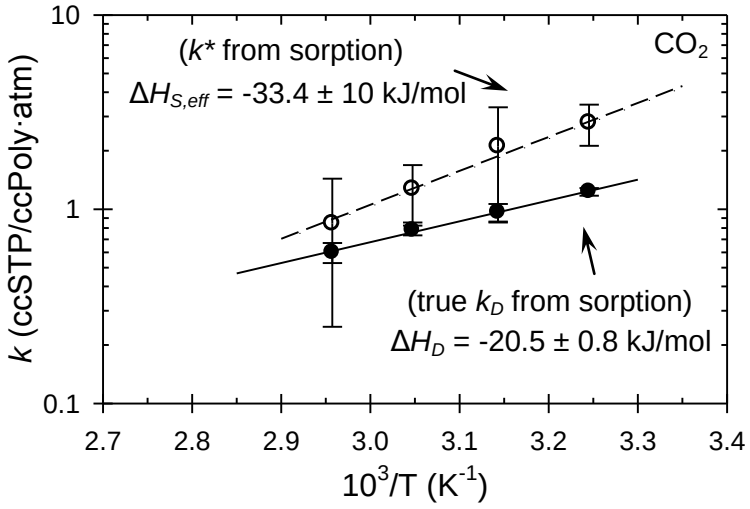

Figure C.3. Van't Hoff plot of k_D and k^* determined from sorption testing for carbon dioxide in PEF.

In contrast to the apparent enthalpy of sorption in the dissolved mode determined from k_D, van't Hoff analysis of the Langmuir affinity parameter can ideally yield the apparent enthalpy of sorption in the Langmuir environment (i.e., ΔH_b). Such analysis is provided in Figure C.4, where the value of -15.9 ± 30 kJ/mol determined for ΔH_b is similar in magnitude to the value of -20.5 kJ/mol determined for ΔH_D. The apparent similarity in ΔH_D and ΔH_b values is not fully understood, since values of ΔH_b are typically more exothermic than ΔH_D in glassy polymers due to sorption in the Langmuir environment occurring in pre-formed penetrant-sized holes [2]. In fact, large uncertainty limits as determined via the fitting program exist for all *b* parameters reported in Table 7.2, and consequently, this error is propagated into the estimate for ΔH_b. Testing at additional temperatures would be required to validate the current trend.

A final note should be mentioned regarding the uncertainty limits for the energetic parameters determined via the Arrhenius and van't Hoff representations employed in this chapter. The uncertainty limits were determined from regression analysis via the standard error of the slope, with exception to the limits for ΔH_b and $\Delta H_{S,eff}$ determined from *b* and *k** (i.e., from sorption, $k^* = k_D + C_H' b$), respectively. The latter two parameters exhibited unusually large uncertainties at all temperatures (cf. Table 7.2), which required the "propagation of such uncertainty" into the uncertainty estimate for the slope. Accommodation of this notion was achieved via application of a MATLAB® routine available online [3], which utilized an estimation method from the literature [4].

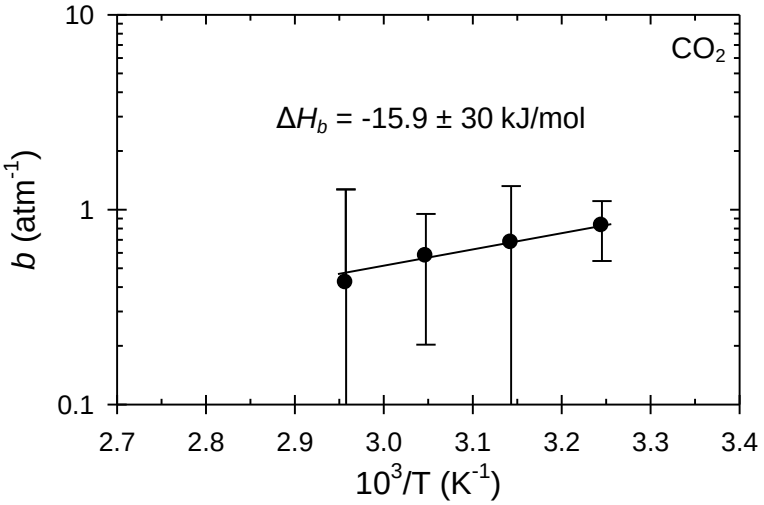

Figure C.4. Van't Hoff plot of *b* (i.e., Langmuir affinity parameter) for carbon dioxide in PEF.

C.2. Partial Immobilization Model Interpretation

The partial immobilization model representations of the permeability and diffusivity are provided in Equations 2.33 and 2.34, respectively, with addition details provided in Chapter 2. As seen in Equation 2.33, a value of $F \approx 0$ (i.e., $D_H \approx 0$) will render the permeability expression independent of upstream pressure. Such behavior occurs in the limit of "total penetrant immobilization" within the Langmuir environment, which is often observed for transport of large, condensable species in glassy polymers (i.e., benzene in PET [5], methanol in PET [6], and sulfur dioxide in Kapton polyimide [7]). As noted in prior work [8], however, F cannot theoretically equal zero, since such reality would render the assumption of "transport equilibrium" between the two modes invalid.

Recall that the dual-mode parameters for carbon dioxide sorption in amorphous PEF at 35°C are reported in Table 7.2 of Chapter 7. These parameters, when incorporated into the partial immobilization model expression for permeability in Equation 2.33, provide a method to determine both F and D_D based on the experimental dependence of

permeability on pressure. The carbon dioxide permeability data at 35°C from Figure 7.1 are re-plotted for illustration purposes in Figure C.5, along with the partial immobilization model expression from Equation 2.33 (dashed line). The optimized model parameters corresponding to carbon dioxide transport in amorphous PEF at 35°C were determined to be $F = 0.3$ and $D_D = 1.4\times10^{-10}$ cm^2/s.

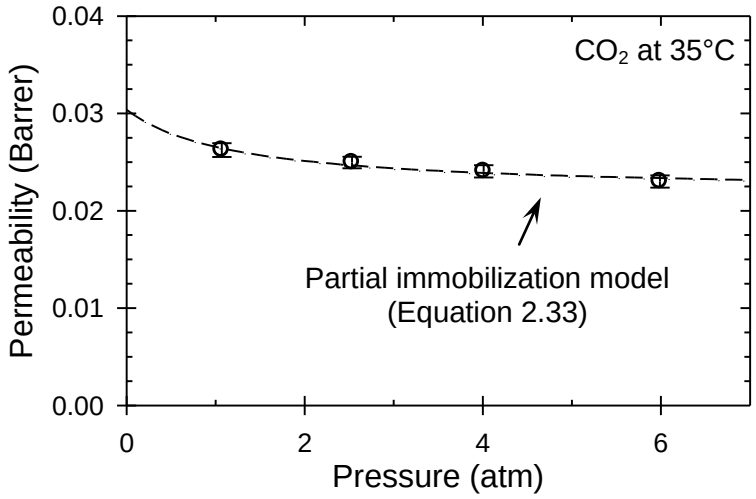

Figure C.5. Permeability at 35°C for CO_2 in PEF (from Figure 7.1). Equation 2.33 is illustrated via the dashed line, with $F = 0.3$ and $D_D = 1.4\times10^{-10}$ cm^2/s.

Inspection of Figure C.5 reveals that the partial immobilization model expression satisfactorily describes the dependence of permeability vs. pressure in the experimental data. The determined value of $F = 0.3$ is larger than expected, especially when considering that respective values for carbon dioxide permeation in various PET samples have been measured between 0.07 to 0.2 [6, 9, 10]. Such a large value of $F = 0.3$ for carbon dioxide in PEF appears to indicate a greater degree of carbon dioxide mobility between sorption modes within PEF compared to PET. This notion is potentially corroborated by the apparent similarity in ΔH_D and ΔH_b discussed previously for PEF,

while ΔH_b is notably more exothermic than ΔH_D for carbon dioxide sorption in semicrystalline PET. This latter reality is consistent with the lower value of F reported for carbon dioxide in PET, which indicates a lower mobility between penetrants in the two sorption modes resulting from the more energetically favorable sorption in the pre-existing microvoids than the dissolved environment.

After determination of F and D_D, Equation 2.34 can provide an estimate for the effective diffusion coefficient for carbon dioxide in PEF as a function of pressure. Diffusivity estimates from Equation 2.34 are plotted in Figure C.6 (dashed line), along with diffusivity estimates determined via application of Equation 7.7 to experimental kinetic uptake data at low pressure (circles). Actual diffusion coefficients were only measured at low pressure; however, as seen in Figure C.6, satisfactory agreement is observed between the estimates determined from Equation 2.34 and the experimentally determined values reported in Chapter 7.

While not illustrated in this Appendix, partial immobilization model parameters were also determined for carbon dioxide transport in PEF at 45°C and 55°C. Values at 45°C were determined to be F = 0.3 and $D_D = 2.4\times10^{-10}$ cm^2/s, while values at 55°C were determined to be F = 0.4 and $D_D = 3.9\times10^{-10}$ cm^2/s. As a consistency check, both F and D_D values exhibit the expected positive correlation with temperature.

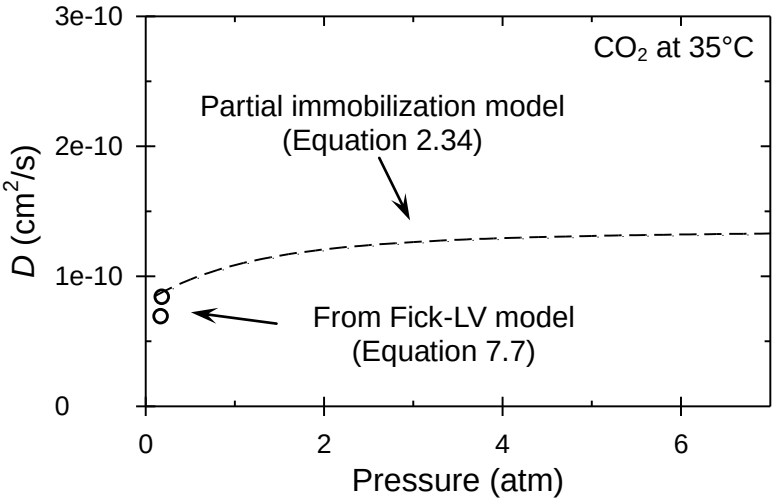

Figure C.6. Diffusivities determined at 35°C for carbon dioxide in PEF via application of the Fick-LV model (Equation 7.7) to kinetic uptake data (hollow circles). The partial immobilization model for D from Equation 2.34 is illustrated via the dashed line, with $F = 0.3$ and $D_D = 1.4\times10^{-10}$ cm^2/s.

C.3. References

1. Koros WJ and Paul DR. CO2 Sorption in Poly(ethylene Terephthalate) above and below the Glass Transition. Journal of Polymer Science: Polymer Physics Edition 1978;16:1947-1963.

2. Barrer RM and Rees LVC. Henry's law adsorption constants. Transactions of the Faraday Society 1961;57(0):999-1007.

3. Linear Regression with Errors in X and Y. http://www.mathworks.com/matlabcentral/fileexchange/26586-linear-regression-with-errors-in-x-and-y.

4. York D, Evensen NM, Martínez ML, and De Basabe Delgado J. Unified equations for the slope, intercept, and standard errors of the best straight line. American Journal of Physics 2004;72(3):367-375.

5. Patton CJ, Felder RM, and Koros WJ. Sorption and transport of benzene in poly(ethylene terephthalate). Journal of Applied Polymer Science 1984;29(4):1095-1110.

6. Lee JS, Chandra P, Burgess SK, Kriegel R, and Koros WJ. An advanced gas/vapor permeation system for barrier materials: Design and applications to poly(ethylene terephthalate). Journal of Polymer Science Part B: Polymer Physics 2012;50(17):1262-1270.

7. Felder RM, Patton CJ, and Koros WJ. Dual-mode sorption and transport of sulfur dioxide in kapton polyimide. Journal of Polymer Science: Polymer Physics Edition 1981;19(12):1895-1909.

8. Paul DR and Koros WJ. Effect of Partially Immobilizing Sorption on Permeability and the Diffusion Time Lag. Journal of Polymer Science: Polymer Physics Edition 1976;14:675-685.

9. Koros WJ and Paul DR. Transient and Steady-State Permeation in Poly(ethylene Terephthalate) Above and Below the Glass Transition. Journal of Polymer Science: Polymer Physics Edition 1978;16:2171-2187.

10. Lee JS, Leisen J, Choudhury RP, Kriegel RM, Beckham HW, and Koros WJ. Antiplasticization-based enhancement of poly(ethylene terephthalate) barrier properties. Polymer 2012;53:213-222.

APPENDIX D

SUPPORTING INFORMATION FOR CHAPTER 9

(KINETIC WATER SORPTION)[1]

D.1. Diffusion Model Justification

As mentioned in Chapters 3 and 9, uptake curves generated from the automated VTI instrument exhibit anomalous curvature at short times due primarily to lag introduced by the automated control scheme (cf. Figure 9.3). Such data were formally modeled using the framework established by Long and Richman [1], which implements an exponential approach to surface concentration at the film surface. In the original application of Long and Richman [1], Equations 2.52 and 2.53 were implemented to account for non-Fickian relaxations occurring in the polymer during vapor sorption. The model parameter τ_S therefore represents an intrinsic property of the material, and will vary based on the penetrant/polymer system being investigated. The current work differs from the original application, in that Equation 2.53 is implemented out of convenience to account for the lag introduced by the automated process control scheme of the VTI instrument. The automated VTI instrument operates by mixing two separate nitrogen streams, one completely humidified and the other dry, using differing respective flow rates to achieve the desired water activity. The resultant mixed stream is then split so that half flows into the chamber which contains the sample, and the other half flows into a separate reference chamber which contains an empty quartz basket. Additional details regarding operation of

[1]Reprinted in part from *Polymer*, 55/26, Burgess, S.K.; Mikkilineni, D.S.; Yu, D.B.; Kim, D.J.; Mubarak, C.R.; Kriegel, R.M.; Koros, W.J., *Water Sorption in Poly(ethylene furanoate) Compared to Poly(ethylene Terephthalate). Part 2: Kinetic Sorption*, 6870-6882, Copyright 2014, with permission from Elsevier.

the VTI instrument are provided in Chapter 3.

A secondary cause of the anomalous sorption kinetics observed in the current work originates from possible variability in water concentration at the film surface due to large residence times of the carrier gas inside the sample chamber. This behavior is conceptually similar to that observed for a concentration step change in a continuous stirred tank reactor (CSTR). The residence time (τ_{Res}) for the carrier gas in the current work is defined as the volume of the sample chamber (cm^3) divided by the volumetric flow rate of the carrier gas (cm^3/min). The volume of the chamber is estimated to be ~152 cm^3 (~3.8 x 3.8 x 10.5 cm), and the combined wet/dry flow rate was automatically set at ~427 cm^3/min for all water activities. Calculation of the residence time for the carrier gas inside the sample chamber is straightforward and equals ~43 s (i.e., 152/(427/2)). The value of τ_{Res} is therefore lower than the value of ~133 s for τ_S averaged over the entire activity range during sorption and desorption in Figure 9.12, but still likely contributes to the overall anomalous kinetic behavior. Consequently, the τ_S parameter in Equation 2.53 reflects contributions from both the process control lag and the secondary residence time effects associated with a step change in water activity. Additional investigation of this notion is provided in Table D.1, which provides D_{Avg} and τ_S data measured for water in PEF using pure helium and pure argon as the carrier gas, in addition to nitrogen operated at lower flow rates via manual control. All data in Table D.1 were measured at 45°C between the sorption interval of 0.1 – 0.2 activity.

Table D.1. D_{Avg} and τ_s values for water in PEF measured at 45°C during sorption between 0.1 – 0.2 water activity. The total flow rate reflects combination of both dry and humid streams, which is split into two separate streams before entering the sample and reference chambers.

Carrier gas	Total flow rate (cm^3/min)	$D_{Avg} \times 10^9$ (cm^2/s)	τ_S (s)	τ_{Res}[c] (s)
Nitrogen	427[a]	4.0	102	~43
	213[b]	4.0	102	~86
	106[b]	4.2	278	~173
Helium	427[a]	4.2	48	~43
Argon	427[a]	3.9	70	~43

a: Measurements obtained using automated flow control.
b: Measurements obtained using manual flow control.
c: $\tau_{Res} \approx$ (chamber volume)/(carrier gas flow rate in the sample chamber).

As seen from Table D.1, values of D_{Avg} and τ_S are similar in magnitude for all cases, with the possible exception being the τ_S value measured using the lowest nitrogen flow rate of 106 cm^3/min. This behavior indicates that neither the carrier gas type nor the flow rate significantly impacts the anomalous contribution to the diffusion process. Furthermore, this behavior is consistent with the notion that the process control lag is the primary cause of the anomalous sorption behavior, with residence time effects likely existing as a secondary cause. These experiments further confirm the utility of Equations 2.52 and 2.53 in the current work for removal of the non-physical "instrument-induced" anomalous behavior, thereby allowing extraction of more accurate intrinsic polymer parameters.

D.2. Quartz Spring Diffusion Coefficient Data at 35°C

Diffusion coefficients obtained during water sorption at 35°C are provided in Figure D.1 for PEF (diamonds) and PET (circles) measured by the automated VTI system (solid

points) and the manual quartz spring system (hollow). The D_{Avg} values in Figure D.1 are plotted at the midpoint of the sorption interval, and exhibit consistency between the two independent methods.

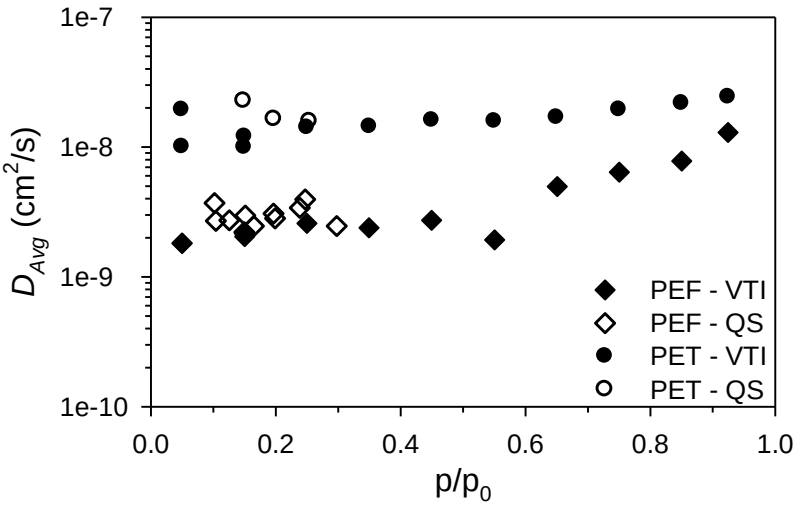

Figure D.1. D_{Avg} values for water in PEF (diamonds) and PET (circles) measured at 35°C by the automated VTI system (solid points) and the manual quartz spring system (QS, hollow points).

D.3. Partial Immobilization Model Interpretation

Diffusion of low-activity vapor in glassy polymers can often be described using the partial immobilization model (PIM), which is described in Chapter 2. As discussed in Chapter 8, simple dual-mode sorption behavior was observed for water at 35°C in both polyesters up to ~0.6 activity (cf. Figure 8.1). Values of the dual-mode model parameters needed to evaluate Equation 2.34 are provided in Table 8.1. The parameter *F* can vary from zero to one, where the former represents the limit of total penetrant immobilization within the Langmuir microvoids and the latter represents no immobilization. Values of *F* near zero are common for condensable gas and vapor transport in PET, such as benzene [2] and methanol [3], and it is expected that corresponding parameters for water in PET

and PEF will be analogously close to zero. Consequently, values of $F \approx 0$ are assumed for water transport in both polyesters in the subsequent discussions. Figures D.2a and D.2b provide diffusion coefficient data for water in PEF and PET, respectively, at 35°C during initial sorption testing using the VTI instrument. The solid lines represent the optimized fit of Equation 2.34 to both respective data sets (with $F \approx 0$), where $D_D \approx 2.6 \times 10^{-9}$ cm^2/s for water in PEF and $D_D \approx 1.5 \times 10^{-8}$ cm^2/s for water in PET. The dashed line represents 0.6 activity (0.033 atm), which marks the departure from dual mode behavior.

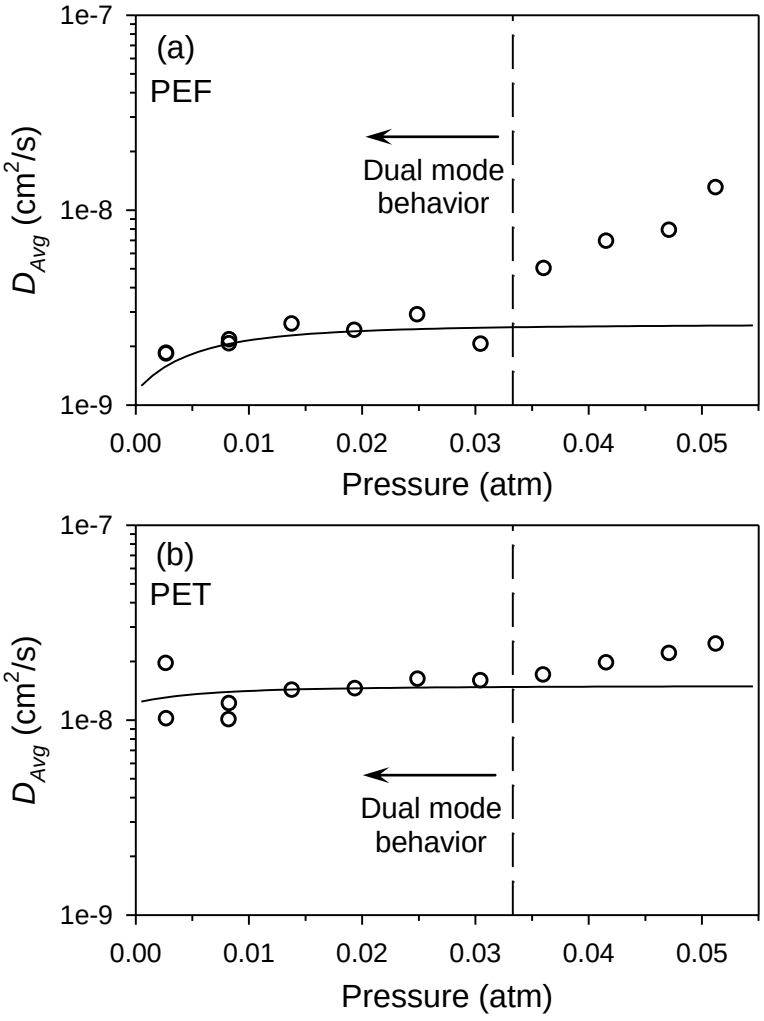

Figure D.2. Diffusion coefficient data for H_2O at 35°C in PEF (a) and PET (b) from Figures 9.6 and 9.7. The solid lines represent the optimized fits from Equation 2.34 ($F \approx 0$) with $D_D = 2.6 \times 10^{-9}$ cm^2/s for PEF and $D_D = 1.5 \times 10^{-8}$ cm^2/s for PET. The dashed lines represent 0.6 activity.

As seen in Figure D.2, the departure from simple dual mode behavior occurs at ~0.033 atm (0.6 activity) for both polyesters and is consistent with plasticization-type behavior. However, independent permeation experiments are needed to truly confirm the presence of plasticization and absence of penetrant clustering.

D.4. References

1. Long FA and Richman D. Concentration Gradients for Diffusion of Vapors in Glassy Polymers and their Relation to Time Dependent Diffusion Phenomena1,2. Journal of the American Chemical Society 1960;82(3):513-519.

2. Patton CJ, Felder RM, and Koros WJ. Sorption and transport of benzene in poly(ethylene terephthalate). Journal of Applied Polymer Science 1984;29(4):1095-1110.

3. Lee JS, Chandra P, Burgess SK, Kriegel R, and Koros WJ. An advanced gas/vapor permeation system for barrier materials: Design and applications to poly(ethylene terephthalate). Journal of Polymer Science Part B: Polymer Physics 2012;50(17):1262-1270.

APPENDIX E

SUPPORTING INFORMATION FOR CHAPTER 11

(MATLAB® DIFFUSION COEFFICIENT MODELING)

E.1. Truncation of an Infinite Decaying Series

As discussed in Chapter 11, 100 terms were used to numerically approximate the infinite series solutions in Equations 11.2, 11.3, 11.6, and 11.7. The use of only 100 terms to approximate the infinite series is well justified, in most cases, due to the functional form of the decaying exponential. Specifically, as "*n*" becomes large, the subsequent terms in the series added to the total sum become exceedingly small, thereby having less impact on the total sum. Furthermore, the error resulting from truncating the series is only realized at short times and manifests as a distinct departure from linearity in M_t/M_∞ plotted as a function of $(\text{time})^{1/2}$. Figure E.1a illustrates the M_t/M_∞ solution obtained from the simple Fickian solution in Equation 11.2 for diffusion in an infinite sheet, with multiple curves calculated using different numbers of terms to approximate the series. The graph depicted in Figure E.1b is an expanded view of the short time behavior to further illustrate the error associated with truncating the series. As seen in Figure E.1b, the difference between using 100 and 1000 terms to approximate the series is negligible, thereby justifying the use of only 100 terms in the current work.

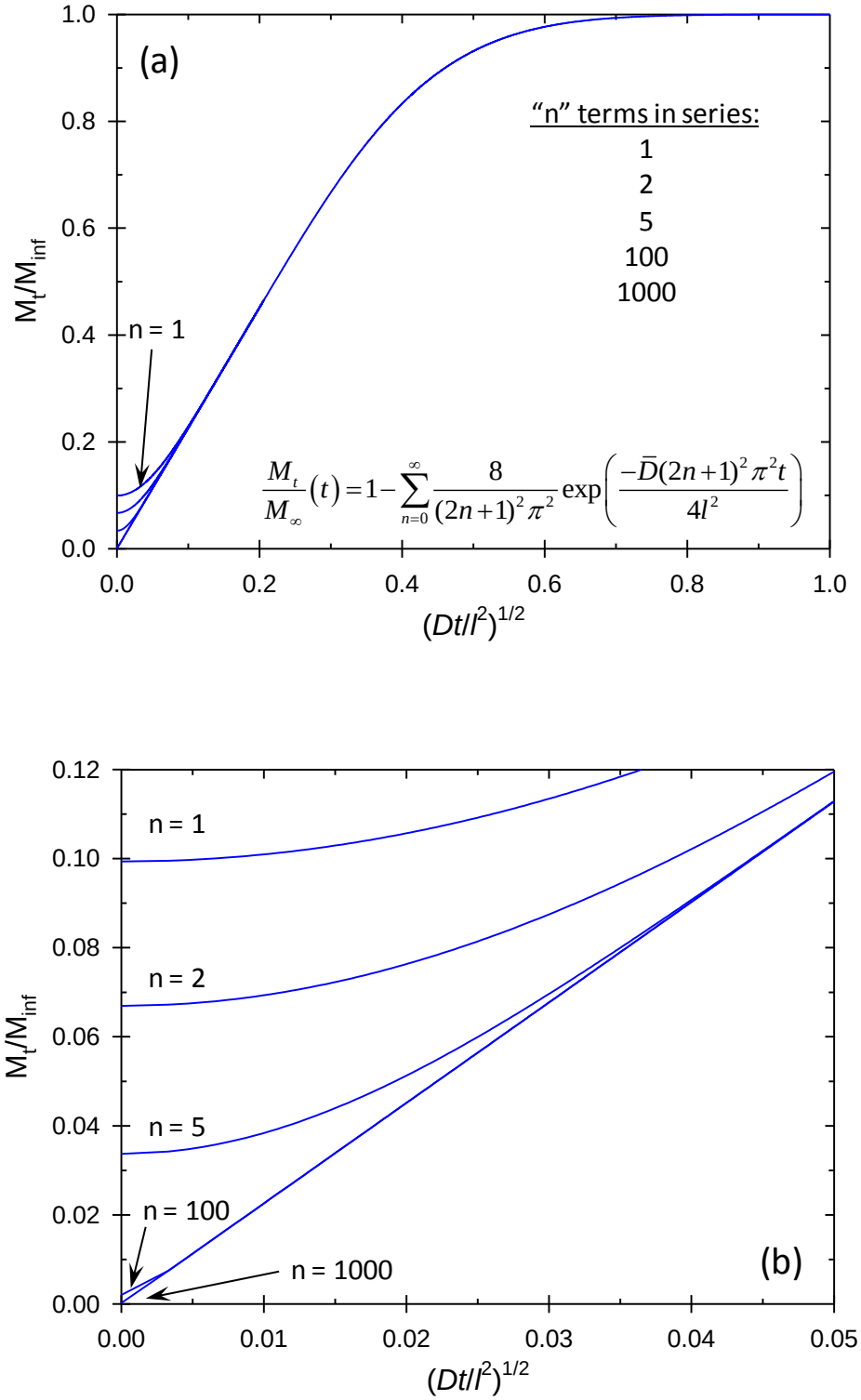

Figure E.1. M_t/M_∞ plot calculated from Equation 11.2 for Fickian diffusion in an infinite sheet. Model parameters: l = 0.178 cm, D = 1e-8 cm^2/s, number of terms in the series: 1, 2, 5, 100, and 1000. Plot (b) represents a close up view of plot (a) to illustrate the short-time behavior.

E.2. Diffusion Analysis—Finite Cylinder Geometry

This section will illustrate the process for modeling Fickian diffusion in a bounded cylinder geometry, which is useful for describing diffusion of ethylene glycol *out of* a cylindrical PEF pellet at high temperature during the solid-state polymerization process. The partial differential equation describing unsteady state diffusion in both the radial (r) and axial (x) cylinder dimensions is provided in Equation E.1 in terms of concentration (C) and assuming a constant diffusion coefficient, D.

$$\frac{\partial C}{\partial t} = \frac{D}{r}\frac{\partial}{\partial r}\left(r\frac{\partial C}{\partial r}\right) + D\frac{\partial^2 C}{\partial x^2} \tag{E.1}$$

The penetrant concentration at the pellet surface can be assumed zero in this application, and a constant initial concentration throughout the pellet is chosen for the initial condition. Analytical solution of linear partial differential equations with non-complex boundary conditions can be simplified via the principle of superposition. Using this technique, solving the original problem described in Equation E.1 (i.e., diffusion in a bounded cylinder) can be separated into two diffusion problems, viz., 1) solving the diffusion equation independently for an infinite sheet geometry, and 2) solving the diffusion equation independently for an infinite cylinder geometry. Superposition then dictates that the product of the solutions derived from the two simple domains will provide the solution over the combined, more restrictive domain (i.e., diffusion in the finite cylinder) [1]. The solutions for the two aforementioned simplified diffusion problems can be obtained by one of many analytical techniques, and are provided in Equations E.2 and E.3 for the *infinite sheet* and *infinite cylinder* geometries, respectively

[2]. Equation E.4 illustrates the product of Equation's E.2 and E.3, and thereby represents the solution to Equation E.1 for diffusion in a *bounded cylinder*.

$$\overline{C}(t,x)=\frac{4}{\pi}\sum_{n=0}^{\infty}\frac{(-1)^n}{2n+1}\cos\left(\frac{(2n+1)\pi x}{2l}\right)\exp\left(\frac{-D(2n+1)^2\pi^2 t}{4l^2}\right) \tag{E.2}$$

$$\overline{C}(t,r)=\frac{2}{a}\sum_{n=1}^{\infty}\frac{J_0(r\alpha_n)}{\alpha_n J_1(a\alpha_n)}\exp\left(-D\alpha_n^2 t\right) \tag{E.3}$$

$$\overline{C}(t,r,x)=\frac{8}{\pi a}\sum_{n=0}^{\infty}\sum_{m=1}^{\infty}\frac{J_0(r\alpha_m)}{\alpha_m J_1(a\alpha_m)}\frac{(-1)^n}{2n+1}\cos\left(\frac{(2n+1)\pi x}{2l}\right)\exp\left(-Dt\left(\alpha_m^2+\frac{(2n+1)^2\pi^2}{4l^2}\right)\right) \tag{E.4}$$

In Equations E.2 – E.4, $\overline{C}$ is the dimensionless concentration (C/C_o), a is the cylinder radius, l is the cylinder half length, J_o is the Bessel function of the first kind (order zero), J_1 is the Bessel function of the first kind (order one), and the α_m's are the non-repeating roots of Equation E.5.

$$J_0(a\alpha_m)=0 \tag{E.5}$$

Equation E.4 is useful because it can be converted to an expression that describes the total penetrant mass *loss* from the cylinder as a function of time. This quantity can be calculated by integrating Equation E.4 over both spatial variables while using the

weighting factor "*r*" and normalizing the quantity by the integral of the weighting factor over the spatial domain. This integration is depicted in Equation E.6, where M_t is the penetrant mass loss from the cylinder at time "*t*" and M_∞ is the equilibrium penetrant mass loss from the cylinder as time goes to infinity.

$$\frac{M_t}{M_\infty}(t) = \frac{\int_0^a \int_{-l}^{l} \overline{C}(t,r,x) \cdot r \; dxdr}{\int_0^a \int_{-l}^{l} r \; dxdr} \tag{E.6}$$

The expression in Equation E.6, after integrating over both spatial variables, can be expressed via Equation E.7, viz.,

$$\frac{M_t}{M_\infty}(t) = \sum_{n=0}^{\infty}\sum_{m=1}^{\infty} \frac{32}{(\pi a \alpha_m)^2 (2n+1)^2} \exp\left(-Dt\left(\alpha_m^2 + \frac{(2n+1)^2 \pi^2}{4l^2}\right)\right) \tag{E.7}$$

Equation E.7 is useful, since it can be directly modeled to experimental penetrant mass loss data for a bounded, cylindrical pellet to yield a value for *D*, considering that all of the aforementioned assumptions are valid and M_∞ is known. The accuracy of Equation E.7 can be verified by calculating and plotting the M_t/M_∞ for an infinite sheet and infinite cylinder and comparing the results to the M_t/M_∞ for the bounded cylinder. Using this approach, the graph of Equation E.7 *should* approach the graph of either the infinite sheet or infinite cylinder uptake curves depending on the model inputs for the radius and cylinder half length. Figure E.2 provides example plots of M_t/M_∞ for a finite cylinder

(i.e., Equation E.7), infinite sheet (i.e., Equation 11.2), and infinite cylinder with model parameters provided in the figure caption. The MATLAB® codes used to generate the curves in Figure E.2 are provided in the next section.

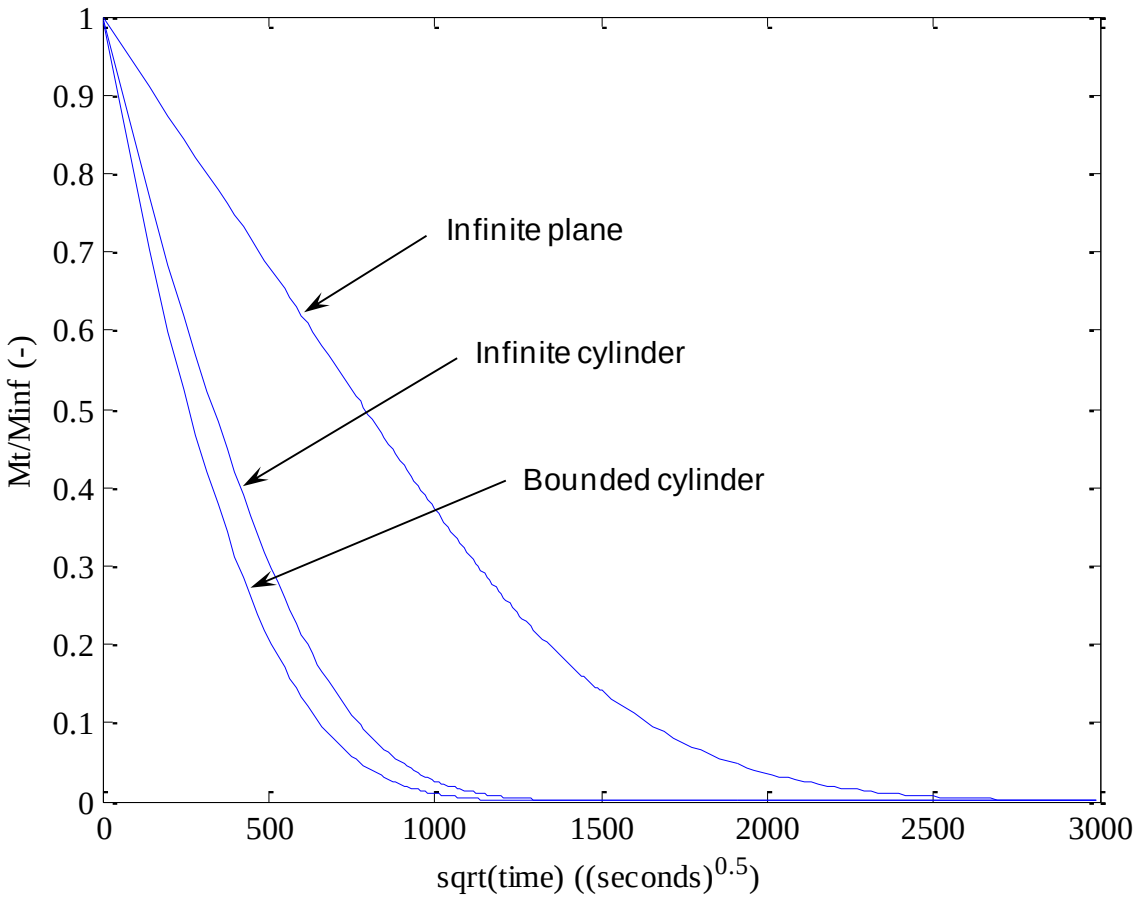

Figure E.2. Example plots of M_t/M_∞ for the finite cylinder, infinite sheet, and infinite cylinder geometries. Model parameters are: a = 0.133 cm, l = 0.178 cm, D = 1e-8 cm^2/s, and 100 terms were used to approximate each infinite series.

The M_t/M_∞ curves for the infinite sheet and infinite cylinder geometries were verified to agree with the corresponding values published in reference [2]. As a final check, the curve for the finite cylinder geometry did indeed converge onto the curve for the infinite sheet and infinite cylinder geometries when the radius and half length values were increased, respectively.

E.3. MATLAB® Code for Plotting Infinite Series Solutions

E.3.1. *Infinite Sheet: Fickian (Equation 2.47)*

```
%%%%%%%%%%%%%%%%%%%%%%%%%%%%%%%%%%%%%%%%%%%%%%%%%%%%%%%%%%%%%%%%%%%%%%%%%%%%
%%% Plots Mt/Minf for Equation 2.47 (Fickian diffusion in an infinite
%%% sheet). File name "Sheet.m"

clear; clc;       %Clear system memory

% Define relevant model input parameters
L = 0.0045;       % Film full thickness (cm)
D = 6.8E-11;      % Diffusion coefficient (cm2/s)

time = 400000;    % Total time of the diffusion process in seconds

% Define the time step of the plotting function
num_steps = 10000;
dt = round(time/num_steps);
terms = 100;      % Number of terms to approximate the infinite series

% Pre-allocate space for the variable matrices
m = zeros(num_steps+1,terms);
t = zeros(num_steps+1,1);

% Discretize the summation term
for n = 1:1:num_steps+1;
    t(n) = (n-1)*dt;
    for i = 0:1:terms-1;
        m(n,i+1) = 8/pi^2*1/(2*i+1)^2*exp(-D*(2*i+1)^2*pi^2*t(n)/L^2);
    end
end
mtminf = 1 - sum(m')';

% Plot Mt/Minf vs. square root of time (i.e., sec^0.5)
sqrtt = sqrt(t);
plot(sqrtt,mtminf)
set(0,'DefaultAxesFontName','Times New Roman');
xlabel('sqrt(time) ((seconds)^0^.^5)');
ylabel('Mt/Minf (-)');

% Plot the Mt/Minf vs. normalized time
% plot(sqrt(D*t./(L^2)),mtminf)
```

E.3.2. *Infinite Sheet: Fickian, Relaxations (Equation 2.55)*

```
%%%%%%%%%%%%%%%%%%%%%%%%%%%%%%%%%%%%%%%%%%%%%%%%%%%%%%%%%%%%%%%%%%%%%%%%%%%%
%%% Plots Mt/Minf for Equation 2.55 (Diffusion in an infinite
%%% sheet with non-Fickian relaxations). File name "Sheet_BH.m"

clear; clc;     %Clear system memory

% Define relevant model input parameters
L = 0.0045;       % Film full thickness (cm)
D = 6.8E-11;      % Diffusion coefficient (cm2/s)
phi = 0.5;        % Weighting parameter
k = 1e-6;         % Relaxation rate constant (1/s)

time = 400000;    % Total time of the diffusion process in seconds

% Define the time step of the plotting function
num_steps = 10000;
dt = round(time/num_steps);
terms = 100;      % Number of terms to approximate the infinite series

% Pre-allocate space for the variable matrices
m = zeros(num_steps+1,terms);
t = zeros(num_steps+1,1);

% Discretize the summation term
for n = 1:1:num_steps+1;
    t(n) = (n-1)*dt;
    for i = 0:1:terms-1;
        m(n,i+1) = 8/pi^2*1/(2*i+1)^2*exp(-(2*i+1)^2*pi^2*D*t(n)/L^2);
    end
end
y = 1 - sum(m')';

% Implement Berens-Hopfenberg framework
mtminf = phi.*y + (1 - phi).*(1 - exp(-k.*t./1));

% Plot Mt/Minf vs. square root of time (i.e., sec^0.5)
sqrtt = sqrt(t);
plot(sqrtt,mtminf)
set(0,'DefaultAxesFontName','Times New Roman');
xlabel('sqrt(time) ((seconds)^0^.^5)');
ylabel('Mt/Minf (-)');

% Plot the Mt/Minf vs. normalized time
% plot(sqrt(D*t./(L^2)),mtminf)
```

E.3.3. *Infinite Sheet: Fickian, Limited Volume (Equation 2.49)*

```
%%%%%%%%%%%%%%%%%%%%%%%%%%%%%%%%%%%%%%%%%%%%%%%%%%%%%%%%%%%%%%%%%%%%%%%%
%%% Plots Mt/Minf for Equation 2.49 (Fickian diffusion in an infinite
%%% sheet--limited volume solution). File name "Sheet_LV.m"

clear; clc;       %Clear system memory

% Define relevant model input parameters
L = 0.0045;       % Film full thickness (cm)
D = 6.8E-11;      % Diffusion coefficient (cm2/s)
alpha = 1;        % From Equation 2.51 (experimentally determined)

time = 400000;    % Total time of the diffusion process in seconds

% Define the time step of the plotting function
num_steps = 10000;
dt = round(time/num_steps);
terms = 100;      % Number of terms to approximate the infinite series

% Pre-allocate space for the variable matrices
m = zeros(num_steps+1,terms);
t = zeros(num_steps+1,1);

% Solve the transcendental equation in Equation 2.50
ep = 0.00001;
qn = zeros(1,terms);
for i = 1:terms
   qn(i) = fzero(@(xD) tan(xD)+alpha*(xD),[pi/2+(i-1)*pi+ep pi/2+i*pi-
ep]);
end

% Discretize the summation term
for n = 1:1:num_steps+1;
    t(n) = (n-1)*dt;
    for i = 0:1:terms-1;
        m(n,i+1) = 2*alpha*(1+alpha)/(1+alpha+alpha^2*qn(i+1)^2)*exp(-
D*(qn(i+1))^2*t(n)*4/L^2);
    end
end
mtminf = 1 - sum(m')';

% Plot Mt/Minf vs. square root of time (i.e., sec^0.5)
sqrtt = sqrt(t);
plot(sqrtt,mtminf)
set(0,'DefaultAxesFontName','Times New Roman');
xlabel('sqrt(time) ((seconds)^0^.^5)');
ylabel('Mt/Minf (-)');

% Plot the Mt/Minf vs. normalized time
% plot(sqrt(D*t./(L^2)),mtminf)
```

E.3.4. *Infinite Sheet: Fickian, Limited Volume, Relaxations (Equation 11.7)*

```
%%%%%%%%%%%%%%%%%%%%%%%%%%%%%%%%%%%%%%%%%%%%%%%%%%%%%%%%%%%%%%%%%%%%%%%%
%%% Plots Mt/Minf for Equation 11.7 (Diffusion in an infinite sheet
%%% with relaxations: limited volume solution). File name
%%% "Sheet_LV_BH.m"

clear; clc;  %Clear system memory

% Define relevant model input parameters
L = 0.0045;        % Film full thickness (cm)
D = 6.8E-11;       % Diffusion coefficient (cm2/s)
alpha = 1;         % From Equation 2.51 (experimentally determined)
phi = 0.5;         % Weighting parameter
k = 1e-6;          % Relaxation rate constant (1/s)

time = 400000;     % Total time of the diffusion process in seconds

% Define the time step of the plotting function
num_steps = 10000;
dt = round(time/num_steps);
terms = 100;       % Number of terms to approximate the infinite series

% Pre-allocate space for the variable matrices
m = zeros(num_steps+1,terms);
t = zeros(num_steps+1,1);

% Solve the transcendental equation in Equation 2.50
ep = 0.00001;
qn = zeros(1,terms);
for i = 1:terms
   qn(i) = fzero(@(xD) tan(xD)+alpha*(xD),[pi/2+(i-1)*pi+ep pi/2+i*pi-
ep]);
end

% Discretize the summation term
for n = 1:1:num_steps+1;
    t(n) = (n-1)*dt;
    for i = 0:1:terms-1;
        m(n,i+1) = 2*alpha*(1+alpha)/(1+alpha+alpha^2*qn(i+1)^2)*exp(-
D*(qn(i+1))^2*t(n)*4/L^2);
    end
end
y = 1 - sum(m')';

% Implement Berens-Hopfenberg framework
mtminf = phi.*y + (1 - phi).*(1 - exp(-k.*t./1));

% Plot Mt/Minf vs. square root of time (i.e., sec^0.5)
sqrtt = sqrt(t);
plot(sqrtt,mtminf)
set(0,'DefaultAxesFontName','Times New Roman');
xlabel('sqrt(time) ((seconds)^0^.^5)');
ylabel('Mt/Minf (-)');
```

E.3.5. *Infinite Sheet: Fickian, Exponential BC (Equation 2.53)*

```
%%%%%%%%%%%%%%%%%%%%%%%%%%%%%%%%%%%%%%%%%%%%%%%%%%%%%%%%%%%%%%%%%%%%%%%%
%%% Plots Mt/Minf for Equation 2.53 (Fickian diffusion in an infinite
%%% sheet with exponential time BC). File name "Sheet_Exp.m"

clear; clc;  %Clear system memory

% Define relevant model input parameters
L = 0.0045;       % Film half thickness (cm)
D = 2.4e-8;       % Diffusion coefficient (cm2/s)
tauS = 500;       % Time constant to reach surface saturation (s)

time = 40000;     % Total time of the diffusion process in seconds

% Define the time step of the plotting function
num_steps = 10000;
dt = round(time/num_steps);
terms = 200;      % Number of terms to approximate the infinite series

% Pre-allocate space for the variable matrices
m = zeros(num_steps+1,terms);
t = zeros(num_steps+1,1);
timeadd = zeros(num_steps+1,1);

% Discretize the summation term
for n = 1:1:num_steps+1;
    t(n) = (n-1)*dt;
    for i = 0:1:terms;
    m(n,i+1) = 8/(pi^2)*(exp(-
D*(2*i+1)^2*pi^2*t(n)/(4*L^2)))/((2*i+1)^2*(1-
((2*i+1)^2*(D*tauS*pi^2/(4*L^2)))));
    end
    timeadd(n) = (exp(-
(1/tauS)*(t(n))).*((D*tauS/(L^2))^(1/2)).*(tan((L^2/(tauS*D))^(1/2))));
end
mtminf = 1 - timeadd - sum(m')';

% Plot Mt/Minf vs. square root of time (i.e., sec^0.5)
sqrtt = sqrt(t);
plot(sqrtt,mtminf)
set(0,'DefaultAxesFontName','Times New Roman');
xlabel('sqrt(time) ((seconds)^0^.^5)');
ylabel('Mt/Minf (-)');

% Plot the Mt/Minf vs. normalized time
%plot(sqrt(D*t./(L^2)),mtminf)
```

E.3.6. *Infinite Sheet: Fickian, Exponential BC, Relaxations (Equation 9.3)*

```
%%%%%%%%%%%%%%%%%%%%%%%%%%%%%%%%%%%%%%%%%%%%%%%%%%%%%%%%%%%%%%%%%%%%%%%%
%%% Plots Mt/Minf for Equation 9.3 (Diffusion in an infinite sheet with
%%% exponential time BC and relaxations). File name "Sheet_Exp_BH.m"

clear; clc;  %Clear system memory

% Define relevant model input parameters
L = 0.0045;         % Film HALF thickness (cm)
D = 2.4e-8;         % Diffusion coefficient (cm2/s)
tauS = 500;         % Time constant to reach surface saturation (s)
phi = 0.5;          % Weighting parameter
k = 1e-6;           % Relaxation rate constant (1/s)

time = 40000;    % Total time of the diffusion process in seconds

% Define the time step of the plotting function
num_steps = 10000;
dt = round(time/num_steps);
terms = 200;      % Number of terms to approximate the infinite series

% Pre-allocate space for the variable matrices
m = zeros(num_steps+1,terms);
t = zeros(num_steps+1,1);
timeadd = zeros(num_steps+1,1);

% Discretize the summation term
for n = 1:1:num_steps+1;
    t(n) = (n-1)*dt;
    for i = 0:1:terms;
    m(n,i+1) = 8/(pi^2)*(exp(-
D*(2*i+1)^2*pi^2*t(n)/(4*L^2)))/((2*i+1)^2*(1-
((2*i+1)^2*(D*tauS*pi^2/(4*L^2)))));
    end
    timeadd(n) = (exp(-
(1/tauS)*(t(n))).*((D*tauS/(L^2))^(1/2)).*(tan((L^2/(tauS*D))^(1/2))));
end
y = 1 - timeadd - sum(m')';

% Implement Berens-Hopfenberg framework
mtminf = phi.*y + (1 - phi).*(1 - exp(-k.*t./1));

% Plot Mt/Minf vs. square root of time (i.e., sec^0.5)
sqrtt = sqrt(t);
plot(sqrtt,mtminf)
set(0,'DefaultAxesFontName','Times New Roman');
xlabel('sqrt(time) ((seconds)^0^.^5)');
ylabel('Mt/Minf (-)');

% Plot the Mt/Minf vs. normalized time
% plot(sqrt(D*t./(L^2)),mtminf)
```

E.3.7. *Infinite Cylinder: Fickian (Equation 5.23 in Ref. 1)*

```
%%%%%%%%%%%%%%%%%%%%%%%%%%%%%%%%%%%%%%%%%%%%%%%%%%%%%%%%%%%%%%%%%%%%%%%%
%%% Plots Mt/Minf for Equation 5.23 in ref 1. (Fickian diffusion in an
%%% infinite cylinder). File name "Cylinder_Infinite.m"

clear; clc;  %Clear system memory

% Define relevant model input parameters
a = 0.133;           % Cylinder radius (cm)
D = 1.1*10^-8;       % Diffusion coefficient (cm2/s)

time = 4000000;      % Total time of the diffusion process in seconds

% Define the time step of the plotting function
num_steps = 10000;
dt = round(time/num_steps);
terms = 100;         % Number of terms to approximate the series

% Pre-allocate space for the variable matrices
m = zeros(num_steps+1,terms);
t = zeros(num_steps+1,1);

% Store the zeros of the J0 bessel function (code by Greg von Winckel:
% available for download on the Mathworks website)
Bzeros = besselzero(0,terms,1);
alphaN = Bzeros/a;   % From Equation E.5

% Discretize the summation term
for n = 1:1:num_steps+1;
    t(n) = (n-1)*dt;
    for i = 1:1:terms;
        m(n,i+1) = 4/(a^2*alphaN(i)^2)*exp(-D*alphaN(i)^2*t(n));
    end
end
mtminf = 1 - sum(m')';

% Plot Mt/Minf vs. square root of time (i.e., sec^0.5)
sqrtt = sqrt(t);
%plot(sqrtt,mtminf)
set(0,'DefaultAxesFontName','Times New Roman');
xlabel('sqrt(time) ((seconds)^0^.^5)');
ylabel('Mt/Minf (-)');

% Plot the Mt/Minf vs. normalized time
plot(sqrt(D*t./(a)^2),mtminf)
```

E.3.8. *Bounded Cylinder: Fickian (Equation E.7)*

```
%%%%%%%%%%%%%%%%%%%%%%%%%%%%%%%%%%%%%%%%%%%%%%%%%%%%%%%%%%%%%%%%%%%%%%%%
%%% Plots Mt/Minf for Equation E.7 (Fickian diffusion in a bounded
%%% cylinder). File name "Cylinder_Bounded.m"

clear; clc;  %Clear system memory

% Define relevant model input parameters
a = 0.133;          % Cylinder radius (cm)
L = 0.178;          % Cylinder half length (cm)
D = 1.1*10^-8;      % Diffusion coefficient (cm2/s)

time = 4000000;     % Total time of the diffusion process in seconds

% Define the time step of the plotting function
num_steps = 10000;
dt = round(time/num_steps);
terms = 100;       % Number of terms to approximate the infinite series

% Pre-allocate space for the variable matrices
m1 = zeros(num_steps+1,terms);
m2 = zeros(num_steps+1,terms);
t = zeros(num_steps+1,1);

% Store the zeros of the J bessel function (code by Greg von Winckel --
% available for download on the Mathworks website)
Bzeros = besselzero(0,terms,1);
alphaN = Bzeros/a;

% Discretize the summation terms
for n = 1:1:num_steps+1;
    t(n) = (n-1)*dt;
    for i = 1:1:terms;
        m1(n,i+1) = 32/(pi*a*alphaN(i))^2*exp(-D*t(n)*alphaN(i)^2);
        m2(n,i+1) = 1/(2*(i-1)+1)^2*exp(-D*t(n)*(2*(i-
1)+1)^2*pi^2/(4*L^2));
    end
end
mtminf = 1 - sum(m1')'.*sum(m2')';

% Plot Mt/Minf vs. square root of time (i.e., sec^0.5)
sqrtt = sqrt(t);
plot(sqrtt,mtminf)
set(0,'DefaultAxesFontName','Times New Roman');
xlabel('sqrt(time) ((seconds)^0^.^5)');
ylabel('Mt/Minf (-)');

% Plot the Mt/Minf vs. normalized time
% plot(sqrt(D*t./(a)^2),mtminf)
% plot(sqrt(D*t./(L)^2),mtminf)
```

E.3.9. *Plotting with a Non-uniform Time Domain*

```
%%%%%%%%%%%%%%%%%%%%%%%%%%%%%%%%%%%%%%%%%%%%%%%%%%%%%%%%%%%%%%%%%%%%%%%%%%%%
%%% The following code defines a non-uniform time-domain, which allows
%%% for more data points at short times, where the extra resolution is
%%% often needed when the data are plotted vs. (time)^0.5.

clear; clc;    % Clear system memory

% Set time parameters -- Two time domains: more points at short times
m = 4500000;      %Maximum time in seconds
step = 10000;     %Step size in time

t_low = 0:(step/5):(m/4);       % "Fine" time spacing at short times
t_high = (m/4):step:m;          % "Coarse" time spacing at longer times
t = horzcat(t_low, t_high);     % Concatenate the two time domains
```

E.4. References

1. Carslaw HS and Jaeger JC. Conduction of Heat in Solids: Oxford Science Publications, 1986.

2. Crank J. The Mathematics of Diffusion, 2nd ed.: Oxford Science Publications, 1975.

APPENDIX F

ACTIVATION ENTROPY OF PENETRANT DIFFUSION IN PEF AND PET

F.1. Activation Entropy of Penetrant Diffusion

As noted in Chapter 2, the pre-exponential factor for the Arrhenius relationship for diffusivity (cf. Equation 2.12) can be represented via Equation F.1, which is derived from transition state theory [1, 2]. Recall that λ is the diffusion path length during a diffusive "jump", k is Boltzmann's constant, h is Planck's constant, R is the universal gas constant, and S_D is the apparent activation entropy of diffusion.

$$D_0 = e\lambda^2 \frac{kT}{h} \exp\left(\frac{S_D}{R}\right) \tag{F.1}$$

Table F.1 provides a compilation of relevant data for oxygen, carbon dioxide, and water diffusion in amorphous PEF and PET at 35°C. The diffusion coefficients originate from Table 7.6, and the corresponding values of λ in Equation F.1 were chosen to be the respective penetrant kinetic diameters from Table 2.2.

Table F.1. Diffusion data for carbon dioxide, oxygen, and water in amorphous PEF and PET at 35°C. *D* values originate from Table 7.6.

	Value at 35°C	Oxygen	Carbon dioxide	Water
PEF	$D \times 10^{10}$ (cm^2/s)	10	0.72	17
	D_0 (cm^2/s)	0.044	0.068	0.21
	E_D[a] (kJ/mol)	44.6	52.0	47.1
	S_D (J/mol·K)	+6	+11	+24
PET	$D \times 10^{10}$ (cm^2/s)	97	22	96
	D_0 (cm^2/s)	0.087	0.15	0.93
	E_D[a] (kJ/mol)	41.0[b]	46.2[b]	46.4
	S_D (J/mol·K)	+12	+17	+36

a: E_D estimates are from: Chapter 6 (O_2), Chapter 7 (CO_2), and Chapter 9 (H_2O).
b: Not explicitly measured in this work. These values represent literature values for PET.

As seen in Table F.1, positive activation entropies of diffusion are observed for all penetrants in both PEF and PET. Such behavior is opposite to that observed for diffusion in carbon molecular sieve (CMS) materials [3], which have well defined pore structures. A negative value for the activation entropy indicates that the "activated" state during a diffusive "jump" exhibits less entropy than the ground state, and such result is logical in the context of pre-formed, well defined pore structures. Amorphous polymers, on the other hand, do not have pre-formed pore structures, and diffusive steps occur via complex, coordinated chain motions involving multiple neighboring chains [4, 5]. Such behavior is thought to contribute to the apparent positive activation entropies for PEF and PET reported in Table F.1. Additional information regarding the mechanics of diffusion in polymers can be found in multiple references in the literature [4, 6-10].

F.2. References

1. Singh A and Koros WJ. Significance of Entropic Selectivity for Advanced Gas Separation Membranes. Industrial & Engineering Chemistry Research 1996;35(4):1231-1234.

2. Singh-Ghosal A and Koros WJ. Energetic and Entropic Contributions to Mobility Selectivity in Glassy Polymers for Gas Separation Membranes. Industrial & Engineering Chemistry Research 1999;38(10):3647-3654.

3. Ning X. Carbon Molecular Sieve Membranes for Nitrogen/Methane Separation. School of Chemical & Biomolecular Engineering, vol. PhD. Atlanta: Georgia Institute of Technology, 2014. pp. 207.

4. Crank J and Park GS. Diffusion in Polymers. London: Academic Press, 1968.

5. Barrer RM. Some Properties of Diffusion Coefficients in Polymers. The Journal of Physical Chemistry 1957;61(2):178-189.

6. DiBenedetto AT. Molecular properties of amorphous high polymers. I. A cell theory for amorphous high polymers. Journal of Polymer Science Part A: General Papers 1963;1(11):3459-3476.

7. DiBenedetto AT. Molecular properties of amorphous high polymers. II. An interpretation of gaseous diffusion through polymers. Journal of Polymer Science Part A: General Papers 1963;1(11):3477-3487.

8. DiBenedetto AT and Paul DR. An interpretation of gaseous diffusion through polymers using fluctuation theory. Journal of Polymer Science Part A: General Papers 1964;2(2):1001-1015.

9. Paul DR and DiBenedetto AT. Diffusion in amorphous polymers. Journal of Polymer Science Part C: Polymer Symposia 1965;10(1):17-44.

10. Kumins CA and Kwei TK. Free Volume and Other Theories. In: Crank J and Park GS, editors. Diffusion in Polymers. London: Academic Press Inc. Ltd., 1968. pp. 107-139.

APPENDIX G

EFFECT OF WATER SORPTION AT UNIT ACTIVITY ON THE THERMAL AND MECHANICAL PROPERTIES OF PEF AND PET

G.1. Introduction

As mentioned in Chapters 8 and 9, it is important to understand the effect of water sorption at unit activity on the thermal, mechanical, and barrier properties of neat PET and PEF since liquid water is present in the end-use application. This Appendix utilizes DSC, DMA, and a range of supplementary characterization techniques to investigate such effects on both dry and water-saturated PEF and PET.

G.2. Materials and Characterization Methods

The poly(ethylene furanoate) (PEF) and poly(ethylene terephthalate) (PET) used in this Appendix are the same materials described previously in Section 3.1.1, and all films were melt-pressed using the method in Section 3.1.3. The "dry" samples were prepared via drying in a vacuum oven at 35°C at least overnight, while the "wet" samples were prepared via submerging in liquid water at 35°C for a time sufficient to allow for complete saturation (i.e., for a time significantly greater than the diffusion time-scale for water at unit activity as determined via the diffusion coefficient estimates provided in Chapter 9).

Differential scanning calorimetry (DSC) measurements were recorded using a TA Q1000 DSC instrument with heating and cooling rates of 20°C/min. Dynamic mechanical

analysis (DMA) measurements pertaining to the beta relaxation were recorded at sub-ambient temperatures using the same procedure described in Chapter 4, and represent at least three measurements. Tensile measurements were recorded using a crosshead speed of 10 mm/min with an Instron 5566 instrument equipped with a 10,000 N load cell. Additional details regarding Instron testing are available in Chapter 3 (cf. Section 3.6.2). Details regarding the FTIR method (using a Perkin Elmer Spectrum 400 instrument) and X-Ray diffraction techniques can be found in Sections 3.7.2 and 3.7.3, respectively.

G.3. Results and Discussion

G.3.1. *X-Ray Diffraction*

X-Ray diffraction data corresponding to the wet and dry PEF and PET samples are provided in Figure G.1, and illustrate that water sorption at unit activity does not shift the peak location of the amorphous halo in both cases. Such notion is consistent with the small volume swelling (<4%) for both polyesters at unit activity reported in Chapter 8 (cf. Table 8.2).

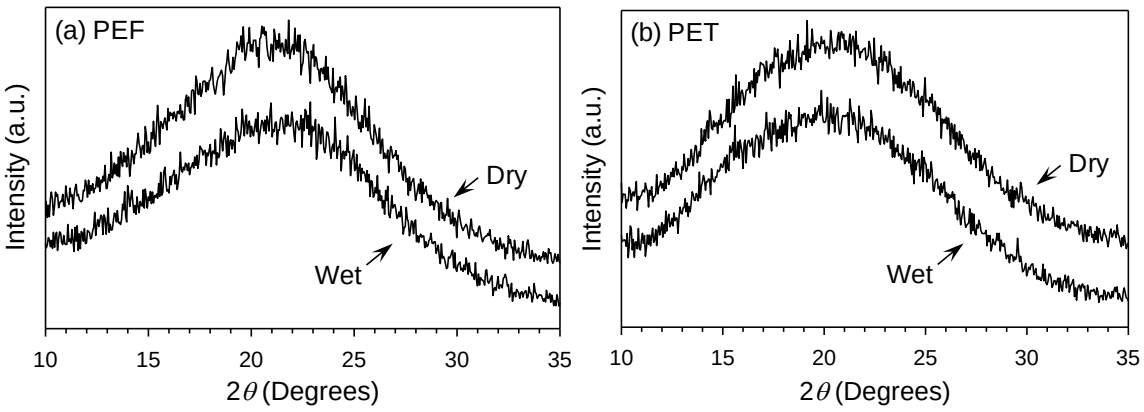

Figure G.1. XRD patterns for PEF (a) and PET (b) in the wet and dry states. The samples are amorphous as indicated by the lack of sharp, crystalline peaks.

G.3.2. *Infrared Spectroscopy (FTIR)*

FTIR spectra between the range of 4000 to 3200 cm^{-1} for dry and wet PET and PEF were measured in both attenuated total reflectance (ATR) mode and transmission modes, with the absorbance data plotted in Figures G.2 and G.3, respectively. Corresponding peak assignments (i.e., for A, B, and C in Figures G.2 and G.3) are provided in Table G.1.

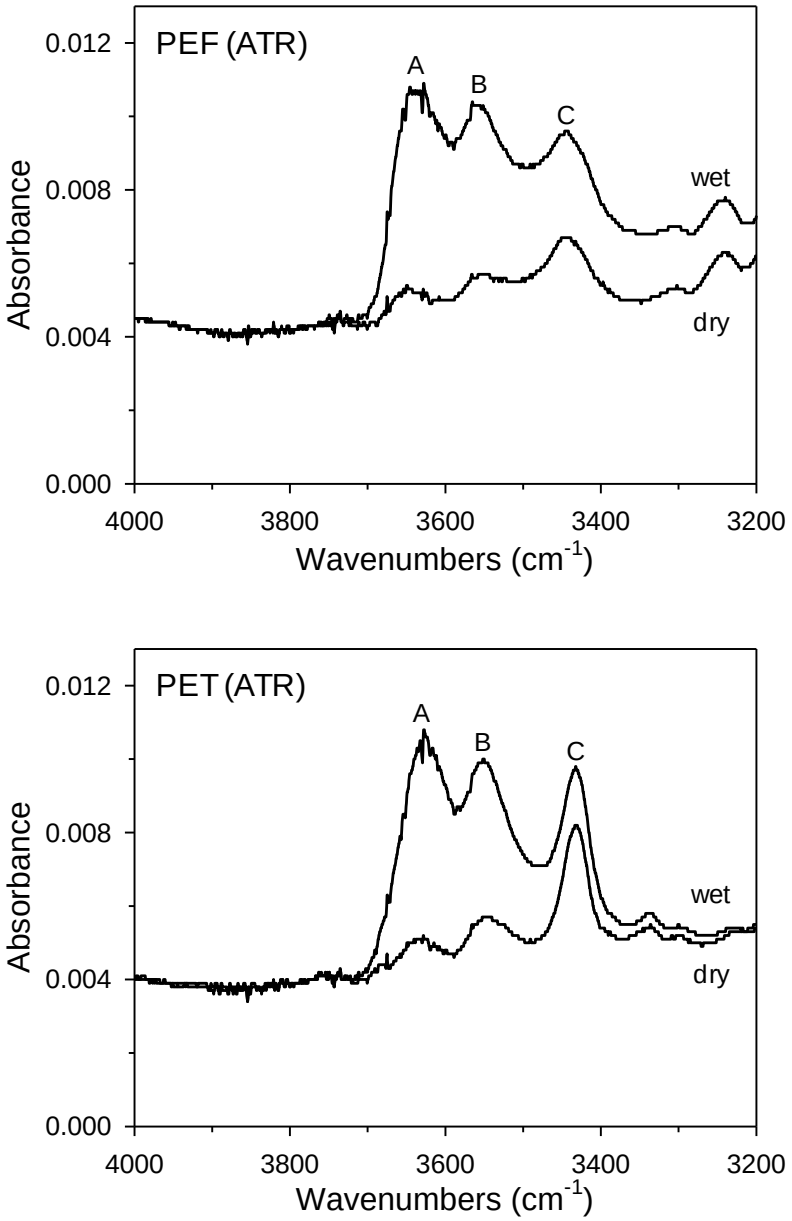

Figure G.2. FTIR spectra (ATR mode) for PEF and PET in the dry and wet states.

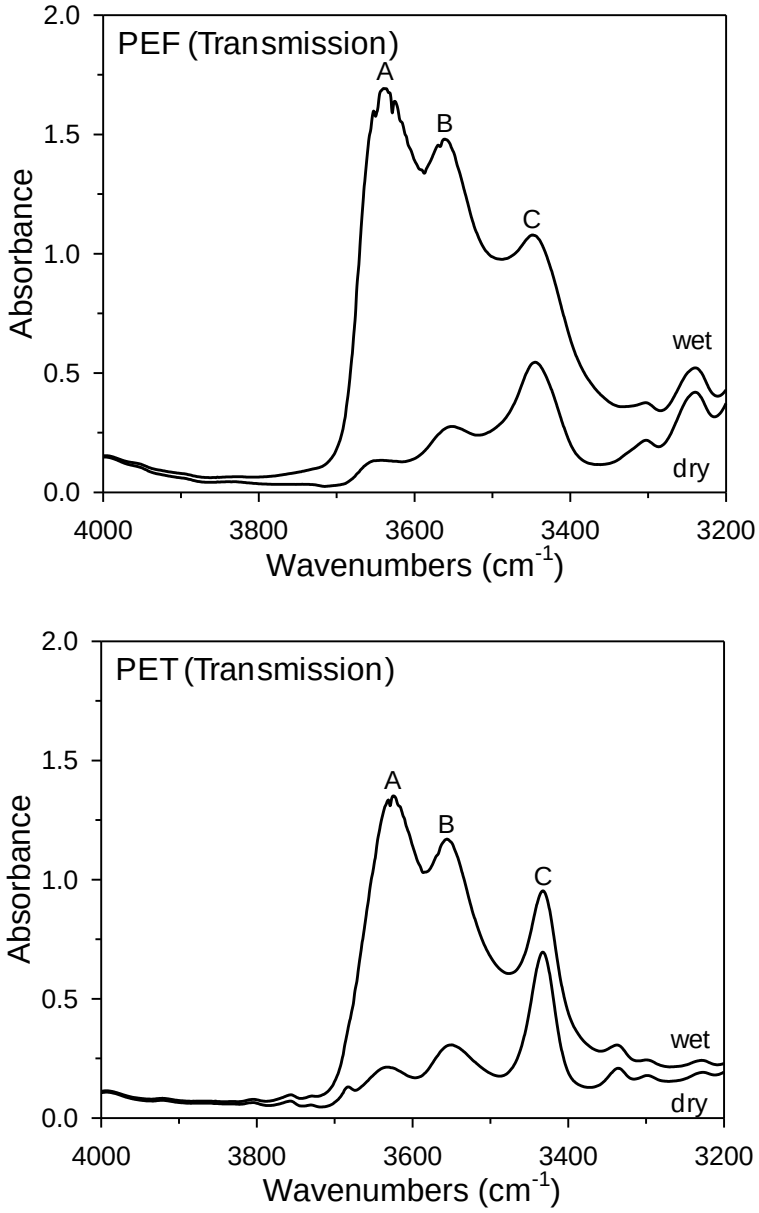

Figure G.3. FTIR spectra (transmission mode) for PEF and PET in the dry and wet states. The film thickness values are as follows: PEF (0.17 mm, dry film; 0.15 mm, wet film), PET (0.16 mm, dry and wet films).

Table G.1. FTIR peak locations corresponding to "A, B, and C" in Figures G.2 and G.3.

	State	Mode	A (cm^{-1})	B (cm^{-1})	C (cm^{-1})
PEF	Dry	ATR	3638	3551	3445
		Transmission	3644	3551	3445
	Wet	ATR	3635	3559	3444
		Transmission	3638	3562	3448
PET	Dry	ATR	3629	3547	3432
		Transmission	3633	3550	3433
	Wet	ATR	3628	3551	3432
		Transmission	3625	3556	3433

As seen in Figures G.2 and G.3, three dominant peaks appear in the spectra for both polyesters over the range 4000 to 3200 cm^{-1}. The peak corresponding to "C", which is the largest peak in the spectra for the dry polyesters, represents an overtone of the primary carbonyl stretching vibration mode [1, 2]. The peaks corresponding to "A" and "B" in Figures G2 and G.3 for the wet samples have been related to the anti-symmetric and symmetric vibration modes, respectively, for "doubly" hydrogen bonded water (as opposed to "free" water) [1, 3-5]. The presence of such strong FTIR peaks for the "bound" water in the wet polyester samples is surprising, since PEF and PET both have relatively small degrees of water uptake at unit activity (i.e., 1.9 wt% for PEF, 1.2 wt% for PET, from Figure 8.3). The FTIR notion that sorbed water within the polyesters is potentially "bound" (via hydrogen bonding) to the polar carbonyl or furan moieties instead of neighboring water molecules is useful, and can potentially give information regarding the presence or lack of water clustering (cf. Chapter 8) [4, 6]. Furthermore, the similarity of the FTIR spectra measured via the ATR method and transmission method is

satisfying, since the ATR method is known to probe only a thin surface layer of the polymer while the transmission method probes the entire thickness of the polymer film [3, 7].

G.3.3. *Differential Scanning Calorimetry*

Preliminary glass transition temperature (T_g) measurements for PEF recorded via DSC indicate that water can cause a reduction in T_g of ~15°C for the wet, amorphous sample compared to the dry, amorphous sample. Similar plasticization effects have been observed in the literature for PET [8]; however, the T_g reduction for PET in the wet vs. dry state should ideally be less significant than for PEF due to the lower water uptake for PET at unit activity. Additional DSC measurements should be performed to verify the T_g reduction for PEF observed in the current work.

G.3.4. *Dynamic Mechanical Analysis*

As discussed in Chapters 4 and 5, characterization of the polymeric sub-ambient beta relaxation can provide molecular level insight into the motional processes occurring in the glassy state. A plot of the beta relaxation curves for dry PET and PEF (from Chapter 5) is provided in Figure G.4 via the solid lines, while corresponding curves for the hydrated polyesters are provided via the dashed lines. Data corresponding to the beta peak activation energy (E_A), activation entropy (ΔS, cf. Equation 3.6), and beta "peak max" temperature are provided in Table G.2.

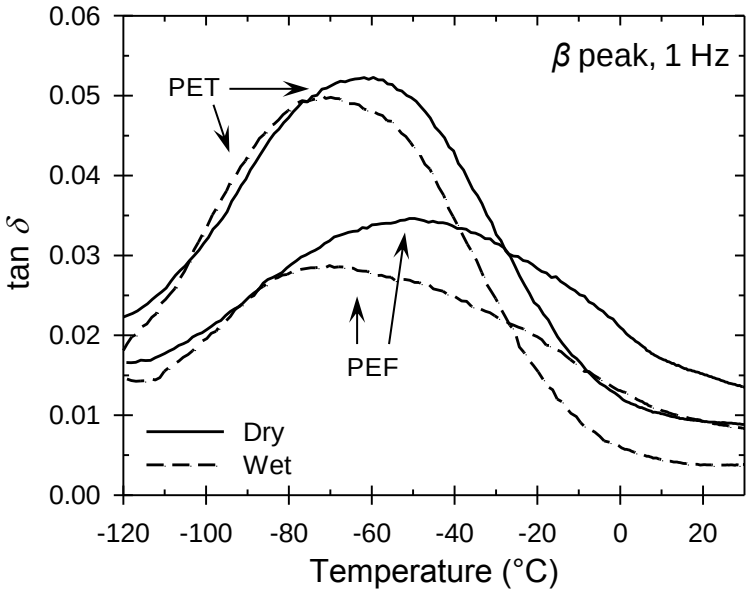

Figure G.4. DMA beta relaxations at 1 Hz for dry and wet PET and PEF films.

Table G.2. DMA data corresponding to the sub-ambient beta (β) relaxation for wet and dry PEF and PET.

Sample	**H_2O activity**	**β peak temp at 1 Hz (°C)**	**$E_A(\beta)$ (kJ/mol)**	**$\Delta S(\beta)$ (J/mol·K)**
PEF	0	–50 ± 1[a]	68 ± 2[a]	68 ± 9[a]
	1	–71 ± 1	52 ± 1	23 ± 7
PET	0	–61 ± 1[a]	72 ± 1[a]	102 ± 3[a]
	1	–69 ± 1	68 ± 3	96 ± 12

a: From Chapter 5, Table 5.5.

As seen in Figure G.4, the beta relaxation tan δ curve is significantly suppressed for the wet vs. dry PEF sample, while the peak suppression is less pronounced for PET. Inspection of Table G.2 also reveals that both the E_A and ΔS values are significantly suppressed for wet vs. dry PEF, while the values are effectively unchanged for wet vs. dry PET. This behavior for PEF, when examined within the context of Starkweather [9-

11], indicates that the dry polymer exhibits a larger degree of cooperativity in the small-scale chain motional processes compared to the wet polymer. This result is interesting, since PEF already exhibits hindered chain mobility compared to PET. Recall from Chapter 5 that the furan ring-flipping motions in PEF are hindered compared to the phenyl ring-flipping motions in PET, while the carbonyl motions in both polymers are thought to be ideally unhindered. Within this context of increased chain rigidity for PEF vs. PET, it is possible that the carbonyl motions in PEF are effectively hindered by the formation of potential hydrogen bonds with sorbed water. Such behavior would reduce both the E_A and ΔS values for wet vs. dry PEF, since the beta relaxation in PEF results primarily from the carbonyl motions (cf. Chapter 5). Hydrogen bond formation between water and the carbonyl moieties in PET is also probable; however, it is possible that the phenyl ring-flipping motions in glassy PET may disrupt the "hindering" effect that is apparently present for water sorbed in PEF. This notion is observed in Table G.2 by the similarity in E_A and ΔS values for wet vs. dry PET.

The large reduction in E_A and ΔS for wet vs. dry PEF is indeed surprising, especially since wet PEF at 35°C contains only 1.9 wt% water (cf. Figure 8.3). Additional proof that water is causing the reduction in E_A and ΔS for wet vs. dry PEF is illustrated in Figure G.5, which provides DMA data corresponding to the beta relaxation for a wet PEF sample before and after "drying". The solid line in Figure G.5 represents data corresponding to the wet sample, and the dashed line represents a second scan on the *same film* after isothermally holding (and by default, "drying") the sample for 8 hours at 40°C after the first temperature scan. The data in Figure G.5 therefore provide a direct investigation into the effect of water sorption on the beta relaxation in PEF, and eliminate

any complications which could arise from using separate samples.

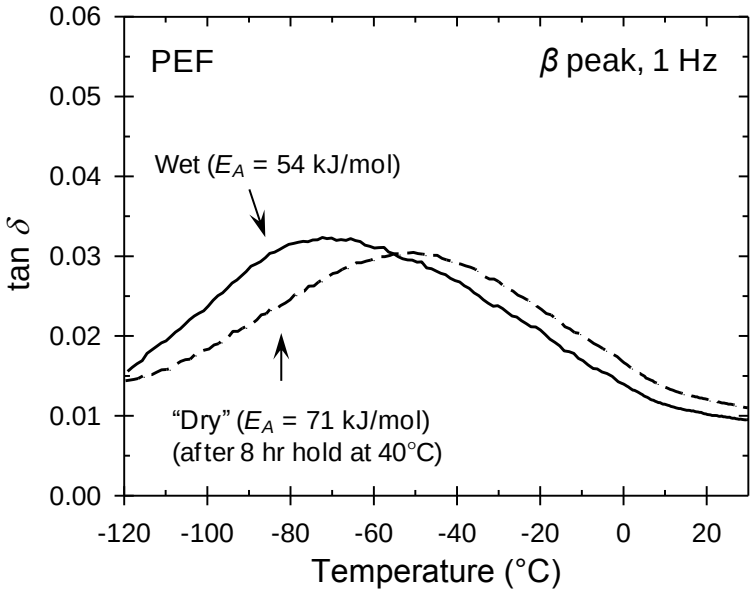

Figure G.5. DMA beta relaxation at 1 Hz for wet PEF (solid line) and "dried" PEF (dashed line) for the same film sample. The test strip was "dried" isothermally at 40°C for 8 hours after the first cycle, before cooling to -120°C and re-testing. Film thickness = 0.16 mm.

As seen in Figure G.5, the beta peak E_A (54 kJ/mol) and peak location for the wet PEF sample are significantly suppressed compared to the "dried" sample, which has a much larger E_A of 71 kJ/mol. The *in situ* "drying" step for the wet PEF film in the DMA instrument may not have removed all of the sorbed water in the film; however, the data in Figure G.5 clearly illustrate the impact of water on the sub-ambient relaxation in PEF.

The DMA data for wet vs. dry PEF in this Appendix are similar to the data reported in Chapter 4 for the PET/caffeine samples compared to neat PET. In light of the large reduction in E_A and ΔS for wet vs. dry PEF in Table G.2, it can be hypothesized that water might exhibit a type of "antiplasticization" effect when sorbed in PEF. Such result would imply a reduction in *short-time* segmental chain mobility for wet vs. dry PEF, which still

allows for the increase in water diffusion coefficient vs. activity observed in Chapter 9, which is consistent with plasticization. In fact, it is possible for wet PEF to exhibit both antiplasticization and plasticization-type phenomena compared to dry PEF depending on the time-scale of testing. Further discussion regarding this notion is provided in the next section.

G.3.5. *Instron Tensile Testing*

Instron tensile testing operates by applying a constant crosshead speed to a film sample and recording the resultant stress, and as a result, is fundamentally different compared to the oscillatory nature of DMA testing. As mentioned previously, wet PEF can exhibit both antiplasticization and plasticization-type phenomena compared to dry PEF depending on the time-scale of testing. For example, tensile testing using a "fast" crosshead speed could potentially indicate an *increase* in Young's modulus (i.e., antiplasticization), while tensile testing using a "slow" crosshead speed could indicate a *decrease* in Young's modulus (i.e., plasticization). Young's modulus data measured at room temperature (20°C) using a crosshead speed of 10 mm/min are provided in Table G.3 for dry, wet, and "re-dried" PEF and PET. The "re-dried" films were prepared by drying wet films in a vacuum oven at 35°C for multiple days, to provide a control for the data corresponding to the wet and dry films. Instron data represent the average of at least six test specimens, and the Young's modulus was estimated using the toe correction method described in ASTM D882. Complex modulus data measured at 20°C from DMA are also provided in Table G.3 as a consistency check for the Young's modulus data measured via Instron testing.

Table G.3. Mechanical data at room temperature (20°C) for dry, wet, and re-dried PEF and PET. All data corresponds to the amorphous morphology.

Sample		(Instron) Young's modulus (MPa)	(DMA) Complex Modulus (MPa)
PEF	Dry	3400 ± 100	3390 ± 50
	Wet	3200 ± 60	–
	Re-dried	3130 ± 70	–
PET	Dry	2030 ± 30	2140 ± 20
	Wet	2010 ± 60	–
	Re-dried	2110 ± 90	–

Inspection of Table G.3 reveals a slightly lower average Young's modulus for the wet vs. dry PEF samples, which potentially indicates that plasticization is occurring for the wet samples as probed by a crosshead speed of 10 mm/min. Additional crosshead speeds need to be investigated to determine if faster speeds will reveal an increase in Young's modulus for the wet vs. dry samples, which would indicate the presence of an antiplasticization-type phenomena for the hydrated samples.

G.4. Summary and Conclusions

This Appendix investigated the effect of water sorption at unit activity on the resultant thermal and mechanical properties of PEF and PET. Infrared spectroscopy (FTIR) for the wet vs. dry polyesters revealed that water is ideally hydrogen bonded to the polar carbonyl moieties in PET or the polar carbonyl and furan moieties in PEF. Thermal investigation via DSC indicated a reduction in T_g for the wet vs. dry polyesters, and DMA investigation of the sub-ambient beta relaxation revealed a significantly lower

E_A and ΔS for wet vs. dry PEF. DMA testing using wet PET should be repeated using thicker films to verify that significant water is not lost during the initial cooling step to sub-ambient temperature. Future testing should also involve Instron testing at faster crosshead speeds than utilized in the current work (i.e., 10 mm/min) to investigate if any antiplasticization-type phenomena is observed for wet vs. dry PEF. Permeation testing for gas feeds in the presence of water should also be conducted, since such antiplasticization phenomena should also be observed via these methods.

G.5. References

1. Rueda DR, Viksne A, Kajaks J, Balta-Calleja FJ, and Zachmann HG. Properties of arylpolyesters with reference to water content. Macromolecular Symposia 1995;94(1):259-268.

2. Rueda DR and Varkalis A. Water Sorption/Desorption Kinetics in Poly(Ethylene Naphthalene-2,6-Dicarboxylate) and Poly(Ethylene Terephthalate). Journal of Polymer Science Part B: Polymer Physics 1995;33:2263-2268.

3. Iwamoto R and Matsuda T. Interaction of water in polymers: Poly(ethylene-co-vinyl acetate) and poly(vinyl acetate). Journal of Polymer Science Part B: Polymer Physics 2005;43(7):777-785.

4. Iwamoto R and Matsuda T. Infrared and Near-Infrared Spectral Evidence for Water Clustering in Highly Hydrated Poly(methyl Methacrylate). Analytical Chemistry 2007;79(9):3455-3461.

5. Du Q, Superfine R, Freysz E, and Shen YR. Vibrational spectroscopy of water at the vapor/water interface. Physical Review Letters 1993;70(15):2313-2316.

6. Buck U and Huisken F. Infrared Spectroscopy of Size-Selected Water and Methanol Clusters. Chemical Reviews 2000;100(11):3863-3890.

7. Ohta K and Iwamoto R. Experimental Proof of the Relation Between Thickness of the Probed Surface Layer and Absorbance in FT-IR/ATR Spectroscopy. Applied Spectroscopy 1985;39(3):418-425.

8. Jabarin SA and Lofgren EA. Effects of water absorption on physical properties and degree of molecular orientation of poly (ethylene terephthalate). Polymer Engineering

& Science 1986;26(9):620-625.

9. Starkweather HW. Simple and Complex Relaxations. Macromolecules 1981;14(5):1277-1281.

10. Starkweather HW. Noncooperative Relaxations. Macromolecules 1988;21:1798-1802.

11. Starkweather HW. Aspects of simple, non-cooperative relaxations. Polymer 1991;32(13):2443-2448.

APPENDIX H

PET/PEF BLENDS AND COPOLYMERS: THERMAL, MECHANICAL, AND TRANSPORT PROPERTIES

H.1. Introduction

As mentioned in Chapter 12, it is important to investigate the thermal, mechanical, and barrier properties of PET/PEF blends and copolymers, since PEF will eventually enter the PET recycle stream. This Appendix provides preliminary data that illustrate the unexpected miscibility of PET with PEF, and the subsequent transesterification reaction that occurs via high temperature treatment.

H.2. Materials and Characterization

The PET used in this Appendix is the same polymer described previously in Section 3.1.1, and the PEF was taken from two separate batches, with one being the same polymer characterized in Section 3.1.1. Specifically, the PEF batch not characterized in this thesis was used solely to illustrate the transesterification reaction as characterized via thermal analysis (cf. Figures H.1 – H.3, discussed later). All additional PEF data in this Appendix correspond to the PEF batch characterized in Section 3.1.1.

The PET/PEF blends in this Appendix were melt-mixed according to the procedure described in Section 3.1.2, and amorphous films were melt-pressed using the method in Section 3.1.3. All mechanical and transport data in this Appendix correspond to the amorphous morphology. PET/PEF copolymers were formed by taking a portion of the

PET/PEF mixed batches (i.e., blends) prepared via melt-mixing and thermally treating at 300°C for 1 hour under vacuum, before melt-pressing according to the method described in Section 3.1.3. The blend samples were dried at 120°C for 24 hours under vacuum prior to the high temperature transesterification step to limit the effect of hydrolytic degradation, and the copolymer samples were subsequently stored at 35°C under vacuum overnight prior to melt-pressing. FTIR spectra for the 50/50 wt% PET/PEF blend exhibited excellent agreement with the 50/50 wt% PET/PEF copolymer, thereby providing confirmation that the heat treatment at 300°C did not significantly degrade the polymer.

Differential scanning calorimetry (DSC) measurements were recorded using a similar procedure to that described in Chapter 4 (i.e., ramp 0 to 280°C at 10°C/min, hold isothermally at 280°C for 1 min, followed by cooling from 280 to 0°C at 10°C/min), and represent the average of three measurements. Multiple heat and cool cycles were used to investigate the effect of PET and PEF transesterification on the relevant thermal transitions (crystal formation and melting), and provide a means to track the progress of copolymer formation. Dynamic mechanical analysis (DMA) measurements pertaining to the beta relaxation were recorded at sub-ambient temperatures using the same procedure described in Chapter 4, and represent four measurements for each blend composition and three measurements for the 50/50 wt% PET/PEF copolymer.

Density measurements for select PET/PEF blends and copolymers were measured at 23°C using a density gradient column containing water and calcium nitrate, as discussed previously in Section 3.7.1.

Permeation and pressure-decay sorption data were measured for oxygen and carbon

dioxide in the 50/50 wt% PET/PEF copolymer according to the methods utilized in Chapters 4, 6, and 7.

H.3. Results and Discussion

H.3.1. *Blend and Copolymer Solubility in DCM*

It is commonly known that dichloromethane (DCM) is able to swell, but not dissolve PET. This notion was experimentally verified for neat PET and neat PEF by adding small pieces of amorphous film into separate vials containing DCM, after which the clear, amorphous polymer films crystallized and became opaque. Similar behavior was qualitatively observed for the 25/75, 50/50, and 75/25 wt% PET/PEF blends, thereby indicating the existence of distinct, pure polymer chains within the blend. On the other hand, amorphous films pressed from the PET/PEF blends (i.e., 25/75, 50/50, and 75/25 wt% PET/PEF blends) which were thermally treated for 1 hour at 300°C under vacuum were *completely* soluble in DCM. Such notion indicates that the aforementioned PET/PEF blends have undergone chain transesterification, which produces a copolymer that is effectively unable to crystallize. Confirmation of this notion is provided in the next section via DSC characterization.

H.3.2. *Differential Scanning Calorimetry*

The presence of blend compatibilization via polymer transesterification is provided by the DSC thermogram in Figure H.1, which illustrates three complete heat/cool cycles for a sample taken from the 90/10 wt% PET/PEF mixed batch (i.e., prior to film formation), followed by a fourth and final heating cycle. As seen in Figure H.1, both the

melt crystallization (T_{mc}) and subsequent melting peaks (T_m) are shifted to lower temperatures as a function of cycle number, indicating that the blend is becoming more "compatible" as a function of exposure to high temperature (i.e., 280°C). This notion is further illustrated in Figure H.2, which shows the thermogram for a sample from the same batch after holding isothermally at 280°C for one hour after the first heat.

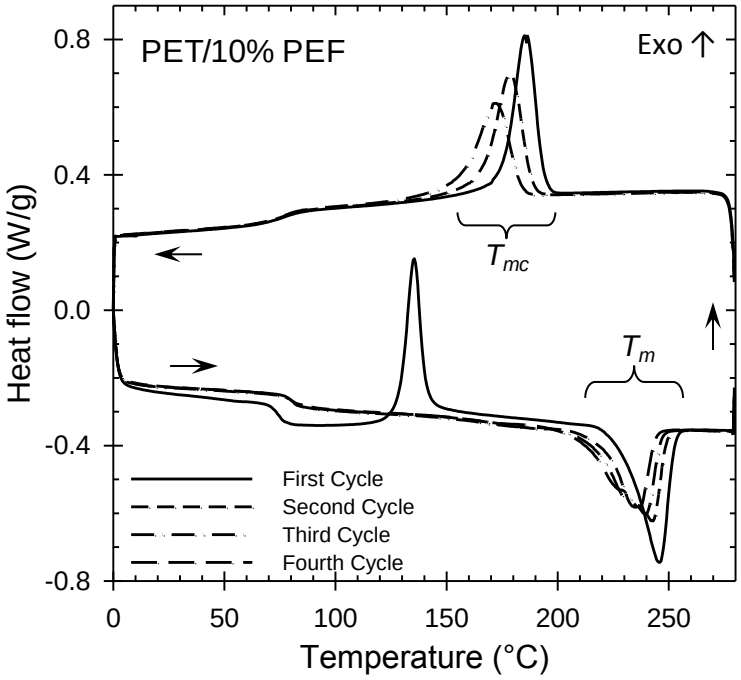

Figure H.1. Example DSC data illustrating multiple heat/cool cycles for the 90/10 wt% PET/PEF blend, with an isothermal hold of 1 min at 280°C after each heating cycle.

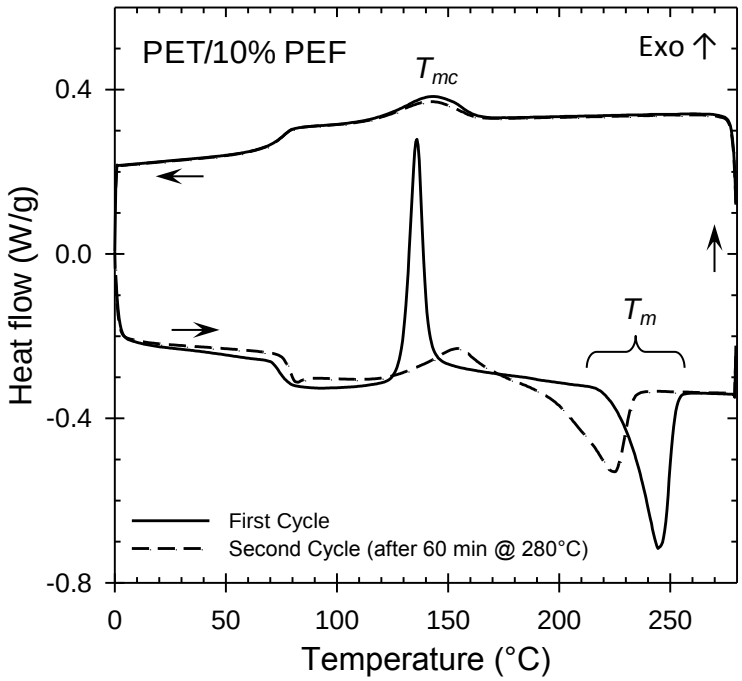

Figure H.2. Example DSC data for the 90/10 wt% PET/PEF blend. The sample was held isothermally at 280°C for *one hour* after the first heat, and 1 min for the subsequent heat.

As seen in Figure H.2, the T_{mc} for the "heat treated" blend (i.e., after exposure to 1 hour at 280°C after the first heat) is lower than the T_{mc}'s illustrated in Figure H.1, thereby indicating that the reduction in T_{mc} for the 90/10 wt% PET/PEF blend occurs due to high temperature exposure. Furthermore, the T_{mc} in Figure H.2 appears to have reached a minimum value, since the T_{mc} for the second cycle is approximately the same as the T_{mc} from the first cycle. Such behavior indicates that the "crystallizability" of the PET/PEF blend is being reduced as the exposure time at high temperature increases, thereby providing evidence for the compatibilization of the blend via polymer transesterification. This trend is further illustrated in Figure H.3, which provides DSC data for the 50/50 wt% PET/PEF mixed batch (i.e., prior to film formation) for three complete heat/cool cycles.

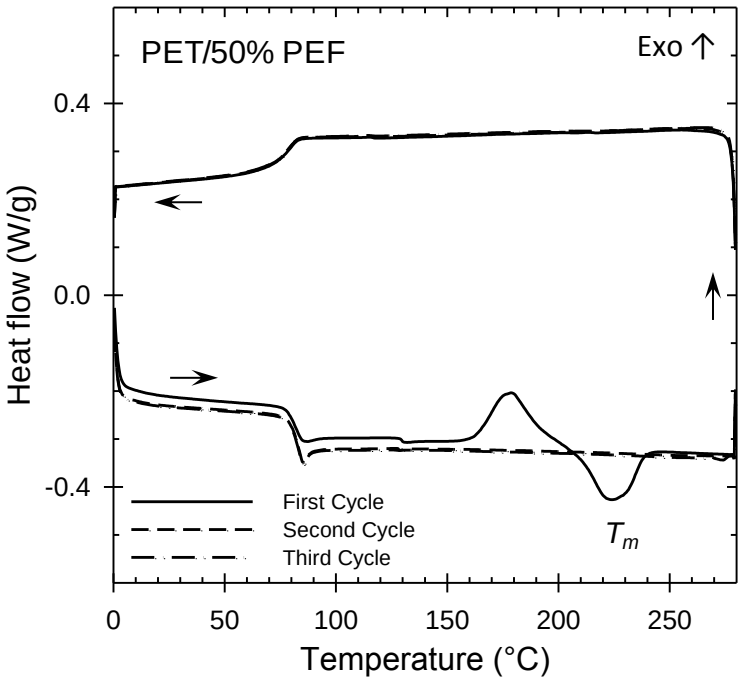

Figure H.3. Example DSC data illustrating multiple heat/cool cycles for the 50/50 wt% PET/PEF blend, with an isothermal hold of 1 min at 280°C after each heating cycle.

Inspection of Figure H.3 reveals the presence of both a cold crystallization peak (T_{cc}) and melting (T_m) peak for the first heat cycle, while such features are absent for all subsequent cooling and heating cycles. This behavior indicates that the 50/50 wt% PET/PEF blend is effectively *unable* to crystallize after the limited high temperature exposure resulting from the first heat. Such data are consistent with the notion of copolymer formation via polymer transesterification, and corroborate the observed copolymer solubility in DCM described previously.

Glass transition temperature (T_g) data for the 25/75, 50/50, and 75/25 wt% PET/PEF "copolymers" are reported in Figure H.4, where the T_g values were recorded via the half-C_p extrapolated tangent method on the *fourth* heat. The samples are referred to as "copolymers", since the data represent measurements for the blends corresponding to the

fourth heat and since only one heat was needed in Figure H.3 to induce transesterification in the 50/50 wt% PET/PEF blend. The heating rate employed in the T_g determination method is indicated in the figure, where a faster heating rate for amorphous PET (i.e., 20°C/min) results in a slightly higher T_g value compared to the respective T_g values measured for the PET/PEF copolymers at a lower heating rate (i.e., 10°C/min).

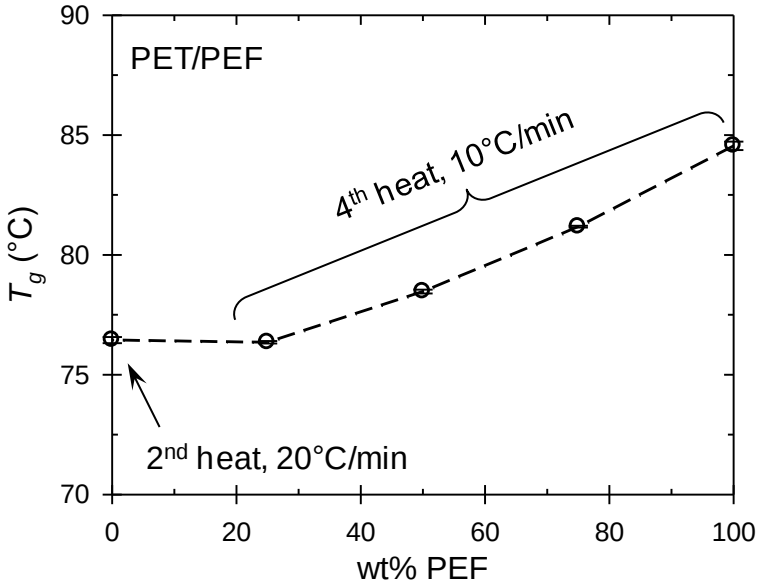

Figure H.4. T_g vs. wt% PEF for various PET/PEF "copolymers" measured on the fourth heating cycle. The heating rate employed in the T_g determination method is indicated in the figure.

It should also be mentioned that only one T_g was observed on the first heat for all PET/PEF blends observed in the current work, thereby indicating that the polymers are miscible *without* extensive transesterification to a domain size of at least ~15 nm [1]. Such notion should be verified, however, since it is often difficult to differentiate a single T_g for the blend when the pure polymer T_g's are only ~10°C apart [1]. The apparent PET/PEF miscibility is further corroborated by the transparency in all amorphous PET/PEF blend films prepared in the current work, which indicates that the polymers are

"miscible enough" to avoid scattering light. The apparent blend miscibility between PET and PEF is indeed surprising, since vary few polymers are known to exhibit true miscibility [2].

H.3.3. *Dynamic Mechanical Characterization*

As discussed in Chapters 4 and 5, characterization of the polymeric sub-ambient beta relaxation can provide molecular level insight into the motional processes occurring in the glassy state. A plot of the beta relaxation curves for virgin PET and PEF (from Chapter 5) is provided in Figure H.5 via the solid lines, while corresponding curves for the various PET/PEF blends are provided via the dashed lines. The curve for the 50/50 wt% PET/PEF *copolymer* is similar to the curve for the corresponding 50/50 blend, and is not shown in Figure H.5.

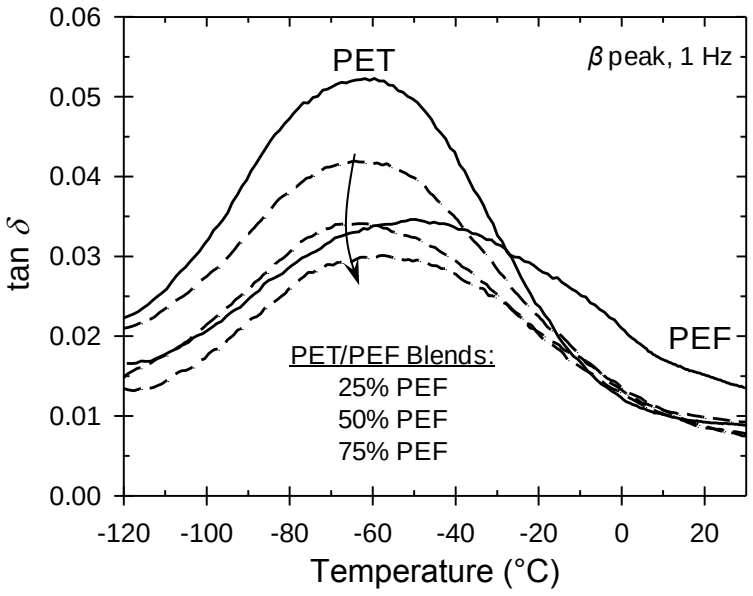

Figure H.5. DMA beta relaxations at 1 Hz for virgin PET and PEF from Chapter 5 (solid lines), and various PET/PEF blends (dashed lines).

A plot of the activation energy (E_A) for the beta relaxation (cf. Equation 3.5) as a function of PEF content is provided in Figure H.5, where the solid circles represent the virgin polymers, the hollow circles represent the *blends*, and the hollow diamond represents the *copolymer* (which was prepared according to the method in Section H.2). Data corresponding to the E_A, activation entropy (ΔS, cf. Equation 3.6), and beta "peak max" temperature are provided in Table H.1.

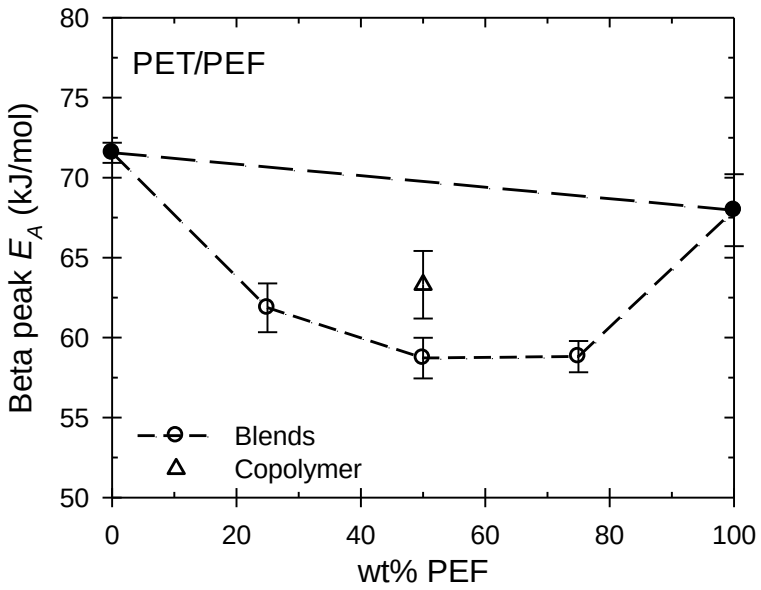

Figure H.6. DMA beta peak E_A vs. wt% PEF for various amorphous films. Solid circles indicate virgin polymers (i.e., *not* Brabender-processed), hollow circles indicate blends, and the hollow triangle represents the 50/50 wt% PET/PEF copolymer.

Table H.1. Mechanical data from DMA pertaining to the sub-ambient beta (β) relaxation for various PET/PEF film samples.

	wt% PEF	β peak temp at 1 Hz (°C)	$E_A(\beta)$ (kJ/mol)	$\Delta S(\beta)$ (J/mol·K)
Virgin[a]	0	-61 ± 1	72 ± 1	102 ± 3
Blends	25	-64 ± 1	62 ± 2	61 ± 8
	50	-62 ± 1	59 ± 1	43 ± 5
	75	-58 ± 2	59 ± 1	38 ± 5
Virgin[a]	100	-50 ± 1	68 ± 2	68 ± 9
Copolymer	50	-60 ± 1	63 ± 2	62 ± 11

a: Virgin PET and PEF *not* brabender-processed.

As seen in Figure H.6, the beta peak E_A is surprisingly reduced for the all of the PET/PEF blends compared to the straight dashed line connecting the two solid points. Such behavior can be interpreted within the framework discussed in Chapter 5, which concluded that the large E_A for pure PEF resulted from an apparent coupling of the carbonyl and furan moieties among neighboring chains. Such coupling between neighboring PEF chains is apparently lost when PEF is incorporated into a PET/PEF blend, where the presence of PET in the matrix effectively "disrupts" the interactions between neighboring PEF chains. This notion is further corroborated by the ΔS values reported in Table H.1, where smaller values of ΔS for the blends compared to the pure polymers indicate an apparent reduction in both complexity and neighboring chain-to-chain coupling of the small-scale motional processes.

It is also interesting to note that the beta peak E_A and ΔS for the 50/50 wt% PET/PEF copolymer is larger than that for the respective blend. Such notion, in the context of Starkweather [3, 4], appears to indicate a larger degree of cooperativity in the small-scale

motional processes for the copolymer compared to the blend. This behavior is perhaps logical, since the copolymer is naturally expected to exhibit a higher degree of compatibility (i.e., homogeneity) compared to the respective blend.

H.3.4. *Density and Free Volume Characterization*

Density data can be used to investigate the presence or lack of volume additivity for the PET/PEF blends. Corresponding data for select PET/PEF blends and the 50/50 wt% PET/PEF copolymer are provided in Figure H.7, with the dashed line illustrating ideal volume additivity between the two pure components.

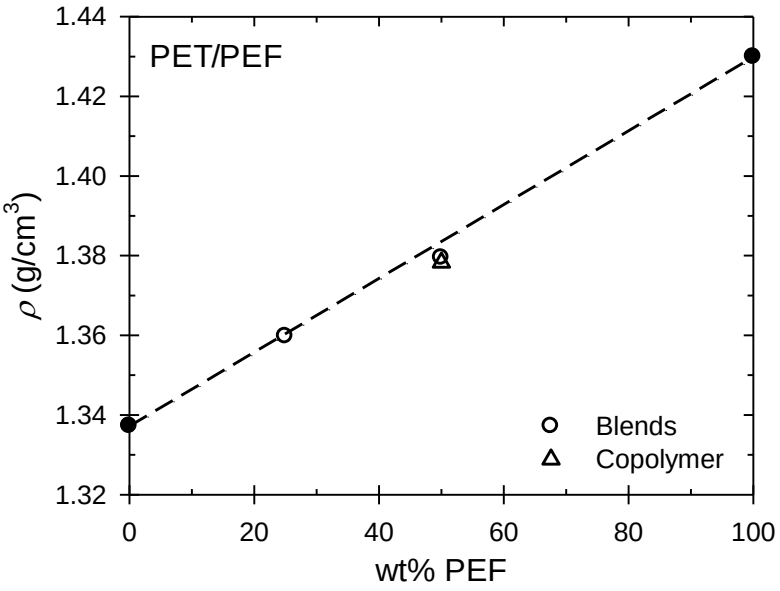

Figure H.7. Density data measured at 23°C for various amorphous PET/PEF samples. Solid circles indicate virgin polymers (i.e., *not* Brabender-processed), hollow circles indicate blends, and the hollow triangle represents the 50/50 wt% PET/PEF copolymer.

As seen in Figure H.7, simple volume additivity is approximately valid for the blend and copolymer samples investigated in the current work. Data corresponding to the

specific volume, occupied volume, free volume, and fraction free volume for the samples studied in this Appendix are provided in Table H.2 Details regard estimation of the parameters in Table H.2 are provided in Chapter 2 (cf. Section 2.3.6).

Table H.2. Density and free volume calculations using Sugden's method [5] for various PET/PEF blends and the 50/50 wt% PET/PEF copolymer at 23°C.

	wt% PEF	**ρ (g/cc)[a]**	**$\hat{V}_g$ (cc/g)[b]**	**$\hat{V}_0$ (cc/g)**	**$\hat{V}_F$ (cc/g)**	***FFV* (–)**
Blends	0	1.3372	0.748	0.652	0.096	0.129
	25	1.3597	0.735	0.637	0.099	0.134
	50	1.3794	0.725	0.622	0.103	0.142
	100	1.4299	0.699	0.592	0.107	0.154
Copolymer	50	1.3783	0.726	0.622	0.104	0.143

a: Uncertainty limits for ρ are $\leq \pm$ 4e-4 g/cc for all samples.

b: Uncertainty limits for $\hat{V}_g$ are $\leq \pm$ 2e-4 cc/g for all samples.

H.3.5. *O_2 and CO_2 Transport: 50/50 wt% PET/PEF Copolymer*

Preliminary pressure-decay sorption data for oxygen and carbon dioxide in the 50/50 wt% PET/PEF copolymer (i.e., "50/50_C") at 35°C are provided in Figures H.8 and H.9, respectively, with the corresponding dual-mode model parameters from Equation 2.26 provided in Table H.3.

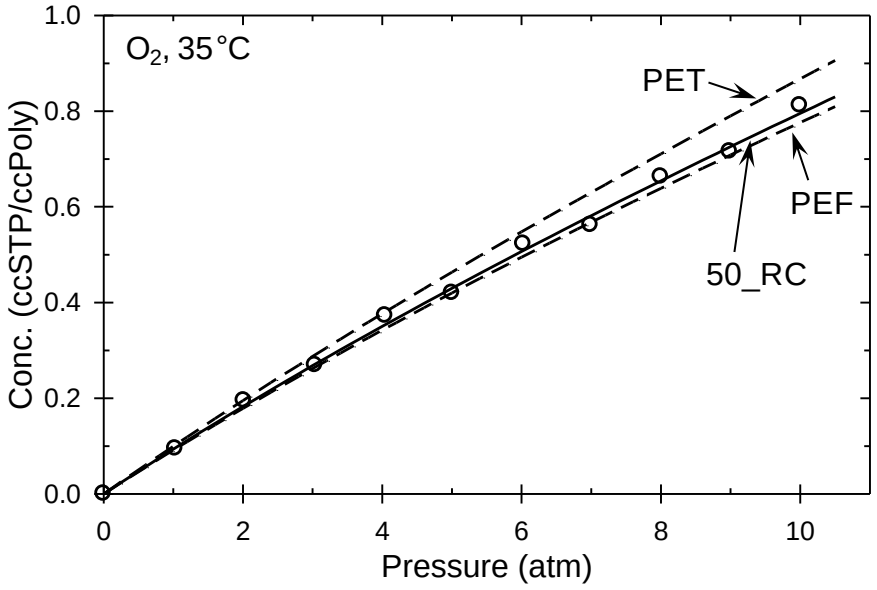

Figure H.8. Oxygen sorption data at 35°C for the amorphous 50/50 wt% PET/PEF copolymer.

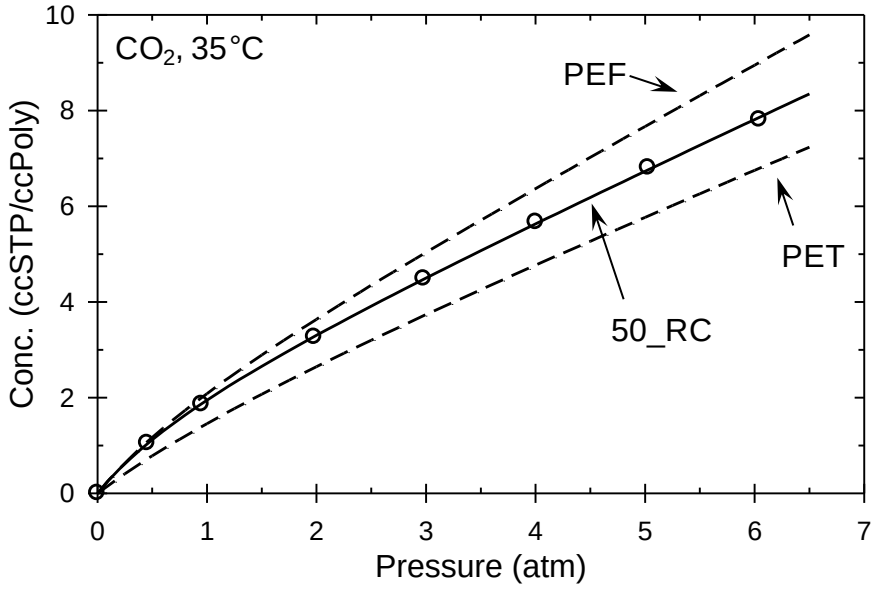

Figure H.9. Carbon dioxide sorption data at 35°C for the amorphous 50/50 wt% PET/PEF copolymer.

Table H.3. Dual-mode model parameters at 35°C for oxygen and carbon dioxide sorption in the amorphous 50/50 wt% PET/PEF copolymer compared to neat PET and neat PEF.

Gas	Sample	k_D (ccSTP/ccPoly·atm)	b (atm^{-1})	C_H' (ccSTP/ccPoly)	k^* (ccSTP/ccPoly·atm)
O_2	PET[a]	0.059	0.055	0.78	0.102
	50/50_C	0.050	0.056	0.81	0.096
	PEF[a]	0.048	0.054	0.85	0.094
CO_2	PET[b]	0.93 ± 0.04	0.50 ± 0.2	1.6 ± 0.4	1.7 ± 0.3
	50/50_C	1.0 ± 0.03	0.93 ± 0.2	1.9 ± 0.2	2.8 ± 0.4
	PEF[c]	1.2 ± 0.06	0.83 ± 0.3	1.9 ± 0.5	2.8 ± 0.7

a: From Chapter 6; b: From Chapter 4; c: From Chapter 7

As seen in Figures H.8 and H.9, the oxygen and carbon dioxide sorption isotherms for the copolymer exist within the upper and lower bounds set forth by the sorption isotherms for the pure polymers. This notion is also observed in Table H.3 via the similarity in dual-mode model parameters for the copolymer compared to the parameters for the respective pure polymers. Further inspection of Table H.3 reveals that the effective low-pressure sorption coefficient (k^*) for the copolymer is practically identical to that for pure PEF, despite the copolymer containing only 50 wt% PEF. This behavior is interesting, and is currently not fully understood at the current time.

Preliminary permeation data for oxygen and carbon dioxide at 6 atm in the 50/50 wt% PET/PEF copolymer (i.e., "50/50_C") at 35°C are provided in Figures H.10 and H.11, respectively, along with the corresponding data for neat PET (Chapter 4) and neat PEF (Chapter 7). The dashed line in both figures represents the permeability prediction from Equation H.1 [2, 6], where ϕ represents the volume fraction, P represents the permeability, and the subscripts 1 and 2 represent the two components in the copolymer.

$$P_{Copolymer} = \exp\left(\phi_1 \ln\left(P_1\right) + \phi_2 \ln\left(P_2\right)\right) \tag{H.1}$$

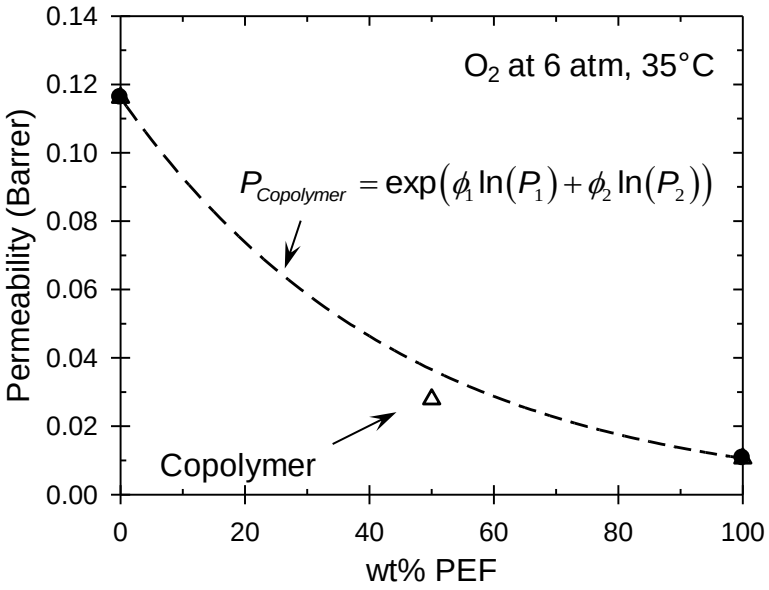

Figure H.10. Oxygen permeation data at 6 atm and 35°C in PET, PEF, and 50/50 wt% PET/PEF copolymer. The dashed line represents Equation H.1.

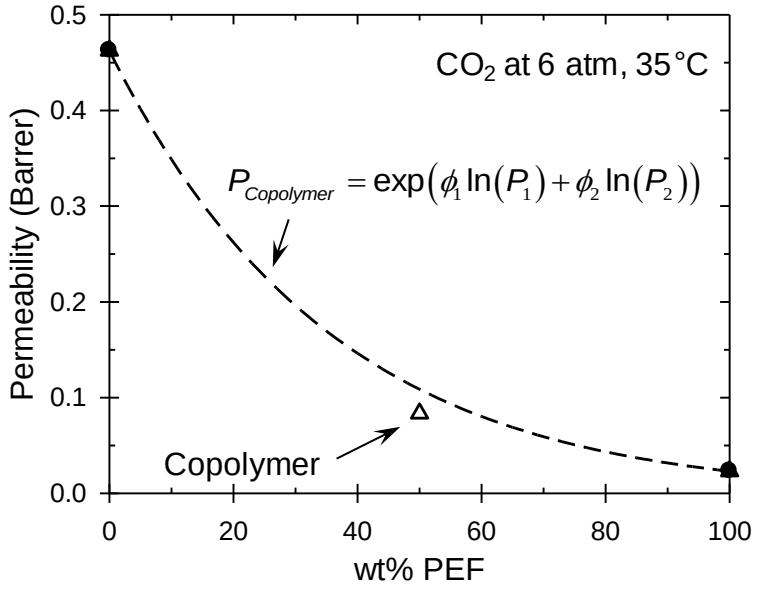

Figure H.11. Carbon dioxide permeation data at 6 atm and 35°C in PET, PEF, and 50/50 wt% PET/PEF copolymer. The dashed line represents Equation H.1.

Inspection of Figures H.10 and H.11 reveal that the preliminary permeability data for both oxygen and carbon dioxide at 6 atm are similar to the permeability prediction from Equation H.1, which is an empirical relationship commonly applied to miscible blends and copolymers [2, 6]. A negative departure from the permeability prediction in Equation H.1 can indicate a highly favorable interaction between the two components [2], however, such systems also often exhibit volume contractions upon mixing, and Figure H.7 indicates that little volume contraction is observed for the PET/PEF blend system. Preliminary diffusion coefficient data for the 50/50 wt% PET/PEF copolymer exhibit a similar trend to that reported for permeability in Figures H.10 and H.11; however, additional measurements need to be performed in order to verify the data.

H.4. Summary and Conclusions

This Appendix focused on the preparation and characterization of various PET/PEF blends and copolymers. All PET/PEF blends investigated in this Appendix were shown to be miscible via thermal analysis (DSC), and the blends could be further compatibilized via polymer transesterification at high temperature. Dynamic mechanical analysis revealed that the blends exhibit a lower beta peak E_A and ΔS vs. the pure polymers, which is consistent with the blends exhibiting a lower degree of cooperative motion between neighboring chains compared to the respective pure polymers. Volume additivity was observed via density measurements for the characterized blends, and the 50/50 wt% PET/PEF blend exhibited close agreement to the density for the respective copolymer.

Pressure-decay sorption measurements revealed that both oxygen and carbon dioxide sorption at low pressure in the 50/50 wt% PET/PEF copolymer were similar to the

respective uptake isotherms at low pressure for pure PEF, despite the copolymer containing only 50 wt% PEF. Preliminary oxygen and carbon dioxide data were measured for the 50/50 wt% PET/PEF copolymer, and were shown to be consistent with the commonly employed permeability prediction useful for modeling permeability in miscible blends and random copolymers. The preliminary transport data reported herein should be verified and extended to include data corresponding to the blends. Additional measurements at multiple temperatures for both the blends and copolymers would also be useful, and would provide insight into the differences in transport (if any) between miscible PET/PEF blends and copolymers. Additional information should also be obtained regarding the catalysts used to polymerize the PET and PEF used in this Appendix, since the transesterification reaction is known to be catalyst-dependent [7].

H.5. References

1. Utracki LA. Thermodynamics of Polymer Blends: Kluwer Academic Publishers, 2003.
2. Robeson LM. Polymer Blends in Membrane Transport Processes. Industrial & Engineering Chemistry Research 2010;49(23):11859-11865.
3. Starkweather HW. Simple and Complex Relaxations. Macromolecules 1981;14(5):1277-1281.
4. Starkweather HW. Noncooperative Relaxations. Macromolecules 1988;21:1798-1802.
5. Sugden S. Molecular Volumes at Absolute Zero. Part II. Zero Volumes and Chemical Composition. Journal of the Chemical Society 1927:1786-1798.
6. Paul DR. Gas transport in homogeneous multicomponent polymers. Journal of Membrane Science 1984;18(0):75-86.
7. Ignatov VN, Carraro C, Tartari V, Pippa R, Scapin M, Pilati F, Berti C, Toselli M, and Fiorini M. PET/PC blends and copolymers by one-step extrusion: 2. Influence of the

initial polymer composition and type of catalyst. Polymer 1997;38(1):201-205.

APPENDIX I

ISOTHERMAL CRYSTALLIZATION OF PEF

I.1. Introduction

As discussed in Chapter 5, the hindered chain mobility for PEF compared to PET results in a slower crystallization rate compared to PET. Such behavior for PEF allowed for the aging study in Chapter 10, which investigated the thermal aging properties of amorphous PEF *in situ* within the differential scanning calorimetry (DSC) instrument. This appendix will further utilize DSC to investigate the isothermal crystallization properties of PEF, and provide a qualitative understanding of such phenomenon.

I.2. Materials and Differential Scanning Calorimetry

The poly(ethylene furanoate) (PEF) used in this Appendix is the same material described previously in Section 3.1.1, and all films were melt-pressed using the method in Section 3.1.3.

DSC measurements were recorded using a TA Q1000 DSC instrument and the method provided in Table I.1. Film samples (~10 mg) were crimped into aluminum pans and heated to 300°C and held isothermally for 5 minutes to melt any residual crystal nuclei in the sample and to provide a common thermal history prior to characterization. After the isothermal step at 300°C, a fast cooling rate of 35°C/min was used to quickly cool the sample from the molten state to the isothermal crystallization temperature (T_c), after which the sample was held isothermally at T_c for 180 min. Crystal formation during

this isothermal step was monitored by the heat flow as a function of time, and crystallization was complete after the heat flow became approximately constant as a function of time. After crystallization, a final ramp to 300°C (cf. Step 8 in Table I.1) allowed characterization of the subsequent polymer crystal melting peaks and determination of the equilibrium melting point for PEF via the Hoffman-Weeks method [1]. Isothermal crystallization temperatures (T_c) investigated in the current work varied from 130°C to 185°C in increments of 5°C, with four separate PEF samples tested at each T_c. The uncertainty limits for all data in this Appendix originate from the standard error of four measurements.

Table I.1. DSC method for measuring isothermal crystallization data for PEF.

Step #	Step Description
1	Equilibrate at 40°C
2	Ramp 35 C/min to 300°C
3	Isothermal for 5 min
4	Mark end of cycle
5	Ramp 35°C/min to isothermal crystallization temperature (T_c)
6	Isothermal for 180 min
7	Mark end of cycle
8	Ramp 10°C/min to 300°C
9	Mark end of cycle / End of method

I.3. Results and Discussion

An example plot of the DSC data recorded during the isothermal crystallization step (cf. step 6 in Table I.1) at 165°C is provided in Figure I.1, and illustrates the method for determining the time required (*after reaching isothermal conditions*) to reach the

maximum in the exothermic crystallization peak.

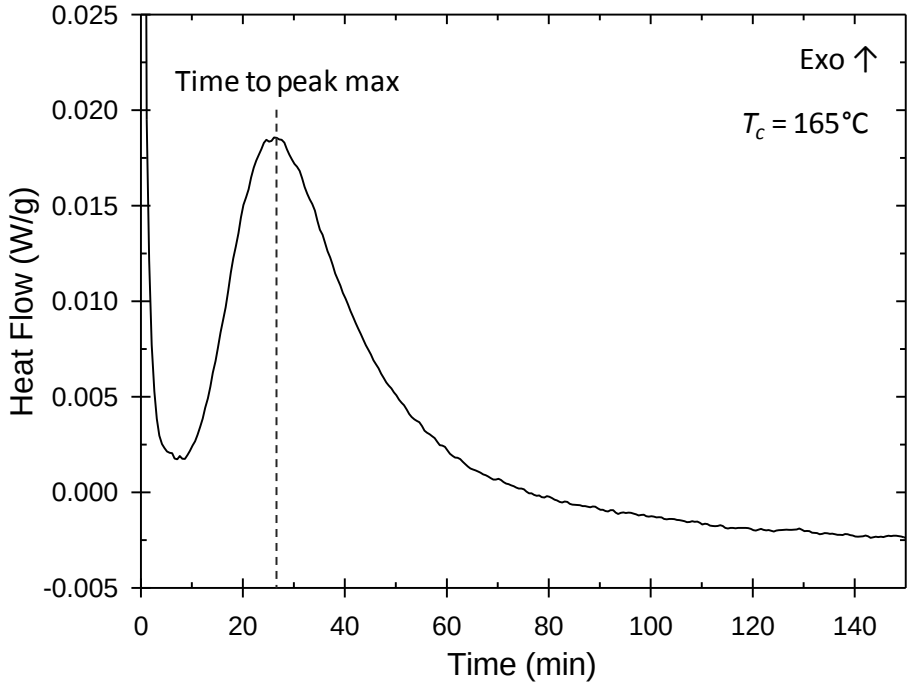

Figure I.1. Evolution of the exothermic crystallization peak for PEF versus time at 165°C.

A plot of the time required to reach the maximum in the crystallization peak as a function of isothermal crystallization temperature (T_c) is provided in Figure I.2 for all samples and crystallization temperatures investigated in the current work, where the dashed line is drawn to aid the eye. The "time to peak max" data can be interpreted as a qualitative indicator of crystallization rate, where a short time indicates a "fast" crystallization rate and a long time indicates a "slow" crystallization rate. As seen in Figure I.2, the "time to peak max" data exhibit the traditional bell shaped curve as a function of T_c, with a minimum time and maximum crystallization rate occurring at approximately 160°C. Crystallization temperatures corresponding to the maximum crystallization rate for PEF have been reported at 155°C [2], 165°C [3], and 167°C [4],

and exhibit excellent agreement with the value of 160°C determined in the current work.

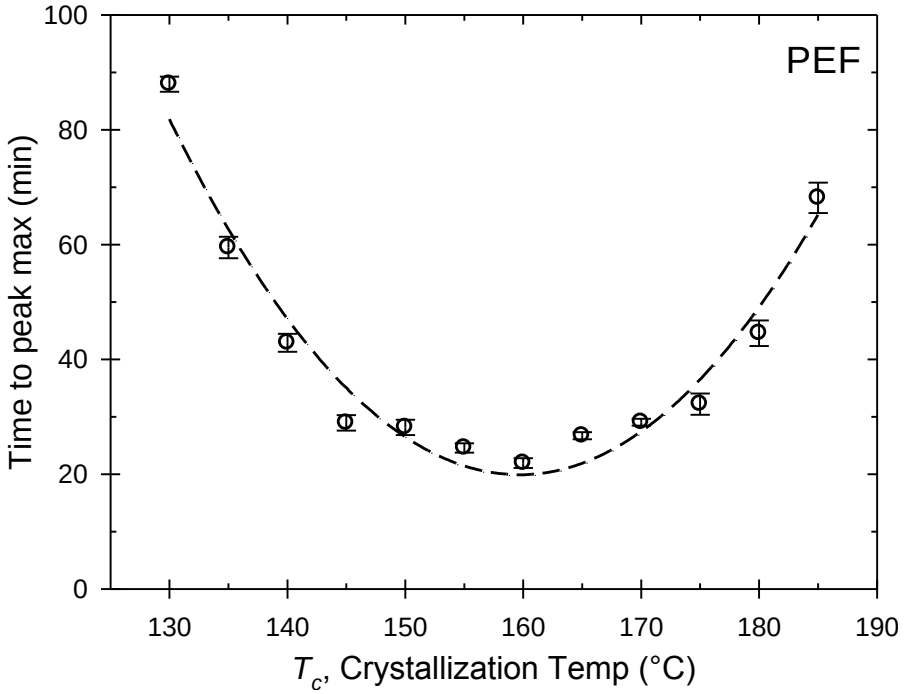

Figure I.2. Time required (after reaching isothermal conditions) to reach the maximum in the exothermic crystallization peak for PEF (cf. Figure I.1).

As described in Table I.1, the PEF samples were heated to 300°C at a rate of 10°C/min after the isothermal crystallization step in order to characterize the subsequent melting peaks. Example DSC data corresponding to Step 8 in Table I.1 are provided in Figure I.3 for selected T_c values used in the current work, and illustrate the presence of two distinct melting peaks in all cases via the dashed lines. The lower temperature melting peak scales directly with T_c, and correlates with the melting of imperfect, secondary crystals, while the higher temperature peak correlates with the melting of primary crystals formed during the isothermal crystallization step. Similar occurrences of multiple melting peaks have been reported in various works in the literature for both PEF

[2-4] and PET [5].

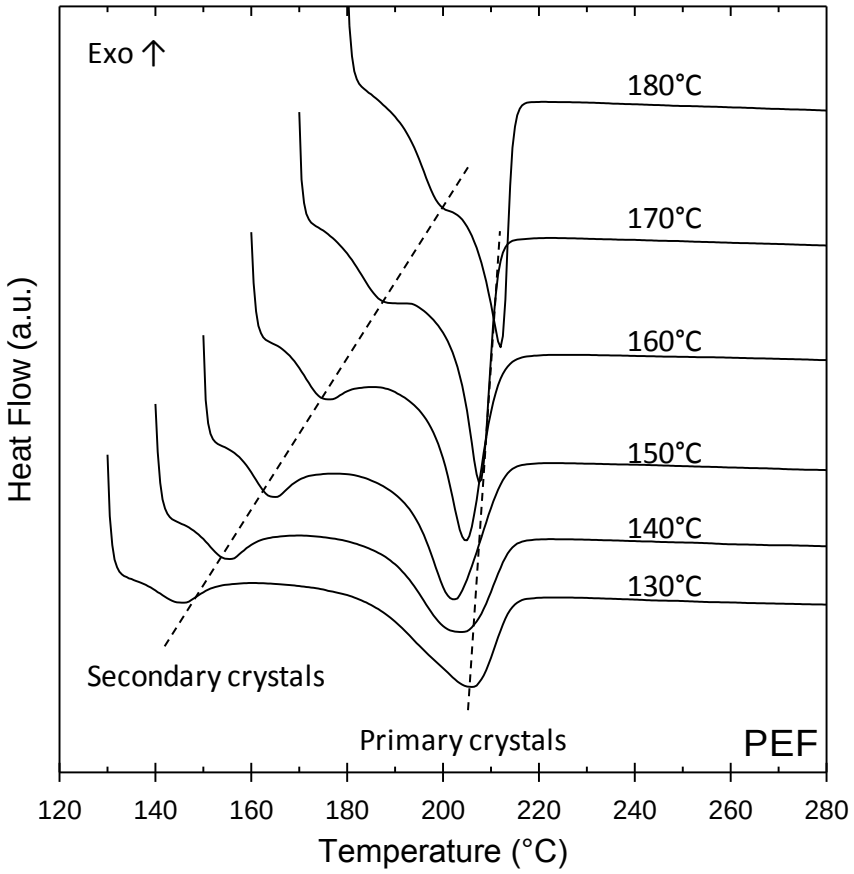

Figure I.3. DSC heating curves for Step 8 in Table I.1, with the corresponding T_c values indicated beside each curve. The dashed lines are drawn to aid the eye.

The shift in primary melting peak as a function of crystallization temperature (T_c) can be used to estimate the equilibrium melting point (T_m^0) for PEF via the Hoffman-Weeks methodology [1]. Figure I.4 provides a plot of the primary melting peak (T_m) vs. T_c, with the long dashed line representing $T_m = T_c$. The equilibrium melting temperature for PEF can be obtained via extrapolating the experimental T_m vs. T_c data to the line of symmetry from $T_m = T_c$. Only the four highest T_c temperatures in the current work (i.e, T_c = 170, 175, 180, and 185°C) were used in the Hoffman-Weeks extrapolation, since the primary

crystals formed at the highest T_c values were less likely to be affected by any shift in primary melting peak due to possible re-crystallization or reorganization phenomena upon heating. The value of T_m^0 from Figure I.4 was determined to be 237°C, which is similar to the value of 240°C reported by Knoop et al. [2], but slightly lower than the values of 247°C [4, 6] and 265°C [3] reported elsewhere.

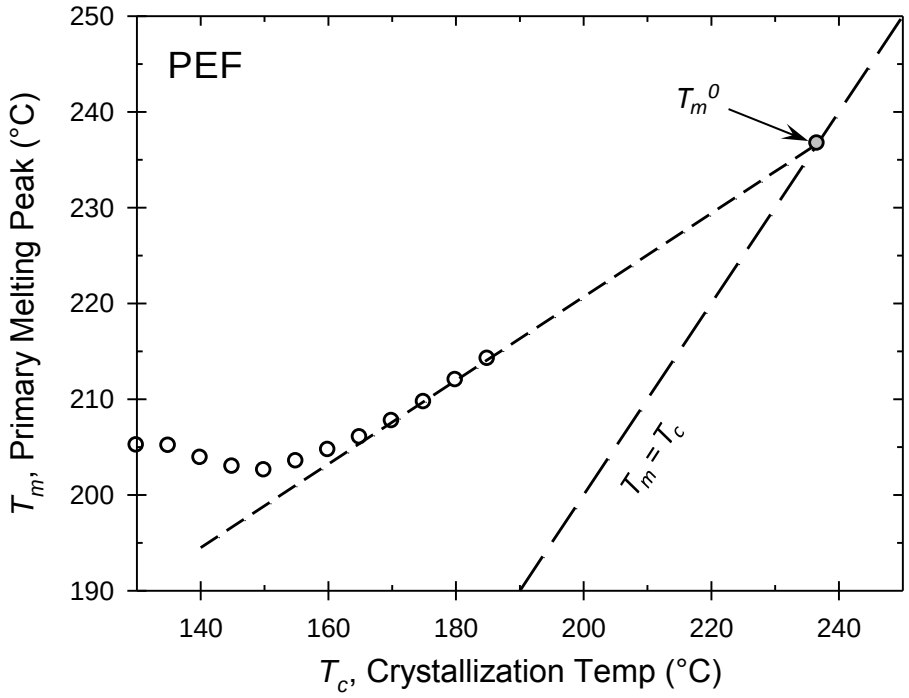

Figure I.4. Hoffman-Weeks plot used to determine the equilibrium melting point (T_m^0) for PEF.

I.4. Summary and Conclusions

DSC was used to investigate the isothermal crystallization properties of PEF. The crystallization temperature (T_c) corresponding to the maximum crystallization rate was determined qualitatively to be 160°C via the minimum in the plot of "time to peak maximum" versus T_c (cf. Figure I.2). The crystallization data in this Appendix were not

modeled using traditional kinetic models found in the literature [7-9]; however, the data herein do provide a qualitative understanding of crystallization in PEF, which is useful since "real-world" beverage containers exhibit some degree of crystallinity. Future work should investigate the differences in crystal shape, size, and rate of formation for PEF crystallized via quiescent (i.e., isothermal) vs. orientation-induced methods, since differences are known to exist for PET [10] and since blow-molded containers are prepared via the latter methodology.

I.5. References

1. Hoffman JD and Weeks JJ. Melting Process and the Equilibrium Melting Temperature of Polychlorotrifluoroethylene. Journal of Research of the National Bureau of Standards-A, Physics and Chemistry 1962;66A(1):13-28.

2. Knoop RJI, Vogelzang W, van Haveren J, and van Es DS. High molecular weight poly(ethylene-2,5-furanoate); critical aspects in synthesis and mechanical property determination. Journal of Polymer Science Part A: Polymer Chemistry 2013;51(19):4191-4199.

3. Papageorgiou GZ, Tsanaktsis V, and Bikiaris DN. Synthesis of poly(ethylene furandicarboxylate) polyester using monomers derived from renewable resources: thermal behavior comparison with PET and PEN. Physical Chemistry Chemical Physics 2014;16:7946-7958.

4. van Berkel JG, Guigo N, Kolstad JJ, Sipos L, Wang B, Dam MA, and Sbirrazzuoli N. Isothermal Crystallization Kinetics of Poly (Ethylene 2,5-Furandicarboxylate). Macromolecular Materials and Engineering 2015, DOI: 10.1002/mame.201400376.

5. Lu XF and Hay JN. Isothermal crystallization kinetics and melting behaviour of poly(ethylene terephthalate). Polymer 2001;42(23):9423-9431.

6. Codou A, Guigo N, van Berkel J, de Jong E, and Sbirrazzuoli N. Non-isothermal Crystallization Kinetics of Biobased Poly(ethylene 2,5-furandicarboxylate) Synthesized via the Direct Esterification Process. Macromolecular Chemistry and Physics 2014;215(21):2065-2074.

7. Avrami M. Kinetics of Phase Change. I. Journal of Chemical Physics 1939;7(12):1103-1112.

8. Ozawa T. Kinetics of non-isothermal crystallization. Polymer 1971;12(3):150-158.

9. Lauritzen JI and Hoffman JD. Extension of theory of growth of chain-folded polymer crystals to large undercoolings. Journal of Applied Physics 1973;44(10):4340-4352.

10. Radhakrishnan J and Kaito A. Structure formation during the isothermal crystallization of oriented amorphous poly(ethylene terephthalate) films. Polymer 2001;42(8):3859-3866.

APPENDIX J

PET/GRAPHENE NANOCOMPOSITES: THERMAL, MECHANICAL, AND WATER TRANSPORT PROPERTIES

J.1. Introduction

This Appendix investigates the effect of melt-mixing graphene with PET on the resultant thermal, mechanical, and water transport properties compared to neat PET. Graphene is a promising additive for barrier property enhancement due to its impermeability to penetrant transport, high aspect ratio, and high tensile strength [1]. PET is an ideal candidate polymer for this study, since it is currently the dominant polymer in the beverage packaging industry and since PET is not considered a "high barrier" polymer regarding oxygen, carbon dioxide, and water transport.

J.2. Materials and Characterization

The PET used in this Appendix is the same polymer described previously in Section 3.1.1, and the graphene was purchased from Angstron Materials, Inc. (Dayton, OH) as product #N002-PDR. The purchased graphene exhibited the following characteristics, as reported by the supplier: surface area ranging from 400 – 800 m^2/g, true density of 2.20 g/cm^3, approximate thickness of less than three graphene layers, and lateral dimensions of less than 10 μm. The pure graphene was extremely fluffy and black, and additional details regarding the physical properties can be found on the supplier's website.

The PET/graphene nanocomposites were melt-mixed using a method similar to that

described in Section 3.1.2 for preparing the PET/caffeine batches. The PET was initially cryogenically ground into a fine powder and physically mixed with the graphene prior to drying the mixture at 120°C for 24 hours under vacuum. The pre-mixing step was necessary due to the fluffy nature of the pure graphene, and such pre-mixing facilitated homogeneous melt-mixing once added into the Brabender. After melt-mixing according to the procedure described in Section 3.1.2, the batches were further processed into amorphous films using the method in Section 3.1.3. PET/graphene compositions of 0, 0.10, 0.53, and 1.0 wt% graphene were investigated in the current work.

Differential scanning calorimetry (DSC) measurements were recorded using the same procedure described in Chapter 4 (i.e., ramp 0 to 280°C at 10°C/min, followed by cooling from 280 to 0°C at 10°C/min), and represent the average of five measurements. Preliminary dynamic mechanical analysis (DMA) measurements pertaining to the beta relaxation were recorded at sub-ambient temperatures using the same procedure described in Chapter 4, and represent one measurement for each graphene composition. X-Ray diffraction measurements for the PET/1 wt% graphene film (not shown in this Appendix) exhibited no polymer crystallinity peaks or graphitic peaks, confirming the amorphous morphology of the samples and the exfoliated nature of the graphene as indicated by the vendor.

Equilibrium and kinetic water sorption measurements at unit activity were measured using thick films (~840 μm) according to the procedure described in Chapter 3 (cf. Section 3.4.3) and Chapter 8. Four measurements were recorded for all samples, with the exception of three measurements for the 1 wt% graphene sample. All transport measurements reported in this Appendix correlate with the amorphous morphology.

J.3. Results and Discussion

J.3.1. *Thermal Characterization*

Figure J.1 provides an example DSC thermogram for data measured upon heating and subsequent cooling for neat PET (solid line) compared to PET mixed with 1.0 wt% graphene (dashed line).

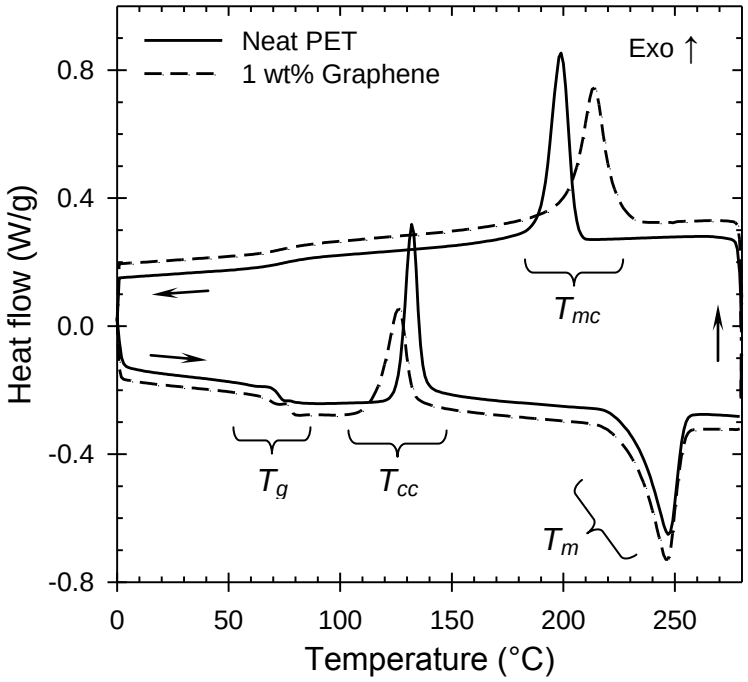

Figure J.1. DSC thermogram for PET (solid line) and PET mixed with 1.0 wt% graphene (dashed line) during heating and subsequent cooling. The heat-cool cycles illustrate the four major thermal events as indicated by the following subscripts: *g* = glass transition, *cc* = cold crystallization, *m* = melting, and *mc* = melt crystallization.

As seen in Figure J.1, the PET/graphene sample exhibits a reduced cold crystallization temperature (T_{cc}) and increased melt crystallization temperature (T_{mc}) compared to neat PET, which indicates that graphene is acting as a nucleating agent for PET crystal formation. This notion is further explored in Figures J.2 and J.3, which plot

T_{cc} and T_{mc} data, respectively, as a function of graphene content.

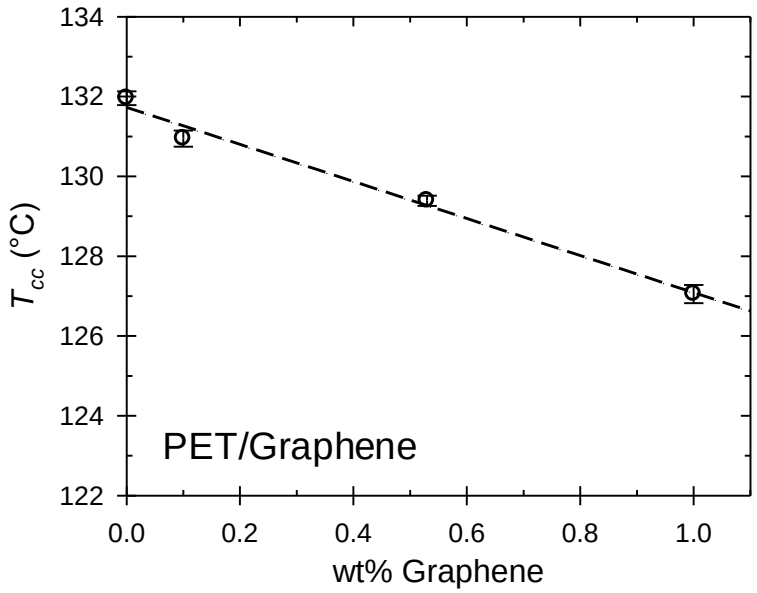

Figure J.2. PET cold crystallization temperature (T_{cc}) vs. graphene content measured via DSC during the first heat cycle. Uncertainty limits originate from five measurements.

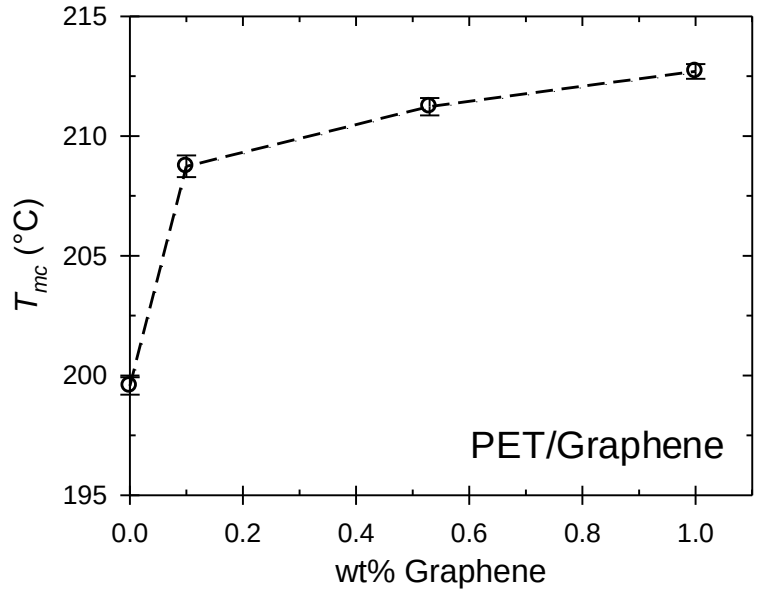

Figure J.3. PET melt crystallization temperature (T_m) vs. graphene content measured via DSC during the first cooling cycle from the melt. Uncertainty limits originate from five measurements.

While the nucleating effects of graphene in PET were not fully characterized via isothermal crystallization experiments, the decrease in T_{cc} and increase in T_{mc} for the graphene containing samples vs. neat PET are significant, especially when considering the low weight fractions of graphene investigated.

J.3.2. *Dynamic Mechanical Characterization*

Preliminary dynamic mechanical measurements corresponding to the sub-ambient beta relaxation are provided in Figure J.4 via the activation energy (E_A) of the beta relaxation as a function of graphene content. The preliminary data in Figure J.4 suggest that the beta peak E_A for PET is not affected by the addition of graphene at low concentrations, thereby implying that graphene is effectively *unable* to hinder the PET phenyl ring-flipping motions. This behavior is opposite to that observed in Chapter 4 for the case of caffeine antiplasticization of PET (cf. Figure 4.10); however, the current results are not surprising, since the transport reductions resulting from graphene occur via the platelet creating a more tortuous diffusion pathway for the penetrant as opposed to antiplasticizing the polymer chains. Preliminary dynamic mechanical data corresponding to the storage modulus revealed little difference between all samples; however, more measurements should be performed to verify this notion. Transport data regarding the water sorption and diffusion properties of the PET/graphene samples are provided in the next section.

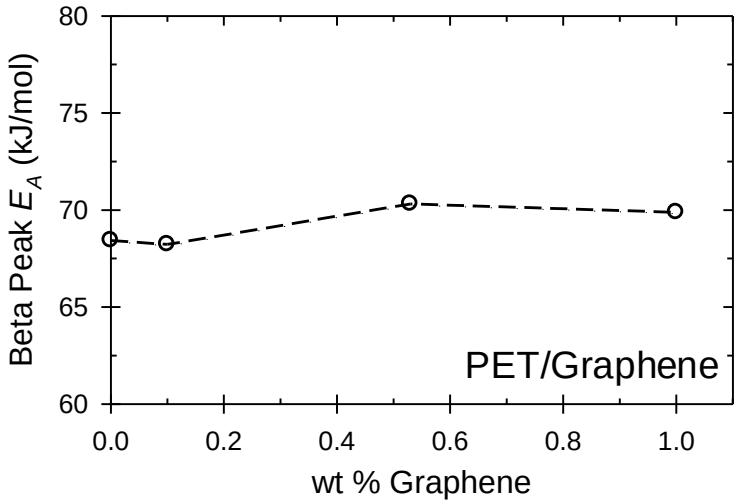

Figure J.4. Beta peak E_A values for various PET/graphene samples vs. graphene content. The dashed line is drawn to aid the eye.

J.3.3. *Water Sorption and Diffusion at Unit Activity*

The water sorption measurements at unit activity in this Appendix were measured in conjunction with the data for neat PET reported previously in Chapters 8 and 9. Solubility (S), diffusivity (D), and permeability ($P = DS$) values for water at unit activity in the PET/graphene samples are provided in Table J.1.

Table J.1. Transport properties for water in amorphous PET/graphene films. Diffusion estimates were determined between zero to unit activity.

wt% Graphene	**Volume fraction graphene[a] (ϕ_g)**	***S* (a = 1) (ccSTP/ccPoly·atm)**	***D*×10^9 (cm^2/s)**	***P* (Barrer)**	***P*/*P*$_0$**
0	0	357 ± 2	6.9 ± 0.2	326 ± 9	1
0.10	0.00061	358 ± 1	6.7 ± 0.1	317 ± 6	0.97 ± 0.03
0.53	0.0032	352 ± 1	5.6 ± 0.1	260 ± 4	0.80 ± 0.03
1.0	0.0061	346 ± 1	4.8 ± 0.1	218 ± 3	0.67 ± 0.02

a: Calculated using ρ = 2.20 g/cc for graphene and ρ = 1.335 g/cc for amorphous PET.

As seen in Table J.1, the water uptake at unit activity is relatively unaffected by the presence of graphene in the PET/graphene samples compared to neat PET. This behavior is expected, since graphene is not envisioned to affect the polymer free volume. On the other hand, the diffusion coefficient decreases with increasing graphene content as a result of the more tortuous diffusion path around the impermeable graphene platelets. The resulting permeability estimates from $P = DS$ can be tentatively described as a function of graphene content using the Nielsen model in Equation J.1, where P is the penetrant permeability in the nanocomposite, P_0 is the penetrant permeability in the neat polymer, ϕ_g is the volume fraction of graphene in the nanocomposite, and α is the platelet aspect ratio [2, 3].

$$\frac{P}{P_0} = \left(\frac{1-\phi_g}{1+\alpha\left(\phi_g/2\right)} \right) \tag{J.1}$$

A plot of the experimental P/P_0 data from Table J.1 for water transport in the PET/graphene nanocomposites is provided in Figure J.5, along with the optimized model fit from Equation J.1 with $\alpha = 160$. As seen in Figure J.5, the Nielsen model describes the experimental data quite well; however, the optimized value of $\alpha = 160$ is *significantly* lower than the aspect ratio estimated from the graphene vendor's specifications (i.e., ~10,000). Such disparities can potentially originate from a variety of factors. Specifically, the Nielsen model assumes that the impermeable platelets are perpendicular to the concentration gradient across the film, and such assumption is potentially not valid for the films in the current application (i.e., the films are essentially un-oriented). It is also a

possibility that the Brabender melt-mixing step could have induced agglomeration of the graphene sheets, thereby decreasing the overall efficacy to transport resistance. Lastly, surprisingly high water fluxes through graphene-based membranes have been linked to capillary formation between graphene sheets [4], and could potentially explain the behavior observed in the current work.

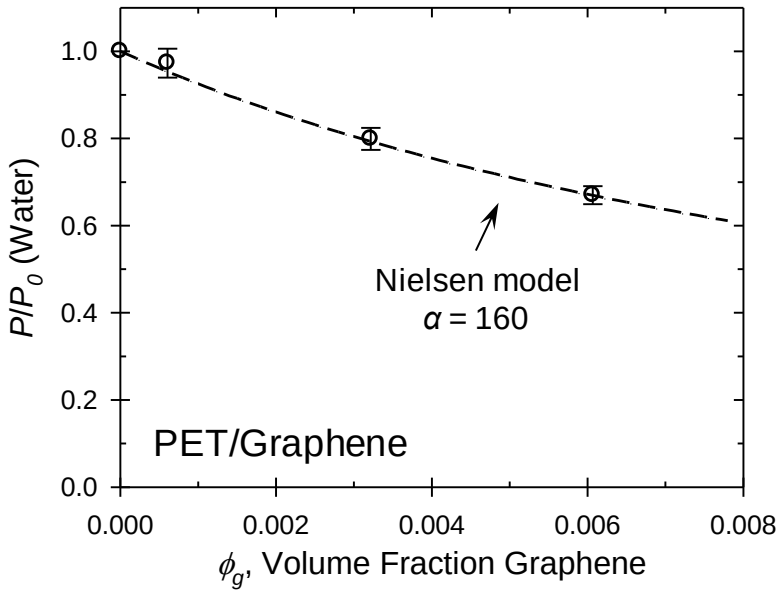

Figure J.5. Experimental P/P_0 data for water transport in PET/graphene from Table J.1. The dashed line represents the Nielsen model fit from Equation J.1 with α = 160.

J.4. Summary and Conclusions

Multiple characterization techniques were used in this Appendix to characterize the effect of graphene on the resultant thermal, mechanical, and water transport properties for various PET/graphene nanocomposites compared to neat PET. Specifically, DSC testing revealed that graphene acts as a nucleating agent for PET as indicated by a reduction in T_{cc} and increase in T_{mc} for the graphene containing samples compared to neat PET. While

not performed in the current study, future work should involve isothermal crystallization experiments to more fully understand the nucleating effects of graphene. Preliminary dynamic mechanical measurements recorded at sub-ambient conditions revealed that graphene is effectively unable to hinder the phenyl ring-flipping motions compared to neat PET, which is expected since graphene is not antiplasticizing the polymer matrix. Mechanical experiments for future study should involve Instron testing, which can accurately assess the effect of graphene on the resultant tensile properties for the nanocomposites compared to neat PET.

Equilibrium water sorption measurements at unit activity revealed little difference in water sorption for the graphene nanocomposites compared to neat PET. Kinetic water sorption measurements, however, revealed a detectable decrease in diffusivity for all graphene containing samples compared to pure PET. Such reduction in diffusivity occurs from the increased penetrant diffusion path length for a penetrant traveling through the nanocomposite compared to the pure polymer. Preliminary water permeability values were estimated via the relationship $P = DS$, and the permeability reduction vs. graphene content was modeled using the Nielson model with the aspect ratio as an adjustable parameter. The optimized aspect ratio obtained via the Nielson model was ~160, which is significantly lower than the estimate based on the platelet specifications as reported via the vendor (~10,000). Future transport experiments regarding PET/graphene nanocomposites should include actual water permeation experiments to verify the permeability estimates reported in the current work.

J.5. References

1. Kim H, Miura Y, and Macosko CW. Graphene/Polyurethane Nanocomposites for Improved Gas Barrier and Electrical Conductivity. Chemistry of Materials 2010;22(11):3441-3450.

2. Nielsen LE. Models for the Permeability of Filled Polymer Systems. Journal of Macromolecular Science: Part A - Chemistry 1967;1(5):929-942.

3. Gupta M, Lin Y, Deans T, Crosby A, Baer E, Hiltner A, and Schiraldi DA. Biaxially oriented poly(propylene-g-maleic anhydride)/phosphate glass composite films for high gas barrier applications. Polymer 2009;50(2):598-604.

4. Nair RR, Wu HA, Jayaram PN, Grigorieva IV, and Geim AK. Unimpeded Permeation of Water Through Helium-Leak–Tight Graphene-Based Membranes. Science 2012;335(6067):442-444.

APPENDIX K

COMPRESSIBLITY FACTORS FOR OXYGEN AND CARBON DIOXIDE

K.1. Compressibility Factors

The compressibility factor (*z*), defined in Equation K.1, can be used to correct the ideal gas law to account for non-ideal gas behavior. In Equation K.1, *p* represents the gas pressure, *V* represents the gas volume, *n* represents the molar quantity of the gas, *R* is the universal gas constant, and *T* is the absolute temperature of the gas.

$$z = \left(\frac{pV}{nRT} \right) \tag{K.1}$$

As noted in Chapter 3 (cf. Section 3.3.1), compressibility factors were calculated using the NIST extended corresponding states equation via the NIST SUPERTRAPP program. The pressure dependence of *z* can be represented by a simple cubic polynomial, where the corresponding equations for oxygen and carbon dioxide used throughout this thesis are provided in Table K.1.

Table K.1. Compressibility factor (z) equations for oxygen and carbon dioxide, with pressure (p) in units of psia.

Gas	Temp (°C)	Compressibility Factor Equation
O_2	35	$z = 1 + \left(-3.581 \times 10^{-5}\right) p + \left(5.654 \times 10^{-9}\right) p^2 + \left(1.602 \times 10^{-12}\right) p^3$
	45	$z = 1 + \left(-2.889 \times 10^{-5}\right) p + \left(5.298 \times 10^{-9}\right) p^2 + \left(1.761 \times 10^{-12}\right) p^3$
	55	$z = 1 + \left(-2.277 \times 10^{-5}\right) p + \left(5.217 \times 10^{-9}\right) p^2 + \left(8.092 \times 10^{-13}\right) p^3$
	65	$z = 1 + \left(-1.735 \times 10^{-5}\right) p + \left(5.167 \times 10^{-9}\right) p^2 + \left(-1.354 \times 10^{-13}\right) p^3$
CO_2	35	$z = 1 + \left(-2.997 \times 10^{-4}\right) p + \left(-6.702 \times 10^{-8}\right) p^2 + \left(-3.020 \times 10^{-11}\right) p^3$
	45	$z = 1 + \left(-2.696 \times 10^{-4}\right) p + \left(-5.207 \times 10^{-8}\right) p^2 + \left(-1.682 \times 10^{-11}\right) p^3$
	55	$z = 1 + \left(-2.432 \times 10^{-4}\right) p + \left(-4.022 \times 10^{-8}\right) p^2 + \left(-9.118 \times 10^{-12}\right) p^3$
	65	$z = 1 + \left(-2.199 \times 10^{-4}\right) p + \left(-3.109 \times 10^{-8}\right) p^2 + \left(-3.751 \times 10^{-12}\right) p^3$